Lead-free Solders: Materials Reliability for Electronics

Wiley Series in Materials for Electronic and Optoelectronic Applications

www.wiley.com/go/meoa

Series Editors

Professor Arthur Willoughby, University of Southampton, Southampton, UK
Dr. Peter Capper, SELEX Galileo Infrared Ltd., Southampton, UK
Professor Safa Kasap, University of Saskatchewan, Canada

Published Titles

Bulk Crystal Growth of Electronic, Optical and Optoelectronic Materials, Edited by P. Capper
Properties of Group-IV, III–V and II–VI Semiconductors, S. Adachi
Charge Transport in Disordered Solids with Applications in Electronics, Edited by S. Baranovski
Optical Properties of Condensed Matter and Applications, Edited by J. Singh
Thin Film Solar Cells: Fabrication, Characterization and Applications, Edited by J. Poortmans and V. Arkhipov
Dielectric Films for Advanced Microelectronics, Edited by M. R. Baklanov, M. Green and K. Maex
Liquid Phase Epitaxy of Electronic, Optical and Optoelectronic Materials, Edited by P. Capper and M. Mauk
Molecular Electronics: From Principles to Practice, M. Petty
Luminescent Materials and Applications, Edited by A. Kitai
CVD Diamond for Electronic Devices and Sensors, Edited by Ricardo S. Sussmann
Properties of Semiconductor Alloys: Group-IV, III-V and II-VI Semiconductors, S. Adachi
Mercury Cadmium Telluride: Growth, Properties and Applications, Edited by P. Capper and J. Garland
Zinc Oxide Materials for Electronic and Optoelectronic Device Applications, Edited by Cole W. Litton, Donald C. Reynolds and Thomas C. Collins

Forthcoming Titles

Silicon Photonics: Fundamentals and Devices, M. J. Deen and P. K. Basu

Lead-free Solders: Materials Reliability for Electronics

Edited by

K. N. SUBRAMANIAN

Department of Chemical Engineering and Materials Science, Michigan State University, Michigan, USA

A John Wiley & Sons, Ltd., Publication

This edition first published 2012

Registered office
John Wiley & Sons Ltd, The Atrium, Southern Gate, Chichester, West Sussex, PO19 8SQ, United Kingdom

Library of Congress Cataloging-in-Publication Data

Subramanian, K. N., Ph. D.
Lead-free solders : materials reliability for electronics / edited by K.N. Subramanian.
p. cm.
Includes bibliographical references and index.
ISBN 978-0-470-97182-6 (cloth)
1. Lead-free electronics manufacturing processes. 2. Solder and soldering. I. Title.
TK7836.S825 2012
621.381–dc23 2011038790

A catalogue record for this book is available from the British Library.

Print ISBN: 9780470971826
Set in 10/12pt Times by Thomson Digital, Noida, India

Printed in [Country] by [Printer]

Contents

Series Preface xv
Preface xvii
List of Contributors xix

Thematic Area I: Introduction 1

1 Reliability of Lead-Free Electronic Solder Interconnects: Roles of Material and Service Parameters 3
K. N. Subramanian

1.1 Material Design for Reliable Lead-Free Electronic Solders Joints 3
1.2 Imposed Fields and the Solder Joint Responses that Affect Their Reliability 5
1.3 Mechanical Integrity 5
1.4 Thermomechanical Fatigue (TMF) 6
1.5 Whisker Growth 7
1.6 Electromigration (EM) 7
1.7 Thermomigration (TM) 8
1.8 Other Potential Issues 8

Thematic Area II: Phase Diagrams and Alloying Concepts 11

2 Phase Diagrams and Their Applications in Pb-Free Soldering 13
Sinn-wen Chen, Wojciech Gierlotka, Hsin-jay Wu, and Shih-kang Lin

2.1 Introduction 14
2.2 Phase Diagrams of Pb-Free Solder Systems 14
2.3 Example of Applications 23
2.3.1 General Applications (Melting, Solidification, Interfacial Reactions) 23
2.3.2 Effective Undercooling Reduction (Co Addition) 28
2.3.3 Unexpected Compound Formation (Sn-Ag/Cu Interfacial Reactions) 32
2.3.4 Unexpected Growth Rates (Sn-Bi/Fe and Sn-Pb/Fe) 32
2.3.5 Unexpected Melting of Solder (Sn-Sb/Ag) 34
2.3.6 Up-Hill Diffusion (Sn-Cu/Ni) 36
2.3.7 Limited Sn Supply (Au/Sn/Cu) 39

2.4 Conclusions 39
Acknowledgments 40
References 41

3 Phase Diagrams and Alloy Development 45
Alan Dinsdale, Andy Watson, Ales Kroupa, Jan Vrestal, Adela Zemanova, and Pavel Broz

3.1 Introduction 45
3.2 Computational Thermodynamics as a Research Tool 48
3.2.1 Concept of the Calculation of Phase Diagrams for Multicomponent Systems 48
3.2.2 Modelling of the Gibbs Energy of the System 50
3.2.3 Critical Assessment of Thermodynamic Properties 51
3.3 Thermodynamic Databases – the Underlying Basis of the Modelling of Phase Diagrams and Thermodynamic Properties, Databases for Lead-Free Solders 51
3.3.1 Creation of the Thermodynamic Databases 52
3.3.2 Three Conditions of Consistency 52
3.3.3 Specialized Databases for the Modelling of Thermodynamic Properties of Systems Relevant for Lead-Free Solders 54
3.4 Application of the SOLDERS Database to Alloy Development 57
3.4.1 Modelling of Phase Diagrams and Thermodynamic Properties 58
3.4.2 Modelling of Other Properties 65
3.5 Conclusions 68
References 68

4 Interaction of Sn-based Solders with Ni(P) Substrates: Phase Equilibria and Thermochemistry 71
Clemens Schmetterer, Rajesh Ganesan, and Herbert Ipser

4.1 Introduction 72
4.2 Binary Phase Equilibria 73
4.2.1 Literature Overview 73
4.2.2 New Experimental Results 77
4.3 Ternary Phase Equilibria Ni-P-Sn 85
4.3.1 Literature Overview 85
4.3.2 Experimental Results 86
4.4 Thermochemical Data 94
4.4.1 Literature Overview 95
4.4.2 New Experimental Results 99
4.5 Relevance of the Results and Conclusion 111
Acknowledgments 113
References 113

Thematic Area III: Microalloying to Improve Reliability 119

5 'Effects of Minor Alloying Additions on the Properties and Reliability of Pb-Free Solders and Joints' 121
Sung K. Kang

5.1 Introduction 122
5.2 Controlling Ag_3Sn Plate Formation 125
5.3 Controlling the Undercooling of Sn Solidification 132
5.4 Controlling Interfacial Reactions 136
5.4.1 Dissolution of UBM and Surface Finishes 137
5.4.2 Cu-Sn Intermetallic Formation 138
5.4.3 Interfacial Void Formation 143
5.4.4 Spalling of Ni-Sn Intermetallics 144
5.5 Modifying the Microstructure of SAC 145
5.6 Improving Mechanical Properties 149
5.6.1 Strength and Hardness 149
5.6.2 Drop Impact Resistance 150
5.6.3 Thermal Fatigue Resistance 150
5.7 Enhancing Electromigration Resistance 151
5.8 Summary 153
References 154

6 Development and Characterization of Nano-composite Solder 161
Johan Liu, Si Chen, and Lilei Ye

6.1 Introduction 162
6.2 Nano-composite Solder Fabrication Process 162
6.2.1 Nano-particle Fabrication 162
6.2.2 Nano-composite Solder Fabrication 163
6.3 Microstructure 166
6.3.1 Grain Size 166
6.3.2 IMC Layer 167
6.4 Physical Properties 167
6.4.1 Viscosity 167
6.4.2 Melting Point 168
6.4.3 Wettability 168
6.4.4 CTE 168
6.4.5 Density and Young's Modulus 169
6.5 Mechanical Properties 169
6.5.1 Microhardness 169
6.5.2 Creep Resistance 170
6.5.3 Mechanical Strength 170
6.5.4 Ductility 170
6.6 Challenges and Solutions 171
6.7 Summary 174

Acknowledgments 175
References 176

Thematic Area IV: Chemical Issues Affecting Reliability 179

7 Chemical Changes for Lead-Free Soldering and Their Effect on Reliability 181
Laura J. Turbini

7.1 Introduction 181
7.2 Soldering Fluxes and Pastes 181
7.3 Cleaning 185
7.4 Laminates 185
7.5 Halogen-Free Laminates 186
7.5.1 Z-axis CTE 187
7.5.2 Interconnect Stress Test (IST) 187
7.5.3 Time to Delamination 187
7.5.4 Temperature to Decomposition 188
7.6 Conductive Anodic Filament (CAF) Formation 189
7.7 Summary 193
References 193

Thematic Area V: Mechanical Issues Affecting Reliability 195

8 Influence of Microstructure on Creep and High Strain Rate Fracture of Sn-Ag-Based Solder Joints 197
P. Kumar, Z. Huang, I. Dutta, G. Subbarayan, and R. Mahajan

8.1 Introduction 198
8.2 Coarsening Kinetics: Quantitative Analysis of Microstructural Evolution 199
8.2.1 Experimental Procedure 199
8.2.2 Results and Discussion 200
8.3 Creep Behavior of Sn-Ag-Based Solders and the Effect of Aging 206
8.3.1 Experimental Procedure 206
8.3.2 Results and Discussion 207
8.4 Role of Microstructure on High Strain Rate Fracture 219
8.4.1 Experimental and Analytical Procedure 220
8.4.2 Results and Discussion 222
8.5 Summary and Conclusions 227
Acknowledgments 227
References 228

9 Microstructure and Thermomechanical Behavior Pb-Free Solders 233
D.R. Frear

9.1 Introduction 233
9.2 Sn-Pb Solder 234

9.3 Pb-Free Solders 237
9.3.1 Pb-Free Solders Microstructure 238
9.3.2 Interfacial Intermetallic Formation of Pb-Free Solders 240
9.3.3 Mechanical Metallurgy of Pb-Free Solder Alloys 243
9.3.4 Thermomechanical Fatigue Behavior of Pb-Free Solder Alloys 245
9.4 Summary 248
References 249

10 Electromechanical Coupling in Sn-Rich Solder Interconnects 251
Q.S. Zhu, H.Y. Liu, L. Zhang, Q.L. Zeng, Z.G. Wang, and J.K. Shang

10.1 Introduction 252
10.2 Experimental 253
10.3 Results 255
10.3.1 Surface Morphology of Sn-3.5Ag-0.7Cu Interconnects after Electromigration 255
10.3.2 Surface Morphology of Pure Sn Interconnect after Electromigration 256
10.3.3 Surface Morphology of Single-Crystal Sn Interconnect after Electromigration 257
10.3.4 Tensile Strength of Solder Interconnects after Electromigration 258
10.3.5 Stress-Relaxation Behavior of Solder Interconnects after Electromigration 260
10.4 Discussion 264
10.4.1 Stress Induced by Vacancy Concentration at the Grain Boundary 264
10.4.2 Compression Stress Induced by the Cu_6Sn_5 Formation on the Surface 265
10.4.3 Vacancy-Concentration Distribution after Current Stressing 266
10.4.4 Effect of High Vacancy Concentration on Strength 267
10.4.5 Effect of High Vacancy Concentration on Stress-Relaxation Rate 268
10.5 Conclusions 269
Acknowledgments 270
References 270

11 Effect of Temperature-Dependent Deformation Characteristics on Thermomechanical Fatigue Reliability of Eutectic Sn-Ag Solder Joints 273
Andre Lee, Deep Choudhuri, and K.N. Subramanian

11.1 Introduction 274
11.2 Experimental Details 275
11.2.1 Test-Specimen Preparation 275
11.2.2 Thermal Cycling 275
11.2.3 Microstructural Characterization 276
11.2.4 Mechanical Testing 276

11.3 Results and Discussion 276
11.3.1 Effects of Temperature 277
11.3.2 Effects of Strain Rate 283
11.3.3 Influence of Temperature Regime of TMF on the Residual Mechanical Properties 286
11.3.4 Effect of Temperature Regime of TMF on Surface-Damage Accumulation 289
11.3.5 Evolution of Microstructural Damages during Low-Temperature Regime TMF 291
11.4 Summary and Conclusions 294
References 295

Thematic Area VI: Whisker Growth Issues Affecting Reliability 297

12 Sn Whiskers: Causes, Mechanisms and Mitigation Strategies 299
Nitin Jadhav and Eric Chason

12.1 Introduction 299
12.2 Features of Whisker Formation 303
12.3 Understanding the Relationship between IMC Growth, Stress and Whisker Formation 308
12.4 Summary Picture of Whisker Formation 314
12.5 Strategies to Mitigate Whisker Formation 316
12.6 Conclusion 318
Acknowledgments 318
References 318

13 Tin Whiskers 323
Katsuaki Suganuma

13.1 Low Melting Point Metals and Whisker Formation 323
13.2 Room-Temperature Tin Whiskers on Copper Substrate 325
13.3 Thermal-Cycling Whiskers on 42 Alloy/Ceramics 326
13.4 Oxidation/Corrosion Whiskers 329
13.5 Mechanical-Compression Whiskers in Connectors 330
13.6 Electromigration Whiskers 331
13.7 Whisker Mitigation 332
13.8 Future Work 334
References 334

Thematic Area VII: Electromigration Issues Affecting Reliability 337

14 Electromigration Reliability of Pb-Free Solder Joints 339
Seung-Hyun Chae, Yiwei Wang, and Paul S. Ho

14.1 Introduction 339
14.2 Failure Mechanisms of Solder Joints by Forced Atomic Migration 342

14.2.1 EM 342
14.2.2 TM 347
14.3 IMC Growth 351
14.3.1 Under Thermal Aging 351
14.3.2 Under Current Stressing 358
14.4 Effect of Sn Grain Structure on EM Reliability 363
14.5 Summary 366
Acknowledgments 369
References 369

15 Electromigration in Pb-Free Solder Joints in Electronic Packaging 375
Chih Chen, Shih-Wei Liang, Yuan-Wei Chang, Hsiang-Yao Hsiao, Jung Kyu Han, and K.N. Tu

15.1 Introduction 376
15.2 Unique Features for EM in Flip-Chip Pb-Free Solder Joints 376
15.2.1 Serious Current-Crowding Effect 377
15.2.2 Joule Heating and Nonuniform Temperature Distribution During EM 378
15.2.3 Effect of Current Crowding and Joule Heating on EM Failure 382
15.2.4 Thermomigration in Solder Joints 385
15.3 Changes of Physical Properties of Solder Bumps During EM 386
15.3.1 Electrical Resistance 386
15.3.2 Temperature Redistribution 390
15.3.3 Mechanical Properties: Electromigration-Induced Brittleness in Solder Joints 391
15.4 Challenges for Understanding EM in Pb-Free Solder Microbumps 393
15.4.1 Fast Dissolution of Cu and Ni under EM 393
15.4.2 Effect of Grain Orientation on Electromigration 393
15.4.3 Stress in Solder Bumps 393
15.5 Thermomigration of Cu and Ni in Pb-Free Solder Microbumps 394
15.6 Summary 394
Acknowledgments 395
References 395

16 Effects of Electromigration on Electronic Solder Joints 401
Sinn-wen Chen, Chih-ming Chen, Chao-hong Wang, and Chia-ming Hsu

16.1 Introduction 401
16.2 Effects of Electromigration on Solders 402
16.2.1 Solder Joints with Primarily Only One Moving Species 403
16.2.2 Solder Joints with Significant Hillock and Void Formation 404
16.2.3 Solder Joints with Phase Segregation 405

16.3 Effects of Electromigration on Interfacial Reactions 408
16.3.1 Asymmetric IMC Layer Growth (Electron from Solder to Substrate: Enhancement, Electron from Substrate to Solder: Suppression) 408
16.3.2 Asymmetric IMC Layer Growth (Electron from Solder to Substrate: Suppression, Electron from Substrate to Solder: Enhancement): Peltier Effect 409
16.3.3 Symmetric IMC Layer Growth (Cathode and Anode: Enhancement or Suppression) 411
16.3.4 No Effect with Passage of Electric Current 411
16.3.5 Effects of Electromigration on Reaction Phases: Evolution of Reaction Phase and Alternating Layer Formation 411
16.3.6 Microstructural Changes Caused by Electromigration 412
16.4 Modeling Description of Effects of Electromigration on IMC Growth 414
16.4.1 The Atomic Flux Summation Model 414
16.4.2 The Atomic Flux Summation with Stress Modification Model 415
16.4.3 Generalized Modeling for Growth of IMC Layer 416
16.5 Conclusions 418
Acknowledgments 418
References 418

Thematic Area VIII: Thermomigration Issues Affecting Reliability 423

17 Thermomigration in SnPb and Pb-Free Flip-Chip Solder Joints 425
Tian Tian, K.N. Tu, Hsiao-Yun Chen, Hsiang-Yao Hsiao, and Chih Chen

17.1 Introduction 425
17.2 Thermomigration in SnPb Flip-Chip Solder Joints 427
17.2.1 Thermomigration in Unpowered Composite SnPb Solder Joints 427
17.2.2 *In-Situ* Observation of Thermomigration in Composite SnPb Solder Joints 429
17.2.3 Thermomigration in Unpowered Eutectic SnPb Solder Joints 431
17.3 Thermomigration in Pb-Free Flip-Chip Solder Joints 432
17.3.1 Thermomigration of Cu and Ni in Pb-Free Flip-Chip Solder Joints 435
17.4 Driving Force of Thermomigration 435
17.4.1 Irreversible Processes of Thermomigration 438
17.5 Coupling between Thermomigration and Creep 439
17.6 Coupling between Thermomigration and Electromigration: Thermoelectric Effect on Electromigration 441
17.7 Summary 441
Acknowledgments 442
References 442

Thematic Area IX: Miniaturization Issues Affecting Reliability **443**

18 Influence of Miniaturization on Mechanical Reliability of Lead-Free Solder Interconnects **445**
Golta Khatibi, Herbert Ipser, Martin Lederer, and Brigitte Weiss

18.1 Introduction 445
18.2 Effect of Miniaturization on Static Properties of Solder Joints (Tensile and Shear) 448
18.2.1 Constraint and Geometry Effects in Model Joints 448
18.2.2 Constraining Effects in Actual Joints 466
18.2.3 Fracture Mechanics Considerations of Solder Joints 473
18.3 Creep and Relaxation of Solder Joints 475
18.4 Summary and Conclusions 478
Acknowledgments 482
References 482

Index **487**

Series Preface

Wiley Series in Materials for Electronic and Optoelectronic Applications

This book series is devoted to the rapidly developing class of materials used for electronic and optoelectronic applications. It is designed to provide much-needed information on the fundamental scientific principles of these materials, together with how these are employed in technological applications. The books are aimed at (postgraduate) students, researchers and technologists, engaged in research, development and the study of materials in electronics and photonics, and industrial scientists developing new materials, devices and circuits for the electronic, optoelectronic and communications industries.

The development of new electronic and optoelectronic materials depends not only on materials engineering at a practical level, but also on a clear understanding of the properties of materials, and the fundamental science behind these properties. It is the properties of a material that eventually determine its usefulness in an application. The series therefore also includes such titles as electrical conduction in solids, optical properties, thermal properties, and so on, all with applications and examples of materials in electronics and optoelectronics. The characterization of materials is also covered within the series in as much as it is impossible to develop new materials without the proper characterization of their structure and properties. Structure–property relationships have always been fundamentally and intrinsically important to materials science and engineering.

Materials science is well known for being one of the most interdisciplinary sciences. It is the interdisciplinary aspect of materials science that has led to many exciting discoveries, new materials and new applications. It is not unusual to find scientists with a chemical engineering background working on materials projects with applications in electronics. In selecting titles for the series, we have tried to maintain the interdisciplinary aspect of the field, and hence its excitement to researchers in this field.

Arthur Willoughby
Peter Capper
Safa Kasap

Preface

Over the last two decades, significant progress has been made to facilitate the replacement of leaded solders in microelectronics. Global pressures to adopt lead-free electronics, brought about by environmental concerns, have made such changes mandatory. This book is intended to update the current state of understanding, and major developments, in electronic lead-free solder interconnects to improve their reliability in service.

At present there are no drop-in lead-free substitutes for leaded solders used in microelectronic packaging. Lead-free solders used in microelectronic packages that use organic polymeric boards need to have low melting points around 200 °C, in addition to having good wettability, thermomechanical fatigue resistance, etc. Among the various possible alloy systems considered, solders with significant amounts of tin have emerged as leading candidates. Sn-Ag-Cu-based solder alloys, known as SAC alloys, are widely adopted in current microelectronic applications based on several suitable attributes like low enough melting point, good wettability, etc. Sn-based solders containing other alloying additions like, Cu, Bi, Zn are also in current use.

At temperatures relevant in microelectronics, Sn exists in body-centered tetragonal structure with a *c*/*a* ratio of about 0.5, and is highly anisotropic. In addition, it is not as compliant as lead to imposed service environments. The layered intermetallics that form at the solder/substrate interfaces, and distributed intermetallics that form within the solder coarsen during service, significantly affecting the mechanical reliability of lead-free solder interconnects. Numerous studies that have been undertaken provide significant insight into the issues and mechanisms. Such studies include alloy development, composite solders with intermetallic or inert reinforcements, etc. In spite of all these efforts, at present, no ideal perfect replacement for leaded solders exists.

Miniaturization of microelectronic components is a constantly advancing area. This raises important issues like electromigration of atoms/ions due to high current densities encountered, and thermomigration due to large temperature gradients. As a consequence, the material developments to address the issues of lead elimination in electronic packaging are facing constantly changing targets. Although whisker growth in tin has been known for over half a century there is no clear understanding of the process and there exists no reliable means to prevent such whisker growth. Miniaturization of microelectronic packages makes whisker growth a very important issue since whiskers can cause short circuits affecting the reliability of such packages.

Studies to face these emerging challenges have resulted in a significant number of important findings at a very rapid phase warranting an update of the current status every few years. This book is aimed at addressing such a goal. Researchers known internationally for their important contributions to the field of lead-free electronic solders were invited to contribute chapters in chosen thematic areas. Most of these invitees have been well

acquainted with the editor for over fifteen years, and the others were recommended by the ones known to the editor.

This effort provides the current understanding of issues and solutions relevant to improving the reliability of lead-free electronic solder interconnects.

K. N. Subramanian
East Lansing, Michigan
July 2011

List of Contributors

Pavel Broz, Institute of Chemistry, Masaryk University, Brno, Czech Republic

Seung-Hyun Chae, Microelectronics Research Center, The University of Texas at Austin, TX, USA

Yuan-wie Chang, Department of Materials Science and Engineering, National Chiao Tung University, Hsin-chu, Taiwan, P.R. China

Eric Chason, School of Engineering, Brown University, Providence, Rhode Island, USA

Chih Chen, Department of Materials Science and Engineering, National Chiao Tung University, Hsin-chu, Taiwan, P.R. China

Chih-ming Chen, Department of Chemical Engineering, National Chung Hsing University, Taichung, Taiwan

Hsiao-Yun Chen, Department of Materials Science and Engineering, National Chiao Tung University, Hsin-chu, Taiwan, P.R. China

Si Chen, SMIT Center & Dept of MicroTechnology and Nanoscience, University of Technology, Göteborg, Sweden and Key Laboratory of New Displays and System Integration, SMIT Center and School of Mechatronics and Mechanical Engineering, Shanghai University, Shanghai, P.R. China

Sinn-wen Chen, Department of Chemical Engineering, National Tsing Hua University, Hsin-Chu, Taiwan

Deep Choudhuri, Department of Chemical Engineering and Materials Science, University of Michigan, East Lansing, MI, USA

Alan Dinsdale, National Physical Laboratory, Teddington, UK

Indranath Dutta, The School of Mechanical and Materials Engineering, Washington State University, Pullman, WA, USA

Darrel R. Frear, Freescale Semiconductor, Tempe, AZ, USA

Rajesh Ganesan, Departments of Materials Chemistry and Inorganic Chemistry, University of Vienna, Vienna, Austria

Yulai Gao, School of Materials Science and Engineering, Shanghai University, Shanghai, P.R. China

Wojciech Gierlotka, Department of Chemical Engineering and Materials Science, Yuan Ze University, Chung-Li, Taiwan

Jung Kyu Han, Department of Materials Science and Engineering, University of California at Los Angeles, Los Angeles, CA, USA

Paul S. Ho, Microelectronics Research Center, The University of Texas at Austin, TX, USA

Hsiang-Yao Hsiao, Department of Materials Science and Engineering, National Chiao Tung University, Hsin-chu, Taiwan, P.R. China

Chia-ming Hsu, Department of Chemical Engineering, National Tsing Hua University, Hsin-Chu, Taiwan

Zhe Huang, The School of Mechanical and Materials Engineering, Washington State University, Pullman, WA, USA

Herbert Ipser, Departments of Materials Chemistry and Inorganic Chemistry, University of Vienna, Vienna, Austria

Nitin Jadhav, School of Engineering, Brown University, Providence, Rhode Island, USA

Sung K. Kang, IBM T.J. Watson Research Center, Yorktown Heights, NY, USA

Golta Khatibi, Physics of Nanostructured Materials, University of Vienna, Vienna, Austria

Ales Kroupa, Institute of Physics of Materials, AS CR, Brno, Czech Republic

Praveen Kumar, The School of Mechanical and Materials Engineering, Washington State University, Pullman, WA, USA

Martin Lederer, Physics of Nanostructured Materials, University of Vienna, Vienna, Austria

Andre Lee, Department of Chemical Engineering and Materials Science, University of Michigan, East Lansing, MI, USA

Shih-wei Liang, Department of Materials Science and Engineering, National Chiao Tung University, Hsin-chu, Taiwan, P.R. China

Shih-kang Lin, Department of Materials Science and Engineering, University of Wisconsin-Madison, Madison, WI, USA

H. Y. Liu, Shenyang National Laboratory for Materials Science, Institute of Metal Research, Chinese Academy of Sciences, Shenyang, China

Johan Liu, SMIT Center & Dept of MicroTechnology and Nanoscience, University of Technology, Göteborg, Sweden and Key Laboratory of New Displays and System Integration, SMIT Center and School of Mechatronics and Mechanical Engineering, Shanghai University, Shanghai, P.R. China

Ravu Mahajan, Assembly Technology Development, Intel Corporation, Chandler, AZ, USA

Clemens Schmetterer, Departments of Materials Chemistry and Inorganic Chemistry, University of Vienna, Vienna, Austria

J. K. Shang, Department of Materials Science and Engineering, University of Illinois, Urbana, IL, USA and Shenyang National Laboratory for Materials Science, Institute of Metal Research, Chinese Academy of Sciences, Shenyang, China

Ganesh Subbarayan, School of Mechanical Engineering, Purdue University, West Lafayette, IN, USA

K. N. Subramanian, Department of Chemical Engineering and Materials Science, University of Michigan, East Lansing, MI, USA

Katsuaki Suganuma, Institute of Scientific and Industrial Research, Osaka University, Suita, Osaka, Japan

Tian Tian, Department of Materials Science and Engineering, University of California at Los Angeles, Los Angeles, CA, USA

K. N. Tu, Department of Materials Science and Engineering, University of California at Los Angeles, Los Angeles, CA, USA

Laura Turbini, Research in Motion Ltd, Cambridge, Ontario, Canada

Jan Vrestal, Institute of Chemistry, Masaryk University, Brno, Czech Republic

Chao-hong Wang, Department of Chemical Engineering, National Chung Cheng University, Chia-Yi, Taiwan

Yiwei Wang, Microelectronics Research Center, The University of Texas at Austin, TX, USA

Z. G. Wang, Shenyang National Laboratory for Materials Science, Institute of Metal Research, Chinese Academy of Sciences, Shenyang, China

Andy Watson, Institute for Materials Research, SPEME, University of Leeds, UK

Brigitte Weiss, Physics of Nanostructured Materials, University of Vienna, Vienna, Austria

Hsin-jay Wu, Department of Chemical Engineering, National Tsing Hua University, Hsin-Chu, Taiwan

Adela Zemanova, Institute of Physics of Materials, AS CR, Brno, Czech Republic

Q. L. Zeng, Shenyang National Laboratory for Materials Science, Institute of Metal Research, Chinese Academy of Sciences, Shenyang, China

Qijie Zhai, School of Materials Science and Engineering, Shanghai University, Shanghai, P.R. China

L. Zhang, Shenyang National Laboratory for Materials Science, Institute of Metal Research, Chinese Academy of Sciences, Shenyang, China

Q. S Zhu, Shenyang National Laboratory for Materials Science, Institute of Metal Research, Chinese Academy of Sciences, Shenyang, China

Thematic Area I

Introduction

1

Reliability of Lead-Free Electronic Solder Interconnects: Roles of Material and Service Parameters

K. N. Subramanian
Department of Chemical Engineering and Materials Science, Michigan State University, East Lansing, MI, 48824-1226, USA

Abstract

This chapter is meant to provide a general overview of the issues affecting the reliability of lead-free electronic solder joints subjected to service environments. It is meant to be an introduction to the various thematic areas that are covered in this book. Hence no attempt to provide references to any of the topics mentioned in this chapter is given at the end of this chapter. Extensive references for each of these topics are cited by the authorities contributing various chapters to this book.

1.1 Material Design for Reliable Lead-Free Electronic Solders Joints

It is important to point out that solder joint is a multicomponent system. Solders used in electronic interconnects are in the joint geometry and its overall response to environmental and in-service parameters are influenced by the constraints present in that configuration. Such a joint has substrates, interface intermetallic compound layers that are necessary

Lead-free Solders: Materials Reliability for Electronics, First Edition. Edited by K. N. Subramanian.

to form the necessary bonding, solder matrix with its own individual phases and intermetallic compounds (IMCs). In addition to geometrical issues, processing method used for fabrication of joints and the resultant microstructural features, service parameters encountered, and the response of the solder material to external influences, play significant roles in determining the reliability of the electronic solder joints. The service environments encountered are becoming more severe and the continuous rapid advances in microminiaturization of the electronic packages impose ever-increasing demands on such solder joints. Since solder joints present in modern microelectronics operate at very high homologous temperatures significant microstructural changes such as coarsening of the features present in the joint occur affecting their reliability. Because of the changes in the joint geometry to accomplish the microminiaturization such joints are expected to provide structural integrity in addition to providing electrical pathways. They are also expected to be mechanically compliant to dissipate the stresses that develop during service but be dimensionally stable.

Most of the lead-free solder alloys that are in current use contain significant amounts of tin. Such alloys have the suitable melting temperatures and wetting characteristics for utilization in consumer electronics. Among these, Sn-Ag-Cu alloys have been widely adopted. In order to minimize the deleterious effects of thermally induced coarsening of the phases present within the solder matrix and at the solder/substrate interfaces, and to improve the mechanical properties, several detailed studies on phase stability along with resultant developments have taken place. They have provided strategies involving minor amounts of additional alloying additions, as well as reinforcements to produce composite solders. Some of these approaches also help to improve the reliability of the lead-free solder joints. Since solders have to bond with substrates, the substrate materials and its finish will interact with the solder during the reflow process and during service. Several studies aim at combating reliability issues arising from the coarsening of these reaction products, which are quite often brittle.

The improvements to address problems listed in the last few paragraphs are the main contributions from those studying phase diagrams to develop suitable lead-free solder alloys, alloy additions to improve their service reliability, and composite solders. Such judicial material design to improve the service reliability invariably can take place only with the clear understanding of the service environments in which the electronic packages will be placed and the material response and resultant behaviors that affect their reliability. Joint geometry is an added contributing factor that can aggravate the influence of the service environment. However, such joint design is outside the realm of the material development to meet the challenges. If material design can either alleviate the material processes that affect the joint reliability either completely (or most of it), joint geometry hopefully will have minimal influence on the joint reliability.

The following sections address the material processes that influence the service reliability of lead-free solder joints. Detailed discussions on the developments in these avenues are brought out by world-renowned researchers in these fields in the chapters presented in various thematic areas.

1.2 Imposed Fields and the Solder Joint Responses that Affect Their Reliability

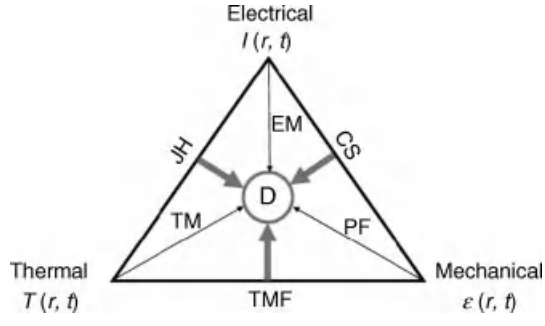

This schematic illustrates damage resulting from multiple fields and their complex interactions. Processes identified in this schematic are EM – electromigration, TM – thermal migration, PF – plastic flow and fracture, JH – Joule heating, CS – current stressing, TMF – thermomechanical fatigue. The scenario presented in this schematic illustrates the complex state of damage accumulation resulting from various fields encountered during service (direct effects: EM, TM, PF), and their mutual interactions (coupled effects: TMF, JH, CS), that affect the reliability of lead-free electronic solder joints.

Even during service these fields are time and position dependent. For example, temperature depends on the environment and Joule heating from the current density that can vary with hills and valleys that form due to electromigration. Similarly, the mechanical stress state will depend on the stresses that develop due to coefficient of thermal expansion (CTE) mismatches between the entities present in the joint, stresses that develop due to atom/ion migration caused by electron wind forces, and externally imposed loads. Among those listed the major damage contributors that affect the reliability of the lead-free electronic solders are (i) mechanical integrity, (ii) thermomechanical fatigue, (iii) whisker growth, (iv) electromigration, and (v) thermomigration. It should be pointed out that this is not an ordered list, and that there are significant mutual interactions between them. Such mutual interactions will become progressively more important with the continued efforts towards microminiaturization of electronic packages. Among the five processes listed above, whisker growth, electromigration, and thermomigration have become reliability concerns mainly due to such miniaturization.

1.3 Mechanical Integrity

An electronic package contains several solder joints and their reliability is what needs to be understood. However, reliability studies carried directly with such complex packages quite often cannot provide the means to evaluate the actual material-related issues that cause the failure, a critical piece of information warranted for material developments. On the other hand, if model system studies are carried out, the model geometries used should be representative of those actually encountered in the electronic packaging. Carrying out

studies on bulk solder specimens, without any of the constraints encountered in the joint configuration, will not be of any relevance to what happens in the joints.

Depending on the application the solder joints present in electronic packages may be experiencing different ranges of temperatures. In addition to the heating that results from passage of electric current, ambient conditions encountered during service can play significant roles. The deformation mode of Sn-based solders is highly sensitive to temperature and strain rate. Any reliability modeling should take this issue into account, along with issues of constraints and joint geometry.

Reliability under impact loading is a very important consideration not only for shipping considerations, but also for accidental dropping of a device. Industrial drop tests are carried out to check for the impact reliability during shipping. Charpy-type impact tests where the impact load is delivered to the individual solder ball attached to the substrate are also employed. In a realistic electronic package the impact delivered to some other location is realized by the solder. Hence, such tests cannot provide the necessary information about the detailed stress states, modes of fracture, and so on, that are critical for material design. In addition, there are several scenarios, like in automotive and aerospace applications, where random bumping can cause repeated impact loading.

1.4 Thermomechanical Fatigue (TMF)

Thermal excursions encountered in service cause significant damage to solder joints affecting their service reliability. Several material-related processes occur during heating, cooling, and dwell at temperature extremes. For example, the heating and cooling rates, temperature regime (high/low), temperature difference, dwell times at high- and low-temperature extremes, do significantly affect the integrity of the solder joints. These studies have shown that heating rate is an important contributor affecting the joint reliability. Damage accumulation in solder joints subjected to TMF results from a highly inhomogeneous stress distribution. Such stresses arise from CTE mismatches between various entities present in the joint. Anisotropy of tin could be a major contributing factor for such damage accumulation since the CTE difference between *a*- and *c*-directions of body-centered tetragonal β-Sn is almost twice that of the CTE difference between polycrystalline copper and polycrystalline Sn. Manifestation of the damage from TMF occurs only after several hundred TMF cycles, although the residual mechanical and electrical properties deteriorate significantly from the very early stages of TMF. Grain-boundary sliding and decohesion are the predominant damage modes that result from TMF. Although such events occur throughout the solder present in the joint, the predominant surface manifestation of the same is highly localized to the solder regions adjacent to solder/substrate IMC layer. Constraints imposed by the substrate appear to cause strain localization to such regions. During the later stages of TMF, when the residual properties tend to stabilize, the surface damage progresses by joining of the individual distributed cracks and cause the catastrophic failure.

Based on TMF evaluation with realistic temperature profiles, and findings from actual electronic packages placed in service, several new solder compositions with various minor alloying additions to Sn-Ag-Cu (SAC) alloy have been developed. A major hurdle encountered in this approach is the coarsening of the intermetallic compounds that form

during service affecting the joint reliability. Studies dealing with dwell-time issues indicate presence of small amounts of Ni in addition to Cu in the solder significantly improves the reliability of the solder joint under situations with longer dwell at the high-temperature extreme. Inert particle reinforcements have not been effective since they do not bond with the solder matrix. An alternate approach to improve service reliability of solder joints is to incorporate compatible nanostructured reinforcements with surface-active radicals to promote bonding with metal, following which they become inert. Such strongly bonded inert reinforcements that do not coarsen during service improve the reliability of lead-free solder joints subjected to TMF during service.

1.5 Whisker Growth

It has long been known that Sn exhibits whisker growth. However, such events did not receive any attention in electronic interconnects till recently. Microminiaturization of electronic components has resulted in close spacing of current carrying lines. Quite often the spacing is of the order of about 100 μm. If whiskers grow to a length of about 50 μm in adjacent lines shorting can occur resulting in electrical failure. Although several models have been proposed for whisker growth from solid substrate, none of them have been proved to be satisfactory. Compressive stresses are believed to make whiskers grow from their base. In Sn-based solder joints such compressive stresses that can arise from the formation of Cu-Sn IMC at Sn grain boundaries present in the solder are believed to cause such whisker growth. Such IMC formation can be facilitated by Cu diffusion from the substrate. For continuous growth of whiskers from the base such compressive stresses need to be present on a continuous basis, and such stresses should not be relaxed. Hence, stresses that are externally applied, or resulting from volume changes involved in formation of IMCs, and those that develop during electromigration, can facilitate whisker growth. There are conflicting views on whisker growth directions and locations from which whiskers grow. If the whisker growth is caused by Cu diffusion from the substrate followed by IMC growth, one should be able to arrive at a solution to this problem. However, no known reliable solution to this problem exists at present. Some of the difficulties in whisker growth investigations are encountered due to uncertainties about when and where will whiskers form and grow. As a consequence evaluation of the effectiveness of attempted mitigation strategies to prevent whisker growth becomes difficult.

1.6 Electromigration (EM)

EM in electronic solders has become an important concern in recent years. Ion migration in the presence of high current density has long been known in computer industry where incorporation of copper atoms at grain boundaries present in aluminum current-carrying lines has provided a solution to such a problem. In electronic interconnects the presence of high current density has not been a significant concern until miniaturization of electronic components and higher service temperatures has caused EM to become a potential reliability issue in electronic interconnects. Although events contributing to this mass

movement are due to material-related issues, it can be further aggravated by geometry in which the material is employed. The latter can impose current crowding and associated localized Joule heating, resulting in enhanced mass movement in localized regions. Based on the intended roles, several alloys used in electronics and energy-related applications are multiphase materials. In these alloys the electromigration-induced changes will depend strongly on the atomic species present, solid solubility, morphological features of the microstructural constituents, and phase stability.

Localized Joule heating and current crowding, have been of great concern. Grain growth and reorientation of grains, phase segregation, and interfacial events; contribute to damage accumulation by electromigration, in addition to hill and valley formation. Unlike the case of aluminum lines in computers, solders present in the electronic interconnects operate at very high homologous temperatures. As a consequence lattice diffusion, in addition to grain-boundary diffusion becomes an important consideration

1.7 Thermomigration (TM)

Microstructural coarsening in solder joints can occur due to the high temperatures encountered during service. Segregation and coarsening of the phases can occur due to electromigration. In addition to these effects, small temperature differences in adjacent regions can result from joint geometry and localized Joule heating during electromigration. Even though such temperature differences can be small, they can result in very significant temperature gradients in the miniaturized electronic solder joints. These large temperature gradients can give rise to additional microstructural evolution and damage. This reliability issue has gained attention in recent years.

1.8 Other Potential Issues

Sn exhibits polymorphism. At temperatures above 13 ^{o}C the stable form of Sn has body-centered tetragonal structure (β-Sn) and below this temperature the stable crystalline form is diamond cubic (α-Sn). Transformation form one form to the other is extremely sluggish and is very sensitive to the purity of the metal. Hence, Sn present in solder joints under environments encountered in service exists in body-centered tetragonal structure. However, if the solder joints are exposed to extremely low temperatures for significant lengths of time in future applications, β to α phase transformation can occur resulting in a significant volume increase of about 27%. Since α-phase is extremely brittle, such increase in volume causes extensive cracking and spalling. Such an event, known as 'tin pest' could potentially become a reliability concern for microelectronics, in applications such as aerospace, and extremely cold locations like in Polar regions.

Synergistic aspects of the various issues that affect the reliability of the solder joint need to be addressed in its entirety. Segmentation to address the individual issues can quite often provide a solution to a particular concern, while totally destroying the integrity of the entity by affecting the other issues. In the current scenario TMF is not the only issue that affects the reliability of a solder joint. EM and whisker growth have become important due to the

microminiaturization of the electronic components. Among these TMF is concerned with flow and adaptation of material to stresses that develop from thermal excursion encountered. However, the other two involve atom/ion migration. EM is concerned with formation of valleys and hillocks. Such events can attribute to significant additional Joule heating that once again should affect the conditions encountered during TMF. Such *self-perpetuating coupled events* cannot be considered as simple additive effects to TMF.

The following block diagram illustrates some such synergistic issues that need to be considered to evaluate the total damage affecting the reliability of lead-free electronic solder joints.

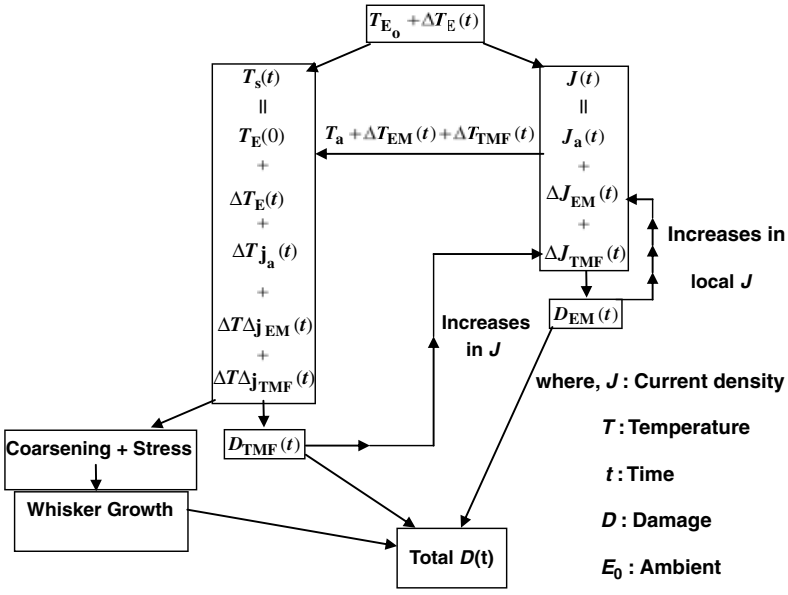

Another major concern is long-term reliability of microelectronic interconnects. Consumer electronics have relatively short life, and reliability evaluation can be carried out with realistic service parameters. In applications like in space or military, lifetime of an electronic component, the expected lifetime could be several decades. Suitable accelerated test methodologies are still to be developed to guarantee reliability for such applications.

Thematic Area II

Phase Diagrams and Alloying Concepts

2

Phase Diagrams and Their Applications in Pb-Free Soldering

Sinn-wen Chen[1], *Wojciech Gierlotka*[2], *Hsin-jay Wu*[1], *and Shih-kang Lin*[3]
[1] *Department of Chemical Engineering, National Tsing Hua University, #101, Sec. 2, Kuang-Fu Rd., Hsin-Chu 300, Taiwan*
[2] *Department of Chemical Engineering & Materials Science, Yuan Ze University, #135, Yuan-Tung Rd., Chung-Li 32003, Taiwan*
[3] *Department of Materials Science and Engineering, National Cheng Kung University, #1, University Rd., Tainan City 701, Taiwan*

Abstract

Pb-free soldering is one of the most important technologies in the electronics industry. A phase diagram is a comprehensive representation of thermodynamic properties of a multicomponent material system. Basic knowledge and information of phase diagrams of Pb-free solder systems are reviewed. In this chapter, several examples of applications of phase diagrams in Pb-free soldering are presented, including general applications of melting, solidification and intermetallic compounds (IMC) formation caused by interfacial reactions. With the aid of phase diagrams, interpretations of some abnormal phenomena in Pb-free soldering such as effective undercooling reduction by Co doping, unexpected IMC growth rate in Sn-Bi/Fe couples, unexpected solder melting in Sn-Sb/Ag joints, special up-hill diffusion in the Cu/Sn-Cu/Ni sandwich structure, and the influence of limited Sn supply upon the interfacial reactions in the Au/Sn/Cu sandwich specimens, and so on, will be given.

Lead-free Solders: Materials Reliability for Electronics, First Edition. Edited by K. N. Subramanian.

2.1 Introduction

Soldering is currently the most important joining process in electronic packaging. Properties of solder joints are crucial to the reliability of electronic products and very often are directly related with their lifetime. As new Pb-free solders are being introduced into the electronics and optoelectronics industries, it is of practical importance to evaluate these emerging materials [1–4]. Although there are several different soldering technologies currently available, they share some common features. During soldering, solders are first melted, followed by wetting and reacting with substrates, and then solidified, and, if necessary, remelted again. Multiple phase transformation steps, such as melting, solidification, and interfacial reactions resulting in the formation of intermetallic compounds (IMC), are involved in the manufacturing processes. Moreover, since solders are usually low melting temperature materials, noticeable interfacial reactions continue in the solid-state solder joints upon Joule heating during device operation. These phases formed via interfacial reaction or solidification during or post soldering determine critically the properties of Pb-free solder joints and thus the reliability of electronic products.

Surface treatments at the soldering position of substrates prepared for soldering processes are under bump metallurgy (UBM). UBM is usually made of multilayers with a dissolvable passivation layer on the top against oxidation [2,4], and Pb-free solders are usually binary or higher-order alloys. Therefore, a Pb-free solder joint is usually at least a quaternary material system. A phase diagram is a comprehensive representation of thermodynamic properties of a multicomponent material system [5–8]. It offers a clear description on multiphase relations as well as doping effects in a complex multicomponent Pb-free system. In addition, solders typically possess relative low melting temperatures, and solder joints are processed and operated in relative medium to high homologous temperatures. The local phase equilibrium approximation is thus generally valid for soldering systems [9–15]. This local phase equilibrium approximation further extends the applications of equilibrium phase diagrams in Pb-free soldering. In this chapter, basic knowledge and information of phase diagrams of Pb-free solder systems are reviewed. Several examples of applications of phase diagrams are presented, and some abnormal phenomena in Pb-free soldering are also illustrated with the aid of phase diagrams.

2.2 Phase Diagrams of Pb-Free Solder Systems

The phase diagram is a type of chart that shows the conditions at which thermodynamically distinct phases can occur at the equilibrium. The phase diagram of the binary Cu-Ni system is shown in Figure 2.1. The composition of the alloy in mole fraction is given by the horizontal axis, while the vertical axis gives temperature in Kelvin.

The mole fraction is defined as follows:

$$x_i = \frac{n_i}{\sum_i n_i} \tag{2.1}$$

where x_i denotes the mole fraction of ith component, and n_i denotes the number of moles of ith components.

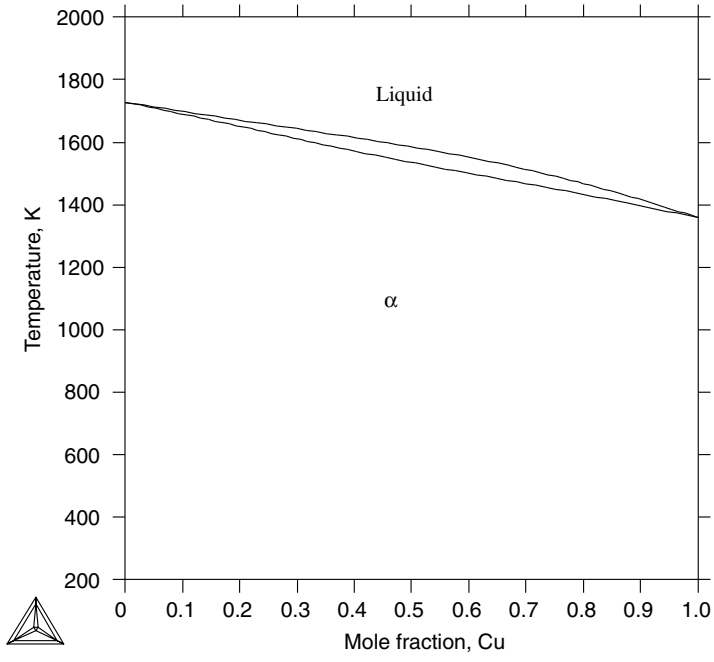

Figure 2.1 *The Cu-Ni binary system.*

In the Figure 2.1, there are two phases, namely the liquid phase and solid phase α, and a region that includes both phases. The border between the two-phase region and the liquid phase is denoted as the liquidus, indicating the temperature at which melting is completed upon heating for each possible alloy composition. On the other hand, the border between the two-phase region and the solid phase is denoted as the solidus, indicating the temperature at which freezing is completed upon cooling. Figure 2.2 shows the lever rule, which is a very useful feature of the phase diagram. The horizontal line AB runs through the binary region connecting two points in the single-phase regions, which are in equilibrium. At point A, the composition of the solid phase α is x_A, the composition of the liquid phase at point B is given by x_B. The lever rule allows the fractional amounts of the phases in equilibrium to be determined. Point O describes the nominal composition of the sample, which equals x_0. At constant temperature, the fraction of solid and liquid phases present can be obtained using Eqs. (2.2) and (2.3):

$$\%\text{solid}(\alpha) = \frac{|x_B - x_0|}{|x_B - x_A|} \cdot 100\% \tag{2.2}$$

$$\%\text{liquid} = \frac{|x_0 - x_A|}{|x_B - x_A|} \cdot 100\% \tag{2.3}$$

Different types of reactions can occur in a binary system. Table 2.1 and Figure 2.3 [18] summarize the possibilities. Figure 2.3 shows the intermediate phases: δ, δ', η, γ, and σ. The homogeneity range of the intermediate phase can vary from strict stoichiometry

Table 2.1 *Invariant reactions in binary systems.*

Name of reaction	Equilibrium	Schematic picture
Eutectic	$L_1 = \alpha + \gamma$	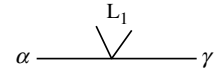
Peritectic	$L + \delta' = \varepsilon$	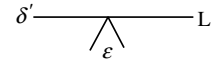
Monotectic	$L_3 = \gamma + L_4$	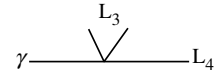
Syntetic	$L_1 + L_3 = \gamma$	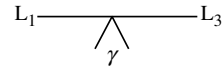
Catetic	$\beta = L_1 + \alpha$	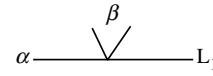
Homotetic	$L_2 = L_1 + L_3$	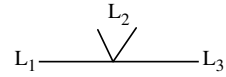
Eutectoid	$\gamma = \eta + \delta'$	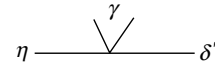
Peritectoid	$\alpha + \gamma = \eta$	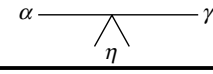

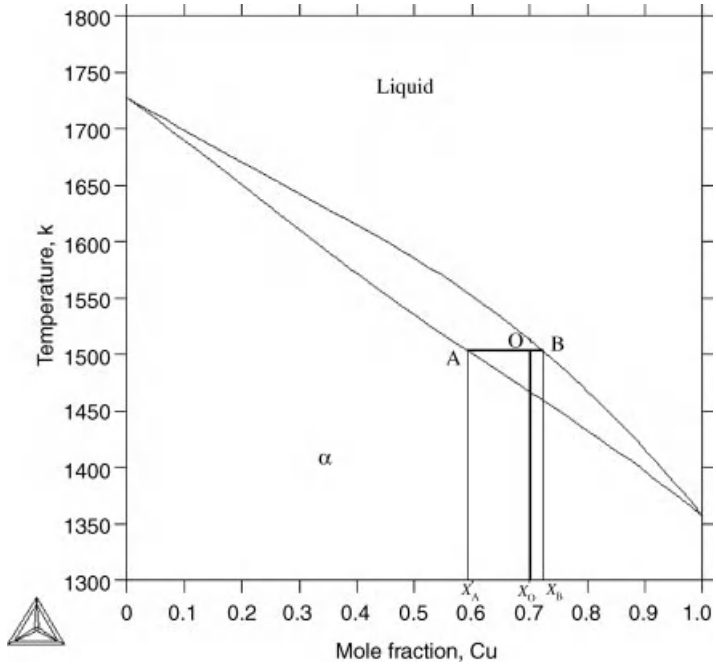

Figure 2.2 *The lever rule.*

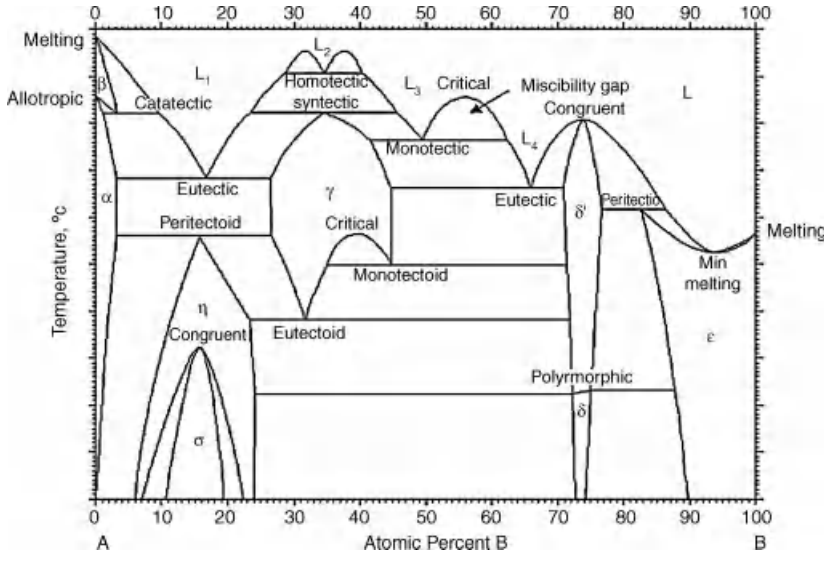

Figure 2.3 *A hypothetical binary A-B phase diagram with different types of reactions [18].*

composition to wide homogeneity range. When an intermediate phase transforms directly (without a two phase region) into another phase at a given temperature for a specific composition (two-phase equilibrium), the transformation is called a congruent transformation. Examples of congruent transformations $\sigma = \eta$ and $\delta' = \mathrm{L}$ can be found in Figure 2.3.

A degree of freedom of the phases in equilibrium is controlled by the Gibbs phase rule:

$$F = C - P + 2 \tag{2.4}$$

where F denotes degree of freedom; C, number of components; and P, number of phases. The possible equilibria for a binary system are listed in Table 2.2.

The phase diagram is related to the thermodynamic properties of phases. The molar Gibbs energy of a phase, which can vary in composition for the whole binary system from A to B and atoms A can be substituted by atoms B without any restrictions (and *vice versa*), is defined as follows:

$$G_{\mathrm{m}}^{\alpha}(T) = x_{\mathrm{A}}^{\alpha}{}^{0}G_{\mathrm{A}}^{\alpha}(T) + \mathrm{x}_{\mathrm{B}}^{\alpha}{}^{0}G_{\mathrm{B}}^{\alpha}\ (T) + {}^{\mathrm{mix}}G_{\mathrm{m}}^{\alpha}\ (T) \tag{2.5}$$

Where $G_{\mathrm{m}}^{\alpha}(T)$ denotes the Gibbs energy of 1 mole of the phase α; x_i^{α}, the mole fraction of component i ($i = \mathrm{A}, \mathrm{B}$); ${}^{0}G_i^{\alpha}\ (T)$, the Gibbs energy of pure component i in the structure of the phase α; and ${}^{\mathrm{mix}}G_{\mathrm{m}}^{\alpha}\ (T)$, the molar Gibbs energy of mixing.

Table 2.2 *The types of equilibrium in the binary systems.*

Name of equilibrium	Number of phases in equilibrium	Degrees of freedom
Invariant	3	0
Monovariant	2	1
Bivariant	1	2

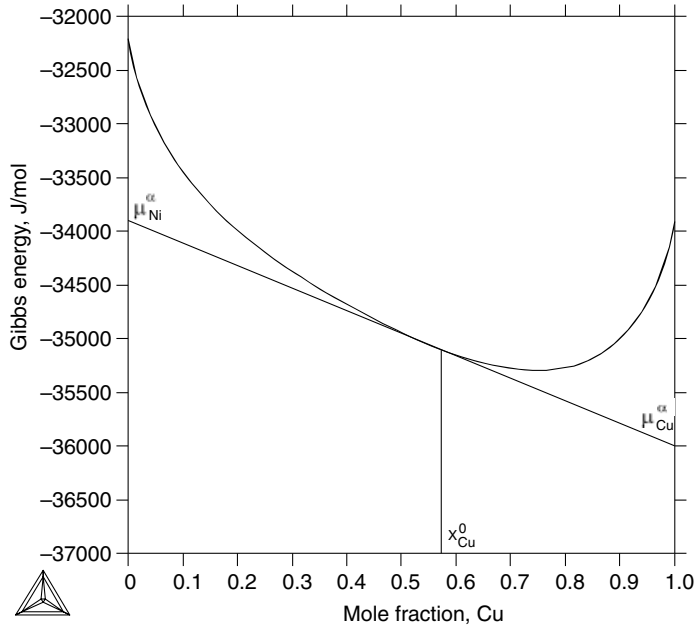

Figure 2.4 *Gibbs energy of the α phase in Cu-Ni system together with partial molar Gibbs energies of Cu and Ni at composition* x^0_{Cu}.

The Gibbs energy of the mixing of one mole of the phase α in the Cu-Ni system at constant temperature is shown in Figure 2.4. The tangent line to the mixing Gibbs-energy curve at composition describes the values of the partial molar Gibbs energies of components Cu and Ni in phase α. The partial molar Gibbs energies that are the chemical potentials of components A and B in phase α at composition x^0_B and are given by:

$$\mu^{\alpha}_{Cu} = {}^{x0}G^{\alpha}_{Cu} = G^{\alpha}_{m} + (1-x_{Cu})\frac{dG^{\alpha}_{m}}{dx_{Cu}} \tag{2.6}$$

$$\mu^{\alpha}_{Ni} = {}^{x0}G^{\alpha}_{Ni} = G^{\alpha}_{m} - x_{Cu}\frac{dG^{\alpha}_{m}}{dx_{Cu}} \tag{2.7}$$

The well-known equilibrium condition between two phases α and β in the binary system is given by equations:

$$\begin{aligned} \mu^{\alpha}_{A} &= \mu^{\beta}_{A} \\ \mu^{\alpha}_{B} &= \mu^{\beta}_{B} \end{aligned} \tag{2.8}$$

The graphical representation of the equilibrium condition given by Eq. (2.8) is shown in Figure 2.5 where the Gibbs energies of two phases, α and liquid, of the binary Cu-Ni system at 1500 K are shown. The α phase has the lowest Gibbs energy for $0 < x_{Cu} < 0.59$, meaning that α phase at temperature 1500 K is a thermodynamically stable phase between these compositions. The same can be said of the stability of the liquid phase for $0.72 < x_{Cu} < 1$. Between

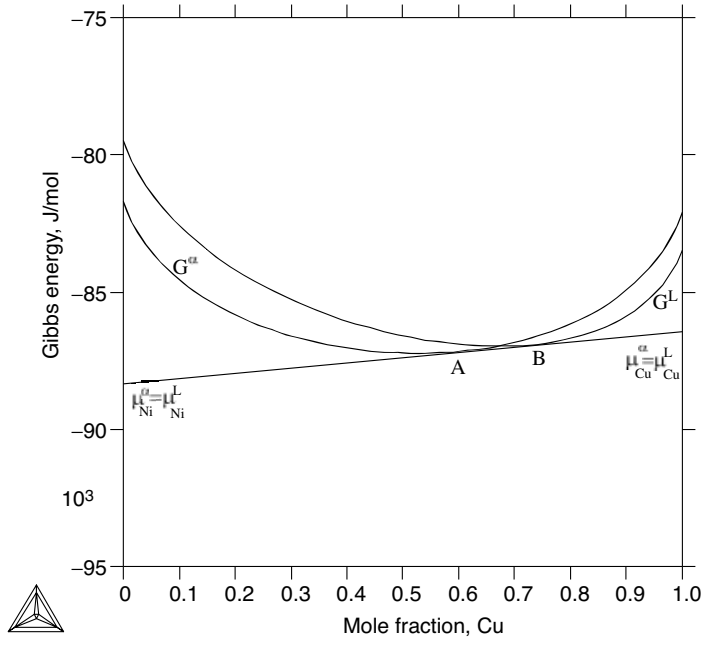

Figure 2.5 *Gibbs energies of solid and liquid phases in Cu-Ni system at 1500 K.*

points A and B, a mixture of α and liquid phases, represented by the common tangent, has lower Gibbs energy than either of the phases alone, implying that the mixture is stable.

The evolution of Gibbs-energy curves is related to the shape of a phase diagram. An example is provided using the Sn-Pb phase diagram given in Figure 2.6 followed by corresponding Gibbs functions at various temperatures plotted in Figures 2.7–2.9

The phase equilibrium criterion of an *n*-phase and *i*-component system is given as follows:

$$\begin{aligned}
&\mu_{\mathrm{A}}^{\alpha} = \mu_{\mathrm{A}}^{\beta} = \mu_{\mathrm{A}}^{\gamma} = \ldots = \mu_{\mathrm{A}}^{n} \\
&\mu_{\mathrm{B}}^{\alpha} = \mu_{\mathrm{B}}^{\beta} = \mu_{\mathrm{B}}^{\gamma} = \ldots = \mu_{\mathrm{B}}^{n} \\
&\mu_{\mathrm{C}}^{\alpha} = \mu_{\mathrm{C}}^{\beta} = \mu_{\mathrm{C}}^{\gamma} = \ldots = \mu_{\mathrm{C}}^{n} \\
&\ldots \\
&\mu_{i}^{\alpha} = \mu_{i}^{\beta} = \mu_{i}^{\gamma} = \ldots = \mu_{i}^{n}
\end{aligned} \tag{2.9}$$

An *i*-component system, under constant pressure, needs *i* dimensions to show the phase relationships as a function of temperature ($i-1$ independent compositional variables and the temperature variable). The ternary system, in the hypothetical version, is shown in Figure 2.10 [18]. For ease of reading, a ternary system can be expressed with three types of two-dimensional plots. The first one is an isothermal section that shows phase equilibria at a given temperature. The second one is a liquidus projection showing the primary solidification phases together with liquidus valleys and, sometimes, isotherms. The third one is an

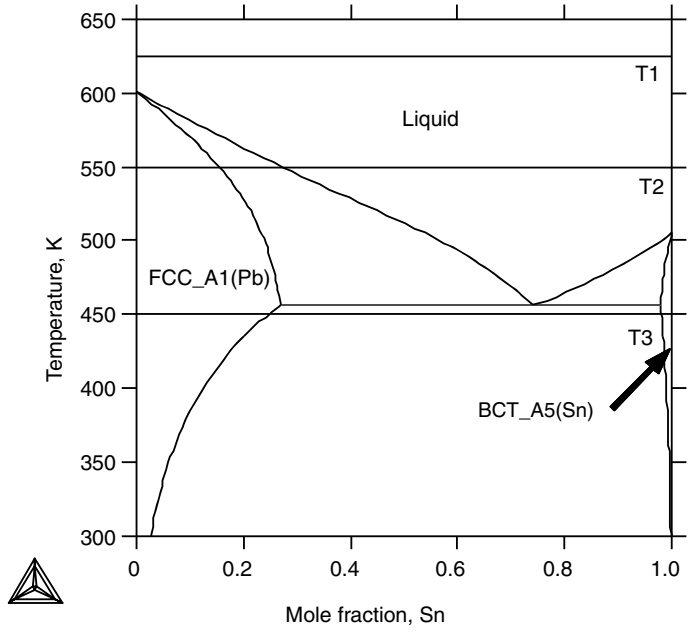

Figure 2.6 *The binary Sn-Pb system together with the marked temperatures T1, T2 and T3.*

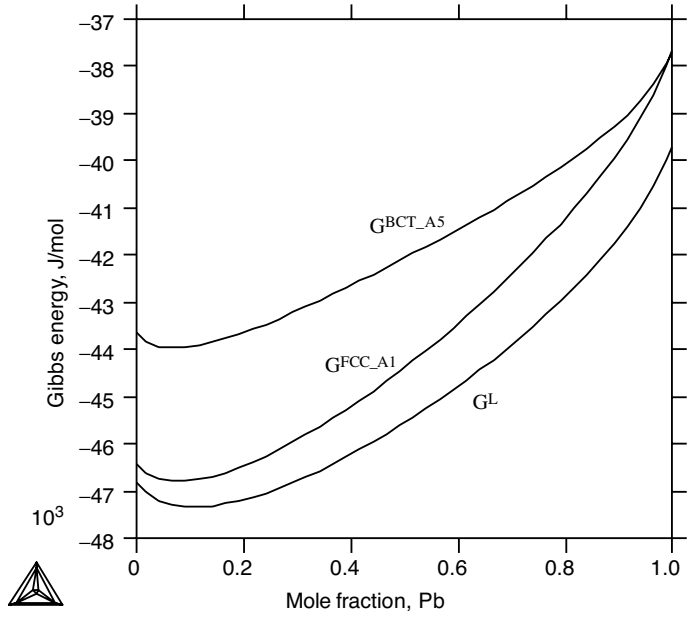

Figure 2.7 *Gibbs energies in the binary Sn-Pb system at 625 K. The liquid phase is stable for all compositions.*

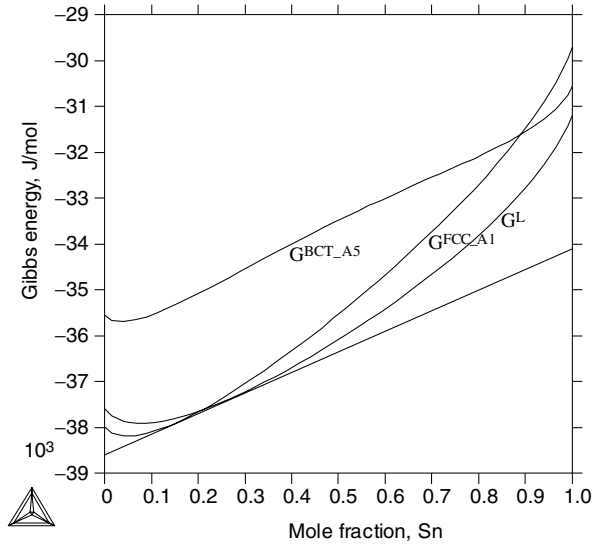

Figure 2.8 *Gibbs energies in the binary Sn-Pb system at 550 K. The FCC_A1(Pb) phase is stable for composition $0 < x_{Sn} < 0.16$, the liquid is stable for composition $0.28 < x_{Sn} < 1$. Between 0.16 and 0.28 mole fraction of Sn the binary region appear. Phase BCT_A5(Sn) is unstable for whole composition.*

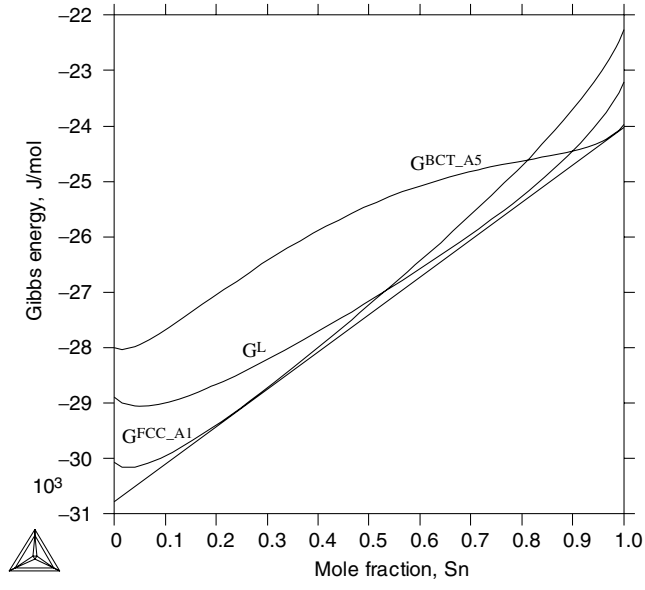

Figure 2.9 *Gibbs energies in the binary Sn-Pb system at 450 K. The FCC_A1(Pb) phase is stable for composition $0 < x_{Sn} < 0.25$, the BCT_A5(Pb) is stable for composition $0.98 < x_{Sn} < 1$. Between 0.25 and 0.98 mole fraction of Sn the binary region (FCC_A1 + BCT_A5) appears. Phase Liquid is unstable for all compositions.*

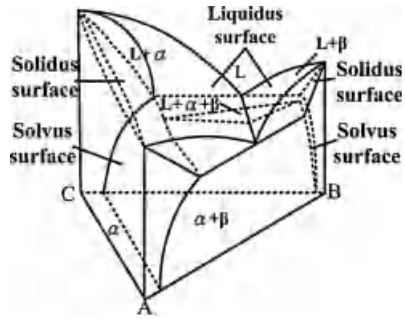

Figure 2.10 *A hypothetical ternary phase diagram [18].*

isoplethal (vertical) section; however, the isoplethal section is not, in fact, an equilibrium phase diagram because the tie-lines (isopotential lines) do not lie on the isopleths plane. Further information about the projections of multicomponent systems can be found in the literature [9,10]

A multicomponent phase diagram can be determined by experiments and by thermodynamic modeling. Key experiments are essentially necessary to explore the phase relationships and reactions. There are several important experimental methods for phase-diagram determination, including thermal analysis, micrography, crystallography, X-ray spectroscopy, and so on. Thermal analysis provides the information about the temperature of phase transformation, and micrography with the aid of microprobe measurements associated with X-ray spectroscopy gives the information about phases in equilibrium. Besides these methods, there are other experimental approaches, such as X-ray diffractometry for lattice parameter and conductivity measurements [5,10].

The phase diagrams can be described using the CALPHAD (CALculation of PHAse Diagrams) method. The flow chart of this method is given in Figure 2.11 [7]. Combining all kinds of experimental information, the parameters of selected thermodynamic model for each phase can be optimized. The final result of the CALPHAD calculation is a database with a set of Gibbs-energy functions that describe the given system. Extrapolating the binary information obtained by the CALPHAD method to higher-order systems can simplify the experimental procedures and make it less time consuming and cost effective.

Several phase diagrams are very important for the lead-free soldering technology. The most important ones include Sn-Ag [12], Sn-Au [13], Sn-Bi [14], Sn-Cu [15], Sn-In [16], Sn-Sb [12], Sn-Zn [14], Cu-In [16] and Ag-In [17]. Figures 2.12–2.20 show the phase diagrams of the systems mentioned above. Significant information about these systems can be found in the ASM Handbook vol. 3 [18] where the phase diagrams of metallic systems are gathered together with crystallographic information.

Both experimental and thermodynamic modeling results are usually available for most of the binary solder-related phase diagrams; however, information regarding the ternary and higher-order systems is relatively limited. Experimental phase equilibrium measurements are available for Sn-Ag-Au [19–22], Sn-Ag-Cu [23–27], Sn-Ag-Ni [28], Sn-Bi-Au [29], Sn-Bi-Ag [30,31], Sn-Bi-Cu [32], Sn-Bi-Fe [33], Sn-Bi-Ni [34], Sn-Cu-Au [35], Sn-Cu-Ni [36,37], Sn-In-Au [38], Sn-In-Cu [39], Sn-In-Ag [40], Sn-In-Ni [41], Sn-Sb-Ag [12,42–44], Sn-Sb-Au [45], Sn-Zn-Ag [46], Sn-Zn-Bi [47], and Sn-Zn-Cu [48], and Sn-Ag-Cu-Ni [49,50] systems.

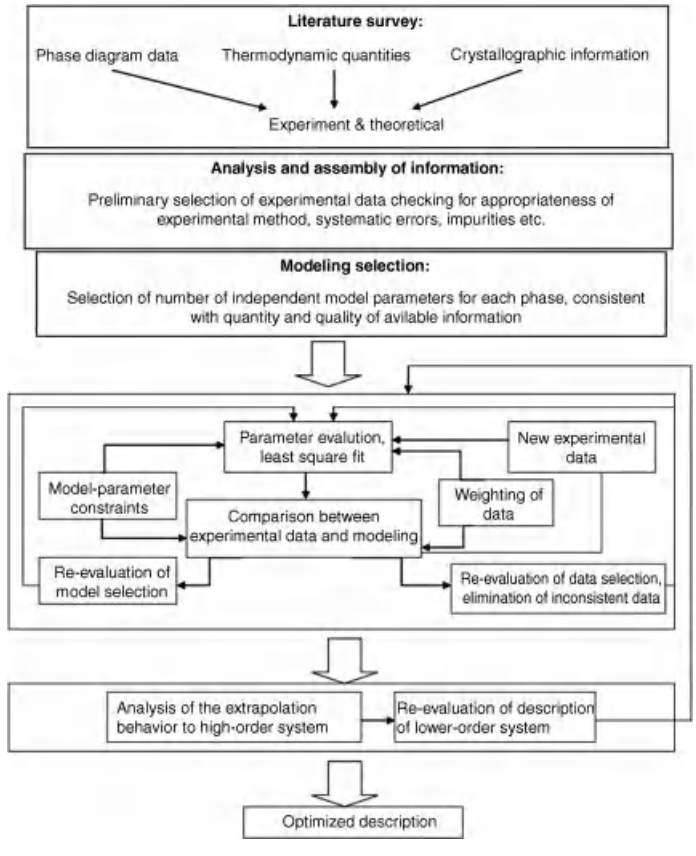

Figure 2.11 *The flow chart of the CALPHAD method [7].*

As for lead-free soldering, there are some commercial thermodynamics databases, such as COST531 database [51], NIST solder database [52] and ADAMIS database [53]. The databases and the software like Pandat [54] or Thermocalc [55] are very powerful tools for engineers, who can predict easily and rapidly the properties of real solders. An example is given in Figures 2.21–2.24. Figure 2.21 shows the calculated isothermal section of Sn-Sb-Ag at 250 °C together with the real micrographs of the samples [12]. Figures 2.22 and 2.23 show the calculated solidification path of the sample Sn-30Ag-50Bi(at%) and DTA results. Additionally, Figure 2.24 displays the solidification path projected on the liquidus surface.

2.3 Example of Applications

2.3.1 General Applications (Melting, Solidification, Interfacial Reactions)

During soldering, phase transformation and reactions occur that include melting of solders, dissolution of connecting substrates in the solder, formation of intermetallic compounds at interfaces, and solidification of molten solders [1,3,4,25]. The melting-point temperature is

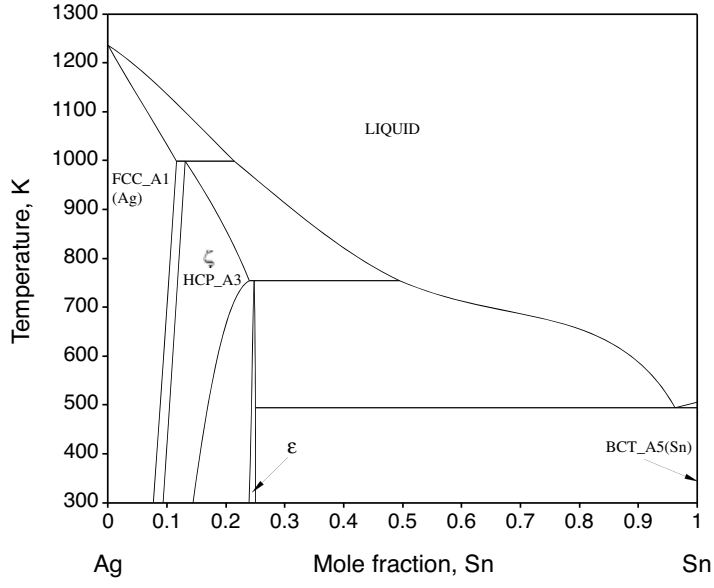

Figure 2.12 *Phase diagram of the binary Sn-Ag system [12].*

the most important property of solders since melting of solders is the first step in the soldering process. The melting point of the eutectic Sn-Pb is at 183 °C. For a long time, it has been the important reference temperature for temperature selections of electronic manufacturing processes. If the solders are not eutectic alloys, such as high-Pb solders,

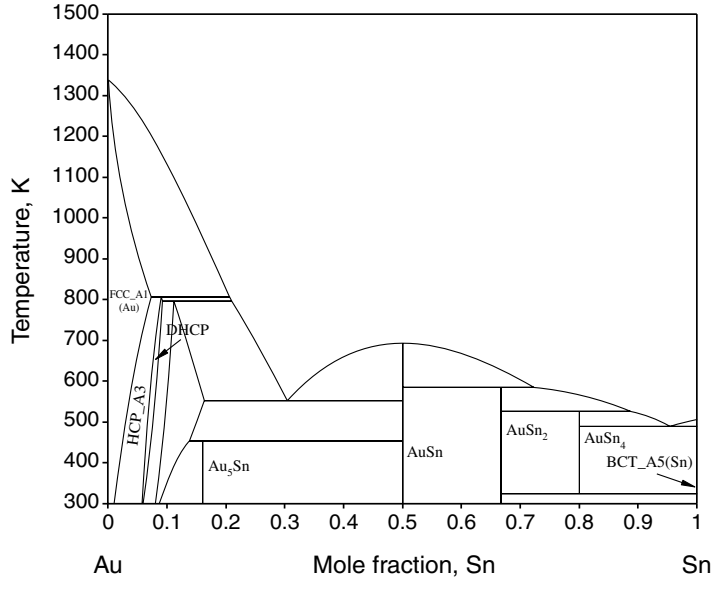

Figure 2.13 *Phase diagram of the Sn-Au binary system [13].*

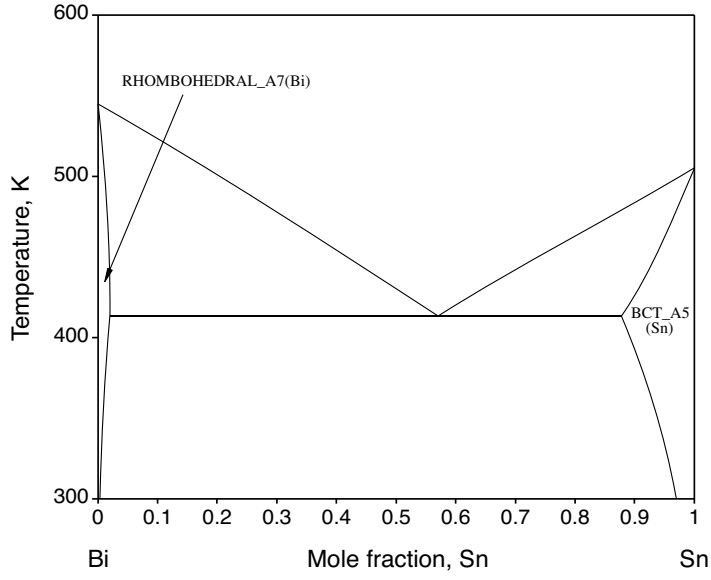

Figure 2.14 *Phase diagram of the Sn-Bi binary system [14].*

the mushy (solid + liquid phase) region is defined by the liquidus temperature and the solidus temperature.

With replacements of Pb-free solders, different soldering temperatures would be required. For example, if the eutectic Sn-Ag solder with eutectic temperature at 221 °C [12]

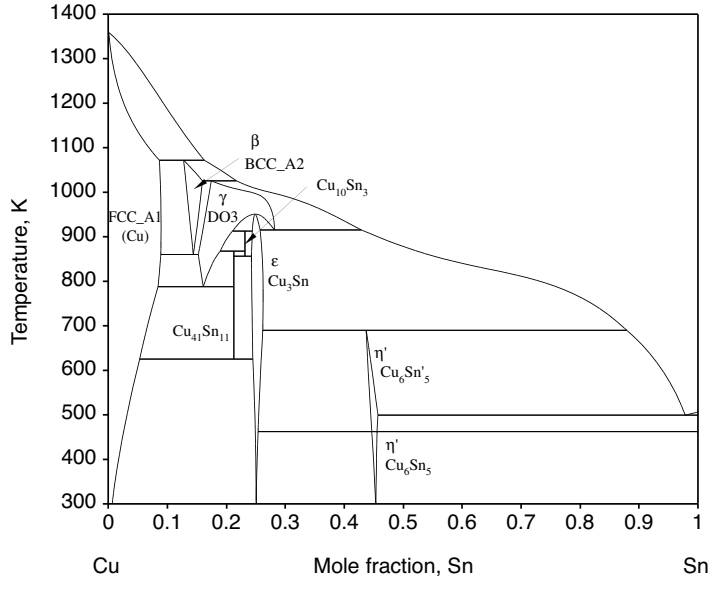

Figure 2.15 *Phase diagram of the Sn-Cu binary system [15].*

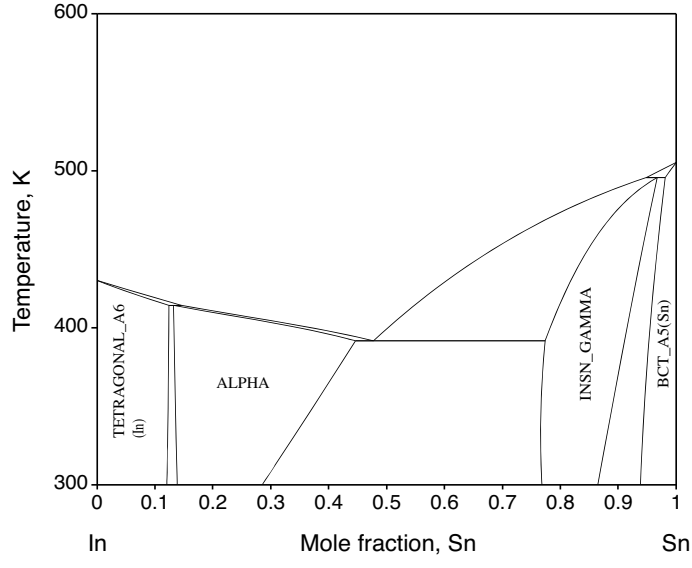

Figure 2.16 *Phase diagram of the Sn-In binary system [16].*

is used, the soldering temperature would be higher compared with that for process using conventional eutectic Sn-Pb solder. Even if the soldering is not necessarily a thermodynamic equilibrium process, the thermodynamic equilibrium melting and solidification temperatures (eutectic, solidus and liquidus temperatures) are the most important bases for

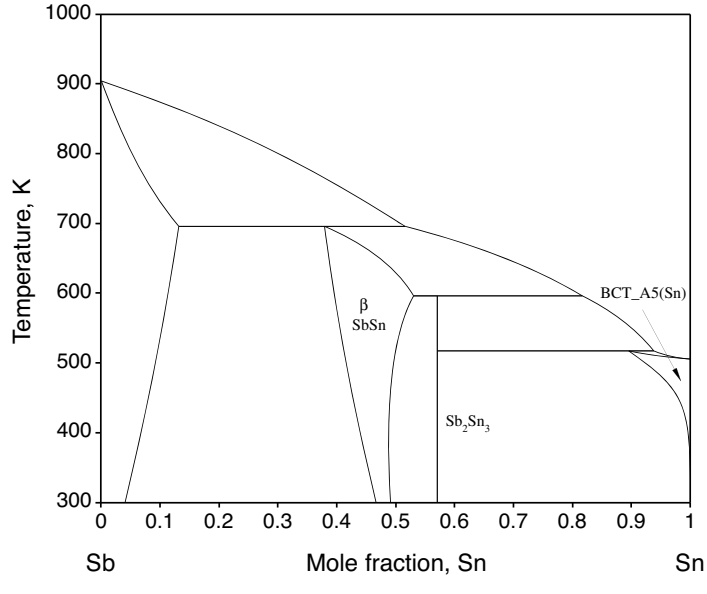

Figure 2.17 *Phase diagram of the Sn-Sb binary system [12].*

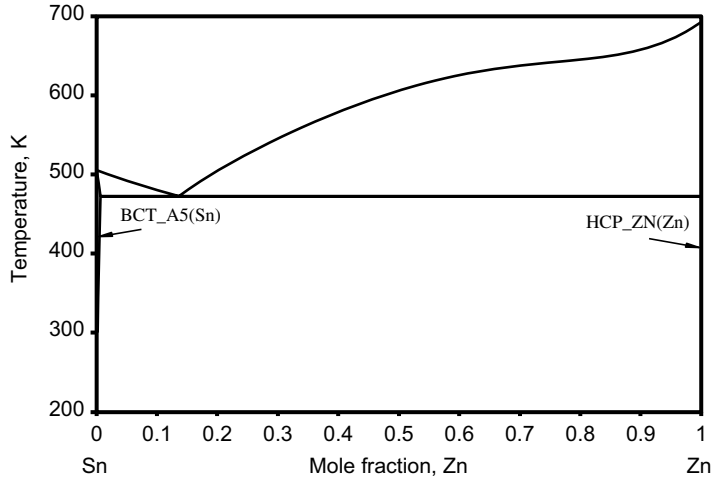

Figure 2.18 *Phase diagram of the Sn-Zn binary system [14].*

processing temperature selections in industry. The eutectic, liquidus and solidus temperatures can be determined directly from a phase diagram, as shown in Figure 2.6.

When dissimilar materials are brought in contact at a solder joint, interdiffusion will occur due to chemical potential gradients across the interface, and usually interfacial reactions would also take place resulting in the formation of IMCs. A schematic diagram illustrating the composition profile through an A-B reaction couple is shown in Figure 2.25. Although the reaction couple is not in thermodynamic equilibrium, the local equilibrium condition usually holds at the interfaces [11,28,33,66,74,85]. When the local equilibrium

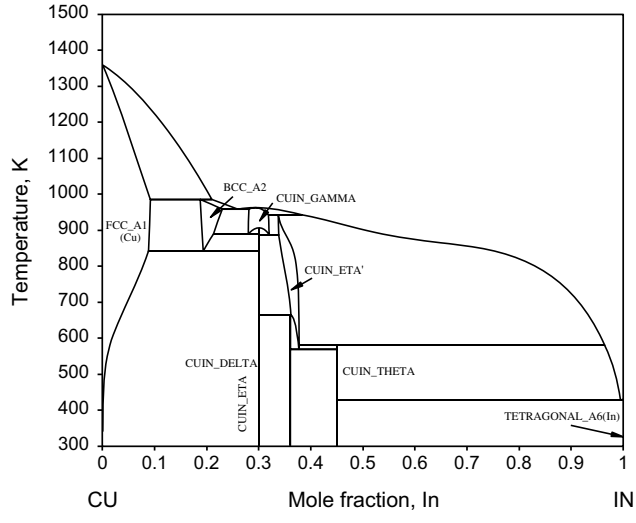

Figure 2.19 *Phase diagram of the Cu-In binary system [16].*

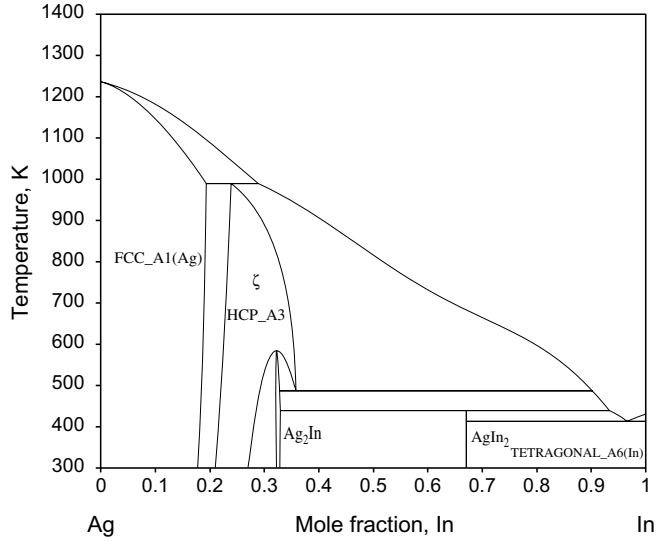

Figure 2.20 *Phase diagram of the Ag-In binary system [17].*

condition is followed, the kinds and compositions of the IMCs can be determined from the phase diagrams. As shown in Figure 2.25, the reaction product is the β phase.

Solders are usually binary or ternary alloys. Together with UBM, a ternary or even higher-order material system would be encountered at solder joints. For a binary system, interfacial reactions and solidification are comprehensible. However, for ternary or higher-order systems, there are diverse possibilities of reaction and solidification paths. An isothermal section of phase equilibria in a ternary system is a useful tool for illustrating interfacial reactions at a binary solder/substrate joint [11,28,33,66,74,85]. It must be mentioned that interfacial reactions and the IMC formation are not only governed by thermodynamics but also kinetics, and it is risky to predict the interfacial reactions using phase diagrams alone.

Liquidus projection is a powerful tool to study solidification behaviors [56–58]. Take, for example, the Sn-Sb-Ag ternary system, which will be discussed later in Section 2.3.5. The liquidus projection of this ternary system is shown in Figure 2.24. Sn-Sb alloys have been used as high melting point solders and Ag is frequently used in surface finishes in electronic products [12]. The interpretation of the solidification made with the aid of the phase diagram and calculations shows that for the sample Sn-50Sb-30Ag(at%), the primary solidification phase will be the Sb phase and the last drop of the liquid will freeze at a temperature around 220 °C. The type of reactions, compositions of both the liquid and solid phases, and phase transformation temperatures can be read from a phase diagram, which can be obtained by using thermodynamic modeling software [54,55] with the databases [51–53].

2.3.2 Effective Undercooling Reduction (Co Addition)

Undercooling refers to the phenomenon that solidification does not occur when the temperature of a liquid phase is below its thermodynamic equilibrium solidification temperature (melting point, liquidus temperature, or eutectic temperature) [59–61].

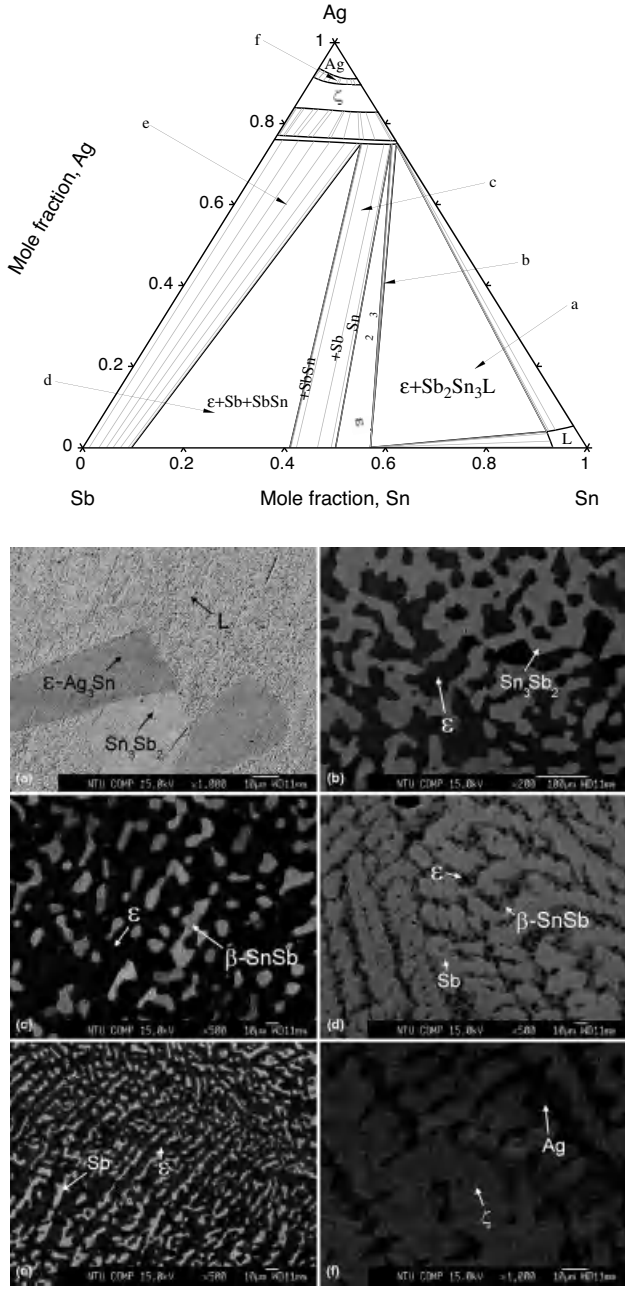

Figure 2.21 *Calculated isothermal section of the Sn-Sb-Ag system at 250°C together with the microstructures of the phase equilibria (a), (b), (c), (d) [12].*

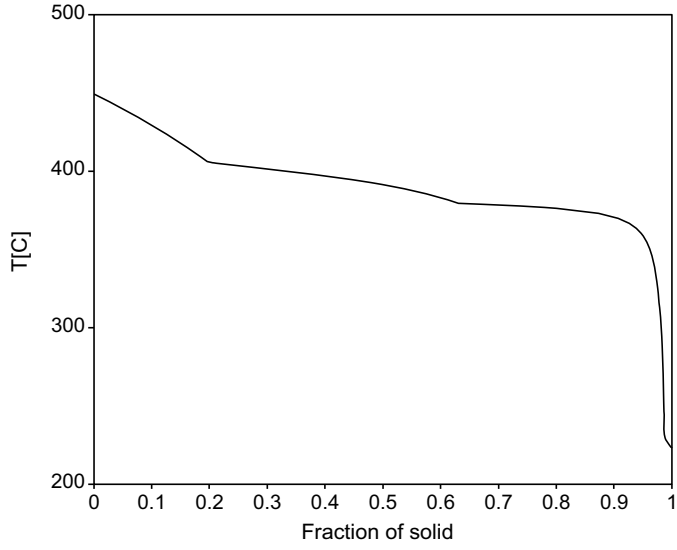

Figure 2.22 *Calculated solidification path of the sample Sn-50Sb-30Ag(at%).*

Undercooling is attributed to nucleation difficulties of the solidification phases, and various factors such as cooling rates and sample size could affect the degree of undercooling [62–64]. Undercooling could change the solidified microstructures and even alter the type of phase formation during solidification. The solidification of the Sn-3.5 wt%Ag solder is a typical example. Because of the significant undercooling, the Ag_3Sn phase solidifies first. At a cooling rate of 6 °C/min, a plate-like Ag_3Sn intermetallic compound formation was observed in the solidified solder [62].

Recently, studies have been devoted to minimizing the undercooling effect via alloying minor elements such as Zn, Co and Ni [65]. Among these candidates, Co is found to be a promising additive for Sn-Ag-Cu (SAC) [65] and Sn-3.5 wt%Ag [62] solders. The degree of undercooling is the difference between the actual solidified temperature (the onset temperature of first peak in the cooling curve of a thermal analysis) and the equilibrium

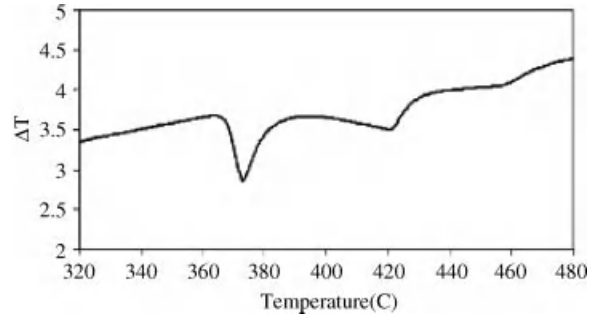

Figure 2.23 *DTA heating curve of the sample Sn-50Sb-30Ag(at%) [12].*

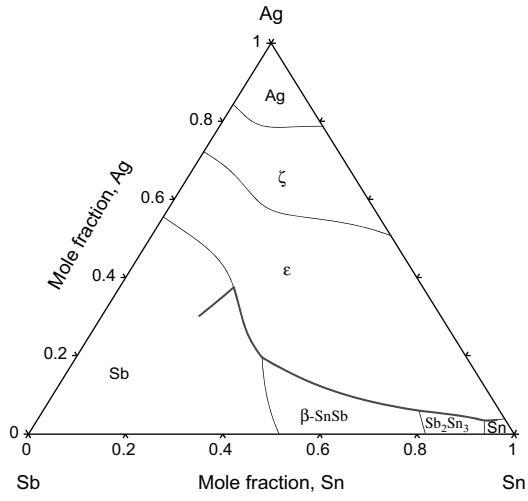

Figure 2.24 *Solidification path of the Sn-50Sb-30Ag(at%) on the liquidus projection [12].*

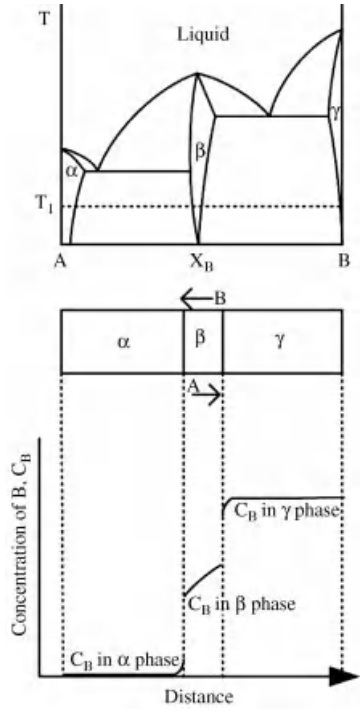

Figure 2.25 *Schematic illustrations of the correlation between the phase diagram and interfacial reaction.*

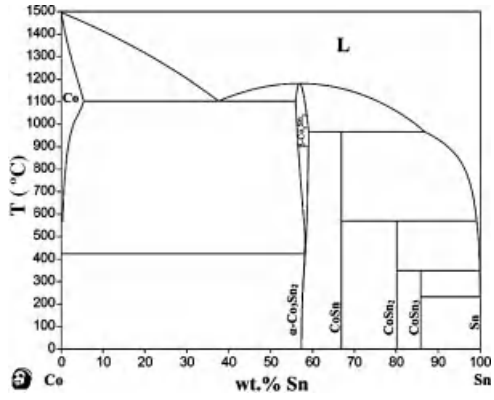

Figure 2.26 *Calculated Sn-Co phase diagram [66].*

melting point, and that of Sn-3.5Ag-0.95Cu (SAC3595, wt%) is reduced from 28–32 °C to 6 °C with only 0.05 wt%Co addition [65].

There are several factors that affect the degree of undercooling, and it is evident that the heterogonous nucleation sites play the main role in promoting nucleation and suppressing the degree of undercooling [64]. Sn-Co intermetallic compounds are heterogonous nucleation sites that would effectively reduce undercooling [62,64,66]. Figure 2.26 is the Sn-Co binary phase diagram determined by Chen *et al.* [66]. The Co solubility in the molten Sn is as low as 0.04 wt%Co at 250 °C and its eutectic composition is 0.03 wt%Co. According to the phase diagram [66], with only 0.03 wt% Co addition, Sn-Co intermetallic compounds would form during cooling. The effective undercooling reduction with minute Co addition is due to the limited solubility of Co in Sn phase, as revealed in the phase diagram.

2.3.3 Unexpected Compound Formation (Sn-Ag/Cu Interfacial Reactions)

Sn-Ag alloy is one of the most promising Pb-free solders, and the interfacial reactions between the Cu substrate and this alloy are of interest [67–70]. Chen and Yen [27] have investigated the solid/solid and liquid/solid interfacial reactions upon Sn-Ag/Cu reaction couples. Figure 2.27 shows the microstructure of the Sn-3.5 wt%Ag/Cu couple reacted at 450 °C for one hour [27]. Three IMCs, δ (Cu_4Sn), ε_1 (Cu_3Sn) and η (Cu_6Sn_5), are observed at the interface and similar results can be found with longer reaction time; however, according to the Sn-Cu binary diagram [15], there are only two stable phases, δ (Cu_4Sn) and ε_1 (Cu_3Sn), at 450 °C. With careful analysis, it is confirmed that the η (Cu_6Sn_5) phase is formed during solidification and not as a result from interfacial reaction. If only the reaction couple results were analyzed without referring to the phase diagram, the η (Cu_6Sn_5) at the interfaces could be concluded as a reaction product by mistake.

2.3.4 Unexpected Growth Rates (Sn-Bi/Fe and Sn-Pb/Fe)

Sn-Bi is a promising lead-free solder for low-temperature applications [69]. Since Fe is the major constituent of steels used in lead frames and solder pots [71,72], understanding the Sn-Bi/Fe interfacial reactions is important. As shown in Figure 2.28, the growth rates of the

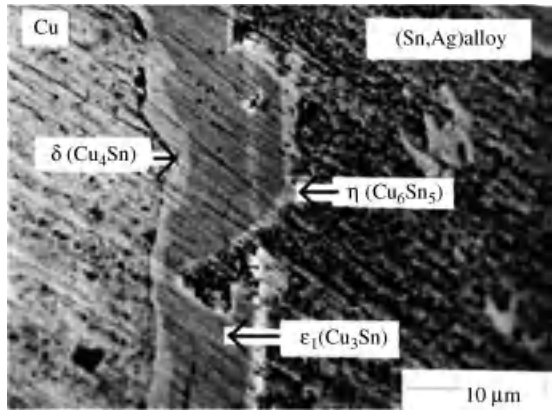

Figure 2.27 *A Sn-3.5 wt%Ag/Cu couple reacted at 450°C for 1 h [27].*

intermetallic compounds in the Sn-57 wt%Bi/Fe couples reacted at 390 °C are higher than those at 500 °C [33]. Further examination reveals that the different reaction rates are results of formation of different reaction phases at different temperatures. The remaining question is what drives the changing of $FeSn_2$ into FeSn phase at reaction temperatures of 390 °C and 500 °C, respectively.

Figures 2.29–2.31 are the isothermal sections of the Sn-Bi-Fe ternary system at 390 °C, 395 °C and 500 °C, respectively [33]. For reaction temperatures lower than 395 °C, there are tie lines between the $FeSn_2$ and molten Sn-Bi eutectic alloy, and the formation of the $FeSn_2$ phase is thermodynamically feasible. However, when the reaction temperature is at 500 °C,

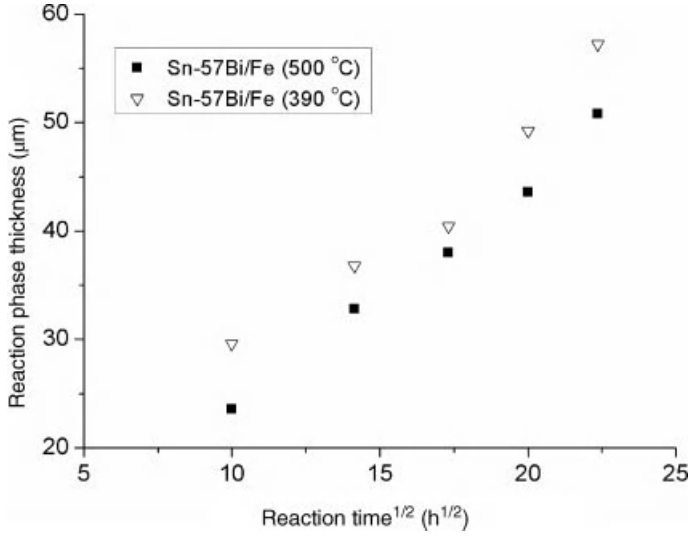

Figure 2.28 *The growth rates of intermetallic compounds in Sn-57wt%Bi/Fe couples reacted at 390°C and 500°C [33].*

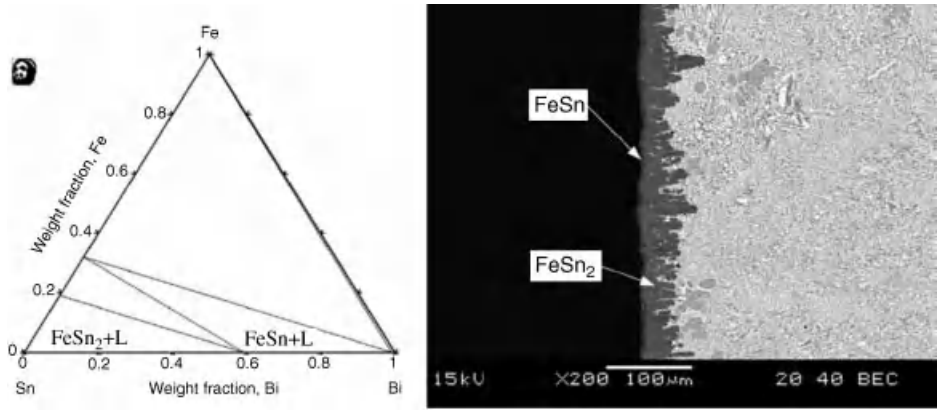

Figure 2.29 *Calculated isothermal sections of Sn-Bi-Fe ternary system at 395 °C together with the resultant microstructures of corresponding Sn-57wt%Bi/Fe couples [33].*

there are no tie lines between these two phases. It can thus be understood that the changing of the reaction product to the FeSn phase when the reaction temperature is raised to 500 °C is a result of the tie-line shift as shown in the Sn-Bi-Fe phase diagrams.

A similar phenomenon has also been found in Sn-37 wt%Pb/Fe couples [72], and the growth rates of the intermetallic compounds at 400 °C are higher than those at 500 °C. The unexpected lower growth rates at higher temperatures are also caused by different reaction products at these two temperatures, which can be successfully illustrated using the Sn-Pb-Fe phase diagrams.

2.3.5 Unexpected Melting of Solder (Sn-Sb/Ag)

Step soldering refers to the manufacturing processes in which soldering is applied more than once, and solders of different melting points are usually needed in step soldering. Sn-5 wt%Sb

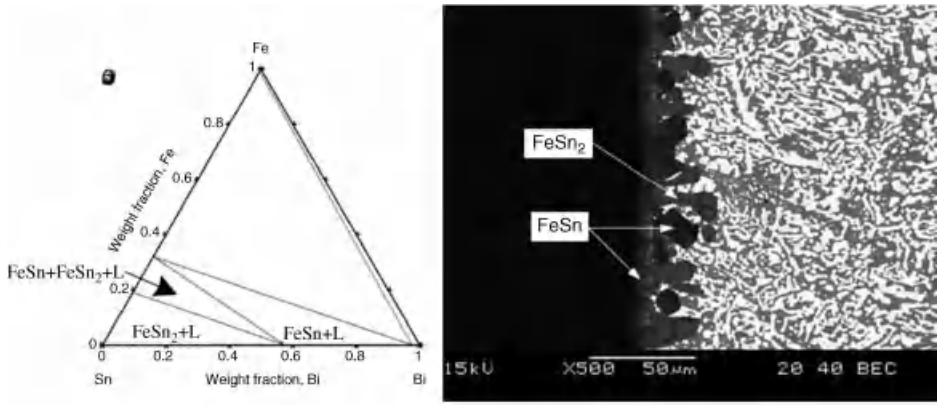

Figure 2.30 *Calculated isothermal sections of Sn-Bi-Fe ternary system at 500 °C together with the resultant microstructures of corresponding Sn-57wt%Bi/Fe couples [33].*

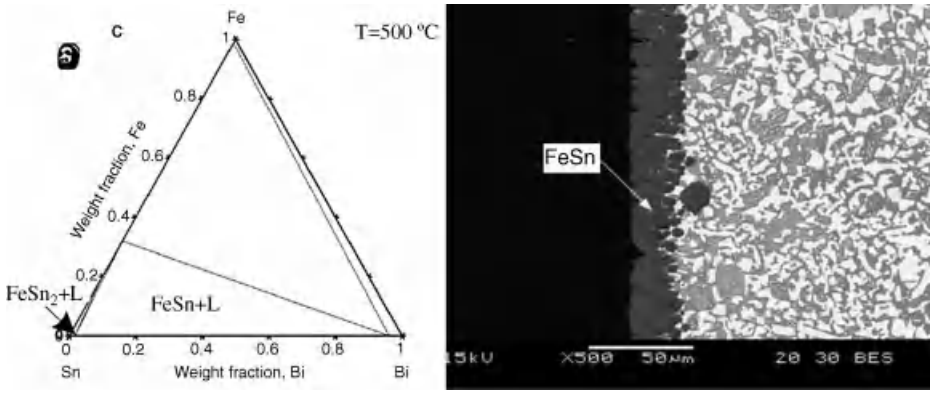

Figure 2.31 *Calculated isothermal sections of Sn-Bi-Fe ternary system at 500 °C together with the resultant microstructures of corresponding Sn-57wt%Bi/Fe couples [33].*

alloy is widely used as a high melting temperature solder, and its solidus and liquidus temperatures are 240 and 245 °C, respectively [73]. Figure 2.32 shows the cross-sectional image of a LTCC (low temperature cofiring ceramic) device. To improve the wetting ability and electrical conduction properties in LTCCs, a thin Ag layer is formed on the ceramic substrate. The solder joint is thus Sn-5 wt%Sb solder in contact with Ag. In LTCC manufacturing processes, an unexpected remelting phenomenon of Sn-5 wt%Sb/Ag solder joints is observed when the products are reflowed at 230 °C [73] in the later stage.

Since the 230 °C reflowing temperature is lower than the 240 °C solidus temperature of the Sn-5 wt%Sb alloy and the 961 °C melting temperature of Ag, the remelting of the

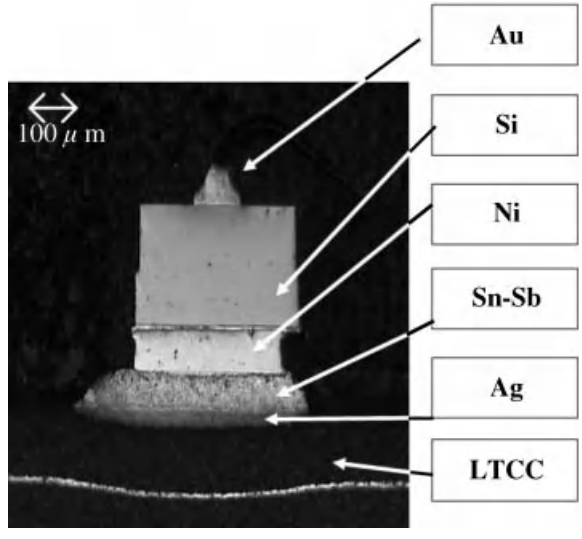

Figure 2.32 *Optical micrograph of a commercial LTCC product.*

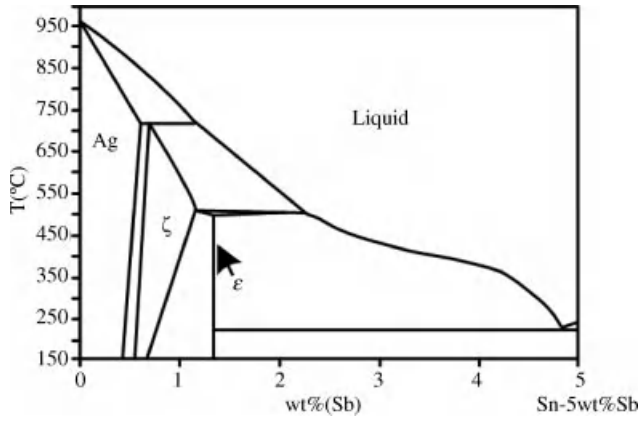

Figure 2.33 *Isoplethal section of the Sn-Sb-Ag ternary system.*

solder joint is puzzling. As mentioned previously, dissolution of the substrate into the solder melt would occur in the solder processes. With the intake of Ag, the Sn-5 wt%Sb solder would become a ternary (Sn-5 wt%Sb)$_{100-x}$Ag$_x$ alloy. Figures 2.33 and 2.34 are the (Sn-5 wt%Sb)-Ag isoplethal sections of the Sn-Sb-Ag ternary system [73]. As shown in the figures, the ternary solubility of Ag in the Sn-5 wt%Sb is very low. With a small amount of Ag added, the (Sn-3.5 wt%Sb)$_{100-x}$Ag$_x$ alloys would encounter the extension of the binary eutectic at 228 °C and a significant lowering of the liquidus temperature is thus observed.

2.3.6 Up-Hill Diffusion (Sn-Cu/Ni)

Flip-chip technology is commonly used in advanced electronic packaging. To simulate the flip-chip structure using Ni as the diffusion barrier layer, a reaction specimen with the

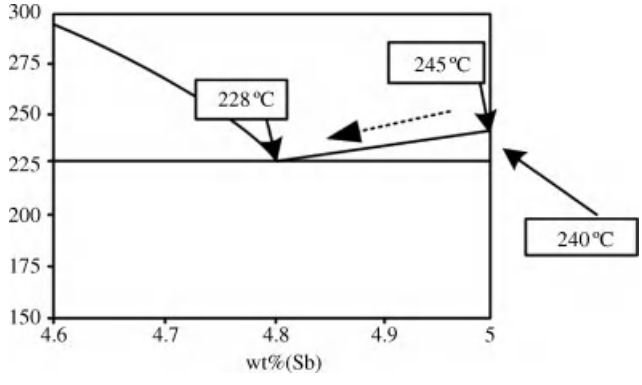

Figure 2.34 *The enlargement of the Sn-5wt%Sb corner, the liquidus and solidus temperatures of the Sn-3.5wt%Sb alloy are at 245°C and 240°C.*

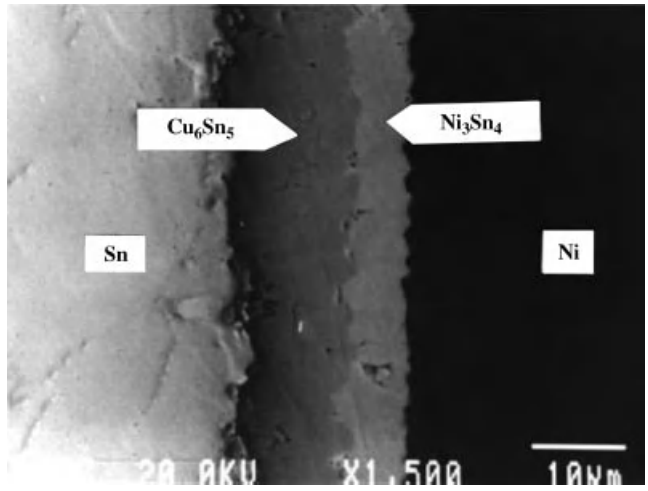

Figure 2.35 *SEI micrograph of the interface between the Sn/Ni in Sn/Cu/Sn/Ni/Sn/Cu/Sn couples [74].*

Cu/Sn/Ni structure is prepared and reacted at 200 °C [74]. The Cu_6Sn_5 and Cu_3Sn phases are formed at the Cu/Sn interface [75–78], while the Cu_6Sn_5 and Ni_3Sn_4 phases are formed at the Sn/Ni interface, as shown in Figure 2.35 [74]. The reaction path is Cu/Cu_3Sn/Cu_6Sn_5/Sn/Cu_6Sn_5/Ni_3Sn_4/Ni. Since Cu atoms diffuse from the Cu side toward

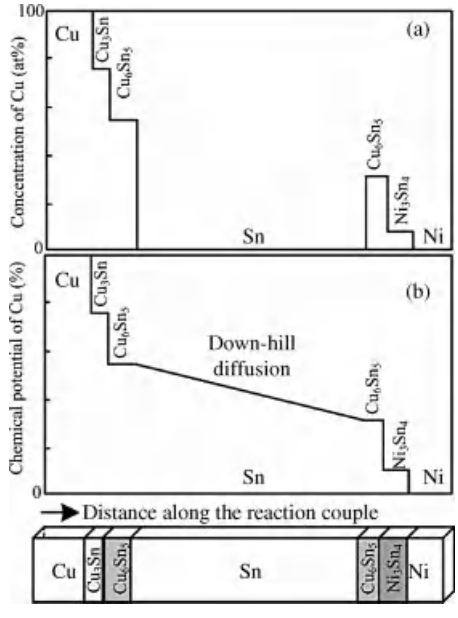

Figure 2.36 *Schematic diagrams of (a) Cu concentration, and (b) Cu chemical potential profile along the reaction couple from the interface of Cu/Sn toward Sn/Ni [74].*

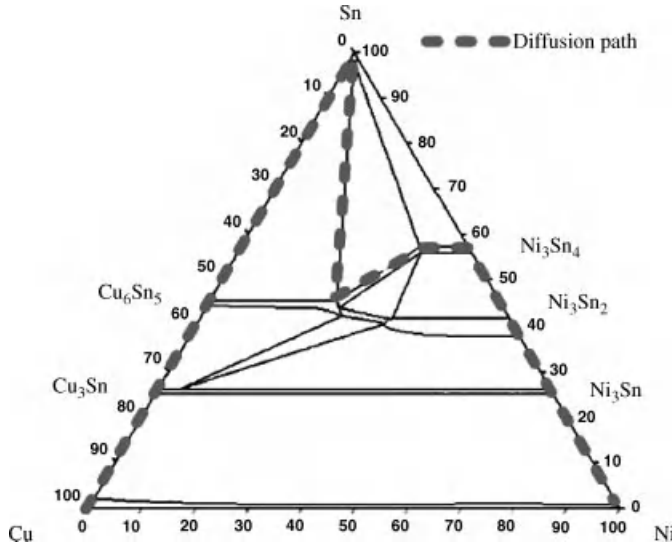

Figure 2.37 *Isothermal section of Sn-Cu-Ni system at 200°C [74].*

the Ni side, the diffusion of Cu from the molten Sn toward the Cu_6Sn_5 phase looks like an up-hill process, that is, from the Cu-depleted side toward Cu-rich side, as shown in the compositional profile along the reaction couple in Figure 2.36a.

As shown in the Sn-Cu-Ni isothermal section at 200 °C in Figure 2.37, the compositional homogeneity range of the Cu_6Sn_5 phase is very significant along the Cu-Ni direction and there are tie lines between the Sn phase and the Cu_6Sn_5 phase. Figure 2.36b is a schematic diagram of Cu chemical potential profile along the reaction couple from the interface of Cu/Sn toward Sn/Ni. Even though the Cu content is very low in the Sn phase, the chemical potentials of Cu in the Sn phase are identical to those in the Cu_6Sn_5 phase that are connected

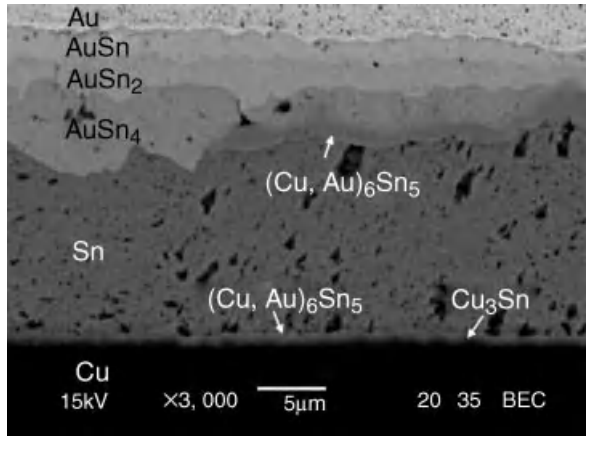

Figure 2.38 *BEI micrograph for Au/Sn(32 μm)/Cu couple reacted at 210 °C for 10 min [85].*

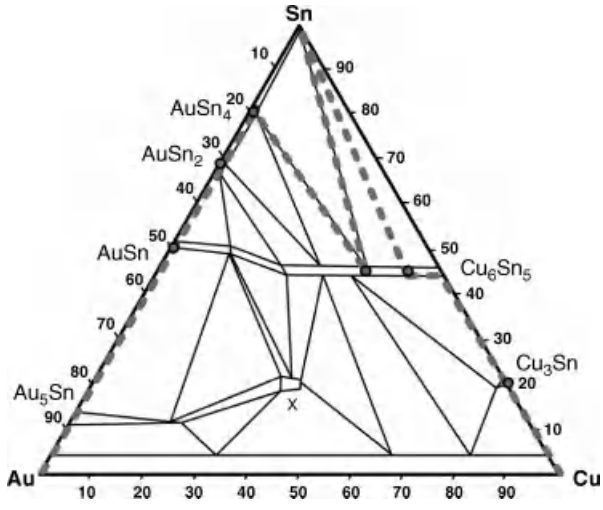

Figure 2.39 *Reaction paths of the Au/Sn(32 μm)/Cu couple reacted at 210 °C superimposed with the Sn-Au-Cu isothermal section.*

by tie lines. As shown in Figure 2.36b, the chemical potential of Cu is decreasing all the way from the pure Cu side toward the Ni side. Since the driving force of atomic diffusion should be the chemical potential gradient instead of the concentration gradient, Cu diffusion from the Sn phase to Cu_6Sn_5 phase is in fact a down-hill process.

2.3.7 Limited Sn Supply (Au/Sn/Cu)

Au is frequently used in electronic products [79–83]. Au bump is used in flexible electronics, and Au finish is important for oxidation prevention. The interfacial reactions in the couples with Au/Sn/Cu sandwich structure have been examined [83–85]. Figure 2.38 shows the metallographic observations for Au/Sn(32 μm)/Cu couple reacted at 210 °C for 10 min, and the reaction path can superimpose with the Sn-Au-Cu isothermal section, as shown in the Figure 2.39, which can be described as Au/AuSn/$AuSn_2$/$AuSn_4$/$(Cu,Au)_6Sn_5$/Sn/$(Cu,Au)_6Sn_5$/Cu_3Sn/Cu. It is observed that the reaction products in the Au/Sn/Cu evolved with reaction time, and the progression of Au/Su/Cu interfacial reactions can be illustrated in Figure 2.40. For example, Sn is completely consumed in the Au/Sn(8 μm)/Cu couple reacted at 210 °C for 10 min. The reaction path is Au/AuSn/$(Cu,Au)_6Sn_5$/Cu_3Sn/Cu, as shown in Figure 2.41 superimposed with the Sn-Au-Cu isothermal section. With the aid of the isothermal section, the reaction phase evolution becomes much easier to comprehend.

2.4 Conclusions

In this chapter, phase diagrams of Pb-free solder systems are reviewed. In addition to the general applications of phase diagram, several examples of interesting phenomena in Pb-free soldering are described and successfully interpreted with the aid of corresponding

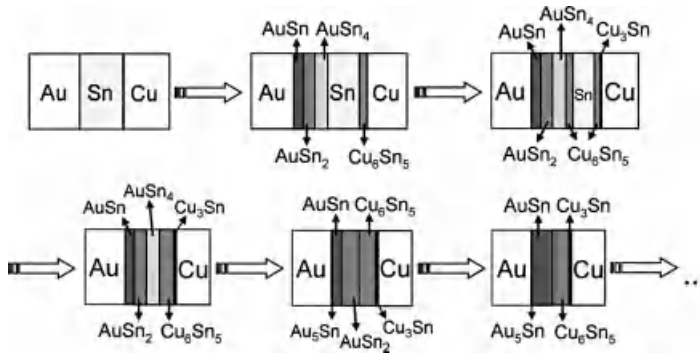

Figure 2.40 *The progression of Au/Su/Cu interfacial reactions with limited Sn supply [85].*

phase diagrams. These examples clearly reiterate the fact that a phase diagram is a condensed presentation of phase relationships and is a powerful tool for evaluating the phase transformations of multicomponent materials systems. Phase diagrams of various Pb-free solder-related systems are still not yet completely understood; hence, continuing efforts devoted to determining these phase diagrams are essential for future Pb-free solder development and their applications.

Acknowledgments

The authors would like to acknowledge the financial support of the National Science Council of Taiwan.

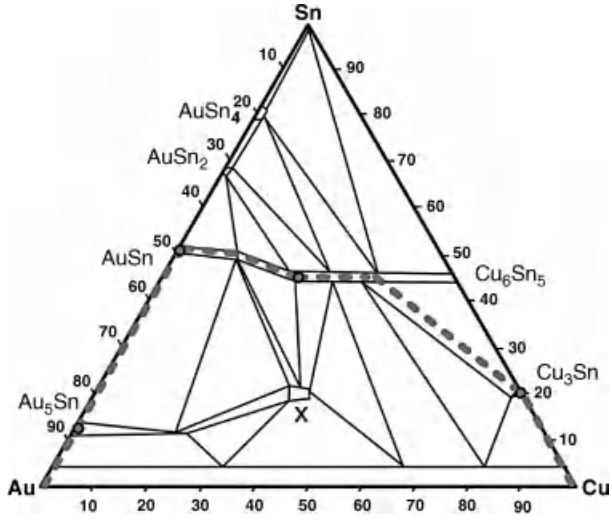

Figure 2.41 *Reaction paths of the Au/Sn(8 μm)/Cu couple reacted at 210° C superimposed with the Sn-Au-Cu isothermal section.*

References

1. Abtew, M. and Selvaduray, G. (2000) Lead-free solders in microelectronics. *Mater. Sci. Eng., R*, **27**, 95–141.
2. Zeng, K. and Tu, K.N. (2002) Six cases of reliability study of Pb-free solder joints in electronic packaging technology. *Mater. Sci. Eng., R*, **38**, 55–105.
3. Laurila, T., Vuorinen, V., and Kivilahti, J.K. (2005) Interfacial reactions between lead-free solders and common base materials. *Mater. Sci. Eng., R*, **49**, 1–60.
4. Frear, D.R., Jang, J.W., Lin, J.K., and Zhang, C. (2001) Pb-free solders for flip-chip interconnects. *JOM*, **53**, 28–32.
5. Zhao, J.C. (ed.) (2007) *Method for Phase Diagram Determination*, Elsevier, Oxford, UK.
6. Hillert, M., (1998) *Phase Equilibria, Phase Diagrams and Phase Transformations*, Cambridge University Press, New York.
7. Lukas, H.L., Fries, S.G., and Sundman, B. (2007) *Computational Thermodynamics: the Calphad Method*, Cambridge University Press, New York.
8. Chang, Y.A. and Oates, W.A. (2010) *Materials Thermodynamics*, John Wiley & Sons, Hoboken, New Jersey.
9. Prince, A. (1966) *Alloy Phase Equilibria*, Elsevier, Amsterdam.
10. Rhines, F.N. (1956) *Phase Diagrams in Metallurgy: Their Development and Application*, McGraw-Hill, New York, USA.
11. Chen, S.W. and Lin, S.K. (2006) Electric current-induced abnormal Cu/γ-InSn4 interfacial reactions. *J. Mater. Res.*, **21**(12), 3065–3071.
12. Chen, S.W., Chen, P.Y., Chiu, C.N. *et al.* (2008) Phase equilibria of the Sn-Sb-Ag ternary system (I): experimental. *Metall. Mater. Trans. A*, **39**, 3191–3198.
13. Liu, X.J., Kinaka, M., Takaku, Y. *et al.* (2005) Experimental investigation and thermodynamic calculation of phase equilibria in the Sn-Au-Ni system. *J. Electron. Mater.*, **34**(5), 670–679.
14. Yang, C.F., Chen, F.L., Gierlotka, W. *et al.* (2008) Thermodynamic properties and phase equilibria of Sn-Bi-Zn ternary alloys. *Mater. Chem. Phys.*, **112**, 94–103.
15. Gierlotka, W., Chen, S.W., and Lin, S.K. (2007) Thermodynamic description of the Cu-Sn system. *J. Mater. Res.*, **22**, 3158–3165.
16. Liu, X.J., Liu, H.S., Ohnuma, I. *et al.* (2001) Experimental determination and thermodynamic calculation of the phase equilibria in the Cu-In-Sn system. *J. Electron. Mater.*, **30**(9), 1093–1103.
17. Moser, Z., Gasior, W., Pstrus, J. *et al.* (2001) Studies of the Ag-In phase diagram and surface tension measurements. *J. Electron. Mater.*, **30**(9), 1120–1128.
18. ASM Handbook, vol. 3, Alloys Phase Diagrams, ASM (1998), Ohio, USA.
19. Chen, S.W. and Yen, Y.W. (2001) Interfacial reactions in the Sn-Ag/Au couples. *J. Electron. Mater.*, **30**, 1133–1137.
20. Yen, Y.W. and Chen, S.W. (2004) Phase equilibria of the Ag-Sn-Cu ternary system. *J. Mater. Res.*, **19**(8), 2298–2305.
21. Loomans, M.E. and Fine, M.E. (2000) Sn-Ag-Cu eutectic temperature and composition. *Metall. Mater. Trans. A*, **31**, 1155–1162.
22. Moon, K.W., Boettinger, W.J., Kattner, U.R. *et al.* (2000) Experimental and thermodynamic assessment of Sn-Ag-Cu solder alloys. *J. Electron. Mater.*, **29**, 1122–1136.
23. Ohnuma, I., Miyashita, M., Anzai, K. *et al.* (2000) Phase equilibria and the related properties of Sn-Ag-Cu based Pb-free solder alloys. *J. Electron. Mater.*, **29**, 1137–1144.
24. Gebhardt, E. and Petzow, G. (1959) The constitution of the silver-copper-tin system. *Z. fuer Metallkunde*, **50**, 597–605.
25. Fedorov, V.N., Osintsev, O.E., and Yuskina, E.T. (1981) *Phase Diagrams of Metallic Systems, 1964–1982* (ed.N.V. Ageev) Acad. Sci. USSR, Moscow.

26. Miller, C.M., Anderson, I.E., and Smith, J.F. (1994) A viable tin-lead solder substitute: Sn-Ag-Cu. *J. Electron. Mater.*, **23**(7), 595–601.
27. Chen, S.W. and Yen, Y.W. (1999) Interfacial reactions in Ag-Sn/Cu couples. *J. Electron. Mater.*, **28**(11), 1203–1208.
28. Hsu, H.F. and Chen, S.W. (2004) Phase equilibria of the Sn-Ag-Ni ternary system and interfacial reactions at the Sn-Ag/Ni joints. *Acta Mater.*, **52**, 2541–2547.
29. Prince, A., Raynor, G.V., and Evans, D.S. (1990) *Phase Diagrams of Ternary Gold Alloys*, Institute of Metals, London.
30. Kattner, U.R. and Boettinger, W.J. (1994) On the Sn-Bi-Ag ternary phase diagram. *J. Electron. Mater.*, **23**(7), 603–610.
31. Chen, S.W., Wu, H.J., Huang, Y.C., and Gierlotka, W. (2010) Phase equilibria and solidification of ternary Sn-Bi-Ag alloys. *J. Alloys Compd.*, **497**, 110–117.
32. Lee, B.J., Hwang, N.M., and Lee, H.M. (1997) Prediction of interface reaction products between Cu and various solder alloys by thermodynamic calculation. *Acta Mater.*, **45**, 1867–1874.
33. Huang, Y.C., Gierlotka, W., and Chen, S.W. (2010) Sn-Bi-Fe thermodynamic modeling and Sn-Bi/Fe interfacial reactions. *Intermetallics*, **18**(5), 984–991.
34. Lee, J.I., Chen, S.W., Chang, H.Y., and Chen, C.M. (2003) Reactive wetting between molten Sn-Bi and Ni substrate. *J. Electron. Mater.*, **32**, 117–122.
35. Karlsen, O.B., Kjekshus, A., and Roest, E. (1992) The ternary system gold-copper-tin. *Acta Chem. Scand.*, **46**, 147–156.
36. Wang, C.H. and Chen, S.W. (2003) Isothermal section of the ternary Sn-Cu-Ni system and interfacial reactions in the Sn-Cu/Ni couples at 800 °C. *Metall. Mater. Trans. A*, **34**, 2281–2287.
37. Lin, C.H., Chen, S.W., and Wang, C.H. (2002) Phase equilibria and solidification properties of Sn-Cu-Ni alloys. *J. Electron. Mater.*, **31**, 907–915.
38. Liu, H.S., Liu, C., Ishida, K., and Jin, Z.P. (2003) Thermodynamic modeling of the Au-In-Sn system. *J. Electron. Mater.*, **32**, 1290–1296.
39. Lin, S.K. and Chen, S.W. (2006) Interfacial reactions in the Sn-20at.% In/Cu and Sn-20at.% In/Ni couples at 160 °C. *J. Mater. Res.*, **21**(7), 1712–1717.
40. Liu, X.J., Inohana, Y., Takaku, Y. *et al.* (2002) Experimental determination and thermodynamic calculation of the phase equilibria and surface tension in the Sn-Ag-In system. *J. Electron. Mater.*, **31**, 1139–1151.
41. Huang, C.Y. and Chen, S.W. (2002) Interfacial reactions in In-Sn/Ni couples and phase equilibria of the In-Sn-Ni system. *J. Electron. Mater.*, **31**(2), 152–160.
42. Oh, C.S., Shim, J.H., Lee, B.J., and Lee, D.N. (1996) A thermodynamic study on the Ag-Sb-Sn system. *J. Alloys Compd.*, **238**, 155–166.
43. Moser, Z., Gasior, W., Pstrus, J. *et al.* (2004) Surface tension and density measurements of Sn-Ag-Sb liquid alloys and phase diagram calculations of the Sn-Ag-Sb ternary system. *Mater. Trans.*, **45**, 652–660.
44. Chen, S.W., Chen, C.C., Gierlotka, W. *et al.* (2008) Phase equilibria of the Sn-Sb binary system. *J. Electron. Mater.*, **37**(7), 992–1002.
45. Kim, J.H., Jeong, S.W., and Lee, H.M. (2002) A thermodynamic study of phase equilibria in the Au-Sb-Sn solder system. *J. Electron. Mater.*, **31**(6), 557–563.
46. Ohtani, H., Miyashita, M., and Ishida, K. (1999) Thermodynamic study of phase equilibria in the Sn-Ag-Zn system. *J. Jpn. Inst. Met.*, **63**(6), 685–694.
47. Malakhov, D.V., Liu, X.J., Ohnuma, I., and Ishida, K. (2000) Thermodynamic calculation of phase equilibria of the Bi-Sn-Zn system. *J. Phase Equilib.*, **21**(6), 514–520.
48. Chou, C.Y. and Chen, S.W. (2006) Phase equilibria of the Sn-Zn-Cu ternary system. *Acta Mater.*, **54**(9), 2393–2400.
49. Chen, S.W., Chiu, C.N., and Hsieh, K.C. (2007) Phase equilibria of the Sn-Ag-Cu-Ni quaternary system at 210 °C. *J. Electron. Mater.*, **36**(3), 197–206.

50. Chen, S.W. and Chang, C.A. (2004) Phase equilibria of the Sn-Ag-Cu-Ni quaternary system at the Sn-rich corner. *J. Electron. Mater.*, **33**(10), 1071–1079.
51. COST 531 database, (2007), http://www.springerlink.com/content/p4684p0t15060148/.
52. NIST solder database, (1999), http://www.metallurgy.nist.gov/phase/solder/solder.html.
53. ADAMIS microsolder database, (2006), http://www.materials-design.co.jp/adamis/msolder.htm.
54. Pandat, CompuTherm LLC, 437 S. Yellowstone Dr. Suite 217 Madison, WI 53719 USA, (2011).
55. ThermoCalc, Foundation Computational Thermodynamic, Stockholm, Sweden, (2006).
56. Chen, S.W., Wang, C.H., Lin, S.K. *et al.* (2007) Phase transformation and microstructural evolution in solder joints. *JOM*, **59**(1), 39–43.
57. Lin, S.K., Yang, C.F., Wu, S.H., and Chen, S.W. (2008) Liquidus projection and solidification of the Sn-In-Cu ternary alloys. *J. Electron. Mater.*, **37**(4), 498–506.
58. Huang, Y.C., Chen, S.W., Chou, C.Y., and Gierlotka, W. (2009) Liquidus projection and thermodynamic modeling of Sn-Zn-Cu ternary system. *J. Alloys Compd.*, **477**, 283–290.
59. Flemings, M.C. (1974) *Solidification Processing*, McGraw-Hill, New York.
60. Allen, W.P. and Perepezko, J.H. (1991) Solidification of undercooled tin-antimony peritectic alloys: part I. Microstructural evolution. *Metall. Trans. A*, **22**, 753–764.
61. Turnbull, D. (1950) Kinetics of heterogeneous nucleation. *J. Chem. Phys.*, **18**, 198–203.
62. Kim, D.H., Cho, M.G., Seo, S.K., and Lee, H.M. (2009) Effects of Co addition on bulk properties of Sn-3.5Ag solder and interfacial reactions with Ni-P UBM. *J. Electron. Mater.*, **38**, 39–45.
63. Huang, Y.C., Chen, S.W., and Wu, K.S. (2010) Size and substrate effects upon undercooling of Pb-free solders. *J. Electron. Mater.*, **39**, 109–114.
64. Perepezko, J.H. (2005) Nucleation controlled phase selection during solidification. *Mater. Sci. Eng., A*, **A413**, 389–397.
65. Anderson, I.E., Walleser, J., and Harringa, J.L. (2007) Observations of nucleation catalysis effects during solidification of SnAgCuX solder joints. *JOM*, **59**, 38–43.
66. Chen, S.W., Chen, Y.K., Wu, H.J. *et al.* (2010) Co solubility in Sn and Interfacial reaction in Sn-Co/Ni couples. *J. Electron. Mater.*, **39**, 2418–2428.
67. Vianco, P.T. and Frear, D.R. (1993) Issues in the replacement of lead-bearing solders. *JOM*, **45**(7),14–19.
68. Melton, C. (1993) The effect of reflow process variables on the wettability of lead-free solders. *JOM*, **45**(7), 33–35.
69. Glazer, J. (1995) Metallurgy of low temperature Pb-free solders for electronic assembly. *Int. Mater. Rev.*, **40**, 65–93.
70. Plumbridge, W.J. (1996) Solders in electronics. *J. Mater. Sci.*, **31**, 2501–2514.
71. Hwang, C.W., Suganuma, K., Lee, J.G., and Mori, H. (2003) Interface microstructure between Fe-42Ni alloy and pure Sn. *J. Mater. Res.*, **18**(5), 1202–1210.
72. Huang, Y.C., Chen, S.W., Gierlotka, W. *et al.* (2007) Dissolution and interfacial reactions of Fe in molten Sn-Cu and Sn-Pb solders. *J. Mater. Res.*, **22**(10), 2924–2929.
73. Chen, S.W., Chen, P.Y., and Wang, C.H. (2006) Lowering of Sn-Sb alloy melting points caused by substrate dissolution. *J. Electron. Mater.*, **35**(11), 1982–1985.
74. Chen, S.W., Wu, S.H., and Lee, S.W. (2003) Interfacial reactions in the Sn-(Cu)/Ni, Sn-(Ni)/Cu, and Sn/(Cu,Ni) systems. *J. Electron. Mater.*, **32**(11), 1188–1194.
75. Tu, K.N. and Thompson, R.D. (1982) Kinetics of interfacial reaction in bimetallic copper-tin thin films. *Acta Metall.*, **30**, 947–952.
76. Bartels, F., Morris, J.W. Jr., Dalke, G., and Gust, W. (1994) Intermetallic phase formation in thin solid-liquid diffusion couples. *J. Electron. Mater.*, **23**(8), 787–790.
77. Bader, S., Gust, W., and Hieber, H. (1995) Rapid formation of intermetallic compounds by interdiffusion in the Cu-Sn and Ni-Sn systems. *Acta Metall. Mater.*, **43**(1), 329–337.

78. Su, L.H., Yen, Y.W., Lin, C.C., and Chen, S.W. (1997) Interfacial reactions in molten Sn/Cu and molten In/Cu couples. *Metall. Mater. Trans. B*, **28**, 927–941.
79. Tsai, J.Y., Chang, C.W., Ho, C.E. *et al.* (2006) Microstructure evolution of gold-tin eutectic solder on Cu and Ni substrates. *J. Electron. Mater.*, **35**(1), 65–71.
80. Nathan, A. and Chalamala, B.R. (2005) Special issue on flexible electronics technology, Part 1: Systems and applications. *Proc IEEE*, **93**, 1235–1238.
81. Nathan, A. and Chalamala, B.R. (2005) Special issue on flexible electronics technology, Part II: Materials and devices. *Proc. IEEE*, **93**, 1391–1393.
82. Baggerman, A.F.J. and Batenburg, M.J. (1995) Reliable Au-Sn flip-chip bonding on flexible prints. *IEEE Trans. Comp., Packag., Manufact. Technol. B*, **18**, 257–263.
83. Tjandra, J., Wong, C.L., How, J., and Peana, S. (1997) Au-Sn Microsoldering on Flexible Circuit. IEEE/CPMT Electronic Packaging Technology Conference, pp. 52–57.
84. Chang, C.W., Lee, Q.P., Ho, C.E., and Kao, C.R. (2006) Cross-interaction between Au and Cu in Au/Sn/Cu ternary diffusion couples. *J. Electron. Mater.*, **35**, 366–371.
85. Yang, C.F. and Chen, S.W. (2010) Interfacial reactions in Au/Sn/Cu sandwich specimens. *Intermetallics*, **18**(4), 672–678.

3

Phase Diagrams and Alloy Development

Alan Dinsdale[1], *Andy Watson*[2], *Ales Kroupa*[3], *Jan Vrestal*[4], *Adela Zemanova*[3], *and Pavel Broz*[4]

[1] *National Physical Laboratory, Teddington, UK*
[2] *Institute for Materials Research, SPEME, University of Leeds, UK*
[3] *Institute of Physics of Materials, AS CR, Brno, Czech Republic*
[4] *Institute of Chemistry, Masaryk University, Brno, Czech Republic*

3.1 Introduction

Phase diagrams have been around for more than 100 years. In Alan Prince's seminal work entitled *Alloy Phase Equilibria* [1], he writes that 'A metallurgist has been defined as someone who thinks in terms of phase diagrams'. He then goes on to write 'Whether one accepts this statement or not, it is self-evident that an ability to interpret phase equilibria is essential to the professional metallurgist'. This last sentence may seem contentious, but it is a fact that the understanding of phase diagrams and phase equilibria has been taught to materials undergraduates for many years, and the subject remains the bedrock of materials research.

At its simplest, the physical properties of materials are governed by microstructure, which to a great extent is in turn governed by phase assemblage. A phase diagram tells the materials scientist which phases are expected to be present under a certain set of conditions of composition, temperature and pressure. Even though, in practice, many materials may be used in a nonequilibrium or metastable state, the phase diagram provides a firm basis for materials design and process development. Underpinning the phase diagram are the *thermodynamic properties* of the material, and once these are known, it is possible to

Lead-free Solders: Materials Reliability for Electronics, First Edition. Edited by K. N. Subramanian.

compute the equilibrium or metastable equilibrium states for any set of conditions. But the availability of sufficient computational power and software to make such complex calculations is a relatively recent development, and traditionally, phase diagrams have been determined through experimentation.

One of the first published phase diagrams was that by Heycock and Neville in the early twentieth century [2]. Inspired by earlier work of Roozeboom [3] and Roberts-Austen and Stansfield [4], they combined cooling curve analysis (which had been in use for a number of years) with metallographic study of solidified Cu-Sn alloys of different compositions. By plotting arrests on the cooling curves with respect to composition, they were able to produce the Cu-Sn phase diagram. They correctly deduced that for all compositions and temperatures above the 'liquidus curve' the alloys are completely liquid, those below the 'solidus curve' are completely solid, and in between the two curves, there is a mixture of the two phases. They were also the first researchers to coin the term 'solid solution' for a solid alloy of '. . .two components (*that*) are capable of being as uniformly mixed as in a liquid solution . . . (*with*) the possibility of continuous variation in the percentage composition of the mixture.' This, what has been considered as a standard work on the subject, led to an explosion in the field, with large experimental programmes being initiated in many countries around the world, as the importance and applicability of a pictorial representation of phase equilibrium became fully appreciated. It is interesting that the quite basic experimental techniques used by Heycock and Neville became standard for the determination of phase diagrams, and they are still in use today, albeit in a more *refined* form. As the effort expended on the study of phase diagrams increased, there was naturally some duplication, which necessitated some form of *assessment* of the phase diagrams originating from different sources or maybe produced using different measurement techniques. This critical evaluation of experimental phase diagram studies is very important for the production of a reliable phase diagram and resulted in a number of highly successful assessment programmes, for binary and ternary systems. Most notable of these were the compendia produced by The Institute of Metals (now the Institute of Materials, Minerals and Mining) in the UK, the ASM (American Society of Metals) and MSI (Materials Science International) based in Germany [5–17]. This effort is ongoing.

An important development in the advancement of phase diagrams was due to the pioneering work of Gibbs and Van Laar [18, 19] in the late nineteenth and early twentieth century. With the derivation of a thermodynamic basis for phase equilibrium a clear link between the thermodynamic properties of an alloy system (or, in principle one of any material type) and its phase diagram exists. Thus, if the thermodynamic properties of the different types of possible phases in a system are known, it is possible to derive the point of equilibrium in the system that is the state that gives the lowest Gibbs energy, and thus calculate the phase diagram. For example tin, in its various crystal forms (phase) will have different thermodynamic properties, such as heat capacity, enthalpy and entropy. These individual properties can be derived from a Gibbs energy expression for each phase, which will be a function of temperature and pressure. By minimizing these functions with respect to temperature and pressure it is possible to calculate the unary phase diagram for tin (Figure 3.1).

Also included in the plot are experimental data points. The regions, or phase fields, bounded by the calculated curves indicate the nature of the stable structure of tin at different temperatures and pressures. The lines themselves represent temperatures and pressures that result in two coexisting phases. The triple point where three phase boundaries meet indicates an invariant point; the single temperature and pressure at which three forms of tin can coexist.

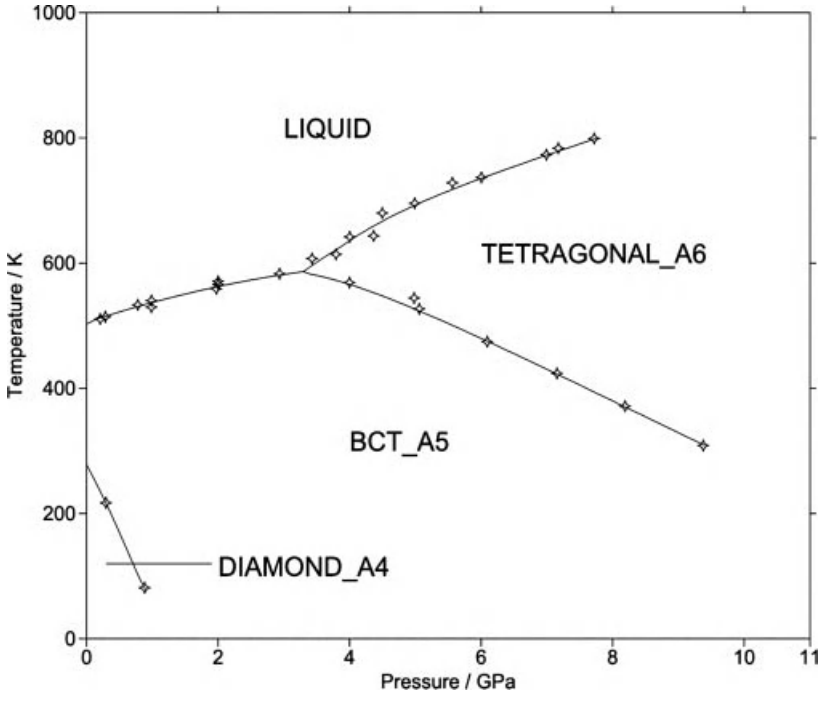

Figure 3.1 *Calculated tin phase diagram.*

Phase diagrams involving 2 components are known as binary phase diagrams, an example of which is given in Figure 3.2. Adding a component to the system should result in needing three dimensions for the phase diagram, but it is often sufficient to show the diagrams at fixed pressure resulting in the need for only two dimensions.

Figure 3.2 shows the lead-tin phase diagram and this indicates the nature of the coexisting phases as a function of system temperature and composition. It is immediately apparent that adding tin to liquid lead (or vice versa) results in a depression of its freezing point leading to a freezing point minimum. At this invariant point, we have three phases in equilibrium, and the reaction associated with this is called a *eutectic reaction.* It is also clear that freezing an alloy of this composition leads directly to a completely solid alloy. This composition is that of traditional electrician's solder, which is in contrast to a range of alloys richer in lead (2 parts lead to 1 part tin, approximately), which freeze over a large temperature range, known as plumber's solders.

The binary phase diagram can be calculated using thermodynamic expressions in the same way as the unary phase diagrams, but in this case we can use expressions as a function of composition as well as temperature, which is necessary for solution phases. Minimization of the system Gibbs energy with respect to composition at different temperatures leads directly to the phase diagram.

Figure 3.3 shows the silver-copper phase diagram together with a second diagram showing Gibbs-energy curves for the liquid and FCC phases at a temperature of 778 °C. The stable phase at any composition should be identified as that which has the minimum Gibbs

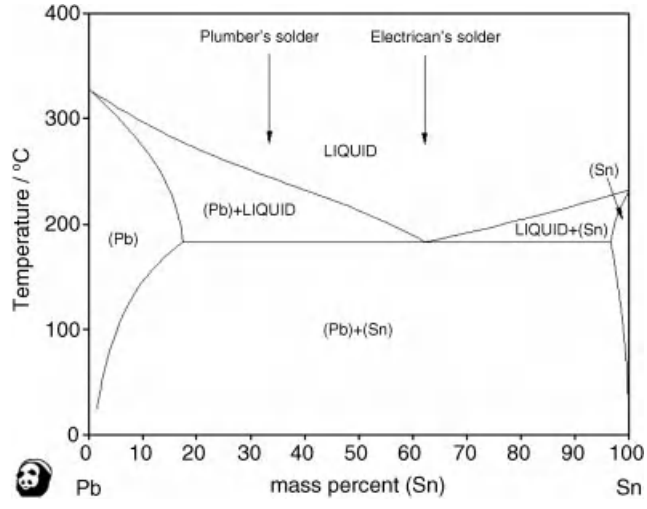

Figure 3.2 *Phase diagram for the lead-tin system.*

energy. However, where the Gibbs-energy curves cross, the minimum in the system Gibbs energy actually lies on tangents to these curves, and the compositions where tangents touch the curves give points on the phase boundaries of the phase diagram, giving a two-phase mixture. In Figure 3.3, there are two Gibbs-energy curves; one for FCC (both silver and copper have the FCC structure) and one for liquid. It can be seen that at 778 °C it is possible to draw a tangent to both curves with three points of contact, which correspond to the compositions of the Cu and Ag-solid solutions in equilibrium with the liquid phase at the eutectic temperature.

The method whereby phase equilibria and phase diagrams can be calculated from molar Gibbs energy expressions is known as the *Calphad* (CALculation of PHAse Diagrams) technique and came to prominence following the publication of *Computer Calculation of Phase Diagrams* by Kaufman and Bernstein [20]. This is an extremely powerful technique that is easily extended to multicomponent systems, which in principle is only limited by computer power, the software used and the availability of thermodynamic data. By having a set of Gibbs-energy expressions for any number of phases it is possible to predict and calculate phase equilibria for a complex set of conditions. With appropriate databases and software it is therefore possible to carry out with relative ease a vast number of 'virtual' experiments with a corresponding saving in resources. The *Calphad technique* gives us 'Phase diagrams for the computer age'.

3.2 Computational Thermodynamics as a Research Tool

3.2.1 Concept of the Calculation of Phase Diagrams for Multicomponent Systems

The *Calphad* approach is based on the sequential modelling of the thermodynamic properties of multicomponent systems, starting from the simplest, the Gibbs energy of phases of the pure elements, followed by its variation as further components (elements) are

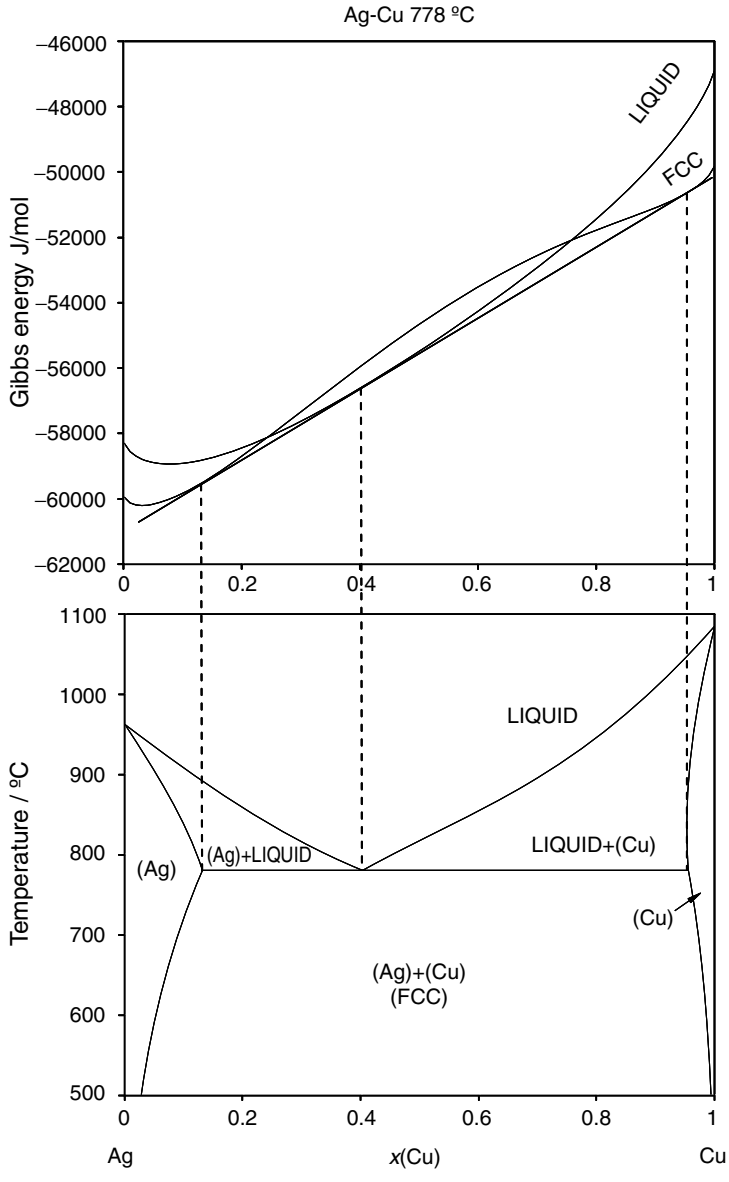

Figure 3.3 *Tangent–intercept construction.*

added. The Gibbs-energy parameters of phases take the form of polynomial coefficients and are fundamental for the calculations of phase diagrams. The thermodynamic properties of a binary system can be calculated using Gibbs-energy expressions comprising contributions for both elements in all of the phases existing in the system, and their mutual interaction. It is possible to model such a system with high precision if reliable experimental data are available that describe both the thermodynamic properties of the individual phases (e.g. heat

capacity, enthalpies of formation or mixing, activities) and the phase equilibria (e.g. invariant temperatures, compositions and amounts of phases). By combining robust thermodynamic descriptions of binary alloy systems, it is possible to predict phase equilibria in ternary and higher-order systems. The deviation of real behavior of the system from the prediction can be minimized by adding appropriate higher-order parameters, describing additional interactions between the elements, as long as these extra parameters do not affect the modelling of the lower-order systems.

3.2.2 Modelling of the Gibbs Energy of the System

For any thermodynamic modelling to be successful it is crucial that it is based on a reliable description of the Gibbs energy of an element or a compound (constituents of the phase) in a crystallographic structure occurring in the system studied, either stable or metastable. In the *Calphad* method, *the Gibbs energy is needed also for crystallographic structures that may appear in the system of interest in which the element or compound does not exist*.

Several methods may be used to obtain the necessary data. If the structure exists in any higher-order system, the data can be derived by extrapolation of measured thermodynamic properties back to the pure component. The second possibility is to model it during the assessment (the optimization of parameters to the thermodynamic functions) of a higher-order system where the phase with the appropriate structure exists and the element dissolves into it. Another possibility, allowed by a rapid development of the computer power and mathematical methods, is the application of *ab-initio* electronic structure calculations to evaluate, for example, the energy of the element in phase in question with respect to the stable phases at 0 K [21].

As outlined in the introduction, a state that, for a given set of conditions (concentration, pressure and temperature), has a minimum total Gibbs energy, may be considered as being in thermodynamic equilibrium. This state may consist of a single phase or a number of phases. The total Gibbs energy of the system may be expressed as the weighted sum of Gibbs energies of the individual phases. The individual Gibbs energy of any phase, G_m, can be expressed as a sum of different contributions:

$$G_m = G_{ref} + G_{id} + G_E + G_{mag} + G_P + \ldots$$

where G_{ref} (reference) is the weighted sum of the molar Gibbs energies of all the constituents in the crystallographic structure corresponding to the structure of the phase in question, relative to their chosen reference states, G_{id} is a contribution to the Gibbs energy from ideal random mixing of the constituents on the crystal lattice, G_E is the excess Gibbs energy, which describes the influence of nonideal behavior on the thermodynamic properties of a phase. In this context, a constituent may be thought of as an entity that mixes in a solution, for example, an element.

Additional terms may be necessary for an accurate description of the Gibbs energy. For example, G_{mag} is the magnetic contribution described in detail by [22] and G_p is an additional term to account for variation of Gibbs energy with pressure.

This general principle applies to a wide variety of materials and types of phases, ranging from simple solid solutions to phases with complex crystallography, such as gamma brass, or liquid phases that show a strong tendency to form molecular species. This approach even allows modelling of particularly complicated phases such as those with order–disorder

transformations. The authors recommend the interested reader to consult [22–26] for a more detailed description.

The thermodynamic equilibrium of the system is calculated through a constrained minimization of the total Gibbs energy for a given temperature, pressure and overall composition. This technique is used in all of the available software packages for the modelling of thermodynamic properties and calculation of phase diagrams for multicomponent systems.

3.2.3 Critical Assessment of Thermodynamic Properties

A reliable set of the Gibbs-energy model parameters is the key to the valid calculation of phase diagrams needed for lead-free solder design and exploitation (in fact, also for any other class of materials). The procedure for deriving these values, known as the assessment procedure, consists initially of summarizing all the relevant experimental and theoretical thermodynamic properties and phase-equilibrium quantities for the system under study. The selection of a set of consistent experimental data from all of the data available is the most important step in the assessment procedure, particularly as the scientific literature often contains different experimental results for the same measured quantity (phase equilibria or thermodynamic properties) and the assessor must decide which should be used.

Following this critical evaluation of the experimental data, a dataset is prepared that is then used as a basis for the optimization of the model parameters using a least-square minimization process. These optimized parameters result in the best agreement between calculated and experimental information.

The choice of the model to represent the Gibbs energy of the phase should be based on crystallographic data, if possible, which makes it easier to take physical properties of the phase into account and makes extrapolation from binary to higher-order systems more reliable.

Optimization, that is the derivation of the best fit to the experimental properties, is carried out by a step-by-step basis. First, it is important to derive a set of parameters that can roughly reproduce the main features of the experimental data. In the second step, using an optimization module within the thermodynamic software package (e.g. PARROT in ThermoCalc [27] or the Assessment module in MTDATA [28]), the parameters are fine tuned to the selected experimental data. Final testing of the derived parameters is essential because mathematical artefacts may occur as a result of the optimization process (e.g. incorrect appearance or disappearance of phases in the phase diagram). A final test of the results of the assessment should be carried out in order to verify that the final dataset is in agreement with all of the experimental properties, that the calculated thermodynamic properties are within reasonable limits, and that the dataset extrapolates reasonably to higher-order systems or higher or lower temperatures.

3.3 Thermodynamic Databases – the Underlying Basis of the Modelling of Phase Diagrams and Thermodynamic Properties, Databases for Lead-Free Solders

Successful modelling of thermodynamic properties and phase equilibria of multicomponent systems depends not only on the existence of theoretically sound methods and software, but

also on the existence of reliable and consistent sources of critically assessed data in the form of thermodynamic databases. The *Calphad* method was described in an earlier part of this chapter, including basic information about models for describing the Gibbs energy of phases and the process for obtaining the necessary parameters of the Gibbs-energy description through thermodynamic assessment.

The parameters for the Gibbs energy are then collected in databases, which are usually orientated towards specific groups of materials (steels, Ni-based alloys, etc.). There are many specialized databases available for the scientific and engineering community, allowing modelling and development of advanced materials, lead-free solders being very important amongst them. This need for such data for lead-free solders is driven by the great practical importance of soldering processes in the electronics industry and by strong legislative pressure arising from possible health hazards associated with the use of 'classical' soldering materials.

3.3.1 Creation of the Thermodynamic Databases

Thermodynamic databases cannot be just collections of critically assessed thermodynamic data for binary and ternary systems gleaned from the scientific literature. Even if these assessments individually reproduce their respective phase diagrams and thermodynamic properties well, a collection of such assessments may contain inconsistencies and present problems, preventing their use in the prediction and calculation of properties in multicomponent systems. This can be caused by different approaches adopted by the individual assessors. Therefore, several important rules must be followed in the process of the creation of any thermodynamic database, and these are described in subsequent parts of this chapter.

3.3.2 Three Conditions of Consistency

Generally, there are three key conditions that must be fulfilled when attempting to create any self-consistent and reliable thermodynamic database. The thermodynamic database must be consistent with respect to:

- the models used to represent the temperature, pressure and composition dependence of the Gibbs energy of a given phase including any additional contributions to it (e.g. related to magnetic properties, surface energy contribution);
- the crystallographic models used for the same or similar crystallographic structure, existing in different systems (binary, ternary, etc.), and the specific names assigned to these phases;
- the data used for the description of the Gibbs energy of an element or compound in a given crystallographic structure, either stable or metastable, in all the systems in the database.

These conditions will be described in more detail below for alloy systems.

3.3.2.1 First Condition of Consistency

Most assessments published today use the Redlich–Kister expression [29] for the concentration dependence of excess Gibbs energy, extended by Muggianu [30] to ternary systems. Alternative composition dependence relationships, for example the modified quasichemical model [31], are incompatible with this formalism. Other formalisms can be used for ternary systems with specific properties, for example the Kohler equation or Toop equation [32].

Therefore, the type of the polynomials used for the expression of excess Gibbs energy has to be checked and the same models applied throughout the database.

The first condition of consistency has to be also checked in connection with the modelling of chemical/short-range ordering (SRO), where several approaches can be used [33]. The sets of parameters for such phases are not compatible when different approaches are used to model the SRO in different assessments.

3.3.2.2 Second Condition of Consistency

The second condition of consistency is usually the most difficult to be fulfilled and careful checks have to be carried out on each assessment that may be included in the database. There are no general rules about how the character of the phase (terminal solid solution, intermediate phases, SRO) and its structural characteristics (crystallographic structure, composition, solubility range) should be described by the individual phase models. Assessors are free to choose the model for the description of a particular phase and to allocate any name to it.

There is general consistency about the way in which the liquid and some terminal solid-solution phases are modelled, where random substitutional mixing of elements is usually assumed within the lattice. Nevertheless, even here some other models are used when the physical properties of the phase demands it, for example, it may be necessary to use the associate model for liquid [25], if the existence of such features is found by experiment or when the thermodynamic properties can't be modelled by a simpler description.

An even more complex situation exists in the case of the sublattice model – implemented in the compound energy formalism [34, 35], which is widely used for metallic systems. Use of this model gives the assessors complete freedom in the selection of the number of sublattices, their ratios, site occupancies, and so on, albeit constrained by any experimental crystallographic information for the phase, for example, number of independent positions in the lattice, mixing of species in different lattice positions and so on.

The main complication with inconsistencies in modelling individual phases can appear when lower-order systems assessed by different assessors are used as a basis for further work on higher-order systems. A typical example of such a problem is the complete solubility between intermediate phases existing in two subsystems (e.g. A-B and A-C) of the ternary system A-B-C. If this complete solubility had not been anticipated during the assessment of both subsystems, then the phase exhibiting complete solubility may be modelled differently by the assessors in such a way as to create difficulties in extending the solubility into the ternary system. Careful adjustment of the models and names of the affected phases must be carried out, sometimes forcing complete reassessment of one or more of the lower-order systems. The In-Ni-Sb system can be shown as an example of such case. In this case, there is complete solubility between Ni_2In and NiSb phases, existing in In-Ni and Ni-Sb binary systems eventually, which was reported by Richter [58]. A further complication is caused by the fact, that the phases have different solubility ranges in the binary systems and even different crystallographic structures. The structure of the Ni_2In-ζ phase is characterized by the Pearson symbol *hP*6, the structure of NiSb phase by *hP*4. Both structures are closely related, which allows complete solubility in the ternary system. Nevertheless, in the assessments of the binary systems both phases had been modelled by different and incompatible models. Therefore, an attempt to reproduce the phase diagram of the

In-Ni-Sb system requires the reassessment of at least one of the subsystems, and the careful selection of a model that would allow the joint modelling of not only these two phases, but also all other phases with such crystallographic structures in any other system of interest.

An even more complex situation is found for the family of γ-brass phases, especially in connection with the Al-Cu-Zn system [36].

3.3.2.3 Third Condition of Consistency

The third major problem is related to the description of the Gibbs energy for an element or compound in a given crystallographic structure, either stable or metastable. This Gibbs energy is typically expressed as its Gibbs energy of formation from the selected standard states of one or more component elements. For an element, this becomes the difference between the Gibbs energy in the required structure and that in its selected standard state (so-called lattice stability). If the same element or compound exists in different binary and ternary systems, it is necessary to carry out a careful check of compatibility between all the datasets. The actual value of the Gibbs energy may differ significantly not only between different assessors, but also between different versions of the same database due to a refinement of these basic data over a period of time.

An example of such an inconsistency is shown in Figure 3.4. Here the phase diagram for the Sb-Sn system, calculated according to the data of Oh [37], is shown in Figure 3.4a. The phase diagram calculated using the same data, except for the use of a more recent lattice stability of pure Sb in the metastable BCT_A5 structure, is shown in Figure 3.4b. Oh [37] used the value of this parameter from version 1 of the SGTE Unary database [38], where this value had been estimated. As a result of assessments of data for other systems the value of this parameter has been changed in subsequent versions of the database [60], resulting in incompatibility with all older assessments such as that given in [37]. It was therefore necessary to reassess the thermodynamic description of the Sb-Sn system, using the more recent value for this lattice stability and changing the data for the concentration dependence of the Gibbs energy in the BCT_A5 phase to maintain agreement with experimental data. The result of such a reassessment is shown in Figure 3.4c. It is clear that the agreement is once again very good.

3.3.3 Specialized Databases for the Modelling of Thermodynamic Properties of Systems Relevant for Lead-Free Solders

Several databases covering the systems relevant for the development of new lead-free solder materials are currently available for use by the scientific and engineering community. The oldest one was developed at The National Institute of Standards and Technology [40] and covers 5 elements (Sn, Ag, Bi, Cu, Pb), 10 assessed binary systems and 10 assessed ternary systems. This database is no longer being developed.

Also available is the ADAMIS database, developed in Japan for calculating phase diagrams for systems suitable for microsoldering by [41, 42]. The ADAMIS database contains 8 elements (Ag, Bi, Cu, In, Pb, Sb, Sn and Zn) and includes critically assessed data for all the component binary systems and a number of important ternary systems covering complete ranges of composition. This database is still being developed, through the incorporation of additional elements relevant to various types of lead-free soldering technologies.

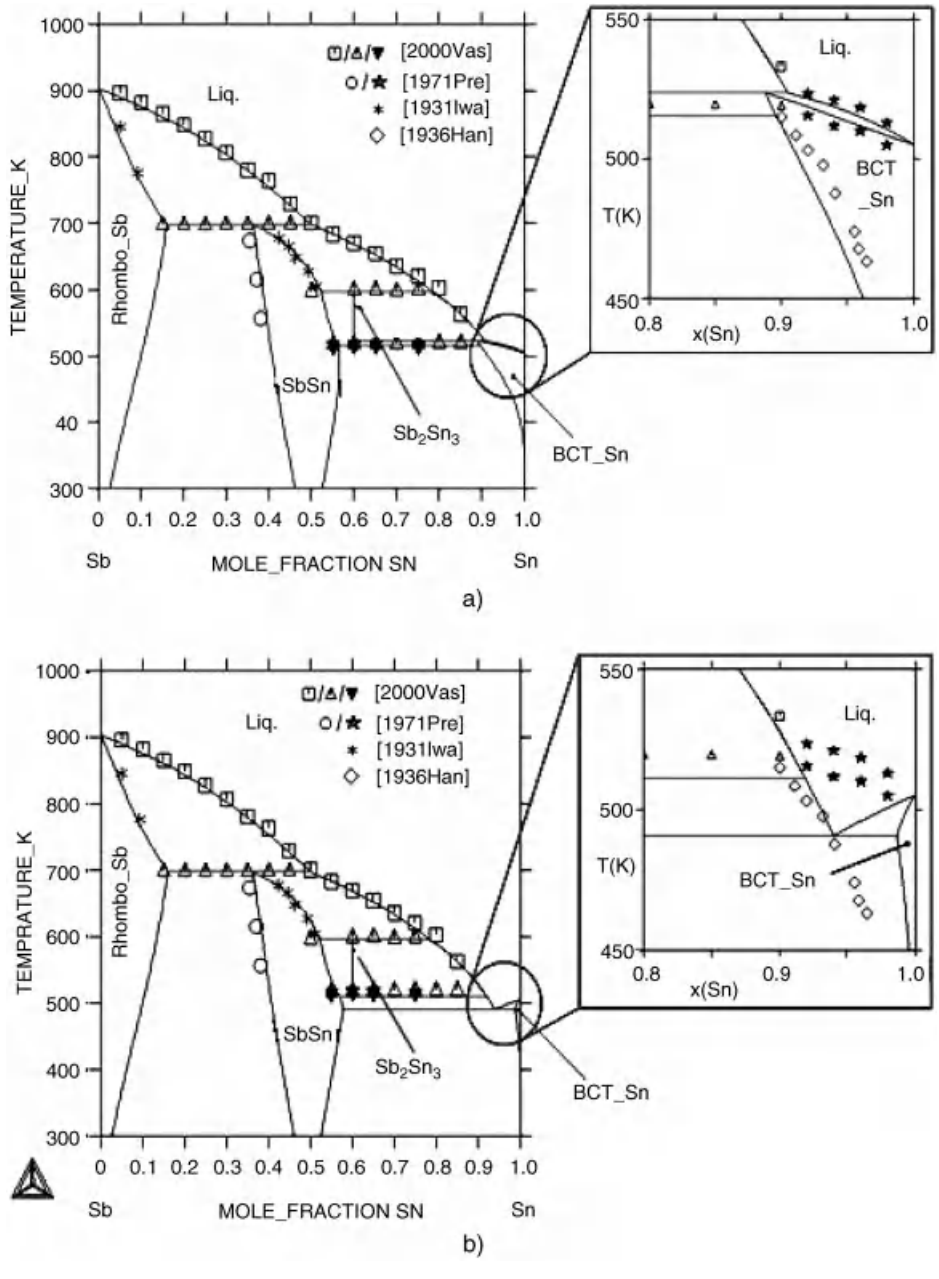

Figure 3.4 *A comparison of Sb-Sn phase diagrams, calculated using the Gibbs energy value from [38] (a) and [60] (b). The result of the reassessment is (c) [39]. (Reproduced from A. Kroupa, J. Vízdal, "The thermodynamic database for the development of modern lead-free solders", Diffusion and Defect Data. Source: Defect And Diffusion Forum 263(2007), pp. 99–104).*

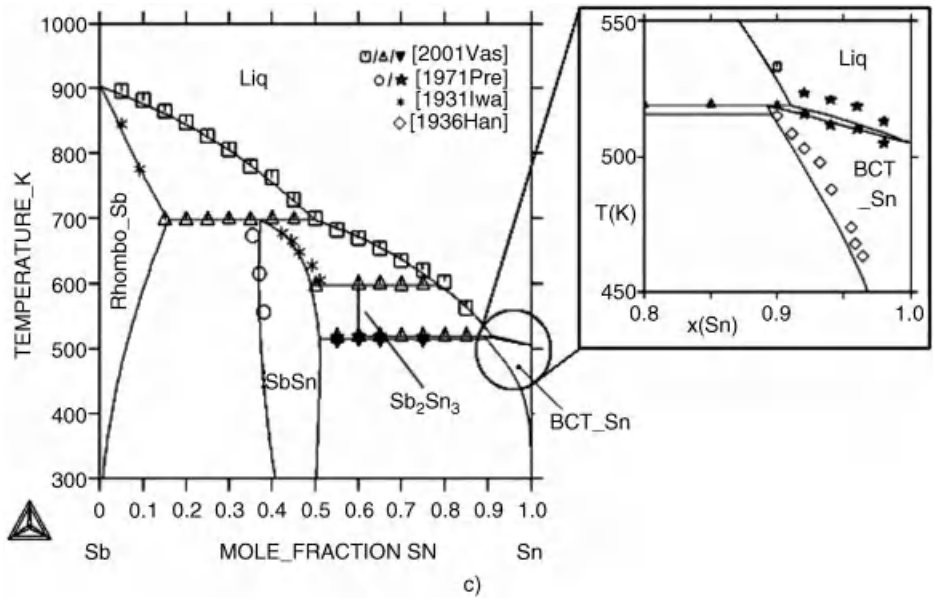

Figure 3.4 *(Continued)*

The most recent thermodynamic database, SOLDERS ([43],[26]), was developed within the scope of the COST 531 Action [44] and covers 11 elements important for lead-free soldering (Ag, Au, Bi, Cu, In, Ni, Pb, Pd, Sb, Sn, and Zn). This database contains complete assessments of all but one binary system (Pd-Sb) and complete assessments of 20 important ternary systems. The development of this database continues within the scope of the COST MP0602 Action [45], through the addition of further elements, thought to be important for high-temperature soldering (service temperatures of approximately 250–300 °C).

3.3.3.1 The SOLDERS Database

The choice of elements required for a lead-free solders database is clear-cut. Tin and copper along with silver have already been identified as important component elements for lead-free soldering materials. Copper may also be used as a substrate material. The properties of solders based on these elements are not completely satisfactory and it was deemed necessary to include other elements in the database in order to provide a tool suitable for optimizing their properties. The low melting point elements In and Bi were included within the scope of the database, along with termination materials as Ni, Au and Pd. Lead was added to the database, as it was important to be able to model the interaction between old and new solders, for example, during the repairs of electronic devices. The reasoning behind the selection of elements for the SOLDERS database is described in more detail in the existing literature ([43],[26]).

Phosphorus also plays an important role in soldering, as it is inseparable from the Ni used in the electronics industry. Layers of Ni are commonly used because of their superior characteristics such as excellent solderability, corrosion resistance, uniform thickness, and selective deposition. The P content in the Ni-P layer can be between about 5 and 15 wt%

and is a result of the deposition procedure. Unfortunately, alloy systems involving P have, in most cases, not been studied sufficiently both experimentally and theoretically and therefore there is a significant lack of critically assessed thermodynamic datasets for Metal-P systems. Therefore, P was not included in the SOLDERS database, at least not during COST 531.

Currently, a new database is under development within the framework of the COST Action MP0602 [45]. The scope of the thermodynamic database was broadened to cover some crucial elements (P) and also elements that may be useful for the development of materials for high-temperature soldering. Currently, the database contains 18 elements: Ag, Al, Au, Bi, Co, Cu, Ga, Ge, Mg, Ni, P, Pb, Pd, Sb, Si, Sn, Ti and Zn. The database is being constructed from assessments taken from the scientific literature and those generated through the research programmes of the COST Actions 531 and MP0602. At each stage, the assessments have been modified where necessary in order to fulfil the criteria described earlier. A number of distinct material types have been identified as having potential for use as high-temperature lead-free solders, alloys based on the Al-Zn, Sb-Sn, Zn-Sn systems, and so on. It is not necessary to have thermodynamic descriptions of all combinations of the elements in the database and so its coverage was limited to those binary and ternary systems with particular relevance to lead-free soldering.

It is important that identical results may be achieved from the database irrespective of the calculation software used. Therefore the databases were, at each stage in their development, tested using three software packages for computational thermodynamics; *Thermo-Calc* [27], *MTDATA* [28], and *Pandat* [46].

3.4 Application of the SOLDERS Database to Alloy Development

Most of the current research effort associated with solders has been concerned with attempts to find replacements for traditional Pb-Sn based materials. Electrician's solder, based on the eutectic composition in the Pb-Sn system (37 wt%Pb, 63 wt%Sn) has long been the material of choice for joining electrical components together. The use of a eutectic material ensures that the solder melts at a single temperature, in this case 183 °C, which provides quicker wetting as the solder heats up and a shorter time for the solder to set. If a noneutectic material is used, the joint must be held fixed while the temperature falls and the solder solidifies. Cracks could occur if the joint is moved while the solder sets, resulting in an unreliable solder joint.

Over the last fifteen years there has been an increasing demand for lead to be removed from all manner of electronic and electrical devices and this led to the search for materials that can be used in place of these traditional Pb-Sn solders. Use of lead does have a number of benefits through its reduction of the surface tension of tin, providing a relatively low eutectic temperature and reflow temperature range as well as supporting intermetallic compounds formed. The ideal lead-free solder would be one that had identical or very similar properties, a so-called drop-in replacement. Computational thermochemistry is the ideal tool to use to search for a new alloy with a eutectic temperature in the region of 183 °C. Of course it has to be recognized that the range of temperatures associated with solidification is only one of a number of properties that are desirable for a new solder material. Amongst other criteria are cost, wettability, good thermal resistance, mechanical strength, creep

resistance and the ability to form an effective bond with substrates and termination materials. It is also desirable that the solder contain no more than three or four elements.

3.4.1 Modelling of Phase Diagrams and Thermodynamic Properties

Figure 3.5 shows the phase diagram for the Cu-Sn binary systems calculated from the SOLDERS database and Table 3.1, the associated table of invariant reactions, published in the Atlas of Phase Diagrams for Lead-Free Soldering [43]. (It's worth noting that in this particular version of the phase diagram, the β and γ phases have been unified into a single phase field.) Of particular interest here is the eutectic reaction close to pure Sn that is calculated to be at 227.2 °C (just under 5° below the melting point of pure Sn). This binary eutectic composition corresponds to one of the common lead-free solders currently in use commercially.

Table 3.1 *Invariant reactions in the Cu-Sn system.*

T/°C	Phases			Compositions/x_{Sn}		
1084.6	LIQUID	FCC_A1		0.000	0.000	
816.3	FCC_A1	BCC_A2	LIQUID	0.069	0.133	0.151
666.5	BCC_A2	CU3SN		0.250	0.250	
647.4	CU3SN	BCC_A2	LIQUID	0.250	0.283	0.412
635.0	BCC_A2	CU10SN3	CU3SN	0.211	0.231	0.250
568.5	BCC_A2	CU41SN11	CU10SN3	0.179	0.212	0.231
540.0	CU41SN11	CU10SN3	CU3SN	0.212	0.231	0.250
523.8	FCC_A1	BCC_A2	CU41SN11	0.086	0.161	0.212
418.1	CU3SN	CUIN_ETA	LIQUID	0.250	0.455	0.868
348.1	FCC_A1	CU41SN11	CU3SN	0.054	0.212	0.250
231.9	LIQUID	BCT_A5		1.000	1.000	
227.2	CUIN_ETA	LIQUID	BCT_A5	0.455	0.985	1.000
[(a)]187.5	CUIN_ETA	CU6SN5_P	BCT_A5	0.455	0.455	1.000
[(a)]187.1	CU3SN	CUIN_ETA	CU6SN5_P	0.250	0.455	0.455
13.1	CU6SN5_P	BCT_A5	DIAMOND_A4	0.455	1.000	1.000
13.0	BCT_A5	DIAMOND_A4		1.000	1.000	

The addition of elements to this Cu-Sn system will generally reduce the eutectic temperature further by stabilizing the liquid phase at the expense of the crystalline phases. The most common lead-free solder is formed by the addition of Ag to the Cu-Sn system. This ternary system has been the subject of many experimental studies in order to fully understand the nature of its phase equilibria. During the course of the COST Action 531 the thermodynamic model parameters of the system were optimized to be consistent with all the experimental thermodynamic and phase-diagram data. Figure 3.6 shows a vertical section through this system with some experimental data superimposed.

In order to explore composition ranges where the liquid can solidify at even lower temperatures the most useful diagram is the liquidus projection. The appropriate diagram for the Ag-Cu-Sn system is shown in Figure 3.7. The diagram shows two different sorts of

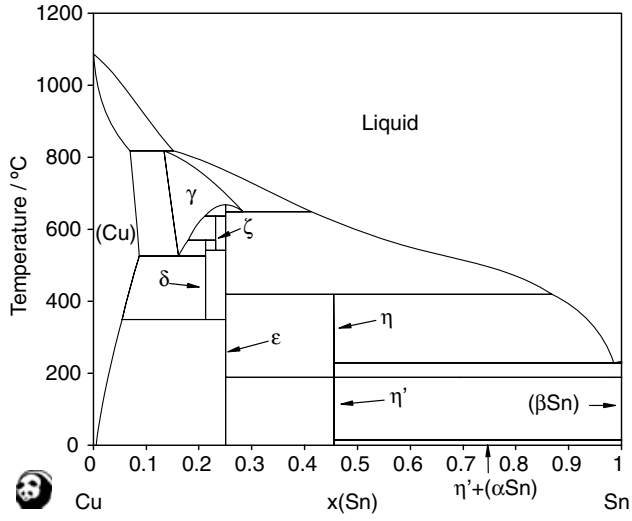

Figure 3.5 *The calculated Cu-Sn phase diagram.*

lines; the eutectic valley follows the compositions with the minimum temperatures for solidifying the liquid, and contour lines showing the actual value where the liquid starts to freeze. Only on compositions where different valleys intersect will liquid solidify at a single temperature.

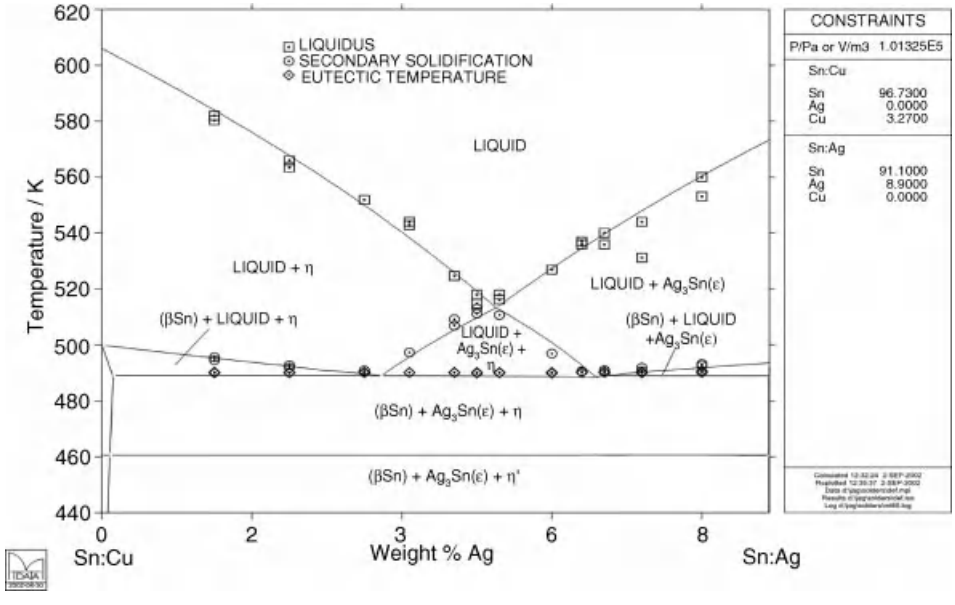

Figure 3.6 *Calculated isopleth through the Ag-Cu-Sn system showing calculated phase boundaries with experimental data superimposed.*

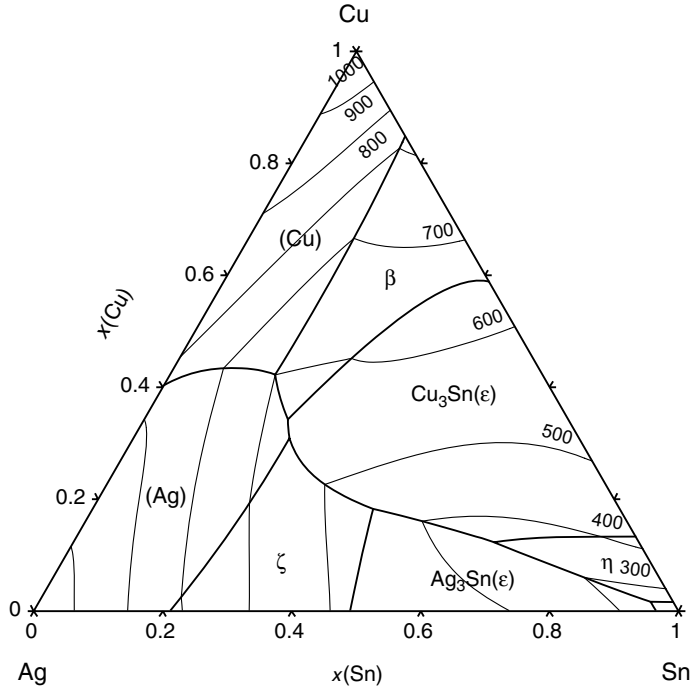

Figure 3.7 *Calculated liquidus projection for the Ag-Cu-Sn system.*

While Figure 3.7 shows very easily the compositions along the eutectic valley, it is less easy to identify the actual freezing temperature. A better way of doing this is shown in Figure 3.8, which represents a projection of the eutectic valley from Figure 3.7 with the temperature as the ordinate. This allows a very clear graphical description of the temperatures and the character of any particular invariant reaction.

Computational thermochemistry also provides an easy way to trace the composition of a noneutectic liquid phase as it solidifies, as shown in Figure 3.9. The composition of the liquid here is one formed from a mixture of lead-free solder based on the Sn-Ag-Cu system and the well-known electrician's Pb-Sn solder.

The results of this calculation are of particular interest where lead-free solders replace, or are used to repair, conventional Pb-Sn solders. There is a significant possibility of the newer solders being contaminated by relatively small amounts of lead from existing solder joints and component terminations. Computational thermochemistry can be used to investigate the phases formed in a lead-contaminated solder and the microstructure that could be expected as such a contaminated solder solidifies [47, 48].

One way to explore the liquidus temperature, the phases that might form and their range of stability, is by calculating a cut or an isopleth through a multicomponent phase diagram.

Figure 3.10 shows such an isopleth between the electrician's solder and the standard Sn-Ag-Cu lead-free solder. It shows that, as the lead-free solder becomes more and more contaminated by the lead solder, the liquidus temperature drops and also the range over which the liquid phase is stable, either on its own or in combination with other phases,

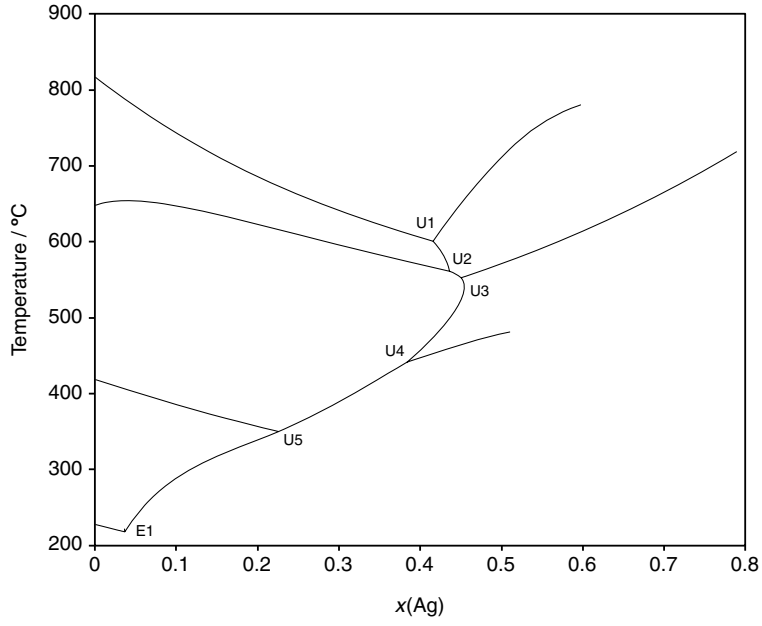

Figure 3.8 *Calculated liquidus projection for the Ag-Cu-Sn system displayed on a temperature–composition axis.*

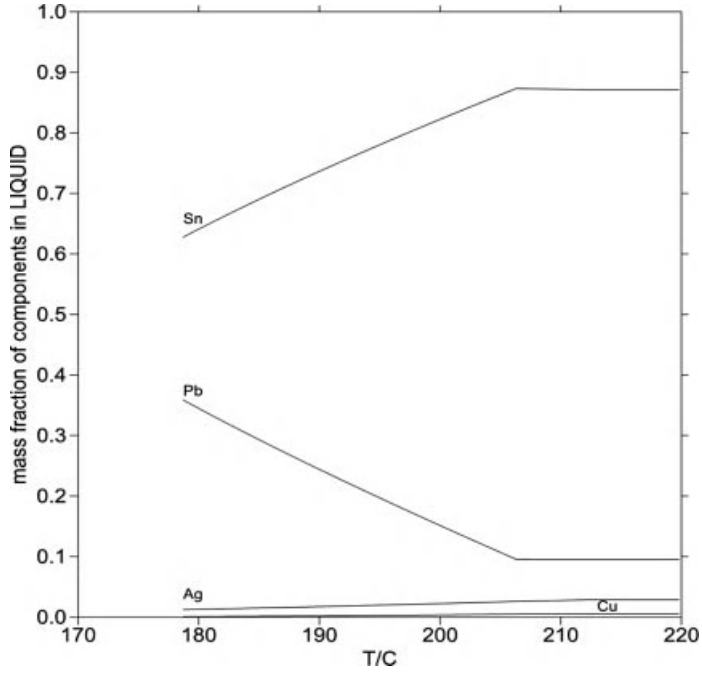

Figure 3.9 *Composition of the liquid phase formed from a mixture of a lead-free solder and a Pb-Sn 'electrician's solder'.*

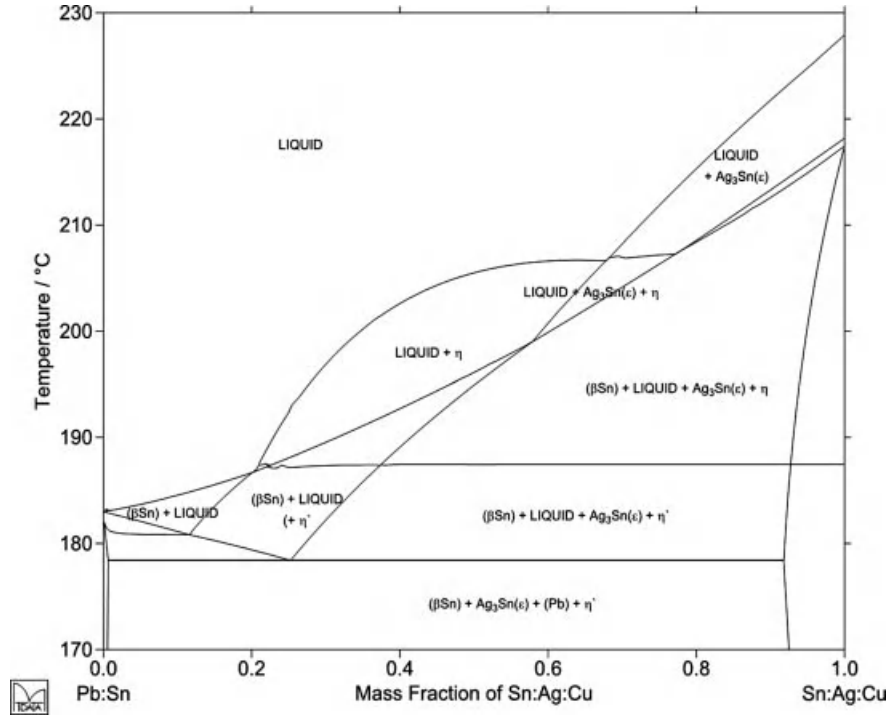

Figure 3.10 *Calculated isopleth between an electrician's solder and the standard Sn-Ag-Cu lead-free solder.*

becomes very much larger. This could lead to unreliability and increased porosity of the solder joint.

Figure 3.9 showed the calculated composition of the liquid phase on the solidification of a Sn-Ag-Cu alloy with 25% contamination of Pb calculated, assuming that equilibrium is maintained as the material is cooled down. The isopleth, Figure 3.10, shows which phases are predicted to appear on cooling down and the appropriate temperature ranges, but it gives no indication of how much of the phase can be expected to form. This, however, can also be calculated, as shown in Figure 3.11. The first phase to appear as the liquid is cooled down is the Ag_3Sn phase, which in this case refers to an intermetallic phase based mainly in the Ag-Sn system. Initially, the amount of this phase is very small and does not seem to affect the total amount of the liquid phase. The next crystalline phase to appear is Cu_6Sn_5, followed by the Sn-based solid-solution phase, BCT_A5. Finally, all the liquid disappears at about 178 °C with the formation of the Pb (FCC) phase.

An analysis of such plots can lead to an understanding of the microstructure of the solidified material, its strength and brittleness.

Other properties can also be calculated and compared directly with experimental properties. For example, the heat capacity measured from DSC is a very good test of the onset of phase transitions and can be compared directly with diagrams such as Figure 3.12, calculated for the same composition.

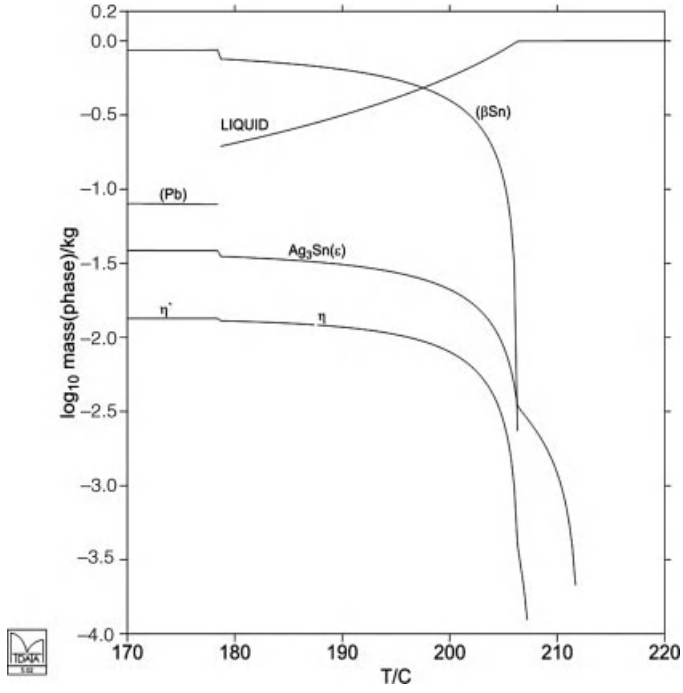

Figure 3.11 *Calculated mass of phases formed on solidification of a mixture of a lead-free solder and a Pb-Sn 'electrician's solder' assuming equilibrium is maintained during solidification.*

The density of the solder is another important property. Since the molar volume is equal to the pressure derivative of the Gibbs energy it can be derived from calculation using an appropriate thermodynamic database. The calculated density as a function of temperature for the solder alloy discussed above is shown in Figure 3.13. It can be seen that most of the change in density is associated with what is called the mushy zone where the liquid is present with one or more crystalline phase.

In the discussion so far, it has been assumed that solidification occurs with thermodynamic equilibrium maintained at each temperature and this could be related to very slow cooling of the material where atoms have a chance to migrate and find the state with the lowest Gibbs energy. In practice, the diffusion of atoms in the liquid phase is likely to be more rapid that in the crystalline phases, particularly in those with a highly ordered structure, and for finite cooling rates the situation is likely to be more complex. At the other extreme, it could be assumed solidification takes place quickly such that rapid diffusion takes place in the liquid phase and no diffusion at all in any solidified material. This is known as Scheil solidification and can simulate the conditions that could give maximum segregation of elements. Reality can be expected to be somewhere between these extremes. Computational thermochemistry can also be used to calculate the properties of the material assuming a Scheil mode of solidification. Figure 3.14 shows the calculated mass of phases, which should be compared with Figure 3.11.

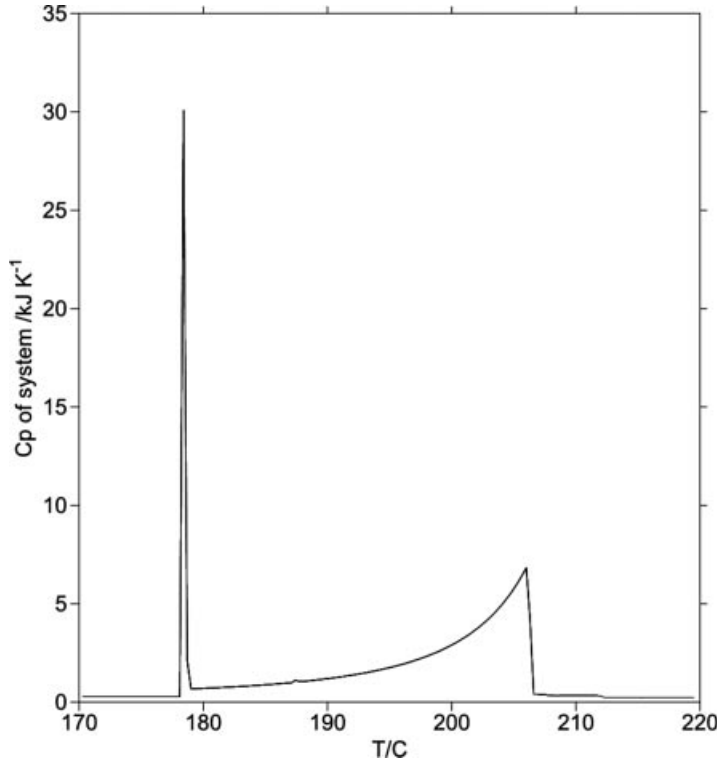

Figure 3.12 *Calculated heat capacity of an alloy formed from a mixture of a lead-free solder and a Pb-Sn 'electrician's solder'.*

Often, the difference between the results from a Scheil calculation and equilibrium calculation are small, however, it is known that even small changes in composition can lead to a large effect on the microstructure of microsolder joints.

Thus far, the discussion has centered on the use of computational thermochemistry to understand and interpret the behavior of conventional and widely used materials. Another feature of computational thermochemistry is its inherently predictive nature. As has been described earlier, the thermodynamic properties of phases in the component binary and ternary systems are represented by well-tested and reliable models, and these can be used to extrapolate these properties into systems with a larger number of components. In this way, the technique can be used to predict the compositions and temperatures of eutectics in systems with more and more components, which may not have been studied experimentally. Nevertheless, it should be remembered that solders, ideally, should not contain more than four elements.

It is also possible to explore, using computational thermochemistry, the interaction between the solder and conductor metals that is component metallizations, board surface finishes and underlying conductors. The formation of a solder joint is thought to proceed through the initial dissolution of the substrate into the solder followed immediately by the formation of intermetallic compound phases within the solder prior to the final solidification

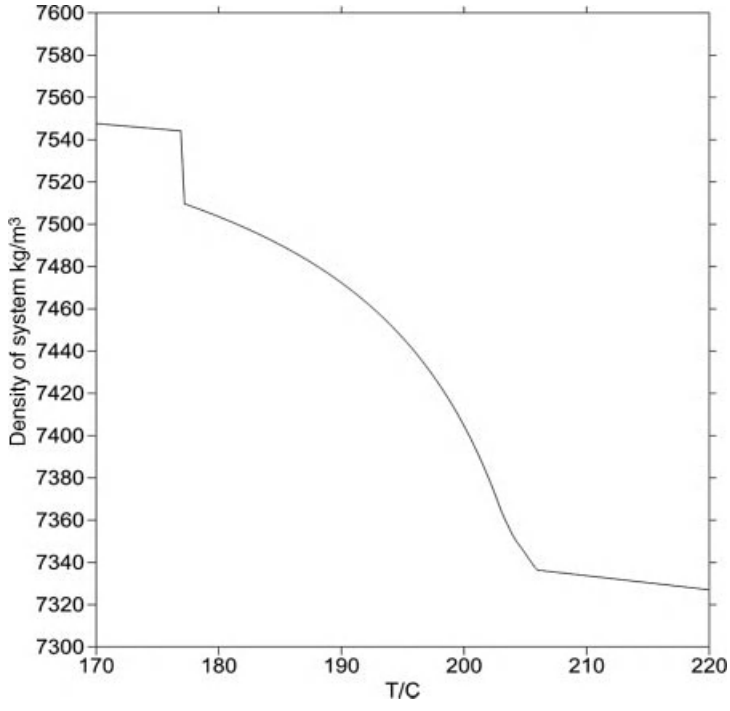

Figure 3.13 *Calculated density of an alloy formed from a mixture of a lead-free solder and a Pb-Sn 'electrician's solder' [49]. (Reproduced with permission from Alan Dinsdale from http://resource.npl.co.uk/mtdata/surfacetension.htm).*

of the solder. As a result, it is important to model the thermodynamic properties and phase equilibria of systems between the solder components and the elements of the contact material. The intermetallic phases formed will tend to have markedly different mechanical and electrical properties than either the solder or the substrate and so being able to predict the nature and the quantity is very important. Ideally, the intermetallic layer should be between 1 and 5 micrometers thick. If the intermetallic layer is too large the solder is usually brittle.

3.4.2 Modelling of Other Properties

It was mentioned earlier how surface tension affects the solderability and that lead had the particularly desirable property of reducing the surface tension. Measurement of surface tension has been carried out systematically within COST Action 531, resulting in the preparation of the Surdat database by Moser and colleagues [50]. While surface tension is not a thermodynamic property of the bulk material it is a reflection of the thermodynamic properties of the atoms near the surface. For a pure material of course, the surface has the same composition as that of the bulk material. However, when it comes to an alloy, the different component elements have different tendencies to be surface active causing the composition of the surface to be quite different from that of the bulk material.

Tanaka [51, 52] has attempted to model the surface tension of a wide range of materials, both ionic and metallic melts, by using an equation developed by Butler [53] that seeks to

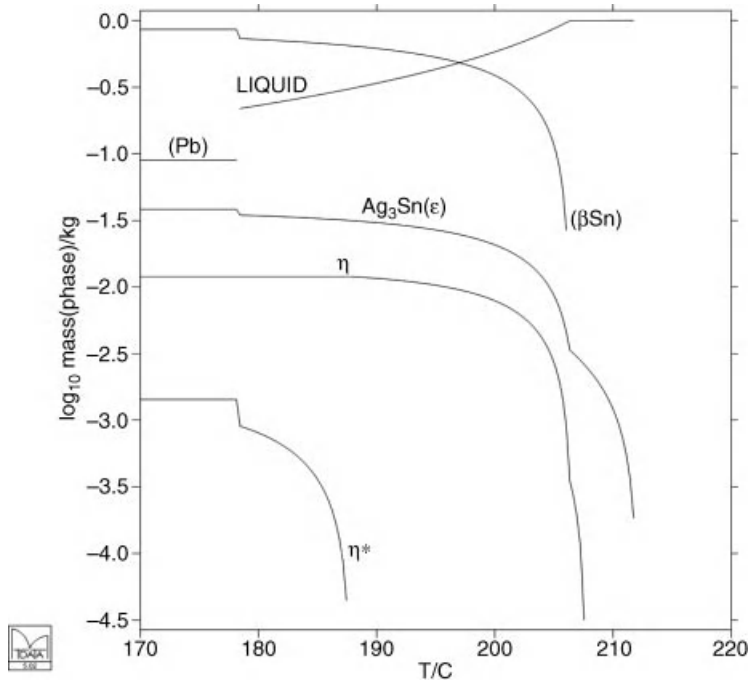

Figure 3.14 *Calculated mass of phases formed on solidification of a mixture of a lead-free solder and a Pb-Sn 'electrician's solder' assuming Scheil solidification.*

express the surface tension in terms of equilibrium between the bulk material and a surface layer. The thermodynamic properties of the bulk are, of course, well represented by standard thermodynamic models and data as stored in the SOLDERS database. The surface thermodynamic properties can be estimated from the excess thermodynamic properties of the bulk, taking into account the reduced number of interatomic bonds at the surface, or derived from experimental surface tension data.

Figure 3.15a shows the calculated surface tension of Bi-Sn liquids with experimental points superimposed. The composition of the surface can also be calculated at the same time as shown in Figure 3.15b, and this shows how Bi is markedly more surface active than Sn.

Figure 3.16a shows the calculated surface tension of Ag-Sn alloys at 1000 °C. While the actual value of the surface tension is important, it is often more important to know how the surface tension changes with temperature. Computational thermochemistry provides this capability, as shown in Figure 3.16b, where the temperature dependence of the surface tension is predicted to change sign.

Thus far, the discussion has focused on the application of thermodynamics to modelling, predicting and understanding the behavior of solders. Many of the reactions taking place during the formation of a solder joint are determined by the geometry of the solder bump, the rates of diffusion of atoms from the substrate into the solder and the rate of reaction to form the intermetallic compounds [54]. This requires the use of a greater level of complexity on top of the equilibrium thermochemistry described earlier. Various approaches have been adopted so far linking together software and data used for equilibrium calculations and other

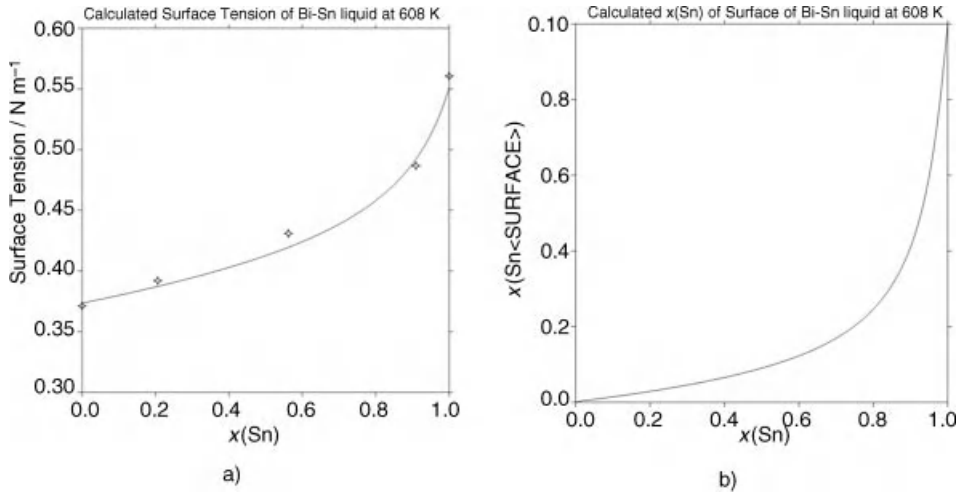

Figure 3.15 *Calculated surface tension and surface composition of Bi-Sn liquid [49]. (Reproduced with permission from Alan Dinsdale from http://resource.npl.co.uk/mtdata/surfacetension.htm).*

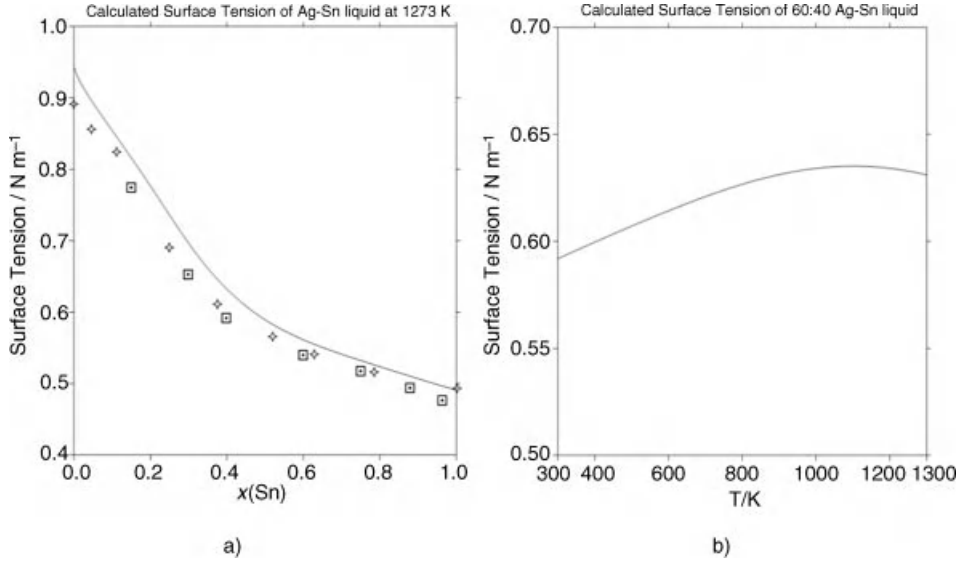

Figure 3.16 *Calculated surface tension for liquids in the Ag-Sn with varying temperature and composition [49]. (Reproduced with permission from Alan Dinsdale from http://resource.npl.co.uk/mtdata/surfacetension.htm).*

packages used to model the nonequilibrium processes. This has been made possible through the development of application programming interfaces that allow packages such as MTDATA to be called directly from within another program to calculate phase equilibria or to provide values of thermodynamic properties. Zhiheng Huang *et al.* [55, 56] for example, have implemented a link between COMSOL, MATLAB and MTDATA in order to model the diffusion of atoms in a Cu-Sn-based solder and study the kinetics of the formation of intermetallic compounds. A more sophisticated treatment is through the use of phase field models [57] to explore the geometry of the crystals formed. Unfortunately, this increased sophistication requires much more information about the properties of the materials.

3.5 Conclusions

The study of phase diagrams and phase equilibria is not new, but the information gained is fundamental to materials science. The advent of computational thermodynamics has unleashed the 'power' of the phase diagram, resulting in a tool that can be used to give an insight into anything from multicomponent, multiphase equilibria to surface tension and microstructural simulation. The creation of the robust self-consistent thermodynamic databases that the technique requires needs a fair amount of effort, but the savings in both time and cost in relation to expensive experimental programmes can be substantial. It's clear that it is essential that phase-diagram assessment programmes relevant to specific fields or topics in materials science, such as lead-free solders, are conducted as soon as the fields themselves become of interest to the scientific community. In this way, the resulting thermodynamic databases can be of maximum benefit to other workers in the field. So our challenge is not in what computational thermodynamics can do for us, but in ensuring that it is allowed to take its rightful place at the forefront of materials research.

References

1. Prince, A. (1961) *Alloy Phase Equilibria*, Elsevier, Amsterdam.
2. Heycock, C.T. and Neville, F.H. (1904) On the constitution of the Copper-Tin series of alloys. *Philos. Trans. Roy. Soc. London Ser. A*, **202**, 1–70.
3. Roozeboom, H.W.B. (1899) Solidification of mixtures of two substances. *Z. Phys. Chem.*, **30**, 385–412.
4. quoted in [1899Roo].
5. Chang, Y.A., Neumann, J.P., Mikula, A. and Goldberg, D. (1979) Phase Diagrams and Thermodynamic Properties of Ternary Copper-Metal Systems, INCRA Monograph VI, The International Copper Research Association, Inc.
6. Chang, Y.A., Neumann, J.P. and Choudary, U.V. (1979) Phase Diagrams and Thermodynamic Properties of Ternary Copper-Sulfur-Metal Systems, INCRA Monograph VII, The International Copper Research Association, Inc.
7. Nayeb-Hashemi, A.A. and Clark, J.B. (1988) *Phase Diagrams of Binary Magnesium Alloys*, ASM International.
8. Raghavan, V. (1987) *Phase Diagrams of Ternary Iron Alloys Part 1*, The Indian Institute of Metals.
9. Petzow, G. and Effenberg, G. (1988–1993) *Ternary Alloys- A Comprehensive Compendium of Evaluated Constitutional Data and Phase Diagrams*, vols. **1–8**, VCH.

10. Raghavan, V. (1988) *Phase Diagrams of Ternary Iron Alloys Part 2 – Ternary Systems Containing Iron and Sulphur*, The Indian Institute of Metals.
11. Raghavan, V. (1988) *Phase Diagrams of Ternary Iron Alloys Part 3 – Ternary Systems Containing Iron and Phosphorus*, The Indian Institute of Metals.
12. Raynor, G.V. and Rivlin, V.G. (1988) *Phase Equilibria in Iron ternary Alloys Part 4*, The Institute of Materials.
13. Raghavan, V. (1989) *Phase Diagrams of Ternary Iron Alloys Part 5 – Ternary Systems Containing Iron and Oxygen*, The Indian Institute of Metals.
14. Smith, J.F. (1989) *Phase Diagrams of Binary Vanadium Alloys*, ASM International.
15. Massalski, R.B., Subramanian, P.R., Okamoto, H. and Kacprzak, L. (1990) *Binary Alloy Phase Diagrams*, 2nd edn, Vols **1, 2 and 3**, ASM International, Materials Park, Ohio.
16. Nash, P. (1991) *Phase Diagrams of Binary Nickel Alloys*, ASM International.
17. Villars, P., Prince, A. and Okamoto, H. (1996) *Handbook of Ternary Alloy Phase Diagrams*, ASM.
18. Gibbs, J.W. (1876) On the equilibrium of heterogeneous substances. *Trans. Connect. Acad.*, **II**, 108–248. and *ibid*, 343–524 (1878).
19. van Emmerik, E.P. (1991) J.J. Van Laar, a mathematical chemist, Thesis, The University of Delft, Netherlands.
20. Kaufman, L. and Bernstein, H. (1970) *Computer Calculation of Phase Diagrams*, Academic Press, New York.
21. Sob, M., Kroupa, A., Pavlu, J. and Vrestal, J. (2009) Application of *ab-initio* electronic structure calculations in construction of phase diagrams of metallic systems with complex phases. *Solid State Phenom.*, **150**, 1–28.
22. Andersson, J.-O. and Sundman, B. (1987) Thermodynamic properties of the Cr-Fe system. *Calphad*, **11**, 83–92.
23. Hillert, M. and Staffansson, L.-I. (1970), Regular solution model for stoichiometric phases and ionic melts, *Acta Chem. Scand.*, **24**, 3618.
24. Hillert, M. and Waldenstrom, M. (1977) Isothermal sections of the Fe-Mn-C system in the temperature range 873 K–1373 K. *Calphad*, **1**, 97–132.
25. Lukas, H.L., Fries, S.G. and Sundman, B. (2007) *Computational Thermodynamics – The Calphad Method*, Cambridge University Press.
26. Kroupa, A., Dinsdale, A.T., Watson, A. *et al.* (2007) The development of the COST 531 lead-free solders thermodynamic database. *JOM*, **59**, 20–25.
27. Andersson, J.-O., Helander, T., Höglund, L. *et al.* (2002) Thermo-Calc & DICTRA, computational tools for materials science. *Calphad*, **26**, 273–312.
28. Davies, R.H., Dinsdale, A.T., Gisby, J.A. *et al.* (2002) MTDATA – Thermodynamics and phase equilibrium software from the National Physical Laboratory. *Calphad*, **26**, 229–271.
29. Redlich, O. and Kister, A. (1948) Algebraic representation of thermodynamic properties and the classification of solutions. *Indust. Eng. Chem.*, **40**, 345.
30. Muggianu, Y.-M., Gambino, M. and Bros, J.-P. (1975) Enthalpies of formation of liquid alloys bismuth-gallium-tin at 723 K – Choice of an analytical representation of integral and partial thermodynamic functions of mixing for this ternary system. *J. Chim. Phys. Physicochim. Biol.*, **72**, 83–88.
31. Guggenheim, E.A. (1952) *Mixtures*, Clarendon Press, Oxford.
32. Saunders, N. and Miodownik, A.P. (1998) *CALPHAD (A Comprehensive Guide)*, Pergamon Press, Oxford.
33. Ansara, I. and Dupin, N. (1998) Thermodynamic modelling, in *Thermodynamic Database for Light Metal Alloys*, vol. **2**(eds I. Ansara, A. Dinsdale and M.H. Rand), European Communities.
34. Sundman, B. and Ågren, J. (1981) A regular solution model for phases with several components and sub-lattices, suitable for computer-applications. *J. Phys. Chem. Solids*, **42**, 297–301.
35. Andersson, J.-O., Fernandez Guillermet, A., Hillert, M. *et al.* (1986) A compound energy model of ordering in a phase with sites of different coordination numbers. *Acta Metall.*, **34**, 437–445.

36. Liang, H. and Chang, Y.A. (1998) A thermodynamic description for the Al-Cu-Zn system. *J. Phase Equilib.*, **19**, 25–37.
37. Oh, C.-S., Shim, J.-H., Lee, B.-J. and Lee, D.-N. (1996) A thermodynamic study on the Ag-Sb-Sn System. *J. Alloys Compd.*, **238**, 155–166.
38. Dinsdale, A.T. (1991) SGTE data for pure elements. *Calphad*, **15**, 317–425.
39. Kroupa, A. and Vízdal, J. (2007) "The thermodynamic database for the development of modern lead-free solders" in DEFECT AND DIFFUSION FORUM vol. 263(2007), *Proc. of the 9th Seminar on Diffusion and Thermodynamics of Materials, Brno, Czech Republic, September* 13–15, 2006 *(eds. J. Cermak, I. Stloukal),* pp. 99–104.
40. http://www.metallurgy.nist.gov/phase/solder/solder.html, (2001) National Institute of Standard and Technology, Maryland, USA.
41. Materials Design Technology, Tokyo, Japan, http://www.materials-design.co.jp/adamis/adamisE.pdf.
42. Ohnuma, I., Liu, X.J., Ohtani, H., and Ishida, K. (1999) Thermodynamic Database for Phase Diagrams in Micro-Soldering Alloys. *J. Electronic Mater.*, **28**, 1163–1170.
43. Dinsdale, A., Watson, A., Kroupa, A. *et al.* (2008) *Atlas of Phase Diagrams for Lead-Free* Soldering, COST 531 Lead-Free Solders vol 1, COST Office, Brussels.
44. Ipser, H.,COST Action 531- Lead-free Solder Materials (End date: March 2007), http://www.cost.esf.org/domains_actions/mpns/Actions/Lead-free_Solder_Materials.
45. Kroupa, A., COST Action MP0602 – Advanced Solder Materials for High Temperature Application (HISOLD) http://w3.cost.esf.org/index.php?id=248&action_number=MP0602.
46. Chen, S.-L., Daniel, S., Zhang, F. *et al.* (2002) The PANDAT software package and its applications. *Calphad*, **26**, 175–188.
47. Hunt, C.P., Nottay, J., Brewin, A. and Dinsdale, A.T. (April 2002) NPL Report MATC(A) 83.
48. Huang, Zhiheng, Conway, P.P., Liu, Changqing and Thomson, R.C. (2003) IEEE/CPMT/SEMI Int'l Electronics Manufacturing Technology Symposium.
49. Dinsdale, A.T. (2002) Unpublished work.
50. Moser, Z., Gasior, W., Debski, A. and Pstrus, J. (2007) SURDAT – database of physical properties of lead-free solders. *J. Min. Metall., Sect. B.*, **43B** (2), 125–130.
51. Tanaka, T., Gokcen, N.A. and Morita, Z. (1990) Relationship between enthalpy of mixing and excess entropy in liquid binary alloys. *Z. Metallkde.*, **81**, 49–54.
52. Tanaka, T., Hack, K. and Hara, S. (1999) Relationship between enthalpy of mixing and excess entropy in liquid binary alloys. *MRS Bull.*, **24** (4), 45–50.
53. Butler, J.A.V. (1932) Thermodynamics of the surfaces of solutions. *Proc. Roy. Soc. London, Ser A*, **135**, 348–375.
54. Laurila, T., Vuorinen, V. and Kivilahti, J.K. (2005) Interfacial reactions between lead-free solders and common base materials. *Mater. Sci. Eng. R*, **49**, 1–60.
55. Huang, Zhiheng, Conway, P.P., Liu, Changqing and Thomson, R.C. (2004) The effect of microstructural and geometrical features on the reliability of ultrafine flip chip microsolder joints. *J. Electron. Mater.*, **33** (10), 1227–1235.
56. Huang, Zhiheng, Conway, P.P., Thomson, R.C. *et al.* (2008) A computational interface for thermodynamic calculations software MTDATA. *Calphad*, **32**, 129–134.
57. Moelans, N., Blanpain, B. and Wollants, P. (2008) An introduction to phase-field modeling of microstructure evolution. *Calphad*, **32**, 268–294.
58. Richter, K.W. (1988) The ternary In-Ni-Sb phase diagram in the vicinity of the binary In-Ni system. *J. Phase Equilib.*, **19**, 455–465.
59. Dinsdale, A.T., Watson, A., Kroupa, A., Vrestal, J., Zemanova, A., and Vizdal, J.,Version 3.0 of the SOLDERS Database for Lead Free Solders. http://www.npl.co.uk/science-technology/advanced-materials/materials-areas/thermodynamics/thermodynamic-databases-for-mtdata.
60. Dinsdale, A.T., SGTE Unary Database, version 4.4., www.sgte.org

4

Interaction of Sn-based Solders with Ni(P) Substrates: Phase Equilibria and Thermochemistry

Clemens Schmetterer[1]*, Rajesh Ganesan*[2]*, and Herbert Ipser*
[1] *Now with ZIK Virtuhcon, TU Bergakademie Freiberg, Freiberg, Germany*
[2] *Now with Chemistry Group, Indira Gandhi Center for Atomic Research, Kalpakkam, Tamilnadu, India*
University of Vienna, Department of Inorganic Chemistry/Materials Chemistry, Vienna, Austria

Abstract

As contradicting results can be found in the literature on the reaction products between tin-based solders and electroless nickel substrates that contain high amounts of phosphorus, a study of the ternary Ni-P-Sn phase diagram was initiated. Since the literature on the binary limiting systems Ni-Sn, Ni-P, and P-Sn was found to contain a number of ambiguities, these were also included in this series of investigations. To provide input data for CALPHAD-type optimizations of the binary and ternary systems, allowing the calculation of consistent phase diagrams, thermodynamic studies of the two binary systems Ni-P and P-Sn were performed.

New experimental results on the binary phase diagrams of Ni-Sn, Ni-P, P-Sn, and Ni-P-Sn are reported here, and their relevance for solder joints and the phases formed during the soldering process are discussed. For the three phosphorus-containing systems Ni-P, P-Sn, and Ni-P-Sn it was found that the phase diagrams show a considerable dependence on the pressure, a variable that is mostly neglected in phase-diagram studies of intermetallic systems. In addition, phosphorus vapor pressures were determined by an isopiestic method

Lead-free Solders: Materials Reliability for Electronics, First Edition. Edited by K. N. Subramanian.

in the two systems Ni-P and P-Sn from which partial Gibbs energies as well as Gibbs energies of formation of some compounds could be derived. With this, the available thermodynamic information on these alloy systems could be significantly extended.

4.1 Introduction

Electroless nickel gold (ENIG), consisting of a 5–10-μm thick Ni layer protected by an ultrathin (some tens of nanometers) Au layer, has been widely used as a reliable surface finish in the production of electronic equipment, in particular on Cu bond pads for flip-chip and ball grid array (BGA) solder bumps [1–5]. Characteristic features of these electroless Ni layers are low stress, uniform thickness, excellent corrosion resistance, and selective deposition that make them more suitable as a diffusion barrier than electrodeposited Ni [2, 6, 7]. Electroless Ni layers can contain up to 15 at% P (and even more), and this is due to the plating process: phosphonites (hypophosphites) are used as reducing agent to deposit Ni from aqueous solutions causing the incorporation of considerable amounts of P into the Ni layer. It has been shown that electroless Ni layers are crystalline for lower P contents (less than 9.5 at%) but exhibit an amorphous structure for P contents above 9.5 at% [8].

In the soldering process itself, the Au layer dissolves immediately in the liquid solder. The exposed Ni(P) layer then reacts with the solder to form various types of reaction products, among them different binary and ternary intermetallic compounds (IMCs). This reaction and the obtained products have been investigated extensively in the recent past (see for example Refs. [1–4, 8–13]), and part of this interest has certainly to do with reliability issues. Thus, the so-called 'black pad' phenomenon is a well-known problem in electronics when electroless Ni(P) plating is used and has been one of the serious causes for failures in the market [5]. It has been shown by Suganuma and Kim to be most probably due to two reasons: first, the appearance of local corrosion of the Ni(P) layer underneath the Au layer, and secondly, the extended reaction of lead-free solders with Ni(P) at higher temperatures and for longer reaction times, resulting in thick phosphorous-rich layers with a defective structure [5].

All the studies of the interfacial reactions between Ni(P) and Sn-based solders were done solely on an empirical basis without any knowledge of the phase relationships in the ternary Ni-P-Sn system, which would be the basis for a scientific approach of the problem. In some of the studies, possible reaction products were identified simply as 'P-rich layer' [8]; others identified Ni_3P as one of the reaction products [1, 14], frequently in combination with other nickel phosphides (like Ni_2P and $Ni_{12}P_5$) [2, 11, 13, 15], depending partly on the P content in the original Ni(P) layer. Several of the studies also reported the observation of an 'Ni-Sn-P' layer [12, 16, 17], whereas others identified one particular ternary IMC, that is, Ni_2PSn [11, 13, 15, 18]. Still other authors [19–22] reported the appearance of an Ni_3PSn layer, suggesting the existence of such a ternary compound.

This confusion on the true nature of the reaction products was the background of a project initiated within the European COST[3] Action MP 0602 (Advanced Solder Materials for High Temperature Application – HISOLD): to establish a reliable phase diagram of the

[3] COST = European Cooperation on Science and Technology (see http://www.cost.esf.org/).

ternary Ni-P-Sn system to understand the interaction of Sn-based solders with Ni(P) substrates. If possible, the experimental study should be finalized by a CALPHAD[4] -type optimization of the ternary system, based on all experimental information on phase equilibria and thermochemistry.

In the following, an overview will be given on the available literature on the limiting binary phase diagrams Ni-Sn, Ni-P, and P-Sn, as well as on recent new experimental work on the phase equilibria of these systems. This will be followed by a description of the Ni-rich part of the ternary Ni-P-Sn phase diagram as it was obtained experimentally. A final chapter will be devoted to thermochemical studies of the two binary systems Ni-P and Sn-P.

4.2 Binary Phase Equilibria

Knowledge of the phase equilibria of the (binary) constituent systems forms the basis for a reliable investigation of any higher-order system. Since the literature survey given below revealed a considerable number of open questions, new experimental investigations were carried out in the three binaries Ni-Sn, Ni-P, and P-Sn.

4.2.1 Literature Overview

4.2.1.1 Ni-Sn

The Ni-Sn phase diagram was considerably modified in a number of recent investigations [23] compared to the version shown by Nash and Nash [24]. Although the basic outline remained the same, the composition regions around Ni_3Sn and Ni_3Sn_2 were altered considerably in Ref. [23]. In the composition range around Ni_3Sn_2, Leineweber *et al.* [25–28] described two incommensurate Ni_3Sn_2 low-temperature phases in addition to the known commensurate phase. The transition reactions from the corresponding high-temperature (HT) phase were investigated in detail by Schmetterer *et al.* [23], and it was suggested that they are of first order throughout.

Ambiguities concerning the Ni_3Sn phases could be resolved, too. The HT phase was shown to be of the cubic BiF_3-type, as originally reported by Schubert *et al.* [29]. The phase cannot be retained by quenching from temperatures above the transition but thermal effects pertinent to the phase transition were clearly observed. HT X-ray diffraction (XRD) indeed proved the HT phase to be of the BiF_3-type. An updated version of the Ni-Sn phase diagram according to Ref. [23] is shown in Figure 4.1, a list of the invariant reactions can be found in Table 4.1.

4.2.1.2 Ni-P

A literature review of the Ni-P system was given by Lee and Nash [30] and more recently by Schmetterer *et al.* [31] (together with new experimental results). The system can be divided into three parts: the Ni-rich part up to 33.3 at% P, the central part up to 66.7 at% P, and the P-rich part. Not surprisingly, most of the phase-diagram-related literature focused on the Ni-rich part.

[4] CALPHAD = CALculation of PHAse Diagrams.

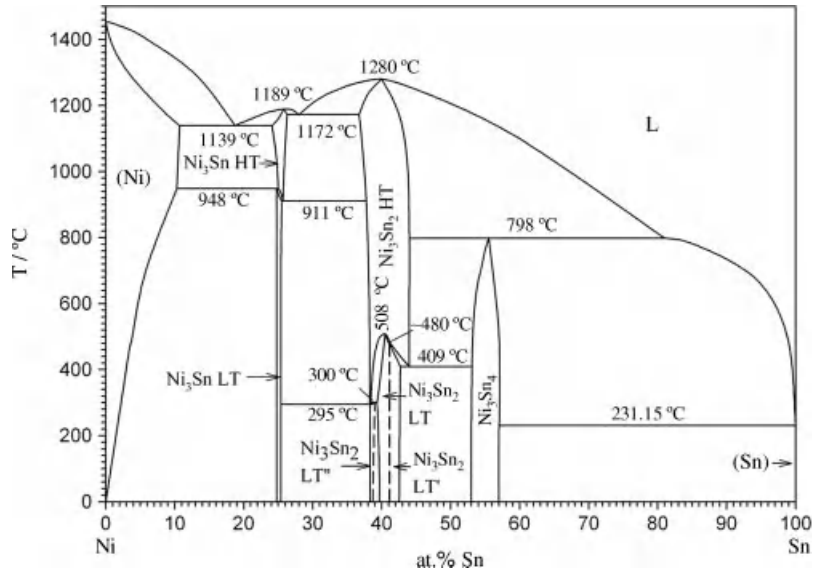

Figure 4.1 *Ni-Sn phase diagram according to Ref. [23]. (Reproduced with permission from Intermetallics, A new investigation of the system Ni–Sn by C. Schmetterer, H. Flandorfer, K.W. Richter, U. Saeed, M. Kauffman, P. Roussel, H. Ipser, 15, 7, 869–884 Copyright (2007) Elsevier Ltd).*

Konstantinov [32] determined the basic outline of the phase diagram using thermal analysis and microscopy and reported the existence of the compounds Ni_3P, Ni_2P and Ni_5P_2, with low-temperature (LT) and high-temperature (HT) modifications for the latter two compounds. Yupko *et al.* [33] investigated the Ni-rich part of the system using XRD, differential thermal analysis (DTA) and metallography confirming the previous results and introducing the HT modification of $Ni_{12}P_5$. Further structural investigations were performed by Nowotny and Henglein [34], Aronsson [35], Rundqvist and coworkers [36], Saini

Table 4.1 *System Ni-Sn: invariant reactions according to the literature [23].*

Reaction	Designation in this work; temperature [°C] and type
$L = (Ni) + Ni_3Sn\ HT$	e2; 1139, eutectic
$Ni_3Sn\ HT + (Ni) = Ni_3Sn\ LT$	p4; 948, peritectoid
$L = Ni_3Sn\ HT$	melting; 1189, congruent
$L = Ni_3Sn\ HT + Ni_3Sn_2\ HT$	e1; 1172, eutectic
$Ni_3Sn\ HT = Ni_3Sn\ LT + Ni_3Sn_2\ HT$	e13; 911, eutectoid
$Ni_3Sn_2\ HT = Ni_3Sn_2\ LT'' + Ni_3Sn\ LT$	e16; 295, eutectoid
$Ni_3Sn_2\ HT + Ni_3Sn_2\ LT = Ni_3Sn_2\ LT''$	p6; 300, peritectoid
$L = Ni_3Sn_2\ HT$	melting; 1280, congruent
$Ni_3Sn_2\ HT = Ni_3Sn_2\ LT$	Congruent transition; 508
$Ni_3Sn_2\ HT + Ni_3Sn_2\ LT = Ni_3Sn_2\ LT'$	p5; ~480, peritectoid
$Ni_3Sn_2\ HT = Ni_3Sn_2\ LT' + Ni_3Sn_4$	e15; 409, eutectoid

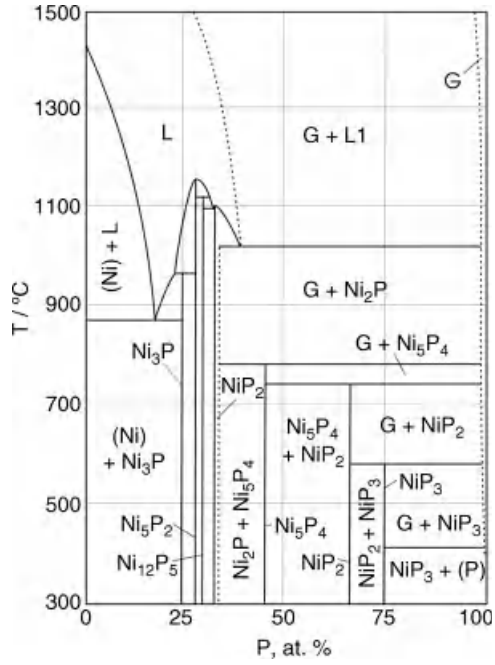

Figure 4.2 *Ni-P phase diagram at a P-pressure of 0.7 bar according to Ref. [41]; several phases are shown to be in direct equilibrium with the gas phase. (Reproduced with permission from Pressure dependent phase diagrams of binary alloys 1997 by Y. Levinsky, G. Effenberg and S. Ilenko, materials Park, Ohio Copyright (1997) ASM International).*

et al. [37], and Oryshchyn *et al.* [38]. Detailed structural information on the HT modifications of Ni_5P_2 and $Ni_{12}P_5$, however, is still missing since their crystal structures cannot be quenched.

The central part of the phase diagram was established by Larsson [39] who described the phases NiP and $Ni_{1.22}P$, while Elfström determined the crystal structure of Ni_5P_4 [40]. Experimental work in this composition range is hampered by the high vapor pressure of P. Due to the lack of reliable thermal analyses in this region the reported invariant reactions have still rather tentative character. A completely different version of this part of the phase diagram was shown by Levinsky *et al.* who established a version of the Ni-P phase diagram [41] at low P pressures, showing actually the formation of the higher nickel-phosphides out of the gas phase (Figure 4.2). However, this phase-diagram evaluation is not based on any experiments but is in fact a reasonable assumption.

Information on the P-rich section is rather poor. Jolibois [42] and Biltz and Heimbrecht [43] performed degradation experiments of P-rich samples from which they concluded the existence and composition of NiP_3, NiP_2 and Ni_2P. The crystal structures of NiP_2 and NiP_3 were determined by Larsson [39] and Rundqvist and Ersson [44], respectively.

A thermodynamic assessment of the system is available from Shim *et al.* [45] that suffers from an incomplete description of the thermodynamic properties and, consequently, from

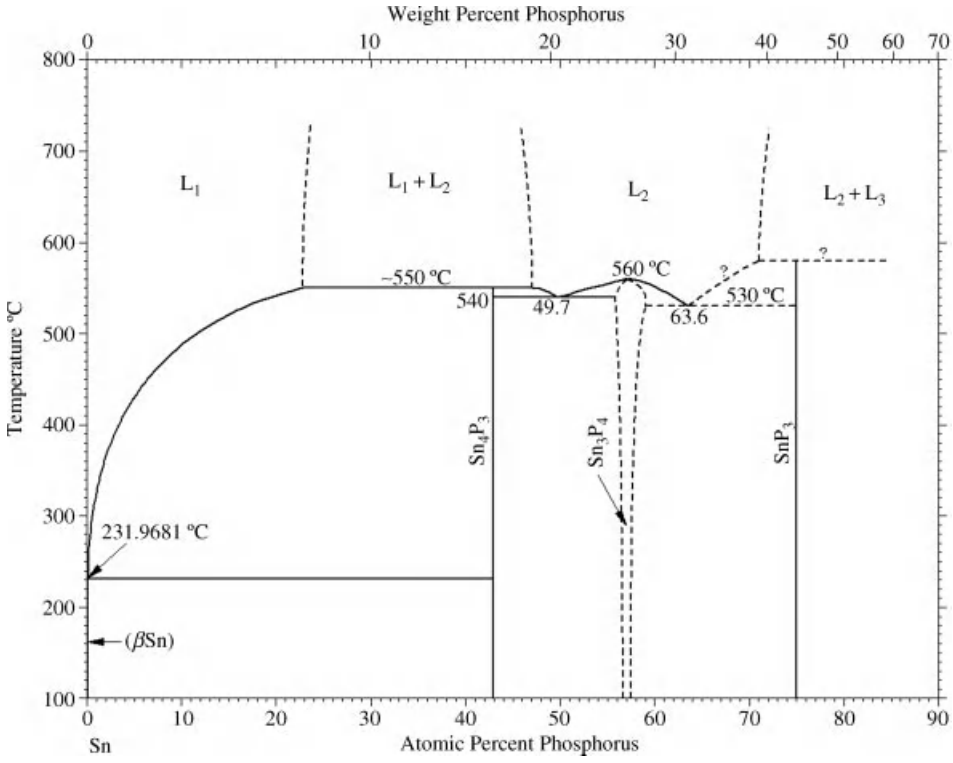

Figure 4.3 *P-Sn phase diagram according to Ref. [46] mainly based on Ref. [47]. (Reproduced with permission from Binary Alloy Phase Diagrams by T. B. Massalski et al.,* Materials Park, Ohio Copyright (1996) ASM International).

severe problems with the liquidus line in the calculated phase diagram that drops down to 0 K at approximately 45 at% P.

4.2.1.3 P-Sn

Not much literature information is available on the P-Sn system; the version of the phase diagram shown in Massalski's compilation [46] is mostly based on the work of Vivian [47] (see Figure 4.3). Olofsson [48] studied the system by XRD but did not establish a phase-diagram version.

Vivian [47] investigated samples prepared in pressure tubes and based his phase diagram on the results of a chemical and micrographical analysis of these samples. He included two liquid miscibility gaps due to the optical appearance of the relevant samples and used simple thermal analysis (cooling curves only) to derive the characteristic temperatures. Based on this, P_3Sn_4 is reported to be formed by a syntectic reaction L1 + L2 = P_3Sn_4 at approximately 550 °C. In the phase diagram shown in Ref. [46] three binary compounds were included. These phases were described in detail, that is, P_3Sn_4 in Ref. [49], P_4Sn_3 in Ref. [50], and P_3Sn in Ref. [51]. Katz *et al.* [52] reported the existence of a fourth compound, PSn, with a hexagonal unit cell.

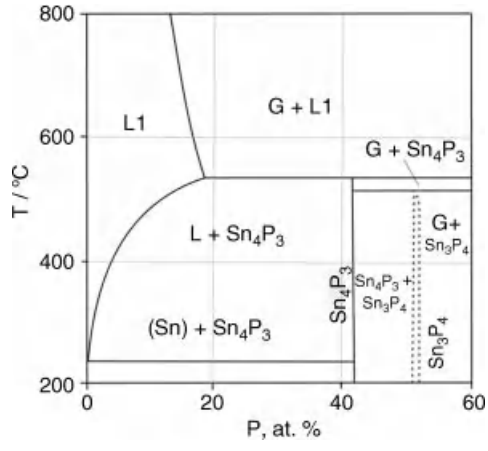

Figure 4.4 *P-Sn phase diagram at a P pressure of 0.3 bar according to Ref. [41]; this phase diagram significantly differs from the version shown in Ref. [46] because several phases are shown to be in direct equilibrium with the gas phase. (Reproduced with permission from Pressure dependent phase diagrams of binary alloys 1997 by Y. Levinsky, G. Effenberg and S. Ilenko, Materials Park, Ohio Copyright (1997) ASM International).*

Samples in the P-Sn system are characterized by high vapor pressures. Vivian [47] claimed that samples with a P content of more than 8.5 wt% have to be made in so-called pressure tubes. Melting of these samples occurred under considerable evaporation of P so that the P-Sn phase diagram cannot be regarded as isobaric. Indeed, a certain P vapor pressure appears to be necessary to allow the formation of the reported phases [50], and evaporation of P from P_4Sn_3 results in the formation of P_3Sn_4 that formally corresponds to the reaction $G + P_3Sn_4 = P_4Sn_3$. This would result in a phase-diagram representation quite different from that by Vivian and by Massalski *et al.* [46, 47]. Indeed, Levinsky *et al.* [41] suggested a pressure-dependent phase diagram also for P-Sn, where at P pressures of less than 1 bar the binary compounds are formed directly out of the gas phase (Figure 4.4) resulting in phase equilibria totally different from the original diagram. (This is, however, again not based on experimental data.)

4.2.2 New Experimental Results

From the very beginning, it has to be noted that the condition of constant pressure that is usually applied to phase diagrams of intermetallic systems does not hold in the present systems Ni-P and P-Sn due to the presence of P vapor of considerable pressure at high temperatures and high P contents. For example, in the DTA experiments the samples are actually heated under their own vapor pressure so that during the measurements the conditions inside the DTA tube can change with the temperature, and with it the composition of the samples may change noticeably.

4.2.2.1 Ni-P

Starting from the literature survey above and based on an extensive experimental study including XRD, electron probe microanalysis (EPMA), and DTA, a new version of the Ni-P

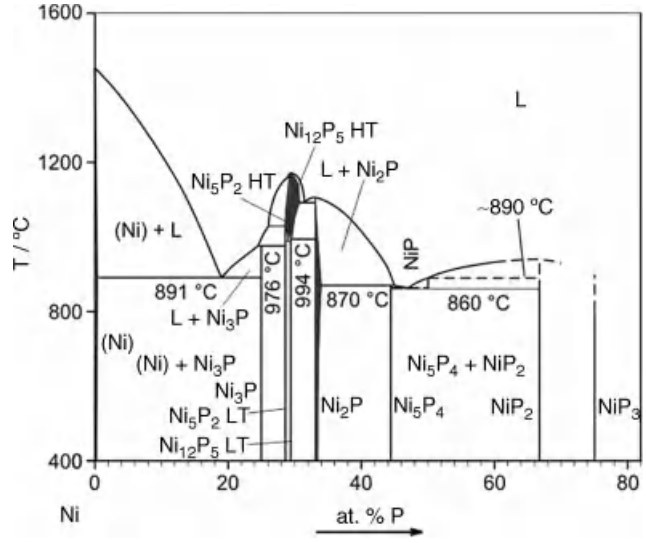

Figure 4.5 *Ni-P phase diagram modified according to the new experimental results, see also Refs. [31, 64]. (Reproduced with permission from Intermetallics, A new investigation of the system Ni-P by Schmetterer, C., J. Vizdal, H. Ipser, 17, 10, 826 Copyright (2009) Elsevier Ltd).*

phase diagram was established by Schmetterer *et al.* [31], which is shown in Figure 4.5. The same intermetallic compounds as previously described were found in this study, except for $Ni_{1.22}P$, for which no evidence whatsoever could be obtained (cf. Table 4.2). In good agreement with the literature, most compounds were found to be line compounds, and the compositions of these phases were also consistent with previous reports.

For Ni_2P, there is a small homogeneity range from 33.2 to 33.8 at% P at 700 °C according to the recent investigation. While this had been tentatively indicated already in Ref. [46], it was now investigated in more detail, and a slight widening of the homogeneity range on the P-rich side was found from 33.5 at% P at 550 °C to 33.9 at% at 810 °C, in good agreement with the results of the thermodynamic study [53] (see Section 4.4.2.1). Difficulties still exist for the Ni_5P_2 LT phase whose XRD pattern could not be described satisfactorily using the structural model from Oryshchyn *et al.* [38]. Further single-crystal studies will be necessary to clarify this situation.

In the literature the existence of HT modifications was reported for Ni_5P_2 and $Ni_{12}P_5$. Indeed, in the recent investigation thermal effects pertinent to the transition between the LT and HT modifications were found at 1029, 987 and 994 °C, whereas the XRD patterns always showed the corresponding LT-phases. Thus, it is concluded that the HT modifications cannot be retained by quenching and that the corresponding transition reactions take place at very high reaction rates, a phenomenon not uncommon with intermetallic HT phases. No crystallographic information is therefore available for these two HT phases. This question could only be solved using high-temperature XRD that is likely to be hampered by severe evaporation of P. The observed thermal effects were assigned to the transformation indicated in Figure 4.6, with one more invariant reaction tentatively placed at approximately 1005 °C, resulting in a congruent transformation of $Ni_{12}P_5$ LT into its HT modification. In

Table 4.2 *System Ni-P: compositions and homogeneity ranges of binary phases.*

Phase Designation	Structure Type	Composition at% P	Reference
(Ni)	Cu	0–0.9	[31]
		0–0.32	[30]
Ni_3P	Ni_3P	25.0	[31]
		25.0	[38]
		25.0	[30]
Ni_5P_2 LT	Ni_5P_2	28.4	[31]
		28.1	[38]
		28.6	[30]
$Ni_{12}P_5$ LT	$Ni_{12}P_5$	29.3	[31]
		29.3	[38]
		29.4	[30]
Ni_2P	Ni_2P	33.2–33.9	[31]
		33.4–n.d.	[38]
		33.3–n.d.	[30]
Ni_5P_4	Ni_5P_4	44.1	[31]
		44.4	[30]
NiP	NiP	50	[30]
NiP_2	NiP_2	65.5	[31]
		66.7	[30]
NiP_3	NiP_3	75	[30]

n.d.: not determined.

addition, several monovariant effects below the liquidus were observed, which were interpreted as the crossing of solvus and solidus curves.[5] This analysis suggested the existence of significant homogeneity ranges of the HT phases, as shown in the phase diagram (Figure 4.6).

Based on extensive DTA data, a modification was introduced in the melting behavior of the HT phases: $Ni_{12}P_5$ HT is shown in the new version as a congruently melting phase, and Ni_5P_2 HT is formed out of $Ni_{12}P_5$ HT in a peritectic reaction p1 at 1161 °C (see also Table 4.3). This is the reverse of the previous version based on the work of Yupko *et al.* [33]. Thus, according to the present data, $Ni_{12}P_5$ HT plays an important role for the solidification behavior of alloys in this composition range: it forms congruently out of the melt and transforms congruently into the LT modification. The other phases Ni_5P_2 HT, Ni_5P_2 LT and Ni_3P are formed by a cascade of peritectic reactions (at 1161, 1029, and 976 °C, respectively) starting from $Ni_{12}P_5$ HT, too. The temperatures of all other invariant reactions are in rough agreement with existing literature reports, with some exceptions: for example, a temperature of 891 °C was obtained for the eutectic L = (Ni) + Ni_3P instead of 870 °C in Ref. [30] (see also Table 4.3).

In the central part of the phase diagram the congruent melting of Ni_5P_4 was shown in Ref. [46] together with a eutectic L = Ni_2P + Ni_5P_4 at either 830 °C [32] or 880 °C [30]. According to Schmetterer *et al.* [31] this phase is formed by a peritectic reaction L + Ni_2P = Ni_5P_4 at 870 °C; this is also supported by metallographic investigations and XRD.

[5] For the interpretation of these monovariant effects the onset temperature of the peak on heating was taken for the precipitation of an additional phase (i.e. the beginning of a two-phase field) and the maximum was taken for the end of this precipitation (i.e. the end of a two-phase field).

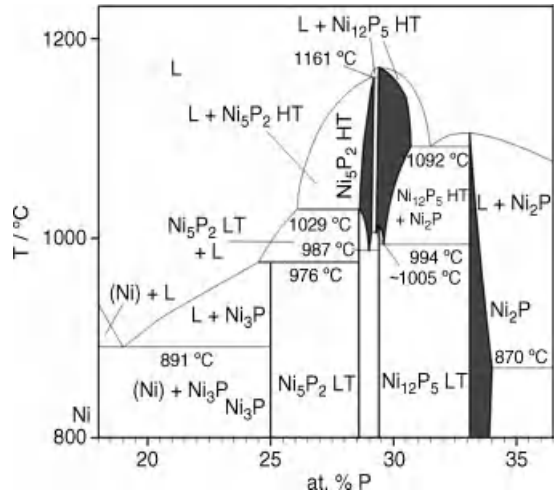

Figure 4.6 *Ni-rich part of the Ni-P phase diagram showing the homogeneity ranges introduced for the high temperature phases and Ni_2P, see also Refs.: [31, 64]. (Reproduced with permission from Intermetallics, A new investigation of the system Ni-P by Schmetterer, C., J. Vizdal, H. Ipser, 17, 10, 826 Copyright (2009) Elsevier Ltd).*

The phase NiP reported by Larsson [39] was found in samples annealed at 900 °C in Ref. [31]. DTA showed an invariant effect at 860 °C, which agrees with the eutectoid decomposition of this phase at about 850 °C according to Ref. [39] ($NiP = Ni_5P_4 + NiP_2$). The phase rule requires the presence of a eutectic $L = Ni_5P_4 + NiP$ between 860 and 870 °C that was actually observed at 863 °C in corresponding DTA curves. In all samples annealed below 860 °C the two phases Ni_5P_4 and NiP_2 were found in XRD and EPMA. As there was absolutely no indication of the existence of the phase $Ni_{1.22}P$ (see Larsson [39]), it was excluded from the present version of the phase diagram.

Considerable evaporation of P complicated the experiments at temperatures above 860 °C for P contents higher than 45 at%. Nonequilibrium was frequently encountered, that is, more than two phases were found in the same sample, and this situation is further aggravated by the presence of a metastable eutectic $L = Ni_2P + NiP$ reported in Ref. [39].

In the light of the phase diagram suggestion by Levinsky [41] and considering the observed severe evaporation of P from (partially) liquid samples, the phase diagram for P contents beyond 40 at% may look quite different for P pressures below 1 bar than that given by Schmetterer *et al.* [31]. Isopiestic measurements (see Section 4.4) suggest equilibrium between the gas phase and Ni_2P or Ni_5P_4, respectively, at lower pressures. Indeed, the degradation experiments done by Biltz and Heimbrecht [43] showed the transformation of NiP_3 into NiP_2 and so on by evaporation of P from the samples meaning that the gas phase is involved in the formation of these phases in the reverse process. This could explain the encountered experimental difficulties in this composition range since samples were prepared in evacuated quartz tubes under the (usual) assumption that changing pressure had little or no influence on the phase equilibria. This, however, is obviously not true.

Table 4.3 *System Ni-P: invariant reactions.*

Reaction	Composition of involved phases [at% P]			Temperature [°C], type and designation		
				This work		Literature [30]
$L = (Ni) + Ni_3P$	19.0	0.32	25.0	891, eutectic	e14	870, eutectic
$L + Ni_5P_2\ LT = Ni_3P$	24.5	28.6	25.0	976, peritectic	p3	970, peritectic
$L + Ni_5P_2\ HT = Ni_5P_2\ LT$	26.1	28.65	28.6	1029, peritectic	p2	1025, peritectic
$Ni_5P_2\ HT = Ni_5P_2\ LT + Ni_{12}P_5\ LT$	29.0	28.6	29.4	987, eutectoid	e8	1000, eutectoid
$Ni_{12}P_5\ HT = Ni_5P_2\ HT + Ni_{12}P_5\ LT$	29.3	29.1	29.4	~1005, eutectoid	e4	1025, peritectoid
$L + Ni_{12}P_5\ HT = Ni_5P_2\ HT$	29.05	29.2	29.4	1161, peritectic	p1	—
$L = Ni_5P_2\ HT$		28.6		—		1170, congruent
$L + Ni_5P_2\ HT = Ni_{12}P_5\ HT$	30.5	28.6	29.4	—		1125, peritectic
$L = Ni_{12}P_5\ HT$		29.4		1170, congruent		—
$Ni_{12}P_5\ HT = Ni_{12}P_5\ LT + Ni_2P$	29.6	29.4	33.2	994, eutectoid	e6	1000, eutectoid
$L = Ni_{12}P_5\ HT + Ni_2P$	31.5	30.7	33.2	1092, eutectic	e3	1100, eutectic
$L = Ni_2P$		33.3		1105, congruent		1110, congruent
Metastable						[39]
$L = Ni_2P + NiP$				n.d.		undetermined, eutectic

Experimental work[6] based on the isopiestic method, as is currently being carried out for the P-Sn system (see Section 4.2.2.2), in combination with thermodynamic modeling would therefore be desirable to provide a solid basis for an improved phase-diagram version and for the introduction of the pressure dependence in this system.

Three samples were prepared in the P-rich part at 69, 72 and 75 at% in Ref. [31] and annealed at 200, 400 and 700 °C. XRD analyses revealed the three phases NiP_3, NiP_2 and Ni_5P_4 (traces) which may be caused by the influence of the gas phase. DTA measurements in this part were abandoned after explosion of a sample, sealed in a quartz capsule, in the DTA apparatus. However, it could be shown that the NiP_3 phase is stable at 200 °C, which is in contrast to the literature, where a lower stability limit of 700 °C is given [30].

4.2.2.2 P-Sn

Despite severe experimental difficulties caused by the evaporation of P, first results are available for the Sn-rich part of the P-Sn phase diagram. All three binary compounds as described in the literature were found in the investigations carried out so far: P_3Sn_4, P_4Sn_3 and P_3Sn. Many samples with P contents higher than 40 at%, prepared in conventional evacuated quartz tubes, contained all three compounds. Recently, Ganesan *et al.* [54] showed that, by the use of the isopiestic method with proper temperature and P-pressure selection, the P_4Sn_3 phase can be obtained in pure form.

Vivian [47] did not specify the type of the most Sn-rich invariant reaction that occurs at temperatures close to the melting of pure Sn (232 °C). A careful DTA experiment with a sample P_2Sn_{98} with pure Sn as a reference indicated a eutectic reaction $L = (Sn) + P_3Sn_4$ with a temperature of 231 °C. Furthermore, the shape of the liquidus curve for compositions up to 23 at% P (which is actually richer in Sn than the [L1 + L2] miscibility gap shown in the literature) could be nicely reproduced using DTA.

Further DTA measurements at higher P concentrations did not yield clear results. None of the invariant reactions suggested in Ref. [46] could be found, and the DTA samples lost large amounts of P due to evaporation, which condensed on the wall of the quartz capsule. Samples placed at compositions and annealing temperatures inside the [L1 + L2] miscibility gap for metallographic investigation lost equally large amounts of P, which resulted in a composition shift of more than 10 at%. Thus, it became clear that samples lose particularly large amounts of P when heated above the liquidus temperature.

In an attempt to suppress this P loss, additional pieces of red P were sealed in a separate crucible together with the sample in the same quartz tube. No clear results were obtained from this method either since the conditions were not identical for each sample and not well defined. Although no useful phase diagram data were obtained from these early experiments they showed several important points:

- P evaporation is excessive in the liquid phase;
- a certain P pressure is required for alloy preparation;
- precisely controlled conditions (p, T) are required for sample preparation to obtain reasonable results;
- liquid samples are partly ejected from the alumina crucibles during quenching due to faster cooling of the quartz capsule than the sample that results in the immediate breakdown of the P pressure inside the tube;

[6] Note that the phase diagram suggestion by Levinsky *et al.* [41] lacks experimental data entirely.

- on air cooling (within 5–10 min) the samples react back with the P in the gas phase, while the vapor pressure of the sample is still high.

From these points, in particular from the latter two, it was concluded that the current version of the phase diagram (Refs. [46, 47]) does not apply to pressures below 1 bar and that a phase-diagram version similar to the suggestion by Levinsky *et al.* for this system [41] seems likely.

In order to provide the required experimental data, and in the light of the previous experience it turned out to be necessary to prepare samples by means of an isopiestic technique (the principle of which will be described in Section 4.4) that had worked well for the preparation of single-phase P_4Sn_3 [54]. This method allows fixing a certain vapor pressure provided by a P reservoir kept at a defined temperature.

In the isopiestic method, the individual alloys are in true equilibrium with the gas phase so that each sample has to be considered as 'condensed phase(s) + gas phase'. Since the gas phase cannot be captured as such by quenching, the samples appear to contain one condensed phase, or occasionally two phases, in a binary system (of course, the liquid phase transforms into solid phases on quenching). From the weight change of the sample due to reaction with gaseous P relative to its initial composition (which, however, is usually pure Sn) the new composition for the fixed temperature and P pressure can be calculated. This new composition represents the limiting P content possible at the given set of pressure and temperature, that is, a sample with a higher P content will lose P and vice versa. From the course of these results it is therefore possible to establish the boundary between the respective condensed phase and the gas phase. An important criterion for the validity of this method is the possibility to retain the high-temperature state during quenching that thus needs to be fast enough.

To meet this requirement a small-scale isopiestic experiment was set up employing tubes of 300 mm length and 12 mm inner diameter. Otherwise, the method was very much like the standard size setup (as described in Section 4.4). The tubes were quenched in such a way that the end with the P reservoir would get immersed into the water last in order to maintain the pressure inside the tube as long as possible.

Due to the numerous experimental problems that had to be overcome (and of which only a brief summary is given above) the investigation of the P-Sn system at various pressures is still in progress. For the construction of the phase-diagram sections shown in Figure 4.7a–d, the primary results from the isopiestic experiments described in Section 4.4 were used for P pressures up to 0.3 bar, while for the 0.7 bar run the described small-scale data were taken. It can be seen that the outline of the phase diagram changed entirely compared to the versions shown in Refs. [46, 47]. Sample compositions after the isopiestic treatment are indicated in the diagrams.

The most significant difference is the presence of the gas phase virtually over the entire composition range that consists of almost pure P at the given temperatures [72]. Furthermore, at these low pressures the binary compounds were found to form out of the gas phase and not out of the liquid phase alone. This interpretation is based on two facts:

- Apparent two-phase samples – that is, in fact three phases including the gas phase – were obtained at certain temperatures, indicating three-phase equilibria between two condensed phases and the gas phase. These phases represent invariant reactions in the binary system involving the gas phase, and the temperature at which this equilibrium was observed was taken as the reaction temperature.

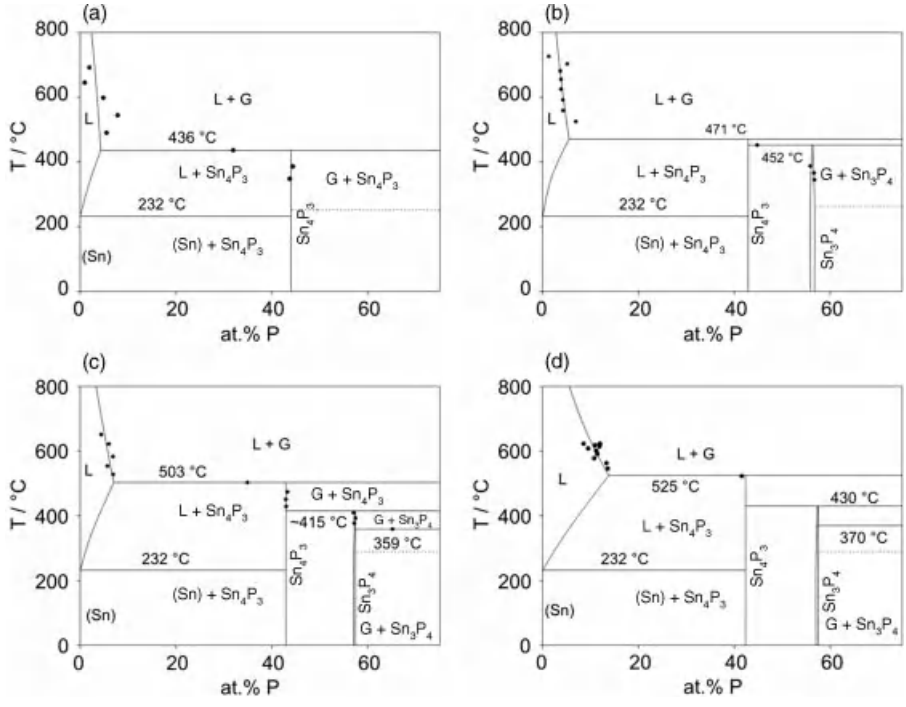

Figure 4.7 *T–x sections of the P-Sn phase diagram at various P vapor pressures: (a) 0.04 bar; (b) 0.16 bar; (c) 0.28 bar; (d) 0.7 bar.*

- The evaporation of P from the samples on heating suggests that the gas phase has to be involved in the decomposition/formation of the compounds.

In this way, P_3Sn_4 is formed by a peritectic-like reaction $G + L = P_3Sn_4$, whereas a syntectic reaction $L1 + L2 = P_3Sn_4$ had been given in Refs. [46, 47]. If there is a change in the formation mechanism of this phase with pressure it has to involve a quadruple point at the composition of the P_3Sn_4 phase, where G, L1, L2, and P_3Sn_4 meet. This could indeed be the case since the limiting liquid composition of the $G + L = P_3Sn_4$ reaction gets richer in P with increasing pressure. This, however, still needs to be checked, as the required investigations between 0.7 and 1 bar have not yet been carried out.

At 0.04 bar the phase P_4Sn_3 was not found at all, and it is likely that it is simply not stable at this low vapor pressure; at higher pressures both phases, P_3Sn_4 and P_4Sn_3, were found, as given in the original phase diagram.

The Sn-rich eutectic was taken as determined by DTA (231 °C); at this low temperature the vapor pressure of P over the alloy is still insignificant. The pressure in the sample container was about 10^{-2} bar, and it was concluded that this reaction involving condensed phases only would not be influenced much by the pressure. The reaction $G + L = Sn_4P_3$ rises from 436 °C at 0.04 bar to 525 °C at 0.7 bar and seems to approach gradually the temperature of the previously reported syntectic reaction so that the quadruple point mentioned before is indeed possible. The formation reaction of P_4Sn_3, $G + Sn_4P_3 = P_4Sn_3$, displays an unusual behavior, since it seems to decrease from 452 °C (0.16 bar) to 415 °C

(0.28 bar) and then to rise to 430 °C (0.7 bar). However, this requires still more experimental data to be clarified. The P-rich reactions were only indicated as dotted lines due to the lack of own data or information from Levinsky *et al.* [41].

4.3 Ternary Phase Equilibria Ni-P-Sn

4.3.1 Literature Overview

In the ternary Ni-P-Sn system most literature deals with the determination of crystal structures of various ternary compounds of which five have been described so far (see Table 4.4): $Ni_{10}P_3Sn$ (T1) [55], $Ni_{21}P_6Sn_2$ (T2) [56], $Ni_{10}P_3Sn_5$ (T3) [57], $Ni_{13}P_3Sn_8$ (T4) [58], and Ni_2PSn (T5) [59]. The structures of T3, T4, and T5 are related to the NiAs

Table 4.4 *System Ni-P-Sn: space groups and compositional and thermal stability ranges of ternary phases.*

Compound	Max. stability temp. [°C]	Melting/ decomposition behavior	Composition [at%]	Literature
$Ni_{10}P_3Sn$ (T1) *P3m1*	~1010	congruent	$Ni_{71.4}P_{21.4}Sn_{7.2}$ $Ni_{71.4}P_{21.4}Sn_{7.2}$	[63, 64] [55]
$Ni_{21}P_6Sn_2$ (T2) *Fm$\bar{3}$m*	991	congruent	$Ni_{72.4}P_{20.7}Sn_{6.9}$ $Ni_{72.4}P_{20.7}Sn_{6.9}$	[63, 64] [56]
$Ni_{10}P_3Sn_5$ (T3) *P$\bar{1}$*	~800	not known	$Ni_{54.2}P_{16.6}Sn_{29.2}$ – $Ni_{57.9}P_{15.3}Sn_{26.8}$ (550 °C) $Ni_{54}P_{16.7}Sn_{29.3}$ – $Ni_{56.2}P_{15.8}Sn_{28.0}$ (700 °C) $Ni_{55.6}P_{16.7}Sn_{27.7}$ (700 °C)[a]	[63, 64] [57]
$Ni_{13}P_3Sn_8$ (T4) *P$\bar{1}$*	700–800	not known	$Ni_{54.2}P_{11.8}Sn_{34}$ – $Ni_{58.2}P_{11}Sn_{30.8}$ (550 °C) $Ni_{54.0}P_{13.5}Sn_{32.5}$[b] (700 °C) $Ni_{54.2}P_{12.5}Sn_{33.3}$ (700 °C)	[63, 64] [58]
Ni_2PSn (T5) *Pnma*	721	peritectic	$Ni_{48.7}P_{25.3}Sn_{26}$ – $Ni_{49}P_{24.5}Sn_{26.5}$ $Ni_{50}P_{25}Sn_{25}$	[63, 64] [59]
Ni_3Sn_2 HT *P6$_3$/mmc*	—	congruent in binary	limiting ternary comp.: $Ni_{52.9}P_{17.6}Sn_{29.5}$ maximum P-Conc.: 17	[63, 64] [60]

[a] from chemical formula; no other composition given.
[b] from nonequilibrium samples.

type, and T3 and T4 form on cooling out of a large ternary solid solution based on Ni_3Sn_2 HT [60]. This ternary solid solution itself was described by Furuseth and Fjellvåg [60], and its homogeneity range was described by the overall formula $Ni_{1+m}P_xSn_{1-x}$ ($0.00 \leq m \leq 0.65, 0.00 \leq x \leq 0.32$). Thorough investigations of ordering phenomena of P and Sn in this ternary solid solution based on electron-diffraction measurements and the elucidation of the crystal structures of T3 and T4 were done later by Furuseth and coworkers [57, 58, 61].

Ni_2PSn (T5) is reported to decompose into Sn (sic!) and Ni_2P at 732 °C [59]. Its crystal structure shows some similarities to the MnP type, but with a complete ordering of P and Sn atoms. $Ni_{10}P_3Sn$ (T1), with its own crystal structure type, was claimed to have a melting point of approximately 850 °C [55].

In the literature dealing with IMC formation in solder joints yet another phase, Ni_3PSn, is cited [19–22]. These findings, however, are highly questionable, and a phase with this stoichiometry has never been explicitly mentioned in the original literature.

No phase-diagram information has been available so far, except for a sketch of the solid solution of P in Ni_3Sn_2 HT in Ref. [60]. Results of the recent phase-diagram study performed by Schmetterer *et al.* [56, 62–64] will be summarized below; a full description is available from the original literature.

4.3.2 Experimental Results

The ternary Ni-P-Sn system was represented in a number of sections in Refs. [62–64]. Four partial isothermal sections between 200 and 850 °C, three partial isopleths, the liquidus surface and the reactions scheme of the Ni-rich part are available from these sources, and several examples out of these will be shown here. Similar to the binary investigations, numerous experimental difficulties had to be overcome to prepare the corresponding samples. Detailed accounts on sample preparation are given in Refs. [62–64] so that a brief description is considered sufficient here.

Weight loss due to evaporation resulted in slight shifts of the composition of some of the samples causing disagreement between the final phase triangulation and observed phases in the samples. A more serious problem was the embrittlement of the quartz capsules employed for alloying on direct contact with the reaction mixture. Although a number of quartz tubes broke after cooling, in most cases the samples were not oxidized and no reaction between quartz and sample had occurred. Thus, it must be assumed that strong wetting forces during cooling caused breaking of the quartz. As a consequence, samples had to be contained in alumina crucibles that were then inserted into the quartz tubes for sealing.

The investigation of the annealed samples followed the standard methods employed in phase-diagram determination. In the DTA measurements, samples needed to be kept in closed quartz crucibles in order to avoid evaporation of P, which limited the maximum temperature to 1200 °C. The primary results from all investigations are available in Refs. [62–64]. Homogeneity ranges of ternary phases and detailed information on the invariant reactions are compiled here in Tables 4.4 and 4.5, respectively.

4.3.2.1 Ternary Compounds

Altogether, five ternary compounds were found during the experimental investigations as mentioned above. Before a detailed description of the phase equilibria is given, several aspects of the ternary phases with significance to the phase diagram shall be discussed.

Table 4.5 *System Ni-P-Sn: invariant reactions in the Ni-rich part of the system.*

Reaction	Designation and Temperature [°C]	Type
$L + Ni_5P_2\ HT = Ni_5P_2\ LT + Ni_{12}P_5\ HT$	U1, ~1015	transition reaction
L = T1	melting, 1010	congruent
L = T2	melting, 991	congruent
$L = Ni_3Sn_2\ HT + T1$	e7, 988	quasibinary eutectic
$L = Ni_{12}P_5\ HT + T1$	e5, 995–1010	quasibinary eutectic
$Ni_5P_2\ HT + Ni_{12}P_5\ HT = Ni_5P_2\ LT + Ni_{12}P_5\ LT$	U2, 987–1005	solid-state reaction
$L + Ni_{12}P_5\ HT = T1 + Ni_5P_2\ LT$	U3, 985–1010	transition reaction
$L + T1 = Ni_5P_2\ LT + T2$	U4, 985	transition reaction
$Ni_{12}P_5\ HT + Ni_2P = L + Ni_{12}P_5\ LT$	U5, 982	transition reaction
L = T1 + T2	e9, 978–991	quasibinary eutectic
$L + T1 = Ni_3Sn_2\ HT + T2$	U6, 978	transition reaction
$L = Ni_3Sn_2\ HT + Ni_{12}P_5\ HT$	e10, ~965	quasibinary eutectic
$Ni_5P_2\ LT + Ni_{12}P_5\ HT = T1 + Ni_{12}P_5\ LT$	U7, 960	solid-state reaction
$L = Ni_3Sn_2\ HT + Ni_{12}P_5\ HT + T1$	E1, 952	ternary eutectic
$L + Ni_3Sn_2\ HT = Ni_3Sn\ HT + T2$	U8, 948	transition reaction
$L + T = Ni_3P + T2$	U9, 947	transition reaction
$Ni_{12}P_5\ HT + T1 = Ni_3Sn_2\ HT + Ni_{12}P_5\ LT$	U10, 941	solid-state reaction
$L + Ni_{12}P_5\ HT = Ni_3Sn_2\ HT + Ni_{12}P_5\ LT$	U11, ~930	transition reaction
$Ni_{12}P_5\ HT = Ni_3Sn_2\ HT + Ni_{12}P_5\ LT$	e11, ~915	quasibinary eutectoid
$L = Ni_3Sn_2\ HT + Ni_2P$	e12, 912	quasibinary eutectic
$L = Ni_{12}P_5\ LT + Ni_2P + Ni_3Sn_2\ HT$	E2, 908	ternary eutectic
$L + Ni_3Sn\ HT = (Ni) + T2$	U12, 872	transition reaction
$L = (Ni) + Ni_3P + T2$	E3, 861	ternary eutectic
$(Ni) + Ni_3Sn\ HT = Ni_3Sn\ LT + T2$	U13, ~830	solid-state reaction
$Ni_3Sn\ HT = Ni_3Sn_2\ HT + Ni_3Sn\ LT + T2$	E4, 808	ternary eutectoid
$T + T2 = Ni_3P + T1$	U14, 700–850	solid-state reaction
$Ni_3Sn_2\ HT + T3 = Ni_{12}P_5\ LT + T4$	U15, 550–700	solid-state reaction

$Ni_{10}P_3Sn$ (T1) was originally described by Keimes *et al.* [55]; it was found to be a line compound, and its stoichiometry was in good agreement with the EPMA results. Primary crystallization of this phase together with a melting temperature of 1010 °C indicate congruent melting, in contradiction to Keimes *et al.* [55] who mentioned a melting point close to 850 °C.

$Ni_{10}P_3Sn$ differs in composition from neighboring $Ni_{21}P_6Sn_2$ (T2) by only one at% in the P content. Its crystal structure (see Refs. [56, 64]) is an ordered ternary variant of the C_6Cr_{23} structure type common to many ternary borides and phosphides of the same stoichiometry. It is a line compound, too, and the obtained EPMA/EDX data agree with the stoichiometry ($Ni_{72.4}P_{20.7}Sn_{6.9}$) of this compound. The congruent melting point of T2 was found at 991 °C by DTA.

The C_6Cr_{23} structure type ($Fm\bar{3}m$ symmetry) of T2 is well known from the literature [65]. Many ternary ordered compounds of this type have been reported, for example, $Fe_{21}W_2C_6$ by Westgren [66], with C often having been replaced by B or P (see e.g., Refs. [67–71]). Although earlier attempts to prepare $Ni_{21}Sn_2P_6$ by Keimes and Mewis were apparently not successful [70] its discovery in the Ni-P-Sn system provides a logic extension of this series.

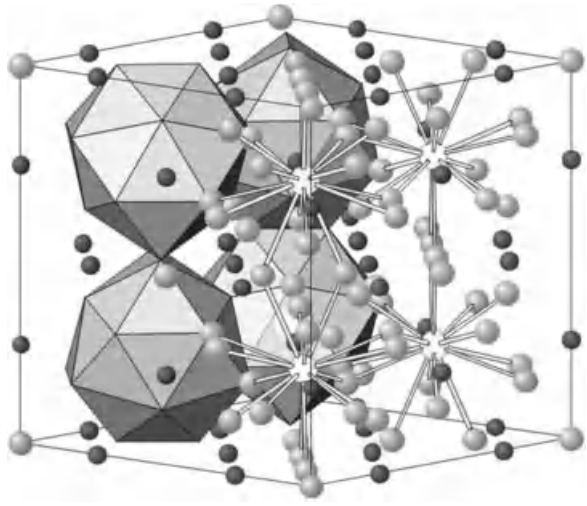

Figure 4.8 *General view of the $Ni_{21}P_6Sn_2$ crystal structure showing the coordination of Sn built from Ni1 and Ni2 atoms. The Ni atoms are shown light gray, P dark black and Sn white, see also Refs. [56, 64].*

The $Ni_{21}Sn_2P_6$ variety of the C_6Cr_{23}-type structure is shown in Figure 4.8; it contains five distinct atom positions: three Ni, one Sn and one P, the latter corresponding to the C position in the prototype. A detailed description of the structure of $Ni_{21}Sn_2P_6$ and its relation to other C_6Cr_{23} structures as well as to the neighboring $Ni_{10}P_3Sn$ phase is given in Refs. [56, 64].

T1 and T2 are the only congruently melting ternary compounds in the Ni-P-Sn system. For the formation of the remaining ternary compounds, the large *ternary solid solution of Ni_3Sn_2HT* plays an important role. At 850 °C it extends up to 17.6 at% P into the ternary system (approximately 17 at % according to Furuseth and Fjellvåg [60]). However, there are differences in the proposed homogeneity ranges: in Ref. [60] a U-like shape was proposed that could not be confirmed in the recent investigation. A strong variation of the lattice parameters of the Ni_3Sn_2 HT phase was found by XRD that is consistent with the inclusion of P in the lattice. On the Ni-rich side the values change from $a = 412.54$, $c = 519.95$ pm in the binary Ni_3Sn_2 HT phase to $a = 387.16$, $c = 521.10$ pm at $Ni_{56.8}P_{14.5}Sn_{28.7}$, which is basically comparable with the evaluation of Furuseth and Fjellvåg. In Ref. [61] Furuseth *et al.* reported the existence of complex modulated structures within the solid solution range around $Ni_{52.4}P_{14.3}Sn_{33.3}$ and proposed a structural model. As it is not clear if this represents a true ternary compound, it was not considered for the present phase diagram as an independent phase.

Between 850 and 700 °C the two ternary compounds $Ni_{10}P_3Sn_5$ (T3) [57] and $Ni_{13}P_3Sn_8$ (T4) [58] develop out of this large ternary solid solution, and the solubility of P in Ni_3Sn_2 HT reduces to 3.3 at % at 550 °C. Composition values for the two phases T3 and T4 can be derived from the crystal-structure determinations mentioned in Refs. [57] and [58] ($Ni_{54.2}P_{12.5}Sn_{33.3}$ and $Ni_{55.6}P_{16.7}Sn_{27.7}$) that are in good agreement with the values obtained in the present study [63, 64] (see Table 4.4). The crystal structures of both phases are triclinic

superstructures of the $InNi_2$-type structure of Ni_3Sn_2 HT [57, 58] from which they form with decreasing temperature by a reaction sequence that is still unknown.

Ni_2PSn (T5) was described in Ref. [59] as a line compound, but was found in the present investigation to have a small homogeneity range at 550 °C that widens at 700 °C. Furthermore, the compound does not seem to be at its exact stoichiometric composition but rather slightly shifted towards the Sn-rich side. It decomposes at 721 °C in a quasibinary peritectic reaction L + Ni_2P = T5 and was not found as a stable phase at 850 °C. This result is in good agreement with the literature where a reaction temperature of 732 °C was given. This quasibinary peritectic is based on the observation of relevant DTA effects only along the section from Ni_2P to T5, but nowhere else. However, the reaction has to be considered tentative because of a few contradicting observations, as discussed in detail by Schmetterer *et al.* [62–64].

4.3.2.2 Development of the Phase Equilibria [62–64]

The liquidus surface of the Ni-P-Sn system has so far been investigated in the Ni-rich part [62] and is shown in Figure 4.9. It is based on DTA results, supported by metallographic investigations of the solidification behavior of a number of samples with the focus on the primary crystallization. A total of 27 ternary invariant reactions have been assigned in this composition range so far, of which five are quasibinary eutectics, twelve are ternary

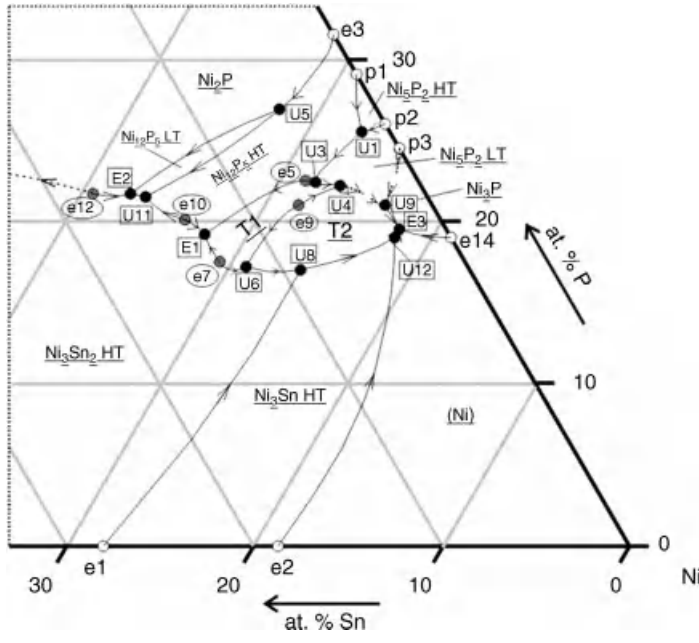

Figure 4.9 *Liquidus projection of the Ni-rich corner of the Ni-P-Sn system. Primary crystallization fields, binary and ternary invariant reactions involving the liquid phase are shown, see also Refs. [62, 64]. (Reproduced with permission from Metallurgical and Materials Transactions A, Ni-rich Part of the System Ni-P-Sn: Thermal Behavior by C. Schmetterer and Herbert Ipser, 41, 1, 43 Copyright (2009) Springer Science + Business Media).*

reactions that involve the liquid phase, eight are solid-state reactions, and two are the melting points of $Ni_{10}P_3Sn$ (T1) and $Ni_{21}P_6Sn_2$ (T2). They are summarized in Table 4.5 with their reaction equation, temperature and type. Those reactions that involve the liquid phase take place in a quite narrow temperature interval of approximately 150 °C. This complex development is also shown in the isopleth from Ni_3Sn to Ni_2P in Figure 4.10.

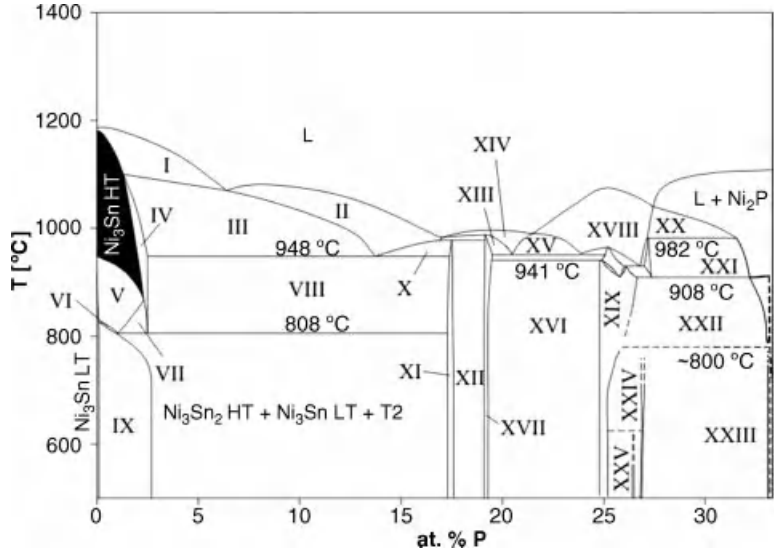

Figure 4.10 *System Ni-P-Sn: isopleth from Ni_3Sn to Ni_2P, see also Refs. [62, 64]. (Reproduced with permission from Metallurgical and Materials Transactions A, Ni-rich Part of the System Ni-P-Sn: Thermal Behavior by C. Schmetterer and Herbert Ipser, 41, 1, 43 Copyright (2009) Springer Science + Business Media).*

Phase-field designations:

I	L + Ni_3Sn HT	XIV	L + T1
II	L + Ni_3Sn_2 HT	XV	L + $Ni_{12}P_5$ LT + T1
III	L + Ni_3Sn_2 HT + Ni_3Sn HT	XVI	Ni_3Sn_2 HT + $Ni_{12}P_5$ LT + T1
IV	Ni_3Sn_2 HT + Ni_3Sn HT	XVII	Ni_3Sn_2 HT + T1
V	Ni_3Sn HT + Ni_3Sn LT	XVIII	L + $Ni_{12}P_5$ HT
VI	Ni_3Sn HT + Ni_3Sn LT + T2	XIX	Ni_3Sn_2 HT + $Ni_{12}P_5$ LT
VII	Ni_3Sn_2 HT + Ni_3Sn HT + Ni_3Sn LT	XX	L + $Ni_{12}P_5$ HT + Ni_2P
VIII	Ni_3Sn_2 HT + Ni_3Sn HT + T2	XXI	L + $Ni_{12}P_5$ LT + Ni_2P
IX	Ni_3Sn LT + T2	XXII	Ni_3Sn_2 HT + $Ni_{12}P_5$ LT + Ni_2P
X	L + Ni_3Sn_2 HT + T2	XXIII	$Ni_{12}P_5$ LT + Ni_2P + T3
XI	Ni_3Sn_2 HT + T2	XXIV	Ni_3Sn_2 HT + $Ni_{12}P_5$ LT + T3
XII	Ni_3Sn_2 HT + T1 + T2	XXV	Ni_3Sn_2 HT + $Ni_{12}P_5$ LT + T4
XIII	L + Ni_3Sn_2 HT + T1		

Large primary crystallization fields of Ni_3Sn HT, Ni_3Sn_2 HT, $Ni_{12}P_5$ HT and Ni_2P were found as well as smaller ones for T1 and T2, and the five quasibinary eutectic reactions link these congruently melting phases. However, the e-type reactions do not belong to true quasibinary systems since the tie lines below the eutectic temperature do not lie in the same vertical plane. Together with the binary invariant reactions they provide starting points for the thermal development of the phase equilibria. The quasibinary reactions divide the liquidus surface into (so far) four distinct regions, three in the Ni-rich part and the fourth being the continuation to the P/Sn-rich parts of the system. The three Ni-rich regions each have a ternary eutectic reaction representing the local liquidus minimum, that is, E1 at 952 °C, E2 at 908 °C, and E3 at 861 °C (see Figures 4.9 and 4.10). The three ternary eutectics E1 to E3 are connected with the binary invariant reactions by a series of U-type reactions in an intricate way, as shown in Figure 4.9 and discussed in full detail in Ref. [62].

The continuation to the P/Sn-rich part of the ternary system is formed by the three-phase field [L + Ni_2P + Ni_3Sn_2 HT] starting from the quasibinary eutectic reaction e12 at 912 °C. Unfortunately, phase equilibria on the P-rich side of the Ni_2P-Sn section are tentative, mostly because evaporation of P becomes significant, but also due to quenching problems.

T1 is the ternary compound with the highest congruent melting point (1010 °C) in the Ni-P-Sn system and is involved in a total of three quasibinary eutectic reactions: e7 at 988 °C, e5 between 995 and 1010 °C, and e9 between 978 and 991 °C. The latter one, e9, forms the connection to the ternary compound T2 with a congruent melting point of 991 °C.

A small part of the reaction sequence, that is, between U4 and U9 and between binary peritectic p3 and U9, could not be fully clarified so far due to unclear results in the proximity of the Ni_5P_2 phases. Here, EPMA measurements indicated a composition $Ni_{72.9}P_{26.3}Sn_{0.8}$ (designated 'T') that does not correspond to any known phase (see below). The reaction sequence described in Figure 4.9 (neglecting the omitted part) continues via reaction U9, L + T = Ni_3P + T2, at 947 °C (T being the phase mentioned above) and terminates in the eutectic reaction E3 at 861 °C that also represents the lowest liquidus temperature in the Ni-rich corner of the Ni-P-Sn system.

The complex reaction sequence so far creates the phase equilibria found in the isothermal section at 850 °C that is shown in Figure 4.11. At this temperature, no single-phase liquid exists in the Ni-rich part any longer but there are otherwise two large two-phase fields containing liquid, [L + Ni_3Sn_2 HT] and [L + Ni_2P], and the liquid phase covers a large part of the P/Sn rich side. The liquid phase frequently decomposes into several solid phases on cooling, and the matrix of partially liquid samples contains up to three decomposition products after quenching [62–64].

As described above, Ni_3Sn_2 HT forms a huge ternary solid solution with a maximum P content of 17.6 at % at 850 °C. On the Ni-rich side of this solid solution broad two-phase fields connect Ni_3Sn_2 HT with $Ni_{12}P_5$ LT and Ni_2P, respectively. The solubility of Sn in the Ni-P binary phases is generally negligible. Some uncertainty is still remaining in the vicinity of the Ni_5P_2 phases, where EPMA measurements revealed a phase with the composition $Ni_{72.9}P_{26.3}Sn_{0.8}$ (designated 'T', see above) in samples in the as-cast condition as well as after annealing at 550, 700 and 850 °C. The XRD patterns also contained peaks that could not be indexed using structure data from any known binary or

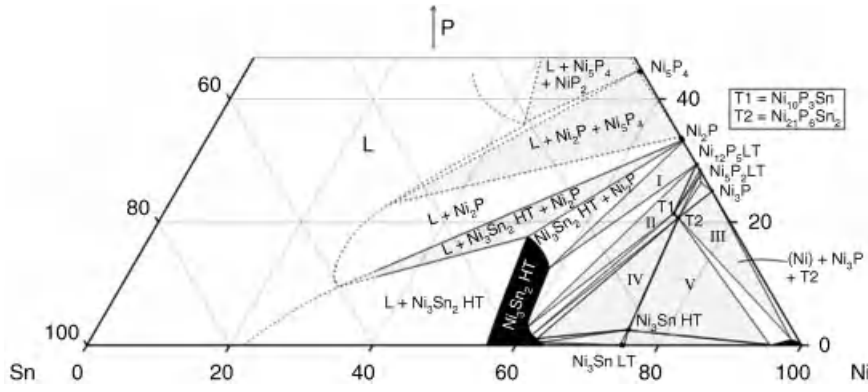

Figure 4.11 *System Ni-P-Sn: isothermal section at 850°C; single-phase regions are shown black, while three-phase fields are shown light gray, see also Refs. [63, 64]. (Reproduced with permission from Journal of Electronic Materials, The Ni-rich Part of the Ni-P-Sn System: isothermal Sections by C. Schmetterer, J. Vizdal, A. Kroupa, A. Kodentsov, H. Ipser, 38, 11, 2275 Copyright (2009) Springer Science + Business Media).*

Phase-field designations:

I = Ni_3Sn_2 HT + $Ni_{12}P_5$ LT + Ni_2P
II = Ni_3Sn_2 HT + $Ni_{12}P_5$ LT + T1
III = (Ni) + Ni_3P + T2
IV = Ni_3Sn_2 HT + Ni_3Sn HT + T2
V = (Ni) + Ni_3Sn HT + T2.

ternary phase. Basically, these observations could indicate the presence of another limited ternary solid solution, the stabilization of the binary Ni_5P_2 HT phase to lower temperatures, or the existence of yet another ternary compound. The phase equilibria shown around this composition T are, therefore, tentative but it is assumed for the phase triangulation in Figure 4.11 that T is the limit of a ternary solid solution of Ni_5P_2 LT (as is shown using dashed lines). If T was a true ternary compound, the related phase fields would have to be added accordingly.

Another important feature of the 850 °C isotherm is the appearance of the Ni_3Sn HT phase (BiF_3-type structure) that dissolves up to 2.5 at% P at this temperature. The diffraction pattern of a sample with the nominal composition $Ni_{71.25}P_5Sn_{23.75}$ annealed at 850 °C shows the Ni_3Sn HT phase together with Ni_3Sn_2 HT and T2. The appearance of Ni_3Sn HT at 850 °C and the fact that it can be retained by quenching are both remarkable; its binary stability range lies above 911 °C [23], and the binary phase cannot be stabilized by quenching. In the ternary system, DTA revealed the HT to LT transformation to occur between 808 and 830 °C, requiring a ternary eutectoid decomposition. It appears that the stabilization of BiF_3-type phases by ternary additions is not uncommon since it was also observed in the ternary systems Cu-Ni-Sn [73] and Ni-Sn-Zn [74]. Considering the present results for Ni_3Sn HT in the Ni-P-Sn system, it can be concluded that small quantities of dissolved elements like P may have a similar stabilizing effect.

Difficulties on the P-rich side of the Ni_2P-Sn section have already been mentioned. Nevertheless, it was possible to establish some of the phase fields, for example, the three-phase field [L + Ni_2P + Ni_5P_4] as shown in Figure 4.11 [63, 64].

The formation of the phases T3 ($Ni_{10}P_3Sn_5$) and T4 ($Ni_{13}P_3Sn_8$) out of the solid solution of Ni_3Sn_2 HT has to be a first-order transition because there is no direct group/subgroup relation between the space groups $P6_3/mmc$ and $P\bar{1}$. Thermal effects observed at approximately 800 °C in some samples placed between Ni_3Sn_2 HT and Ni_2P were interpreted to be related to the formation of the T3 phase. This temperature agrees nicely with a value of 797 °C mentioned by Furuseth and Fjellvåg [60] as the lower stability limit of the Ni_3Sn_2 HT ternary solid solution at a composition of $Ni_{53.5}P_{16.3}Sn_{30.2}$, although the exact formation mechanism of T3 out of Ni_3Sn_2 HT has so far not been elucidated.

Further solid-state reactions have to occur between 700 and 800 °C in order to yield the phase triangulation between [Ni_2P + T3] and [Ni_3Sn_2 HT + $Ni_{12}P_5$ LT + T3] at 700 °C. However, due to the fact that no thermal effects related to these reactions have so far been observed by DTA, the temperature range between 850 and 700 °C is left open or shown by dotted lines in the corresponding composition range of the isopleths in Figure 4.10.

The Ni_3Sn HT phase transforms into the LT phase via reaction U13 at approximately 830 °C and a eutectoid reaction at 808 °C that is also the lower stability limit of Ni_3Sn HT in the ternary system. At 700 °C the large homogeneity range of Ni_3Sn_2 HT has reduced to about 2 at % P, and the two ternary compounds, T3 and T4, have formed out of this phase. The composition of $Ni_{10}P_3Sn_5$ is close to the limiting P concentration found in Ni_3Sn_2 HT at 850 °C (see Table 4.4). According to García-García *et al.* [57] the crystal structure of T3 (triclinic superstructure of the $InNi_2$-type structure of Ni_3Sn_2 HT) was determined from a sample $Ni_{60}P_8Sn_{32}$ quenched from 700 °C containing the phases Ni_3Sn_2, Ni_2PSn and T3 (major component). However, in the present work no such three-phase field was found, and a sample at this nominal composition would in fact be placed within the three-phase field [Ni_3Sn_2 HT + $Ni_{12}P_5$ LT + T3].

In addition to T3 and T4, T5 is stable at 700 and 550 °C. Its formation, which is assumed to be quasibinary peritectic, is accompanied by a significant change in the phase equilibria. This requires the occurrence of a number of solid-state reactions between 850 and 700 °C that are listed in Table 4.5. Between 700 and 550 °C the phase equilibria in this area change once more, most likely according to the solid-state U-type reaction Ni_3Sn_2 HT + T3 = $Ni_{12}P_5$ LT + T4, in order to yield the three-phase fields [Ni_3Sn_2 HT + $Ni_{12}P_5$ LT + T4] and [$Ni_{12}P_5$ LT + T3 + T4] that were observed at 550 °C (see Figure 4.12).

On the Sn-rich side of $Ni_{10}P_3Sn_5$ (T3) the three-phase fields [L + T3 + T5] and [L + Ni_3Sn_4 + T3] were found according to the phase analysis. The remaining phase triangulation in the vicinity of Ni_3Sn_2 HT is shown by dotted lines, because inhomogeneities, fine-grained microstructures and precipitation of a dark phase within Ni_3Sn_2 HT grains hampered a reliable analysis by EPMA.

The remainder of the Ni-rich phase equilibria shows two significant aspects, when compared to the situation at 850 °C. First, the Ni_3Sn LT-phase was found at 700 and 550 °C, consistent with the transition temperatures of 808 and 830 °C. In contrast to the HT modification, the LT phase does not show any appreciable ternary solubility of P. The two-phase field [Ni_3Sn_2 HT + $Ni_{12}P_5$ LT] appears to exist down to the temperature of the HT to

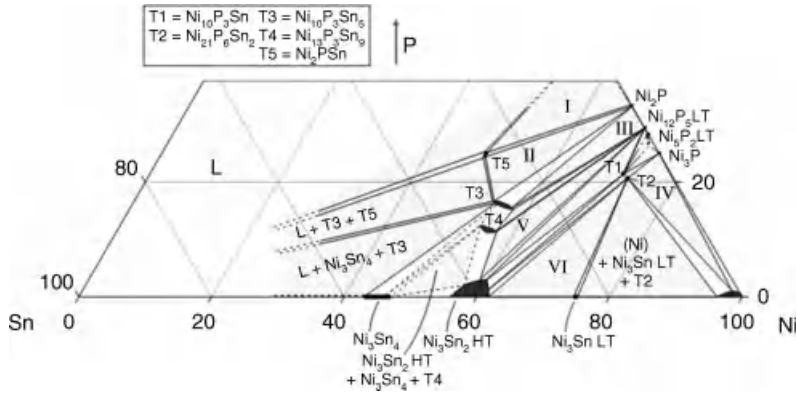

Figure 4.12 *System Ni-P-Sn: partial isothermal section at 550°C, see also Refs. [63, 64]. (Reproduced with permission from Journal of Electronic Materials, The Ni-rich Part of the Ni-P-Sn System: isothermal Sections by C. Schmetterer, J. Vizdal, A. Kroupa, A. Kodentsov, H. Ipser, 38, 11, 2275 Copyright (2009) Springer Science + Business Media).*

Phase-field designations:

I = Ni_2P + Ni_5P_4 + T5
II = Ni_2P + T3 + T5
III = $Ni_{12}P_5$ LT + Ni_2P + T3
IV = (Ni) + Ni_3P + T2
V = Ni_3Sn_2 HT + $Ni_{12}P_5$ LT + T4
VI = Ni_3Sn LT + Ni_3Sn_2 HT + T2.

LT transition in Ni_3Sn_2 (between 295 and 508 °C [23]) and can still be found at 550 °C. At this temperature, however, it has become significantly narrower.

The phase equilibria on the P-rich side of the Ni_2P-Sn section require still further work for clarification, since contradictory results were obtained here.

4.4 Thermochemical Data

Thermochemical data are an indispensable input for a reliable CALPHAD-type optimization of binary or higher-order systems. Therefore, it had been planned to extend the available thermodynamic information by experimental measurements in the two binary systems Ni-P and P-Sn and in the ternary Ni-P-Sn system. The so-called isopiestic method that allows obtaining partial pressures of volatile components [75] was considered a proper method to derive partial thermodynamic properties of P since its vapor pressure is higher by many orders of magnitude than that of Ni or Sn. In order to ascertain that the vapor phase over P-Sn alloys contains only the different molecular species of P and no mixed P-Sn molecules (a basic requirement for the application of the isopiestic method), Knudsen effusion mass spectrometry (KEMS) was additionally employed (see Section 4.4.2.2).

Due to experimental difficulties and due to problems with the interpretation of the results of isopiestic measurements in the ternary system, these measurements were restricted to the two binary systems Ni-P and P-Sn, and the ternary isopiestic experiments were abandoned altogether. A short account of the results of the thermodynamic experiments will be given below after the corresponding literature survey.

4.4.1 Literature Overview

4.4.1.1 Ni-P

A brief survey of the literature on the thermochemistry of the system was given by Lee and Nash [30] as well as by Schlesinger [76]. Details of the available thermochemical data, such as heat capacities, enthalpies of formation, vapor pressure and activity data, as well as Gibbs-energy data are summarized below, as well as in Table 4.6.

Heat capacity measurements in this system were carried out by Lu *et al.* [77, 78] and by Sarsenbaev *et al.* [79]. Lu *et al.* [77] measured the heat capacities of Ni-20 at% P alloys prepared in nanocrystalline, amorphous and crystalline forms over the temperature range 310–400 K and reported the average values. The corresponding data for a much larger temperature interval, that is, ∼200–600 K, were reported by Lu *et al.* in Ref. [78]. Sarsenbaev *et al.* [79] measured the heat capacity of Ni_2P over the temperature range 298–450 K and derived other thermodynamic functions assuming that $S^o(298.15\,K)$ of Ni_2P is the average of the corresponding values for Fe_2P and Co_2P reported in the literature.

Three different reports can be found in the literature on the direct determination of the *enthalpy of formation* of various nickel phosphides. Weibke and Schrag [80] determined the enthalpy of formation of Ni_3P and Ni_5P_2 by direct reaction calorimetry and reported values of -202.5 and $-401.2\,kJ\,mol^{-1}$, respectively at 903 K. Boone and Kleppa [81] measured the enthalpy of formation (ΔH_f^0 at 298.15 K) of "$Ni_{2.55}P$" with black phosphorus as the reference state and reported a value of $-180 \pm 8\,kJ\,mol^{-1}$. Recently, Delsante *et al.* [82] measured the enthalpy of formation of several Ni-P alloys by direct reaction drop calorimetry and reported interpolated values corresponding to the compounds Ni_3P, Ni_5P_2, $Ni_{12}P_5$, and NiP_2, as well as an estimated value for Ni_5P_4.

Four experimental investigations of equilibrium *vapor pressures* in the system have been reported in the literature. Biltz and Heimbrecht [43] determined equilibrium vapor pressures over two-phase mixtures (NiP_3 + NiP_2), (NiP_2 + "Ni_6P_5"), and ("Ni_6P_5" + Ni_2P), where most probably the compound "Ni_6P_5" is actually Ni_5P_4. The second study is that of Myers and Conti [83] who employed a Knudsen effusion mass-loss technique to measure the vapor pressure of P_2 over the mixtures (Ni_2P + $Ni_{12}P_5$) and ($Ni_{12}P_5$ + "$Ni_{2.55}P$"). Viksman and Gordienko [84] also used a Knudsen method to determine phosphorus partial pressures in equilibrium with Ni_3P and elemental Ni over the temperature range 1380–1790 K and derived ΔH_f^0 for Ni_3P. Zaitsev *et al.* [85] carried out extensive measurements by Knudsen cell mass spectrometry in the composition range 26–32.5 at% P between 971 and 1440 K and derived the values of ΔH_f^0 and ΔS_f^0 for the compounds Ni_3P, α-Ni_5P_2, γ-$Ni_{12}P_5$, and Ni_2P. For all the above cases, wherever applicable, the reported raw data were least-squares fitted, and the corresponding expressions are given Table 4.6. Finally, an emf method was employed by Kawabata *et al.* [86] to determine *activities* of P in liquid Ni-P alloys saturated with solid Ni over the temperature range 1477–1663 K.

Table 4.6 *System Ni-P: thermochemical data.*

No.	Reference	Data	Temp. Range (K)	Reported error
		(a) Heat capacity		
1.	Lu *et al.* 1991 [77]	$C_p^0(Ni_{80}P_{20})/J\,g^{-1}\,K^{-1} = 0.465$ (nanocrystalline) $= 0.446$ (amorphous) $= 0.414$ (crystalline)	310–400	<1% relative error
2.	Lu *et al.* 1993 [78]	$C_p^0(Ni_{80}P_{20})/J\,mol^{-1}\,K^{-1}$ = range from 21.037 to 28.687 (nanocrystalline) = range from 21.487 to 28.872 (amorphous) = range from 21.629 to 27.400 (crystalline)	205–565 205–565 205–595	
3.	Sarsenbaev *et al.* 1994 [79]	$C_p^0(Ni_2P)/J\,mol^{-1}\,K^{-1} = 154.1 - 0.065 \times 10^3(T/K) - 0.438 \times 10^5(T/K)^{-2}$	298–450	±10%
		(b) Enthalpy of formation		
4.	Weibke and Schrag 1941 [80]	$\Delta H_f^0(Ni_3P)/kJ\,mol^{-1} = -202.5^a$ $\Delta H_f^0(Ni_5P_2)/kJ\,mol^{-1} = -401.2^a$	903	±2%
5.	Boone and Kleppa 1991 [81]	$\Delta H_f^0(Ni_{2.55}P)/kJ\,mol^{-1} = -181^b$	298.15	±8 kJ mol^{-1}
6.	Delsante *et al.* [82]	$\Delta H_f^0(Ni_3P)/kJ\,mol\,at^{-1} = -48.0$ $\Delta H_f^0(Ni_5P_2)/kJ\,mol\,at^{-1} = -55.0$ $\Delta H_f^0(Ni_{12}P_5)/kJ\,mol\,at^{-1} = -56.0$ $\Delta H_f^0(NiP_2)/kJ\,mol\,at^{-1} = -61.0$ $\Delta H_f^0(Ni_5P_4)/kJ\,mol\,at^{-1} \sim -39.0$	927–1065	±2 kJ mol^{-1}
		(c) Vapor pressure		
7.	Biltz and Heimbrecht 1938 [43]	$\log(p_{P_4}/bar) \pm 0.014 = 9.927 - 9290 \cdot (K/T)$ over NiP_3–NiP_2[c, d]	870–940	Given in the expression
		$\log(p_{P_4}/bar) \pm 0.012 = 11.605 - 12\,606 \cdot (K/T)$ over NiP_2-"Ni_6P_5"[c, d] $\log(p_{P_4}/bar) \pm 0.026 = 12.241 - 13\,915 \cdot (K/T)$ over "Ni_6P_5"-Ni_2P[c, d]	1013–1077 1015–1096	

8.	Myers and Conti 1985 [83]	$\log (p_{P_4}/\text{bar}) \pm 0.131 = 14.586 - 24\,877 \cdot (\text{K}/T)$ over Ni_2P-$Ni_{12}P_5$[c, d]	1237–1362	Given in the expression
		Four data points over $Ni_{12}P_5$-$Ni_{2.55}P$ (2 degrees temperature interval)	1399–1401	
9.	Viksman and Gordienko 1992 [84]	Derived data $\Delta H_f^0(Ni_3P)/\text{kJ mol}^{-1} = -206.6$	1380–1790	$\pm 12.0\,\text{kJ mol}^{-1}$
10.	Zaitsev *et al.* 2003 [85]	Derived data[a] Ni_3P: $\Delta H_f^0 = -198.0 \pm 4.8\,\text{kJ mol}^{-1}$; $\Delta S_f^0 = -8.0 \pm 4.0\,\text{J.K}^{-1}.\text{mol}^{-1}$ α-Ni_5P_2: $\Delta H_f^0 = -379.4 \pm 9.1\,\text{kJ mol}^{-1}$; $\Delta S_f^0 = -10.5 \pm 7.0\,\text{J.K}^{-1}.\text{mol}^{-1}$ γ-$Ni_{12}P_5$: $\Delta H_f^0 = -931.6 \pm 22.1\,\text{kJ mol}^{-1}$; $\Delta S_f^0 = -27.2 \pm 17.0\,\text{J.K}^{-1}.\text{mol}^{-1}$ Ni_2P: $\Delta H_f^0 = -167.1 \pm 3.9\,\text{kJ mol}^{-1}$; $\Delta S_f^0 = -3.6 \pm 2.7\,\text{J.K}^{-1}.\text{mol}^{-1}$	971–1440	Given along with the data
		(d) Activity		
11.	Kawabata *et al.* 1995 [86]	$2 \log a_P \equiv \log p_{P_2} = -5.6\text{–}9700\,(\text{K}/T)$	1477–1612	
		$2 \log a_P \equiv \log p_{P_2} = -22.0\text{–}17\,000\,(\text{K}/T)$	1612–1663	
		$\Delta G^0_{P(Ni),1wt\%} = -210\,\text{kJ. g atom P}^{-1}$	1728	
		(e) Estimation		
12.	Ghosh and Hess 1962 [87]	$^1/_2\ P_2\ (g) + 3\ Ni\ (s) = Ni_3P\ (s)$; $\Delta G_T/\text{kJ mol}^{-1} = -266.9 + 0.0473\,(T/\text{K})$	298–1243	
		$P_2\ (g) + 5\ Ni\ (s) = Ni_5P_2\ (g?)$; $\Delta G_T/\text{kJ mol}^{-1} = -528.4 + 0.0941\,(T/\text{K})$		
		$^1/_2\ P_2\ (g) + 2\ Ni\ (s) = Ni_2P\ (s)$; $\Delta G_T/\text{kJ mol}^{-1} = -231.8 + 0.0473\,(T/\text{K})$	298–1298	
		$P_2\ (g) + Ni\ (s) = NiP_2\ (s)$; $\Delta G_T/\text{kJ mol}^{-1} = -262.8 + 0.0941\,(T/\text{K})$		
		$3/2\ P_2\ (g) + Ni\ (s) = NiP_3\ (s)$; $\Delta G_T/\text{kJ mol}^{-1} = -343.9 + 0.1414\,(T/\text{K})$	298–1383	
			298–?	
			298–?	
13.	Press *et al.* 1987 [89]	Ni_3P: $\Delta H = 1.2\,\text{eV atom}^{-1}$	—	
		$Ni_{12}P_5$: $\Delta H = 1.4\,\text{eV atom}^{-1}$		
		Ni_2P: $\Delta H = 0.7\,\text{eV atom}^{-1}$		

(*continued*)

Table 4.6 (*Continued*)

No.	Reference	Data	Temp. Range (K)	Reported error
14.	Shim *et al.* 1999 [90]	Ni_3P: ΔG_f^0/J g-atom^{-1} = − 50383.1 − 3.4658 (*T*/K) αNi_5P_2: ΔG_f^0/J g-atom^{-1} = − 55392.7 − 5.0530 (*T*/K) βNi_5P_2: ΔG_f^0/J g-atom^{-1} = − 55292.7 − 5.1300 (*T*/K) $\gamma Ni_{12}P_5$: ΔG_f^0/J g-atom^{-1} = − 56690.6 − 4.9716 *T* $\delta Ni_{12}P_5$: ΔG_f^0/J g-atom^{-1} = − 56590.6 − 5.0501 *T* Ni_2P: ΔG_f^0/J g-atom^{-1} = − 62790.4 − 4.4249 *T*	—	

[a] red (l) phosphorus as reference state.
[b] black phosphorus (orthorhombic) as reference state.
[c] original raw data given by authors were least squares fitted.
[d] standard deviation from straight line.

An *estimation of thermodynamic data* was done by Ghosh and Hess [87] based on the data reported by Kubaschewski and Evans [88]. In this way, they derived the Gibbs energies of formation of nickel phosphides from P_2(g) and Ni(s). Press *et al.* [89] reported values of the enthalpies of formation of Ni_3P, $Ni_{12}P_5$, and Ni_2P obtained by *ab-initio* calculations. Shim *et al.* [90] derived thermodynamic parameters by CALPHAD-type calculations based on available experimental data. Finally, Ren *et al.* [91] estimated the stability of nickel phosphides based on density functional theory and reported their lattice enthalpies.

4.4.1.2 P-Sn

Information on thermochemical data of P-Sn alloys is rather scarce. Guadagno and Pool [92] measured the relative partial molar heats of solution of P at infinite dilution in liquid Sn at 750 K by calorimetry, and they obtained a value of $24\,355 \pm 418$ J mol^{-1}. No concentration dependence was found up to 2 at% P. Suleimanov and Kuliev [93] studied the system by an emf method using a molten-salt electrolyte. The authors reported the Gibbs energy of formation, enthalpy of formation and entropy values at 673 K for the compounds P_4Sn_3, P_3Sn_4 and for a new compound PSn_5, and for the compound P_4Sn_3, also at 373 K. However, the energy units were not explicitly mentioned in their paper. Arita and Kamo [94] measured the activity of phosphorus over Sn-P alloys containing up to 45 at% P and derived the Gibbs energy of formation and enthalpy of formation for P_3Sn_4. Based on the experimental data reported by Arita and Kamo [94] and by Guadagno and Pool [92], Heuzey and Pelton [95] optimized the thermodynamic and phase equilibrium data for the P-Sn liquid solution and arrived at an expression for the Gibbs free energy of the liquid solution that can well account for the experimental data.

4.4.2 New Experimental Results

For both systems, Ni-P and P-Sn, partial pressures of P were determined by means of an isopiestic vapor pressure method. The basic principles of the isopiestic method have been described repeatedly [75, 96–98]. A schematic diagram of the experimental setup used in the present investigation is shown in Figure 4.13. The setup consists of an outer tube made of quartz glass where a graphite crucible with 25 mm O.D. is placed at the bottom serving as a reservoir for phosphorus. On top of the reservoir, a quartz glass spacer of suitable height is placed. Approximately 150–200 mg of pure Ni or Sn samples are filled into the crucibles (made from quartz or graphite for Ni-P and P-Sn, respectively) which are in turn placed inside graphite crucible holders having provisions for easy insertion of a quartz glass thermocouple well. About 10–15 of the holders are stacked along the thermocouple well, with excess amounts of red P placed in several of the holders at the top, that is, at high temperatures, which would recondense as white phosphorus in the reservoir during the experiment. The fully assembled apparatus is sealed under a dynamic vacuum of less than 10^{-3} mbar and is then heated in a vertical two-zone furnace for a period of about three weeks, with the P reservoir at the lowest temperature. The temperatures of the samples (T_S) and of the reservoir (T_R) are measured by raising a Pt/Pt10%Rh thermocouple inside the thermocouple well. After equilibration, the isopiestic apparatus is quenched in water and cut open under Ar atmosphere in a glove box. The individual samples (which have become Ni-P or P-Sn alloys during the equilibration) are weighed again and their compositions are derived from the mass difference, which is attributed to the uptake of phosphorus. Several

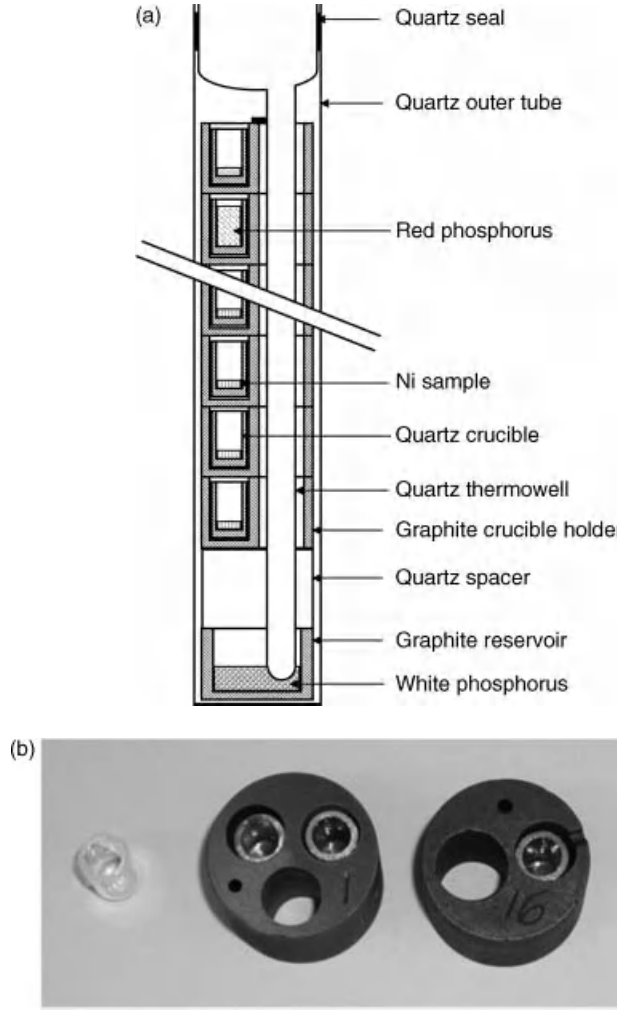

Figure 4.13 *Experimental isopiestic apparatus; (a) Schematics of isopiestic experimental setup; (b) Photograph showing single and dual sample holders.*

isopiestic experiments were carried out with sample holders that contain duplicate samples. Figure 4.13.b shows a photograph of single- and dual-sample holders. After equilibration, representative samples were characterized by powder XRD.

In all experiments it was found that liquid white phosphorus had condensed in the reservoir at the lowest temperature. As the vapor pressure of white phosphorus is dominant over that of the red modification for the reservoir temperatures employed, the phosphorus vapor pressure in the apparatus is clearly defined by the temperature of the reservoir of white phosphorus (see above).

Calculation of the activities of the individual samples can be carried out by using phase equilibrium software such as MTDATA® or ThermoCalc® with appropriate thermodynamic databases: first, the phosphorus vapor pressure above the reservoir is calculated, and then the phosphorus activity at the sample temperature relative to the selected reference phase. If phase equilibrium software packages are not available the pressure of phosphorus above the reservoir is given by Eq. (4.1) fitted to calculations carried out using the SGTE[7] pure substance database [99].

$$\log(p_{\text{total}}/\text{bar}) = 16.363 - 3408.2 \cdot (\text{K}/T) - 3.71177 \cdot \log(T/\text{K}) \qquad T : 370 - 500\,\text{K} \tag{4.1}$$

The calculation of the activity of phosphorus at the sample temperature is more complicated because it requires some knowledge of the speciation in the gas phase. The data for phosphorus species in the SGTE pure substance database are derived from those in the IVTAN[8] compilation that recognizes the following species: P, P_2, P_3 and P_4. However, for practical purposes, the vapor pressures of P and P_3 are several orders of magnitude smaller than those of P_2 and P_4, and can therefore be neglected. Thus, the total vapor pressure can be approximated by

$$p_{\text{total}} = p_{\text{P}_2} + p_{\text{P}_4} \tag{4.2}$$

The equilibrium between P_2 and P_4 is governed by the corresponding equilibrium constant

$$K_{\text{eq}} = \frac{p_{\text{P}_2}^2}{p_{\text{P}_4}} \tag{4.3}$$

Values of this equilibrium constant were calculated for the range of temperature and pressures appropriate to the samples and the resultant fit is given in Eq. (4.4)

$$\log(K_{\text{eq}}) = 10.89 - 12109.2 \cdot (\text{K}/T) - 0.914126 \cdot \log(\text{T}/K) \qquad T : 900 - 1450\,\text{K} \tag{4.4}$$

Arita and Watanabe [100] determined the equilibrium constant K_{eq} based on their own measurement of phosphorus vapor pressures between 373 and 1423 K, and their values are in close agreement with the data given by Eq. (4.4).

Equation (4.4) now allows the partial pressure of P_4 (and P_2) species to be calculated corresponding to the sample temperature and the pressure defined by the reservoir. For the calculation of phosphorus activities the species P_4 was chosen since its partial pressure is the highest:

$$a_{\text{P}} = \sqrt[4]{\frac{p_{\text{P}_4}(T_{\text{S}})}{p^0_{\text{P}_4}(T_{\text{S}})}} \tag{4.5}$$

[7] Scientific Group Thermodata Europe.
[8] Institute of High Temperature of the Russian Academy of Science.

According to the definition of the activity, the denominator in Eq. (4.5) is the partial pressure of P_4 at the sample temperature of the gas in equilibrium with pure liquid phosphorus. This can be obtained by Eq. (4.6), again calculated using data from the SGTE pure substance database [99].

$$\log(p_{P_4}/\text{bar}) = 13.511 - 3162.6 \cdot (\text{K}/T) - 2.82757 \cdot \log(T/\text{K}) \qquad T : 900 - 1450\,\text{K} \tag{4.6}$$

In the case of the P-Sn system additional measurements were performed using two different Knudsen effusion methods, that is, Knudsen effusion mass loss (KEML) and Knudsen effusion mass spectrometry (KEMS); the former for the determination of the equilibrium vapor pressures of the two-phase mixtures (L + P_3Sn_4) and (P_3Sn_4 + P_4Sn_3), the latter to ascertain the nature of the molecular species in the vapor.

The basic principles of the KEML method are well described in Ref. [101]. In the present study the cylindrical effusion cells employed (10 mm in diameter and 16 mm in height) were machined from high-density graphite and had effusion orifices of various diameters ranging from 0.165 to 1.0 mm. The geometrical dimensions of the effusion holes were measured with a traveling microscope, and Clausing factors were calculated from the table of values reported in Ref. [102]. The high-temperature furnace is made with a cylindrical graphite resistance tube properly tapered in order to guarantee an isothermal zone in the central section. Temperatures were measured by a Pt/Pt10%Rh thermocouple.

In the KEMS experiments, whose features are well summarized in Ref. [103], a single focusing 12-inch 90° magnetic sector mass spectrometer (Patco) was used. A secondary electron multiplier provided the detection of ions that were produced from the vapors effusing from the Knudsen cell by electron impact, with an electron emission current generally regulated at 1.0 mA. The ion source features allowed the determination of the ionization efficiency curves (IEC) by continuously varying the energy of the electrons up to 100 V. The effusion cell made by high-density graphite was heated by means of a tungsten coil and its temperature was measured with a W-Re/W-Re 5/26% thermocouple.

A detailed description of the experimental methods can be found in the original literature [53, 72].

4.4.2.1 Ni-P

Seven successful isopiestic experiments were carried out in the Ni-P system with reservoir temperatures between 375 and 495 K that correspond to a total vapor pressure of phosphorus between about 5 and 310 mbar, respectively, and sample temperatures between 977 and 1325 K. The experimental results are shown in Figure 4.14 as a plot of the equilibrium sample temperatures versus composition (the so-called equilibrium curves) superimposed on the phase diagram given originally by Lee and Nash [30].

From the figure it can be seen that the equilibrium samples are covering the Ni-P phase diagram between about 32 and 44 at% P although the majority of the samples are single phase, namely Ni_2P, with a few data points in single-phase liquid and in the neighboring two-phase regions (Ni_5P_4 + Ni_2P) and (Ni_2P + L). It is interesting to note that, even though the equilibration of Ni samples was carried out over a wide range of phosphorus pressures (between 5 and 310 mbar), the majority of the samples were restricted to a narrow composition range, essentially representing the phosphorus-rich side of the

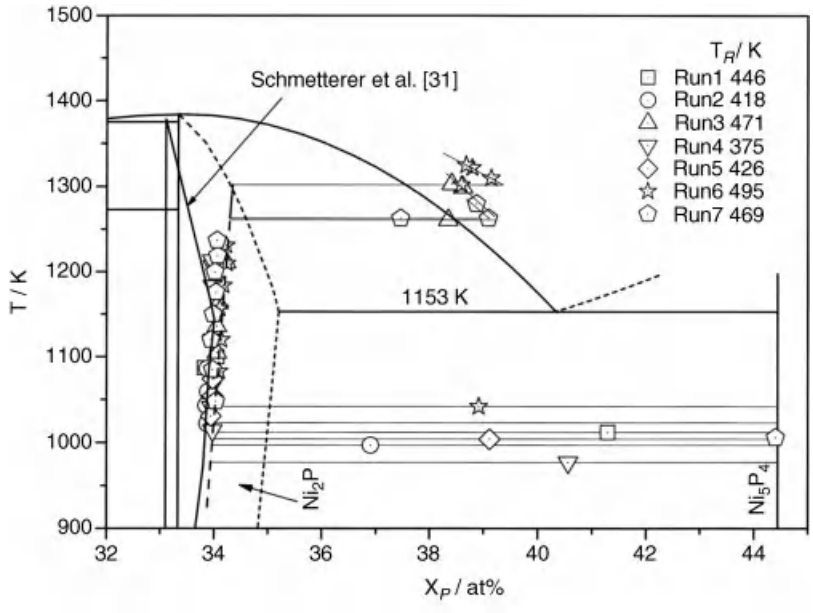

Figure 4.14 *System Ni-P: isopiestic equilibrium sample temperature vs. composition superimposed over the phase diagram by Lee and Nash [30].*

nonstoichiometric Ni_2P phase. Thus, the P-rich phase boundary of nonstoichiometric Ni_2P can be estimated from the present results, in reasonable agreement with the data by Schmetterer *et al.* [31] but shifted in comparison with the assessed phase diagram by Lee and Nash [30].

In order to derive partial enthalpies, natural logarithms of the phosphorus activities for selected close compositions between 33.85 and 34.20 at% P within the nonstoichiometric Ni_2P phase were plotted as a function of the reciprocal sample temperature. (The details of this approach are described elsewhere [75, 96–98].) For this purpose, the sample temperatures for the selected compositions were obtained by interpolation of the equilibrium curves in the Ni_2P phase region in Figure 4.14. They were used to calculate the partial enthalpies of mixing of P according to:

$$\frac{\partial \ln a_P}{\partial (1/T)} = \frac{\Delta \overline{H}_P}{R} \tag{4.7}$$

The obtained enthalpy data were used to convert the activity of P of samples in the Ni_2P phase, originally calculated for the individual sample temperature, to a common temperature of 1123 K, which is the average temperature of the obtained data points. The results are shown in Figure 4.15 together with values for the neighboring two-phase fields: the value for (Ni_2P + Ni_5P_4) was derived from the present study, the one for (γ-$Ni_{12}P_5$ + Ni_2P) from Zaitsev *et al.* [85] after conversion to white P as standard state. On extrapolation of the ln a_P data in the Ni_2P phase to the values for the neighboring two-phase fields it was possible to

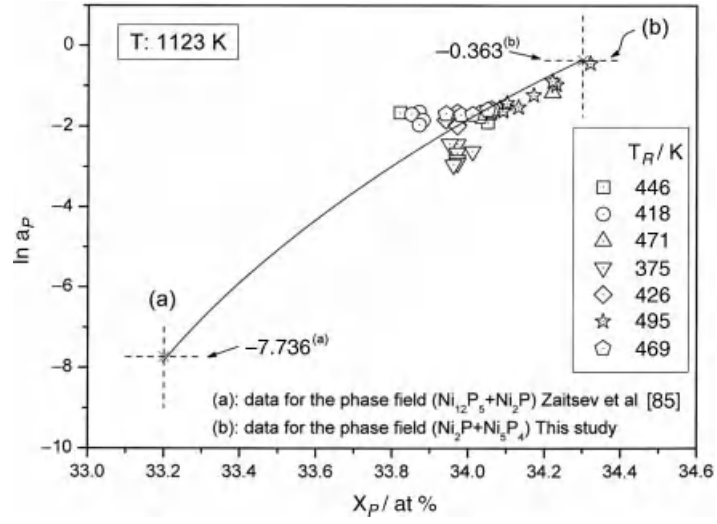

Figure 4.15 *System Ni-P: natural logarithm of the phosphorus activity as a function of composition in the Ni_2P phase at 1123 K; standard state: liquid P.*

estimate the corresponding phase boundaries (33.2 to 34.3 at% P at 1123 K) that are again in good agreement with Ref. [31]. Figure 4.15 shows that the value of a_P varies by about three orders of magnitude over the narrow homogeneity range of Ni_2P, indicating the high stability of this particular phase. This is supported by the enthalpy measurements by Delsante *et al.* [82] where the most negative value of ΔH_f^0 in the entire Ni-P system was found for the compound Ni_2P.

The phosphorus vapor pressures measured over the phase fields ($Ni_2P + Ni_5P_4$) and ($Ni_2P + L$) are shown in Figure 4.16 including also literature data by Biltz and Heimbrecht [43] for the phase field ("Ni_6P_5" + Ni_2P) that are in good agreement with the present data at lower temperatures, whereas they differ significantly at higher temperatures. These phosphorus pressure data correspond to the following equilibrium

$$5\,\mathrm{Ni_2\,P(s)} + 3/4\,\mathrm{P_4(g)} = 2\,\mathrm{Ni_5}\,P4(s) \tag{4.8}$$

which can be represented by the expression

$$\log(p_{\mathrm{P_4}}/\mathrm{bar}) \pm 0.119 = 26.021 - 27577 \cdot (\mathrm{K}/T) \qquad T : 977 - 1042\,\mathrm{K} \tag{4.9}$$

With this, the standard Gibbs energy of formation of Ni_5P_4(s) can be obtained using the value of $\Delta_f G_m^o(\mathrm{Ni_2\,P})$ from Zaitsev *et al.* [85], in the following way:

$$2\Delta_f G_m^o(\mathrm{Ni_5\,P_4})(\mathrm{s}) = 5\Delta_f G_m^o(\mathrm{Ni_2\,P})(\mathrm{s}) + (3/4)\,\mathrm{RT}\ln p_{\mathrm{P_4}} \tag{4.10}$$

and is calculated as (referred to liquid white P as reference state)

$$\Delta_f\, G_m^o(\mathrm{Ni_5\,P_4})(\mathrm{s}) \pm 9.8/(\mathrm{kJ\,mol^{-1}}) = -631.5 + 0.2130\,(\mathrm{T}/K) \qquad T : 977 - 1042\,\mathrm{K} \tag{4.11}$$

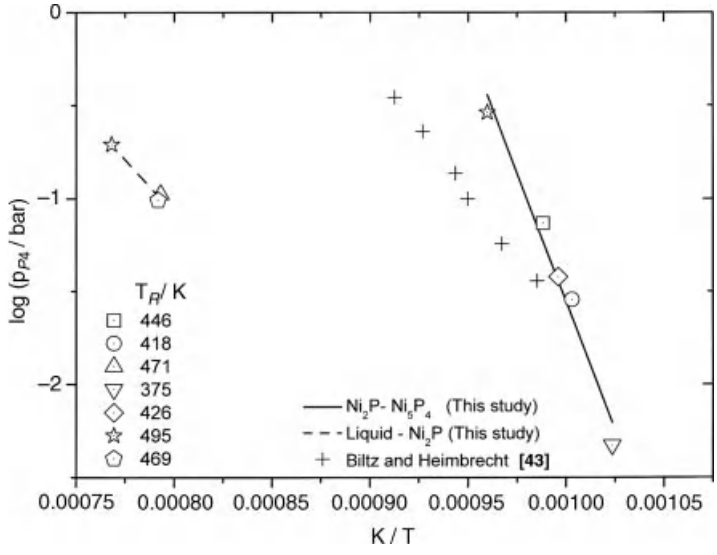

Figure 4.16 *System Ni-P: variation of phosphorus partial pressure (P_4) with temperature in the two-phase fields ($Ni_2P + Ni_5P_4$) and ($L + Ni_2P$).*

To the best of our knowledge, this is the first experimentally determined thermochemical value for the compound Ni_5P_4.

4.4.2.2 P-Sn

Six successful isopiestic experiments were carried out with reservoir temperatures between 315 and 518 K (corresponding to a total vapor pressure of P between 4 and 515 mbar, respectively) and sample temperatures between 618 and 998 K. The equilibrium sample temperatures and compositions (the so-called equilibrium curves) for each isopiestic run are shown in Figure 4.17 superimposed on the phase diagram given by Okamoto [104]. The uncertainty in the compositions is estimated to be less than 0.50 at% for samples containing <10 at% P, whereas it is estimated to be less than 0.25 at% for the rest of the samples. The temperatures are accurate within ± 2 K.

It can be seen from Figure 4.17 that the equilibrium samples obtained in all experimental runs cover the Sn-P phase diagram up to 71 at% P. The majority of the samples are single phase, namely liquid, P_3Sn_4, or P_4Sn_3, with a few data points in the two-phase regions ($L + P_3Sn_4$), ($P_3Sn_4 + P_4Sn_3$), and ($P_4Sn_3 + P_3Sn$). From the present results, the homogeneity range of the phases P_3Sn_4 and P_4Sn_3 at the corresponding temperature ranges can be estimated to be about 0.5 and 0.8 at%, respectively. It is to be pointed out that Zaikina *et al.* [50] were discontented with the present version of the phase diagram as reported by Massalski *et al.* [46], since the phase PSn was not incorporated. However, all the additional phases mentioned in the earlier literature, such as PSn, $P_{10}Sn_7$ and PSn_5, could not be found in the present investigations (see also Section 4.2.2.2), at least not under the pressure and temperature conditions employed. Since the isopiestic method is a true equilibrium method, that is, all compounds stable under the given experimental conditions should be formed, it

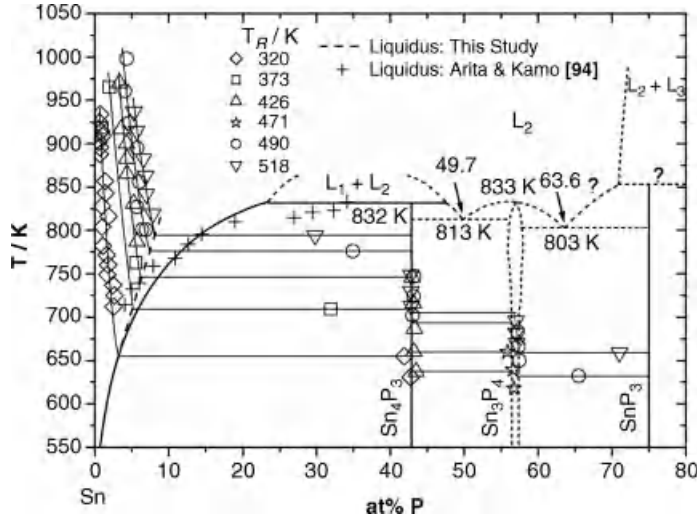

Figure 4.17 *System P-Sn: isopiestic equilibrium sample temperature vs. composition superimposed over the phase diagram according to Okamoto [104].*

must be concluded that they do not exist under the present temperature and pressure conditions.

Partial enthalpies of mixing $\Delta\overline{H}_P$ for the tin-rich liquid were obtained as described in Eq. (4.7). The obtained values were used to convert the activity of phosphorus to a common temperature of 750 K, as shown in Figure 4.18.

The kinks in the so-called equilibrium curves in Figure 4.17 provide valuable information on the shape of the phase boundaries, especially for the liquidus curve in the Sn-rich part of the system. The liquidus curve in the phase diagram by Okamoto [104] agrees reasonably well with the present data at lower temperatures (<675 K) but deviates distinctly towards more phosphorus-rich composition at higher temperatures. This has certainly to do with experimental problems in the original study by Vivian [47] as well as with the noticeable pressure dependence of the P-Sn phase diagram, as discussed in Section 4.2.2.2. Similarly, liquidus data by Arita and Kamo [94], obtained from their dew-point measurements, are also included in Figure 4.17, but they show a distinct deviation towards higher P contents at temperatures above 760 K. Again, this is most probably connected with the pressure dependence of the phase diagram, although some simplifications in the data evaluation in Ref. [94] may also contribute to the deviation (see the discussion in Ref. [72]). Actually, the present shape of the liquidus line refers to varying pressures according to the different reservoir temperatures. It is in reasonable agreement with the P-Sn phase diagram at pressures between 0.28 and 0.7 bar shown in Figure 4.7 and supports the results of the present phase-diagram study, independently of the nature of the invariant reaction(s) above 400 °C.

The P vapor pressures measured over the two-phase fields (L + P_3Sn_4), (P_3Sn_4 + P_4Sn_3), and (P_4Sn_3 + P_3Sn), both by the isopiestic method and the KEML method, are shown in Figure 4.19. It can be seen that the isopiestic data cover mainly the high

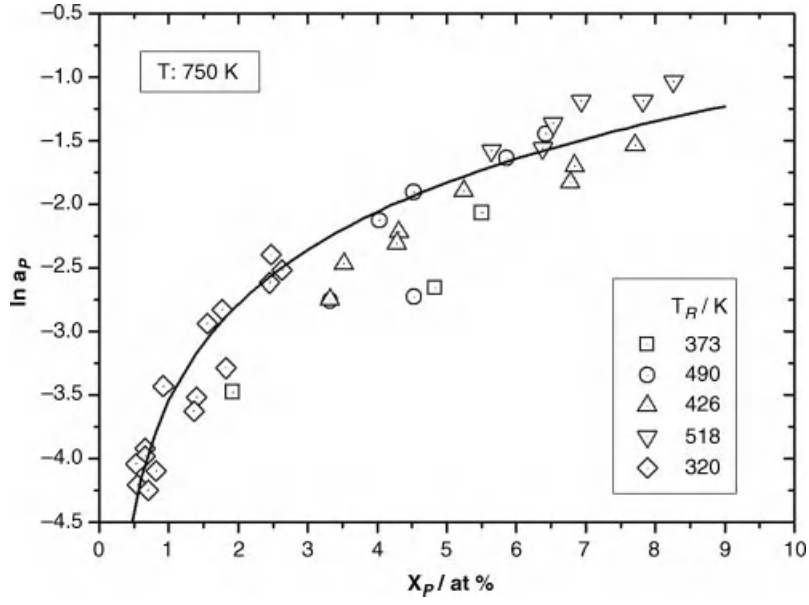

Figure 4.18 *System P-Sn: natural logarithm of the phosphorus activity as a function of composition in the liquid phase at 850 K; standard state: liquid P.*

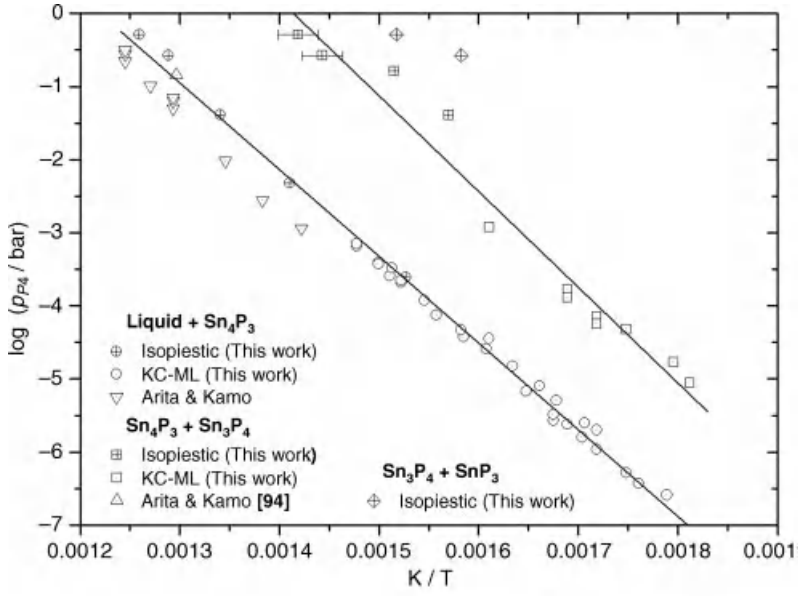

Figure 4.19 *System P-Sn: variation of phosphorus partial pressure (P_4) with temperature over the two-phase fields (L + P_3Sn_4), (P_3Sn_4 + P_4Sn_3), and (P_4Sn_3 + P_3Sn).*

temperature range whereas the low-temperature data were obtained from the KEML measurements, thus together covering a wide temperature range. Note that two of the high-temperature data for the phase field ($P_3Sn_4 + P_4Sn_3$) from isopiestic measurements are given with error bars as they could not be obtained directly from individual samples but had to be taken from the horizontal branches of the equilibrium curves of Runs 3 and 5. The rather good agreement between the results obtained by the two different methods indicates the reliability of the measurements, and hence they were combined for further interpretations. The data by Arita and Kamo [94] are also included in Figure 4.19, and it can be seen that their partial pressures for the phase field ($L + P_3Sn_4$) are somewhat lower (about 0.5 orders of magnitude) than the present data. On the other hand, there is only one data point by these authors for the phase field ($P_3Sn_4 + P_4Sn_3$) that seems to be more than two orders of magnitude lower than the present data on extrapolation. Due to the good agreement of the results of the two independent experimental methods of the present study they are thought to be more reliable.

Based on the obtained vapor pressure data and the information derived from the isopiestic experiments about the temperature ranges of coexistence of phases at various phosphorus pressures, a plot of the P activity as a function of composition is shown in Figure 4.20 for selected temperatures. It is evident from the figure that the P activity at 650 K increases drastically for alloys with phosphorus contents of more than 75 at%. With increase in temperatures, this dramatic increase of the P activity shifts more and more to lower P content.

The measured P pressure data over the two-phase field ($L + P_3Sn_4$) correspond to the equilibrium

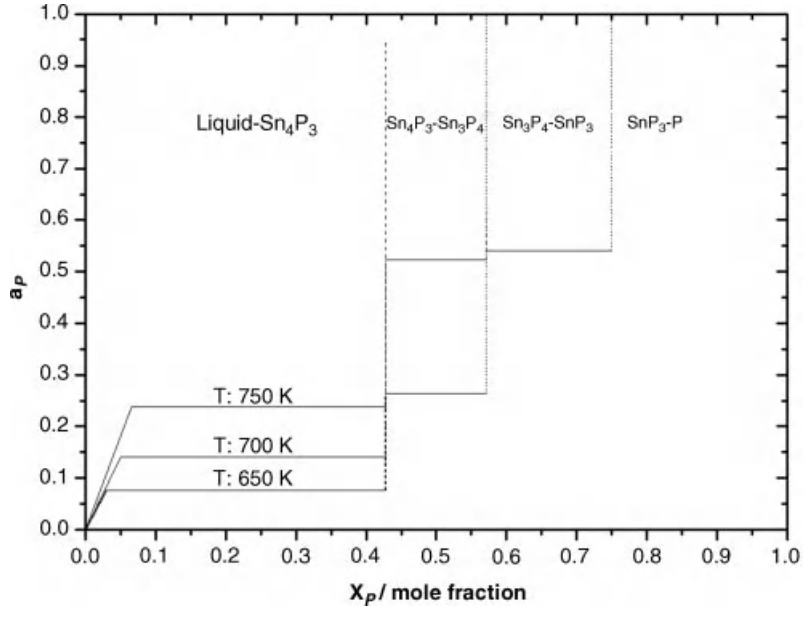

Figure 4.20 *System P-Sn: variation of the phosphorus activity with composition for selected temperatures.*

$$4[\mathrm{Sn}]_{\mathrm{Sn-P(l)}} + {}^{3}\!/_{4}\mathrm{P_4(g)} = \mathrm{P_3Sn_4(s)} \tag{4.12}$$

and can be represented by the following least squares fitted expression:

$$\log(p_{\mathrm{P_4}}/\mathrm{bar}) \pm 0.118 = 14.449 - 11851 \cdot (\mathrm{K}/T) \qquad T : 559 - 794\ \mathrm{K} \tag{4.13}$$

From this the standard Gibbs energy of formation of P_3Sn_4(s) can be obtained in the following way:

$$\Delta_{\mathrm{f}} G^{\mathrm{o}}_{\mathrm{m}}(\mathrm{P_3Sn_4})(\mathrm{s}) = 4\,RT \ln a_{\mathrm{Sn}} + {}^{3}\!/_{4}\,RT \ln p_{\mathrm{P_4}} \tag{4.14}$$

Extrapolating the liquidus line obtained from the isopiestic experiments to lower temperatures, assuming Raoult's law behavior for the Sn-rich liquid, and neglecting nonstoichiometry in P_3Sn_4, $\Delta_{\mathrm{f}} G^{\mathrm{o}}_{\mathrm{m}}(\mathrm{P_3Sn_4})(\mathrm{s})$ can be computed from the phosphorus pressure data as

$$\Delta_{\mathrm{f}} G^{\mathrm{o}}_{\mathrm{m}}(\mathrm{P_3\,Sn_4})(\mathrm{s}) \pm 1.1/(\mathrm{kJ\,mol^{-1}}) = -166.5 + 0.2007(T/\mathrm{K}) \qquad T : 559 - 794\ \mathrm{K} \tag{4.15}$$

where mol means one mole of formula unit of P_3Sn_4.

Figure 4.21 compares the standard Gibbs energy of formation of P_3Sn_4 obtained from the present measurements with data reported in the literature. The data point by Suleimanov and Kuliev [93] at low temperature is in good agreement with the present data (assuming the values given by these authors were in kcal); the values by Arita and Kamo [94] are in reasonable agreement with the present results at temperatures around 800 K, however, they deviate significantly towards lower temperatures. The mean value for the enthalpy of

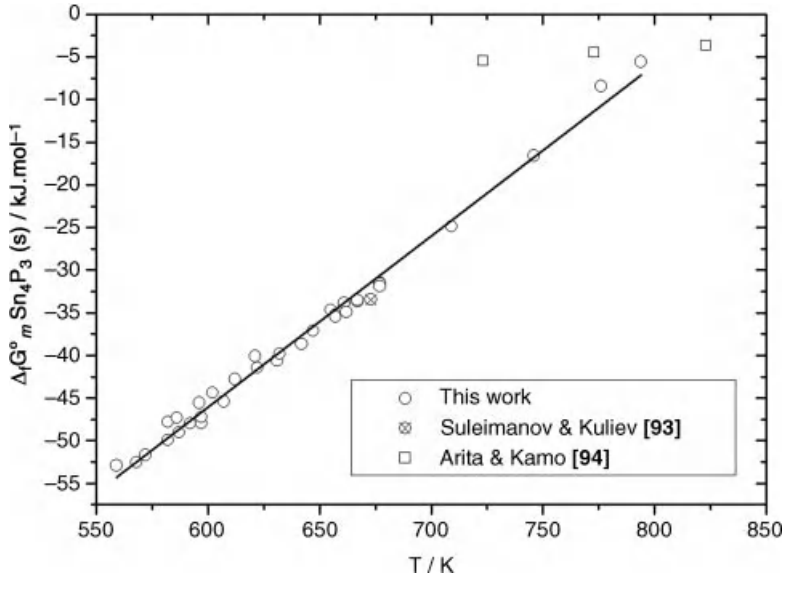

Figure 4.21 *System P-Sn: variation of standard molar Gibbs energy of formation of P_3Sn_4(s) with temperature.*

formation of this compound within the temperature range of the present measurements is $-166.5 \pm 1.1\ \mathrm{kJ\ mol^{-1}}$ whereas a value of $-100.4 \pm 5.0\ \mathrm{kJ\ mol^{-1}}$ had been reported by Suleimanov and Kuliev for 673 K [93]; Arita and Kamo [94] arrived at a value of $-18.4 \pm 0.6\ \mathrm{kJ\ mol^{-1}}$ for the temperature range 723–823 K, which is about one order of magnitude smaller than the present result.

In a similar way, the measured phosphorus pressure data obtained over the phase field ($P_3Sn_4 + P_4Sn_3$) correspond to the equilibrium

$$3\,P_3\,Sn_4(s) + 7/4\,P_4(g) = 4\,P_4\,Sn_3(s) \tag{4.16}$$

and can be represented by the following least squares fitted expression:

$$\log(p_{P_4}/\mathrm{bar}) \pm 0.118 = 18.533 - 13106 \cdot (\mathrm{K}/T) \qquad T : 552 - 705\ \mathrm{K} \tag{4.17}$$

The standard Gibbs energy of formation of $P_4Sn_3(s)$ can be obtained from the measured phosphorus pressure data in Eq. (4.17) and from $\Delta_f G^o_m(P_3\,Sn_4)$ in the following way:

$$4\,\Delta_f G^o_m(P_4\,Sn_3)(s) = 3\Delta_f G^o_m(P_3\,Sn_4)(s) + (7/4)RT\ln p_{P_4} \tag{4.18}$$

Neglecting any nonstoichiometry for the compounds P_3Sn_4 as well as P_4Sn_3, $\Delta_f G^o_m(P_4Sn_3)(s)$ was obtained from $\Delta_f G^o_m(P_3\,Sn_4)$ (as calculated by Eq. (4.15) and extrapolated to lower temperatures) and from the measured phosphorus pressure data, resulting in

$$\Delta_f G^o_m(P_4\,Sn_3)(s) \pm 1.8/(\mathrm{kJ\ mol^{-1}}) = -234.4 + 0.3053(T/\mathrm{K}) \qquad T : 552 - 705\ \mathrm{K} \tag{4.19}$$

Figure 4.22 compares the present data with those reported by Suleimanov and Kuliev [93]. Whereas their data point for 673 K is in excellent agreement with the present data, their

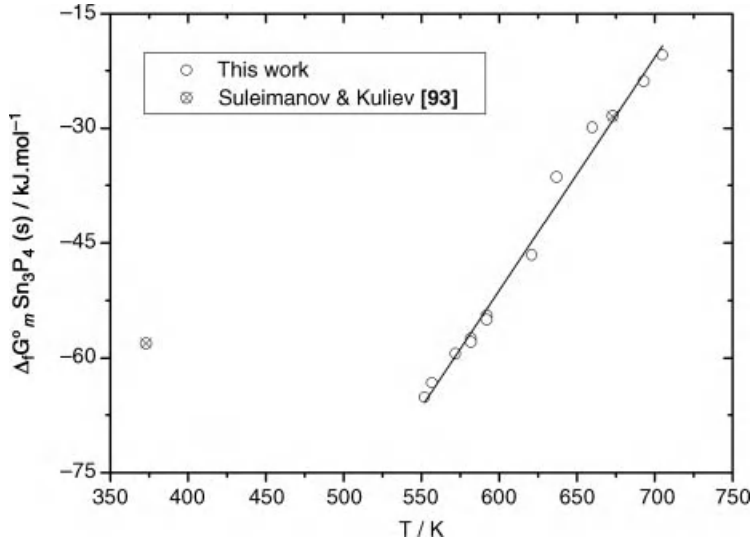

Figure 4.22 *System P-Sn: variation of standard molar Gibbs energy of formation of $P_4Sn_3(s)$ with temperature.*

result for 373 K deviates to a large extent, which can possibly be attributed to nonequilibrium conditions at such low temperatures. The mean enthalpy of formation of this compound within the temperature range of the present measurement is $-234.4 \pm 1.8\,\mathrm{kJ\,mol^{-1}}$ whereas a value of $-120.25 \pm 5.02\,\mathrm{kJ\,mol^{-1}}$ at 373 K was reported by Suleimanov and Kuliev [93].

Only two data points were obtained in the two-phase field (P_4Sn_3 + P_3Sn) representing the following equilibrium:

$$P_4Sn_3(s) + 5/4\,P_4(g) = 3\,P_3Sn(s) \tag{4.20}$$

Relying on these two points the following expression can be derived:

$$\log(p_{P_4}/\mathrm{bar}) = 6.343 - 4370 \cdot (\mathrm{K}/T) \qquad T : 632 - 659\,\mathrm{K} \tag{4.21}$$

The standard Gibbs energy of formation of $P_3Sn(s)$ can then be obtained from the measured phosphorus pressure data and from the data on $\Delta_f G^o_m(P_4Sn_3)$ by the following equation:

$$3\Delta_f\, G^o_m(P_3Sn)(s) = \Delta_f G^o_m(P_4Sn_3)(s) + (5/4)RT \ln p_{P_4} \tag{4.22}$$

Neglecting again any nonstoichiometry for Sn_3P_4, $\Delta_f G^o_m(P_3\,Sn)(s)$ was computed using $\Delta_f G^o_m(P_4\,Sn_3)$ from Eq. (4.18) and phosphorus pressure data:

$$\Delta_f G^o_m(P_3\,Sn)(s)/(\mathrm{kJ\,mol^{-1}}) = -113.0 + 0.1523(T/\mathrm{K}) \qquad T : 632 - 659\,\mathrm{K} \tag{4.23}$$

To the best of our knowledge, this is the first thermochemical value for the compound P_3Sn giving at least an estimate of the stability of this compound.

4.5 Relevance of the Results and Conclusion

As most of the experimental results obtained in this work concern phase equilibria and thermochemical data at elevated temperatures, above the usual working temperatures in soldering, the relevance of this work to the application in soldering may not be immediately obvious. The solder materials themselves are mostly Sn-rich alloys with low melting temperatures in the range between 200 and 230 °C, or in the case of high-temperature solders alloys with melting temperatures of up to 300 °C. On the other hand, IMCs that are formed during the soldering process exhibit frequently much higher melting temperatures and contain significant amounts of high-melting components. In order to understand the reactions during soldering and aging of the joints it is absolutely necessary to know practically the entire phase diagram. Phase-diagram studies at such low temperatures are usually no problem for the low-melting composition regions, but they become problematic in the rest of the alloy system where melting temperatures are high: very low diffusion rates hamper an equilibration of the samples within a reasonable time period.

One possible solution is to study the corresponding alloy systems at higher temperatures where well-equilibrated samples can be obtained within a reasonable time. With the support of thermochemical data (the more the better) the CALPHAD method provides a means to extrapolate, in a reliable way, the phase equilibria to those low temperatures which are of significance for soldering applications.

For the Ni-P-Sn system, this means that an isothermal section at 200 °C, for which there would be a strong demand, is only experimentally accessible in the very Sn-rich part since the liquidus rises steeply towards higher Ni concentrations. In order to construct the full isotherm, CALPHAD modeling will be required. As CALPHAD is a semiempirical method, the experimental high-temperature results provide an excellent starting point for the creation of the necessary dataset. In addition, the activity measurements that were carried out parallel to the phase-diagram studies provide an extension to the available literature information and will be valuable by themselves.

In the case of Ni-P-Sn additional experimental difficulties are caused by the behavior of the element phosphorus. The P-Sn-rich side of the system is especially characterized by the development of high P vapor pressures due to the evaporation of P from the alloys. Indeed, experiments in this part showed a number of unclear results that have so far prevented the definite determination of the phase equilibria at 200 °C. Frequently, four to six phases were observed in samples annealed at this temperature, which is caused by decomposition of the liquid, unfinished formation of low-temperature phases out of their parent phases, and the presence of P vapor at the alloying temperature, in combination with a complicated behavior on cooling. Low-temperature annealing, even for several months, did not allow establishing equilibrium and removing the nonequilibrium effects frozen in at higher temperatures. Furthermore, a number of samples revealed phase equilibria that violated the clear-cross principle, that is, the results indicated contradicting phase fields. As inconvenient as this may be from the viewpoint of experiments, it is at the same time a nice showcase for the points mentioned above: such a situation can only be clarified if the development of the phase equilibria from higher to lower temperature (in the form of the reaction scheme) can be obtained, for example by the support of CALPHAD-type calculations.

Despite all these difficulties the present results allow already answers to be given to two issues that were noticed in the existing solder-related literature, that is, the existence of a large ternary solid solution of P in Ni_3Sn_2 and the presumed existence of the Ni_3PSn phase: From the binary Ni-Sn phase diagram [23] it is clear that at temperatures relevant for soldering (around 200 °C) there are three Ni_3Sn_2 LT-phases. Furthermore, two ternary compounds exist in the Ni-P-Sn phase diagram, and the ternary solubility of the LT phases is rather limited at 550 °C and is unlikely to increase at 200 °C. The existence of a large ternary solid solution of a Ni_3Sn_2 phase, as claimed in the literature, is therefore rather unlikely.

As far as Ni_3PSn is concerned, there is no indication at all for the existence of such a compound in the present study, and the information from the literature is inconclusive. According to the literature the phase Ni_3PSn is said to be reported by Furuseth and Fjellvåg in Ref. [60] (see ICSD, Ref. [105]), but it is not even mentioned in their original paper. Ni_3PSn is claimed to be an $InNi_2$-type phase (cf. the TEM investigations by Hwang *et al.* [22]), which contradicts the observation of superstructure phases at lower temperatures. Furthermore, the phase composition given by the ICSD fits rather to a stoichiometry Ni_3PSn_2. Thus, the existence of a thermodynamically stable phase Ni_3PSn is highly improbable.

From an experimental point of view a lot of experience was gained during work on the phase diagrams of the P-containing systems. Since a significant P vapor pressure develops above a certain P content in the alloy, none of the P-containing systems is truly isobaric; for Ni-P this limit can be given at about 40 at% P, for P-Sn it is even lower. Of course, this limit also varies with the temperature. For P-Sn the gas phase has to be clearly included in the

phase-diagram work, even at compositions as low as a few at% P in the alloy at temperatures above approximately 500 °C.

This has severe consequences for the sample preparation and the interpretation of the acquired data:

- The common method of preparing alloys in evacuated quartz glass ampoules cannot be employed, because the phase equilibria are strongly pressure dependent. The practical assumption of pressure independence is not valid.
- Certain compounds require the presence of the gas phase to form.
- Nonequilibrium is frequently encountered in P-rich samples.
- During sample preparation, care has to be taken to allow sufficient reaction time; too fast heating can result in the build up of high pressures inside the tube causing explosions.

As the example of the P-Sn phase diagram shows, the conventional investigation techniques have to be modified in order to cope with the peculiarities of these systems.

Acknowledgments

The authors want to thank A. Ciccioli and G. Gigli (University La Sapienzia, Rome, Italy), A. Kodentsov (Eindhoven University of Technology, Netherlands), and J. Vizdal (University of Vienna, Austria) for valuable experimental help. Financial support of these studies by the Austrian Science Fund (FWF) under Project Nos. P17346 and P18968 is gratefully acknowledged. They are a contribution to the European COST Action MP0602 (HISOLD).

References

1. Zeng, K., Vuorinen, V., and Kivilahti, J.K. (2002) Interfacial reactions between lead-free SnAgCu solder and Ni(P) surface finish on printed circuit boards. *IEEE Trans. Electron. Pack. Manufact.*, **25**, 162–167.
2. Alam, M.O., Chan, Y.C., and Tu, K.N. (2003) Effect of reaction time and P content on mechanical strength of the interface formed between eutectic Sn-Ag solder and Au/electroless Ni(P)/Cu bond pad. *J. Appl. Phys.*, **94**, 4108–4115.
3. Yoon, J.-W. and Jung, S.-B. (2004) Growth kinetics of Ni_3Sn_4 and Ni_3P layer between Sn-3.5Ag solder and electroless Ni-P substrate. *J. Alloys Compd.*, **376**, 105–110.
4. Sohn, Y.C., Yu, Jin., Kang, S.K. *et al.* (2004) Effects of phosphorus content on the reaction of electroless Ni-P with Sn and crystallization of Ni-P. *J. Electron. Mater.*, **33**, 790–795.
5. Suganuma, K. and Kim, K.-S. (2008) The root causes of the "Black Pad" phenomenon and avoidance tactics. *JOM*, **60**(6), 61–65.
6. Yoon, J.W., Lee, C.B., and Jung, S.B. (2003) Growth of an intermetallic compound layer with Sn-3.5Ag-5Bi on Cu and Ni-P/Cu during aging treatment. *J. Electron. Mater.*, **32**, 1195–1202.
7. Jeon, Y.-D., Paik, K.-W., Bok, K.-S. *et al.* (2002) Studies of electroless nickel under bump metallurgy – Solder interfacial reactions and their effects on flip chip solder joint reliability. *J. Electron. Mater.*, **31**, 520–528.
8. Alam, M.O., Chan, Y.C., and Hung, K.C. (2002) Reliability study of the electroless Ni–P layer against solder alloy. *Microelectron. Reliab.*, **42**, 1065–1073.

9. Cho, M.G., Paik, K.W., Lee, H.M. *et al.* (2006) Interfacial reaction between 42Sn-58Bi solder and electroless Ni-P/immersion Au under bump metallurgy during aging. *J. Electron. Mater.*, **35**, 35–40.
10. Kao, Sz.-Ts., Lin, Y.-Ch., and Duh, J.-G. (2006) Controlling intermetallic compound growth in SnAgCu/Ni-P solder joints by nanosized Cu_6Sn_5 addition. *J. Electron. Mater.*, **35**, 486–493.
11. Lin, Y.-C., Shih, T.-Y., Tien, Sh.-K., and Duh, J.-G. (2007) Morphological and microstructural evolution of phosphorous-rich layer in SnAgCu/Ni-P UBM solder joint. *J. Electron. Mater.*, **36**, 1469–1475.
12. Chen, K., Liu, C., Whalley, D.C. *et al.* (2008) A comparative study of the interfacial reaction between electroless Ni–P coatings and molten tin. *Acta Mater.*, **56**, 5668–5676.
13. Lin, Y.-C., Wang, K.-J., and Duh, J.-G. (2010) Detailed phase evolution of a phosphorous-rich layer and formation of the Ni-Sn-P compound in Sn-Ag-Cu/Electroplated Ni-P solder joints. *J. Electron. Mater.*, **39**, 283–294.
14. Chun, H.-S., Yoon, J.-W., and Jung, S.-B. (2007) Solid-state interfacial reactions between Sn-3.5Ag-0.7Cu solder and electroless Ni-immersion Au substrate during high temperature storage test. *J. Alloys Compd.*, **439**, 91–96.
15. Kang, H.-B., Bae, J.-H., Lee, J.-W. *et al.* (2008) Characterization of interfacial reaction layers formed between Sn-3.5Ag solder and electroless Ni-Immersion Au-plated Cu substrates. *J. Electron Mater.*, **37**, 84–89.
16. Lin, Y.-C., Duh, J.-G., and Chiou, B.-S. (2006) Wettability of electroplated Ni-P in under bump metallurgy with Sn-Ag-Cu solder. *J. Electron. Mater.*, **35**, 7–14.
17. Linand, Y.-C. and Duh, J.-G. (2006) Optimal phosphorous content selection for the soldering reaction of Ni-P under bump metallization with Sn-Ag-Cu solder. *J. Electron. Mater.*, **35**, 1665–1671.
18. Yoon, J.-W. and Jung, S.-B. (2008) Effect of surface finish on interfacial reactions of Cu/Sn–Ag–Cu/Cu(ENIG) sandwich solder joints. *J. Alloys Compd.*, **448**, 177–184.
19. Jee, Y.K., Yu, J., and Ko, Y.H. (2007) Effects of Zn addition on the drop reliability of Sn-3.5Ag-xZn/Ni(P) solder joints. *J. Mater. Res.*, **22**, 2776–2784.
20. Sohn, Y.C., Jin, Yu., Kang, S.K. *et al.* (2004) Spalling of intermetallic compounds during the reaction between lead-free solders and electroless Ni-P metallization. *J. Mater. Res.*, **19**, 2428–2436.
21. Sohn, Y.-C. and Yu, J. (2005) Correlation between chemical reaction and brittle fracture found in electroless Ni(P)/immersion gold-solder interconnection. *J. Mater. Res.*, **20**, 1931–1934.
22. Hwang, Ch.-W., Suganuma, K., Kiso, M., and Hashimoto, Sh. (2003) Interface microstructures between Ni-P alloy plating and Sn-Ag-(Cu) lead-free solders. *J. Mater. Res.*, **18**, 2540–2543.
23. Schmetterer, C., Flandorfer, H., Richter, K.W. *et al.* (2007) A new investigation of the system Ni-Sn. *Intermetallics*, **15**, 869–884.
24. Nash, P. and Nash, A. (1991) *Ni-Sn (Nickel-Tin). Phase Diagrams of Binary Nickel Alloys* (ed. P. Nash), ASM International, Materials Park, OH, pp. 310–318.
25. Leineweber, A., Ellner, M., and Mittemeijer, E.J. (2001) A NiAs/Ni2In-Type Phase Ni1 + xSn (0.35<x<0.45) with incommensurate occupational ordering of Ni. *J. Solid State Chem.*, **159**, 191–197.
26. Leineweber, A. (2004) Variation of the crystal structures of incommensurate LT′-$Ni_{1+\delta}Sn$ ($\delta = 0.35$, 0.38, 0.41) and commensurate LT-$Ni_{1+\delta}Sn$ ($\delta = 0.47$, 0.50) with composition and annealing temperature. *J. Solid State Chem.*, **177**, 1197–1212.
27. Leineweber, A., Oeckler, O., and Zachwieja, U. (2004) Static atomic displacements of Sn in disordered NiAs/Ni_2In type HT-$Ni_{1+\delta}Sn$. *J. Solid State Chem.*, **177**, 936–945.
28. Leineweber, A., Mittemeijer, E.J., Knapp, M., and Baehtz, C. (2004) *In situ* and *ex situ* observation of the ordering kinetics in $Ni_{1.50}Sn$. *Mater. Sci. Forum*, **443–444**, 247–250.

29. Schubert, K., Burkhardt, W., Esslinger, P. *et al.* (1956) Some structural results on metallic phases. *Naturwiss.*, **43**, 248–249.
30. Lee, K.J., and Nash, P. (1991) Ni-P (Nickel-Phosphorus), in *Phase Diagrams of Binary Nickel Alloys* (ed. P. Nash), ASM International, Materials Park, OH, pp. 235–246.
31. Schmetterer, C., Vizdal, J., and Ipser, H. (2009) A new investigation of the system Ni-P. *Intermetallics*, **17**, 826–834.
32. Konstantinow, N. (1908) Verbindungen von Nickel und Phosphor. *Z. Anorg. Allg. Chem.*, **60**, 405–415.
33. Yupko, L.M., Svirid, A.A., and Muchnik, S.V. (1986) Phase equilibriums in nickel-phosphorus and nickel-phosphorus-carbon systems. *Poroshk. Metallurg. (Kiev)* (9), 78–83.
34. Nowotny, H. and Henglein, E. (1938) X-ray investigation in the system nickel-phosphorus. *Z. Phys. Chem.*, **B40**, 281–284.
35. Aronsson, B. (1955) The crystal structure of Ni_3P (Fe_3P type). *Acta Chem. Scand.*, **9**, 137–140.
36. Rundqvist, S., Hassler, E., and Lundvik, L. (1962) Refinement of the Ni_3P structure. *Acta Chem. Scand.*, **16**, 242–243.
37. Saini, G.S., Calvert, L.D., and Taylor, J.B. (1964) Compounds of the type M_5X_2: Pd_5As_2, Ni_5Si_2, and Ni_5P_2. *Can. J. Chem.*, **42**, 1511–1517.
38. Oryshchyn, S., Babizhetskyy, V., Chykhriy, S. *et al.* (2004) Crystal Structure of Ni_5P_2. *Inorg. Mater.*, **40**, 380–385; (2004) *Neorg. Mater.*, **40**, 450–456.
39. Larsson, E. (1964) X-ray investigation of the Ni-P system and the crystal structures of NiP and NiP_2. *Arkiv foer Kemi*, **23** (32), 335–365.
40. Elfström, M. (1965) Crystal structure of Ni_5P_4. *Acta Chem. Scand.*, **19**, 1694–1704.
41. Levinsky, Y., Effenberg, G., and Ilenko, S. (1997) *Pressure Dependent Phase Diagrams of Binary Alloys*, ASM International, Materials Park, OH.
42. Jolibois, P. (1910) Two new phosphides of nickel. *Compt. Rend.*, **150**, 106–108.
43. Biltz, W. and Heimbrecht, M. (1938) Systematic study of affinity. 78. The nickel phosphides. *Z. Anorg. Allg. Chem.*, **237**, 132–144.
44. Rundqvist, S. and Ersson, N.O. (1968) Structure and bonding in skutterudite-type phosphides. *Arkiv foer Kemi*, **30** (10), 103–114.
45. Shim, J.-H., Chung, H.-J., and Lee, D.N. (1999) Calculation of phase equilibria and evaluation of glass-forming ability of Ni-P alloys. *J. Alloys Compd.*, **282**, 175–181.
46. Massalski, T.B., Okamoto, H., Subramanian, P.R., and Kacprzak, L. (1996) *Binary Alloy Phase Diagrams*, ASM International, Materials Park, OH.
47. Vivian, A.C. (1920) Tin-phosphorus alloys. *J. Inst. Met.*, **23**, 325–366.
48. Olofsson, O. (1970) X-ray investigations of the tin-phosphorus system. *Acta Chem. Scand.*, **24**, 1153–1162.
49. Eckerlin, P. and Kischio, W. (1968) Preparation and crystal structure of tin arsenide (Sn_4As_3) and tin phosphide (Sn_4P_3) phases. *Z. Anorg. Allg. Chem.*, **363**, 1–9.
50. Zaikina, J.V., Kovnir, K.A., Sobolev, A.N. *et al.* (2008) Highly disordered crystal structure and thermoelectric properties of Sn_3P_4. *Chem. Mater.*, **20**, 2476–2483.
51. Gullman, J. and Olofsson, O. (1972) Crystal structure of tin phosphide and a note on the crystal structure of germanium phosphide. *J. Solid State Chem.*, **5**, 441–445.
52. Katz, G., Kohn, J.A., and Broder, J.D. (1957) Crystallographic data for tin monophosphide. *Acta Cryst.*, **10**, 607.
53. Ganesan, R., Dinsdale, A.T., and Ipser, H. (2011) Thermochemistry of the nickel-phosphorus system. *Intermetallics*, **19**, 927–933.
54. Ganesan, R., Richter, K.W., Schmetterer, C. *et al.* (2009) Synthesis of single-phase Sn_3P_4 by an isopiestic method. *Chem. Mater.*, **21**, 4108–4110.
55. Keimes, V., Blume, H.M., and Mewis, A. (1999) Preparation and crystal structure of $ANi_{10}P_3$ (A: Zn, Ga, Sn, Sb). *Z. Anorg. Allg. Chem.*, **625**, 207–210.

56. Schmetterer, C., Wildner, M., Giester, G. *et al.* (2009) The crystal structure of $Ni_{21}Sn_2P_6$. *Z. Anorg. Allg. Chem.*, **635**, 301–306.
57. García-García, F.J., Larsson, A.K., and Furuseth, S. (2002) The crystal structure of $Ni_{10}Sn_5P_3$. *J. Solid State Chem.*, **166**, 352–361.
58. Garcia-Garcia, F.J., Larsson, A.K., and Furuseth, S. (2003) The crystal structure of $Ni_{13}Sn_8P_3$ elucidated from HREM. *Solid State Sci.*, **5**, 205–217.
59. Furuseth, S. and Fjellvaag, H. (1985) Crystal structure and properties of nickel tin phosphide (Ni_2SnP). *Acta Chem. Scand. A*, **A39**, 537–544.
60. Furuseth, S. and Fjellvaag, H. (1994) Properties of the NiAs-type phase $Ni_{1+m}Sn_{1(x}P_{x.}$ *Acta Chem. Scand.*, **48**, 134–138.
61. Furuseth, S., Larsson, A.K., and Withers, R.L. (1998) An electron diffraction study of Sn/P and interstitial Ni ordering in $Ni_{1+m}Sn_{1(x}P_x$ B8-type solid solutions. *J. Solid State Chem.*, **136**, 125–133.
62. Schmetterer, C. and Ipser, H. (2010) The Ni-rich part of the Ni-P-Sn system: Thermal behavior. *Met. Mater. Trans. A*, **41**, 43–56.
63. Schmetterer, C., Vizdal, J., Kroupa, A. *et al.* (2009) The Ni-rich Part of the Ni-P-Sn system: Isothermal sections. *J. Electron. Mater.*, **38**, 2275–2300.
64. Schmetterer, C. (2009) *The System Ni-P-Sn and Binary Constituents*, Südwestdeutscher Verlag für Hochschulschriften (SVH), Saarbrücken.
65. Yakel, H.L. (1987) Atom distributions in tau-carbide phases: iron and chromium distributions in chromium iron carbide $(Cr_{23(x}Fe_x)C_6$ with $x = 0$, 0.74, 1.70, 4.13 and 7.36. *Acta Cryst. B*, **B43**, 230–238.
66. Westgren, A. (1933) Complex chromium and iron carbides. *Nature*, **132**, 480.
67. Khan, Y. and Wibbeke, H. (1991) Formation of the τ-phase in the iron-boron alloys. *Z. Metallkde.*, **82**, 703–705.
68. Idzikowski, B. and Szajek, A. (2003) Formation of the nanocrystalline cubic $(FeNi)_{23}B_6$ phase in the nickel-rich FeNiZrB alloys and its magnetic behavior. *J. Optoelectron. Adv. Mater.*, **5**, 239–244.
69. Stadelmaier, H.H., Draughn, R.A., and Hofer, G. (1963) The structure of ternary borides of the chromium carbide ($Cr_{23}C_6$) type. *Z. Metallkde.*, **54**, 640–644.
70. Keimes, V. and Mewis, A. (1992) Magnesium and manganese nickel phosphides, $Mg_3Ni_{20}P_6$ and $Mn_3Ni_{20}P_6$ – two new phosphides with $Cr_{23}C_6$-type structure. *Z. Anorg. Allg. Chem.*, **618**, 35–38.
71. Andersson-Soederberg, M. and Andersson, Y. (1990) The crystal structure of nickel indium phosphide ($Ni_{21}In_2P_6$). *J. Solid State Chem.*, **85**, 315–317.
72. Ganesan, R., Ciccioli, A., Gigli, G., and Ipser, H. (2011) Thermochemical Investigations in the Tin-Phosphorus System. *Int. J. Mater. Res.*, **102**, 93–103.
73. Schmetterer, C., Flandorfer, H., Luef, Ch. *et al.* (2009) Cu-Ni-Sn – a key system for lead-free soldering. *J. Electron. Mater.*, **38**, 10–24.
74. Schmetterer, C., Rajamohan, D., Ipser, H., and Flandorfer, H. (2011) The high-temperature phase equilibria of the Ni-Sn-Zn system: isothermal sections. *Intermetallics*, **19**, 1489–1501.
75. Ipser, H., Krachler, R., and Komarek, K.L. (1989) The isopiestic method and its application to a thermodynamic study of the Au-Zn system, in *Thermochemistry of Alloys* (eds H. Brodowsky and H.-J. Schaller), Kluwer Academic Publishers, Dordrecht, NL, pp. 293–306.
76. Schlesinger, M.E. (2002) The thermodynamic properties of phosphorus and solid binary phosphides. *Chem. Rev.*, **102**, 4267–4301.
77. Lu, K., Wang, J.T., and Wei, W.D. (1991) Thermal expansion and specific heat capacity of nanocrystalline Ni-P alloy. *Scripta Met. Mater.*, **25**, 619–623.
78. Lu, K., Lück, R., and Predel, B. (1993) Investigation of the heat capacities of Ni-20 at.% P in different states. *Z. Metallkde.*, **84**, 740–743.

79. Sarsenbaev, B.S., Kasenov, B.K., Bukharitsyn, V.O., and Baeshov, A. (1994) Heat capacity and thermodynamic functions of cobalt and nickel phosphides at 298.15–450 K. *Kompleksn. Ispolz. Miner. Syr'ya*, (6), 54–57.
80. Weibke, F. and Schrag, G. (1941) Heats of formation of the lower phosphides of several heavy metals. *Z. Elektrochem.*, **47**, 222–238.
81. Boone, S. and Kleppa, O.J. (1991) Determination of the standard enthalpy of formation of nickel phosphide ($Ni_{2.55}P$) by high-temperature drop calorimetry. *J. Chem. Thermodyn.*, **23**, 781–790.
82. Delsante, S., Schmetterer, C., Ipser, H., and Borzone, G. (2010) Thermodynamic investigation of the Ni-rich side of the Ni-P system. *J. Chem. Eng. Data*, **55**, 3468–3473.
83. Myers, C.E. and Conti, T.J. (1985) Vaporization behavior, phase equilibria, and thermodynamic stabilities of nickel phosphides. *J. Electrochem. Soc.*, **132**, 454–457.
84. Viksman, G.S. and Gordienko, S.P. (1992) Behavior in vacuum at high temperatures and thermodynamic properties of nickel phosphide Ni_3P. *Sov. Powder Metall. Metal. Ceram.*, **31**, 1052–1052.
85. Zaitsev, A.I., Zaitseva, N.E., and Shakhpazov, E.K. (2003) Thermodynamic Properties of Intermediate Ni-P Phases (26–32.5 at. % P) between 971 and 1440 K. *Neorg. Mater.*, **39**, 519–524; (2003) *Inorg. Mater.*, **39**, 427–432.
86. Kawabata, R., Ichise, E., and Iwase, M. (1995) Activities of phosphorus in liquid Ni + P alloys saturated with solid nickel. *Met. Mater. Trans. B*, **26**, 783–787.
87. Ghosh, P.C. and Hess, E.G. (1962) Thermodynamics of phosphides. *Sci. Cult.*, **28**, 386–387.
88. Kubaschewski, O. and Evans, L. (1956) *Metallurgical Thermochemistry*, Pergamon Press, London.
89. Press, M.R., Khanna, S.N., and Jena, P. (1987) Electronic structure, magnetic behavior, and stability of nickel-phosphorus alloys. *Phys. Rev. B*, **36**, 5446–5443.
90. Shim, J.-H., Chung, H.-J., and Lee, D.-N. (1999) Calculation of phase equilibria and evaluation of glass-forming ability of Ni-P alloys. *J. Alloys Compd.*, **282**, 175–181.
91. Ren, J., Wang, J.G., Li, J.F., and Li, Y.W. (2007) Density functional theory study on crystal nickel phosphides. *J. Fuel Chem. Technol.*, **35**, 458–464.
92. Guadagno, J.R. and Pool, M.J. (1965) Heats of solution of phosphorus, arsenic, and antimony in liquid tin at 750 K. *Trans. Met. Soc. AIME*, **233**, 1439–1440.
93. Suleimanov, D.M. and Kuliev, A.A. (1974) Thermodynamic study of the tin-phosphorus system, in *Tezisy Dokl. - Vses. Konf. Kristallokhim. Intermet. Soedin*, 2nd edn (ed. R.M. Rykhal), L'vov. Gos. Univ., Lvov, USSR, p. 168.
94. Arita, M. and Kamo, K. (1985) Measurement of vapor pressure of phosphorus over tin-phosphorus alloys by dew point method. *Trans. Jpn. Inst. Metals*, **26**, 242–250.
95. Heuzey, M.C. and Pelton, A.D. (1996) Critical evaluation and optimization of the thermodynamic properties of liquid tin solutions. *Met. Mater. Trans. B*, **27**, 810–828.
96. Ipser, H. and Komarek, K.L. (1974) Thermodynamic properties of iron-tellurium alloys. *Monatsh. Chem.*, **105**, 1344–1361.
97. Leubolt, R., Ipser, H., and Komarek, K.L. (1986) Thermodynamic properties and defect mechanism of nonstoichiometric .gamma.-nickel antimonide (NiSb). *Z. Metallkde.*, **77**, 284–290.
98. Ganesan, V., Feufel, H., Sommer, F., and Ipser, H. (1998) Thermochemistry of ternary liquid Cu-Mg-Si alloys. *Met. Mater. Trans. B*, **29**, 807–813.
99. Dinsdale, A.T. (1991) SGTE Data for Pure Elements, *CALPHAD*, 15, 317–425 see also: http://www.sgte.org/.
100. Arita, M. and Watanabe, M. (1985) Equilibrium constant of gaseous reaction 2P2 = P4 and vapor pressure of liquid phosphorus. *Trans. Jpn. Inst. Metals*, **26**, 175–182.
101. Carlson, K.D. and Paule, R.C. (1967) *The Characterization of High Temperature Vapours* (ed. J.L. Margrave) Wiley, New York.

102. Freeman, R.D. and Edwards, J.G. (1967) *The Characterization of High Temperature Vapours, Appendix C* (ed. J.L. Margrave), Wiley, New York.
103. Drowart, J. *et al.* (2005) High-temperature mass spectrometry: Instrumental techniques, ionization cross-sections, pressure measurements, and thermodynamic data. *Pure Appl. Chem.*, **77**, 683–737.
104. Okamoto, H. (1993) P-Sn (phosphorus-tin). *J. Phase Equil.*, **14**, 263–264.
105. *Inorganic Crystal Structure Database*, in version 1.4.1., (2009) Fachinformationszentrum Karlsruhe.

Thematic Area III

Microalloying to Improve Reliability

5

'Effects of Minor Alloying Additions on the Properties and Reliability of Pb-Free Solders and Joints'

Sung K. Kang
IBM T.J. Watson Research Center, Yorktown Heights NY 10598, USA

Abstract

Since July, 2006, following the EUs RoHS legislation, the consumer electronics industry has been offering 'green' products by eliminating Pb-containing solders and other toxic materials. This transition has been relatively smooth, because the reliability requirements are less stringent. However, the Pb-free transition for high-performance electronic systems (such as servers and telecommunication) is still on-going due to their rigorous reliability requirements. For example, the research and development efforts to implement Pb-free flip-chip interconnections for high-end applications are still very active.

In this chapter, the recent progress in Pb-free solder development, especially minor alloy additions to Sn-rich solders is reviewed in light of improving various physical, mechanical, metallurgical or electrical properties of solder joints. The topics to be discussed include those such as control of undercooling, microstructure, interfacial reactions, or void formation, as well as enhancing impact resistance, electromigration, and other mechanical properties.

Lead-free Solders: Materials Reliability for Electronics, First Edition. Edited by K. N. Subramanian.

5.1 Introduction

Extensive searches for Pb-free solders have been conducted in the 1990s to find an ideal 'drop-in' replacement of eutectic Pb/Sn solder predominantly used in microelectronic applications [1–9]. However, such a replacement was not found. Instead, several promising candidates of Sn-rich solders were identified for different soldering applications as listed in Table 5.1. Among them, binary eutectic solders, Sn-Cu or Sn-Ag, and ternary Sn-Ag-Cu or Sn-Ag-Bi were recommended for major soldering applications, such as SMT card assembly [3–7].

When the European Union passed the RoHS (*R*estriction *o*f *H*azardous *S*ubstances) directive in October 2002, banning several toxic materials including Pb in electrical and electronic systems from July 1, 2006, the R&D activities on Pb-free solders became more intensified. By the early 2000s, the near-ternary eutectic Sn-Ag-Cu (SAC) alloy compositions of melting temperatures around 217 °C became a consensus candidate in the US as well as abroad [10–18]. Some variations of SAC solders are included in Table 5.1. In general, low-Ag SAC compositions were adopted in Japan, while high-Ag versions were preferred initially in the US.

Subsequently, extensive research and development efforts have been focused on the Sn-Ag-Cu system to evaluate the reliability risk factors associated with SAC solder joints, compared to the well-established Pb-containing solder joints [19–29].

Recently, many new findings on fundamental issues of Sn-rich solders have been reported, especially on Sn-Ag-Cu system. A few examples are listed here, such as severe interfacial reactions during reflow or thermal aging [6, 19], large Ag_3Sn plate formation [14], large undercooling during Sn solidification [17, 18], unique twining microstructure in Sn-Ag or Sn-Ag-Cu [28], anisotropic physical/mechanical properties of Sn crystals [28], fast diffusions of Cu, Ag and Ni solute atoms along the *c*-axis of β-Sn crystal [30–32], only a few grains in BGA or flip-chip joints [15] and others. These new findings have also closely related with the reliability issues of Sn-rich solder joints. To name a few items, such as excessive Cu consumption [26], easy fatigue crack growth along large Ag_3Sn plates [16], chip-joining issues due to large undercooling [33], void formation and

Table 5.1 *Pb-free solders used in microelectronic applications.*

Composition (wt%)	Liquidus/ Solidus (°C)	Applications	Notes
Sn-0.7Cu	227	PTH, Flip-chip	Cu dissolution, Wetting, excessive IMCs
Sn-3.5Ag	221	SMT, Flip-chip	Cu dissolution, Excessive IMCs, Voids
Sn-3.5Ag-3Bi	208–215	SMT	Cu dissolution Fillet lift, low mp phase
Sn-3.0Ag-0.5Cu (SAC305)	217	SMT, PTH, BGA	Japanese Comm/Consortia Alloy Choice
Sn-3.8Ag-0.7Cu (SAC3807)	217	SMT, PTH, BGA	US Comm Alloy/Europ IDEALS Consortium
Sn-3.9Ag-0.6Cu (SAC3906)	217	SMT, PTH, BGA	NEMI Consortium Alloy
Sn-3.0Ag-0.9Cu (SAC309)	217	SMT, PTH, BGA	US Commercial Alloy

Table 5.2 *US Patents on Pb-free solders issued during 1988–1999.*

US Patents on Pb-Free Solders (1988–1999)

Patent No.	Assignee	Sn (wt%)	Bi	Ag	In	Sb	Cu	Zn	Others
4758407	Harris	87–93		0.1–0.5		4.0–6	3.0–5		Ni
4778733	Engelhard	92–99		0.05–3			0.7–6		
4806309	Willard	90–95	1.0–4	0.1–0.5		3.0–5			
5229070	Motorola	90	1.0-5		5				
5328660	IBM	78	10	2	10				
5344607	IBM	90	2		8				
5352407	Seelig	93–98		1.5–3.5		0.2–2	0.2–2		
5368814	IBM	42	56		2				
5393489	IBM	93	2	3		1	1		
5405577	Seelig	90–99		0.5–3.5		0.2–2	0.1–3		
5410184	Motorola	92–97					3.0–8		
5411703	IBM	94	2			3	1		
5414303	IBM	70–90	2.0–10		8.0–20				
5435968	Touchston	79–97	0–1	0–4			3.0–15		Se
5429689	Ford	80	4.5–14.5		5–14.5				
5455004	Indium Co.	82–90	1.0–5		3.5–6			4.5–6	
5538686	Lucent	>70	>10		3.0–10	>5		6.0–10	
5569433	Lucent	40–60	40–60	0.2–0.5					
5520572	US Army	86–97	0–5	0.3–4.5	0–9.3		0–5		
5527628	Iowa St. U.	89	(5–10)	3.5–7.7			1.0–4	(Si,Sb,Zn)	(Mg,Ca,RE)
5580520	Indium Co.	71–92		2.0–4	4.0–26				
5658528	Mitsui	90	0.5–1.5	1.0–4	3.0–4				
5698160	Lucent	59–82		2.0–11				16–30	
5718868	Mitsui	90	2.0–3				~0.5	7.0–9	
5733501	Toyota	65–95	0.1–9.5	0.8–5	0.1–9.5	0.1–10			
5730932	IBM	80	12	3	5				
5762866	Lucent	76–98	0.2–6	1.0–6	0.2–6			0.2–6	
5755896	Ford	37–57	37–57		6.0–10				
	Ford	48–58	40–50		2.0–5				

(*continued*)

Table 5.2 (*Continued*)

US Patents on Pb-Free Solders (1988–1999)

Patent No.	Assignee	Sn (wt%)	Bi	Ag	In	Sb	Cu	Zn	Others
5833921	Ford	43–58	38–52	1.0–2	2	2.0–15	1.0–4		
5837191	Johnson	95		0.6		0.75–2	~0.6		Ni
5843371	Samsung	77–89	6.0–14	3.0–4	2.0–5				
5851482	KIMM	80	1.0–20		0.1–3			0.01–3	Al,Mg,
5863493	Ford	91–97		2.0–5			0–3		Ni
5874043	IBM	70–74		6.5–7.5	12.0–24				
5938862	Delco	84–90		2.5–3.5	7.0–11		0.5–1.5		
5942185	Hitachi	72–87	10.0–23					3.0–5	
5985212	H-Tech	> 75			0–6		0.1–9.5		Ga
5993736	Mitsui	91–95	2.0–3	2.0–4				0.5–2	

drop impact failure [22–24], crystal-orientation effects on thermal fatigue [28] and electromigration [34], and others.

In an effort to mitigate the reliability risk factors associated with Sn-Ag-Cu joints, the worldwide research community on Pb-free solders has lately directed their efforts on modifying the compositions of the SAC solders by adding minor alloying elements.

In this chapter, some of the new findings and their impacts on the reliability and integrity of Pb-free solder joints are discussed in order to reduce the reliability risk factors in implementing Pb-free solder technology.

It is remarkable to note that numerous alloy modifications of Sn-rich solders have already been well documented in the patent literature on Pb-free solders for the past 20 years or so. Tables 5.2–5.4 collect about 100 US patents on Pb-free solders, mostly with Sn-rich compositions and a few Bi-rich compositions. The tables also show the composition ranges of various alloying elements, such as Ag, Bi, Cu, In, Ni, Sb, Zn and others. Since this patent literature covers a wide range of minor alloying elements added to Sn-rich solders, it will be very useful to the following discussion.

5.2 Controlling Ag_3Sn Plate Formation

The microstructure of ternary eutectic Sn-Ag-Cu solder consists of three different phases β-Sn (m.p., 232 °C), Cu_6Sn_5 (415 °C), and Ag_3Sn (480 °C), with the ternary eutectic temperature, about 217 °C [10]. Figure 5.1 shows a typical microstructure of near-ternary SAC formed at a relatively low cooling rate. The β-Sn dendrite cells were surrounded by the ternary eutectic regions that are a mixture of fine intermetallic particles of Cu_6Sn_5 and Ag_3Sn in the β-Sn matrix. This microstructure suggests that Sn dendrites solidified first and then immediately followed by the eutectic solidification. In the middle of Figure 5.1, a large plate-like Ag_3Sn phase grown across the Sn dendrite cells is noted. This large Ag_3Sn plate is a proeutectic phase of an intermetallic compound (IMC), nucleated well above the ternary eutectic temperature and continued to grow in the liquid solder until the solidification process ends. The presence of the large Ag_3Sn plate indicates that the overall solidification process was not under equilibrium and its microstructure must be off the ternary eutectic as shown. From the microhardness test on each phase, it was confirmed that the large Ag_3Sn plate has a considerably higher hardness (HVN ∼126.5) than the Sn dendrite matrix (HVN; 15.2 to 26.5) [35]. This suggests the formation of large Ag_3Sn plates being regarded as not desirable in view of their microstructure and mechanical properties of SAC joints.

Figure 5.2 shows an example of a large Ag_3Sn plate adversely affected the fatigue life of a CBGA (ceramic ball grid array) package [13]. Due to the strain localization at the boundary between the Ag_3Sn plates and the bounding β-Sn phase, the interface provided a preferential crack-propagation path, leading to a premature failure during the thermal cycling testing. To improve thermal fatigue life of near-ternary SAC joints, it is desirable to suppress the formation of large Ag_3Sn plates.

A systematic study on the formation of large Ag_3Sn plate in near-ternary SAC solder and joints was conducted in terms of cooling rate, Ag and Cu content [35, 36]. The cooling rate was found to be a crucial factor in forming large Ag_3Sn plates. At a high cooling rate, there would be not enough time for Ag_3Sn plates to grow into a large size, even if they were

Table 5.3 *US Patents on Pb-free solders issued during 2000–2004.*

US Patents on Pb-Free Solders (2000–2004)									
Patent No	Assignee	Sn (wt%)	Bi	Ag	In	Sb	Cu	Zn	Others
6077477	Matsushita	81–91	5.0–10	3.0–6	0.1–1.0		0.1–2		
6086687	Alpha Fry	> 90	0–9.25	0–9.25	0–9.25	0–9.25	0–9.25	0–0.2	Ti
6139979	Murata	92–96				3.0–5	0.7–2.0		Ni
6156132	Fuji Elec	40–70	30–58	0–5		0–5	0–1		Ni, Ge
6176947	H–Tech	balance	0.5–5	2.5–4.5	6.0–12	(0.5–2)	0.5–2.5		
6179935	Fuji Elec	balance		0–4.0		(0–3.5)	0–2.0		Ni, Ge
6180055	Nihon Supr	balance					0.3–07		Ni
6184475	Fujitsu	34–40	46–55	(Ag)	5.0–20	(Sb)		(Zn)	(Ge, Ga, P)
6187114	Matsushita	balance					(0.1–5)		Ni, Pd
6229248	Murata Mfg	balance		1.0–2.0		1.0–3.0	0.5–1.0		
6224690	IBM	balance	1.0–20	1.0–5	(0.5–10)	1.0–10	(0.5–5)	(0.5–5)	Ni,Co
6228322	Sony	balance	0.5–8.0	1.5–6.0			0.1–5.0		La,Ce,Sm,Gd
6231691	Iowa St. U.	balance		3.0–7.7			0.5–4		Fe, Co
6241942	Matsushita	balance	(0.2–6)	0.1–3.5	(0.5–3)		0.1–3	7.0–10	P
	Matsushita	balance	10.0–30	0.05–2				2.0–10	P
6253988	Antaya Tec	30	0.3	4.5	65.0	–0.8	0.5		
6267823	Matsushita	balance	5.0–18	2–3.5	(0.1–1.5		(<0.7)	(<10)	
6296722	Nihon Supr	balance					0.1–2		Ni, Ga
6319461	Nippon Gls	balance	< 10	0.1–6		<10	0.1–6	0.1–3	Al,Ti
6325279	Matsushita	balance	5.0–10	3.0–6.0	0.1–1.0		0.1–2		
6361626	Fujitsu	balance	3.0–6					3.0–14	Al
6440360	Tokyo First	balance					0.8		Ni
6416883	Ecosolder	balance	20–30	1.0–3.0		<4.0	<2.0		

6488888	Matsushita	balance	15–25	0.05–2				2.0–10	
	Matsushita	balance	(0.2–6)	0.1–3.5	(0.5–3)		0.1–3	7.0–10	Ni
6521176	Fujitsu	77–87	10.0–20	2.8–3.1					
6648210	Multicore	balance	1.0–10	< 6		<5	<3		
6660226	Murata	> 88		0.5–9			0.5–2.0		Co
	Murata	> 88		3.0–5.0			0.5–1.0		Co
6689488	Taiho Kogyo	balance		1.0–3.5	0.1–2.0		0.1–0.7		Ni Co Fe
6692691	Nihon	balance		3.5–6.0					Ni
	Nihon	balance		3.5–6.0					Ni, P Ga Ge
6703113	Murata	0.1–3.0	>90	0.1–9	0.1–3.0	0.1–3.0	0.1–9/9	0.1–9.9	P, Ge
6805974	IBM	90–95	0.1–0.2	<2.8			<1.5		Sb
6824039	IHC	balance		3.0–14					Mg

Table 5.4 *US Patents on Pb-free solders issued during 2005–2010.*

US Patents on Pb–Free Solders (2005–2010)									
Patent No.	Assignee	Sn (wt%)	Bi	Ag	In	Sb	Cu	Zn	Others
6837947	NCK Univ	balance		4.0>				7.0–10	Al, Ga
6843862	Quantum	88–94		3.5–4.5	2.0–6		0.3–1.0		
6884389	Kabushiki	balance	43–47	0.9–2.2	0.4–0.6		0.4–0.6		Ni Sb Ge
6936219	IKA	balance						7.5–9.0	Mn
6984254	Fujitsu	77–87	10.0–20	2.8–3.1					
	Fujitsu	34–40	46–55		10.0–20				
7022282	Murata	>90.5		0.5–9.0		0.5–5.0			Mn, Cr
7111771	Intel	balance	(Bi)	(Ag)	5.0–15	(Sb)	(Cu)	(Zn)	(Ni,Ge,Pt)
7148426	Hitachi	balance		2.0–5.0			0.01–2.0		P
7172726	Senju	90–98					1.5–8.0		Ni, Co
7175804	Nippon	balance	0.5–6.0					6.0–10	Mg, Al
7175805	Nippon	balance						6.0–10	Mg
7220493	Koa Kabush	balance						30–70	Ni, Al
7224067	Intel		63–67		33–37			(Zn)	Li,Ti,Zr,Re
7250135	MK	> 94.79		2.8–4.2	0.2		0.3–0.8		Ge
7273540	Shinryo	balance		2.6–3.4			0.4–0.7		
7282174	Senju	balance	0.5–12			< 1.0		5.0–10	AuPtPdFe
7282175	Senju	balance		0.05–5			0.01–0.5		P Ni Co
7335269	Aoki	99>		0.3–0.4			0.6–0.7		P
7338567	Senju	98>					0.1–1.5		Ni, P
7410833	IBM	>90	(Bi)	(Ag)		(Sb)	(Cu)	(Zn)	
7425299	Senju	balance		4.0–6.0			1.0–2.0		
7422721	Murata	90.5					0.5–2		Pd, Co
7576428	Int Tech Res	0.01–30	30–60		20–70				Ga

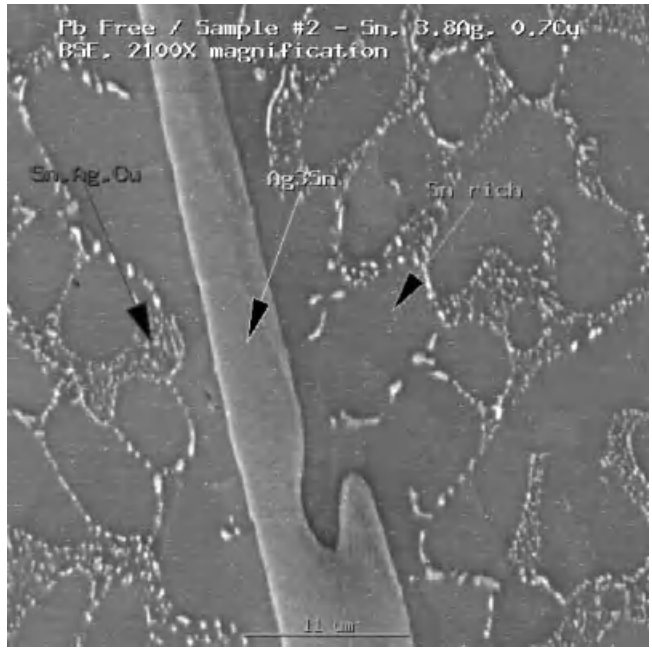

Figure 5.1 *Backscattered electron SEM micrograph showing a typical solidified microstructure of Sn-3.8Ag-0.7Cu alloy in a BGA solder ball. Sn dendrite cells are surrounded by Ag3Sn and Cu6Sn5 particulate arrays [15]. (Reproduced with permission from J. Mater. Res., The Microstructure of Sn in Near Eutectic Sn-Ag-Cu Alloy Solder Joints and its Role in Thermomechanical Fatigue by D. Henderson et al., 19, 6, 1608–1612 Copyright (2011) Cambridge University Press).*

nucleated. This is consistent with the observation that large Ag_3Sn plates are not commonly observed in solder joints rapidly cooled at a rate of 1 °C/s or higher. Hence, the formations of large Ag_3Sn plates can be *kinetically* controlled by employing a high cooling rate, such as 1.5 °C/s or higher during a reflow process. However, providing a high cooling rate is not always practical, especially with a substrate of a large thermal mass because of unwanted high thermal stress or strain induced. In the same study, complete dissolution of large Ag_3Sn plates (about 500 micrometer long) was demonstrated after 3 min reflow at 250 °C [35]. However, in a conventional reflow large Ag_3Sn plates would not dissolve completely due to a limited time provided above the liquidus temperature, and the remaining Ag_3Sn plates can grow back quickly to a large size in a subsequent cooling step.

To investigate the effect of Ag content, several SAC solders with reduced Ag contents were evaluated from 2.0 to 3.8% with a fixed Cu content. Table 5.5 lists the melting point and the amount of undercooling measured with these SAC alloys. The melting point of SAC solders is not sensitive to Ag content, while the amount of the undercooling varied from 18 to 34 °C. A strong correlation between the Ag content and the population of large Ag_3Sn plates (larger than 100 micrometer long) was observed in this study. Solder balls were heated to 250 °C, held there for 10 min, and then cooled slowly at a rate of 0.02 °C/s to room temperature. The microstructure of about 100 solder balls from each group was examined to count the number of solder balls containing at least one large Ag_3Sn plate of 100 μm or

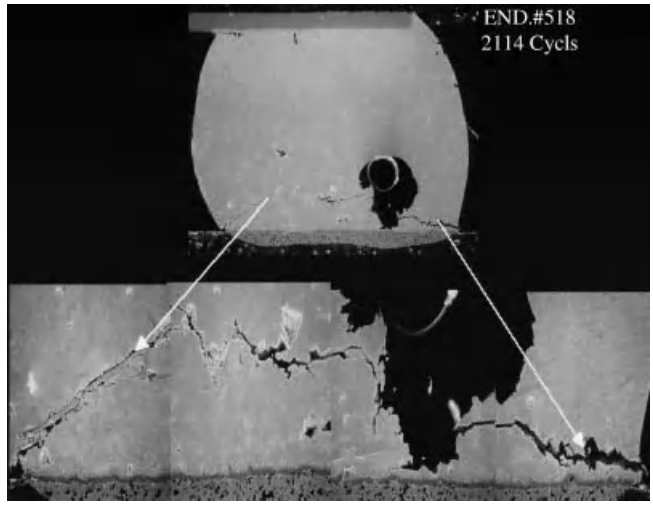

Figure 5.2 *A BGA solder joint failed by thermomechanical fatigue showing preferred crack propagation along the interface between the Ag_3Sn plate (indicated by arrows) and β-Sn phase [13]. (Reproduced with permission from J. Mater. Res., Ag_3Sn Plate Formation in the Solidification of Near Ternary Eutectic Sn-Ag-Cu Alloys by D. W. Henderson et al., 17, 11, 2775–2778 Copyright (2011) Cambridge University Press).*

longer. The frequency of observation of large Ag_3Sn plates is summarized in Table 5.6. For the SAC alloy with 3.8% Ag, 76 out of 100 balls contained large Ag_3Sn plates, while almost no balls contained large Ag_3Sn plates in the slow-cooled solders with the Ag content less than 3.0 wt%. Large Ag_3Sn plates were substantially reduced in the SAC alloys of less than 3 wt% Ag, even in an extremely slow-cooled condition, such as 0.02 °C/s. Hence, the formation of large Ag_3Sn plates can be *thermodynamically* suppressed by lowering the Ag content below 3 wt%. This dependence on Ag content was further explained by a thermodynamic calculation using an isopleth phase diagram of Sn-XAg-0.7Cu [35]. The Ag_3Sn liquidus was determined in the metastable region by directly extrapolating the liquidus from the ternary eutectic temperature. As listed in Table 5.5, the solidification process in the Sn-3.8Ag-0.7Cu alloy requires an undercooling of 15–30 °C before the

Table 5.5 *Melting temperature and undercooling of Sn-Ag-Cu solder alloys [35]. (Reproduced from Proceedings of 53rd ECTC, Formation of Ag_3Sn Plates in Sn-Ag-Cu Alloys and Optimization of their Alloy).*

Alloy Composition (wt%)	Melting Temperature (°C)	Undercooling (°C)*
Sn-3.8Ag-0.7Cu	216.9	28.6
Sn-3.4Ag-0.9Cu	217.0	18.0
Sn-3.0Ag-0.9Cu	216.8	21.9
Sn-2.5Ag-0.9Cu	216.8	34.3
Sn-2.0Ag-0.9Cu	216.9	29.3

Table 5.6 *Population of large Ag_3Sn plates in Sn-Ag-Cu solder alloys solidified at a rate of 0.02 °C/s [35]. (Reproduced from Proceedings of 53rd ECTC, Formation of Ag_3Sn Plates in Sn-Ag-Cu Alloys and Optimization of their Alloy).*

Solder Composition (wt%)	Solder Form	# of Solder Balls with Large Ag_3Sn Plates
Sn-3.8Ag-0.7Cu	BGA balls	76/100
Sn-3.4Ag-0.9Cu	BGA balls	5/100, 10/100
Sn-3.0Ag-0.9Cu	BGA balls	6/100, 3/100
Sn-2.5Ag-0.9Cu	BGA balls	1/100, 0/100
Sn-2.0Ag-0.9Cu	BGA balls	0/100, 0/100
Sn-3.5Ag	Ingot	few
Sn-3.8Ag-0.35Cu	Ingot	many
Sn-3.8Ag-0.7Cu	Ingot	many

Sn phase solidifies. The metastability of the liquid Sn phase depends on the available sites for heterogeneous nucleation to take place. At a nominal Cu concentration of 0.7% in the liquid, the composition of the liquidus intersecting at 20 °C undercooling is approximately 2.7 wt% Ag. Thus, for compositions equal to or less than 2.7 wt% Ag, the Ag_3Sn phase would be difficult to nucleate or grow within the liquid in a solder joint without undercooling in excess of 20 °C.

The effect of Cu content on large Ag_3Sn plate formation was somewhat different from Ag content. Many large Ag_3Sn plates were found in slowly cooled ingots of Sn-3.8Ag-0.35Cu and Sn-3.8Ag-0.7Cu, but much less in Sn-3.5Ag [35]. The presence of Cu in the solder appears to promote the formation of large Ag_3Sn plates, but it is not explicitly clear how this effect occurs. One possible explanation was provided by noting that more Cu atoms were measured in a large Ag_3Sn plate (about 0.36 wt% Cu) than in β-Sn dendrites (about 0.16 wt% Cu), [10]. Hence, the role of Cu atoms in nucleating a large Ag_3Sn plate, not in growth, was suggested. Since only a small number of Cu atoms may need to nucleate an Ag_3Sn plate in an undercooled SAC alloy, this may explain why no difference in the population of large Ag_3Sn plates was observed for a different Cu composition, such as 0.35 vs 0.7 wt%.

Another method of controlling the formation of large Ag_3Sn plates was reported by adding a small amount of Zn to the near-ternary SAC solders [14]. As discussed in the following section, the Zn addition into SAC (such as 0.1 wt%) is very effective to reduce the undercooling required for β-Sn solidification and thereby to suppress the formation of large Ag_3Sn plates even at a very slow cooling rate (such as 0.02 °C/s). The Zn addition did coarsen Sn dendrites and increase the volume fraction of the eutectic regions. It was also reported that a preferential reaction between Zn and Cu atoms occurred in the solder matrix as well as at the interface of Cu metallization. To control the formation of large Ag_3Sn plates, the Zn addition in the range from 0.1 to 0.7 wt% was recommended, depending on its metallization or solder volume [14].

The presence of large Ag_3Sn plates in small solder joints such as flip-chip solder bumps can be a serious issue of affecting the joint integrity and reliability. Figure 5.3 shows an example of a flip-chip joint made of Sn-3.8Ag-0.7Cu solder reflowed twice at 260 °C on a Cu substrate [19]. The large plate-like Ag_3Sn IMCs extended to a substantial distance in a small flip-chip joint after reflow, while relatively small Cu_6Sn_5 IMCs were mostly attached to the interface. The microstructure and mechanical properties of this joint would be

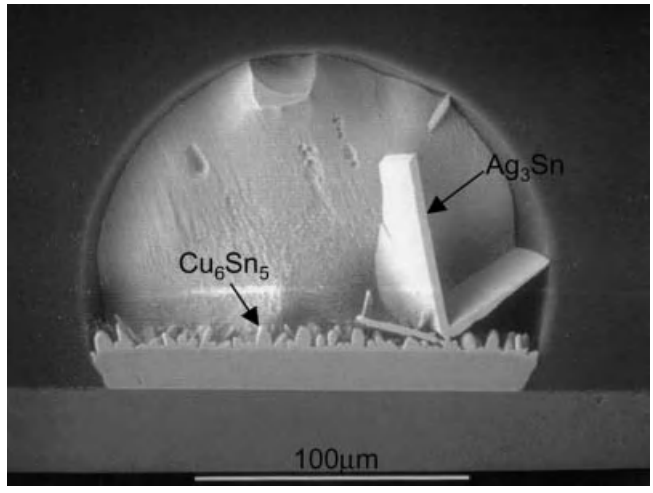

Figure 5.3 *The intermetallic compounds of Ag3Sn and Cu6Sn5 formed in a flip-chip solder joint of Sn-3.8Ag-0.7Cu joined to a Cu substrate by reflowing twice at 260°C (courtesy of T.Y. Lee at UCLA, from [19]). (Reproduced with permission from Mater. Sci. Eng. R: Rep., Six cases of reliability study of Pb-free solder joints in electronic packaging technology by K. Zeng, K.N. Tu, 38, 2, 55–105 Copyright (2002) Elsevier Ltd).*

seriously altered by the large IMCs, and consequently the reliability of the joint would be affected.

Another interesting example of large Ag_3Sn plates was reported with electroplated Sn-Ag solder bumps fabricated by a wafer bumping process for flip-chip applications, as shown in Figure 5.4 [37]. Large Ag_3Sn plates or needles were precipitated on top of solder bumps after multiple reflows. Some of the large Ag_3Sn plates were even shorting neighboring bumps. To avoid this undesirable situation, the Ag content of electroplated Sn-Ag bumps was reduced below 2.7 wt%, following the recommendations provided by the previous works [13, 35, 36]. Since then, the low Ag content in electroplated Sn-Ag bumps has been adopted for Pb-free flip-chip wafer-bumping applications.

5.3 Controlling the Undercooling of Sn Solidification

The undercooling is defined as the temperature difference between the melting temperature of a solder during heating and the solidification temperature during cooling. A typical DSC (differential scanning calorimetry) thermal profile recorded during the heating and cooling cycle of one solder ball of Sn-0.9%Cu (50-mil diameter) is shown in Figure 5.5. The onset and peak temperatures during heating are 228.6 °C and 230.5 °C, respectively, and those during cooling are 199.7 °C (onset) and 202.0 °C (peak). The undercooling is then estimated to be about 28–29 °C depending on either the onset or peak temperatures [29]. Table 5.7 reports the amount of the undercooling measured with several Pb-free solders. The undercooling of Sn-rich solders, namely, Sn-Cu, Sn-Ag and Sn-Ag-Cu, is not significantly affected by varying Cu or Ag content or both. This suggests that Cu and Ag solute atoms

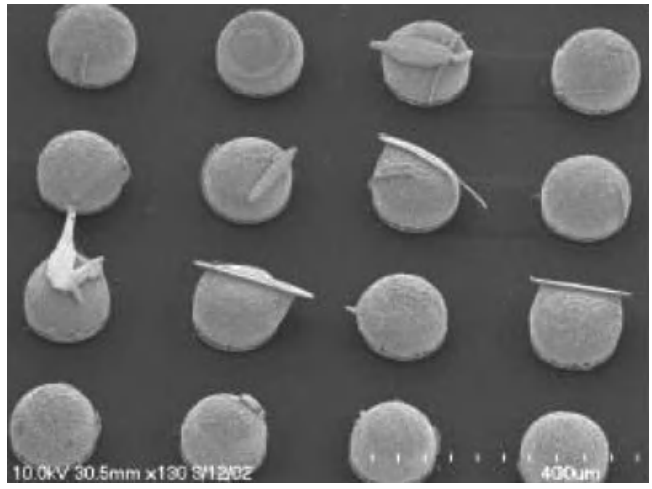

Figure 5.4 *Electroplated Sn-4.3Ag solder bumps after 20 times reflow. Some solder was etched to reveal Ag_3Sn plates within bumps [37]. (Reproduced from presentation at Peaks in Packaging Symposium, October 2003, Unitive's Plated Pb-free Solder Solution by D. Mis Copyright (2002) D. Mis).*

themselves or their intermetallic compounds, such as Cu_6Sn_5 or Ag_3Sn, may not provide preferential nucleation sites for β-Sn solidification. However, the addition of a small amount of Co, Fe, or Zn is found to be very effective to reduce the undercooling by more than 20 °C, as listed in Table 5.7.

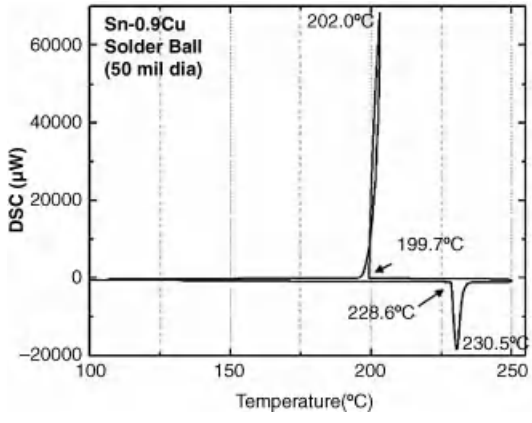

Figure 5.5 *A typical DSC thermal profile recorded during the heating and cooling cycle of one solder ball of Sn-0.9%Cu (50-mil diameter). The undercooling is estimated to be about 28–29 °C depending on either the onset or peak temperatures [29]. (Reproduced from Proceedings of 57th ECTC (Reno), Critical Factors Affecting the Undercooling of Pb-free, Flip-chip Solder Bumps and In-situ Observation of Solidification Process by S.K. Kang, M.G. Cho, P. Lauro, D-Y Shih, 1597–1603 Copyright (2007) IEEE).*

Table 5.7 *The amount of the undercooling measured by DSC with Pb-free Solders [29]. (Reproduced from Proceedings of 57th ECTC (Reno), Critical Factors Affecting the Undercooling of Pb-free, Flip-chip Solder Bumps and In-situ Observation of Solidification Process by S.K. Kang, M.G. Cho, P. Lauro, D-Y Shih, 1597–1603 Copyright (2007) IEEE).*

Composition (wt%)	Onset Temp (heating) (T_1)	Onset Temp (cooling) (T_2)	ΔT ($T_1 - T_2$)	Peak Temperatures[a]
Sn-0.9Cu	228.6	199.7	28.9	230.5 (H), 202.0 (C)
Sn-2Ag	228.7	201.5	27.2	230.2(H), 204.5(C)
Sn-l.OAg-0.9Cu	218.2	192.3	25.9	220.2. 226.0(H). 195.6 (C)
Sn-0.9Cu-0.6Zn	226.8	220.0	6.8	228.7(H) 223.0(C)
Sn-lAg-0.9CU-lZn	217.4	219.2	(−1.8)	219.2, 224.8 (H) 213.0, 219.6(C)
Sn-0.9Cu-0.3Fe	228.7	208.5	20.2	230.8 (H), 211.9 (C)
Sn-0.9Cu-0.2Co	229.4	224.7	4.7	231.3 (H), 226.3 (C)
Sn-3.0A_2-0.5Cu[a]	218.7	195.0	23.7	219.7 (H), 195.2 (C)

[a] DSC 22OC, Seiko, heating at 6 °C/min, cooling at 6 °C/min.

[b] All solder balls are 1.27 mm (50 mil) diameter (~8 mg), except for Sn-3.0Ag-0.5Cu, 25 mil diameter (~1 mg).

The undercooling required for solidification of near-ternary Sn-Ag-Cu solders is generally much larger than high-Pb solders or Sn-Pb eutectic solders [17, 35]. This large undercooling is also responsible for the growth of large primary phases of Ag_3Sn or Cu_6Sn_5, as shown in Figure 5.1. It is also known that the undercooling amount in Sn-Ag-Cu solders is inversely proportional to sample size, suggesting a larger undercooling in a smaller solder joint (such as flip-chip vs. BGA solder joints) [38]. A large undercooling and random solidification among flip-chip solder bumps can adversely affect the reliability of solder joints, since this would yield a situation of some bumps already solidified while others not, causing stress concentration to certain bumps and possibly leading to mechanical or electrical failures within solder joints or other weak structures within the package or in a Si device.

Controlling the undercooling of Sn-rich solders is an important issue in such a new wafer-bumping process, C4NP (C4 new process), where melting/solidification of multiple solder bumps in a small volume is a key metallurgical process involved [33, 39]. In C4NP, a molten solder is filled into a glass mold containing prefabricated cavities of I/O footprint of a silicon wafer, and then solder bumps are transferred from the glass mold to the wafer by aligning/melting the solidified bumps.

To understand the critical factors affecting the undercooling of Pb-free, flip-chip solder bumps in the C4NP process, a systematic investigation was conducted in terms of solder composition, solder volume, and minor alloying elements, UBM (under bump metallization), cooling rate, impurity level, and others [29]. The undercooling of Pb-free, flip-chip solder bumps was evaluated by DSC and the direct observation of individual solder bumps in a glass mold during melting and solidification [29, 40]. The amount of the undercooling of Sn-rich solders was confirmed to be strongly affected by solder volume, inversely proportional to its volume (or effective diameter of solder balls). It was also found that the solder composition and UBM significantly affected the undercooling, but the cooling rate and holding temperature of the mold plate used in C4NP did not so much. Sn-0.7Cu C4NP solder bumps in a mold plate were undercooled by as much as 90 °C from its melting

point, while a less amount of undercooling (40–60 °C) was observed on a Si chip having a wettable Cu/Ni UBM [29].

The effects of UBM on the undercooling were evaluated by comparing various Cu vs. Ni metallization, which included electroplated Cu, electroplated Ni, electroless Ni(P), electroless Ni(P)/immersion Au [41, 42]. The Ni-based UBM was found to be more effective than Cu UBM in reducing the undercooling of Pb-free solders investigated. To explain, the superior behavior of Ni over Cu UBM, both minor Cu- and Ni-doped solders were evaluated for their undercooling behaviors [42]. It was concluded that the type of interfacial IMC phases (Cu_6Sn_5 vs. Ni_3Sn_4) was not the primary contributing factor, but the Ni atoms dissolved from Ni UBM and concurrent precipitation of Ni_3Sn_4 particles inside the solder matrix.

The direct observation of individual flip-chip-size solder bumps on a glass mold during their solidification process revealed the random nature of the molten solder nucleation process, and also confirmed the similar amount of the undercooling as measured by DSC [29, 40]. As the solder volume continuously decreases in the future flip-chip interconnect technologies, minimizing the undercooling of molten solders like in C4NP will become a more critical issue for reliable solder joints.

Since the undercooling phenomenon is related to the difficulty of nucleating a solid phase in a liquid solder, many studies have been reported by adding minor alloying elements into Sn or Sn-rich solders in order to provide some preferential nucleation sites. These minor alloying elements reported include such as Al, Be, Bi, Co, Fe, Hf, Mg, Mn, Mo, Ni, Pt, Ti, Zn, Zr, W, and others [9, 12, 14, 18, 25, 26, 35, 41–45]. Among them, Zn has been extensively investigated, because it is most effective and practical to be used with Sn or alloys [14, 25, 26, 43, 44].

In order to address why Zn or Co addition is so effective in reducing the undercooling, a variety of minor alloying elements to Sn-rich solders has been investigated in terms of their crystal structure [43]. Table 5.8 summarizes the amounts of the undercooling measured by DSC with several different crystal structures of the minor alloying elements. The content of the minor alloying elements is 0.2 wt% in all cases. It is quite interesting to note that the hexagonal crystal structure (HCP) of minor alloying elements is very effective in reducing the undercooling of pure Sn compared to other crystal structure groups. The minor additions of Zn and Ti of the hexagonal crystal structure are again confirmed to be most effective

Table 5.8 *The minor alloying effects on the undercooling during Sn solidification [43]. (Reproduced from PhD thesis of M. G. Cho, Effects of Zn Addition on Undercooling of Pb-free Solder Alloys and Their Interfacial Reactions with Cu and Ni-P UBMs, KAIST, Korea Copyright (2008) M. G. Cho).*

composition (wt%)	ΔT (undercooling)	composition (wt%)	ΔT (undercooling)
pure Sn	31.2	Sn-0.2Zn (HCP)	1.4
Sn-0.2Pb (FCC)	34.6	Sn-0.2Ti (HCP)	5.4
Sn-0.2Cu (FCC)	35.1	Sn-0.2In (tetragonal)	22
Sn-0.2Au (FCC)	15.5	Sn-0.2Bi (rhombohedral)	21.9
Sn-0.2Cr (BCC)	21.4	Sn-0.2Sb (rhombohedral)	25.5
Sn-0.2Fe (BCC)	13.2	Sn-0.2Se (rhombohedral)	19.6
Sn-0.2Mn (BCC)	22	Sn-0.2Ga (orthorhombic)	23.5

Table 5.9 *The undercooling of Sn-rich solders with minor alloying elements with a hexagonal crystal structure [43]. (Reproduced from PhD thesis of M. G. Cho, Effects of Zn Addition on Undercooling of Pb-free Solder Alloys and Their Interfacial Reactions with Cu and Ni-P UBMs, KAIST, Korea Copyright (2008) M. G. Cho).*

Composition (wt%)	ΔT (undercooling)
Sn-0.2Zn	1.4
Sn-0.2Co	6.3
Sn-0.2Mg	6.3
Sn-0.2Ti	5.4
Sn-0.2Sc	4.1
Sn-0.2Zr	5.3

among others. Subsequently, several other HCP metals, such as Co, Mg, Sc and Zr, were evaluated to verify their effectiveness. Table 5.9 summarizes the results of the undercooling measurement with all the HCP metals investigated. Indeed, the minor alloying elements of HCP crystal structure are confirmed to be very effective in reducing the undercooling of the pure Sn down to about 6 °C or less. The Zn addition is again shown to be most effective among all other HCP metals.

In his Ph.D. thesis, M. G. Cho has further explained why the hexagonal metals, especially Zn is most effective by comparing the lattice coherency between Pb/β-Sn and Zn/β-Sn, finding an excellent matching surface, (10–11) of Zn to the β-Sn lattice, while not possible with the Pb structure. This matching surface is suggested to act as a more favorable nucleation site for the Sn nucleation. In addition, employing DFT (density function theory) calculations, it has been shown that the interfacial energy between β-Sn and Zn is relatively low, and is lowest on the (10–11) surface of Zn [46].

5.4 Controlling Interfacial Reactions

The interfacial reactions with UBM (under bump metallization) or surface finishes of solder joints start during a joining/rework process and continue in testing or field service of electronic packages. Proper interfacial reactions are required to provide good wetting of a molten solder, to form metallurgical bonds to wettable surfaces, and thereby to yield a decent joint strength. Factors such as intermetallic compound (IMC) formation, IMC spalling, UBM dissolution, interfacial void formation, all affect the integrity and reliability of solder joints. The failure mechanisms identified in thermal fatigue or electromigration stressing of solder joints are often influenced by the interfacial reactions.

When Sn-rich solders are used for Pb-free applications, the interfacial reactions become more aggressive since Sn-rich solders have a larger Sn content and require a higher reflow temperatures than eutectic Sn-Pb solders. To control the aggressive reactions, a reaction barrier layer, such as Ni, electrolytic or electroless, is commonly used, because Ni has a much lower solubility than Cu in molten Sn at the corresponding reflow temperature. The solubility of Cu in Sn is approximately seven times larger than Ni at a reflow temperature of 260 °C, and is about five times larger at a typical aging temperature of 150 °C [10, 47].

Table 5.10 *Dissolution of surface metallization and intermetallic growth in Sn-Ag, Sn-Ag-Cu, Sn-Ag-Bi at 250 °C [55]. (Reproduced from IEEE Trans. Elec. Pack. Manuf., Interfacial Reaction Studies on Lead (Pb)-Free Solder Alloys by S.K. Kang, et al., 25, 3, 155 Copyright (2002) IEEE).*

Solder	Surface Metallization	Dissolution Rate (μm/min)	IMC Growth Rate (μm/min)
Sn-3.5%Ag	Cu (4 μm)/Cu	0.20	0.67
	Au/Ni(P)/Cu	0.08	0.49
	Au/Pd/Ni(P)/Cu	0.09	0.42
Sn-3.8%Ag-0.7%Cu	Au/Ni(P)/Cu	0.05	0.47
	Au/Pd/Ni(P)/Cu	0.08	0.55
Sn-3.5%Ag-3.0%Bi	Au/Ni(P)/Cu	0.08	0.70
	dAu/Pd/Ni(P)/Cu	0.10	0.67

Recently, numerous research works have been performed to control various aspects of the interfacial reactions by adding various minor alloying elements to Sn-rich solders, such as Bi, Co, Cu, Fe, Ge, Mn, Ni, Sb, Ti, Zn, rare-earth metals (Ce, La), and others [9, 12, 14, 16–18, 22, 25, 26, 29, 34–36, 42–46, 48–54]. In this section, controlling the interfacial reactions in Pb-free solders is briefly discussed in terms of UBM dissolution, IMC formation, void formation and IMC spalling.

5.4.1 Dissolution of UBM and Surface Finishes

The interfacial reactions between Sn-rich solders (Sn-3.5Ag, Sn-3.8Ag-0.7Cu, Sn-3.5Ag-3.0Bi) and several surface finishes commonly used in printed circuit boards were investigated in terms of their dissolution kinetics and interfacial IMC growth [55]. Table 5.10 summarizes the dissolution and IMC growth rates at 250 °C up to 20 min reflow. The dissolution rates of Ni-based metallization, (Au/Ni(P) or Au/Pd/Ni(P), are much smaller than that of Cu metallization (about one half at 250 °C). It is also noted that the dissolution rate of Ni-based metallization is the least in Sn-3.8Ag-0.7Cu among other solders, suggesting the small amount of Cu in SAC to significantly suppress the Ni dissolution. In the same study, as shown in Table 5.11, the dissolution kinetics of

Table 5.11 *Dissolution and intermetallic growth of Ni metallization (electroless vs. electroplated) in Sn-Ag, Sn-Ag-Cu, Sn-Ag-Bi at 250 °C [55]. (Reproduced from IEEE Trans. Elec. Pack. Manuf., Interfacial Reaction Studies on Lead (Pb)-Free Solder Alloys by S.K. Kang, et al., 25, 3, 155 Copyright (2002) IEEE).*

Solder	Surface Metallization	Dissolution Rate (μm/min)	IMC Growth Rate (μm/min)
Sn-3.5%Ag	Au/Ni(P)-(electroless)	0.08	0.49
	Au/Ni-(electroplated)	0.06	0.17
Sn-3.8%Ag-0.7%Cu	Au/Ni(P)-(electroless)	0.05	0.47
	Au/Ni-(electroplated)	0.05	0.29
Sn-3.5%Ag-3.0%Bi	Au/Ni(P)-(electroless)	0.08	0.70
	Au/Ni-(electroplated)	0.05	0.25

electroplated Ni is shown to be much slower than the electroless Ni (one half to one third).

In an attempt to reduce the Cu dissolution and void formation during thermal aging, several minor alloying elements, such as Co, Fe, Ni/In, and Zn, were added to the standard Sn-3.0Ag-0.5Cu (SAC305), [26]. Low-level Zn additions to SAC305 are found to be most beneficial in reducing Cu pad consumption, Cu_3Sn phase, and interfacial void formation. The increased Cu content in SAC309 (0.9Cu) is also beneficial to reduce Cu consumption [26].

In a study to control the interfacial reactions with various Ni UBMs (electroless, electrolytic, sputtered), a small amount of Ni (0.2 wt%) was added to Sn-rich solders, intending to saturate to the solubility limit in Sn at 260 °C [56]. In addition, an overlayer of thin Cu (0.5 or 1.0 μm) was deposited on Ni UBM to investigate the effects of an additional Cu layer on the interfacial reactions. It is found that the consumption of Ni UBM is significantly reduced by the addition of 0.2 wt% Ni to pure Sn and Sn-2Ag solders, but rather increased in Sn-0.7Cu with Ni(P) or sputtered Ni. A metallurgical explanation for this composition dependence is also discussed. The Ni addition is more effective with Ni alloy UBMs (NiSi, NiW, Ni(P) than pure Ni (electrolytic or sputtered). The Cu overlayer is only beneficial in Sn-0.7Cu, but not in pure Sn and Sn-2Ag.

5.4.2 Cu-Sn Intermetallic Formation

When a Sn-rich solder is melted (or reflowed) on Cu metallization, the first IMC to be formed at the interface is Cu_6Sn_5, and subsequently the second IMC, Cu_3Sn phase is formed in between Cu_6Sn_5 and Cu. Since the Cu_6Sn_5 phase is formed in contact with a molten solder, it has an irregular morphology (round or jagged), reflecting the liquid–solid reaction, while the Cu_3Sn phase has a planar interface with a rather uniform thickness. Since a solid-state diffusion of Cu and/or Sn through Cu_6Sn_5 is required to form Cu_3Sn, it is usually much thinner than Cu_6Sn_5. Excessive formation of Cu-Sn IMCs is not desirable because of their brittle nature of mechanical properties, especially when the relative volume of IMCs to a solder joint become significant, such as flip-chip or microbumps of 3D interconnects.

An extensive literature is available on the formation of Cu-Sn intermetallics in Pb-free solders/joints for their growth kinetics, mechanisms, morphological evolution, compositional analysis, mechanical/electrical/physical properties, and others [19, 25, 43, 48, 49, 57, 58].

The IMC growth kinetics in Sn-3.8Ag-0.7Cu PBGA joints was investigated as a function of reflow cycle and UBM (Cu vs. Ni(P) [59]. The IMC on Cu UBM grew much thicker (9–17 μm) than on Ni(P) UBM (4–6 μm) after 12 reflows at 260 °C (peak temperature), as summarized in Table 5.12. When a Cu UBM was coupled with a Ni(P) at an opposite interface, the growth of IMC layers formed on both interfaces were enhanced, compared to the case of having the same UBM on both sides. This suggests the UBM on one side strongly influences the IMC growth on the opposite interface in multiple reflows.

Minor addition of Zn to Sn-3.8Ag-0.7Cu was found to be very effective in reducing the IMC growth on Cu pads in multiple reflows, while the effect was not significant for Au/Ni (P) [25]. The Cu-Sn IMC growth during high-temperature aging at 150 °C was also reduced in Zn-added SAC, especially for the second Cu_3Sn layer. Retardation of the Cu-Sn IMC layers during reflow and aging was attributed to the accumulation of Zn atoms at the Cu_3Sn and Cu interface [25].

Table 5.12 *IMC growth kinetics as a function of reflow cycle and surface finish at 260 °C [59]. (Reproduced from Proc 52nd Elec. Comp. & Tech Conf, San Diego, CA, Interfacial Reactions, Microstructure and Mechanical Properties of Pb-Free Solder Joints in PBGA Laminates by S.K. Kang et al., p. 147 Copyright (2002) IEEE).*

Module #	Surface Finish (side B)	IMC Thick. (μm)	Surface Finish (side *L*)	IMC Thick. (μm)	Reflow # at 260 °C
1	Cu	5–7	Cu	4–5	2, 1
2	Cu	7–12	Cu	7–9	7, 6
3	Cu	9–17	Cu	9–15	12, 11
4	Au/Ni(P)	3–4	Cu	10–12	2, 1
5	Au/Ni(P)	7–10	Cu	10–11	7, 6
6	Au/Ni(P)	6–10	Cu	8–12	12, 11
7	Au/Ni(P)	3–4	Au/Ni(P)	3–4	2, 1
8	Au/Ni(P)	4–5	Au/Ni(P)	5–6	7, 6
9	Au/Ni(P)	4–6	Au/Ni(P)	4–6	12, 11
10	Au/Pd/Ni(P)	3–5	Cu	5–7	2, 1
11	Au/Pd/Ni(P)	5–8	Cu	5–8	7, 6
12	Au/Pd/Ni(P)	5–12	Cu	8–10	12, 11
13	Au/Pd/Ni(P)	3–5	Au/Pd/Ni(P)	2–5	2, 1
14	Au/Pd/Ni(P)	5–7	Au/Pd/Ni(P)	3–5	7, 6
15	Au/Pd/Ni(P)	4–6	Au/Pd/Ni(P)	3–5	12, 11

In another study, the influence of low-level doping of Co, Cu, Fe, Ni/In and Zn to SAC 305 was investigated with BGA solder joints thermally aged at 150 °C up to 2000 h [26]. Table 5.13 summarizes the results on IMC thickness and Cu pad consumption for each minor alloying element in comparison with SAC305. The Cu consumption was significantly reduced by the addition of Zn, Cu, or Fe, but rather increased with Co or Ni/In. The Cu_3Sn thickness was significantly reduced by the addition of Zn, Co, Fe, or Ni/In, while it was similar with SAC309. The Zn addition was most effective in reducing the total IMC thickness as well as the Cu_3Sn thickness after 2000 h aging at 150 °C among other alloying elements examined.

Minor Ni addition to Sn-3.5Ag was reported to increase the Cu dissolution and to enhance the growth of $(CuNi)_6Sn_5$ during reflow, but to suppress the growth of Cu_3Sn during solid-state aging [60]. The reduced growth of Cu_3Sn was regarded to be beneficial to suppress the Kirkendall voids and thereby to improve the impact strength of the corresponding joint. However, in a search for the fourth element addition to Sn-Ag-Cu solders to improve the

Table 5.13 *Thickness of Cu-Sn IMCs and Cu consumption in Pb-free solder joints annealed for 2000 h at 150 °C (in μm) [26]. (Reproduced from Proc 56th ECTC, The Influence of Low Level Doping on the Thermal Evolution of SAC Alloy Solder Joints with Cu Pad Structures by I. de Sousa et al., p.1454, Copyright (2006) IEEE).*

	SAC 305	Zn	Co	Fe	In/Ni	SAC 309	Pb/Sn
Cu Consumption	8.7	5.6	10.9	7.3	11.9	4.9 7.1	
Cu_3Sn	4.3	0.4	1.5	1.2	1.8	4.2	5.9
Cu_6Sn_5	7.5	3.4	9.0	9.2	12.2	5.5	5.7

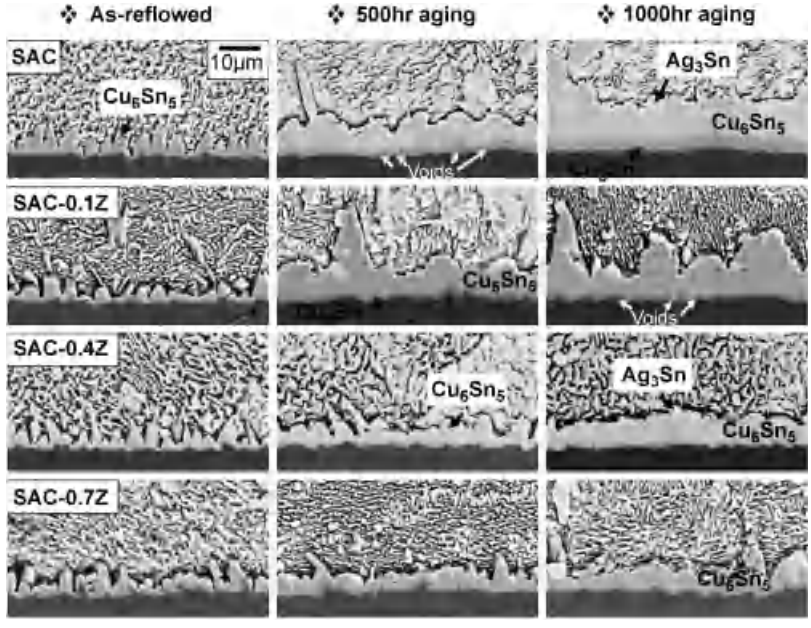

Figure 5.6 *The cross-sectional images of Sn-3.8Ag-0.7Cu, Sn-3.8Ag-0.7Cu-0.1Zn, Sn-3.8Ag-0.7Cu-0.4Zn and Sn-3.8Ag-0.7Cu-0.7Zn solders on electroplated Cu after the reflow and aging for 500 h and 1000 h at 150°C [63]. (Reproduced from J. Electron. Mater., Effects of Minor Addition of Zn on Interfacial Reactions of Sn-Ag-Cu and Sn-Cu Solders with Various Cu Substrates during Thermal Aging by S. K. Kang et al., 36, 11, 1501–1509 Copyright (2007) Springer Science + Business Media).*

high-temperature aging resistance, the Ni addition was not favorably recommended, because it could cause a brittle failure or reduction in the impact strength after high-temperature aging [61].

The beneficial effects of minor Ti or Mn addition were reported with SAC joints by controlling their microstructure, improving drop impact strength as well as suppressing the interfacial IMC growth [62].

The beneficial effects of minor Zn addition (0.1 to 0.7 wt%) to Sn-Cu and Sn-Ag-Cu solders were systematically investigated with various Cu substrates, such as high-purity Cu, oxygen-free Cu, electroplated Cu and sputtered Cu [63]. Figure 5.6 shows typical cross-sectional images of Sn-3.8Ag-0.7Cu, and Sn-3.8Ag-0.7Cu-(0.1, 0.4, 0.7)Zn solders on electroplated Cu after the reflow and aging for 500 h and 1000 h at 150 °C. The thickness of Cu-Sn IMC layers was plotted as a function of Zn content in SAC, as shown in Figure 5.7. In general, the thickness of each IMC decreases as the Zn content increases. All IMCs of SAC-0.7Zn are much thinner than others, especially for Cu_3Sn. The 0.4 wt% addition was recommended to control the IMC growth as well as the interfacial void formation with electroplated Cu substrates, which were prone to void formation upon high-temperate aging at 150 °C [63].

The beneficial effects of Zn addition on the interfacial reactions were earlier explained by observing accumulation of Zn atoms at the interface between Cu_3Sn and Cu after multiple

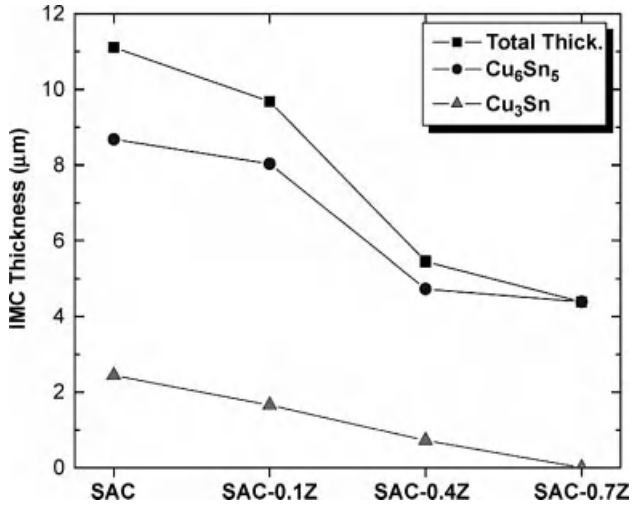

Figure 5.7 *The thickness of each IMC layer plotted as a function of Zn composition in SAC after aging for 1000 h at 150°C on electroplated Cu [63]. (Reproduced from J. Electron. Mater., Effects of Minor Addition of Zn on Interfacial Reactions of Sn-Ag-Cu and Sn-Cu Solders with Various Cu Substrates during Thermal Aging by S. K. Kang et al., 36, 11, 1501–1509 Copyright (2007) Springer Science + Business Media).*

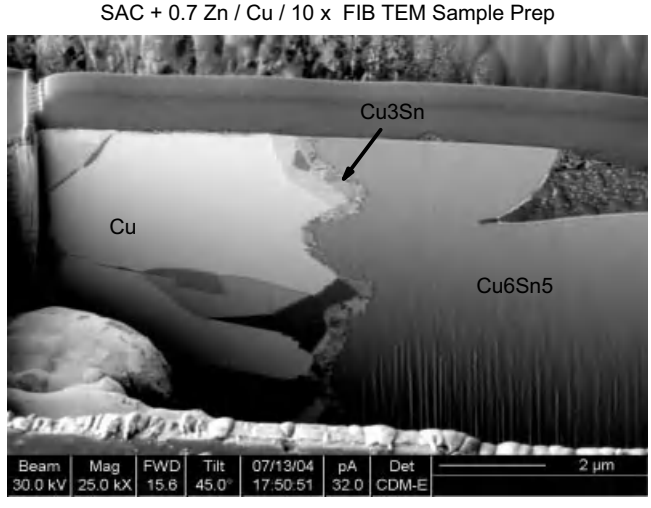

Figure 5.8 *A secondary electron image of the interfacial region in a SAC + 0.7Zn solder joint formed on a Cu pad. The joint was reflowed 10 times with the peak temperature ranging from 235 to 245°C. The sample was prepared by focused ion beam milling a thin slice perpendicular to the joint interface [25]. (Reproduced from J. Electron. Mater., Interfacial Reactions of Sn-Ag-Cu Solders Modified by Minor Zn Alloying Addition, by S. K. Kang, 35 (3), 479–485 Copyright (2006) Springer Science + Business Media).*

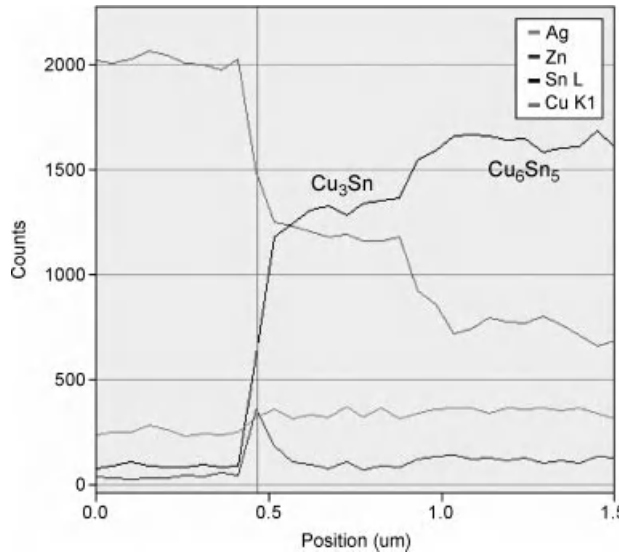

Figure 5.9 *An example of energy-dispersive X-ray (EDX) spectroscopy performed on the sample shown in Figure 5.7. The compositional profiles of Cu, Sn, Ag and Zn were plotted along the distance perpendicular to the IMC interfaces [25]. (Reproduced from J. Electron. Mater., Interfacial Reactions of Sn-Ag-Cu Solders Modified by Minor Zn Alloying Addition, by S. K. Kang, 35 (3), 479–485 Copyright (2006) Springer Science + Business Media).*

reflows, employing the high-resolution TEM/FIB technique combined with EDX [25]. Figure 5.8 exhibits a representative image of the interfacial region in a SAC + 0.7Zn solder joined to a Cu pad. The ion-beam image clearly shows the well-known double-layer structure of Cu_6Sn_5 and Cu_3Sn formed on top of the Cu pad. The IMC layer attached to Cu, Cu_3Sn is very thin, less than 1 μm thick, even after 10 reflows, while the Cu_6Sn_5 in contact with the solder has progressively grown to a few micrometer thickness. The EDX analysis was conducted across the IMC interfaces to identify the IMC layers as well as any segregation of Zn atoms. As shown in Figure 5.9, an accumulation of Zn atoms at the interface between the Cu and Cu_3Sn layer was noted [25].

To further reveal the amount and location of Zn atoms dissolved in the IMC layers, the Zn-accumulated regions in Sn-0.7Cu-0.4Zn joints after aging at 150 °C were reinvestigated by the high-resolution STEM microanalysis [43]. Figure 5.10 shows a typical example of a high-resolution TEM image of the interface between Sn-0.7Cu-0.4Zn and electroplated Cu aged at 150 °C for 1000 h. The microanalysis of EDS results of the regions, (a), (b), (c), (d) and (e) marked in Figure 5.10 are also tabulated in Figure 5.10. A significant level of Zn accumulation, 1–2 wt%, was detected in the regions of (b), (c) and (d), which correspond to the interface between Cu_3Sn/Cu, the layer of Cu_3Sn, and the Cu_6Sn_5 layer, respectively. In addition, an appreciable number of Zn atoms, 0.8 wt%, was also detected in the region (a) of the Cu substrate underneath the Cu_3Sn layer. The results strongly support the view that Zn atoms exist in Cu-Sn IMCs or Cu-Zn solid solution, not in a form of Cu-Zn IMCs [63]. In addition, a thermodynamic calculation for the driving force to form the Cu_3Sn phase as a

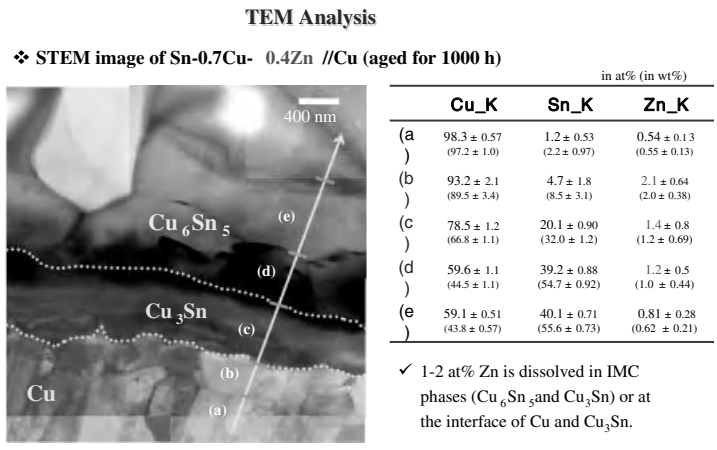

Figure 5.10 *A high-resolution STEM image of the interface between Sn-0.7Cu-0.4Zn and electroplated Cu, aged at 150°C for 1000 h. The microanalysis results of EDS of the corresponding areas are listed for Cu, Sn and Zn content [43]. (Reproduced from PhD thesis of M. G. Cho, Effects of Zn Addition on Undercooling of Pb-free Solder Alloys and Their Interfacial Reactions with Cu and Ni-P UBMs, KAIST, Korea Copyright (2008) M. G. Cho).*

function of Zn content at 150 °C in the Sn-Cu-Zn system was conducted to explain the reduced growth of Cu_3Sn layer in Zn-added solders [43].

5.4.3 Interfacial Void Formation

The formation of voids between the interfacial IMCs and Cu substrate has been well recognized as an important reliability issue affecting the integrity of Pb-free solders joints [22–24, 64]. The void formation is possibly caused due to an imbalance in atomic flux across the diffusing interface, that is, Cu atoms diffuse out faster across the Cu-Sn IMC layer(s) toward the solder than Sn atoms diffuse through the IMCs from the Sn-rich solder. This phenomenon is known as the Kirkendall effect, which was originally observed to occur during an interdiffusion experiment between Cu and Cu-Zn alloy, where Zn atoms diffuse faster than Cu atoms across the interface [65].

Upon an extended annealing of SAC joints in contact with Cu, at 150 °C, voids were observed at the interface between Cu and IMCs, and could grow and coalescence into a void layer as the annealing progresses [23]. This void structure would drastically reduce the impact drop strength of Pb-free solder joints [23]. Accordingly, several approaches have been proposed to improve the impact reliability of Sn-rich solder joints. Among these are the placement of a diffusion barrier layer over Cu, such as electroless Ni(P) or electroplated Ni [22], and additions of minor alloying elements into the SAC alloys to control the IMC growth [18, 22] or to suppress the interfacial void formation [17, 25, 26, 52].

In the efforts to maintain the solder joint shear strength and ductility after an extended high-temperature aging, several minor alloying elements, such as Co, Fe, Mn, Ni, Ge, Ti, Si, Cr, and Zn, were added to modify a strong (high Cu content) SAC solder alloy [52, 61]. Of the choices tested, Co, Fe, and Zn substitutions for Cu were found to be attractive in terms of IMC segregation effects, suppression of IMC growth and void formation, and mechanical

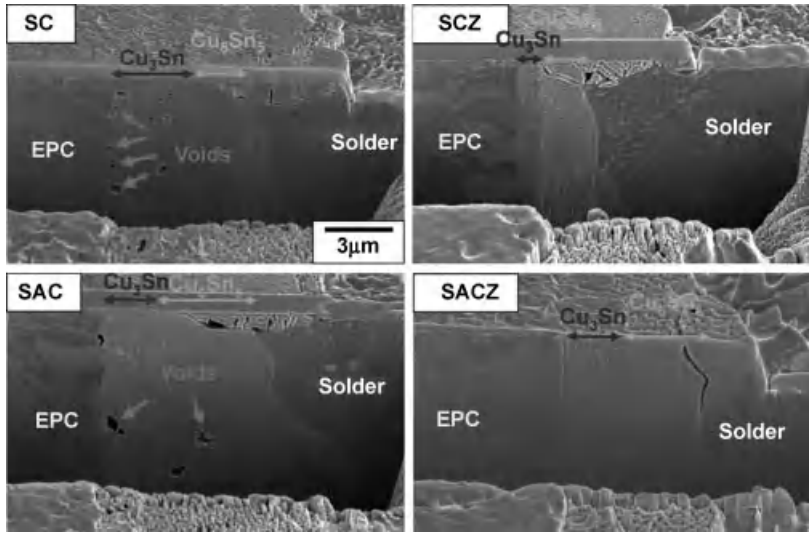

Figure 5.11 *Secondary electron images of the interface area between each solder and electroplated Cu after aging for 1000 h at 150°C, which was cut out by the focused ion beam (FIB) technique [63]. (Reproduced from J. Electron. Mater., Effects of Minor Addition of Zn on Interfacial Reactions of Sn-Ag-Cu and Sn-Cu Solders with Various Cu Substrates during Thermal Aging by S. K. Kang et al., 36, 11, 1501–1509 Copyright (2007) Springer Science + Business Media).*

properties of joints [61], while the Ni addition was not recommended based on the brittle fracture observed in shear tests. By using the WDS (wavelength-dispersive spectroscopy) technique, it was also demonstrated the interfacial segregation of minor alloying elements of Fe, Co or Zn at the joint interfaces after 1000 h aging at 150 °C [61], consistent with the similar findings [25, 43].

As discussed earlier, a small addition of Zn to SAC significantly reduced the growth of a Cu_3Sn IMC layer, and thereby the formation of interfacial voids during the solid-state annealing, when in contact with Cu metallization [25, 26, 63]. Figure 5.11 displays an example of void formation at the interfacial regions of electroplated Cu substrates reacted with or without Zn additions. Several voids are noted in the Cu_3Sn phase, while no voids were detected in the Zn-added solders [63].

In order to estimate the propensity of void formation, the average distance between voids was measured with SAC solders of several minor alloying elements, such as Co, Cu, Fe, and Zn, aged at 150 °C, up to 2000 h, as tabulated in Table 5.14 [26]. The Zn addition almost completely suppressed the void formation compared to other minor alloying elements after the aging of 2000 h. It is also interesting to note that SAC309 has 50% more voids for 1000 h aging, while the difference became insignificant for the longer aging time of 2000 h.

5.4.4 Spalling of Ni-Sn Intermetallics

Recently, electroless Ni(P) metallization has received great attention as a reaction barrier layer for Pb-free solder joints, because of its low cost and simple processing steps. However,

Table 5.14 *Void propensity evaluation for Pb-free solder joints annealed at 150°C [26]. (Reproduced from Proc 56th ECTC, The Influence of Low Level Doping on the Thermal Evolution of SAC Alloy Solder Joints with Cu Pad Structures by I. de Sousa et al., p.1454, Copyright (2006) IEEE).*

Aging at 150 °C–1000 h	
Solder type	Average distance between voids (μm)
SAC305	4
SAC309	2
Aging at 150 °C–2000 h	
Solder type	Average distance between voids (μm)
SAC305	2.5
SAC + Zn	570
SAC + Co	3
SAC + Fe	5
SAC309	2

the interfacial reactions with Ni(P) are more complex than electroplated Ni, owing to the formation of a P-rich layer between the Ni-Sn IMC and Ni(P) during reflow and solid-state annealing [66–69]. Spalling of Ni-Sn IMCs from the interface is commonly observed when the interfacial reactions progress [68–71]. The IMC spalling was found to be strongly influenced by P content, solder volume or deposition method [70]; higher P content and larger solder volume causing more spalling. In addition, a higher tendency of IMC spalling was noted from screen-printed solder paste over electrodeposited solder. It was also determined that the solder-deposition method (plating vs. solder paste) was important to the IMC spalling behavior. Upon reflow, solder paste reflowed causes more spalling than electroplated solder under equivalent conditions [68]. The IMC spalling from a Ni(P) layer is also closely related to the crystallization process. A Ni-Sn-P layer forms between Ni_3Sn_4 and crystalline Ni_3P, causing Ni-Sn IMC spalling to occur from the Ni-Sn-P surface [68]. The IMC spalling becomes less severe from a Ni(P) layer when Sn-rich solders contain a small amount of Cu, possibly by altering the structure or composition of Ni-Sn IMCs [55, 57, 69].

To prevent IMC spalling, a thin intermediate layer of Sn or Cu was deposited on top of Ni (P) by electro- or electroless plating. During the reflow reaction of Sn-3.5%Ag solder paste, the intermediate layers effectively suppressed Ni-Sn IMC spalling during the reflow reaction at 250 °C, 30 min, while most IMC already spalled off the Ni(P) in a few minutes in the control samples without an intermediate layer [71]. The Sn layer provided protection of the Ni(P) surface and a good wettable surface during reflow. The thin Cu layer changed the chemical structure of the interfacial IMCs in addition to providing a good wettable surface.

5.5 Modifying the Microstructure of SAC

The microstructure of a solder joint is determined by the complex interplay among several factors such as solder composition, solidification conditions (reflow temperature, dwell time, cooling rate, etc.), solder volume, minor alloying elements, UBM, and

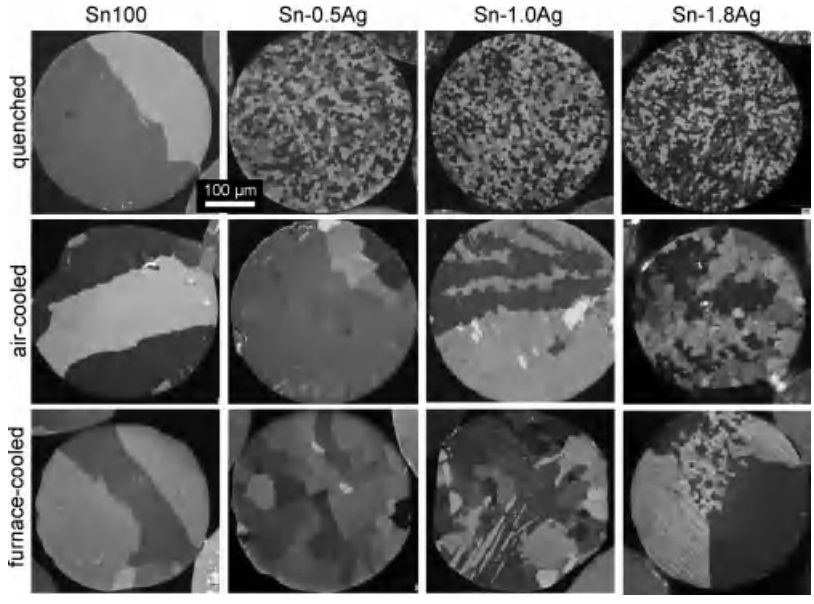

Figure 5.12 *Cross-polarized images of Sn-Ag solder balls (380 μm diameter) as a function of cooling rate and Ag composition (0, 0.5, 1.0 and 1.8 wt%) [72]. (Reproduced from J. Electron. Mater. An Investigation of Microstructure and Microhardness of Sn-Cu and Sn-Ag Solders as a Function of Alloy Composition and Cooling Rate by S. K. Kang et al., 38(2), 257–265 Copyright (2009) Springer Science + Business Media).*

others. A typical microstructure of a ternary Sn-3.8Ag-0.7Cu alloy in a BGA solder joint is a nonequilibrium one, as shown in Figure 5.1, consisting of Sn dendrite cells surrounded by a network of fine intermetallic particles of Ag_3Sn and Cu_6Sn_5. Occasionally, the large primary Ag_3Sn plates and/or Cu_6Sn_5 rods may be found, as noted in Figure 5.1. A large amount of undercooling required for Sn solidification promotes growth of the primary phases once nucleated in a undercooled liquid, by prolonging their growth time until the solidification is completed. The large undercooling is also responsible for the large grain structure commonly observed in Sn-rich solder joints [15, 28, 72, 73]. When a solid phase nucleates in a significantly undercooled liquid Sn, the solidification process occurs in a very short time and its latent heat released becomes large enough to heat up the melt and thereby to make additional nucleation difficult. This situation leads to formation of a large-grain microstructure of one or a few grains.

The grain structure observed in Sn-Ag-Cu solders is often related with cyclic twinning orientations. Two different cyclic twinning morphologies have been observed [28, 73]; a twining structure of 60^o rotations with 3 dominant twin orientations cyclically repeating around the nucleus (known as Kara's beach ball structure), and a highly interpenetrating dendrite structure with no well-defined twin regions [74]. It is also reported that Sn grain size in Sn-Ag-Cu solders significantly increases as Cu content increases from 0 to 1.1%, while the Ag addition to Sn decreases the grain size of Sn-Ag [73].

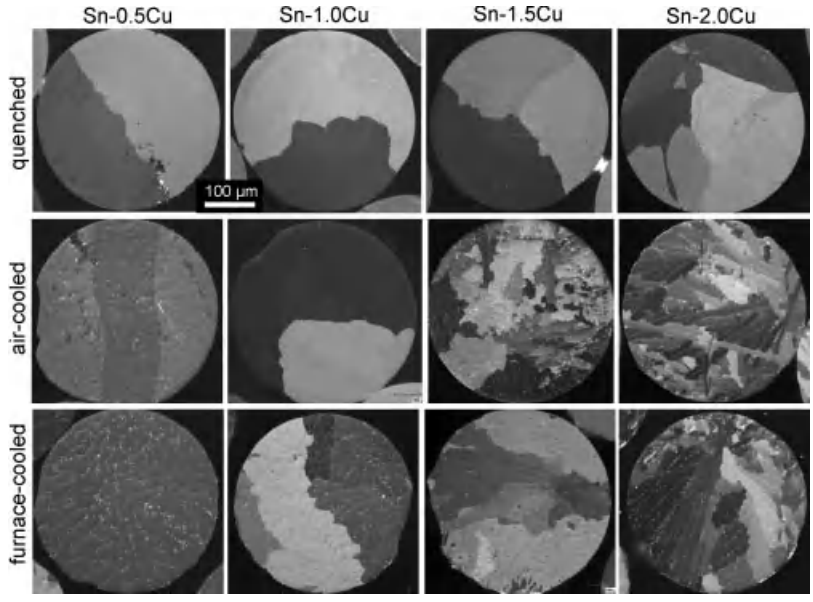

Figure 5.13 *Cross-polarized images of Sn-Cu solder balls (380 μm diameter) as a function of cooling rate and Cu composition (0.5, 1.0, 1.5 and 2.0 wt%) [72]. (Reproduced from J. Electron. Mater. An Investigation of Microstructure and Microhardness of Sn-Cu and Sn-Ag Solders as a Function of Alloy Composition and Cooling Rate by S. K. Kang et al., 38(2), 257–265 Copyright (2009) Springer Science + Business Media).*

The microstructure and mechanical properties of binary Sn-Cu and Sn-Ag solders were systematically investigated in terms of their composition and cooling rate [72]. Figure 5.12 exhibits the microstructure variations in Sn-Ag solders revealed by crosspolarized light microscopy. The grain size of Sn-xAg ($x = 0, 0.5, 1.0, 1.8$ wt%) solders generally increases as the cooling rate is reduced from the quenched rate ($\sim$100 °C/s) to the air cooled ($\sim$10 °C/s) to the furnace cooled ($\sim$0.02 °C/s), while the grain size of pure Sn appears to be independent of cooling rate. A small addition of Ag is found to be very effective to reduce Sn grain size, especially in the quenched condition. In the quenched Sn-0.5Ag samples, about 50% of solder balls has the fine grain structure, while the remaining ones have one or a few grains. As the Ag content increases, the ratio of having the fine grains increases. For the quenched Sn-1.8Ag, over 90% have the fine grain structure. The similar fine grain structure was also observed in high Ag or near-ternary eutectic Sn-Ag-Cu solders [73, 74]. For low-Ag solders, the microstructure is more sensitive to Ag content than cooling rate [72]. The fine-grain structure in the quenched sample of Sn-0.5%Ag was analyzed by EBSD and found to be a mixture of cyclic twins (with 60° misorientation) and low-angle boundaries, not general grain boundaries [72]. The propensity of forming fine cyclic twins in Sn-Ag solders was explained by noting a large supersaturation of Ag atoms in the quenched Sn matrix compared to Sn-Cu solders from the thermodynamic data of their solubility in Sn [72].

To compare the alloying effects of Ag versus Cu in Sn-rich solders, the microstructure of Sn-xCu ($x = 0, 0.5, 1.0, 1.5, 2.0$ wt%) was investigated in terms of Cu content and cooling,

as shown in Figure 5.13. In the quenched condition, contrary to Ag, the Cu addition did not produce any fine-grain microstructure at all, while the grain size generally decreases as Cu content increases for the air-cooled and the furnace-cooled case. The microstructure of low Cu solders (0.5 and 1.0 wt%) is pretty similar to pure Sn of large grains, not sensitive to its cooling rate. Another interesting feature was reported on the Sn grain orientations of the fine-grain structure observed such as in Sn-2.0Cu by the EBSD analysis [72]. The misorientation between neighboring grains was distributed over a wide range of 0–95 deg, indicating the fine-grain structure being general grain boundaries, not related to the twinning structure, as observed in Sn-Ag solders. The microstructure (or Sn grain size) in Sn-Cu solders was found to be closely related to the distribution of Cu_6Sn_5 particles, which are strongly influenced by both Cu content and cooling rate.

Another important effect of Cu content reported is on the pasty range of SAC solder joints [35]. The pasty range is defined as the difference between the liquidus and solidus temperature of a given alloy composition. It is desirable to have a smallest pasty range as possible to reduce the defect rate in solder joints. The pasty range of SAC solder joints is quite sensitive to Cu content, above the eutectic composition, but not to Ag content. For Ag contents ranging from 2.1 to 2.7%, the pasty range is estimated to be 2 to 4 °C for 0.7%Cu and 15 to 17 °C for 0.9%Cu. Comparing the microstructure of Sn-3.5%Ag [76] with the near-eutectic ternary SAC alloys [75], it is noted that the presence of Cu in SAC alloys promotes more dendrite growth of β-tin.

The effect of Zn addition to SAC was investigated to control the formation of large Ag_3Sn plates [14, 77]. It was also reported that Zn additions modified the microstructure of the β-tin dendrite, as well as the ternary eutectic microstructure. For Zn-added solders, Sn dendrites become coarser and the volume fraction of the eutectic phase increases at an equivalent cooling rate. Considering Zn atoms preferentially react with Cu atoms, the role of Zn is regarded to influence the nucleation of the eutectic microstructure and thereby to promote the formation of the eutectic microstructure. Since Zn can be easily oxidized in a molten solder and can hence degrade solder wettability, the amount of Zn addition should be limited to a minimum and the reflow process is required to be performed in an inert atmosphere, such as nitrogen.

A minute amount of Ni and Ge additions to Sn-0.7Cu solders has been practiced to improve soldering characteristics, fluidity, to reduce shrinkage defects, to reduce the volume fraction of Sn dendrite and to promote a more eutectic microstructure, [78–80].

The additions of rare-earth metals, such as Ce, La, or Y, have been reported to improve wettability, creep strength and tensile strength, and to refine the microstructure of Pb-free solder joints [81–85]. The addition of a small amount of La (up to 0.5 wt%) to SAC refined the microstructure by decreasing the length and spacing of Sn dendrites and decreased the interfacial Cu-Sn IMC thickness [82], which significantly enhanced its elongation with a small decrease in shear strength. In addition, some refinement of Sn grain size and IMC particles was also reported [83, 84]. However, in the case of Ce-added SAC, abnormal Sn whisker growth was reported even after 1 day at an extremely high growth rate (~8.6 Å/s) [85]. The high growth rate was owing to Sn whisker formation from the oxidizing $CeSn_3$ phase.

The influence of the interfacial reactions on the microstructure of solder joints was reported [86]. When Sn-Ag and Sn-Cu solders are reacted with Cu or Ni(P) UBM, Cu and Ni atoms dissolve quickly to saturate to their solubility limits in molten solders, causing the

changes in composition and microstructure. A few large grains in pure Sn and Sn-0.5Cu solders change to many columnar grains after being reacted on a Cu UBM, influenced by the large increase in Cu content (~1.3 wt%). In contrast, when reacted on Ni(P), a few large grains are maintained, probably due to the small increase in Ni content (~0.07 wt%). The fine twins in Sn-Ag solders also changed to a few large grains after being reacted with Cu or Ni(P) UBM. This microstructure change is attributed to the compositional changes during reflow and the accompanied precipitation of IMC particles in solder joints [86].

5.6 Improving Mechanical Properties

5.6.1 Strength and Hardness

The mechanical properties of Pb-free solders and joints have been extensively investigated in terms of alloying elements, solidification conditions or other processing parameters [4, 8, 12, 15–17, 59, 72, 75, 76, 87]. Several Pb-free solders were evaluated as a function of alloying composition, plastic deformation and annealing condition [87]. The strain-hardening behavior of Sn-rich solders is significantly affected by the amount of alloying elements and plastic deformation. More plastic deformation and more alloying elements yield larger strain hardening, confirmed by their microhardness measurement. However, pure Sn does not exhibit substantial strain hardening, due to the recrystallization and grain growth occurring at room temperature. For high-solute solders, such as Sn-3.5Ag and Sn-3.5Ag-0.7Cu, recrystallization requires both a considerable amount of plastic deformation, such as 30% or higher, and an annealing condition, such as 150 °C for 48 h. This confirms that high-solute solders of SAC have a better microstructure stability than low-solute solders, such as Sn-0.7Cu or pure Sn [87].

High-solute solders or near-ternary eutectic Sn-Ag-Cu solders are usually not chosen for flip-chip applications, because they have high modulus and high tensile strength. Recently, low-Ag solders have become popular for the solder interconnects required for low strength and high ductility. Figure 5.14 exhibits the microhardness data of low-solute solders, Sn-Ag and Sn-Cu, measured in terms of alloy composition and cooling rate [72]. Sn-Cu solders follow a general structure–property relationship, that is, a higher hardness for more alloy additions and faster cooling. However, Sn-Ag solders do not follow this relation with regard to cooling rate; the air-cooled solders exhibit a higher hardness than the rapidly quenched, as shown in Figure 5.14a. Sn-Ag quenched solders have a fine twin structure, while air-cooled Sn-Ag have a relatively coarse microstructure revealed by the crosspolarized images in Figure 5.12. Generally, for metals and alloys a finer grain structure is responsible for a higher yield strength (or higher hardness) due to the grain-boundary strengthening mechanism (known as the Hall–Petch relationship). But the fine twin structure observed in Sn-Ag solders seems to not contribute for the hardening of Sn-rich solders. Further, it is reported that the microhardness data of Sn-Ag and Sn-Cu are better correlated with the characteristics of IMC particles (quantity, size, distribution) rather than Sn grain or twin size revealed in crosspolarizing images [72].

Comparing the hardness data of Sn-Ag and Sn-Cu solders, it is evident that the addition of Cu solute atoms to Sn matrix is much more effective than Ag to Sn at the same cooling rate, as shown in Figure 5.14. This is explained by two reasons. First, the volume fraction of

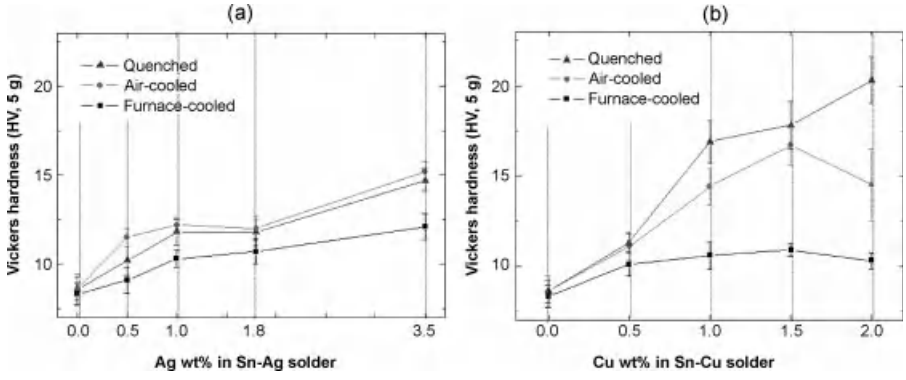

Figure 5.14 *Microhardness variations of (a) Sn-Ag and (b) Sn-Cu solders in terms of solute content and cooling rate [72]. (Reproduced from J. Electron. Mater. An Investigation of Microstructure and Microhardness of Sn-Cu and Sn-Ag Solders as a Function of Alloy Composition and Cooling Rate by S. K. Kang et al., 38(2), 257–265 Copyright (2009) Springer Science + Business Media).*

Cu_6Sn_5, formed at 220 °C, just below the eutectic temperature, is estimated to be always larger than Ag_3Sn for the same wt% of Cu or Ag [72]. The second reason is such that the bulk hardness of Cu_6Sn_5 (∼4.5 GPa) is much higher than Ag_3Sn (∼1.5 GPa) [88]. Hence, for the same amount of Ag or Cu, Sn-Cu solders are expected to be harder than Sn-Ag, assuming each IMC system has a similar size and distribution characteristics.

5.6.2 Drop Impact Resistance

Drop impact resistance is an important reliability issue for Pb-free solders joints, especially for mobile electronics. The brittle fracture of solder joints during drop impact test is often caused by the weak interface owing to the formation of voids along IMC layers [23]. To improve the drop impact resistance of Pb-free solder joints, two approaches have been taken; reducing Ag or Cu content in SAC solder to increase the ductility of the solder matrix [89–91], and/or adding minor alloying elements to suppress the interfacial void formation and IMC growth [52, 58, 62, 78, 89, 90].

A small addition of Ti, Mn, Ni, or In is also reported to improve the impact resistance of Sn-Ag-Cu joints [62, 90], while Ni and Ge are added to Sn-Cu [78], or Zn added to Sn-Ag-Cu or Sn-Cu for the same purpose [25, 43]. Examples of void suppression by Zn addition to Sn-Cu or Sn-Ag-Cu are already shown in Figure 5.11 [63]. However, when an excessive amount of Zn is added to Sn-rich solders, the drop impact resistance rather degrades [54].

5.6.3 Thermal Fatigue Resistance

In the early Pb-free, flip-chip development, thermal-fatigue performance of Pb-free solders was compared with Pb-containing solder joints [21, 92–94]. Three Pb-free solders, Sn-0.7Cu, Sn-3.8Ag-0.7Cu and Sn-3.5Ag, formulated as solder paste, were evaluated for flip-chip applications [94]. Among the solders and UBM evaluated, Sn-0.7Cu bump on both Ni (P) and TiW/Cu had the longest fatigue life, while Sn-3.5Ag on Ni(P) had the shortest

life [94]. The Sn-3.8Ag-0.7Cu on TiW/Cu had a better fatigue life than Sn-3.5Ag, worse than Sn-0.7Cu, and a similar life to Sn-37Pb on Ni(P). The better fatigue performance of Sn-0.7Cu joints were explained by the fatigue crack initiation/propagation mechanism through the grain boundaries. For Sn-0.7Cu joints, the cracks were observed to propagate at the grain boundaries, significantly removed from the UBM/bump interface near the center of the joint. This solder was claimed to be most compliant in thermal fatigue and to undergo massive deformation before failing by crack propagation [93].

The effect of silver content on thermal fatigue life of flip-chip interconnects was systematically investigated for the packages assembled to FR-4 substrate with Sn-Ag-Cu solder balls [95]. From the thermal cycling test (between −45 and 125 °C), solder joints with a high Ag content, 3 and 4 wt%, were found to have a longer fatigue life compared to solder joints with a lower Ag content, 1 and 2 wt%. The better fatigue performance of high-Ag solders was attributed to their stable microstructure owing to a uniform dispersion of fine Ag_3Sn particles. In low-Ag joints, significant coarsening of the microstructure was observed during the thermal cycling test [95].

In another study, the effect of Ag content on thermal fatigue life of ceramic BGA modules assembled on an organic substrate was evaluated in terms of Ag content, cooling rate and thermal cycling condition [16, 96]. The fatigue life was influenced by Ag content as well as thermal cycling test condition. The low-Ag joints (2.1%) had the best thermal fatigue life for the thermal cycling test between 0 and 100 °C with a long cycle time of 120 min, while the high-Ag joints (3.8%) had the best life for the short cycle time of 30 min. The slow cooling rate (0.5 °C/s) used during assembly was beneficial to the thermal fatigue life regardless of Ag content or thermal cycling conditions compared to the fast cooling rate (1.7 °C/s).

Since the microstructure of Pb-free BGA or flip-chip joints are known to be either a single crystal or composed of a few grains [28, 97], the fatigue performance of Pb-free solder joints would be strongly affected by the crystal orientation of Sn matrix. In the conventional thermal cycling test, solder bumps at the corner of a Si chip or module with the largest DNP would expect to fail first, but this situation would not be warranted when the crystal orientation of Sn matrix plays into the failure process. An example was discussed with Pb-free BGA solder joints, where the *c*-axis of Sn-crystal was oriented parallel to the substrate direction, premature failures were observed regardless of the position of solder joints [28, 97].

5.7 Enhancing Electromigration Resistance

Recently, the electromigration (EM) in Pb-free solder joints for flip-chip applications has become a critical reliability challenge, largely because of lower melting temperatures of Sn-rich solders in comparison to high-Pb solders as well as the remarkable anisotropy in diffusion rates of common solute atoms such as Cu, Ni, or Ag in Sn matrix, as discussed earlier.

Early EM test results obtained from actual flip-chip solder joints are often complicated to compare with each other because their solder temperature and current density significantly vary among samples due to current crowding and local Joule heating. In order to avoid these

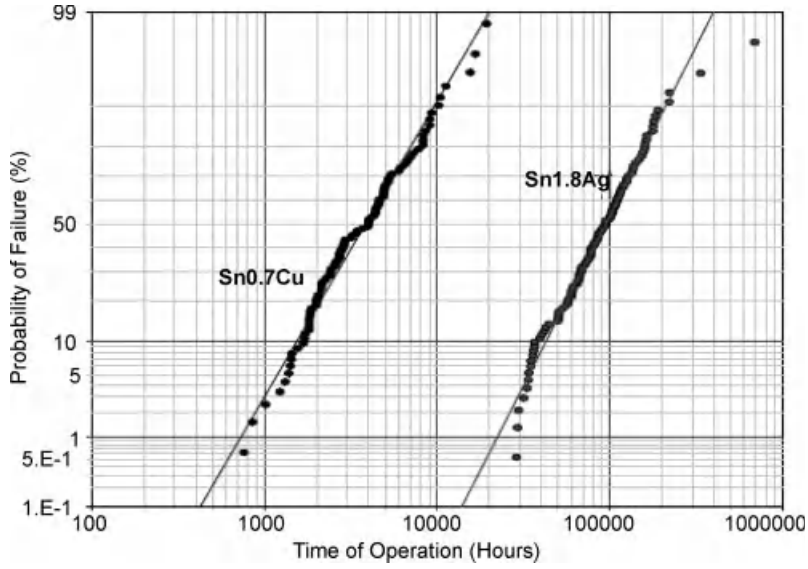

Figure 5.15 *Cumulative failure probability plot comparing Sn-0.7Cu vs. Sn-1.8Ag. Both solder joints were tested at 90°C at 200 mA [34]. (Reproduced from Proc. of the 59th ECTC, The Effects of Cu, Ag Compositions And Zn Doping on the Electromigration Performance of Pb-Free Solders, 922 Copyright (2009) IEEE).*

complications, a model wire test structure, providing uniform current density and minimal gradients, was adopted to compare pure electromigration effects of solder composition, UBM, and surface finish [34, 98, 99]. From this study, it was found that Sn-Ag joints have a superior EM performance over Sn-Cu under the same conditions of other variables, as shown in Figure 5.15 [34, 99]. In addition, two failure mechanisms are identified [98]; Mode-I, probably dominated by Sn self-diffusion resulting in separation between IMC and solder. Mode-II is responsible for premature failures in EM tests, which is dominated by a fast diffusion process of Ni and/or Cu in Sn, when the *c*-axis of Sn grain orientation is parallel to the direction of electron flow. EM failure mechanism in Sn-Ag joints with higher Ag content is dominated by Mode-I failure, while more Mode-II was observed in Sn-Cu joints. In the subsequent study, the alloying effects of Ag, Cu and Zn on the EM performance of Sn-rich solders have been systematically investigated using the Cu wire structure [34, 100]. For Sn-Ag joints, the frequency of early EM failures (associated with Mode-II) significantly decreases as Ag content increases, while Mode-II failures are more commonly observed in Sn-Cu joints for all Cu concentrations tested. The EM lifetime of Sn-Cu joints is generally shorter than Sn-Ag or Sn-Ag-Cu joints. The better EM performance of Sn-Ag over Sn-Cu is explained by the stable network of Ag_3Sn particles during EM or high-temperature aging experiments [101].

The beneficial effect of Zn doping on EM performance is also reported for Sn-Ag joints, as shown in Figure 5.16 [34, 100]. It is observed that Zn combines closely with Cu and Ag that stabilizes the IMC network and effectively slows down Cu diffusion. Hence, EM reliability is significantly improved in Zn-doped Sn-Ag joints. The effects of other alloying

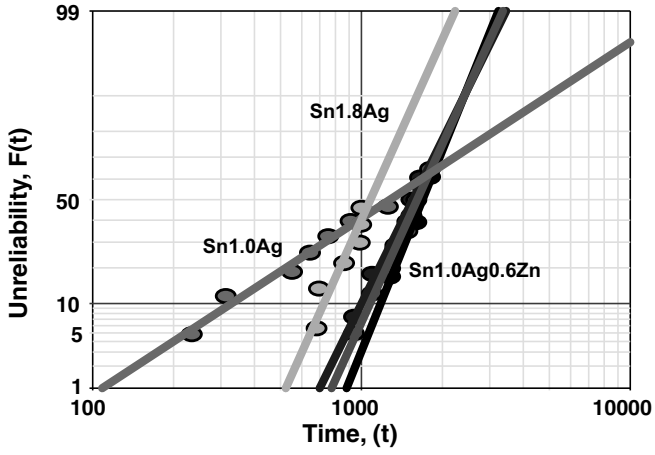

Figure 5.16 *The lognormal probability plot of the unreliability function for three solder joints; Sn-1.0Ag, Sn-1.8Ag, and Sn-1.0Ag-0.6Zn [34]. (M. Lu, et al). (Reproduced from Proc. of the 59th ECTC, The Effects of Cu, Ag Compositions And Zn Doping on the Electromigration Performance of Pb-Free Solders, 922 Copyright (2009) IEEE).*

elements such as Ni, Sb or Bi were also investigated, but no appreciable improvement on EM performance was found.

In a recent study, the EM performance of Pb-free solder joints is investigated in terms of solder composition (Sn-0.5Cu vs Sn-1.8Ag) and joining path to Cu or Ni(P) UBM [102]. It is again confirmed that Sn-Ag joints are superior to Sn-Cu regardless of the choice of UBM and its joining path. For Sn-1.8Ag joined first to Cu UBM, Cu atoms migrate fast through 60° twin boundary under current stressing. However, since Ag atoms hardly migrate to the anode side under current stressing, Sn-1.8Ag joints have a longer EM lifetime than Sn-0.5Cu joints. When Sn-1.8Ag is joined first to Ni(P), because of their stable microstructure and initially thicker IMC layers, Cu migration through low-angle boundaries and the Sn lattice is much slow and its EM lifetime is enhanced accordingly [102].

5.8 Summary

Near-ternary eutectic SAC solders are widely used in Pb-free microelectronic applications, such as surface mount or plated-through-hole joints in printed circuit boards, BGA (ball grid array) or CSP (chip-scale package), and others. Many variations of near-ternary SAC compositions are available depending on their applications, as listed in Table 5.1.

However, near-ternary SAC compositions are not well implemented for Pb-free solder joints requiring a high ductility, low modulus, or enhanced impact resistance. The applications for mobile electronics and flip-chip interconnect of high-performance systems are the few examples of this kind. Here, low-Ag or low-solute SAC solders have been recommended at the expense of stable microstructure and other physical/mechanical properties.

Recently, the anisotropic properties of Sn grain orientations were found to critically affect key reliability performance of Pb-free solder joints, such as electromigration, thermal fatigue, or chip-to-package interaction (CPI). Since the microstructure of small solder joints such as flip-chip or BGA consists of a few grains or even a single crystal, the orientation of Sn crystal(s) is crucial in determining the integrity or reliability of solder joints. The fast diffusion of common solute atoms (such as Ag, Cu, Ni) along the *c*-axis of Sn crystal often causes premature failures of Pb-free flip-chip joints during their electromigration stressing. Moreover, since the elastic constant and CTE (coefficient of thermal expansion) are a few times larger along the *c*-axis of Sn crystal than the *a*- or *b*-axis, this situation provides more challenging technical issues to compromise several important reliability risk factors of Pb-free solder joints.

The addition of minor alloying elements (such as Zn, Co, Fe, Mn, Al, Ti, Ni, and others) to Sn-rich solders is actively being investigated to improve the integrity or reliability of Pb-free solders joints. Among them, Zn addition is the most promising and extensively investigated. Some beneficial effects of Zn addition to Sn-rich solders include

1. suppression of large Ag_3Sn plate growth;
2. reduction of the undercooling during Sn solidification;
3. suppression of IMC growth, especially Cu_3Sn at the Cu/solder interface;
4. reduction of void formation at the Cu/Sn IMC interface;
5. reduction of Cu consumption during reflow and aging;
6. promotion of uniform Sn dendrite microstructure;
7. improved drop impact resistance;
8. enhanced electromigration resistance.

Further research and development activities are needed to fully understand the beneficial effects of minor alloying elements on other important technical issues such as Sn whisker formation, Sn pest transformation, and others.

References

1. Allenby, B.R. *et al.* (1992) An assessment of the use of lead in electronic assembly. *Proc. Surface Mount Int.*, (San Jose, CA), **1**, 1–28.
2. Vianco, P. and Frear, D. (1993) Issues in the replacement of Pb-bearing solders. *J. Met.*, **45**(7), 14.
3. Kang, S.K. and Sarkhel, A. (1994) Lead (Pb)-free solders for electronic packaging. *J. Electron. Mater.*, **23**(8), 701.
4. Glazer, J. (1994) Microstructure and mechanical properties of Pb-free solder alloys for low-cost electronic assembly: A review. *J. Electron. Mater.*, **23**(8), 693.
5. Anderson, I.E. (1996) Tin Silver Copper: A Lead Free Solder for Broad Applications. Proc. NEPCON West'96 Conf., vol. 2, p. 882.
6. Kang, S.K., Rai, R.S., and Purushothaman, S. (1996) Interfacial reactions during soldering with Lead-Tin eutectic and lead (Pb)-free, Tin-rich solders. *J. Electron. Mater.*, **25**(7), 1113.
7. NCMS (Aug 1997) "Lead-Free Solder Project Final Report," National Center for Manufacturing Sciences Report 0401RE96 Ann Arbor, MI.
8. Ninomiya, R., Miyake, K., and Matsunaga, J. (1997) Microstructure and Mechanical Properties of New Lead Free Solder. Proc. InterPACK'97. (Kohala Coast, HI), p. 1329.

9. Kang, S.K., Horkans, J., Andricacos, P., Carruthers, R., Cotte, J., Datta, M., Gruber, P., Harper, J., Kwietniak, K., Sambucetti, C., Shi, L., Brouillette, G., and Danovitch, D. (1999) "Pb-Free Solder Alloys for Flip Chip Applications". Proc.49th Elec. Comp. Tech. Conf., San Diego, CA, June 1999, pp. 283–88.
10. Moon, K.W., Boettinger, W.J., Kitten, U.R. *et al.* (2000) Experimental and thermodynamic assessment of Sn-Ag-Cu solder alloys. *J. Electron. Mater.*, **29**, 1122.
11. Kang, S.K. (2001) Recent progress in Pb-free solders and soldering technologies. *J. Miner., Metal. Mater. (JOM)*, **53**(6), 16.
12. Anderson, I.E., Foley, J.C., Cook, B.A. *et al.* (2001) Alloying effects in near-eutectic Sn-Ag-Cu solder alloys for improved microstructural stability. *J. Electron. Mater.*, **30**, 1050.
13. Henderson, D.W., Gosselin, T., Sarkhel, A. *et al.* (2002) Ag3Sn plate formation in the solidification of near ternary eutectic Sn-Ag-Cu alloys. *J. Mater. Res.*, **17**(11), 2775.
14. Kang, S.K., Shih, D.Y., Leonard, D. *et al.* (2004) Controlling Ag3Sn plate formation in near-ternary-eutectic Sn-Ag-Cu Solder by minor Zn alloying. *J. Miner., Met. Mater. (JOM)*, **56**(6), 34.
15. Henderson, D., Woods, J., Gosselin, T. *et al.* (2004). The microstructure of Sn in near eutectic Sn-Ag-Cu alloy solder joints and its role in thermomechanical fatigue. *J. Mater. Res.*, **19**, 1608.
16. Kang, S.K., Lauro, P., Shih, D.Y. *et al.* (2004) The microstructure, thermal fatigue, and failure analysis of near-ternary eutectic Sn-Ag-Cu solder joints. *Mater. T. JIM*, **45**(3), 695.
17. Kang, S.K., Lauro, P., Shih, D.Y. *et al.* (2005) The microstructure, solidification, mechanical properties, and thermal fatigue behavior of lead(Pb)-free solders and solder joints used in microelectronic applications. *IBM J. Res. Dev.*, **49**(4/5), 606.
18. Anderson, I.E. (2007) Development of Sn–Ag–Cu and Sn–Ag–Cu–X alloys for Pb-free electronic solder applications. *J. Electron. Mater.*, **34**, 55.
19. Zeng, K. and Tu, K.N. (2002) Six cases of reliability study of Pb-free solder joints in electronic packaging technology. *Mater. Sci. Eng., R*, **38**, 55–105.
20. Lin, J.K., Jang, J.W., and White, J. (2003) Characterization of Solder Joint Electromigration for Flip Chip Technology. Proc. 53rd ECTC, p. 816.
21. Lin, J.K., Jang, J.W., and Frear, D. (2004) Lead-Free Flip Chip Interconnect Reliability for DCA and FC-PBGA packages. Proc. 54th ECTC, p. 642.
22. Date, M., Shoji, T., Fujiyoshi, M. *et al.* (2004) Impact Reliability of Solder Joints. Proc. 2004 ECTC, p. 668.
23. Chiu, T.C., Zeng, K., Stierman, R. *et al.* (2004) Effect of Thermal Aging on Board Level Drop Reliability for Pb-Free BGA Packages. Proc. 54th ECTC, p. 1256.
24. Mei, Z., Ahmad, M., Hu, M., and Ramakrishna, G. (2005) Kirkendall Voids at Cu/Solder Interface and their Effects on Solder Joint Reliability. Proc. 55th ECTC, p. 415.
25. Kang, S.K., Leonard, D., Shih, D.Y. *et al.* (2006) Interfacial reactions of Sn-Ag-Cu solders modified by Minor Zn alloying addition. *J. Electron. Mater.*, **35**(3), 479.
26. de Sousa, I., Henderson, D.W., Patry, L. *et al.* (2006) The Influence of Low Level Doping on the Thermal Evolution of SAC Alloy Solder Joints with Cu Pad Structures. Proc. 56th ECTC, p. 1454.
27. Lin, K.L. and Kuo, S.M. (2006) The Electromigration and Thermomigration Behaviors of Pb-Free Flip Chip Sn-3Ag-0.5Cu Solder Bumps. Proc. 56th ECTC, p. 667.
28. Bieler, T.R., Jiang, H., Lehman, L.P. *et al.* (2006) Influence of Sn Grain Size and Orientation on the Thermomechanical Response and Reliability of Pb-Free Solder Joints. 46th ECTC Proc., p. 1462.
29. Kang, S.K., Cho, M.G., Lauro, P., and Shih, D.-Y. (2007) Critical Factors Affecting the Undercooling of Pb-Free, Flip-Chip Solder Bumps and *In-Situ* Observation of Solidification Process. Proc. 2007 ECTC, Reno, NV, p. 1597–1603.
30. Dyson, B.F., Anthony, T.R., and Turnbull, D. (1967) Interstitial diffusion of copper in tin, *J. Appl. Phys.*, **37**, 3408.

31. Yeh, D.C. and Huntington, H.B. (1984) Extreme Fast-Diffusion System: Nickel in Single-Crystal Tin *Phys. Rev. Lett.*, **53**(15), 1469.
32. Huang, F.H. and Huntington, H.B. (1974) Diffusion of Sb^{124}, Cd^{109}, Sn^{113}, and Zn^{65} in tin. *Phys. Rev. B*, **9**(4), 1479.
33. Gruber, P. *et al.* (2005) Low cost wafer bumping. *IBM J. Res. Dev.*, **49**(4/5), 621.
34. Lu, M., Lauro, P., Shih, D.-Y. *et al.* (2009) The Effects of Cu, Ag Compositions and Zn Doping on the Electromigration Performance of Pb-Free Solders. Proc. 59th ECTC, p. 922.
35. Kang, S.K., Choi, W.K., Shih, D.Y. *et al.* (2003) Formation of Ag3Sn Plates in Sn-Ag-Cu Alloys and Optimization of their Alloy Composition. Proc. 53rd ECTC, p. 64.
36. Kang, S.K., Choi, W.K., Shih, D.Y. *et al.* (2003) Ag3Sn plate formation in the solidification of near ternary eutectic Sn-Ag-Cu alloys. *J. Miner., Metal. Mater. (JOM)*, **55**, 61.
37. Mis, D. (2003) Unitives' Plated Pb-free Solder Solution. presented at. Symposium on Peaks in Packaging.
38. Kinyanjui, R., Lehman, L.P., Zavalij, L., and Cotts, E. (2006) Effect of sample size on the solidification of temperature and microstructure of SnAgCu near eutectic alloys. *J. Mater. Res.*, **20** (11),2914–2918.
39. Kang, S.K., Gruber, Peter, and Shih, Da-Yuan (2008) An overview of Pb-free, flip-chip wafer bumping technologies. *JOM*, **60**(6), 66.
40. Kang, S.K., Cho, M.G., Lauro, P., and Shih, D.-Y. (2007) Study of the undercooling of Pb-free, flip-chip solder bumps and In-situ observation of solidification process. *J. Mater. Res.*, **22**(3), 557.
41. Cho, M.G., Kang, S.K., and Lee, H.M. (2008) Undercooling and microhardness of Pb-free solders on various UBMs. *J. Mater. Res.*, **23**(4), 1147.
42. Cho, M.G., Kang, S.K., Seo, S.K. *et al.* (2009) Effects of under bump metallization and nickel alloying element on the undercooling behavior of Sn-based, Pb-free solders. *J. Mater. Res.*, **24**(2), 534.
43. Cho, M.G. (2008) "Effects of Zn Addition on Undercooling of Pb-free Solder Alloys and Their Interfacial Reactions with Cu and Ni-P UBMs," Ph.D. Thesis, Dept. of Mater Sci. Eng., KAIST, Daejeon, Korea.
44. Anderson, I.E., Walleser, J.W., Harringa, J.L. *et al.* (2009) Nucleation control and thermal aging resistance of near-eutectic Sn-Ag-Cu-X solder joints by alloy design. *J. Electron. Mater.*, **38**(12), 2770–2779.
45. Hougham, G.G., Srivastava, K.K., Kang, S.K. *et al.* (2010) Method and process for reducing undercooling in a Lead-free Tin-rich solder alloy, US Pat. #7,703,661B2 issued Apr. 27.
46. Cho, M.G., Kim, H.Y., Seo, S.K., and Lee, H.M. (2009) Enhancement of heterogeneous nucleation of b-Sn phases in Sn-rich solders by adding minor alloying elements with hexagonal closed packed structures. *Appl. Phys. Lett.*, **95**, 021905.
47. Ghosh, G. (1999) Thermodynamic modeling of the nickel-lead-tin system. *Metall. Mater. Trans. A*, **30**, 1481–1494.
48. Tsai, J.Y. and Kao, C.R. (2002) The Effect of Ni on the Interfacial Reaction BETWEEN Sn-Ag Solder and Cu Metallization. Proc 4th International Symposium on Electronic Materials and Packaging, Kaohsiung, Taiwan, p. 271.
49. Choi, W.K., Kim, J.H., Jeong, S.W., and Lee, H.M. (2002) Interfacial microstructure and joint strength of Sn-3. 5Ag-X (X=Cu, In, Ni) solder joint. *J. Mater. Res.*, **17**(1), 43.
50. Yu, D.Q., Zhao, J., and Wang, L. (2004) Improvement on the microstructure stability, mechanical and wetting properties of Sn-Ag-Cu lead-free solder with the addition of rare earth elements. *J. Alloys Compd.*, **376**(1/2), 170.
51. Kim, K.S., Huh, S.H., and Suganuma, K. (2003) Effects of fourth alloying additive on microstructure and tensile properties of Sn-Ag-Cu and joints with Cu. *Microelectron. Reliab.*, **43**, 259.

52. Anderson, I.E. and Harringa, J.L. (2006) Suppression of void coalescence in thermal aging of Tin-Silver-Copper-X solder joints. *J. Electron. Mater.*, **35**(1), 94.
53. Rizvi, M.J., Chan, Y.C., Bailey, C. *et al.* (2006) Effects of adding 1 wt% Bi into the Sn-2.8Ag-0.5Cu solder alloy on the intermetallic formation with Cu substrate during soldering and isothermal aging. *J. Alloys Compd.*, **407**(1/2), 208.
54. Jee, Y.K., Yu, J., and Ko, Y.H. (2007) Effects of Zn addition on the drop reliability of Sn-3.5Ag-xZn/Ni(P) solder joints. *J. Mater. Res.*, **22**(10), 276.
55. Kang, S.K., Shih, D.Y., Fogel, K. *et al.* (2002). Interfacial reaction studies on Lead (Pb)-free solder alloys. *IEEE Trans. Elec. Pack. Manuf.*, **25**(3), 155.
56. Kang, S.K., Cho, M.G., Shih, D.-Y. *et al.* (2008) Controlling the Interfacial Reactions in Pb-Free Interconnections by Adding Minor Alloying Elements to Sn-Rich Solders. Proc. 58th ECTC, Orlando, FL, p. 478.
57. Choi, W.K., Kang, S.K., Sohn, Y.C., and Shih, D.Y. (2003) Study of IMC Morphologies and Phase Characteristics Affected by the Reactions of Ni and Cu Metallurgies with Pb-Free Solder Joints. Proc. 53rd Elec Comp. & Tech Conf, New Orleans, LA, CA, p. 1190.
58. Chen, W.T., Ho, C.E., and Kao, C.R. (2002) Effects of Cu concentration on the interfacial reactions between Ni and Sn-Cu solders. *J. Mater. Res.*, **17**(2), 263.
59. Kang, S.K., Choi, W.K., Shih, D.Y. *et al.* (2002) Interfacial Reactions, Microstructure and Mechanical Properties of Pb-Free Solder Joints in PBGA Laminates. Proc 52nd Elec Comp. & Tech Conf, San Diego, CA, p. 147.
60. Ho, C.E., Yang, S.C., and Kao, C.R. (2007) Interfacial reaction issues for lead-free electronic solders. *J. Mater. Sci.*, **18**, 155.
61. Anderson, I.E. (2007) Development of Sn-Ag-Cu and Sn-Ag-Cu-X alloys for Pb-free electronic solder applications. *J. Mater. Sci.; Mater. Electron.*, **18**, 55–76.
62. Liu, W., Bachorik, P., and Lee, N.C. (2008) The Superior Drop Test Performance of SAC-Ti Solders and its Mechanism. Proc. 58th ECTC, p. 452.
63. Cho, M.G., Kang, S.K., Shih, D.-Y., and Lee, H.M. (2007) Effects of minor addition of Zn on interfacial reactions of Sn-Ag-Cu and Sn-Cu solders with various Cu substrates during thermal aging. *J. Electron. Mater.*, **36**(11), 1501.
64. Borgesen, P., Yin, L., Kondos, R. *et al.* (2007) Sporadic Degradation in Board Level Drop Reliability – those aren't all Kirkendall Voids!. Proc. 2007 ECTC, p. 136.
65. Kirkendall, E., Thomassen, L., and Upthegrove, C. (1939) Rates of diffusion of Copper and Zinc in Alpha Brass. *Trans. AIME*, **133**, 186–203.
66. Tu, K.N., Gusak, A.M., and Li, M. (2003) Physics and materials challenges for lead-free solders. *J. Appl. Phys.*, **93**(3), 1335.
67. Sohn, Y.C., Yu, Jin, Kang, S.K. *et al.* (2003) Study of the reaction mechanism between electroless Ni-P and Sn and its effect on the crystallization of Ni-P. *J. Mater. Res.*, **18**(1), 4.
68. Sohn, Y.C., Yu, J., Kang, S.K. *et al.* (2004) Study of Spalling Behavior of Intermetallic Compounds During the Reaction between Electroless Ni(P) Metallization and Lead-Free Solders. Proc. 54th Elec. Comp. & Tech. Conf., Las Vegas, NV, p. 75.
69. Paik, W., Jeon, Y.D., and Cho, M.G. (2004) Interfacial Reactions and Bump Reliability of Various Pb-Free Solder Bumps on Electroless Ni-P UBMs. Proc. 54th ECTC, p. 675.
70. Sohn, Y.C., Yu, Jin, Kang, S.K. *et al.* (2004) Spalling of intermetallic compounds during the reaction between lead-free solders and electroless Ni-P metallization. *J. Mater. Res.*, **19**(8), 2428.
71. Sohn, Y.C., Yu, J., Kang, S.K. *et al.* (2005) Effect of Intermetallics Spalling on the Mechanical Behavior of Electroless Ni(P)/Pb-free Solder Interconnection. Proc. 55th ECTC, p. 83.
72. Seo, S.K., Kang, S.K., Shih, D.-Y., and Lee, H.M. (2009) An investigation of microstructure and microhardness of Sn-Cu and Sn-Ag solders as a function of alloy composition and cooling rate. *J. Electron. Mater.*, **38**(2), 257–265.

73. Lehman, L.P., Athavale, S.N., Fullem, T.Z. *et al.* (2004) Growth of Sn and intermetallic compounds in Sn-Ag-Cu solder. *J. Electron. Mater.*, **33**(12), 1429.
74. Telang, A.U., Bieler, T.R., Lucas, J.P. *et al.* (2004) Grain-boundary character and grain growth in bulk tin and bulk lead-free solder alloys. *J. Electron. Mater.*, **33**(12), 1412.
75. Vianco, P.T., Rejent, J.A., and Matin, J.J. (2003) The compression stress-strain behavior of Sn-Ag-Cu solder. *JOM*, **55**(6), 50–55.
76. Ochoa, F., Williams, J.J., and Chawla, N. (2003) The effects of cooling rate on microstructure and mechanical behavior of Sn-3.5Ag solder. *JOM*, **55**(6), 56–60.
77. Buckmaster, K.L., Dziedzic, J.J., Masters, M.A., Poquette, B.D., Tormoen, G.W., Swenson, D., Henderson, D.W., Gosselin, T., Kang, S.K., Shih, D.-Y., Goldsmith, C., and Puttlitz, K.J. (2003) The Effects of Minor Zn Alloying Additions on the Solidification Behavior and Microstructure of Near-Eutectic Sn-Ag-Cu Solder Joints. presented at the TMS 2003 Fall Meeting, Chicago.
78. Sawamura, T., Komiya, H., Inazawa, t., and Nakagawa, F.(Feb. 17, 2004) Pb-free Soldering Alloy, US Patent No. 6,692,691 B2.
79. Nogita, N., Read, J., Nishimura, T. *et al.* (2005) Microstructure control in Sn-0,7mass%Cu alloys. *Mater. T.*, **46**(11), 2419.
80. Ventura, T., Gourlay, C.M., Nogita, K. *et al.* (2008) The influence of 0–0.1 wt% Ni on the microstructure and fluidity length of Sn-0.7Cu-xNi. *J. Electron. Mater.*, **37**(1), 32.
81. Wu, C.M.L., Yu, D.Q., Law, C.M.T., and Wang, L. (2004) Properties of Pb-free solder alloys with rare earth element additions. *Mater Sci. Eng. R*, **44**(1), 1–44.
82. Dudek, M.A., Sidhu, R.S., Chawla, N., and Renavikar, M. (2006) Microstructure and mechanical behavior of novel rare-earth containing Pb-free solders. *J. Electron. Mater.*, **35**(12), 2088.
83. Xia, Z., Chen, Z., Shi, Y. *et al.* (2002) Effect of rare earth element additions on the microstructure and mechanical properties of Sn-Ag-Bi solder. *J. Electron. Mater.*, **31**(6), 564.
84. Hao, H., Tian, J., Shi, Y.W. *et al.* (2007) Properties of Sn3. 8Ag0. 7Cu solder alloy with trace rare earth element Y. *J. Electron. Mater.*, **36**(7), 766.
85. Chuang, T.H. and Yen, S.F. (2006) Abnormal growth of Tin whiskers in a Sn3Ag0. 5Cu0. 5Ce solder ball grid array package. *J. Electron. Mater.*, **35**(8), 1621.
86. Seo, S.K., Kang, S.K., Cho, M.G. *et al.* (2009) The crystal orientation of b-Sn grains in Sn-Ag and Sn-Cu solders affected by their interfacial reactions with Cu and Ni(P) under bump metallurgy. *J. Electron. Mater.*, **38**(12), 2461.
87. Lauro, P., Kang, S.K., Choi, W.K., and Shih, D.Y. (2003) Effects of mechanical deformation and annealing on the microstructure and hardness of Pb-free solders. *J. Electron. Mater.*, **32**(12), 1432.
88. Albrecht, H.-J., Juritza, A., Muller, K. *et al.* (2003) Interface Reactions in Microelectronic Solder Joints and Associated Intermetallic Compounds: An Investigation of their Mechanical Properties Using Nanoindentation. Proc. 5th Elec. Pack. Tech. Conf. (Piscataway NJ: IEEE), pp. 726–731.
89. Syed, A., Kim, T.S., Cha, S.W. *et al.* (2007) Effect of Pb-free Alloy Composition on Drop/Impact Reliability of 0.4, 0.5, 0.8 mm Pitch Chip Scale Packages with NiAu pad Finish. Proc. 2007 ECTC, p. 951.
90. Amagai, M., Toyoda, Y., Ohnishi, T., and Akita, S. (2004) High Drop Test Reliability: Lead-Free Solders. Proc. 2004 ECTC, p. 1304.
91. Kim, H., Zhang, M., Kumar, C.M. *et al.* (2007) Improved Drop Reliability Performance with Lead Free Solders of Low Ag Content and their Failure Modes. Proc. 2007 ECTC, p. 962.
92. Elenius, P., Leal, J., Ney, J. *et al.* (1999) Recent Advances in Flip Chip Wafer Bumping Using Solder Paste Technology. Proc. of the 49th ECTC, pp. 260–265.
93. Frear, D.R., Jang, J.W., Lin, J.K., and Zhang, C. (2001) Pb-free solders for flip-chip interconnects. *JOM*, **53**(6), 28–33.
94. Zhang, C., Lin, J.K., and Li, Li, (2001). Thermal Fatigue Properties of Pb-Free Solders on Cu and NiP Under Bump Metallurgies. Proc. 51st ECTC, p. 463.

95. Terashima, S., Kariya, Y., Hosoi, T., and Tanaka, M. (2003) Effect of silver content on thermal fatigue life of Sn-xAg-0.5Cu flip-chip interconnects. *J. Electron. Mater.*, **32**(12), 1527.
96. Kang, S.K., Lauro, P., Shih, D.-Y. *et al.* (2004) Evaluation of Thermal Fatigue Life and Failure Mechanism of Sn-Ag-Cu Solder Joints with Reduced Ag Contents. Proc. 54th ECTC, p. 661.
97. Arfaei, B., Xing, Y., Woods, J. *et al.* (2008) The Effect of Sn Grain Number and Orientation on the Shear Fatigue Life of SnAgCu Solder Joints. Proc. 58th ECTC, p. 459.
98. Lu, M., Shih, D.-Y., Lauro, P. *et al.* (2008) Effect of Sn grain orientation on electromigration degradation mechanism in high Sn-based Pb-free solders. *Appl. Phys. Lett.*, **92**, 211909.
99. Lu, M., Shih, D.-Y., Polastre, R. *et al.* (2008) Comparison of Electromigration Performance for Pb-free Solders and Surface Finishes with Ni UBM. Proc. 58th ECTC, p. 360.
100. Lu, M., Shih, D.-Y., Kang, S.K. *et al.* (2009) Effect of Zn doping on SnAg solder microstructure and electromigration stability. *J. Appl. Phys.*, **106**, 053509.
101. Seo, S.-K., Kang, S.K., Shih, D.-Y., and Lee, H.M. (2009) The evolution of microstructure and microhardness of Sn-Ag and Sn-Cu solders during high temperature aging. *Microelectron. Reliab.*, **49**, 288.
102. Seo, S.K., Kang, S.K., Cho, M.G., and Lee, H.M. (2010) Electromigration performance of Pb-free solder joints in terms of solder composition and joining path. *JOM*, **62**(7), 22–29.

6

Development and Characterization of Nano-composite Solder

Johan Liu[1,2], *Si Chen*[1,2], *and Lilei Ye*[3]

[1] *SMIT Center & Dept of MicroTechnology and Nanoscience, University of Technology, Kemivägen 9, Se-412 96, Göteborg, Sweden*

[2] *Key Laboratory of New Displays and System Integration, SMIT Center and School of Mechatronics and Mechanical Engineering, Shanghai University, Box 282, Yanchang Road 149, Shanghai 200072, P.R. China*

[3] *SHT Smart High-Tech AB, Fysikgränd 3, Se 412 96b, Göteborg, Sweden*

Abstract

Lead-free solder and its soldering processing has been well developed and applied in the electronics industry as an interconnection material to replace Sn37Pb solder. However, in recent years with the rapid development of high-density, thin and 3D packaging technology, disadvantages of lead-free solder, such as high soldering processing temperature, which can result in unstable microstructure and thermal stress build-up, have been gradually exposed, limiting its application. Therefore, nanocomposite solder, as a possible replacement for traditional lead-free solder, has been developed and studied for the past decade.

The purpose of this chapter is to present the development status and achievements of nanocomposite solder. It will first describe two kinds of fabrication processing of nanoreinforcement and nanocomposite solder. It will then summarize the type of nanocomposite solder and categorize it based on different kinds of nanoreinforcement. Finally, the influences of nanoreinforcement on microstructure, its physical properties and mechanical properties on solder are illustrated in detail and analyzed. In addition, theory and the studies on how nanoreinforcements work on the enhancement of solder performances are also mentioned in this chapter.

Lead-free Solders: Materials Reliability for Electronics, First Edition. Edited by K. N. Subramanian.

6.1 Introduction

Solder is a traditional interconnection material that has been applied in the electronics packaging industry for several decades. Its development significantly depended on the development of electronics technology and the requirements of the market. In the past decade, solder underwent its first revolution, from Sn-Pb solder to lead-free solder, which had a tremendous impact on the entire electronics packaging industry, especially processing and evaluation systems. For instance, the soldering processing temperature had to be increased to cater to the higher melting point of lead-free solder compared to Sn37Pb solder. This change led to a series of problems in quality and reliability because of the harmful effects of heat-stress accumulation in the packaging system as well as high energy costs. In addition to a high melting point, the problems of grain coarseness and exceeded growth of intermetallic compound (IMC) layers with aging time still exist in lead-free solder. As we know, grain coarseness and excess growth of the IMC layer will dramatically decrease the mechanical performance of solder, and in turn decrease the reliability and service life of electronics products. In recent years, although new processing and evaluation systems have been set up for lead-free solder, the trend of ultrathin-miniature and multi-functionalized electronics products led to an urgent need for development of new interconnect materials in advanced packaging. Therefore, we are now approaching the second revolution in solder. The basic requirements for new-generation solder are that it must be green, energy saving and high performance.

Solders with intentionally incorporated reinforcements are termed composite solders [1]. Composite solder is a possible candidate for a new-generation solder. According to previous summary work [1], reinforced composite solder can effectively enhance mechanical strength, increase creep resistance and stabilize the microstructure of solder, as reinforcements are able to pin the grain boundary and constrain grain growth and crack propagation. Studies on composite solder have proved that composite solder is a feasible method to enhance performance of solder in packaging.

In recent years, nanotechnology has developed rapidly. Particles in the nanometer size could present extraordinary properties including large surface area per unit volume, large surface energy, low melting point, supermagnetism, quantum-size effects and self-purification [2]. Therefore, people have shown great enthusiasm about nanosized materials and made great efforts to apply these characteristics in their fields. In the field of solder, with the development of nanoparticle fabrication processing, various nanoreinforcements have been used to form nanocomposite solders. As the size of reinforcement has reached the nanometer scale, nanocomposite solder was considered to be more effective for enhancement of mechanical properties and improvement of microstructure [1].

The purpose of this chapter is to present and analyze the development of nanocomposite solder, provide an elementary guidance to those who want to join the research work of nanocomposite solder and build a communication platform for groups who are studying nanocomposite solder.

6.2 Nano-composite Solder Fabrication Process

6.2.1 Nano-particle Fabrication

There are two main approaches used in the manufacture of nanoparticles, namely top-down and bottom-up techniques. Top-down techniques are those in which the particles are

fabricated from larger pieces of material (bulk material), and bottom-up techniques are those in which the particles are built atom by atom, or molecule by molecule. Typical top-down methods are mechanical milling and spark erosion. Some processes belonging to the bottom-up technique are chemical vapor deposition (CVD), microemulsion, sol-gel, and chemical reduction. One method that seems very promising in the manufacture of solder nanoparticles is the spark erosion method, also known as consumable-electrode direct current arc (CDCA) or arc discharge. Three main advantages of this method are that the synthesis takes place at room temperature, it is highly suitable for high-volume production and it is versatile. The manufacturing setup, schematically shown in Figure 6.1 [2], shows the cathode (1) and the anode (2) that are connected to a high-current and low-voltage power source, the bulk alloy electrodes (3 and 4), the arc discharge taking place between the electrodes (5), and the dielectric coolant (6). The nanoparticles are fabricated when the two electrodes come close enough that a stable arc is formed [2]. This method has been successfully used and published [3]. Figure 6.2 shows the synthesized Sn3.0Ag0.5Cu [34] nanoparticles were in the same size range between 20 and 80 nm, and nearly spherical in shape.

Chemical reduction is a process that also offers some advantages since it takes place at relatively low temperature (~65 °C) resulting in better thermal oxidation control, and where particle size and oxidation can also be controlled. Since it is a chemical process, it is considered a somewhat more complicated and not as straightforward method compared to top-down methods. In the chemical reduction method, three main ingredients are required in order to manufacture metallic nanoparticles, namely metal precursor, reducing agent and solvent. There are different metal precursors available for the manufacture of nanoparticles. These can, for example, be acetates or chlorides of the metallic elements that constitute the nanoparticles [2].

6.2.2 Nano-composite Solder Fabrication

As we know, solder products come in various forms according to different soldering processing and application. For the electronics industry, the three most common forms of solder product are paste, bar and wire. Based on practice product, some researchers fabricate

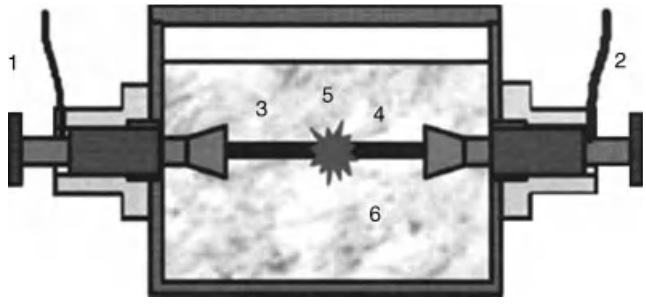

Figure 6.1 *Schematic of arc-discharge setup. (Reproduced from Proceedings of 2nd Electronics System Integration Technology Conference, Greenwich, Recent Advances in the Synthesis of Lead-free Solder Nanoparticle by C. Andersson, C.D. Zou, B. Yang, Y.L. Gao, J. Liu, Q.J. Zhai, 915–922 Copyright (2010) IEEE).*

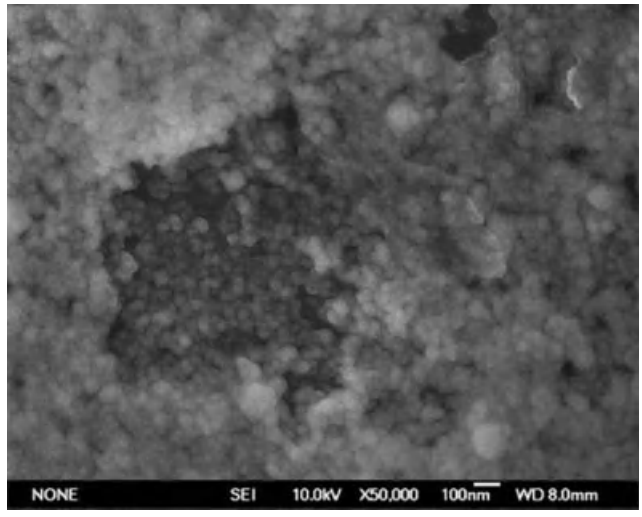

Figure 6.2 *SEM image of Sn-Ag-Cu nanoparticles. (Reproduced from Proceedings of International Symposium on High Density Packaging and Microsystem Integration, Shanghai, 2007, Preparation Techniques and Characterization for Sn-3.0Ag-0.5Cu Nanopowders by X.Z. Xia, C. D. Zou, Y.L. Gao, J. Liu, Q.J. Zhai, 10.1109/HDP.2007.4283616).*

their nanocomposite solder in the form of a paste to meet the requirements of surface mount technology (SMT) processing, while other researchers prefer to fabricate their nanocomposite solder in the form of bar and wire.

For the fabrication of nanocomposite solder paste the preweight nanoreinforcements and matrix solder powders will generally be blended to form a mixture filler system at first. Then, the proper flux will be added and stirred together with the filler system to form the nanocomposite solder paste. For simplified processing, some researchers also add a certain volume of nano-reinforcements directly into a kind of commercial solder paste. So far, the processing parameters of nanocomposite solder paste fabrication have not yet been standardized due to selection of different materials and machines. But, whatever materials or machines were used to form nanocomposite solder paste, due to the high surface energy of nano-reinforcements and agglomeration phenomenon, uniform distribution of nano-reinforcements and processing compatibility should be considered as the most two important keys for nanocomposite solder paste fabrication.

For processing the nanocomposite solder in bar form, Li *et al.* [4] presented integration and systematic processing parameters. They successfully fabricated Al_2O_3-, SnO_2- and Cu-reinforced nano-composite solder. From their description, the processing could be divided into primary processing and secondary processing. During primary processing, a blend-press-sinter powder metallurgy technique is applied. The solder alloy powder with certain volume percentage of nano-particulates was mixed in a V-blender. The blended mixture was uniaxially cold compacted to billets. The billets were then coated with colloidal graphite and sintered in a tube furnace under argon atmosphere to prevent oxidation of the alloy. During the processing, they further developed microwave-assisted

hybrid sintering technology to create a uniform temperature gradient within the billet and circumvent the disadvantages of heating using either conventional heating or microwave only [5]. In secondary processing, the sintered billets were extruded with a certain extrusion ratio. The billets were held at a constant temperature in the furnace before extrusion. From their literature [6, 7], the porosity level and morphology of pores in the microstructure are two dominating factors in their processing and will significantly affect the mechanical properties of nanocomposite solder. In this fabrication processing, Kumar *et al.* [8–10] also successfully fabricated single-wall carbon nanotube (SWCNT) reinforced nano-composite solder. Tsao *et al.* [11, 12] prepared their bulk form nanocomposite solder by mechanically dispersing nano-powders of different weight percentages into the lead-free Sn-Ag-Cu solder by subsequently remelting in vacuum furnace at 650 °C for 2.5 h and casting in a mold. The solder was melted in a crucible and chill cast in a water-cooled copper mold to form square ingots.

So far, most nano-composite solders were fabricated using the above-detailed processing. Nano-composite solder could be roughly divided into four types, according to different kinds of reinforcement, namely monolithic metal-reinforced nano-composite solder, metallic-oxide-reinforced nano-composite solder, metal alloy reinforced nano-composite solder and nonmetallic reinforced nano-composite solder. Table 6.1 summarizes partial information from the literature about nanocomposite solder.

Table 6.1 *List of studies of nanocomposite solder.*

Nanoreinforcement		Matrix	Form
Monolithic Metal	Cu	Sn37Pb [13, 14]	paste
		Sn3.5Ag [15]	bulk
		Sn [7]	bulk
	Ag	Sn37Pb [16, 17]	paste
		Sn0.7Cu [14]	paste
		Sn9Zn [18]	paste
	Al	Sn3.5Ag0.5Cu [19]	paste
Metallic Oxide	TiO_2	Sn37Pb [20, 21]	paste
		Sn3.5Ag0.5Cu [22]	paste
		Sn3.5Ag0.25Cu [12]	bulk
	Al_2O_3	Sn37Pb [21]	paste
		Sn4In4.1Ag0.5Cu [4]	bulk
		Sn0.7Cu [6]	bulk
		Sn9Zn [23]	paste
		Sn3.5Ag0.5Cu [11]	bulk
	SnO_2	Sn3.5Ag [5]	bulk
	$SrTiO_3$	Sn3.0Ag0.5Cu [24]	paste
	ZrO_2	Sn3.0Ag0.5Cu [25]	paste
Metal alloy	Sn3.0Ag0.5Cu	Sn58Bi [26]	paste
Nonmetallic	POSS	Sn3.5Ag [27, 28]	paste
	SWCNT	Sn37Pb [9]	bulk
		Sn3.8Ag0.7Cu [10]	bulk
	MWCNT	Sn3.5Ag0.7Cu [29]	bulk

6.3 Microstructure

6.3.1 Grain Size

The addition of nano-reinforcements into conventional micrometer-sized solders results in finer microstructures and grain size. Lin *et al.* [13, 20] found when adding Cu and TiO_2 nanoparticles into Sn37Pb solder, both the grain size and spacing between the eutectic lamella were reduced. Actually, this conclusion could be observed and proved in almost all nano-composite solders. Currently, there are two possible explanations that can be induced for this phenomenon. One is the theory of absorption of the surface-active materials [30]. According to this theory, with the increase of absorption amounts of surface-active materials on a plane, the surface free energy of this plane will decrease, and in turn the growth speed of this plane will decrease. This theory has been widely accepted. For example, in research work on nanoparticle reinforced Sn-Ag-Cu nano-composite solder [11, 22, 25, 28], nano-reinforcements acted as a kind of surface-active material at the Ag_3Sn grain boundaries and decreased surface free energy of Ag_3Sn, in turn decreasing the grain growth speed of Ag_3Sn. Another explanation for this phenomenon is that nanoparticles promote a high nucleation density in the eutectic colonies during solidification [12, 24, 25].

Liu *et al.* also found this phenomenon in their research work on Sn3.0Ag0.5Cu reinforced Sn58Bi. Figure 6.3 [26, 31] shows the microstructures of the Sn58Bi solder joint and the nanocomposite solder joint. The features observed are quite typical of a eutectic Sn58Bi solder and consist of fine alternating lamellae of two constituent phases. From Figures 6.3a and b, it can be seen that the addition of a small amount of Sn3.0Ag0.5Cu nanoparticles to the eutectic Sn58Bi solder marginally altered the as-solidified microstructure. Compared with the pure eutectic solder, the addition of nanoparticles tends to form a large number of nanosized grains with uniform distribution. This indicates that the dispersed nanoparticles will result in grain refining.

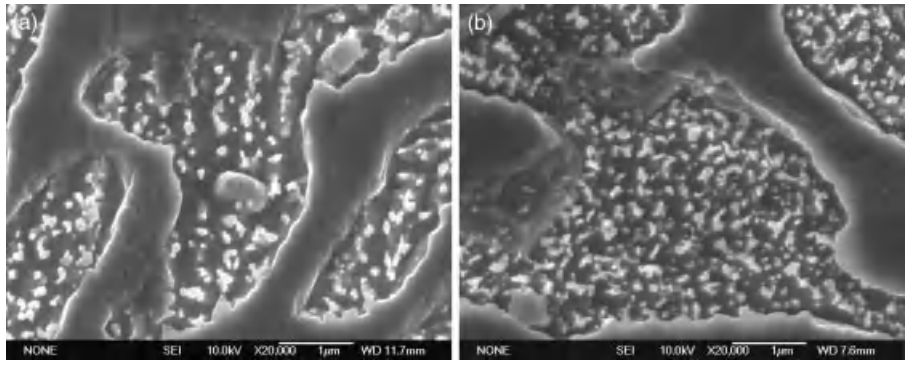

Figure 6.3 *SEM micrographs of eutectic Sn-Bi solder and composite solder joint: (a) Morphology of the eutectic Sn-Bi solder joint (b) Morphology of the composite solder joint. (Reproduced from Proc. Of Electronic Packaging Technology & High Density Packaging, 2008. ICEPT-HDP 2008, Manufacture, microstructure and microhardness analysis of Sn-Bi lead-free solder reinforced with Sn-Ag-Cu nano-particles by L.L. Zhang, W.K. Tao, J. Liu, Y. Zhang, Z.N. Cheng, C. Anderson, Y.L. Gao, Q. J. Zhai, 10.1109/ICEPT.2008.4607057, 1–5 Copyright (2008) IEEE).*

6.3.2 IMC Layer

The growth of the IMC layer could also be controlled by the addition of nano-reinforcements. From Tsao's research [22], a large amount of nano-Ag_3Sn could be formed by addition of TiO_2 nanoparticles due to the theory of absorption of surface-active materials. Then, nano-Ag_3Sn particles, which are located at the scallop-type Cu_6Sn_5 IMCs layer or embedded on the prism-type Cu_6Sn_5 IMCs layer, could reduce the surface energy of Cu_6Sn_5 grains and effectively slow the growth of the Cu_6Sn_5 IMCs layer. Chan *et al.* [24, 25] also found this phenomenon in their research work on ZrO_2 and $SrTiO_3$ nanoparticle reinforced nanocomposite solder. They pointed out that the possible reason is the second phase nanoparticles change the driving force and diffusivity of the IMC layer growth.

6.4 Physical Properties

6.4.1 Viscosity

Due to high surface energy, nano-reinforcements readily increase the viscosity of nanocomposite solder paste. As we know, viscosity is one of the most important parameters of solder paste. It will significantly affect the quality of solder joints in stencil printing processes and dispensing processes. Therefore, in the future, viscosity controls will be critical to the extensive application of nanocomposite solders in the electronics industry. Liu at el. measured the viscosity of Sn3.0Ag0.5Cu nanoparticles reinforced Sn58Bi nanocomposite solder paste with different weight percentages of nanoparticles. As shown in Figure 6.4 [32], after only 3 wt% nanoparticles addition the viscosity of the solder paste increased by 20%.

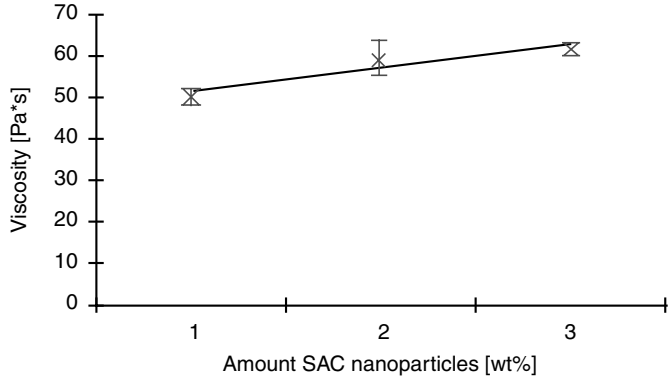

Figure 6.4 *Solder paste viscosity as a function of amount Sn-Ag-Cu nanoparticles added to Sn-Bi microsized solder. (Reproduced from Electronics Packaging Technology Conference, 2008, Singapore, Recent Development of Nano-solder Paste for Electronics Interconnect Applications by J. Liu, C. Andersson, Y.L. Gao, Q.J. Zhai, 84–93 Copyright (2008) IEEE).*

6.4.2 Melting Point

Some research studies on nanocomposite solder have proved that the addition of reinforcements will affect the melting point. Lin at el. [33] found copper nanoparticles could reduce the melting point of Sn37Pb-based nano-composite solder due to the alloying effect of copper. Meanwhile, TiO_2 nanoparticles could increase the melting point because of melt undercooling before solidification. Tsao *et al.* [12] also proved this phenomenon in their research work on TiO_2 reinforced Sn3.5Ag0.25Cu nanocomposite solder. Kumar *et al.* [8–10] pointed out that the melting point of SWCNT-reinforced composite solder is slightly lower due to the higher surface free energy and interfacial instability compared to that of unreinforced solders. However, in some other research studies, such as research on Ni-coated multiwall carbon nanotube (MWCNT) reinforced nanocomposite solder [29] and research on nano-ZrO_2 reinforced nanocomposite solder [25], there is almost no change to the melting point with the addition of nano-reinforcements. So, whether the melting point changes with the addition of nano-reinforcements will be partially decided by which kind of nanoreinforcement is chosen. But, whether or not the melting point changes at all, it would not change greatly, as the weight percentage of nanoreinforcement is very low in all nanocomposite solders. This is very beneficial for the extensive application of nanocomposite solder in the electronics industry, as the current soldering process temperature would not need adjustment following the introduction of nano-composite solder.

6.4.3 Wettability

Wettability is a critical property of solder because it affects the bonding quality between solder and substrate, and in turn, affects electrical, thermal and mechanical performance of a solder joint. The wettability of nanocomposite solder has been studied in some groups, where it has been proven that the addition of nano-reinforcements does not decrease wettability, or in some cases can even increase the wettability. Lee *et al.* [27] found that the addition of polyhedral oligomeric silsesquioxanes (POSS) in Sn-Ag would not significantly affect the wettability from measurement results of the contact angle. Therefore, implementation of POSS-silanol in eutectic Sn-Ag electronic solder joints with copper substrates will not require any major modifications to current industrial processing practices. Han *et al.* [29] observed that with the addition of 0.05 and 0.1 wt% of Ni-coated CNT in Sn3.5Ag0.7Cu, the contact angles decreased by 12.5 and 13.2%, respectively.

6.4.4 CTE

By decreasing the coefficient of thermal expansion (CTE) mismatch between nano-composite solder and other parts in packaging, thermomechancial fatigue (TMF) resistance of nano-composite solder joints can be effectively enhanced. Li *et al.* [4] found the increasing presence of nanosized Al_2O_3 particulates led to a reduction in CTE values. This could be attributed to the judicious selection of the reinforcement that has a much lower CTE value than the matrix. Another reason is the ability of the reinforcements to effectively constraint the expansion of the matrix. Kumar *et al.* [9] and Han *et al.* [29] also observed CTE decrease in their research on SWCNT and Ni-coated MWCNT-reinforced nanocomposite solder, respectively.

6.4.5 Density and Young's Modulus

Some literature also mentions density [29] and Young's modulus [8] in nano-composite solder studies. These properties will affect the quality and performance of solder joints to a greater or lesser extent according to application atmosphere and service temperature. According to the literature, this kind of property of matrix solder will change slightly when nano-reinforcements are added into the matrix to form nano-composite solder due to property mismatch between reinforcement and matrix.

6.5 Mechanical Properties

6.5.1 Microhardness

The mechanical properties of metallic materials are frequently quantified by its hardness. The value of hardness provides a measure of the resistance of the material to deformation, densification, and cracking [13]. Lin *et al.* found the microhardness of the solidified composite solder to increase by about 40% for 5 wt% addition of copper nano-powders to a eutectic solder mixture. The observed increase in hardness of the composite solder was attributed to the presence of intermetallic phases in the microstructure [13]. Liu's group also found this phenomenon in their Sn3.0Ag0.5Cu nanoparticles reinforced nanocomposite solders. The influence of Sn3.0Ag0.5Cu nanoparticles on the microhardness of Sn58Bi solder is shown in Figure 6.5 [31]. From Figure 6.5, an increase in microhardness with an increase in the weight percentage of nanoparticles is observed [32]. Other research studies have also proved the strengthening effect of nano-reinforcements on the microhardness of solder [4, 5, 8, 11, 12, 15, 20, 28]. Theoretically, this phenomenon could be basically explained and supported by the Hall–Petch mechanism [9, 32] and dispersion strengthening theory [11, 28] because the grain size and spacing between particles could be effectively

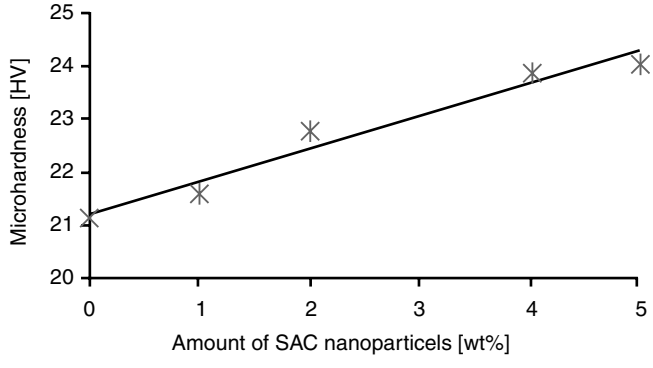

Figure 6.5 *Effect of the amount of Sn-Ag-Cu nanoparticles on microhardness of Sn-Bi solder. (Reproduced from Electronics Packaging Technology Conference, 2008, Singapore, Recent Development of Nano-solder Paste for Electronics Interconnect Applications by J. Liu, C. Andersson, Y.L. Gao, Q.J. Zhai, 84–93 Copyright (2008) IEEE).*

refined by the addition of nano-reinforcements, as mentioned in microstructure section of this chapter.

Babaghorbani *et al.* [5, 15] also found that with the addition of Cu and SnO_2 nanoparticles in Sn3.5Ag solder, respectively, the microhardness of Sn3.5Ag solder increased. They point out that harder nanopowder reinforcement in the matrix and higher constraint to the localized matrix deformation due to the presence of nanosized particulates are possible reasons for the increase in hardness.

6.5.2 Creep Resistance

The creep resistance of nano-composite solder has also been evaluated. Liu *et al.* [16] analyzed the effect of Ag nano-particles in Sn-Pb solder. They found that the nano-composite solder showed improvement on both creep resistance and creep-rupture life. Shi *et al.* [21] also investigated the creep behavior of nanocomposite solders with Cu, Ag, Al_2O_3 and TiO_2 nano-reinforcements. They found, however, that creep-rupture life first increased with an increase in volume fraction of reinforcement, but decreased when the reinforcement content exceeded a certain value. They also found, from a creep-resistance point of view, and from all assessed nanoparticles, that Ag nanoparticles were the best. The reason that creep resistance normally increases as a function of nanoparticle addition is because when nanoparticles are uniformly distributed in the solder, at the grain boundaries, they pin the movement of dislocations [16].

6.5.3 Mechanical Strength

Well-dispersed nanoparticles and fine grain size in nano-composite solder result in the enhancement of shear strength. Lee *et al.* [27] found that well-dispersed POSS nano-clusters reinforce the eutectic Sn-Ag matrix, resulting in improved shear strength. The tensile strength of solder can also be improved by addition of nano-reinforcements. Li *et al.* [4] found 0.2% yield strength and ultimate tensile strength of monolithic solder could be significantly increased by addition of Al_2O_3 nanoparticles. The possible reason for tensile strength improvement could mainly be attributed to higher dislocation density due to CTE mismatch between solder matrix and nano-reinforcement [4, 5, 9, 12, 29] and load transfer from matrix to nano-reinforcement [4, 29]. The effects of nano-reinforcement on mechanical strength improvement have also been obtained and proven by other research groups [14, 26].

6.5.4 Ductility

Unlike mechanical strength, the ductility of solder normally decreases with the addition of nano-reinforcements. Gupta *et al.* [4, 5, 15] found the decrease in ductility with an increase of nano-reinforcement content in nanocomposite solder can be attributed to the presence of the harder reinforcing phase, such as nanosized Al_2O_3, Cu and SnO_2, that serve as crack nucleation sites. Kumar *et al.* [8] also found similar results in their research on ductility of SWCNT reinforced nanocomposite solder. They pointed out that SWCNT acts as crack nucleation, which is responsible for the lower ductility of Sn37Pb and Sn3.8Ag0.7Cu-based nano-composite solder.

6.6 Challenges and Solutions

So far, most studies on nanocomposite solder have selected high melting point lead-free solder or Sn37Pb as the base material. As we know, due to its toxic nature, lead has been banned from many electronic applications with the implementation of legislation, such as the Restriction of the use of certain Hazardous Substances (RoHS), which came into force on July 1st 2006 [32]. Therefore, at present, lead-free solder is the only choice as base material of nanocomposite solder. However, the soldering processing temperature of lead-free solder is still high due to its high melting point. In addition, mismatch of nano-particles and base material is also a potential issue to nano-composite solders performance, especially TMF resistance. High soldering processing temperature and large CTE mismatch can result in thermal stress build-up, various defects and warpage during reflow processing, which will limit application and development of advanced packaging technology, such as high-density packaging, 3D packaging, chip-scale packaging and so on.

Work on improvement of TMF resistance and soldering processing temperature has been carried out by some research groups. Lee *et al.* [27] developed nanostructured POSS particulates that can promote bonding between nano-reinforcements and the metallic matrix, and then can effectively pin the grain boundary of solder joints, which lead to enhancement of TMF resistance. According to their experimental results on TMF, the residual shear strength of nano-composite solder after exposure to 1000 TMF cycles (-15 to $+150\,^{\circ}C$) was around 48 MPa, which is higher than the as-fabricated Sn4.0Ag0.5Cu solder joints.

Focusing on the disadvantages of current nano-composite solder, Liu's group also developed a kind of metallic-alloy nano-particle-reinforced nano-composite solder [26, 31]. They added nanosized Sn3.0Ag0.5Cu particles into Sn58Bi solder matrix to form nano-composite solder. The advantages of this kind of nano-composite solder are: Firstly, both nano-reinforcement and metallic matrix are Sn-based materials. This will be beneficial for minimizing mismatch and bonding formation between reinforcement and matrix. Secondly, the processing temperature of nano-composite solder could be decreased due to low melting point of based metallic material Sn58Bi. Thirdly, the dispersing strengthening effect of Sn3.0Ag0.5Cu nanoparticles on Sn58Bi solder alloy can effectively resolve the natural problems in mechanical performance of Sn58Bi.

For evaluating TMF resistance of nano-composite solder, thermal cycling (-40 to $+125\,^{\circ}C$) was carried out in a single chamber. Monolithic Sn58Bi and Sn3.0Ag0.5Cu were also tested together with nano-composite solder for comparison. The variation of average contact resistance of the solder joints during thermal cycling is presented in Figure 6.6 [26]. For all solder joints, the contact resistance exhibited was quite stable, in the range of 0, 260, 320, 380, 440 and 500 cycles. The shear test of solder joints was also performed before and after 500 cycles of thermal cycling. Figure 6.7 shows the average shear strength and standard deviation for nano-composite solder joints with two kinds of pure eutectic solders. From Figure 6.7 [26], we see that before thermal cycling, the average shear strength of all composite solders was above 30 MPa. These values were 2 times higher than the 15 MPa of Sn58Bi and close to the average shear strength of Sn3.0Ag0.5Cu. The enhancement of shear strength of composite solder could be attributed to finer crystal grains due to the addition of nano-particles and well-dispersed nanoparticles in solder matrix, as mentioned above. From Figure 6.7, we can also see that after 500 cycles of thermal cycling,

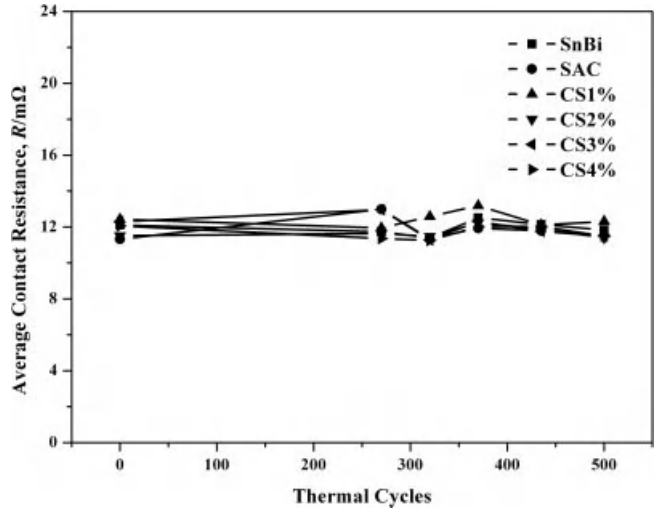

Figure 6.6 *Average contact resistance during thermal cycling. (Reproduced from Materials Transactions, A Reliability Study of Nanoparticles Reinforced Composite Lead-Free Solder by S. Chen, L.L. Zhang, J. Liu, Y.L. Gao, Q.J. Zhai, 51, 10, 1720–1726 Copyright (2010) Japan Institute of Metals).*

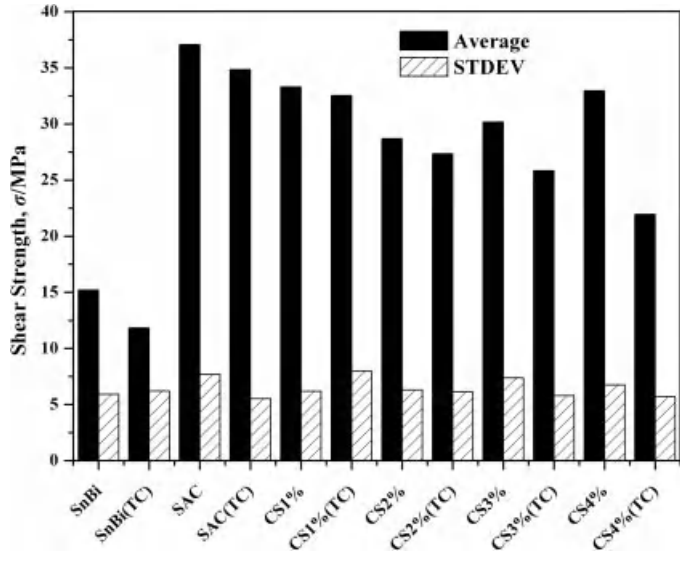

Figure 6.7 *Average and standard deviation (STDEV) of shear strength of composite solder with two conventional eutectic solders before and after thermal cycling. (Reproduced from Materials Transactions, A Reliability Study of Nanoparticles Reinforced Composite Lead-Free Solder by S. Chen, L.L. Zhang, J. Liu, Y.L. Gao, Q.J. Zhai, 51, 10, 1720–1726 Copyright (2010) Japan Institute of Metals).*

though the average shear strength of composite solder was lower than before thermal cycling, the percentage decrease in shear strength of nano-composite solder is much lower than monolithic Sn58Bi and Sn3.0Ag0.5Cu when the weight percentage of nano-particles was lower than 2 wt%. The results of the shear strength tests after thermal cycling indicated clearly that TMF resistance of the composite solder with 1 wt% nanoparticles increased 16 times in comparison to Sn58Bi and 4 times in comparison to Sn3.0Ag0.5Cu. This could be attributed to the fact that grain-boundary slide was constrained effectively during thermal cycling due to the nanoparticles in grain boundaries, as shown in Figure 6.8 [26, 31]. From Figure 6.8, we can see that some of the nano-particles were located at crystal grain boundaries or near the grain boundaries. However, adding too many nanoparticles resulted in a degradation of shear strength. These results indicate that on the one hand the addition of nano-particles would be helpful to refine the crystal grain, but on the other hand the addition of nano-particles could easily cause the initiation and propagation of microcracks at the interfaces between the nano-particles and solder matrix during thermal cycling. A cross-sectional inspection was made to detect any crack initiation and propagation in the solder matrix after thermal cycling. The fatigue cracks in Sn58Bi and composite solders with 3 mass% and 4 mass% nanoparticles are shown in Figure 6.9 [26]. In the cases of Sn3.0Ag0.5Cu and composite solders with 1 mass% and 2 mass% nanoparticles, no cracking was found after 500 cycles of thermal cycling. The results of cross sections corresponded well with the data of shear strength, indicating that the initiation and propagation of cracks in solder joints after thermal cycling resulted in decreased shear strength, though the cracks had not yet developed enough to cause obvious change in contact resistance during thermal cycling.

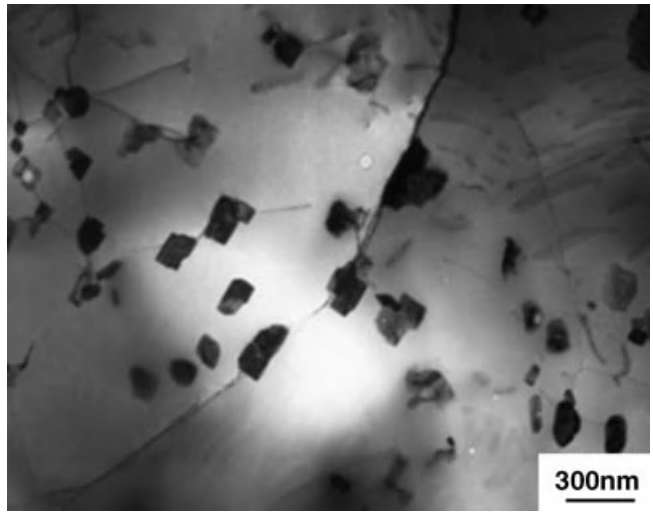

Figure 6.8 *TEM images of Sn3.0Ag0.5Cu-reinforced nanocomposite solder joint. (Reproduced from Materials Transactions, A Reliability Study of Nanoparticles Reinforced Composite Lead-Free Solder by S. Chen, L.L. Zhang, J. Liu, Y.L. Gao, Q.J. Zhai, 51, 10, 1720–1726 Copyright (2010) Japan Institute of Metals).*

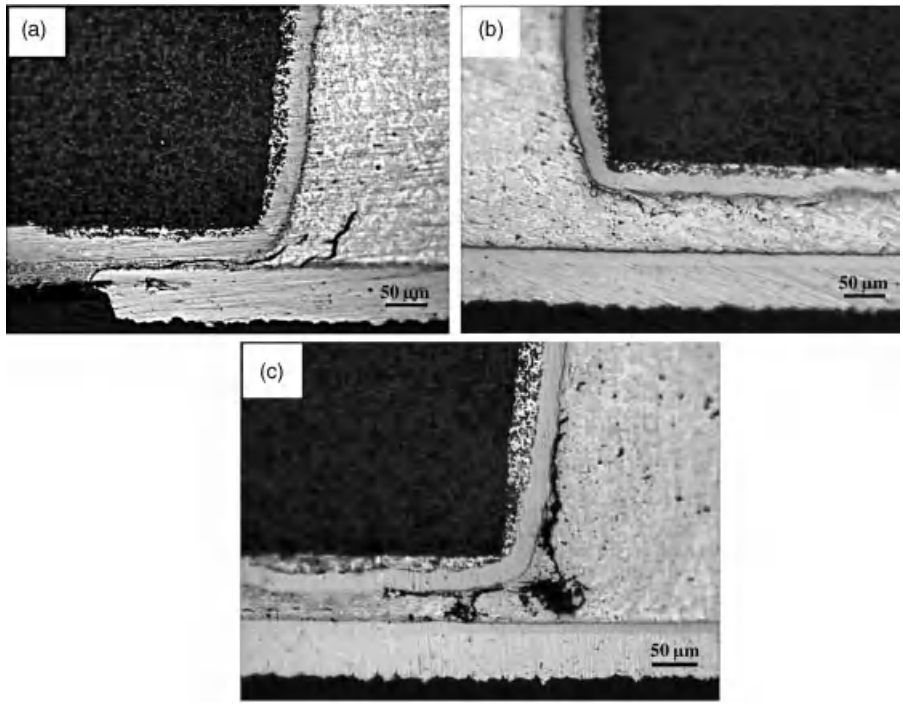

Figure 6.9 *Cross-sectional observations after thermal cycling: (a) Cracking in Sn58Bi solder joint after thermal cycling (b) Cracking in composite solder joint with 3 wt% nanoparticles (c) Cracking in composite solder joint with 4 wt% nanoparticles. (Reproduced from Materials Transactions, A Reliability Study of Nanoparticles Reinforced Composite Lead-Free Solder by S. Chen, L.L. Zhang, J. Liu, Y.L. Gao, Q.J. Zhai, 51, 10, 1720–1726 Copyright (2010) Japan Institute of Metals).*

6.7 Summary

Increasing attention has been paid to the development of nano-composite solder because it is regarded as a possible candidate for new-generation solder. With the development of nanoparticle fabrication technology, studies of nano-composite solder continue to increase. Summarizing the achievements of these studies, we can conclude that the effects of nanoparticles on solder are as follows:

The addition of nano-reinforcements into conventional micrometer-sized solders results in finer microstructures because of the theory of absorption of surface-active materials. The IMC layer growth can also be limited by nano-particles due to nanoparticles changing the driving force and diffusivity of IMC layer growth as well as the theory of absorption of surface-active materials.

The physical properties of matrix solder, such as viscosity, melting point, wettability, CTE, density and modulus, will be affected by the addition of nanoparticles because of the differences in properties between nano-reinforcement and matrix. However, these properties would not change too much due to relatively low nano-particle content in

nano-composite solder. Therefore, it is not necessary to adjust the current soldering processing and parameters for monolithic solder.

Microhardness could be obviously increased with the addition of nanoparticles, which can be attributed to finer grain size and smaller spacing between grain particles in nano-composite solder. Currently, this phenomenon can be theoretically supported by the Hall–Petch mechanism and dispersion strengthening theory.

Creep resistance can be improved because uniformly distributed nanoparticles can be located at the grain boundaries and pin the movement of dislocations.

The mechanical strength of monolithic solder can also be enhanced by addition of nano-particles due to fine grain size and good dispersion of nanoparticles in nanocomposite solder. However, according to some literature, too high a nano-particle content could decrease mechanical strength. A possible reason for this phenomenon is that it is caused by the increased number of interfaces between nano-particles and matrix with increase of nanoparticle content. The number of interfaces will significantly increase the possibility of defects, such as microcracks and microvoid, and in turn, degrade the mechanical strength of nanocomposite solder.

The ductility of nano-composite solder is normally lower than matrix solder because nanoparticles in the solder could act as crack nucleation sites and decrease ductility of the solder.

Currently, TMF resistance and melting point are two critical issues for nano-composite solder. Some new kinds of nano-reinforcement, such as POSS and Sn3.0Ag0.5Cu, have been applied to the formation of nanocomposite solder in order to enhance bonding quality and minimize mismatch between nano-reinforcement and matrix. Low melting point monolithic solder alloy, such as Sn58Bi, is also used to decrease the melting point.

Although research about nano-composite solder has obtained plenty of valuable results, a lot of problems still need to be considered for the wide application of nanocomposite solder. First, the choice of nano-reinforcement and matrix still need to be studied further in order to balance the performance of stiffness, toughness and TMF resistance. Secondly, large-scale production, storage, transportation devices and fabrication processes of nanoparticles and nanocomposite solder must be designed and developed because of the ultrahigh surface energy of nanoparticles. Finally, the cost and environment factors of nano-composite solder and nano-waste recycling also need to be planned for and considered in the future.

Acknowledgments

This work was supported by EU programs “Thema-CNT”, “Nanopack”, “Smartpower”, “Nanotec”, “Nanocom”, “Nanoteg”, “Mercure”, and the Swedish National Science Foundation (VR) under the project “on-chip cooling using thermo-electrical device with the contract no: 2009-5042. This work was also carried out within the Sustainable Production Initiative and the Production Area of Advance at Chalmers. J.L. also acknowledges the support from the Chinese Ministry of Science and Technology for the International Science and Technology Cooperation program of China (No.2010DFA14450) and from the Chinese 02 special program with the contract No: 2011ZX02602.

References

1. Guo, F. (2007) Composite lead-free electronic solders. *J. Mater. Sci: Mater. El.*, **18**(1–3), 129–145.
2. Andersson, C., Zou, C.D., Yang, B. *et al.* (2008) Recent Advances in the Synthesis of Lead-free Solder Nanoparticle. Proceedings of 2nd Electronics Systemintegration Technology Conference, Greenwich, UK, pp. 915–922.
3. Guan, W.B., Verma, S.C., Gao, Y.L. *et al.* (2006) Characterization of Nanoparticles of Lead Free Solder Alloys. Proceedings of 2006 Electronics System Integration Technology Conference, Dresden, Germany, pp. 7–12.
4. Zhong, X.L. and Gupta, M. (2005) High Strength Lead-Free Composite Solder Materials using Nano Al_2O_3 as Reinforcement. *Adv. Eng. Mater.*, **7**(11), 1049–1054.
5. Babaghorbani, P., Nai, S.M.L., and Gupta, M. (2009) Development of lead-free Sn-3.5Ag/SnO_2 nanocomposite solders. *J. Mater. Sci.:Mater. Electron.*, **20**, 571–576.
6. Nai, S.M.L., Kum, J.V.M., Alam, M.E. *et al.* (2009) Using microwave-assisted powder metallurgy route and nano-size reinforcements to develop high-strength solder composites. *J. Mater. Eng. Perform.* **19**(3), 335–341.
7. Alam, M.E. and Gupta, M. (2010) Effect of addition of nano-copper and extrusion temperature on the microstructure and mechanical response of tin. *J. Alloys Compd.*, **490**, 110–117.
8. Kumar, K.M., Kripesh, V., Shen, L., and Tay, A.A. (2006) Study on the microstructure and mechanical properties of a novel SWCNT-reinforced solder alloy for ultra-fine pitch applications. *Thin Solid Films*, **504**, 371–378.
9. Kumar, K.M., Kripesh, V., and Tay, A.A. (2008) Influence of single-wall carbon nanotube addition on the microstructural and tensile properties of Sn–Pb solder alloy. *J. Alloys Compd.*, **455**, 148–158.
10. Kumar, K.M., Kripesh, V., and Tay, A.A. (2008) Single-wall carbon nanotube (SWCNT) functionalized Sn–Ag–Cu lead-free composite solders. *J. Alloys Compd.*, **450**, 229–237.
11. Tsao, L.C., Chang, S.Y., Lee, C.I. *et al.* (2010) Effects of nano-Al_2O_3 additions on microstructure development and hardness of Sn3.5Ag0.5Cu solder. *Mater. Des.*, **31**, 4831–4835.
12. Tsao, L.C. and Chang, S.Y. (2010) Effects of Nano-TiO_2 additions on thermal analysis, microstructure and tensile properties of Sn3.5Ag0.25Cu solder. *Mater. Des.*, **31**, 990–993.
13. Lin, D., Wang, G.X., Srivatsan, T.S. *et al.* (2002) The influence of copper nanopowders on microstructure and hardness of lead–tin solder. *Mater. Lett.*, **53**, 333–338.
14. Shi, Y.W., Liu, J.P., Yan, Y.F. *et al.* (2008) Creep Properties of Composite Solders Reinforced with Nano- and Microsized Particles. *J. Electron. Mater.*, **37**(4), 507–514.
15. Babaghorbani, P., Nai, S.M.L., and Gupta, M. (2009) Integrating copper at the nanometer length scale with Sn–3.5Ag solder to develop high performance nanocomposites. *Mater. Sci. Technol.*, **25** (10), 1258–1264.
16. Liu, J.P., Guo, F., Yan, Y.F. *et al.* (2004) Development of Creep-Resistant, Nanosized Ag Particle-Reinforced Sn-Pb Composite Solders. *J. Electron. Mater.*, **33**(9), 958–963.
17. Shi, Y.W., Liu, J.P., Xia, Z.D. *et al.* (2010) Study on creep characterization of nano-sized Ag particle-reinforced Sn–Pb composite solder joints. *J. Mater. Sci.: Mater. Electron.*, **21**, 256–261.
18. Gain, A.K., Chan, Y.C., Sharif, A. *et al.* (2009) Interfacial microstructure and shear strength of Ag nano particle doped Sn–9Zn solder in ball grid array packages. *Microelectron. Reliab.*, **49**, 746–753.
19. Gain, A.K., Fouzder, T., Chan, Y.C. *et al.* (2010) The influence of addition of Al nano-particles on the microstructure and shear strength of eutectic Sn–Ag–Cu solder on Au/Ni metallized Cu pads. *J. Alloys Compd.*, **506**, 216–223.
20. Lin, D.C., Wang, G.X., Srivatsan, T.S. *et al.* (2003) Influence of titanium dioxide nanopowder addition on microstructural development and hardness of tin–lead solder. *Mater. Lett.*, **57**, 3193–3198.

21. Shi, Y.W., Liu, J.P., Xia, Z.D. *et al.* (2008) Creep property of composite solders reinforced by nano-sized particles. *J. Mater. Sci.: Mater. Electron.*, **19**, 349–356.
22. Tsao, L.C. (2010) Evolution of nano-Ag_3Sn particle formation on Cu–Sn intermetallic compounds of Sn3.5Ag0.5Cu composite solder Cu during soldering. *J. Alloys Compd.*, **509**(5), 2326–2333.
23. Fouzder, T., Gain, A.K., Chan, Y.C. *et al.* (2010) Effect of nano Al_2O_3 additions on the microstructure, hardness and shear strength of eutectic Sn–9Zn solder on Au/Ni metallized Cu pads. *Microelectron. Reliab.*, **50**, 2051–2058.
24. Fouzder, T., Shafiq, I., Chan, Y.C. *et al.* (2010) Influence of $SrTiO_3$ nano-particles on the microstructure and shear strength of Sn–Ag–Cu solder on Au Ni metallized Cu pads. *J. Alloys Compd.*, **509**(5), 1885–1892.
25. Gain, A.K., Fouzder, T., Chan, Y.C., and Yung, Winco K.C. (2010) Microstructure; kinetic analysis and hardness of Sn-Ag-Cu-1wt% nano-ZrO_2 composite solder on OSP-Cu pads. *J. Alloys Compd.*, **509**(7), 3319–3325.
26. Chen, S., Zhang, L.L., Liu, J. *et al.* (2010) A Reliability Study of Nanoparticles Reinforced Composite Lead-Free Solder. *Mater. T. JIM*, **51**(10), 1720–1726.
27. Lee, A. and Subramanian, K.N. (2005) Development of Nano-Composite Lead-Free Electronic Solders. *J. Electron. Mater.*, **34**(11), 1399–1407.
28. Tai, F., Guo, F., Xia, Z.D. *et al.* (2010) Effects of nano-structured particles on microstructure and microhardness of Sn–Ag solder alloy. *J. Mater. Sci.: Mater. El.*, **21**, 702–707.
29. Han, Y.D., Nai, S.M.L., Jing, H.Y. *et al.* (2010) Development of a Sn–Ag–Cu solder reinforced with Ni-coated carbon nanotubes. *J. Mater. Sci.: Mater. El.*, **22**(3), 315–322.
30. Xia, Z.D., Chen, Z.G., Shi, Y.W. *et al.* (2002) Effect of rare earth element additions on the microstructure and mechanical properties of Tin-Silver-Bismuth solder. *J. Electron. Mater.*, **31**, 564–567.
31. Zhang, L.L., Tao, W.K., Liu, J. *et al.* (2008) Manufacture, Microstructure and Microhardness Analysis of Sn-Bi Lead-Free Solder Reinforced with Sn-Ag-Cu Nano-particles. Proc. IEEE CPMT Int. Conf. on Electronics Packaging Technology and High Density Packaging, p. 167.
32. Liu, J., Andersson, C., Gao, Y.L., and Zhai, Q.J. (2008) Recent Development of Nano-solder Paste for Electronics Interconnect Applications. Proceedings of 10th Electronics Packaging Technology Conference.
33. Lin, D.C., Liu, S., Guo, T.M. *et al.* (2003) An investigation of nanoparticles addition on solidification kinetics and microstructure development of tin/lead solder. *Mater. Sci. Eng. A Struct.*, **360**, 285–292.
34. Xia, X.Z., Zou, C.D., Gao, Y.L. *et al*. (2007) Preparation Techniques and Characterization for Sn-3.0Ag-0.5Cu Nanopowders. Proc. IEEE CPMT Int. Symp. on High Density Packaging and Microsystem Integration, p. 302–304.

Thematic Area IV

Chemical Issues Affecting Reliability

7

Chemical Changes for Lead-Free Soldering and Their Effect on Reliability

Laura J. Turbini
Research in Motion Limited, Cambridge, Ontario, Canada

7.1 Introduction

The introduction of lead-free solders has had a profound effect on the materials used in manufacturing today's electronics. This is due in part to the higher processing temperatures, as well as to the increased circuit density and functionality required for all product types, but particularly portable and handheld product. iNEMI (International Electronics Manufacturing Initiative) [1], the IPC Association Connecting Electronics Industry [2] and ITRS (Industrial Technology Roadmap for Semiconductors) [3] have concluded that materials research is critical to meeting the needs of tomorrow's electronics. This chapter will narrow the focus on a subset of materials and failure modes associated with electronic assemblies to (a) soldering fluxes and pastes, (b) cleaning materials, (c) laminates and (d) conductive anodic filament (CAF) formation.

7.2 Soldering Fluxes and Pastes

Soldering fluxes and pastes are essential ingredients for joining two metals, since their purpose is to remove oxides and other contaminants from the metal surfaces to be soldered

Lead-free Solders: Materials Reliability for Electronics, First Edition. Edited by K. N. Subramanian.

so that intermetallic formation can occur. There are several types of ingredients in a soldering flux:

- *Activators* react with and remove the metal oxides.
- The *vehicle* carries the solder powder when present and the activators, evenly coating the surfaces to be soldered. It dissolves the metal salts produced when the activator reacts with the oxides and it must also protect the clean metal surfaces until joining takes place. In the case of solder paste for SMT, this also protects the solder powder within the paste, as well as the metallization on the board or package.
- The *solvent* helps dissolve the activators and vehicle to provide uniform coverage of the metal surfaces to be joined.
- *Special additives* are required for solder pastes and cored-wire fluxes and these include rheological agents, corrosion inhibitors and other special ingredients.

The flux formulator must consider the thermal profile for soldering, the metallization present, and the reactive and decomposition temperatures of the activator and vehicle as well as the vaporization temperature of the solvent. In traditional flux chemistry for Sn/Pb solder using a soak profile the assembly is preheated to around 100–125 °C to remove the solvent and begin to activate the chemicals used to remove the metal oxide. After this plateau, the temperature is increased above the melting point of the solder (183 °C) to 240 °C for sufficient time to reflow the solder paste. The assembly is then cooled, solidifying the solder and creating a metallurgical bond between the board metallization and the components. For lead-free soldering the preheat plateau temperature is higher – 150–200 °C – and the peak temperature is 245–260 °C, depending on the complexity of the product. This requires solvent combinations that evaporate at a higher temperature, and activators that become chemically active at a higher temperature. In addition, new activators had to be developed to address the new metallurgy on board and component surfaces, and new lead-free solders alloys containing Ag, Cu and much higher levels of Sn as well as other metals in smaller amounts.

Fine-pitch components such as ball grid arrays (BGAs) and quad flat pack no leads (QFNs) present important challenges. Often, the solder powder in the paste is Type 4, which has a higher surface to volume area of oxidized metal that requires stronger fluxing action to remove. Special formulations are required to prevent voiding (Figure 7.1) that occurs when the solvent, gaseous flux residues and the vehicle are trapped in the solder when it solidifies. The optimization of the reflow profile and the use of stronger activators are other factors important in reducing voids [4].

Lee [5] suggests a number of chemical changes to solder flux formulations for SAC alloys. For higher thermal stability, he proposed introducing cyclic or aromatic structures, or strong chemical bonds such as C—F or Si—O. He suggests a higher concentration of covalent bonding using high molecular weight cyclic or aromatic structures and high crosslink density. Also recommended are hydrogen-bonding groups such as —OH, —NH, —O— and —N—. Higher fluxing action can be achieved using more organic acids or halides. One solder flux patent for lead-free soldering recommends acid phosphate esters and their derivatives [6].

Head-on-pillow (HOP) [7] defects will occur if the flux does not stay active in protecting the surface of the reflowed solder paste until the solder balls coalesce with it Figure 7.2. This prevents the solder ball on the package from merging with the solder paste on the board.

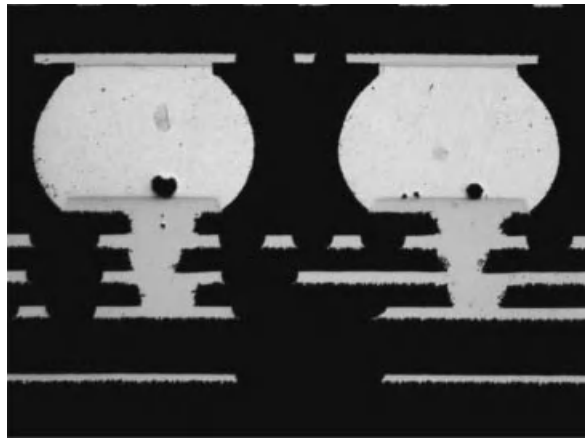

Figure 7.1 *Voids in lead-free solder joints.*

Figure 7.3 is a 3D X-ray image showing that some solder balls of the BGA merged with the solder paste, while others did not. This latter situation causes intermittent electrical failures.

An additional concern is the problem of graping, which becomes more visible when type-4 solder powder is required for fine-pitch μ-BGA attachment. Graping, as the name implies, is a grape-like cluster formation of partially coalesced solder spheres that make up the solder joint after reflow [8, 9]. The role of the flux is to protect the solder powder from

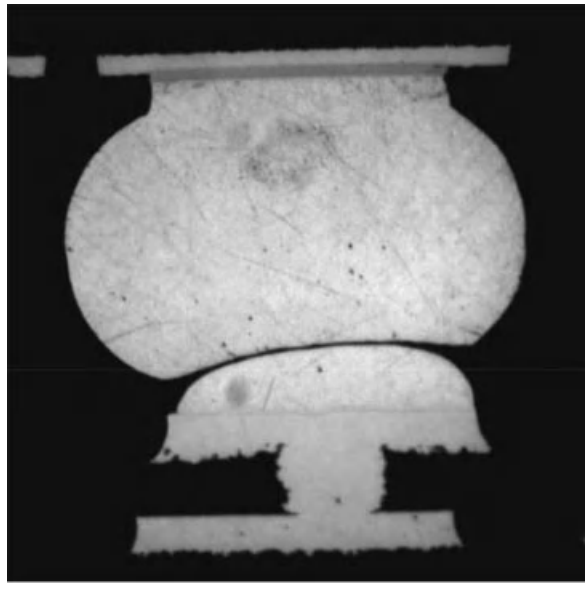

Figure 7.2 *Head-on-pillow defect.*

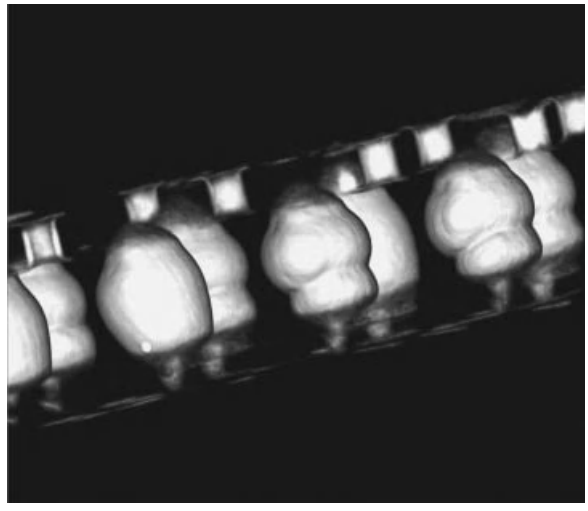

Figure 7.3 *Computed X-ray tomography image of the head on pillow defect. (Reproduced with permission from Chris Cherry, Xylon International).*

oxidation and to remove the oxidation on the component. As the flux to powder ratio decreases, there may not be enough flux or the flux may not be strong enough to protect all the solder powder, thus leading to graping. This condition is more prevalent with lead-free solder profiles, decreased solder paste for small components and with slow reflow ramp rates. Figure 7.4 shows an example of graping under a resistor or capacitor.

Changes in flux chemistry to deal with the higher soldering temperature can create flux residues that are more reactive and less benign. In some cases these residues have been implicated in tin whisker growth. Sweatman *et al.* [10] evaluated a series of halogenated liquid fluxes, solder pastes and cored-wire fluxes including one halogen-free cored-wire flux. Coupons processed by hand soldering, dip soldering or reflow soldering were aged under 3 different temperature/humidity conditions: 40 °C/95% RH, 60 °C/90% RH and 85 °C/85% RH. The halogenated fluxes created tin whiskers along the side walls of the comb lines where corrosion products were observed (Figure 7.5) [10]. At 85 °C/85% RH the first

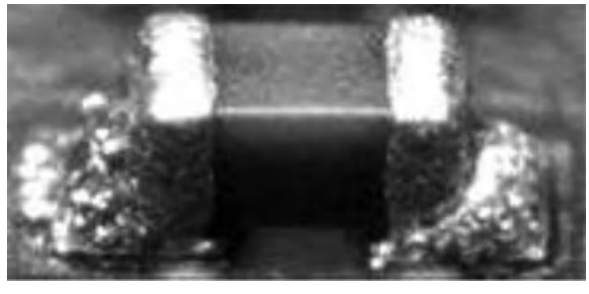

Figure 7.4 *An example of graping associated with fine powder solder paste.*

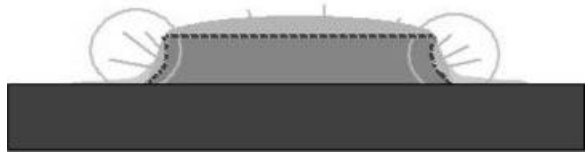

Figure 7.5 *Tin-whisker formation can be enhanced by the presence of halides in flux residues. The highest incidence of whiskers is at the edges of the trace where flux residues concentrate [10]. (Reproduced with permission from EIPC Apex Expo, Effect of Soldering Method, Temperature and Humidity on Whisker Growth in the Presence of Flux Residues by K. Sweatman et al., IPC, Las Vegas, NV Copyright (2010) Nihon Superior Co., Ltd).*

whiskers were observed at approximately 500 h, much sooner than at the lower accelerating conditions.

7.3 Cleaning

The chemicals used in fluxes for lead-free soldering use higher molecular weight constituents that experience a longer time at higher temperatures. This creates residues that are more difficult to remove because of increased polymerization. Formerly, organic acid (water soluble) fluxes were cleaned with water alone, but today's higher-temperature water-soluble flux formulations require chemical additions to the water for flux removal. Low stand-off components and high-density designs provide a cleaning challenge that has required new cleaning chemistries, and new cleaning equipment [11–13].

The lead-free flux formulations must deal with higher processing temperatures, reduced wetting speeds and the increased surface tension of SAC (SnAgCu) alloys as compared with Sn/Pb. New cleaning chemicals require high solvency and higher cleaning temperatures. The cleaning agent must be matched to the flux chemistry with nonpolar solvents needed for fluxes with high thermal stability, high oxidation resistance, low surface tension and low moisture pickup. On the other hand, polar solvent cleaners are needed for fluxes with chemicals that deal with high polarity, high oxide penetration, high fluxing capacity and halogen-free fluxes. Both alkaline, pH-neutral and polar cleaners are required.

Due to today's miniaturization, more demands are made on the cleaning equipment. The cleaning solution requires a higher temperature, longer cleaning times, higher concentrations of cleaning agent and specialized equipment to clean residues under low-profile components. The latter may include agitation, or specialized spray nozzles with both increased spray intensity as well as specialized angles. Increased cleaning time may be achieved by slower conveyor speed.

7.4 Laminates

The higher temperatures of lead-free soldering require substrates with a higher glass-transition temperature (T_g). Traditional FR-4 epoxy is made by curing the epoxy precursor

with dicyandiamide (DICY). Newer epoxy-based polymers use a phenolic novolac (PN) resin to cure the epoxy. There is a significant difference in the properties of these two polymers [14]. DICY-cured epoxy has excellent processing characteristics and good adhesion of copper but only fair T_g, CTE and thermal cycle properties. It absorbs more moisture and is more susceptible to CAF. On the other hand, PN-cured epoxy is very rigid and has poor adhesion of copper. However, it has excellent humidity resistance and reported to be less susceptible to CAF. The thermal properties of these resins are important under lead-free soldering conditions and while the polymers have similar glass-transition temperatures, thermogravimetric analysis shows that the PN-cured material has a higher thermal decomposition temperature and a much higher time to delamination at 288 °C.

7.5 Halogen-Free Laminates

There is a move today to manufacture halogen-free electronics. Laminates have led the way because of the potential for dioxin formation if the incineration of the printed wiring boards (PWBs) is not properly controlled. Traditional FR-4 epoxy uses bisphenol A as a precursor to the dicyandiamide (DICY) cured epoxy with about 10% of the bisphenol A brominated forming tetrabromobisphenol A. This brominated precursor provides flammability protection. The same flame retardant is used in PN-cured epoxies. In halogen-free (HF) laminates [15] the brominated material is removed, and replaced by metal hydroxides such as aluminum and magnesium hydroxides (Figure 7.6) [16] that release water vapor upon heating. Phosphorous-doped epoxy is also used to suppress the flame by causing the polymer to char [17]. Silica fillers are added to lower the CTE of the laminate (Figure 7.7) [16, 18].

The fillers and the modified epoxy significantly affect the thermal properties of the laminate that are important to the manufacturing process. These include the CTE in the *z*-axis, time to delamination, temperature to decomposition, and interconnect stress test performance.

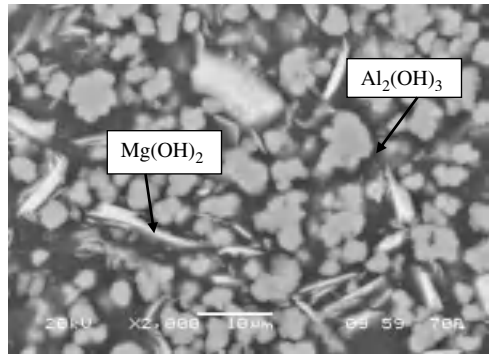

Figure 7.6 *Magnesium and aluminum hydroxide fillers [16, 19]. (Reproduced with permission from Proceedings of SMTAI 2009, San Diego, CA, October 2009, Evaluation of Halogen-Free Laminates Used in Handheld Electronics by David Y. Lau, Laura Turbini, J. Liu and Y. N. Zhou Copyright (2009) David Y. Lau).*

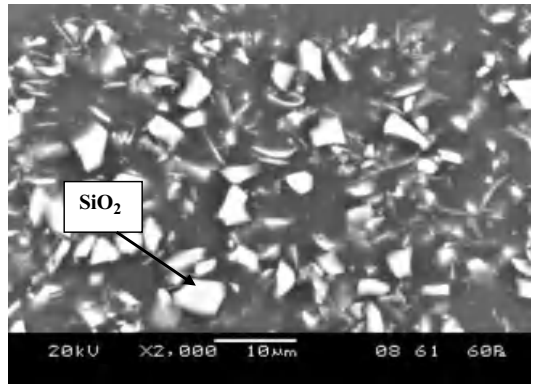

Figure 7.7 *Silica fillers added to reduce the CTE of the laminate [19]. (Reproduced with permission from Proceedings of SMTAI 2009, San Diego, CA, October 2009, Evaluation of Halogen-Free Laminates Used in Handheld Electronics by David Y. Lau, Laura Turbini, J. Liu and Y. N. Zhou Copyright (2009) David Y. Lau).*

A series of materials with T_g between 142 and 154 °C were examined [18]. The materials included one traditional FR-4 brominated epoxy, one brominated with fillers, and several phosphorous-doped epoxies with fillers. The most common hydroxide flame-retardant filler was $Al(OH)_3$ and only two materials tested had $Mg(OH)_2$. Silica was present in 5 of the 6 materials examined.

7.5.1 Z-axis CTE

PWBs with a high CTE in the *Z* direction experience greater thermal stress during lead-free soldering, which causes plastic deformation of the copper that ultimately fatigues, inducing crack formation. As the total filler percentage increases the CTE both before and after T_g decreases; silica filler percentage is a major factor in the decrease in CTE.

7.5.2 Interconnect Stress Test (IST)

IST was developed to measure plated through via and interconnect reliability under temperature cycling [20]. The resistance of a sensing circuit is monitored and when it changes by 10%, it is considered a failure. Cross-sectioning of suspected failure areas can show barrel cracks or even knee cracks (Figure 7.8) [16, 19].

7.5.3 Time to Delamination

Delamination is a failure due to separation of layers of a PWB caused by either mechanically or thermally induced stress. It is measured using IPC Test Method 2.4.24.1 at either 260 °C or 288 °C by ramping the sample up to the desired temperature using a thermomechanical analyzer (TMA) holding it there for 30 min and noting when delamination takes place (sharp increase in the thickness of the sample). Since the manufacturing process involves a number of thermal cycling steps, this property is important. Delamination can occur in one of three

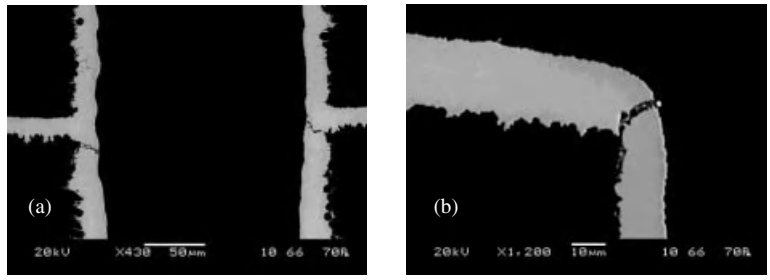

Figure 7.8 *(a) Barrel crack in plated through hole; (b) knee crack [16, 19]. (Reproduced with permission from Evaluation of Halogen-Free Laminates Used in Handheld Electronics, MAS thesis of David Y. H. Lau in Mechanical Engineering, University of Waterloo, Waterloo, Ontario, Canada Copyright (2009) David Y. H. Lau).*

ways: (a) copper/epoxy delamination, (b) glass/epoxy delamination or (c) epoxy/epoxy delamination (Figure 7.9).

HF laminates with aluminum hydroxide fillers start decomposing by releasing water above 200 °C [15]. The creation and expansion of the water vapor within the epoxy degrades the cohesive strength and promotes epoxy/epoxy delamination. Also, the CTE mismatch between the epoxy and the glass fibers lead to interfacial separation. As a result, materials with predominantly silica fillers exhibit a longer time to delamination than those with only aluminum hydroxide fillers and show predominantly copper/epoxy delamination mode. (Table 7.1) [18].

7.5.4 Temperature to Decomposition

The temperature to decomposition is related to the physical degradation of the resin system during high-temperature reflow. It can affect the long-term reliability for PWBs if delamination occurs during assembly and rework. When $Al(OH)_3$ is used as a filler, we note an interesting phenomenon. Aluminum hydroxide decomposes at 350 °C, but actually begins to decompose at 200 °C [15]. A plot of the derivative weight change of the laminate

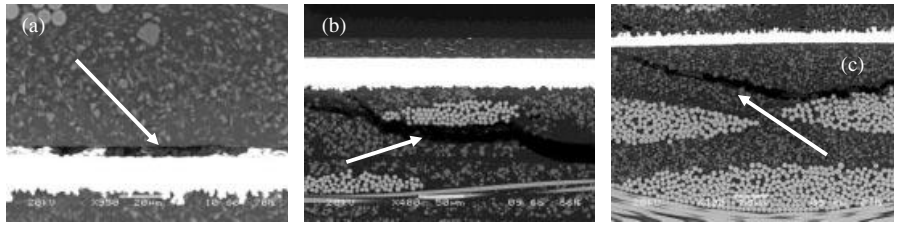

Figure 7.9 *Delamination can occur either between (a) the copper and epoxy, (b) the epoxy and glass or (c) within the epoxy [18]. (Reproduced with permission from Evaluation of Halogen-Free Laminates Used in Handheld Electronics, MAS thesis of David Y. H. Lau in Mechanical Engineering, University of Waterloo, Waterloo, Ontario, Canada Copyright (2009) David Y. H. Lau).*

Table 7.1 *Delamination modes and fillers associated with the materials tested [18]. (Reproduced with permission from Evaluation of Halogen-Free Laminates Used in Handheld Electronics, MAS thesis of David Y. H. Lau, University of Waterloo, Waterloo, Ontario, Canada Copyright (2009) David Y. H. Lau).*

Materials	Majority Fillers		Delamination Modes		
	SiO_2	Al_2O_3	Copper/Epoxy	Epoxy/Epoxy	Epoxy/Glass
A			x		
B	x		x		
C	x		x		
D		x		x	x
E		x		x	x
F	x		x		
G	x	x	x	x	x

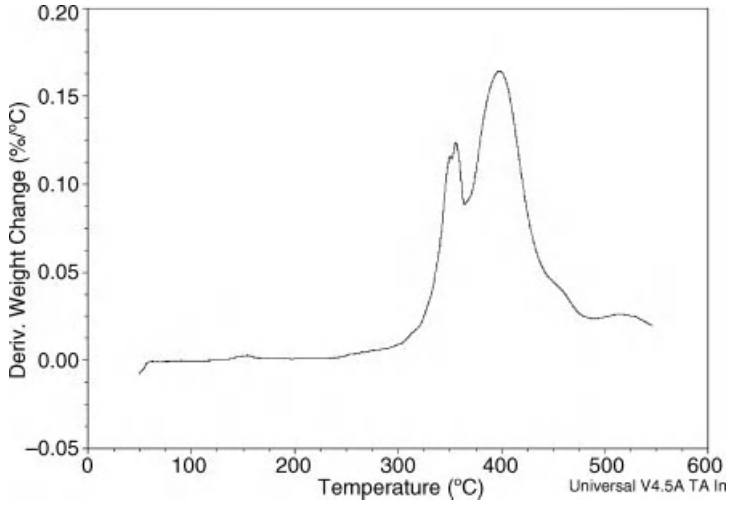

Figure 7.10 *Derivative weight change of $Al(OH)_3$-filled epoxy laminate shows the decomposition of the $Al(OH)_3$ at 350°C followed by the epoxy decomposition that peaks around 400°C [18, 19]. (Reproduced with permission from Evaluation of Halogen-Free Laminates Used in Handheld Electronics, MAS thesis of David Y. H. Lau in Mechanical Engineering, University of Waterloo, Waterloo, Ontario, Canada Copyright (2009) David Y. H. Lau).*

shows a peak for the $Al(OH)_3$ decomposition followed by a second peak representing the epoxy decomposition (Figure 7.10) [18, 19].

7.6 Conductive Anodic Filament (CAF) Formation

CAF is failure mode in PWBs in which an electrochemical reaction causes a copper salt to grow from the anode to the cathode along the polymer/glass interface (Figure 7.11) [21].

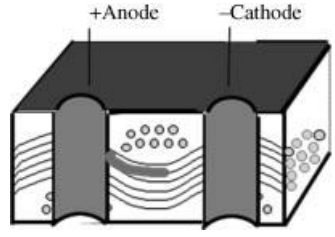

Figure 7.11 *CAF grows from the anode to the cathode, usually along the glass/polymer interface [21]. (Reproduced with permission from Materials Science and Engineering, Reliability Investigation of Printed Wiring Boards Processed with Water Soluble Flux Constituents by W. J. Ready (PhD thesis), Georgia Institute of Technology, Atlanta, Georgia Copyright (2000) W. Judson Ready).*

This failure mode was first reported on in 1976 by both Bell Labs [22] and Raytheon [23], but it was not until 1979 that it was named CAF [24] by Bell Labs.

It can cause catastrophic failure, as seen in Figure 7.12 [21] where the CAF has grown to the cathode and when it bridged the gap, the large current flow heated the epoxy to the point of decomposition and the gases that were released broke the glass fibers and caused the copper barrel of the plated through hole to expand into the vacant space.

Normally, conductive filaments are metal dendrites that grow from the cathode based on the following reaction (where M is a metal):

$$\begin{array}{ll} \text{Anode :} & \text{Cathode :} \\ \mathrm{M} \rightarrow \mathrm{M}^{+n} + ne^- & \mathrm{M}^{+n} + ne^- \rightarrow \mathrm{M} \\ \mathrm{H_2O} \rightarrow 0.5\mathrm{O_2} + 2\mathrm{H}^+ + 2\mathrm{e}^- & \mathrm{O_2} + \mathrm{H_2O} + 4\mathrm{e}^- \rightarrow 4(\mathrm{OH})^- \end{array}$$

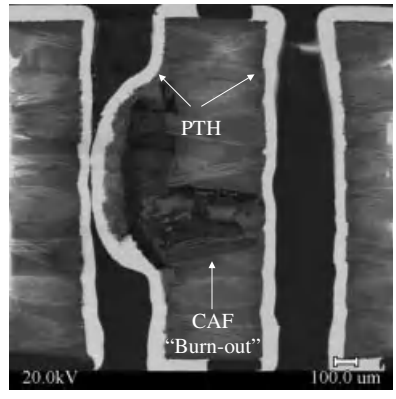

Figure 7.12 *An example of catastrophic failure caused by CAF bridging the gap between anode and cathode [21]. (Reproduced with permission from Materials Science and Engineering, Reliability Investigation of Printed Wiring Boards Processed with Water Soluble Flux Constituents by W. J. Ready (PhD thesis), Georgia Institute of Technology, Atlanta, Georgia Copyright (2000) W. Judson Ready).*

In the case of CAF, the metal is Cu from the anode that reacts with residual chloride from the reaction of epichlorhydrin with bisphenol A (the first step in creating the prepolymer in the formation of epoxy) by the following reaction:

$$Cu^{+} + Cl^{-} = CuCl$$

The CuCl then reacts with the water and oxygen to form $Cu_2(OH)_3Cl$ (CAF), which precipitates at the anode because it is insoluble in acid [25].

$$12CuCl + 3O_2 + 6H_2O = 4Cu_2(OH)3Cl + 4Cu^{2+} + 8Cl^{-}$$

The Pourbaix diagram [26], Figure 7.13 shows this compound (written as $3Cu(OH)_2{\cdot}CuCl_2$) to be insoluble below pH 4.

$Cu_2(OH)_3Cl$ has semiconductor properties that makes it more conductive under the accelerated testing conditions of 85 °C.

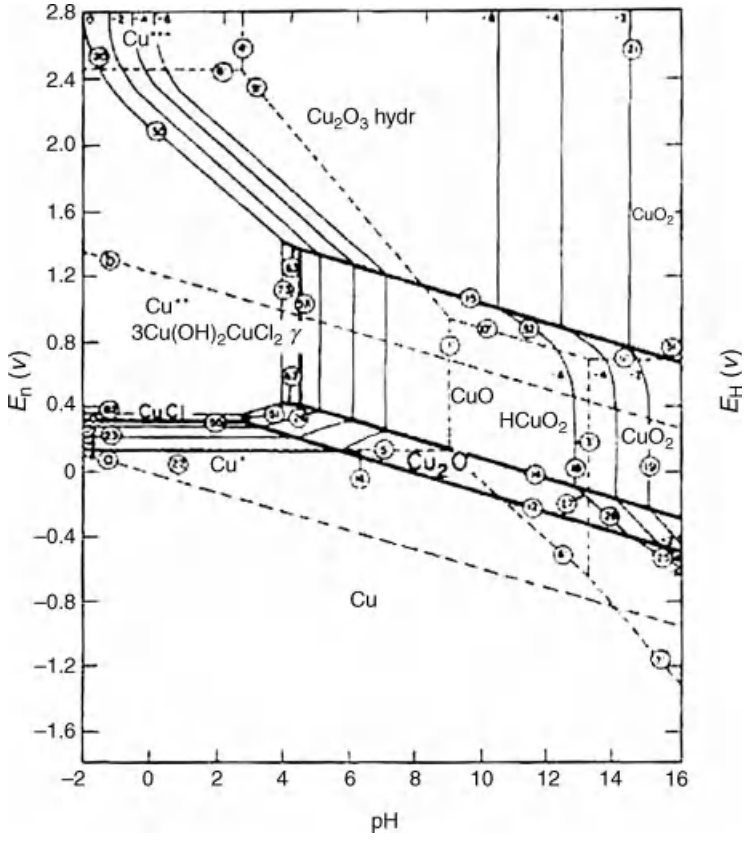

Figure 7.13 *Pourbaix diagram for Cu-Cl-H_2O system [26]. (Reproduced with permission from Lectures on Electrochemical Corrosion by M. Pourbaix, New York, Plenum Press Copyright (1973) Springer Science + Business Media).*

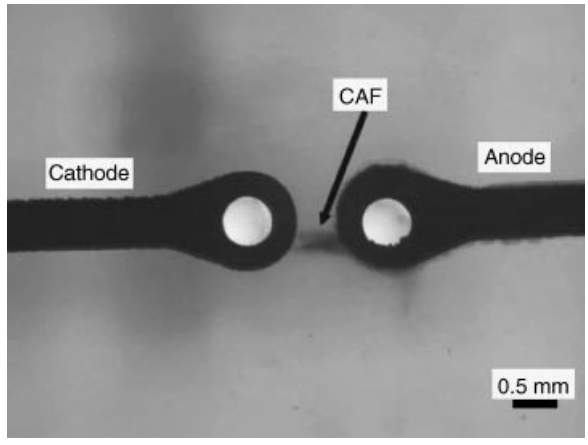

Figure 7.14 *CAF shadows seen using backlighting [28]. (Reproduced with permission from Journal of Electronic Materials, Conductive Anodic Filament (CAF) Formation Part 1: The Influence of Water-Soluble Flux on Its Formation by A. Caputo, 39, 1, 85-91 Copyright (2009) Springer Science + Business Media).*

In 2000, Turbini and Bent [27] were studying a series of water-soluble fluxes and their propensity for CAF formation. The IPC-B-24 comb patterns were processed at either 201 °C or 241 °C, representing SnPb wave soldering vs. lead-free wave soldering. Since CAF shows up as a dark shadow when a single- or double-sided board is viewed with backlighting (Figure 7.14) [28], they were able to count the number of CAF observed on the comb patterns of each processed board.

The coupons processed at the lead-free temperature created greater than 2 orders of magnitude more CAF in most cases than those processed at SnPb soldering temperatures (Table 7.2) [27].

Table 7.2 *Comparison of SIR levels and number of CAF associated with two different reflow temperatures [27].*

Flux	SIR (Ω) Reflow 201 °C	SIR (Ω) Reflow 241 °C	#CAF at Reflow 201 °C	#CAF at Reflow 241 °C
Polyethylene glycol 600 (PEG)	$<10^6$	$<10^6$	90	55
PEG/HCl	$<10^6$	High 10^8	None	None
PEG/HBR	$<10^6$	High 10^8	None	None
Polypropylene glycol 1200 (PPG)	High 10^9	$>10^{10}$	None	455
PPG/HCl	High 10^9	$>10^{10}$	None	379
PPG/HBr	10^{10}	$>10^{10}$	1	423
Polyethylene propylene glycol 1800 (PEPG)	High 10^9	High 10^9	1	406
PEPG/HCl	High 10^9	High 10^9	10	135
PEPG/HBr	High 10^9	High 10^9	9	279

This is caused by the large difference in coefficient of thermal expansion (CTE), between the glass (5.5 ppm/°C) and the epoxy (15.8 ppm/°C), which increases with increased processing temperature.

As mentioned earlier in this chapter, newer PWBs are made with PN-cured epoxies that create more moisture-resistant boards, but are also more brittle. This can cause cracking between holes during drilling, as well as weakening at the epoxy/glass interface enhancing CAF. The halogen-free laminates are also more brittle due to the presence of fillers. Often, plating salts or copper deposits in cracks between closely spaced holes are mistaken for CAF failure. One can distinguish between the two because the plating deposits will fail as soon as the test coupon stabilizes at the typical 85% RH used for the testing, whereas CAF growth takes a certain amount of time to bridge the gap between anode and cathode.

7.7 Summary

The requirement for lead-free electronics has created many challenges that relate to quality and reliability. This chapter has focused on the impact this change has had on the chemical constituents of the manufacturing process for lead-free product. New solder fluxes and pastes are needed for the higher processing temperature and cleaning of flux residues that have become more polymerized and difficult to remove, have been discussed. New laminate materials have been discussed, those that contain brominated epoxy as well as those that are halide free. Finally, the failure mode called CAF has been described and the enhancement of its formation at higher soldering temperatures has been explained.

References

1. McElroy, J. (2009) iNEMI 2009 Research Priorities. [cited; Available from http://thor.inemi.org/webdownload/RI/2009_Research_Priorities.pdf].
2. IPC International Technology Roadmap for Electronic Interconnections. (2009) [cited; Available from http://www.ipc.org/toc/Roadmap-09.pdf#xml=http://localhost/texis/searchipc/pdfhi.txt?query=Roadmap&pr=IPC-NonMember&prox=page&rorder=500&rprox=500&rdfreq=0&rwfreq=1000&rlead=750&rdepth=31&rpop=0&sufs=1&order=r&cq=&sr=-1&id=4d55eaf6b2].
3. Chen, William, Bottoms, W.R., Pressel, Klaus and Wolf, Jurgen (2009) The next step in assembly and packaging: system level integration in the package (SiP), in *International Technology Roadmap for Semiconductors*, ITRS.
4. Aspandiar, R.F. (2006) Voids in solder joints. *SMTA J.*, **19**(4), 28–36.
5. Lee, N.-C. (2010) Lead-free flux technology and influence on cleaning. *SMTA J.*, **23**(2), 31–36.
6. Kawamata, Y. et al., (issued Dec. 17, 2009) Flux for lead-free solder and soldering method, USA, Patent 2009/0308496 A1,
7. Oliphant, C. *et al.* (2010) Head-on-pillow – a pain in the neck or head-on-pillow BGA solder defect, in APEX, IPC, Las Vegas, NV.
8. Poole, N. and Toleno, B., Solder materials science gets small as miniaturization challenges old rules, Volume, SMTnet Express, March 10, 2011 (http://www.smtnet.com/express/20110310/)
9. Briggs, E. and Lasky, R. (2010) Process optimization to prevent graping, in SMTA International Conference on Soldering and Reliability, SMTA, Toronto, ON, Canada.

10. Sweatman, K. *et al.* (2010) Effect of soldering method, temperature and humidity on whisker growth in the presence of flux residues, in IPC Apex Expo, IPC, Las Vegas, NV.
11. Wack, H. *et al.* (2007) A new definition of low stand off cleaning, in SMTA International, SMTA, Orlando, Florida.
12. Brooks, R. and Bixenman, M. (2010) Issues and concerns in cleaning under low profile components, in SMTA International, SMTA, San Diego, CA.
13. Bixenman, M., Zhang, P. and Shi, C. (2009 , August) White Residue on Printed Wiring Boards Post Soldering/Cleaning. SMTA China South, Shenzhen, PR China.
14. Peng, Y.-R., Qi, X. and Chrisafides, C. (2005) The influence of curing systems on epoxide-based pcb laminate performance. *Circuit World*, **41**(4), 14–20.
15. Doering, M. and Diederichs, J. (eds) (2007) *Halogen-free flame retardants in E and E applications*, Karlsruhe, Germany Forschungszentrum Karlsruhe GmbH.
16. Lau, D.Y.H. *et al.* (2009) Evaluation of halogen-free laminates used in handheld electronics, in SMTA International, SMTA, San Diego, CA.
17. Jeng, R.-J. *et al.* (2002) Flame retardant epoxy polymers based on all phosphorous containing components. *Eur. Polym. J.*, **38**(4), 683–6993.
18. Lau, D.Y.H. (2009) Evaluation of halogen-free laminates used in handheld electronics, in Mechanical Engineering, University of Waterloo, Waterloo, 99.
19. Lau, D.Y.H. *et al.* (2010) Experimental techniques for characterizing the thermal and mechanical properties of halogen-free laminates, in International Conference on Soldering and Reliability, SMTA, Toronto, Ontario.
20. Freda, M. and Reid, P. (2009) Thermal cycling testing of PWBs - methodology, in International Conference on Soldering and Reliability, SMTA, Toronto, Ontario.
21. Ready, W.J. (2000) Reliability investigation of printed wiring boards processed with water soluble flux constituents, in *Material Science and Engineering*, Georgia Institute of Technology, Atlanta, p. 196.
22. Body, P.J. *et al.* (1976) Accelerated life testing of flexible printed circuits, in *IEEE Reliability Physics*, IEEE.
23. DeMarderosian (1976) Raw material evaluation through moisture resistance testing, in *IPC Spring Meeting*, IPC, San Francisco, CA.
24. Lando, D.J., Mitchell, J.P. and Welsher, T.L. (1979) Conductive anodic filaments in reinforced polymeric dielectrics: Formation and prevention. IEEE 17th Annual Reliability Physics Conference.
25. Caputo, A., Turbini, L.J. and Perovic, D.D. (2010) Conductive anodic filament formation part II: Electrochemical reactions leading to CAF. *J. Electron. Mater.*, **39**, 92–96.
26. Pourbaix, M. (1973) *Lectures on Electrochemical Corrosion*, Plenum Press, New York.
27. Turbini, L.J., Bent, W.R. and Ready, W.J. (2000) Impact of higher melting lead-free solders on the reliability of printed wiring assemblies, in Surface Mount International, San Jose, CA, Surface Mount Technology Association.
28. Caputo, A., Turbini, L.J. and Perovic, D.D. (2010) Conductive anodic filament (CAF) formation part I: The influence of water-soluble flux on its formation. *J. Electron. Mater.*, **39**, 85–91.

Thematic Area V

Mechanical Issues Affecting Reliability

8

Influence of Microstructure on Creep and High Strain Rate Fracture of Sn-Ag-Based Solder Joints

P. Kumar[1], *Z. Huang*[1], *I. Dutta*[1], *G. Subbarayan*[2], *and R. Mahajan*[3]
[1] *The School of Mechanical and Materials Engineering, Washington State University, Pullman, WA 99164*
[2] *School of Mechanical Engineering, Purdue University, West Lafayette, IN 47907*
[3] *Assembly Technology Development, Intel Corporation, Chandler, AZ 85226*

In an electronic package, numerous tiny solder joints provide mechanical and electrical interconnections the chip, substrate and the printed wiring board. Among the various lead-free solders, Sn-Ag-based solders have found the widest acceptance in electronics to date due to their superior mechanical properties and solderability [1, 2]. During service, these joints are subjected to extreme thermomechanical cycling conditions, wherein high homologous temperatures are superimposed with large shear strains. In addition to making the joints highly susceptible to creep and thermomechanical fatigue, these conditions cause substantial *in situ* microstructural coarsening, resulting in continuous evolution of mechanical properties during service. In addition to deformation via creep during thermomechanical fatigue, solder joints can also be subjected to dynamic impact loading when a portable electronic device is inadvertently dropped, resulting in fracture under high-strain-rate conditions. The specifics of the solder microstructure, which depends on the thermomechanical history of the joint, control both the creep and fracture responses. This chapter summarizes recent and ongoing efforts on: (1) quantitatively characterizing microstructural evolution of Sn-Ag-based solders during service, (2) incorporating these *in situ* microstructural changes into a unified creep model combining primary and secondary creep to make the model "microstructurally adaptive;" and (3) elucidating the role of microstructure on fracture

Lead-free Solders: Materials Reliability for Electronics, First Edition. Edited by K. N. Subramanian.

of solder joints at high strain rates. A microstructurally adaptive unified creep law for solders has not been proposed before, nor has the effect of microstructure on the dynamic fracture behavior of solder joints been studied until now. As such, both of these areas of recent and ongoing research represent some of the latest developments in structure–property relationships in solders under practical service conditions.

8.1 Introduction

The microstructure of Sn-Ag-based solders typically consists of two components: (i) a proeutectic composing β-Sn dendrites, and (ii) a eutectic microconstituent with dispersed Ag_3Sn and Cu_6Sn_5 precipitates in the β matrix, as illustrated in Figure 8.1a, which shows a typical microstructure of the interior of a Sn-3.8Ag-0.7Cu (SAC387) solder joint. Figure 8.1b shows the microstructure of the solder joint near the interface with a Cu bond-pad. A continuous layer of intermetallic compounds, IMCs, which comprise mostly

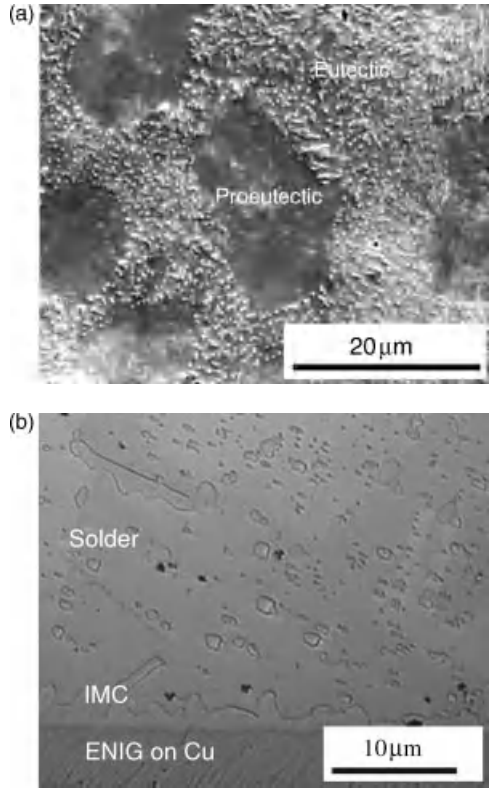

Figure 8.1 *(a) The microstructure SAC387 solder showing two components a proeutectic composing β-Sn dendrites, and a eutectic microconstituent with dispersed Ag_3Sn and Cu_6Sn_5 precipitates in the β matrix). (b) a continuous layer of intermetallic compounds (IMCs) at the interface between SAC387 and Cu.*

Cu_6Sn_5, and a very thin layer of Cu_3Sn, forms at the interface during reflow and thickens during service. The size and distribution of Ag_3Sn and Cu_6Sn_5 precipitates in the interior the solder joint, and the thickness and composition of the IMC layer at the interface between the solder and the bond-pad depend on the reflow parameters (reflow temperature, dwell time and cooling rate). Details of the effect of reflow parameters on the initial microstructure and the mechanical properties of a solder joint can be found in references [1, 2].

Diffusion-controlled phenomena, such as precipitate coarsening and creep become important in Sn-Ag-Cu (SAC) solders during service owing to its low melting temperature ($\sim$220 °C) [3]. Several studies [4–11] have addressed the problem of microstructural coarsening in Sn-Ag-based lead-free solders during aging. Both Ag_3Sn and Cu_6Sn_5 particles undergo coarsening via diffusion-controlled Ostwald ripening [5, 7, 11]. The larger precipitate particles grow at the expense of smaller particles, eventually leading to only a few large particles after a sufficiently long exposure to high homologous temperatures (T/T_m). In addition, coarsening is severely accelerated under thermomechanical cycling (TMC) conditions where a joint is subjected to large plastic strains in addition to exposure to high temperatures [8–13]. In addition to coarsening of the solder microstructure, the interfacial microstructure also evolves during aging. The interfacial IMC layer thickens during aging due to continued interdiffusion and reaction between the bond-pad metallization and the solder [e.g., 14–16], and solute elements (such as Cu) from the solder react with the pad metallization (e.g., Ni) to form complex interfacial IMCs (e.g., $(Cu,Ni)_6Sn_5$) [17–19]. The resultant depletion of certain solute elements (e.g., Cu) from the solder matrix may enhance the solubility of other solutes (e.g., Ag) in the β-Sn matrix of the solder, and thereby further enhance the coarsening rate of Ag_3Sn precipitates [17, 18].

Since continuous microstructural changes within solder joints during the service life leads to continuous evolution of joint properties, quantitative linkages between the microstructure and the property evolution need to be established for accurate reliability and performance predictions. This requires developing a quantitative description of coarsening under generalized temperature and strain combinations, and incorporating this in constitutive laws. Here, a synopsis of the kinetics of microstructural coarsening in Sn-Ag-based lead-free solders is provided, highlighting the differences between static and strain-enhanced coarsening. Some results elucidating the impact of the microstructural coarsening on the creep behavior are then summarized and a microstructurally adaptive model to capture primary-cum-secondary creep is presented. The impacts of aging on the mechanical properties of SAC solder alloys at intermediate and high strain rates are then briefly discussed. Finally, some results of recent work on the impact of microstructure and IMC layer thickness on the fracture toughness of SAC joints under dynamic (or drop) conditions is presented.

8.2 Coarsening Kinetics: Quantitative Analysis of Microstructural Evolution

8.2.1 Experimental Procedure

The effect of thermomechanical excursion on the coarsening kinetics of solder was studied using a range of Sn-Ag-based lead-free solder alloys. The details of the experiments are reported elsewhere [8, 12, 20], and are summarized below:

The effect of aging under isothermal and thermomechanical cycling (TMC) conditions were studied by subjecting 80-μm diameter flip-chip (FC) Sn-3.5Ag solder joints in a microelectronic package to isothermal aging at 150 °C up to 500 h, and TMC between −65 and 150 °C up to 1500 cycles [8, 12].

The effect of thermomechanical excursions on particle size and interparticle spacing was quantified using 650-μm diameter and 350-μm high ball joints attached between two alumina plates with electroless Ni immersion gold (ENIG) metallization [11]. These samples were subjected to one of the following thermomechanical excursions: (i) isothermally aged (IA) at 125 °C for 4 days, (ii) thermally cycled (TC) between −25 °C and 125 °C for 105 cycles, and (iii) thermomechanically cycled (TMC) between −25 °C and 125 °C for 105 cycles with an imposed shear strain (γ) of either 0.04 or 0.16 per cycle. The TMC experiments were conducted by affixing the sample to a bimetallic frame made of Al and Invar, and cycling the temperature. The difference between the thermal expansion coefficients of Al and Invar ($\alpha_{Al} = 23 \times 10^{-6}$/K and $\alpha_{Invar} = 1.2 \times 10^{-6}$/K) resulted in loading of the solder joint in shear, imposing a shear strain proportional to the temperature excursion ΔT ($=T - T_{ambient}$).

8.2.2 Results and Discussion

8.2.2.1 Microstructural Coarsening: Isothermal Aging and Thermomechanical Cycling
Figure 8.2 shows secondary electron micrographs of an Sn-3.5%Ag flip-chip (FC) joint after: (a) reflow, (b) isothermal aging for 500 h at 180 °C, and after TMC over −65 to +150 °C for (c) 1500 cycles, and (d) 750 cycles [12]. Initially, the microstructure contains a dispersion of Ag_3Sn precipitates. During static aging, the particle size and spacing coarsen. The coarsening is much more rapid during TMC (Figure 8.2c), during which most of the fine particles are replaced by a few very coarse platelets, evidencing substantial strain-enhanced coarsening. The role of strain is further elucidated in Figure 8.2d, which shows a FC joint with a large protrusion (fillet) after 750 cycles. The main joint, which is subjected to strain during TMC, shows severe coarsening similar to Figure 8.2c, whereas the fillet, which is not strained during TMC, shows a much finer Ag_3Sn distribution. Clearly, microstructural evolution during TMC is dominated by *in situ* strain-enhanced coarsening [12, 20].

Figure 8.3 shows the effect of four types of thermomechanical excursion on the SAC387 joints with ENIG bond-pad. These are representative micrographs from the central region (defined as a 100-μm wide band along the middle of the joint) of the ball joints following four types of thermomechanical excursions. Figure 8.3a shows the microstructure of a BGA ball in the as-reflowed condition, revealing proeutectic β-Sn dendrites and an interdendritic eutectic comprising a fine dispersion Ag_3Sn and Cu_6Sn_5 in β. Aging leads to progressive loss in the definition of the β dendrites, with commensurate coarsening of the eutectic. Backscattered electron (BSE) imaging and energy dispersive spectroscopy (EDS) were employed to distinguish between Cu_6Sn_5 and Ag_3Sn particles and it was observed that the number fraction of Ag_3Sn particles was substantially (∼100 times)[1] larger than that of

[1] Assuming that all Ag and Cu are in compound form, the Ag_3Sn and Cu_6Sn_5 volume fractions for SAC387 can be calculated to be ∼5.5% and 1.9%, respectively, consistent with (i) the measured Cu_6Sn_5 volume fraction of 1.6% reported for aged SAC387 [5] and (ii) the measured Ag_3Sn volume fraction of 4.7% for Sn-3.5%Ag [21]. The volume fraction of Cu_6Sn_5 will further decrease in a solder ball joint with ENIG bond-pad as Cu from solder diffuses into the bond-pad forming $(Cu, Ni)_6Sn_5$ tertiary IMCs [13].

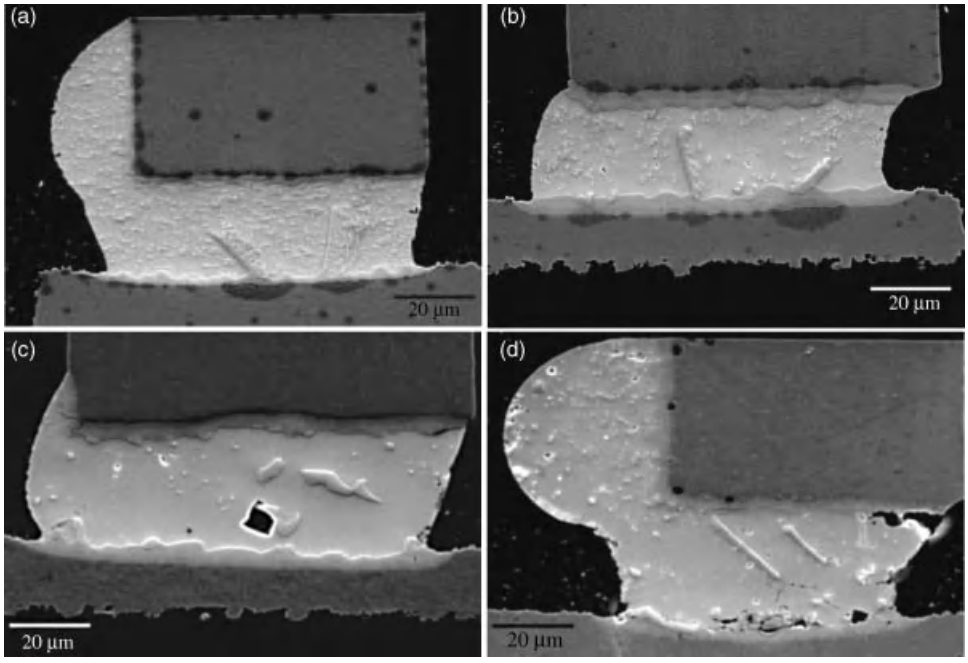

Figure 8.2 *SEM micrographs of SA FC joints: (a) in the as reflowed state, (b) after 500 h aging at 150 °C, (c) after 1500 thermal cycles, and (d) after 750 thermal cycles from −65 to 150 °C [12]. (Reproduced with permission from Materials Science and Engineering: A, Effect of thermo-mechanically induced microstructural coarsening on the evolution of creep response of SnAg-based microelectronic solders by I. Dutta, D. Pan, R. A. Marks and S. G. Jadhav, Nov 2005, 410–411 Copyright (2005) Elsevier Ltd).*

Cu_6Sn_5. Furthermore, the Cu_6Sn_5 particles coarsen much faster than Ag_3Sn owing to the faster diffusion of Cu in Sn as compared to the diffusion of Ag in Sn [20]. As a result, it is adequate to consider only the coarsening of Ag_3Sn precipitates when quantifying the coarsening of kinetics of Sn-Ag-Cu solders. Table 8.1 lists the particle sizes of the solder following different thermomechanical treatments.[2] The data show that the particle size coarsens faster with the severity of the aging condition. It is noted that the major axis of the particles following thermomechanical cycling (TMC) is ∼25% larger than those after only thermal cycling (TC), even though the temperature profile were identical for both conditions. In order to compare the effects of aging, the median value of the particle size was employed because it better represents the Ag_3Sn particle size (rather than the mean value, which may be affected by the few but rapidly growing Cu_6Sn_5 particles).

[2] These particle-size measurements did not attempt to differentiate between Ag_3Sn and Cu_6Sn_5 particles, since the vast majority of the particles are Ag_3Sn and hence the Cu_6Sn_5 particles will have little impact on the particle growth kinetics.

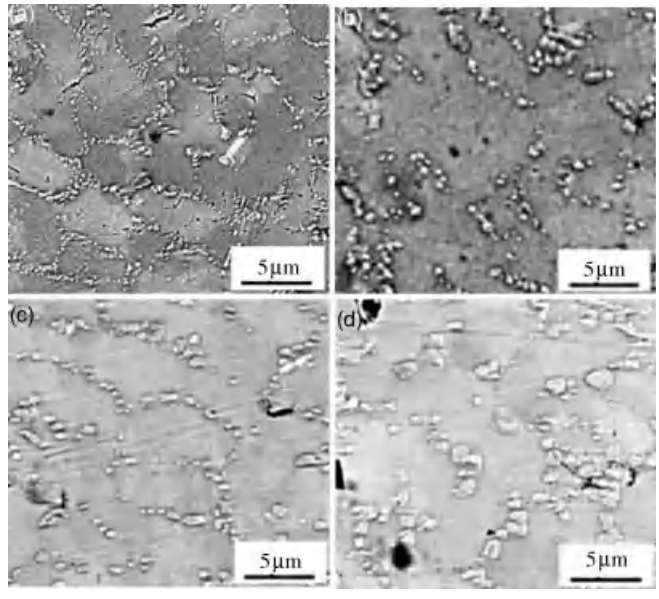

Figure 8.3 *Representative SEM micrographs from the central region of BGA samples with different thermomechanical history: (a) as-reflowed, (b) thermally cycled between −25 to 125 °C for 110 cycles, (c) thermomechanically cycled between −25 to 125 °C for 110 cycles with an equivalent shear strain of 0.04 per cycle, and (d) isothermally aged at 125 °C for 4 days.*

8.2.2.2 Quantification of Coarsening Kinetics

The coarsening kinetics of precipitates in a solder is governed by diffusion of solute atoms (e.g., Ag, Cu) through Sn, and can be written as [8, 12]:

$$d_{\mathrm{p}}^{m} - d_{0}^{m} = K.C_{\mathrm{sol}}.D_{\mathrm{sol}}t \tag{8.1}$$

Table 8.1 *The size variation of Ag_3Sn in the central region of SAC387 BGA samples after various thermomechanical excursions. The effective particle diameter is defined as $d = \sqrt{6A_{\mathrm{p}}/\pi}$ [22].*

Condition	Axis	Median (μm)	Variance (μm)	Mean (μm)	Standard Deviation (μm)	Effective Particle Diameter (μm)
AR	Major	0.21	0.009	0.23	0.09	0.2
	Minor	0.14	0.001	0.014	0.04	
TC	Major	0.50	0.04	0.53	0.20	0.48
	Minor	0.32	0.01	0.33	0.10	
TMC ($\gamma = 0.16$)	Major	0.84	0.057	0.82	0.24	0.78
	Minor	0.49	0.019	0.50	0.14	
TMC ($\gamma = 0.06$)	Major	0.62	0.06	0.66	0.24	0.56
	Minor	0.35	0.01	0.36	0.11	
IA	Major	0.69	0.07	0.74	0.26	0.65
	Minor	0.39	0.02	0.42	0.14	

where d_p is the instantaneous particle size, d_0 is the initial particle size, C_{sol} and D_{sol} are the solubility and diffusivity of solute atoms in Sn, respectively, t is time, K is a constant, and $m = 2$ or 3 for two-dimensional growth of platelet-shaped precipitates or 3-dimensional growth of spherical precipitates, respectively [12]. Here, the term $\sqrt{D_{sol}t}$ represents a length parameter signifying the diffusion distance of the solute atoms in Sn, which depends on the thermomechanical history of the solder. For thermal and thermomechanical cycling conditions, where the temperature varies, $\sqrt{D_{sol}t}$ may be replaced by an effective diffusion length $\sqrt{(\overline{D_{sol}t})}$, which depends on the temperature and strain range to which the joint is subjected, as well as the number of elapsed cycles. $\sqrt{(\overline{D_{sol}t})}$ for an entire cycles is given by:

$$\overline{D_{sol}t} = v_c \left[\overline{(D_{sol}t)}_{\text{ramp up}} + D_{sol}^{T_{max}}\, t_{\text{dwell, } T_{max}} + \overline{(D_{sol}t)}_{\text{ramp down}} + D_{sol}^{T_{min}}\, t_{\text{dwell, } T_{min}} \right] \tag{8.2}$$

where v_c is the total number of elapsed cycles, and the terms within the brackets on the right-hand side represent the square of the diffusion distances during different segments of the thermal cycle (ramp up of temperature, dwell at the maximum temperature, rampdown of temperature and dwell at the minimum temperature). $D_{sol}^{T_{max}}$ and $D_{sol}^{T_{min}}$ are the diffusivity of solute atoms in Sn at the maximum and minimum temperatures, respectively, $t_{\text{dwell, } T_{max}}$ and $t_{\text{dwell, } T_{min}}$ are the dwell times at the maximum temperature and the minimum temperatures, respectively, and $\overline{(D_{sol}t)}_{\text{ramp up}}$ and $\overline{(D_{sol}t)}_{\text{ramp down}}$ are the diffusion lengths during the rampup and rampdown thermal cycling. $\overline{(D_{sol}t)}_{\text{ramp up}}$ and $\overline{(D_{sol}t)}_{\text{ramp down}}$ are given by:

$$\begin{aligned} \overline{(D_{Ag}t)}_{\text{ramp up}} &= \int_0^{t_{\text{ramp up}}} D_{o_{sol}} \exp\left[\left(-\frac{Q_{sol}}{RT(t)} \right) \right] \mathrm{d}t \\ \overline{(D_{Ag}t)}_{\text{ramp down}} &= \int_0^{t_{\text{ramp down}}} D_{o_{sol}} \exp\left[\left(-\frac{Q_{sol}}{RT(t)} \right) \right] \mathrm{d}t \end{aligned} \tag{8.3}$$

where, $D_{o,sol}$ and Q_{sol} are the frequency factor and activation energy, respectively, for diffusion of the solute atoms in Sn, and R is the universal gas constant. During thermal cycling rampup and rampdown, the temperature is assumed to vary linearly with time at the rate of $\beta_1 = \mathrm{d}T/\mathrm{d}t$. Hence, for thermal cycling conditions, Eq. (8.3) can be rewritten as:

$$\overline{(D_{Ag}t)}_{\text{ramp}} = \int_{T_{min}}^{T_{max}} D_{o_{sol}} \exp\left(-\frac{Q_{sol}}{RT(t)} \right) \frac{\mathrm{d}T}{\beta_1} = D_{min} \frac{e^{a/4b}}{\sqrt{ab}} \frac{\sqrt{\pi}}{2} [\mathrm{erf}(\eta_o) - \mathrm{erf}(\eta_c)] \tag{8.4a}$$

where,

$$D_{\min} = D_{\mathrm{o}}^{\mathrm{sol}} \exp\left[\left(-\frac{Q_{\mathrm{sol}}}{R}\right)\frac{1}{T_{\min}}\right]$$
$$a = \left(\frac{Q_{\mathrm{sol}}}{R}\right)\frac{\beta_1}{T_{\min}^2}, b = \frac{\beta_1}{2T_{\min}}, \eta_{\mathrm{o}} = \frac{\sqrt{ab}}{2b}, \eta_{\mathrm{c}} = \sqrt{ab}\left(\frac{1}{2b} - t_{\mathrm{ramp}}\right) \tag{8.4b}$$

whereas for thermomechanical cycling conditions, where strains accumulate during the cycling:

$$\begin{aligned}\overline{(D_{\mathrm{Ag}}t)}_{\mathrm{ramp}} &= \left[\frac{1}{t_{\mathrm{ramp}}}\int_{T_{\min}}^{T_{\max}} D_{\mathrm{o_{sol}}} \exp\left(-\frac{Q_{\mathrm{sol}}}{RT(t)}\right)\frac{\mathrm{d}T}{\beta_1}\right] t_{\mathrm{ramp,eff}} \\ &= D_{\min}\frac{\mathrm{e}^{a/4b}}{\sqrt{ab}}\frac{\sqrt{\pi}}{2}\left[\mathrm{erf}(\eta_{\mathrm{o}}) - \mathrm{erf}(\eta_{\mathrm{c}})\right]\frac{t_{\mathrm{ramp,eff}}}{t_{\mathrm{ramp}}}\end{aligned} \tag{8.5}$$

where $t_{\mathrm{ramp,eff}}$ is given by [8]:

$$t_{\mathrm{ramp,\ eff}} = t_{\mathrm{ramp}}(1 + N\dot{\gamma}_{\mathrm{TMC}}\phi) \tag{8.6}$$

where N (in seconds) is a kinetic constant representing strain-enhanced aging ($\sim 10^4$ s [12]), $\dot{\gamma}_{\mathrm{TMC}}$ is the strain rate during thermomechanical cycling and ϕ is the plastic fraction of the total strain ($\phi \sim 1$). Equation (8.6) captures the essence of the effect of strain, especially at the high strain rates, in generating vacancies enhancing the coarsening rate.

Figure 8.4 shows the variation in effective particle diameter of Ag_3Sn and Cu_6Sn_5 particles with $\overline{D_{\mathrm{sol}}t}$. The diffusion constants used in the calculations are: $D_{\mathrm{o,Ag}} = 7 \times 10^{-7}$ m^2/s, $Q_{\mathrm{Ag}} = 51.5$ kJ/mol, $D_{\mathrm{o,Cu}} = 2.4 \times 10^{-7}$ m^2/s and $Q_{\mathrm{Cu}} = 33.1$ kJ/mol [20]. These diffusivity values correspond to the diffusion of Ag and Cu atoms in the direction perpendicular to the c-axis of Sn and give the fastest diffusion rates as compared to other directions. It is apparent from Figure 8.4 that the Cu_6Sn_5 particles grow very rapidly early on since the diffusivity of Cu in Sn is very high compared that of Ag in Sn. But the coarsening rate saturates at larger $\overline{D_{\mathrm{Cu}}t}$ values, since the small number of Cu_6Sn_5 particles makes the interparticle spacing very large following initial coarsening, making further coarsening very slow. In contrast, the Ag_3Sn particles coarsen continuously with $\overline{D_{\mathrm{Ag}}t}$ according to the 2-dimensional platelet

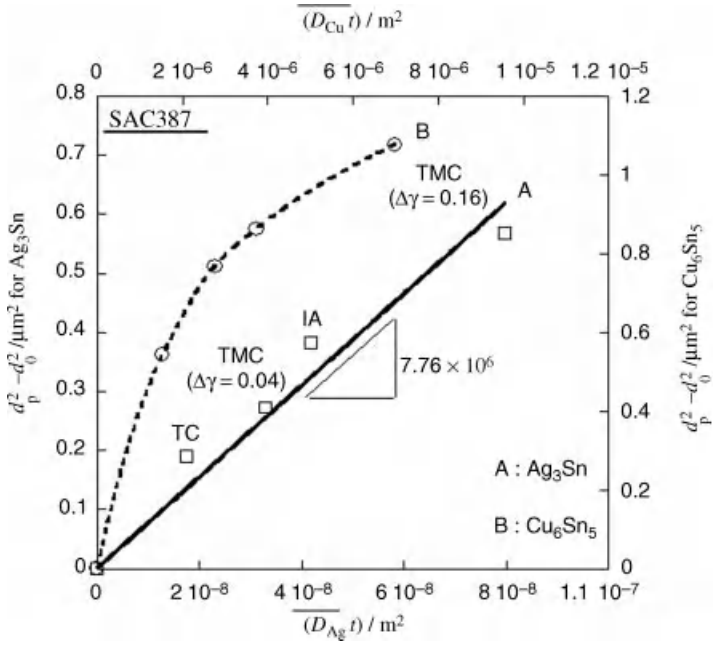

Figure 8.4 *The relationship between the particle size with mean effective diffusion distances for Cu and Ag in SAC387. Reasonably good linear curve fit between the square of the effective diameter of Ag_3Sn and the mean effective diffusion distance suggests that coarsening kinetics of Ag_3Sn can be represented well by the use of average effective diffusion distance.*

coarsening law:

$$d_p^2 - d_0^2 = M\,\overline{D_{Ag}t} \tag{8.7}$$

where M is the proportionality constant equal to $\sim 7.758 \times 10^{-6}$ for SAC387. The nominally linear dependence of Ag_3Sn coarsening data on $\overline{D_{Ag}t}$ for several different thermomechanical excursions demonstrates that the effective diffusion length, $\sqrt{\overline{D_{Ag}t}}$, adequately describes the thermomechanical history dependence of Ag_3Sn coarsening in Sn-Ag-based solders.

Typically, the Ag_3Sn particles are concentrated within bands of the divorced eutectic microconstituent (Ag_3Sn + β-Sn) in the interdendritic spaces of primary β-Sn. Assuming a cubic array of precipitates within the eutectic, the average interparticle spacing may be estimated as:

$$\lambda = \sqrt[3]{\frac{\pi\, V_{f,\text{eutectic in solder}}}{6\, V_{f,\ Ag_3Sn\text{ in solder}}}}\, d_p \tag{8.8}$$

where $V_{f,\text{eutectic in solder}}$ is the volume fraction of eutectic in solder and $V_{f,\ Ag_3Sn\text{ in solder}}$ is the volume fraction of Ag_3Sn in solder. The volume fraction of the eutectic region and Ag_3Sn particles in the solder, and particle size of Ag_3Sn were measured using several SEM micrographs for each condition. These values were used in Eq. (8.8) to calculate the

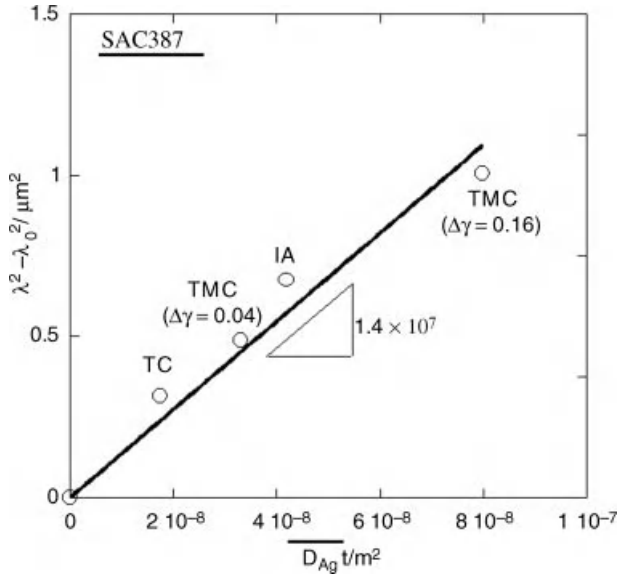

Figure 8.5 *Relationship between Ag_3Sn interparticle spacing and mean effective diffusion distance. Reasonably good linear curve fit shows that the effective diffusion distance can be used as the microstructural parameter, which is dependent only on the thermomechanical history of the solder.*

interparticle spacing. Figure 8.5 shows the relationship between the interparticle spacing and the effective diffusion distance for the various thermomechanical histories. Similar to the particle-size variation, the interparticle spacing is given by:

$$\lambda^2 - \lambda_0^2 = P_1 \overline{D_{\mathrm{Ag}} t} \tag{8.9}$$

where λ_0 is the initial interparticle spacing and P_1 is the proportionality constant equal to $\sim 1.4 \times 10^{-5}$ for SAC387. Equation (8.9), which provides a mathematical description of the effect of thermomechanical history on λ may now be used to substitute for λ in creep formulations to render creep models microstructurally adaptive.

8.3 Creep Behavior of Sn-Ag-Based Solders and the Effect of Aging

There is substantial literature available on creep of SA and SAC alloys [12, 23, 25–35]. In the following, some previously published results are summarized. Then, a microstructurally adaptive model for primary-cum-secondary creep is developed.

8.3.1 Experimental Procedure

The role of coarsening on the steady-state creep response was studied via impression creep testing on 750-μm diameter Sn-4.0%Ag-0.5%Cu (SAC405) balls attached to a BGA

substrate, in the as-reflowed condition, and following aging at 180 °C for 24 and 100 h [11]. Details of the experiments are available in [11].

Creep tests were also conducted on 650-μm diameter and 350-μm high SAC387 solder ball joints attached between two Al_2O_3 substrates with ENIG metallization using a double lap-shear geometry at shear stresses ranging from 26.1 to 52.2 MPa at temperatures ranging from 25 to 125 °C. Details on the test geometry are reported elsewhere [36, 37]. In addition to the as-reflowed samples, joints isothermally aged at 125 °C for 30, 60 and 90 days were also tested. These samples are identical to those utilized for quantitative assessment of microstructural coarsening (as reported in Section 8.2.2). Hence, these results are directly usable for the development of the microstructurally adaptive unified creep model.

8.3.2 Results and Discussion

8.3.2.1 Role of Microstructure on Steady-State Creep

During an impression creep test, the steady-state impression velocity *V*, which is proportional to the steady-state creep rate, may be expressed as [12, 38]:

$$\frac{VT}{G} \propto \left(\frac{\sigma_p}{G}\right)^n e^{-Q/RT} \tag{8.10}$$

where σ_p is the punch stress, *T* is the temperature, *G* is the shear modulus, and *n* and *Q* are the stress exponent and activation energy for creep, respectively. Here, $\sigma_p = \kappa\sigma$, where σ is the equivalent uniaxial stress, κ being a material-dependent constant [12, 33, 38]. A summary of the creep data for SAC405 solder at different temperatures and stresses is presented in Figure 8.6. Figure 8.6a shows a plot of (VT/G) vs. (σ_p/G) at various temperatures. Except for 25 °C (298 K) at which creep tests were conducted only at high punch stresses, the plots for all other temperatures (323, 348, 373 K and 423 K) naturally divide into low- and high-stress regimes with different stress exponents, *n*. This suggests a mechanism transition from power-law creep with $n \approx 6$ in the low-stress regime, to a power-law behavior with a greater stress dependence at higher stresses. This mechanism transition from low to high stresses is consistent with other observations of two distinct regimes of creep in SAC [e.g., 28, 32]. Figure 8.6b shows a plot of $(VT/G)^{1/n}$ vs. σ_p for the data in the high-stress regime with $n = 6$, revealing that at each temperature, there is a threshold stress $\sigma_{p,th}$, below which the relevant mechanism produces negligible creep, and that the true stress exponent in this regime is the same as that in the low-stress regime ($n = 6$).

A transition from a low to high apparent *n* may occur when the increase in the length of the dislocation segment undergoing local climb over particles is stress dependent [39, 40]. At low stresses, this results in a backstress σ_b that is directly proportional to the applied stress, thereby producing a simple power-law stress-dependence of the strain rate (i.e. $\sigma_b \propto \sigma$, so $\sigma - \sigma_b \propto \sigma$). At high stresses, the σ_b reaches a maximum constant value σ_{th}, yielding a discernible threshold behavior and consequently, a high apparent *n* value. This maximum value of σ_b may be attributed to either (a) the stress necessary to bypass particles via the Orowan mechanism [40], or (b) the stress necessary to overcome departure-site pinning of dislocation segments undergoing local climb around attractive particles [41, 42]. In either case, the back stress is inversely proportional to the interparticle spacing λ. In the case of thermally activated release of departure-site-pinned dislocations, the backstress also

depends on temperature [42]; however, this dependence is often weak, as frequently observed in Sn-Ag-based solders [e.g., 29, 43].

Plotting $\ln(VT/G)$ vs. $1/T$ for a constant value of $\sigma_{p,eff}/G = (\sigma_p - \sigma_{p,th})/G$, an activation energy value of $Q \sim 61$ kJ/mole is obtained in both the low- and high-stress regimes, which

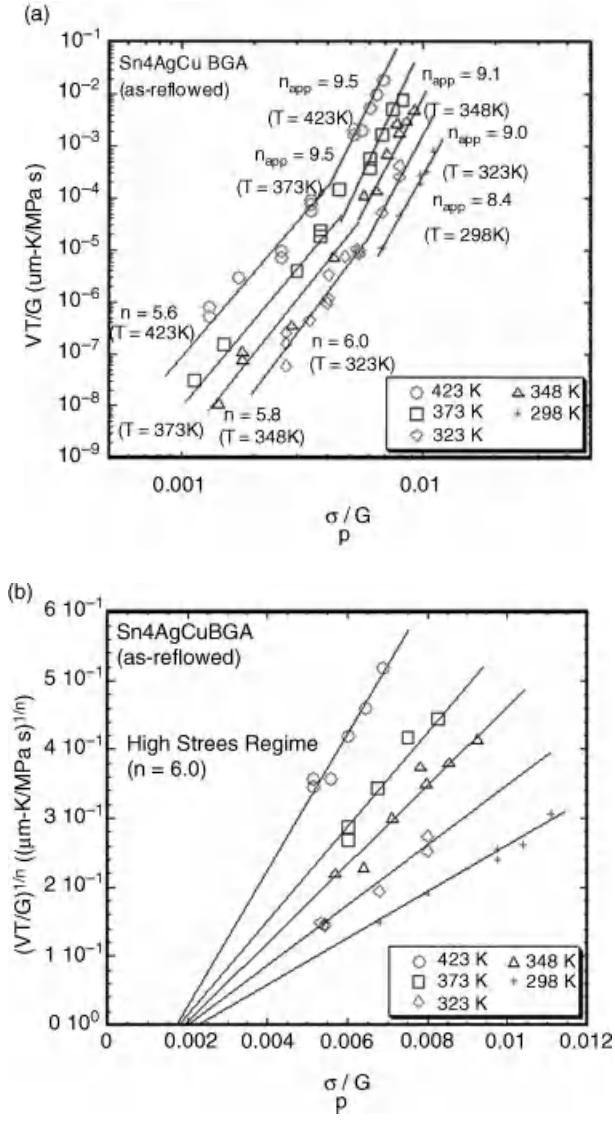

Figure 8.6 *(a) Punch-stress dependence of impression velocity of as-reflowed SAC405 BGA, showing. two stress regimes; (b) Plot of $(VT/G)1/^{6.0}$ versus $\sigma p/G$ for the high-stress data, illustrating the presence of a threshold stress; (c) Plot of temperature-compensated impression velocity versus modulus-compensated effective punch stress, showing that a stress exponent of 6 and an activation energy of 61–62 kJ/mol fit the data in both stress regimes.*

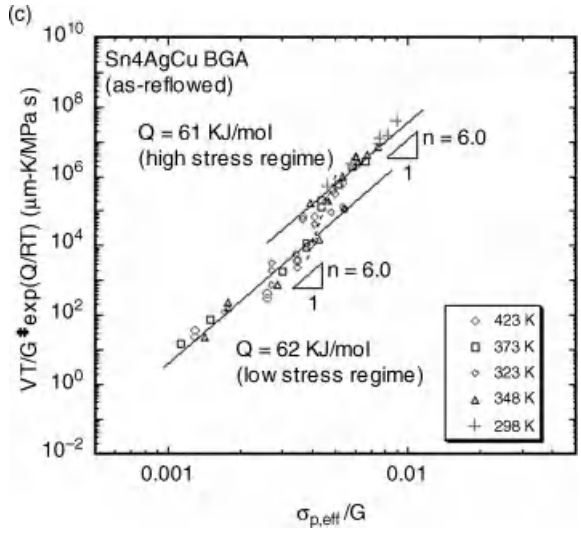

Figure 8.6 *(Continued)*

is consistent with $Q \sim 40$–65 kJ/mole for Sn self-diffusion through dislocation cores [43–45]. A plot of temperature-compensated impression velocity $V(T/G)e^{Q/RT}$ vs. modulus compensated effective punch stress, $\sigma_{p,eff}/G$, is presented in Figure 8.6c for both low- and high-stress regimes. Clearly, $Q \approx 61$–62 kJ/mole and $n = 6$ describe both stress regimes adequately, with a transition from low-stress to high-stress behavior occurring at $\sigma_{p,eff}/G \sim 4$–5×10^{-3}. The n value of 6 is consistent with dislocation-core diffusion-controlled climb, the stress exponent for volume-diffusion-controlled climb being ~ 4, with n increasing by 2 due to the stress dependence of dislocation density. Therefore, the creep mechanism in both stress regimes is dislocation-core diffusion-controlled climb, but with a threshold stress associated with the high-stress regime.

Figure 8.7 shows the dependence of the creep data on aging conditions. The coarsening of the Ag_3Sn dispersion enhances the creep kinetics in both stress regimes, but the mechanisms of creep remain unchanged, based on the computed n and Q values. For all three conditions (as-reflowed, aged at 453 K for 24 h, and aged at 453 K for 100 h), the n value is ~ 6 in both stress regimes (following threshold stress analysis), and the Q value is 57–61 kJ/mole. The invariance of n and Q with aging condition is an important result, which, as will be shown in the next section, facilitates an easy to use microstructurally adaptive creep model.

8.3.2.2 Development of a Unified Primary-Cum-Secondary Creep Model

Since the solder microstructure continuously evolves during service, accurate prediction of solder-joint reliability warrants the development of microstructurally adaptive creep models, which can self-adjust to *in situ* changes in microstructure during thermomechanical excursions. Steady-state microstructurally adaptive creep models based on a power law [8, 12] or a hyperbolic sine model [25] have been proposed earlier. However, microstructurally adaptive features have not been incorporated into a combined primary and

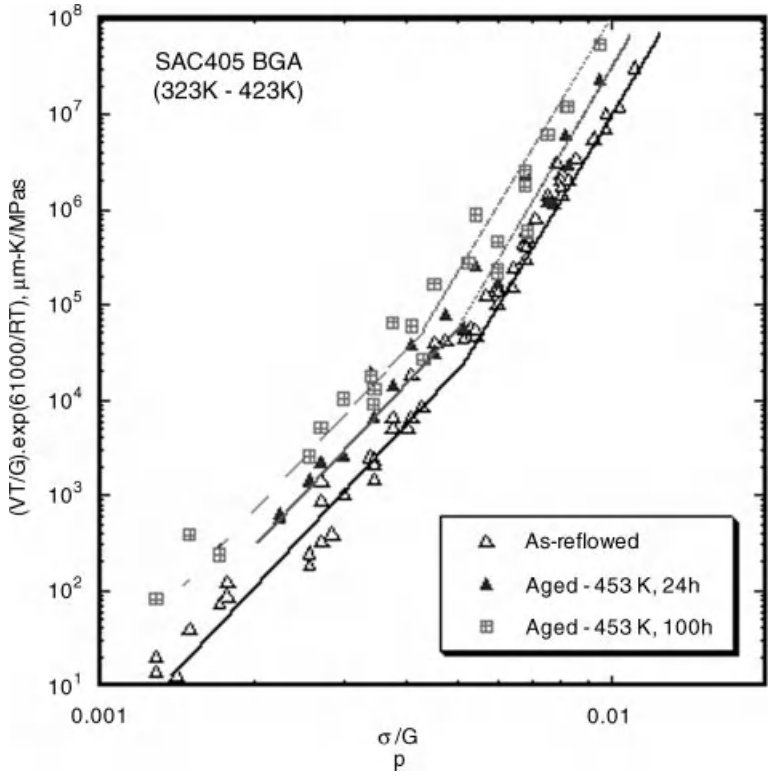

Figure 8.7 *Comparison of the creep response of SAC405 at 25, 50, 100 and 150°C (298, 323, 373 and 423 K) and stresses following aging to various extents.*

secondary creep law. Since under most thermomechanical cycling conditions, where the applied mechanical load changes continuously, primary creep is expected to play a significant role, it is of interest to develop microstructurally adaptive modes for primary as well as steady-state creep.

The creep behavior of Sn-Ag-based solders is controlled by the eutectic microconstituent, which is the harder of the two microstructural components (eutectic and the proeutectic β) [33]. Within the eutectic, the creep response is controlled by dislocation interaction with the precipitate particles (Ag_3Sn and/or Cu_6Sn_5), giving rise to a particle size/spacing dependent threshold stress [32–34], as well as a direct dependence of the creep rate on the interparticle spacing (λ) [8, 12, 13]. Hence, incorporating a mathematical description of the history dependence of particle size (or interparticle spacing), as discussed in Section 8.2.2.2, proffers a mechanism for developing microstructurally adaptive creep models [8, 12, 13].

Unified Creep Model. The total creep strain is expressed as the sum of primary and secondary creep, using an exponential formulation for primary creep as follows [46, 47]:

$$\gamma_{\text{creep}} = \alpha\left(1-e^{-\beta t}\right) + \dot{\gamma}_{ss} t \tag{8.11}$$

where γ_{creep} is the total shear creep strain, α is the saturation primary creep strain, β is the exhaustion rate of primary creep and $\dot{\gamma}_{ss}$ is the steady-state shear creep strain rate. The first part of the right-hand side of Eq. (8.11) gives the primary creep and its second term gives the steady-state creep. The exponential expression utilized here for primary creep gives a finite creep rate even at small times, and is therefore advantageous over conventional expressions with power dependence on time [46–49]. Figures 8.8a and b show representative creep curves obtained on ball grid joints between alumina plates in the double shear-lap geometry. Regressed curves using Eq. (8.11) are also shown, and the fits are observed to be reasonably good, establishing the efficacy of Eq. (8.11) in describing both primary and secondary creep of SAC alloys.

Mechanistic Basis for Creep Constants in Unified Model. In order to develop a microstructurally adaptive model for primary creep, it is necessary to develop a physical basis for the constants α and β, and relate them to the microstructure and the steady-state creep rate $\dot{\gamma}_{ss}$. $\dot{\gamma}_{ss}$ may be expressed as:

$$\dot{\gamma}_{ss} = A' \frac{Gb}{kT} \left(\frac{\tau_{eff}}{G}\right)^n e^{-\frac{Q}{RT}} \tag{8.12}$$

where A' and n are constants, b is the Burgers vector, k is Boltzmann's constant, and τ_{eff} is the effective shear stress on the joint. All the double shear-lap experiments on BGA joints were conducted in the high-stress regime, and therefore, τ_{eff} includes a threshold stress τ_{th}

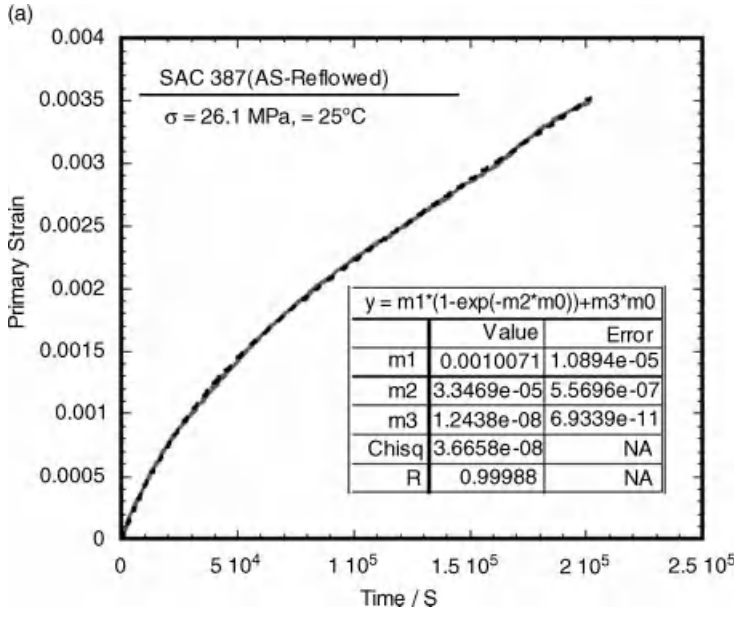

Figure 8.8 *Creep response of ball solder joints tested using double shear-lap geometry. The solid line is the measured creep response, whereas the broken line is the best-fit curve using Eq. (8.11). The legend shows the curve fit parameters.*

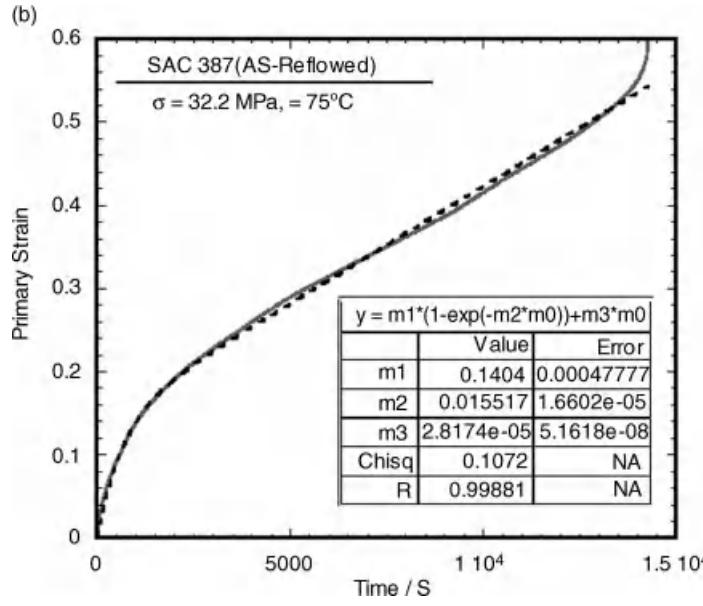

Figure 8.8 *(Continued)*

($\tau_{eff} = \tau - \tau_{th}$). Figure 8.9a, which plots the τ dependence of $\dot{\gamma}_{ss}$ for multiple temperatures (assuming $Q = 61$ kJ/mole, as per the discussion in Section 8.3.2.1 and refs. [32, 33, 35]), reveals an apparent creep stress exponent of 9.8 without accounting for the threshold stress. Replotting the data as $\left[(\dot{\gamma}_{ss}kT)/\left(Gbe^{-Q/RT}\right)\right]^{1/n}$ vs. τ/G assuming a true n value of 6 (as discussed in Section 8.3.2.1), gives an excellent fit (Figure 8.9b), and reveals a weakly temperature-dependent threshold stress,[3] consistent with previous studies on Sn-Ag and Sn-Ag-Cu solders [32, 33, 35, 43]. Figure 8.9c replots the data as $\left[(\dot{\gamma}_{ss}kT)/\left(Gbe^{-Q/RT}\right)\right]^{1/n}$ vs. $(\tau - \tau_{th})/G$ using the τ_{th}/G value obtained in Figure 8.9b, and shows that $n = 6$ and $Q = 61$ kJ/mole gives a good fit for all temperatures, yielding the value of A' for SAC387 ($=4.32 \times 10^7$ m^2/s).

By subtracting the steady-state creep strain $\dot{\gamma}_{ss}t$ from the total creep strain, the primary creep strain γ_{pri} may now be plotted and fitted to the first term of Eq. (8.11), as shown in Figure 8.10, thereby yielding the values of α and β for each test condition. Figure 8.11 shows some of the salient features of these parameters. First, Figure 8.11a shows that α, β and $\dot{\gamma}_{ss}$ are related to each other as:

$$\dot{\gamma}_{ss} \approx \alpha\beta/3 \tag{8.13}$$

This observed proportionality between $\alpha\beta$ and $\dot{\gamma}_{ss}$ is consistent with data reported for various metallic materials [46, 47, 50, 51], and allows reduction of the number of unknown parameters in Eq. (8.11) from three (α, β, $\dot{\gamma}_{ss}$) to two. Secondly, Figure 8.11b shows

[3] The threshold stress showed a weak temperature dependence within the range of temperatures used here (within a factor of ~1.5). This allowed representing t_{th} with an average value, as shown in Figure 8.9b.

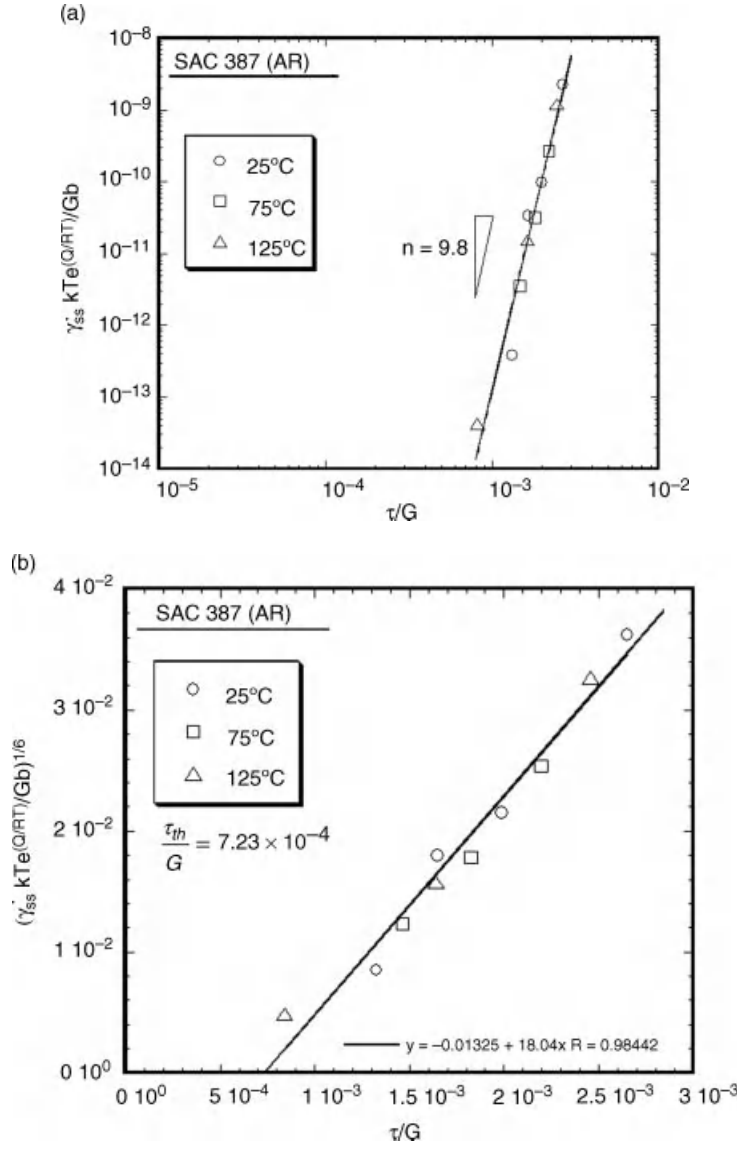

Figure 8.9 *(a) Variation of steady-state creep with the applied stress. A high stress exponent value of 9.8 for all the test condition suggests a high stress behavior with a threshold stress. (b) Plot of* $[(\dot{\gamma}_{ss}kT|)/(Gbe^{-Q/RT})]^{1/6}$ *vs.* τ/G *that demonstrates the presence of a threshold stress below which creep does not take place. The x-intercept of such a plot gives the value of threshold stress if the 'n' used is the real stress exponent. An average modulus compensated stress,* τ_{th}/G*, equal to* 7.23×10^{-4} *was calculated as the threshold stress for the as-reflowed samples. (c) Variation of temperature-compensated steady-state strain rate with respect to the modulus compensated net stress. All the samples were in as-reflowed conditions. A threshold stress,* τ_{th}/G*, equal to* 7.23×10^{-4} *was subtracted from the applied stress to calculate the net stress.*

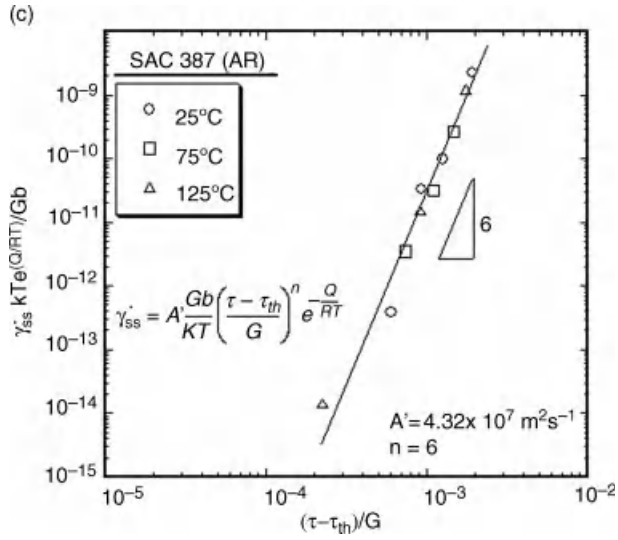

Figure 8.9 *(Continued)*

that the saturation primary creep strain α is independent of temperature and depends on stress as:

$$\alpha = C_1[(\tau - \tau_{th})/G]^2 \tag{8.14}$$

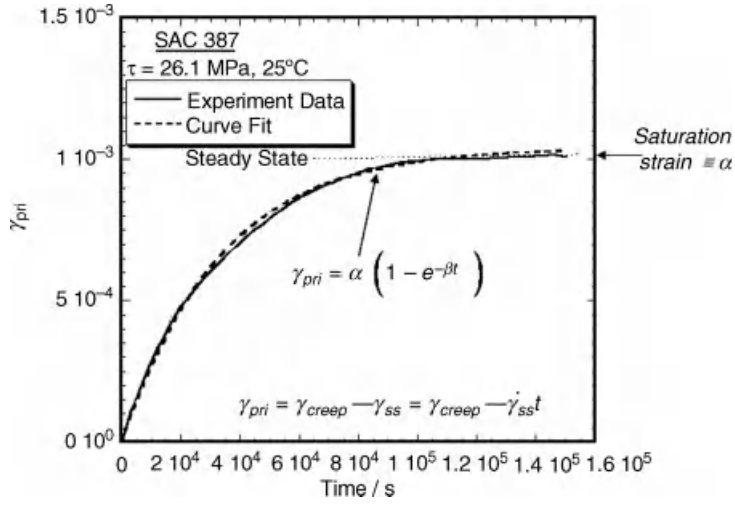

Figure 8.10 *A typical primary creep curve (continuous line) for SAC 387. The best fit curve is shown by dashed line. From the curve fitting, a value of* $\alpha = 1.04 \times 10^{-3}$ *and* $\beta = 3.05 \times 10^{-5}\ s^{-1}$ *was calculated for the shown curve.* γ_{pri} *is the primary creep strain and* γ_{ss} *is the steady-state creep strain.*

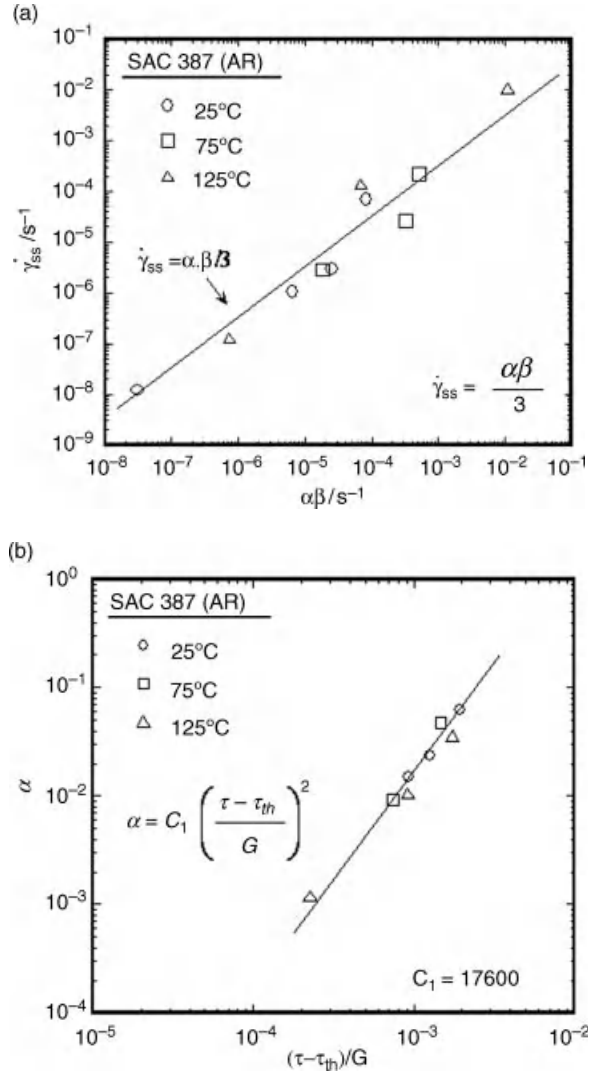

Figure 8.11 *(a) Variation of steady-state creep rate with respect to the product of the saturated primary strain and the exhaustion rate. (b) dependence of α on the modulus compensated net stress, (c) dependence of temperature-compensated β on the modulus-compensated net stress.*

where C_1 is a constant. This is consistent with the fact that the saturation creep strain depends on the dislocation density and therefore on the square of the effective shear stress. The temperature independence of α is consistent with previous reports on other metallic systems [47, 52, 53]. Thirdly, Figure 8.11c shows that β, the exhaustion rate of primary creep, shows similar dependencies on temperature and applied stress as $\dot{\gamma}_{ss}$, but with a stress

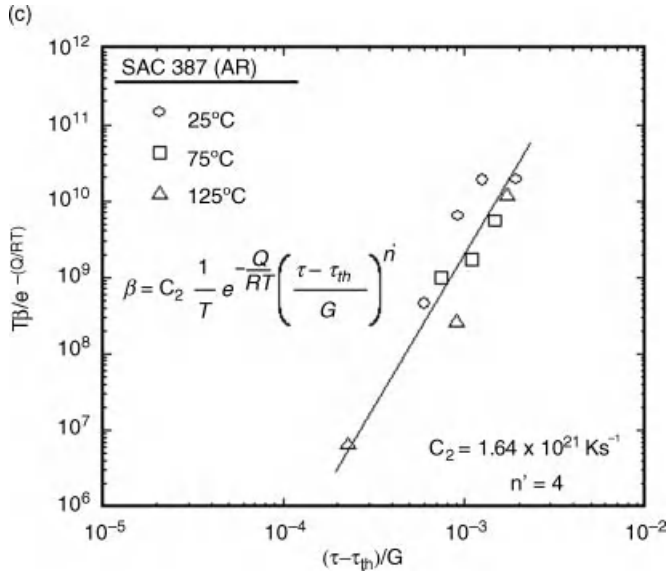

Figure 8.11 *(Continued)*

exponent n' that is 2 less than that for $\dot{\gamma}_{ss}$ (i.e. 4 instead of 6), according to:

$$\beta = C_2[(\tau - \tau_{th})/G]^{n'}.(1/T)e^{-Q/RT} \tag{8.15}$$

where C_2 is a constant, and Q is identical to the activation energy for creep (61 kJ/mol for SAC387). Equation (8.15) is consistent with the fact that the exhaustion rate of primary creep depends on the rate at which dislocations recover into a stable subgrain structure, and is therefore related to both the applied stress and the temperature.

8.3.2.3 Incorporation of Aging Effects in Unified Creep Law

In order to incorporate aging effects into the unified creep law (Eq. (8.11)), the functional dependencies of α, β and $\dot{\gamma}_{ss}$ on the interparticle spacing λ, and hence the effective diffusion distance, $\sqrt{D_{Ag}t}$, have to be established. Figures 8.12a–c show the aging dependence (30, 60 and 90 days at 125 °C) of α, β and $\dot{\gamma}_{ss}$, respectively. The dependence of α, β and $\dot{\gamma}_{ss}$ on the stress and the temperature is identical before and after aging, suggesting that only the creep kinetics, but not the mechanism, depend on thermomechanical history. Clearly, α and $\dot{\gamma}_{ss}$ depend on the extent of aging, whereas β shows negligible dependence on microstructural coarsening. Based on prior work [8, 13], $\dot{\gamma}_{ss}$ shows a direct dependence on λ, and may be expressed as:

$$\dot{\gamma}_{ss} = \frac{BD_{Sn}Gb}{kT}\left[\frac{\tau}{G} - \frac{\tau_{th}}{G}\right]^{n}\lambda \tag{8.16}$$

where B is a constant, and D_{Sn} is the self-diffusivity of Sn. In addition, the term τ_{th}/G also shows an inverse proportionality on λ (for both departure-site pinning and Orowan pinning),

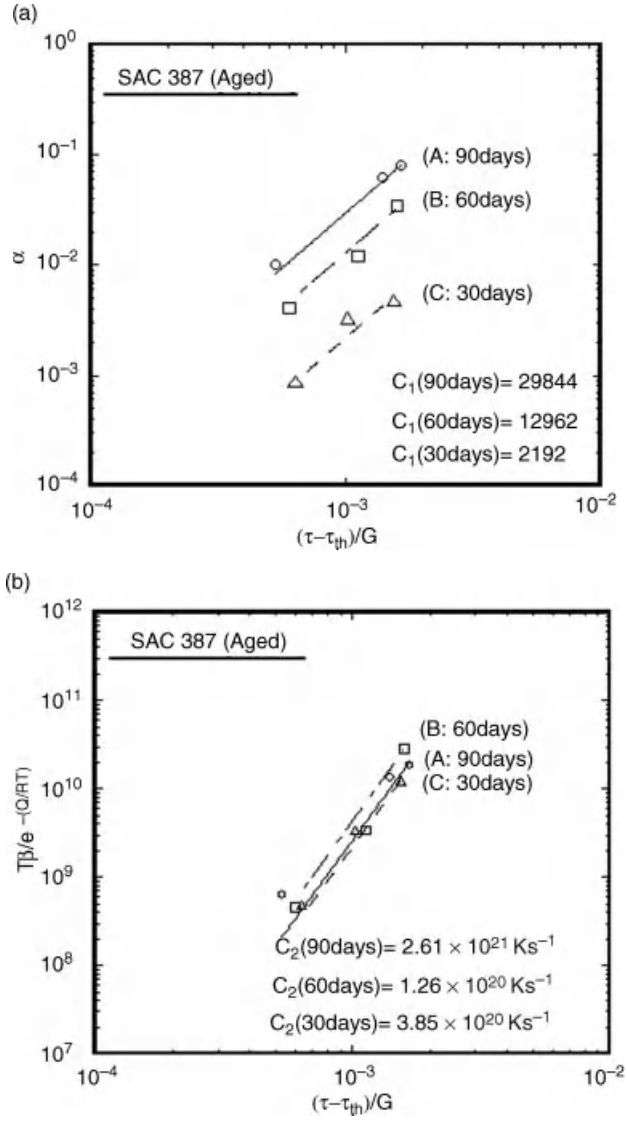

Figure 8.12 *Variation in parameters α, β and $\dot{\gamma}_{ss}$ with the modulus compensated net stress for samples isothermally aged for different periods. Aging for all samples was conducted at 125°C. Aging time is shown in parenthesis. The constants C_1, C_2 and A′ are defined in Figure 8.11.*

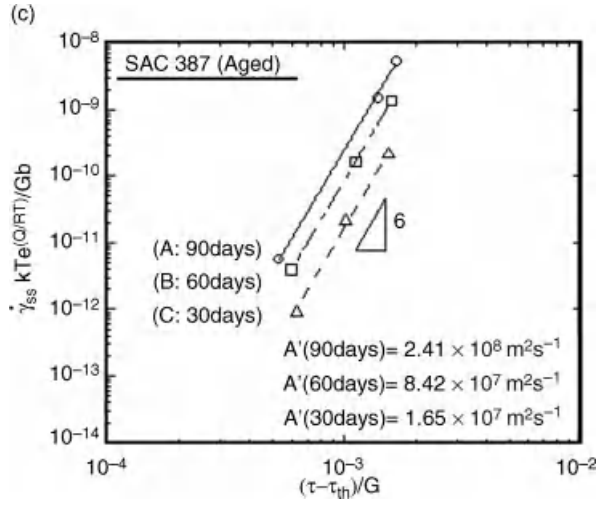

Figure 8.12 *(Continued)*

and hence $\sqrt{D_{Ag}t}$, as follows:

$$\frac{\tau_{th}}{G} = \left(\frac{\tau_{th}}{G}\right)_{\infty} + \frac{L}{\sqrt{D_{Ag}t}} \tag{8.17}$$

where $(\tau_{th}/G)_{\infty}$ is a constant representing the threshold stress for an infinitely long aging time, and L is a constant. For SAC387, $(\tau_{th}/G)_{\infty}$ and L are equal to 4.85×10^{-4} and 3×10^{-7} m^{-1}, respectively. Because of the small value of L, however, the λ dependence of (τ_{th}/G) is relatively small, and can be ignored, giving $(\tau_{th}/G) \approx (\tau_{th}/G)_{\infty}$. Thus, the λ dependence of $\dot{\gamma}_{ss}$ is given by Eq. (8.15) with $(\tau_{th}/G) \approx (\tau_{th}/G)_{\infty}$.

Since β is independent of aging condition (and hence λ), and $\alpha\beta \propto \dot{\gamma}_{ss}$, α must have the same λ dependence as $\dot{\gamma}_{ss}$. Based on the discussion in Section 8.3.3.2, α and β may therefore be written as:

$$\alpha = \frac{3B}{C}\left[\frac{\tau}{G} - \frac{\tau_{th}}{G}\right]^2 \lambda \tag{8.18}$$

$$\beta = C_{\beta}\frac{D_{Sn}Gb}{kT}\left[\frac{\tau}{G} - \frac{\tau_{th}}{G}\right]^{n-2} \tag{8.19}$$

$$\text{where} \quad \lambda = \sqrt{\lambda_0^2 + P\overline{D_{Ag}t}} \tag{8.20}$$

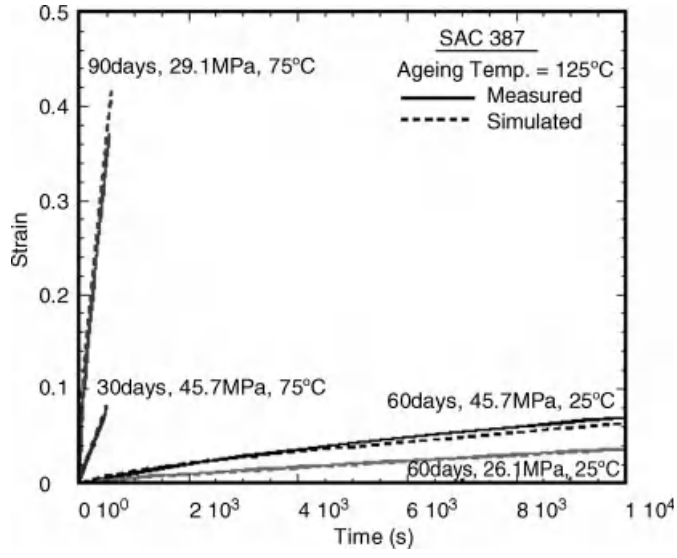

Figure 8.13 *A comparison of the model and the experiment.*

and, for SAC387 solder, $(\tau_{th}/G) \approx (\tau_{th}/G)_{\infty} = 4.8 \times 10^{-4}$, $B = 2.21 \times 10^{25}\,\mathrm{m}^{-1}$, $C_{\beta} = 6.43 \times 10^{39}$, $\lambda o \sim 2 \times 10^{-7}$ m, $P_1 = 1.4 \times 10^{-5}$, $G = 20632 - 37.67T$ (MPa) [24], $b = 3.18 \times 10^{-10}$ m, $D_{0,\mathrm{Sn}} = 1.0 \times 10^{-9}$, $Q_{\mathrm{Sn}} = 61$ kJ/mol [32, 33, 35], $D_{0,\mathrm{Ag}} = 7.7 \times 10^{-7}\,\mathrm{m/s}^2$ and $Q_{\mathrm{Ag}} = 51.5$ kJ/mol [20]. Equations (8.16) and (8.18)–(8.20), when combined with the unified creep law presented in Eq. (8.11), provides a methodology to incorporate thermomechanical history into the creep law, thereby rendering it "microstructurally adaptive."

Figure 8.13 shows entire experimental creep curves, including both primary and secondary stages, for several different thermomechanical aging histories and test conditions (stress and temperature). Simulated creep curves utilizing the above model, where the thermomechanical history has been accounted for by incorporating the appropriate $\sqrt{D_{Ag}t}$ value (which determines λ), are also shown. The agreement between the experimental and simulated results is excellent, clearly demonstrating the effectiveness of the proposed microstructurally adaptive unified creep model.

8.4 Role of Microstructure on High Strain Rate Fracture

Most handheld devices undergo thermomechanical cycling during service and therefore, tiny low-cycle fatigue cracks form early in the service life of solder joints. These pre-existing cracks may propagate under a combination of tensile and shear loading when the package sustains an impact during a drop. Thus, solder joints that are resistant to brittle fracture under drop-loading conditions are critical to the robustness of portable devices. Whereas during low strain rate loading, significant plastic deformation of the solder precedes catastrophic failure of joints, under high strain rate loading, fracture is typically confined to the interfacial regions of Sn-Ag-Cu solder joints. Depending on the

microstructural condition of the solder, the surface finish of the bond pads, processing history and test conditions, the flow properties of the solder, details of the fracture path, as well as the joint fracture toughness can be quite different [54, 55].

A few studies have addressed the quasistatic fracture of Sn-Ag-based solder joints, outlining the effects of mode-mixity, bond-pad metallization, interfacial IMC composition and thickness, and so on, on the fracture toughness of the solder joints [56–61]. However, there is a lack of general consensus on the effect of mode-mixity on the fracture toughness of solder joints, for example, Choi *et al.* [57] and Siow *et al.* [60] reported an increase in fracture toughness with an increase in mode-mixity for solder joints, whereas Nayeb-Hashemi *et al.* [57] reported a corresponding decrease. A linear relationship between the crack-opening displacement and J-integral has been noted for a cohesive crack in a solder joint [59]. It has been generally observed that at relatively low strain rates ($\sim 8.3 \times 10^{-3}$/s), longer solder-reflow times shift the dominant failure mode from ductile (i.e. through bulk solder) to brittle (i.e. interfacial delamination of different layers of IMCs, e.g., Cu_3Sn and Cu_6Sn_5) [61]. However, the relationship between solder microstructure, the IMC morphology and the fracture behavior of solder joints at high strain rate has never been systematically studied, nor has the evolution of the relative contributions of these mechanisms with increasing loading mode-mixity. In the following, these relationships and their dependence on various process and loading conditions are explored.

The parameters affecting fracture toughness can be divided into three groups: (i) reflow parameters, which include dwell time at the reflow temperature and the cooling rate following reflow, and on which the initial solder microstructure and interfacial layer characteristics depend, (ii) thermomechanical history, which, as discussed earlier, also affects the solder microstructure and IMC layer morphology, and (iii) test conditions, which include strain rate and loading mode mixity. In this section, a methodology for measurement of fracture toughness of adhesive joints undergoing elastoplastic deformation is developed. This methodology utilizes a compact mixed mode (CMM) specimen wherein a 0.5-mm thick solder joint is sandwiched between two massive copper substrates, and the sample is loaded under far-field mixed-mode conditions [54, 55, 63]. On the basis of this methodology, the effect of the above three parameters on solder joint fracture toughness is studied.

8.4.1 Experimental and Analytical Procedure

The test samples comprised a 0.5-mm thick solder joint between two "massive" copper substrates in the modified compact mixed mode (CMM) sample configuration [63]. A thin Al film (which is not wetted by solder) was deposited on a Cu substrate on one side of the joint to provide an interfacial starter crack. The following reflow parameters were used: (a) reflow temperature: 260 °C, (b) dwell time: 30 s, 90 s, 180 s or 300 s, and (c) cooling rate: $\sim 10\,^{\circ}\mathrm{C\,s^{-1}}$ (water quenched, WC) or $\sim 3\,^{\circ}\mathrm{C\,s^{-1}}$ (air cooled, AC). Some samples were aged at 150 °C for 48 h after being soldered. Fracture tests were conducted using a servohydraulic test frame at joint strain rates of 0.01–200 $\mathrm{s^{-1}}$, using a fixture that enabled the loading angle to be changed from 0° to 90° relative to the loading axis in increments of 15°. The details of the experimental setup are reported elsewhere [54, 55].

For small-scale yielding problems, where failure is catastrophic, the fracture toughness may be expressed as the critical strain energy release rate, G_C. Finite element analysis by the

authors has revealed that although the solder is inherently ductile, the adhesive joint between the "massive" elastic substrates is severely constrained, and when the sample is thick compared to the joint thickness (the experimental samples were 6.35 mm thick, the joints being 0.5 mm thick), the calculated J-integral values were very close to the G values after accounting for any subcritical crack growth. Therefore, the strategy utilized for computing G_C comprised two steps: (i) estimate the actual crack length just prior to fracture by accounting for any subcritical crack growth, and (ii) utilize available formulations for the stress intensity factors for adhesive joints in CMM samples under mode I and II, K_{Ia} and K_{IIa} [64–66]:

$$K_{\mathrm{Ia}}(CMM) = \frac{P\cos\theta\sqrt{\pi a}}{wh} f_{\mathrm{Ia}}\left(\frac{a}{w}\right)$$
$$K_{\mathrm{IIa}}(CMM) = \frac{P\sin\theta\sqrt{\pi a}}{wh} f_{\mathrm{Ia}}\left(\frac{a}{w}\right) \tag{8.21}$$

where P is the applied load, θ is the loading angle, a is the critical crack length (at which unstable crack propagation initiates), w is the joint width, h is the thickness of the Cu pieces, and f_{Ia} and f_{IIa} are factors that depend on the sample geometry and the crack length.

To estimate the actual crack length just prior to catastrophic crack propagation (accounting for any subcritical crack growth, which can be significant), a methodology based on ASTM standard E561-05 [67] was employed. This involved comparing the secant modulus just prior to fracture from the load–displacement plot with the initial modulus during loading to determine the fractional decrease in modulus (or increase in compliance C). For this, a master plot of the fractional compliance change ($\Delta C/C_0$) versus the fractional crack-length increase ($\Delta a/a_0$) was developed using finite element modeling (FEM), and the experimentally obtained $\Delta C/C_0$ value was utilized to determine $\Delta a/a_0$, and hence the critical crack length a_{c} just prior to fracture. G_{C} can then be expressed as [68]:

$$G_C = \frac{K_{\mathrm{Ia}}^2 + K_{\mathrm{IIa}}^2}{E'_{\mathrm{a}}\cosh^2(\pi\varepsilon)} \tag{8.22}$$

where ε is a constant depending on Dundurs parameter, β', and E'_{a} is given by:

$$E'_{\mathrm{a}} = 2\frac{E'_1.E'_2}{E'_1 + E'_2} \tag{8.23}$$

where E'_1 and E'_2 are the plane strain Young's moduli [$=E/(1-\nu^2)$] of substrate and adhesive, respectively, E and υ being the Young's modulus and Poisson's ratio, respectively, and ε and β' are:

$$\varepsilon = \frac{1}{2\pi}\ln\frac{1-\beta'}{1+\beta'} \text{ and } 2\beta' = \frac{\mu_1(1-2\nu_2)-\mu_2(1-2\nu_1)}{\mu_1(1-\nu_2)+\mu_2(1-\nu_1)} \tag{8.24}$$

where μ_1 and μ_2 are the shear modulus of the substrate and the adhesive layer, respectively, and ν_1 and ν_2 are Poisson's ratio of the substrate and the adhesive layer, respectively. The

mode-mixity ψ (which may be different from the phase angle ϕ for interfacial fracture [65–67, 69] is:

$$\psi = \tan^{-1} \frac{K_{\mathrm{IIa}}}{K_{\mathrm{Ia}}} \tag{8.25}$$

8.4.2 Results and Discussion

8.4.2.1 Effect of Test Parameters on Fracture

Figure 8.14 shows the effect of strain rate on the fracture toughness of SAC387 solder joints for various dwell times at the reflow temperature (260 °C). Irrespective of reflow conditions, the fracture toughness monotonically decreases with strain rate. This is due to the higher solder yield strength and work-hardening rates at higher strain rates [62]. Longer dwell time makes G_{C} less sensitive to the strain rate. This is mainly due to the increase in the IMC thickness as well as roughness at the Cu/solder interface with increasing dwell times, which increases the proclivity of crack propagation through the interfacial IMC layer, making the fracture path less dependent on the solder properties. Figure 8.15 shows the effect of mode mixity on the fracture toughness. G_{C} decreases with increasing shear component. This trend is the same for all reflow conditions. At higher ψ, early microvoid nucleation occurs at the tip of the interfacial IMC scallops, leading to fracture by linkage of microvoids at the IMC tips and consequent decohesion along the solder/IMC interface [54]. Another general inference that can be drawn from post-testing inspection of fracture surfaces (shown in Figure 8.16) is that lower strain rates and smaller mode-mixities tend to promote a meandering crack path

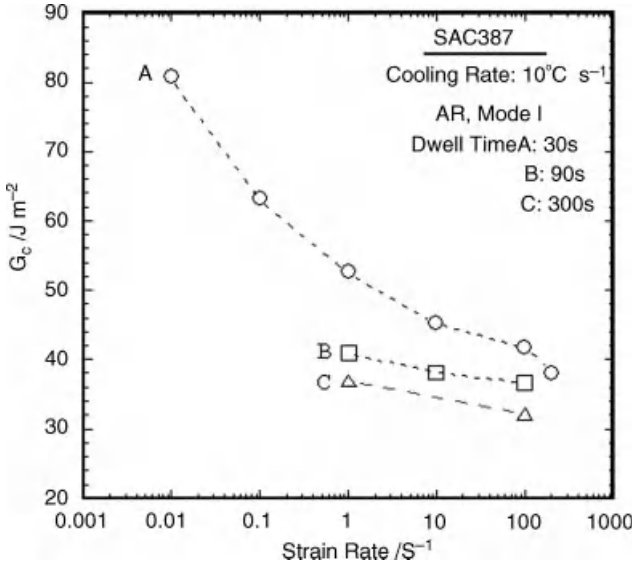

Figure 8.14 *Effect of strain rate on fracture toughness.*

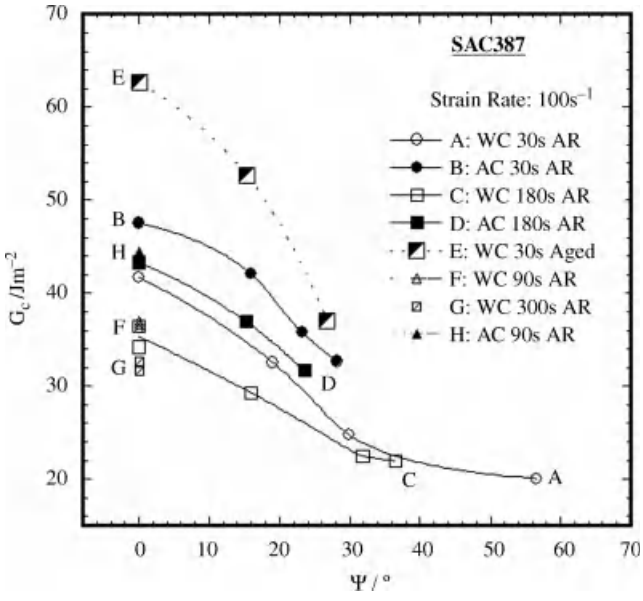

Figure 8.15 *Effect of reflowing and aging parameter.*

(often passing through the solder), which is more energy expensive, and therefore leads to higher G_C. Conversely, at high strain rates and large loading angles (high mode-mixity), the crack typically passes either through the IMC or along the IMC/solder interface, thereby lowering G_C.

8.4.2.2 Effect of Reflow Parameters on Fracture

Samples with different dwell time (30 s, 90 s, 180 s and 300 s) and cooling rate (water cooled and air cooled) were tested at the strain rate of 100 s^{-1} at different loading angles.

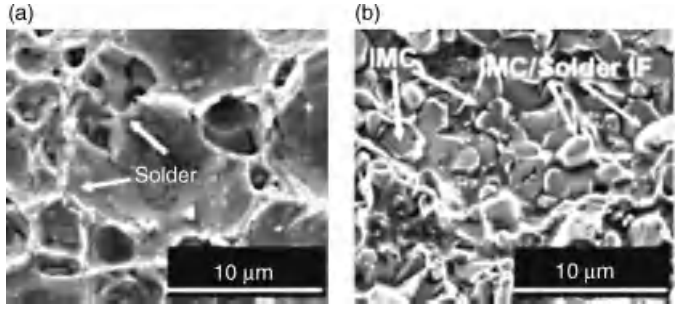

Figure 8.16 *Fracture surface of as-reflowed solder joints with identical reflow conditions (reflow temperature = 260°C, dwell time = 90 s, cooling rate = 10°C/s) and tested in mode I at: (a) 1 s^{-1} and (b) 100 s^{-1}. The fracture surface of the sample tested at lower strain rate shows relatively many more dimples as compared to the sample tested at higher strain rate, suggesting a meandering crack path at lower strain rates.*

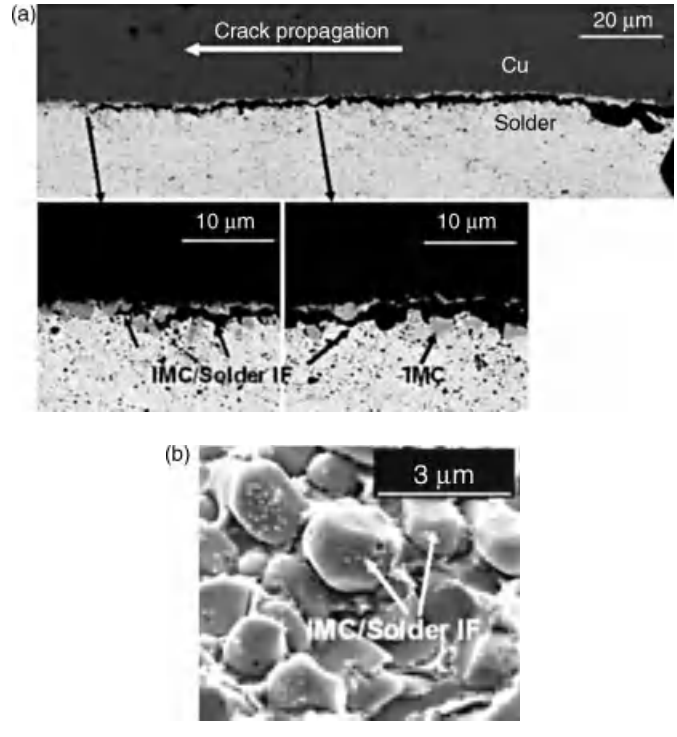

Figure 8.17 *(a) Crack profile and (b) fracture surface of the sample tested at 100 s^{-1} in mode I. The sample was prepared using a dwell time of 30 s and a cooling rate of 10° C/s (water cooled).*

Figure 8.15 shows that G_C decreased with an increase in the dwell time. As discussed above, this is attributable to the formation of coarser IMC scallops and greater overall IMC thickness at longer dwell times, which increases the propensity of the crack to remain confined to the IMC (Figures 8.17 and 8.18). As mentioned earlier, the thickness of IMC layer increases with dwell time. A thicker IMC layer not only increases the fraction of brittle material near the crack tip but also increases the elastic–plastic stresses at the solder/IMC interface, arising due to the elastic mismatch between IMC and solder. This proffers a faster nucleation rate of microvoids, resulting in degradation of fracture toughness [55].

G_C decreases with increase of cooling rate (Figure 8.15). Higher cooling rate (i.e. WC) samples have finer microstructures leading to a higher yield strength. Thus, a smaller plastic zone at the crack tip results in smaller G_C as compared to a sample produced using a slower cooling rate. It is confirmed by Figures 8.18 and 8.19 that for the same dwell time, the crack path in WC sample is much flatter than the one in the AC sample, thus the ratio of solder fracture as well as G_C value is lower.

8.4.2.3 Effect of Aging on Fracture

Aging affected the solder joints in two opposite directions. On the one hand, it caused a much thicker IMC layer, degrading the joint property (see the effect of dwell time); on the

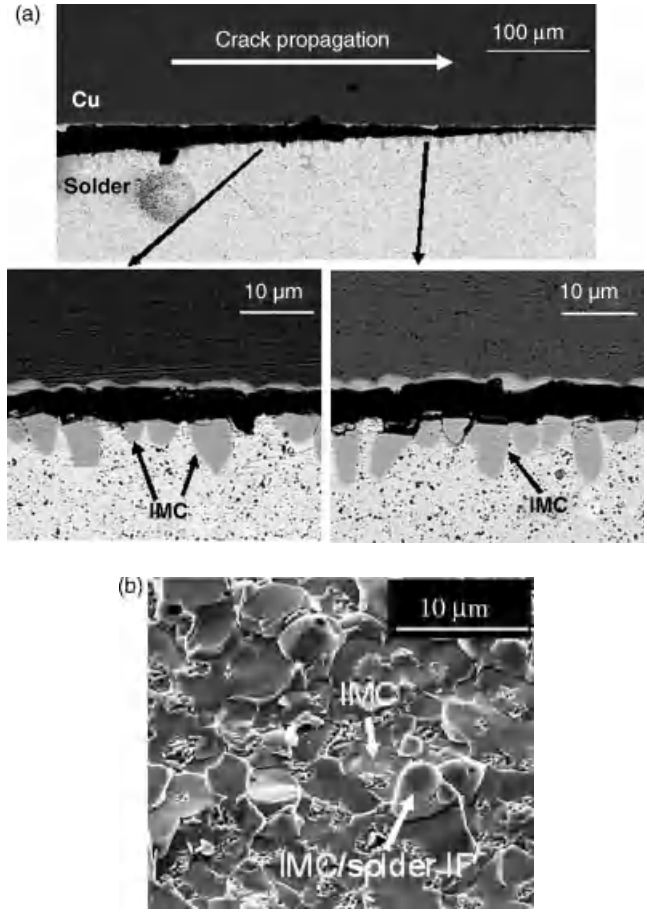

Figure 8.18 *(a) Crack profile and (b) fracture surface of the sample tested at 100 s^{-1} in mode I. The sample was prepared using a dwell time of 180 s and a cooling rate of 10 °C/s (water cooled).*

other hand, aging softened the solder, allowing the crack-propagation path to transition from the being largely along the interface to partly through the solder. The latter effect appears to dominate, enabling a greater degree of aging to make the joint tougher (higher G_C). Examination of both the crack profiles and the fracture surfaces (Figure 8.20) revealed that following aging, the majority of the crack path lay in the solder close to interface, resulting in much higher G_C values than those observed for the as-reflowed samples. During aging, Ag_3Sn precipitates in the solder (see Section 8.2 for details about coarsening) coarsen substantially. Therefore, both the yield strength and the work-hardening rate of the solder decrease significantly, resulting in enhanced. crack tip plasticity and higher fracture toughness [54, 55, 62]. However, the positive effect of aging diminished with an increase in the shear component of the loading (i.e. increasing mode-mixity). This is attributable to an increased propensity for crack propagation through the interfacial IMC layer at higher mode-mixity. The effect of lower cooling rate is similar to that for aging in that it too reduces the solder yield strength and work-hardening rate.

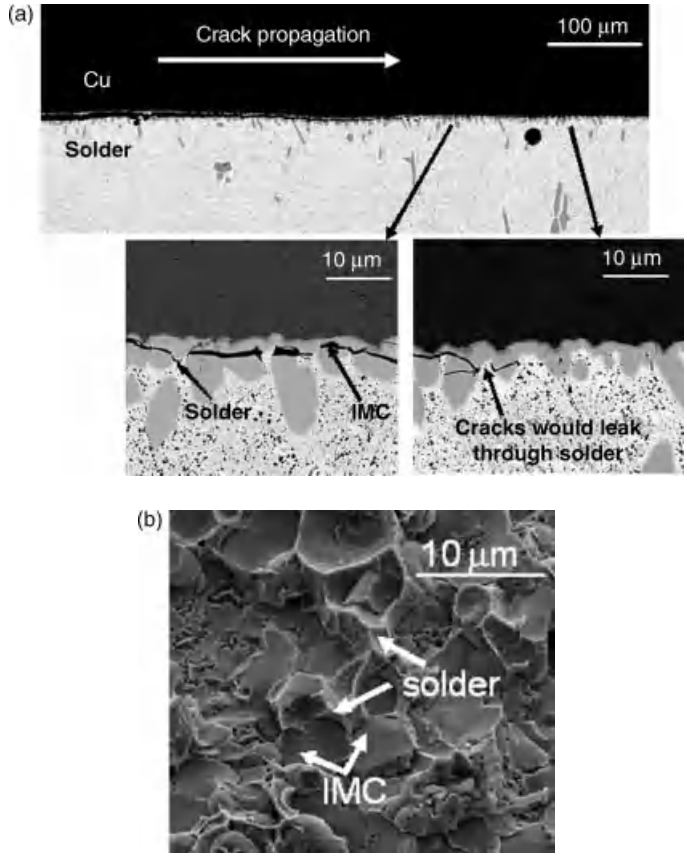

Figure 8.19 *(a) Crack profile and (b) fracture surface of the sample tested at 100 s^{-1} in mode I. The sample was prepared using a dwell time of 180 s and a cooling rate of 3 °C/s (air cooled).*

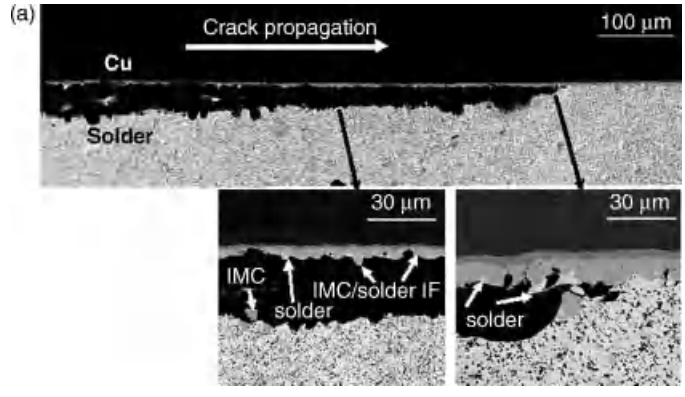

Figure 8.20 *(a) Crack profile and (b) fracture surface of the sample tested at 100 s^{-1} in mode I. The sample was prepared using a dwell time of 30 s and a cooling rate of 10 °C/s (water cooled) and was thermally aged at 150 °C for 48 h.*

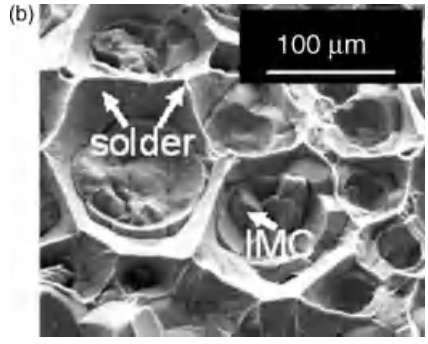

Figure 8.20 *(Continued)*

8.5 Summary and Conclusions

A quantitative study of the coarsening kinetics of a Sn-Ag-Cu solder alloy has been presented. The coarsening kinetics of these alloys is controlled by that of Ag_3Sn, as their number is substantially larger than that of Cu_6Sn_5 particles. The coarsening rate of Ag_3Sn can be mathematically described in terms of a parameter $\sqrt{(\overline{D_{sol}t})}$, termed the effective diffusion distance, which depends on the thermomechanical history of the solder. A methodology for determining this parameter has been presented, and it has been shown that both particle size and interparticle spacing may be expressed in terms of $\sqrt{(\overline{D_{sol}t})}$.

As the microstructure coarsens, both primary and secondary creep behavior of the solder change. Representing the primary creep behavior using an exponential formulation, and the secondary creep behavior using a power-law equation with a threshold stress, a microstructurally adaptive unified creep model has been developed. The model can self-adjust to *in situ* changes in microstructure during thermomechanical excursions, and utilizes the term $\sqrt{(\overline{D_{sol}t})}$ to account for the coarsening kinetics.

The mixed-mode fracture behavior of Sn-Ag-Cu solder joints attached to Cu substrates under drop conditions has also been examined. The effects of the following parameters on fracture toughness G_C under dynamic loading conditions has been examined: (i) fracture-test conditions (strain rate and loading angle), (ii) solder-reflow parameters (dwell time and cooling rate) and (iii) thermal-mechanical history of the solder joint. G_C decreases as strain rate increases because of lower yield strength of the solder at high strain rates, with increasing mode-mixity (up to a phase angle ψ of 60°). A faster cooling rate and a longer dwell time during reflow decrease G_C; whereas softening the solder matrix by isothermal aging enhanced G_C. Aging makes the solder softer, which enhances G_C, but makes the interfacial intermetallics thicker (albeit smoother), which tends to reduce G_C, the final impact of aging being determined by a balance of these factors.

Acknowledgments

This work has been supported through grants from the National Science Foundation (DMR-0209464, DMR-0705734, DMR-0939392), the Semiconductor Research Corporation

(Tasks 1394, 1630 and 1855), Intel Corporation, and the Strategic Environmental Research and Development Program (SERDP contract #W912HQ-10-C-0041). The authors gratefully acknowledge the contributions of several colleagues (Drs M. Renavikar and R. Sidhu of Intel Corp. and Dr Vikas Gupta of Texas Instruments) and former/current students and postdoctoral associates (Dr Deng Pan, Dr Tiandan Chen, Dr Dhruv Bhate, and Ms Sri Chaitra Chaveli) to the results reported herein.

References

1. Tu, K.N. (2007) *Solder Joint Technology: Materials, Properties, and Reliability*, Springer Science + Business Media, LLC, New York, NY.
2. Subramanian, K.N. (2007) *Lead-Free Electronic Solders: A Special Issue of the Journal of Materials Science: Materials in Electronics*, Springer Science + Business Media, LLC.
3. Kang, S.K., Lauro, P.A. Shih, D.Y. *et al.* (2005) Microstructure and mechanical properties of lead free solders and solder joints used in microelectronic applications. *IBM J. Res. Dev.*, **49**, 607–620.
4. Choi, S., Bieler, T.R. Lucas, J.P., and Subramanian, K.N. (1999) Characterization of the growth of intermetallic interfacial layers of Sn-Ag and Sn-Pb eutectic solders and their composite solders on Cu substrate during isothermal long-term aging. *J. Electron. Mater.*, **28**, 1209–1215.
5. Snugovsky, I., Perovic, D.D., and Rutter, J.W. (2005) Experiments on the aging of Sn-Ag-Cu solder alloys. *Powder Metall.*, **48**, 193–198.
6. Guo, F., Choi, S. Lucas, J.P., and Subramanian, K.N. (2001) Microstructural characterization of reflowed and isothermally-aged Cu and Ag particulate reinforced Sn-3.5Ag composite solders. *Solder. Surf. Mount Technol.*, **12**, 7–18.
7. Allen, S.L., Notis, M.R. Chromik, R.R., and Vinci, R.P. (2004) Microstructural evolution in lead-free solder alloys: Part I. Cast Sn-Ag-Cu eutectic. *J. Mater. Res.*, **19**, 1417–1424.
8. Dutta, I. (2003) A constitutive model for creep of lead-free solders undergoing strain-enhanced microstructural coarsening: A first report. *J. Electron. Mater.*, **32**, 201–207.
9. Fix, A.R., Lopez, G.A. Brauer, I. *et al.* (2005) Microstructural development of Sn-Ag-Cu solder joints. *J. Electron. Mater.*, **34**, 137–142.
10. Fix, A.R., Nuchter, W., and Wilde, J. (2008) Microstructural changes of lead-free solder joints during long-term aging, thermal cycling and vibration fatigue. *Solder. Surf. Mt. Tech.*, **20**, 13–21.
11. Kumar, P., Cornejo, O., Dutta, I. *et al.* (2008) Joint Scale Dependence of Aging Kinetics in Sn-Ag-Cu Solders. *10th Electronics Packaging Technology Conference (EPTC), Singapore*, pp. 903–909.
12. Dutta, I., Pan, D. Marks, R.A., and Jadhav, S.G. (2005) Effect of thermo-mechanically induced microstructural coarsening on the evolution of creep response of SnAg-based microelectronic solders. *Mater. Sci. Eng. A Struct.*, **410–411**, 48–52.
13. Dutta, I., Kumar, P., and Subbarayan, G. (2009) Microstructural coarsening in Sn-Ag-based solders and its effects on mechanical properties. *JOM-J. Min. Met. Mat. S.*, **61**(06), 29–38.
14. Pang, H.L.J., Tan, K.H. Shi, X.W., and Wang, Z.P. (2001) Microstructure and intermetallic growth effects on shear and fatigue strength of solder joints subjected to thermal cycling aging. *Mater. Sci. Eng. A Struct.*, **307**, 42–50.
15. Lee, T.Y., Choi, W.J., Tu, K.N. *et al.* (2002) Morphology, kinetics, and thermodynamics of solid-state aging of eutectic SnPb and Pb-free solders (Sn-3.5Ag, Sn-3.8Ag-0.7Cu and Sn-0.7Cu) on Cu. *J. Mater. Sci.*, **17**, 291–301.

16. Chana, Y.C., Soa, A.C.K., and Laib, J.K.L. (1998) Growth kinetic studies of Cu–Sn intermetallic compound and its effect on shear strength of LCCC SMT solder joint. *Mater. Sci. Eng. B*, **55**, 5–13.
17. Zribi, A., Clark, A., Zavalij, L. *et al.* (2001) The growth of intermetallic compounds at Sn-Ag-Cu Solder/Cu and Sn-Ag-Cu Solder/Ni interfaces and the associated evolution of the solder microstructure. *J. Electron. Mater.*, **30**, 1157–1164.
18. Suh, D., Kim, D.W., Liu, P. *et al.* (2007) Effects of Ag content on fracture resistance of Sn–Ag–Cu lead-free solders under high-strain rate conditions. *Mater. Sci. Eng. A Struct.*, **460–461**, 595–603.
19. Ho, E., Tsai, R.Y. Lin, Y.L., and Kao, C.R. (2002) Effect of Cu concentration on the reactions between Sn-Ag-Cu solders and Ni. *J. Electron. Mater.*, **31**, 584–590.
20. Butterworth-Heinemann (1992) *Smithells Metals Reference Book*, 7th edn, Brook GB, Brandes EA.
21. Sidhu, R. and Chawla, N. (2006) Three-dimensional (3D) visualization and microstructure-based modeling of deformation in a Sn-rich solder. *Scr. Mater.*, **54**, 1627–1631.
22. Underwood, E.E. (1970) *Quantitative Stereology*, Addison-Wesley Publishing, Menlo Park.
23. Lu, H.Y., Balkan, H., and Ng, K.Y.S. (2006) Effect of Ag content on the microstructure development of Sn-Ag-Cu interconnects. *J. Mater. Sci.: Mater. Electron.*, **17**, 171–188.
24. Vianco, P.T., Rejent, J.A., and Kilgo, A.C. (2004) Creep behavior of the ternary 95.5Sn-3.9Ag-0.6Cu solder: Part II-Aged condition. *J. Electron. Mater.*, **33**, 1473–1484.
25. Xiao, Q., Nguyen, L., and Armstrong, W.D. (2004) Aging and Creep Behavior of Sn3.9Ag0.6Cu Solder Alloy. *Electronic Components and Technology Conference (ECTC)*, 2, 1325–1332.
26. Dutta, I., Pan, D. Marks, R.A., and Jadhav, S.G. (2005) Effect of thermo-mechanically induced microstructural coarsening on the evolution of creep response of SnAg-based microelectronic solders. *Mater. Sci. Eng. A Struct.*, **410–411**, 48–52.
27. Sidhu, R.S., Deng, X., and Chawla, N. (2008) Microstructure characterization and creep behavior of Pb-free Sn-Rich solder alloys: Part II. creep behavior of bulk solder and solder/copper joints. *Metall. Mater. Trans. A*, **39**, 349–362.
28. Song, H.G., Morris, J.W., and Hua, F. (2002) Anomalous creep in Sn-rich solder joints. *Mater. Trans.*, **43**, 1874–1853.
29. Rist, M.A., Plumbridge, W.J., and Cooper, S. (2006) Creep-constitute behavior of Sn-3.8Ag-0.7Cu solder using an internal stress approach. *J. Electron. Mater.*, **35**, 1050–1058.
30. Shin, S.W. and Yu, J. (2005) Creep deformation of Sn-3.5Ag-xCu and Sn-3.5Ag-xBi solder joints. *J. Electron. Mater.*, **34**, 188–195.
31. Guo, Z., Pao, Y.H., and Conrad, H. (1995) Plastic deformation kinetics of 95.5Sn4Cu0.5Ag solder joints. *J. Electron. Packag.*, **117**, 100–104.
32. Kerr, M. and Chawla, N. (2004) Creep deformation behavior of Sn-3.5Ag solder/Cu couple at small length scales. *Acta Mater.*, **52**, 4527–4535.
33. Dutta, I., Park, C., and Choi, S. (2004) Impression creep characterization of rapidly cooled Sn-3.5Ag solders. *Mater. Sci. Eng. A Struct.*, **379**, 401–410.
34. Huang, M.L., Wang, L., and Wu, C.M.L. (2002) Creep behavior of eutectic Sn-Ag lead-free solder alloy. *J. Mater. Res.*, **17**, 2897–2903.
35. Mathew, M.D., Yang, H. Movva, S., and Murty, K.L. (2005) Creep deformation characteristics of tin and tin-based electronic solder alloys. *Metall. Mater. Trans. A*, **36**, 99–105.
36. Bhate, D., Chan, D., Subbarayan, G. *et al.* (2008) Constitutive behavior of Sn3.8Ag0.7Cu and Sn1.0Ag0.5Cu alloys at creep and low strain rate regimes. *IEEE T. Compon. Pack. Technol.*, **31**, 622–633.
37. Kumar, P., Huang, Z., Chavali, S.,*et al.* (2010) A thermomechanical history dependent microstructurally adaptive model for primary and secondary creep of Sn-Ag based Solders. *IEEE T. Compon. Pack. T.* (in press).

38. Park, C., Long, X., Haberman, S. *et al.* (2007) A comparison of impression and compression creep behavior of polycrystalline Sn. *J. Mater. Sci.*, **42**, 5182–5187.
39. Brown, L.M. and Ham, R.K. (1971) *Dislocation-Particle Interactions in Strengthening Methods in Crystals*, Elsevier, Amsterdam.
40. Lagneborg, R. (1973) Bypassing of dislocation past particles by a climb mechanism. *Scr. Metall. Mater.*, **7**, 605–614.
41. Arzt, E. and Rosler, J. (1988) The kinetics of dislocation climb over hard particles-II. Effects of an attractive particle-dislocation interaction. *Acta Metall. Mater.*, **36**, 1053–1060.
42. Rosler, J. and Arzt, E. (1990) A new model-based creep equation for dispersion strengthened materials. *Acta Metall. Mater.*, **38**, 671–683.
43. Huang, M.L., Wang, L., and Wu, C.M.L. (2002) Creep behavior of eutectic Sn-Ag lead-free solder alloy. *J. Mater. Res.*, **17**, 2897–2903.
44. Adeva, P., Caruana, G. Ruano, O.A., and Torralba, M. (1995) Microstructure and high-temperature mechanical properties of tin. *Mater. Sci. Eng. A Struct.*, **194**, 7–23.
45. Reinikainen, T. and Kivilahti, T.J. (1999) Deformation behavior of dilute SnBi (0.5 to 6 At. Pct) solid solutions. *Metall. Mater. Trans. A*, **30**, 23–132.
46. Evans, R.W. and Wilshire, B. (1985) *Creep of Metals and Alloys*, The Institute of Metals, London.
47. Garofalo, F., Richmond, C. Domis, W.F., and von Gemmingen, F. (1963) *Strain-time, rate-stress, and rate-temperature relations during large deformations in creep, Joint International Conference on Creep, London*, 1, pp. 31–39.
48. Li, J.C.M. (1963) A dislocation mechanism of transient creep. *Acta Metall. Mater.*, **11**, 1269–1270.
49. Dobes, F. and Dobes, J. (1985) Description of primary creep by means of the stochastic model. *Czech. J. Phys.*, **B35**, 333–336.
50. Garofalo, F. (1965) *Fundamentals of Creep and Creep Rupture in Metals*, MacMillan, New York.
51. Evans, W.J. and Wilshire, B. (1970) The high temperature creep and fracture behavior of 70–30 alpha brass. *Metall. Trans.*, **1**, 2133–2139.
52. Evans, W.J. and Wilshire, B. (1968) Transient and steady-state creep behavior of nickel, zinc, and iron. *Trans. Am. I. Min. Met. Eng.*, **242**, 1303–1307.
53. Klopp, W.D., Titran, R.H., and Sheffler, K.D. (1980) Long-time creep behavior of the tantalum alloy Astar 8llC. NASA TP.-1691, 1–20.
54. Kumar, P., Dutta, I., Sarihan, V. et al. (2008) Effects of strain rate and aging on deformation and fracture of Sn-Ag-Cu solder joints, 11th thermal and thermomechanical phenomena in electronic systems (Itherm.), *Lake Buena Vista*, pp. 660–667.
55. Kumar, P., Huang, Z., and Dutta, I. (2009) Roles of process and microstructural parameters of mixed mode fracture of Sn-Ag-Cu solder joints under dynamic loading conditions. *Proc. InterPACK, San Francisco*.
56. Choi, S.H., Song, B.G. Kang, K.J., and Fleck, N.A. (2001) Fracture of a ductile layer constrained by stiff substrates. *Fatigue Fract. Eng. M.*, **23**, 1–13.
57. Nayeb-Hashemi, H. and Yang, P. (2001) Mixed mode I/II fracture and fatigue crack growth along 63Sn-37Pb solder/brass interface. *Int. J. Fatigue*, **23**, S325–S335.
58. Kang, K.J., Kim, D.H., and Choi, S.H. (2002) Effects of mode mix upon fracture behavior of a solder joint. *Int. J. Fracture*, **113**, 195–212.
59. Sun, Y. and Pang, J.H.L. (2008) Experimental and numerical in investigations of near-crack-tip deformation in a solder alloy. *Acta Mater.*, **56**, 537–548.
60. Siow, K.S. and Manoharan, M. (2005) Mixed mode fracture toughness of lead-tin and tin-silver solder joints with nickel-plated substrate. *Mater. Sci. Eng. A Struct.*, **404**, 244–250.
61. Hayes, S.M., Chawla, N., and Frear, D.R. (2009) Interfacial fracture toughness of Pb-free solders. *Microelectron. Reliab.*, **49**, 269–287.

62. Long, X., Dutta, I. Sarihan, V., and Frear, D.R. (2008). Deformation behavior of Sn-3.8Ag-0.7Cu solder at intermediate strain rates: effect of microstructure and test conditions. *J. Electron. Mater.*, **38**, 2746–2755.
63. Arcan, M., Hashin, Z., and Voloshin, A. (1978) A method to produce uniform plane- stress states with applications to fiber-reinforced materials. *Exp. Mech.*, **28**, 141–146.
64. Hutchinson, J.W. and Suo, Z. (1991) Mixed mode cracking in layered materials. *Adv. Appl. Mech.*, **29**, 63–191.
65. Shi, X.Q., Zhang, X.R., and Pang, J.H.L. (2006) Determination of interface fracture toughness of adhesive joint subjected to mixed-mode loading using finite element method. *Int. J. Adhes. Adhes.*, **26**, 249–260.
66. Pang, H.L.J. and Seetoh, C.W. (1997) A compact mixed mode (CMM) fracture specimen for adhesive bonded joints. *Eng. Fract. Mech.*, **57**, 57–65.
67. (2008) ASTM, E561-05: Standard test method for, K-R, curve, determination. Annual book of, ASTM, standards, 04.01 pp. 593–611.
68. Majumdar, B.S. and Ahmad, J. (1991) Fracture of ceramic-metal joints: Zirconia/nodular cast iron system. In: *Metal-Ceramic Joining* (eds P. Kumar and V.A. Greenhut), TMS, pp. 67–97.

9

Microstructure and Thermomechanical Behavior Pb-Free Solders

D.R. Frear
Freescale Semiconductor, 2100 East Elliot Road, Tempe, AZ 85284, USA

9.1 Introduction

An electronic package integrates metal conductors, organic/ceramic dielectrics and semiconductors into a functional device. This variety of materials results in a complex system to build and, increasingly, retain high levels of reliability. Adding to complexity to this situation is European Union's Waste in Electrical and Electronic Equipment (WEEE) and Restriction of Hazardous Substances (RoHS) [1] and the China RoHS [2] directives that ban Pb in electronics. Pb-based alloys have always been the solder alloy of choice for electronic interconnects. The need for Pb-free solders not only changes the solder alloys used for interconnects in electronic packages but also affects other materials in the package due to the need for higher processing temperatures associated with the Pb-free solders. Reliability is influenced by the operation of the device (e.g., power dissipated, current carried, etc.) and the environment (e.g., ambient temperature, temperature changes and imposed mechanical strains). The differences in thermal expansion coefficients of the materials in a package (ranging from 3 ppm/°C for Si to >100 ppm/°C for some organic dielectrics) results in imposed strains and potential cracks when the temperature changes.

Thermomechanical fatigue occurs when materials with different coefficient of thermal expansion (CTE) are joined and used in an environment that experiences cyclic temperature fluctuations resulting in imposed cycling strain. Thermomechanical fatigue is a major deformation mechanism concern for solder interconnects in electronic packages from flip-chip interconnects to board mount solder joints. Even small temperature fluctuations can

Lead-free Solders: Materials Reliability for Electronics, First Edition. Edited by K. N. Subramanian.

have a large effect, depending upon the joint thickness and CTE difference of the joined materials. The imposed shear strain on solder joints due to bonding materials with differing CTE can be defined as:

$$\gamma = \Delta\alpha * \Delta T^* a/h \tag{9.1}$$

where γ is the shear strain, $\Delta\alpha$ is the difference in CTE of the joined materials, ΔT is the temperature difference that occurs over a thermal cycle, a is the distance from the neutral point of the joined materials and h is the thickness of the solder joint. After a critical number of thermal excursions, such as machine on/off cycles or changes in ambient temperature, the solder joints experience cyclical damage and are susceptible to fatigue failure. The failure of the solder joints can lead to electrical opens and device failure. The type and magnitude of strains in solder joints under conditions of thermomechanical fatigue are often quite complex. For surface-mount applications, the strain is nominally in shear. However, tensile and mixed-mode strains can occur due to bending of the chip-carrier or board.

In addition to the thermomechanical strain, the microstructure of the solder alloys defines the behavior of the interconnect. Therefore, the thermomechanical fatigue behavior of solder joints must be fundamentally understood from a microstructural perspective to be able to improve and predict the lifetime of solder joints used in electronic applications.

Microstructure defines behavior, so the focus of this chapter is solder microstructure under conditions of thermomechanical fatigue. Included in this discussion are both Pb-based and Pb-free solder as it is illustrative to compare and contrast the alloy systems.

9.2 Sn-Pb Solder

The as-solidified microstructure of near-eutectic Sn-Pb solders consists of lamellar and globular regions that, in optical micrographs, appear as dark Pb-rich and light appearing Sn-rich phases (Figure 9.1). The regions of similarly oriented lamella form separate individual

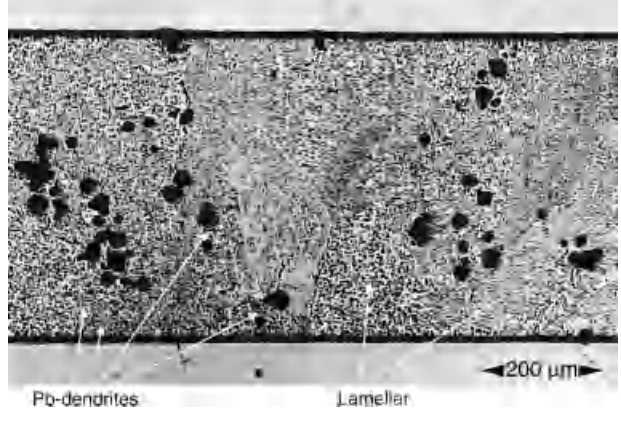

Figure 9.1 *Optical micrograph of the Sn-Pb near eutectic as-solidified microstructure. Light phases are Sn-rich, dark phases are Pb-rich.*

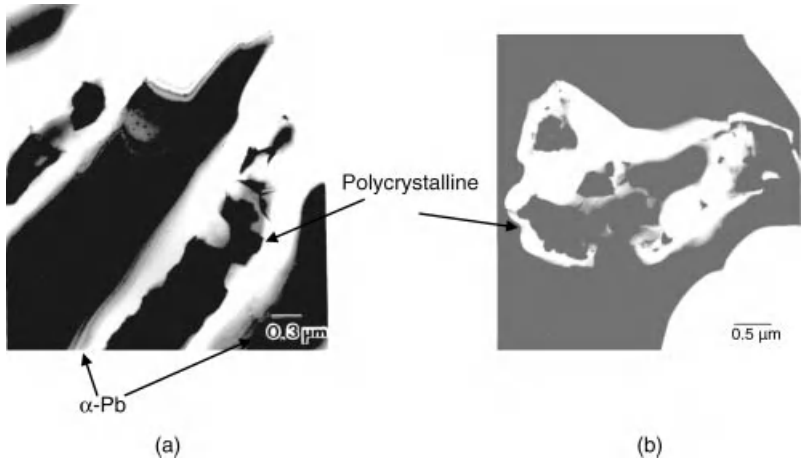

Figure 9.2 *TEM micrographs of the near-eutectic Sn-Pb microstructure. (a) lamellar region and (b) globular region.*

cells, or colonies. These colonies develop during solidification of the eutectic and initiate at nuclei on the solid base metal surface. The solidifying lamella grow into the molten solder and eventually intersect with other solidifying cells. The regions where the cells intersect are the last regions of the joint to solidify and exhibit the coarsest structure (i.e. largest lamellar spacing). Consequently, these regions also contain the majority of rejected impurities in the solder. Eutectic colonies are often mistaken for individual solder grains. The colonies often dictate the mechanical response of the solder but the actual grain size of the solder is much smaller because individual Sn and Pb lamella are polycrystalline, as shown in the TEM micrograph of Figure 9.2 that depicts the grain structure. The Pb grains are much larger (on the order of 1 μm) than the Sn grains (0.25 μm) as shown in the TEM micrograph. High-angle grain boundaries exist between the grains, as evidenced by the contrast between the Sn grains. It is interesting to note that when the individual lamella form during solidification they are single crystals. Stresses that develop due to the difference in thermal expansion coefficients between Sn and Pb upon cooling results in recrystallization of both the Sn- and Pb-rich phases. The Pb-rich regions do not have the small grains observed in Sn-rich regions because slip deformation is much easier to achieve with the face-centered-cubic crystal structure of Pb compared to the body-centered-tetragonal (BCT) structure of the Sn. Tin does not have a simple slip system to dissipate strain so recrystallization occurs. The as-solidified structure of 60Sn-40Pb is metastable due to the large surface area created as a consequence of the fine-phase spacing. Recalling that surface area represents internal energy, microstructural evolution of this alloy results from the fact that there is a substantial amount of internal energy stored in the microstructure. Thus, with the application of external energy (i.e. heat) the microstructure evolves and coarsens in a manner that lowers its high-energy configuration (i.e. one with a reduced overall surface area).

The combination of strain and temperature during thermomechanical fatigue has a large effect on the microstructure, and microstructural evolution of eutectic Sn-Pb solder

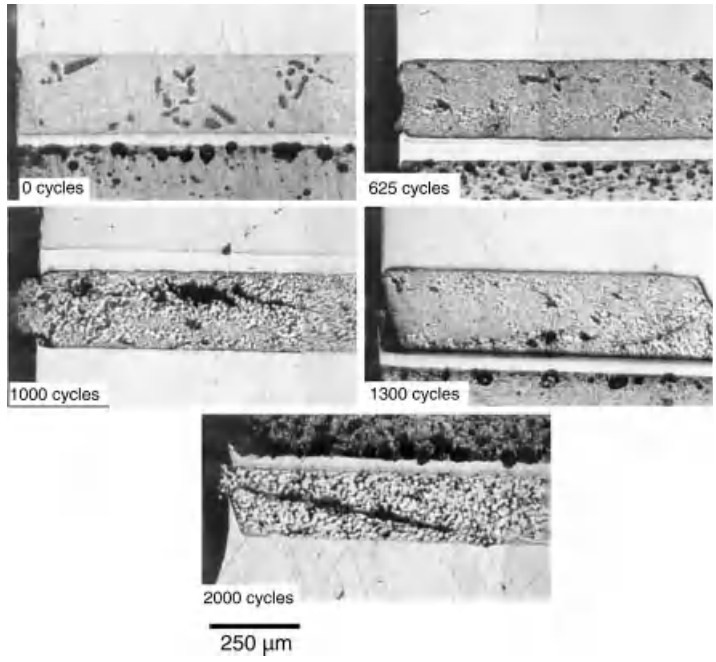

Figure 9.3 *Optical micrographs of the near-eutectic Sn-Pb microstructure after various degrees of thermomechanical fatigue damage (increasing number of thermal cycles −55 °C to 125 °C). The microstructure undergoes heterogeneous coarsening in regions of high strain that eventually crack and fail.*

joints [3–6]. The microstructural evolution of near-eutectic Sn-Pb solder as a function of the number of thermal cycles (−55° to 125 °C) is shown in Figure 9.3.

Microstructures evolve through deformation that concentrates at the colony boundaries closely parallel to the direction of imposed shear strain, causing the cells to slide or rotate relative to one another. The structure within the cell boundaries becomes slightly coarsened relative to the remaining solder-joint microstructure and, thus are the 'weak links' of the joint. Damage (in the form of defects or dislocations) is created at the cell boundaries at the low-temperature portion of a thermal cycle. As the temperature rises, the deformation is annealed by recrystallization or stress-assisted diffusion, where material diffuses to regions of high stress. This results in coarsening the Sn-rich and Pb-rich grains and phases in colony boundaries. The heterogeneously coarsened colony boundaries are weaker than the rest of the joint and any further deformation concentrates in the coarsened regions resulting in further coarsening.

Failure eventually occurs due to cracks that form in the coarsened regions of a joint as shown in Figure 9.4. The first indications of impending failure are associated with cracking of coarsened Sn-rich grains in the heterogeneous region whose initial as-solidified grain size is in the submicrometer range. As cracks initiate due to thermomechanical fatigue, the Sn-grain size grows to a range of about 5 to 10 μm. Failure occurs when grains can no longer slide and rotate to accommodate the imposed strain resulting in intergranular separation.

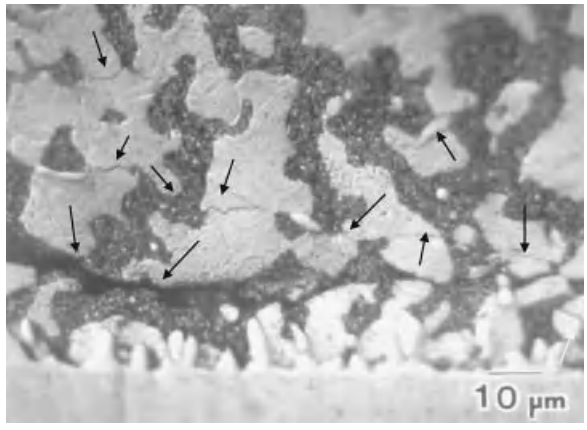

Figure 9.4 *Optical micrograph that shows the cracking of Sn-rich and Pb-rich heterogeneously coarsened phases in near-eutectic Sn-Pb solder.*

9.3 Pb-Free Solders

Pb-free solders alloy are typically Sn-rich. Tin is the primary element that drives wetting and solderability. The alloy additions to Sn are intended to keep the melting point of the resultant alloy relatively low because an increase in the processing temperature of the solder would have a detrimental effect on the polymer materials in the electronic assembly that have low glass-transition or melting temperatures. Above 260 °C many organic materials used in electronic packaging start to oxidize or char. The melting temperature of eutectic Sn-Pb is 183 °C with a typical processing temperature of joining of 220 °C. The maximum processing temperature for Pb-free solder alloys is 260 °C meaning the melting temperature should not exceed 230 °C. Several alloying alternatives to Pb have been investigated that include: Ag, Bi, Cd, Cu, In, Sb, Zn. [7–11]. The candidate Pb-free solder alloy should also have similar or better thermal, mechanical and electrical behavior as eutectic Sn-Pb. A maximum liquidus temperature of 230 °C and a narrow liquid + solid melting range of no more than 30 °C has been recommended by several consortia of manufacturers and producers due to constraints on processing and manufacturing tools and materials. [8] A chart of the melting temperature of potential solder alloys is shown in Figure 9.5.

Many of the alloy additions can be eliminated from consideration for issues including: toxicity (Cd), high cost (In), processing temperature (Sn-Sb melts at 240 °C). Bi can be eliminated because it is a residual of the Pb refinement process. Zn oxidizes quickly and must be reflowed in a reducing environment that is not typically available in the industry. As a result, Sn-Cu, Sn-Ag, and Sn-Ag-Cu have emerged as the primary Pb-free solder alloys. The following is a discussion of the microstructure of these Pb-free alloys and the metallurgical reaction of the solder when it forms a joint including interfacial intermetallic formation. This is followed by a discussion of the mechanical and thermomechanical behavior of these solder alloys.

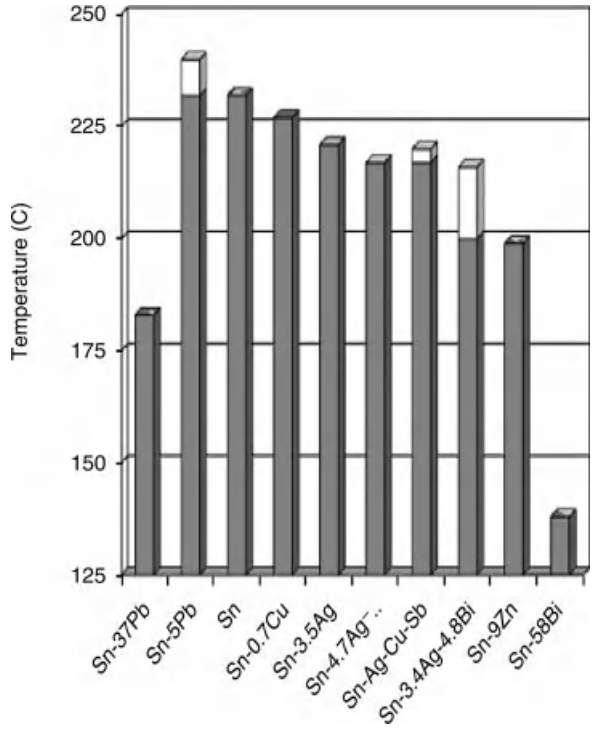

Figure 9.5 *Chart of Pb-free solder temperatures (dark = solidus, light = liquidus).*

9.3.1 Pb-Free Solders Microstructure

Figure 9.6 shows the eutectic Sn-0.7Cu microstructure. This alloy melts at 227 °C and is composed of large Sn-rich grains with a fine dispersion of Cu_6Sn_5 intermetallics. The solder grains form and grow out from the bond-pad interfaces. The grains are large; on the order of 20–50 μm in size. The Sn-Cu binary alloy does not vary from the Sn-0.7Cu eutectic because small changes in composition result in significant increases in melting temperature and increases in two-phase liquid + solid that are undesirable to form electronic interconnects.

The Sn-3.5Ag solder is a eutectic solder alloy with a melting point (221 °C). The Sn-3.5Ag microstructure consists of a fine structure of alternating Sn-rich/Ag_3Sn intermetallic lamella, Figure 9.7. Grain colonies also form in this microstructure but the boundaries are not coarsened. In addition to the fine Ag_3Sn intermetallics, large needles of Ag_3Sn are present and are typically attached to one of the bump-pad interfaces. Similar to the Sn-Cu eutectic alloy, variations in Sn-Ag binary alloys are not found due to small compositional changes dramatically affecting melting temperature.

The Sn-3.8Ag-0.7Cu solder microstructure is shown in Figure 9.8 and is very similar to that of the Sn-3.5Ag. The addition of a small amount of Cu (0.5–2%) lowers the melting point of the Sn-Ag alloy and forms a near-ternary eutectic. In addition to the lamellar structure of Sn/Ag_3Sn intermetallics with large needles of Ag_3Sn there are also discrete Cu_6Sn_5 intermetallics that precipitate throughout the bulk of the solder.

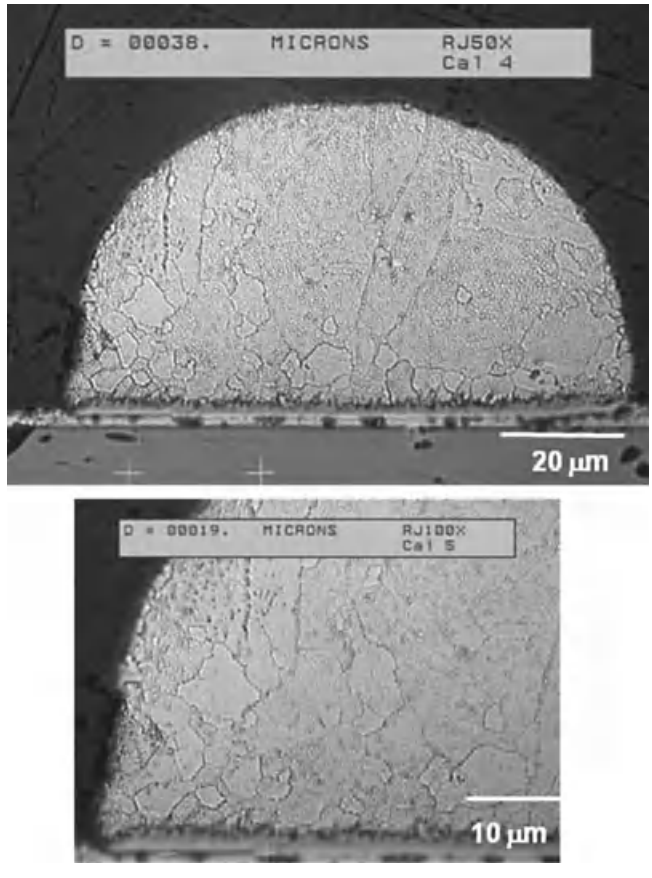

Figure 9.6 *Optical micrograph of the microstructure of Sn-0.7Cu solder on a Cu metallization.*

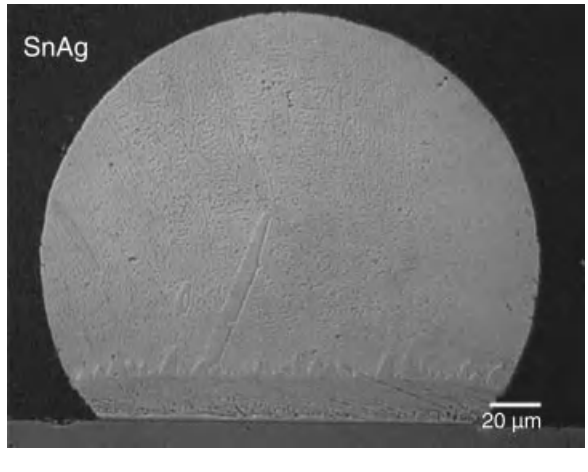

Figure 9.7 *Optical micrograph of the microstructure of Sn-3.5Ag solder on Cu.*

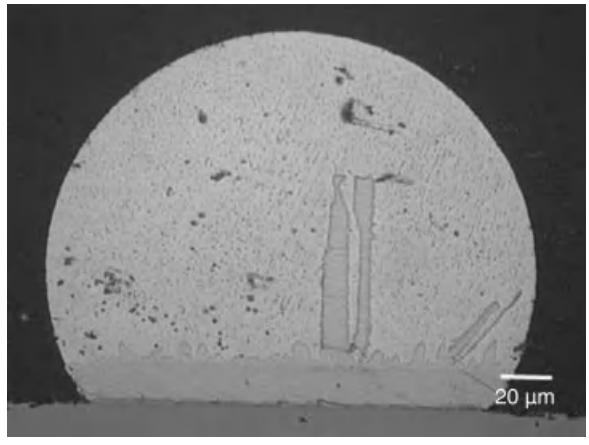

Figure 9.8 *Optical micrograph of the microstructure of Sn-3.8Ag-0.7Cu solder on Cu.*

9.3.2 Interfacial Intermetallic Formation of Pb-Free Solders

The metallization typically used for solder interconnects is Cu or Ni as both are readily wet by Sn when the surfaces are oxide free. Often, Au is plated or sputtered on the Ni to limit oxidation and enhance wetting. The Au layer is typically very thin and dissolves into the solder playing no role on intermetallic formation or joint mechanical behavior.

When molten Sn-based solders come into contact with the Ni or Cu surfaces they wet and react to form interfacial intermetallics. The intermetallics grow out into the solder as rods, or plates, and continue to grow when the solder is in the solid state. Even though all the solders studied are Sn-rich, the morphology and reaction kinetics differ between alloys. The growth of interfacial intermetallics is of concern because the intermetallic is brittle and if it becomes a significant fraction of the solder joint it can act as a site for crack initiation and propagation when the joint is deformed.

On Cu, Sn-37Pb forms a two-phase intermetallic of Cu_6Sn_5 adjacent to the solder and Cu_3Sn adjacent to the Cu. The Cu_3Sn is planar with a columnar grain structure and the Cu_6Sn_5 consists of elongated nodules. On Ni, eutectic Sn-Pb forms irregularly shaped Ni_3Sn_4. The formation and growth of the interfacial intermetallics between Cu, Ni and eutectic Sn-Pb solder are well known [12–14]. The intermetallics follow parabolic growth kinetics and do not extensively spall off into the solder.

The intermetallics formed upon reacting the Sn-Ag, Sn-Cu and Sn-Ag-Cu solders with typical metallizations are the same as found with eutectic Sn-Pb, that is a compound layer of Cu3Sn/Cu6Sn5 forms on Cu and a Ni3Sn4 layer forms on Ni. The kinetics of intermetallic growth is also similar to eutectic Sn-Pb.

Figure 9.9 shows SEM micrographs of the Pb-free solders (compared with eutectic Sn-Pb) on Cu after 2 reflows. The intermetallic that forms is Cu_6Sn_5, no Cu_3Sn was found but it may have been too thin to be observed. The interfacial intermetallic has the same morphology for all the Pb-free alloys as for Sn-Pb eutectic. The intermetallic consists of regularly spaced nodules of Cu_6Sn_5. The Ag-containing solders all have large Ag_3Sn intermetallics that are attached to the Cu_6Sn_5 interface. All three Pb-free alloys also have

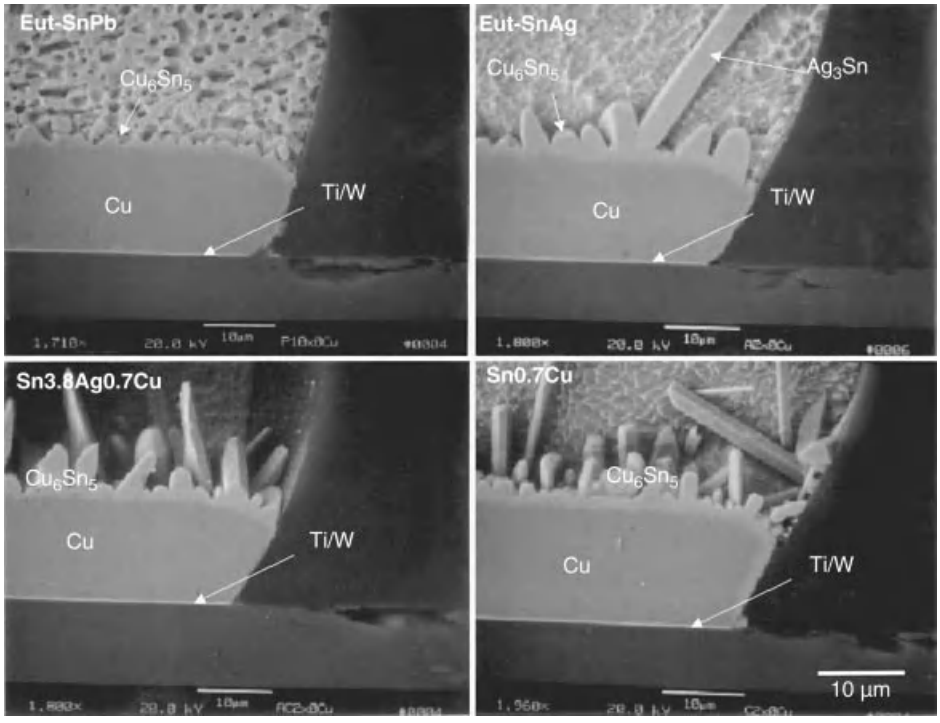

Figure 9.9 *SEM micrographs of the Pb-free solders on Cu compared with eutectic Sn-Pb.*

small discrete particles of Cu_6Sn_5 present in the bulk of the solder. For Sn-0.7Cu, the Cu is present in the solder before joining. For the Sn-3.5Ag solder the Cu_6Sn_5 is present due to the dissolution of some of the Cu into the solder. Spalling of the interfacial intermetallics into the molten solder was not observed and this is believed to be due to the presence of Cu in each of the solders during reflow. The Cu inhibits growth and spalling of the intermetallic because it saturates the solder [15]. Of the three Pb-free alloys on Cu, the Sn-0.7Cu solder structure is the most uniform and has the thinnest intermetallic structure.

One of the concerns of using Sn-rich Pb-free solders is the reaction of the Cu with the solders is feared to be so fast that the metallization will dissolve during reflow. A plot of the Cu consumed after 2 reflows for Sn-Pb and the Pb-free solders is shown in Figure 9.10. The Pb-free solders consume only 10–20% more Cu than Sn-Pb and this is less than 2 µm after 2 reflows. A plot of consumed Cu during solid-state aging is shown in Figure 9.11 for the solders on Cu at 150 °C for 500 and 1000 h. In the solid state, the Cu was consumed at a slower rate in Pb-free solders than for eutectic Sn-Pb. The Pb appears to play a role in accelerating intermetallic growth, perhaps by enhancing Sn diffusion to the intermetallic/solder interface. Sn-0.7Cu had the slowest consumption rate of the Cu metallization.

The intermetallic formation for the Pb-free solders on Ni after 2 reflows is shown in Figure 9.12. Figure 9.12 shows the structure of the interface on electroless Ni-P but the same observations were made for electrolytic Ni metallization. The intermetallic that forms is Ni_3Sn_4. The Ni_3Sn_4 intermetallic between Sn-0.7Cu and Ni is thin and regular and is the

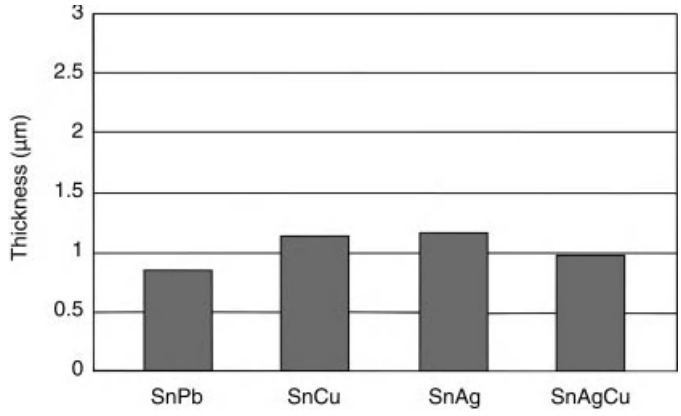

Figure 9.10 *Consumed Cu thickness after 2 reflows for the solders on Cu.*

most uniform of the Pb-free alloys. The Sn-3.5Ag solder on Ni has a different intermetallic morphology that consists of nodules and chunks of Ni_3Sn_4 that spall off into the solder. This morphology has been attributed to the lack of Cu in the solder. It is hypothesized that the Cu acts to saturate the solder with respect to the Ni and inhibits dissolution and spalling of the intermetallic into the solder [16]. However, this mechanism remains to be fully understood.

The consumption of the Ni layer by the formation of Ni_3Sn_4 intermetallic during solid-state aging for each of solder alloy is shown in Figure 9.13 for 1000 h aging at 150 ° and 170 °C. Figure 9.13 shows results on an electroless Ni-P/Au (similar results were observed on the electrolytic Ni). For these solders, less than 2 μm transformed into Ni_3Sn_4. The Ni reacts slowly with Sn and is why it is often preferred for Sn-rich solders. The Pb-free solders consume more Ni and form more intermetallic than Sn-Pb eutectic solder, but this increase is

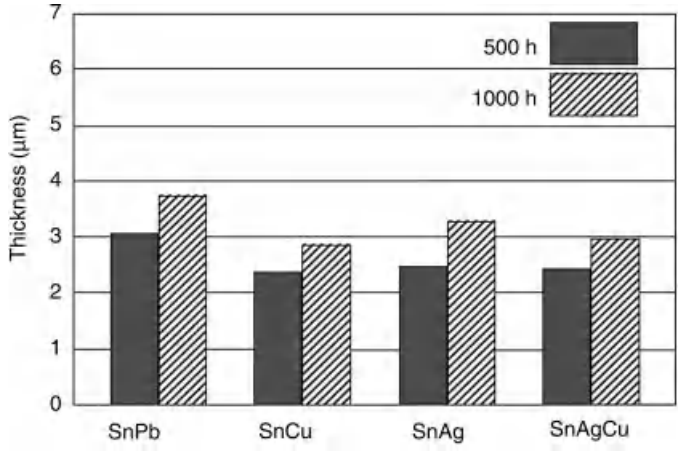

Figure 9.11 *Bar chart of the consumed Cu thickness of the solders on Cu after aging for 500 and 1000 h at 150 °C.*

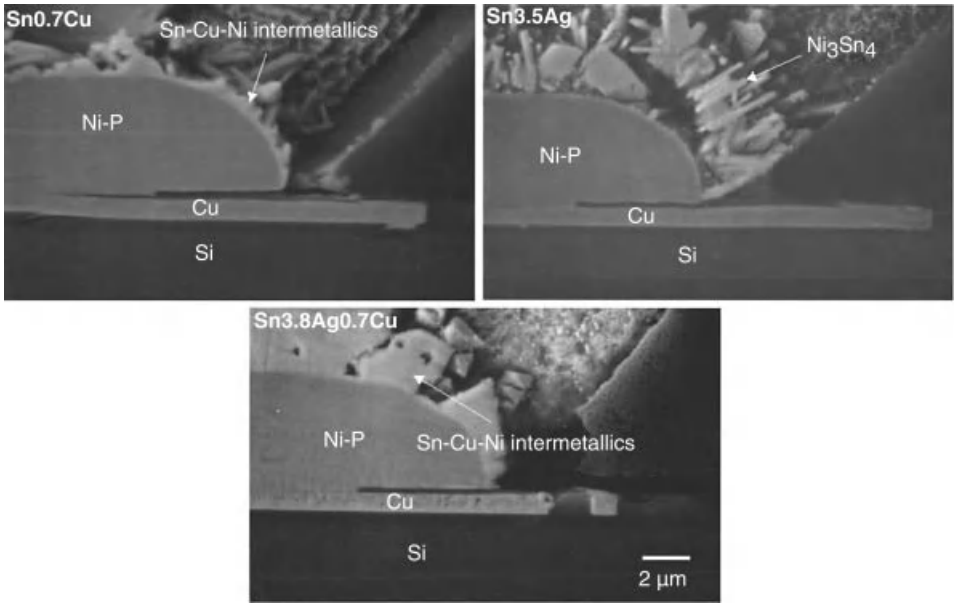

Figure 9.12 *SEM micrographs of the Pb-free solders on electroless Ni showing the morphology of the interfacial intermetallics.*

relatively small. The Ag_3Sn intermetallic plates are attached to the Ni_3Sn_4 interfacial intermetallics, similar to that observed on Cu metallizations.

9.3.3 Mechanical Metallurgy of Pb-Free Solder Alloys

The solder joint must be both an electrical and mechanical interconnect in an electronic package. However, the solder also cannot impose significant strain to the semiconductor

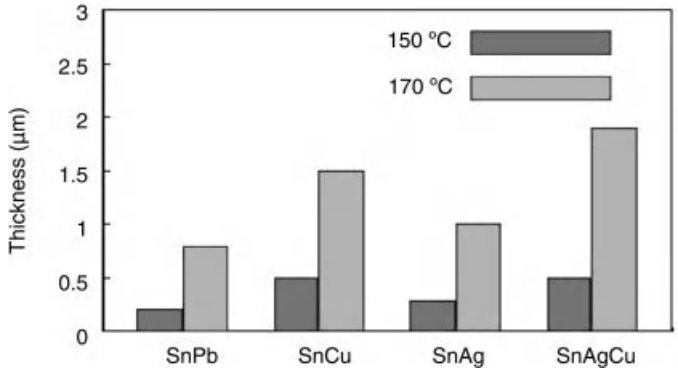

Figure 9.13 *Thickness of consumed Cu for the solders on electroless Ni after 1000 h aging at 150°C and 170°C.*

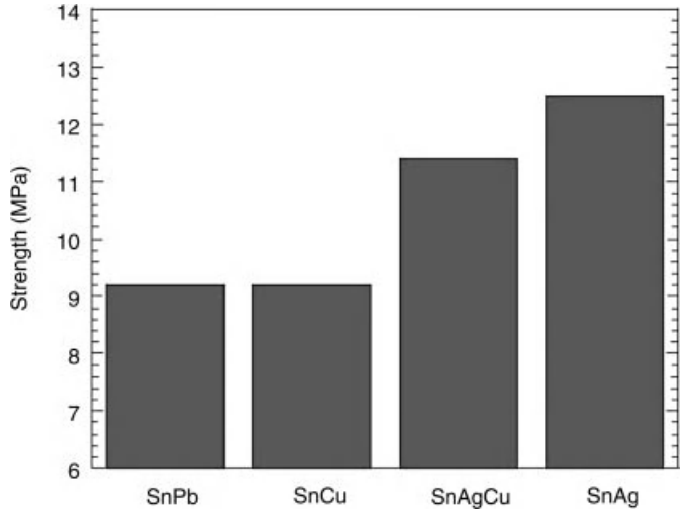

Figure 9.14 *Shear strength of the solder alloys.*

device or the device could crack and fail. The shear strength of the Pb-free solder alloys compared to Sn-Pb eutectic is shown in Figure 9.14. The strength of the solder alloys is a measure of the ability of the interconnect to be compliant to the imposition of strain. Sn–37Pb and Sn–0.7Cu solder joints have similar values of shear strength. The Sn–3.5Ag solder alloy has the highest shear strength (25% greater than Sn–0.7Cu) with the Sn–3.8Ag–0.7Cu having a slightly lower strength than Sn–3.5Ag. The shear failure for all joints tested occurred solely through the solder. The solder-joint strength and failure mode were similar to, and independent of, the metallization the solder was reflowed upon. Eutectic Sn–3.5Ag has shown susceptibility to brittle interfacial delamination in tensile [12] and shear tests [17] for surface-mount interconnects. The failure occurs at the intermetallic/solder interface where one side of the fracture shows intermetallic and the other side reveals an impression of where the intermetallic grew into the solder.

Creep behavior is important for solder interconnects because the solders deform to relax stress over time when held at a constant strain, which is what occurs during thermo-mechanical fatigue. The creep rate of a solder must be sufficiently fast so that the strain is minimized in joined bulk components. However, the creep rate must not be so fast that the components move over time. The creep behavior of solders can be summarized empirically using one of two equations:

$$\mathrm{d}\gamma/\mathrm{d}t = A\sigma^{n}\mathrm{e}^{-Q/RT} \tag{9.2a}$$

$$\mathrm{d}\gamma/\mathrm{d}t = A\,\sinh(\alpha\sigma)^{n}\mathrm{e}^{-Q/RT} \tag{9.2b}$$

where $\mathrm{d}\gamma/\mathrm{d}t$ is the creep rate in shear, A is a constant, α is the stress constant, σ is the flow stress, n is the stress exponent, and Q is the creep activation energy. Equation (9.2a) works well for creep mechanisms that remain constant over all test temperatures. Equation (9.2b) is the Garofalo, or sinh, creep relation that captures up to two different creep mechanisms in

Table 9.1 *Constitutive creep relations.*

Alloy	A (s^{-1})	α	n	Q (kJ/mol)	Ref.
Sn-40Pb	2.48×10^{4}	0.0793	3.04	56.9	[18]
Sn-40Pb	1.1×10^{-12}		6.3	20	[30]
Sn-3.5Ag	9.3×10^{-5}		6.05	61.2	[31]
Sn-3.8Ag-0.7Cu	2.6×10^{-5}		3.69	36	[31]
Sn-1Cu	1.41×10^{8}		8.1	79.4	[32]

a single formulation. Creep results for Pb-free solders can be found in the published literature [17–29].

Table 9.1 shows fitted results of creep tests on Pb-free solders using Eqs (9.2a) and (9.2b). The creep rate of high Sn-content solders is slower than Sn-Pb.

Eutectic Sn-3.5Ag has greater strength and a higher creep resistance than eutectic Sn-Pb [33]. The creep behavior Sn-3.5Ag has been found to have one of the highest levels of creep resistance of the Pb-free alloys [34]. The steady-state creep behavior for Sn-Cu has been found to be much faster than eutectic Sn-Pb and Sn-Ag-Cu faster than Sn-Pb. A faster creep rate is desired for electronic packaging applications because damage can be accommodated by the solder, rather than the more brittle joined components. Furthermore, a faster creep rate often translates into a longer thermomechanical fatigue lifetime.

9.3.4 Thermomechanical Fatigue Behavior of Pb-Free Solder Alloys

Temperature variations encountered during use conditions, combined with the materials of differing coefficients of thermal expansion in the electronic package, result in cyclic temperature and strain on the solder joints. Glazer presented a summary of work on Pb-free solders and concluded that additional data on thermomechanical fatigue data for low melting point solders are is growing, but more is needed [7, 35].

A diagram of thermal fatigue life vs. applied strain range is shown in Figure 9.15, using the characteristic life extracted from Weibull plots of the thermomechanical fatigue data and thermal strain calculated for the 0° to 100 °C and −40° to 125 °C thermal ranges. The thermal fatigue failure data follows a power law function. In Figure 9.15, the thermal fatigue data from Sn-0.7Cu solder joints on both NiP and Cu metallizations fall onto the same straight line. The thermal fatigue performance of Sn-0.7Cu is metallization independent and is confirmed by the failure analysis discussed below, where failures occurred solely through the solder joint. Sn-3.5Ag has the shortest characteristic thermal fatigue lifetime. Sn-Ag-Cu has a slightly longer lifetime than eutectic Sn-Pb solder alloy.

Pb-free solder alloys have a different deformation behavior, and lifetime, than Sn-Pb alloys and representative microstructures after thermomechanical fatigue are shown in Figure 9.16.

The eutectic Sn-0.7Cu solder exhibited a failure mode that differed from the other solder alloys studied. The initiation and propagation of fatigue cracks is through the grain boundaries in the Sn-0.7Cu solder, as shown in Figure 9.16. The fatigue cracks initiated on the highest point of strain in the joint, closer to the edge of the joint, and then propagated across to the center of the joint. After thermal cycling, the surface of the solder bumps is no longer smooth. The Sn-0.7Cu solder deforms by grain-boundary sliding. The cracks were

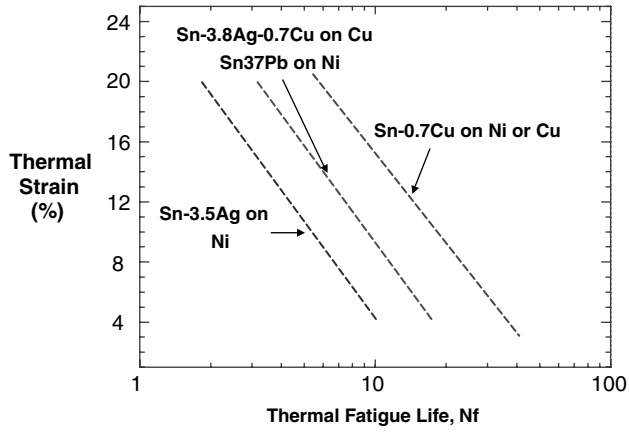

Figure 9.15 *Plot of thermal fatigue life as a function of applied thermal strain for the Sn-3.5Ag, Sn-37Pb, Sn-3.8Ag-0.7Cu and Sn-0.7Cu.*

observed to propagate at the grain boundaries significantly removed from the solder/metallization interface, near the center of the joint. No microstructural evolution is observed in Sn-0.7Cu in thermomechanical fatigue. This solder is the most compliant in thermal fatigue and undergoes massive deformation before failing by crack propagation.

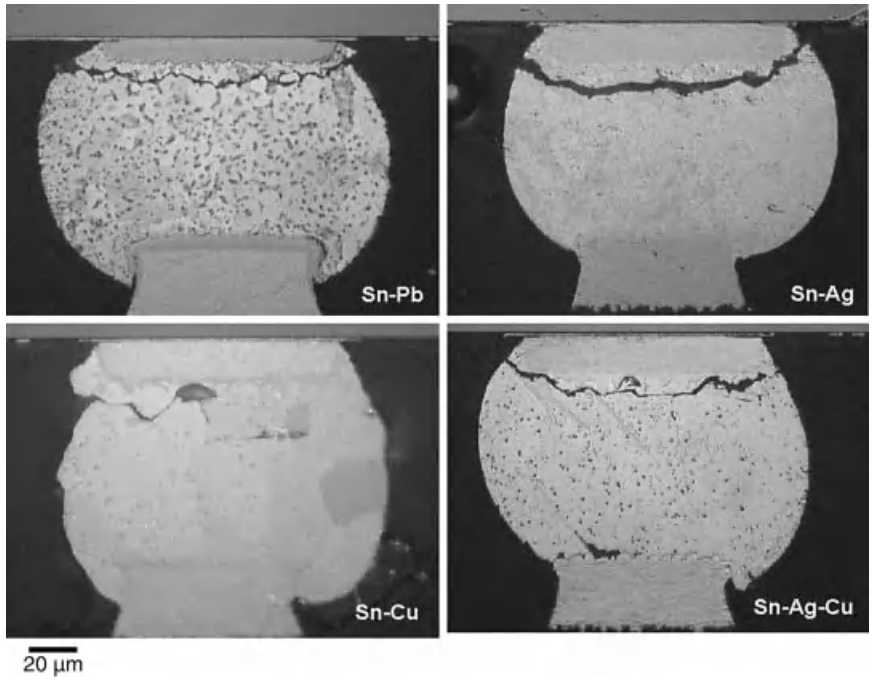

Figure 9.16 *Optical micrographs of solder joint cross sections of solder joints on Cu on organic substrates after thermal cycling 0° to 100°C.*

The failure behavior of Sn-3.5Ag solder and the Sn-3.8Ag-0.7Cu alloy behave similarly with crack initiation and propagation at the highest strain region of the solder joint and cracks can form through the intermetallics and at the intermetallics/solder interface. Sn-3.5Ag and Sn-Ag-Cu eutectic-based solders, experience thermomechanical fatigue damage and failure at Sn grain boundaries. The microstructural evolution in these alloys tends to be phase coarsening with minimal grain size coarsening. Sn-Ag-X alloys tend to have longer thermomechanical fatigue lifetimes than near-eutectic Sn-Pb solders (Figure 9.15). These alloys typically have longer fatigue lives than Sn-Pb alloys and do not exhibit evidence of extensive microstructural evolution during thermomechanical fatigue. Failure is observed in the portion of solder joints that experiences the highest strain, with intergranular cracks formed at Sn-grain boundaries. Typically, the Sn grain size is slightly larger in the failed region compared with the rest of the joint. Tin grains coarsen at high-strain regions due to enhanced diffusivity in the damaged regions during thermal cycling. Tin grains coarsen to the point where, as the grains slide and rotate to accommodate the strain, voids are created that are too large to be backfilled by diffusion. The surface of the solder bump exhibited no deformation with the damage concentrated at the solder/intermetallic interface. Conversely, eutectic Sn-3.5Ag solder has a shorter thermal fatigue lifetime than the other Pb-free alloys. This appears to be due to the higher strength of this alloy (Figure 9.14) that may be due to the large Ag_3Sn intermetallic plates (Figure 9.17) present in the joints that increase the structural strength and reduce the compliance of the solder thereby shortening the thermal fatigue life.

The weaker, more compliant, and faster steady-state creep rate solders (e.g., Sn-0.7Cu) have a longer thermomechanical fatigue lifetime. Eutectic Sn-Pb has the same low shear strength as Sn-0.7Cu but has a shorter thermal fatigue lifetime due to heterogeneous coarsening that concentrates the strain into a small band in the solder and reduces lifetime. The Sn-0.7Cu alloy undergoes massive deformation during thermal cycling. This deformation protects the semiconductor device and package from damage due to imposed strain. Interestingly, even with significant surface deformation, the crack formation takes longer in

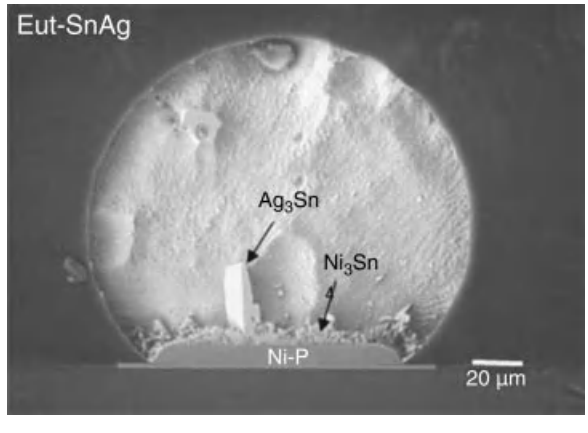

Figure 9.17 *SEM micrograph of Sn-3.6Ag solder with large interfacial Ag_3Sn intermetallic plates.*

Sn-0.7Cu than the other solders that had no surface deformation. The Sn-0.7Cu accommodates the thermal strain by grain-boundary sliding and rotation. The self-diffusion of Sn to accommodate the sliding and rotation is sufficient to delay the formation of cracks. An additional positive aspect of the Sn-0.7Cu solder is that failure is only observed in the solder joint away from the brittle intermetallic/solder interface.

Shear strength and time-dependent deformation have a direct correlation to thermomechanical fatigue performance of Pb-free solders. The weaker, more compliant, and faster steady-state creep rate solders (e.g., Sn-0.7Cu) have a longer fatigue lifetime. Eutectic Sn-Pb has the same low shear strength as Sn-0.7Cu but has a shorter thermal fatigue lifetime due to heterogeneous coarsening. It is well established that heterogeneous coarsening concentrates strain in the joint to the coarsened band and accelerates crack formation and propagation [5, 36, 37]. The stronger Sn-Ag-Cu alloys has a slightly improved life compared to Sn-Pb due to the limited heterogeneous microstructural coarsening so strain does not concentrate on microstructural features in the joint as they do with eutectic Sn-Pb.

9.4 Summary

As microelectronic devices become more complex and reduce in size they are increasingly used in a growing broad array of applications ranging from hand-held consumer gaming to cell phones to automotive electronics. One of the most critical aspects of the electronic devices in these applications is electronic package solder-joint reliability and thermomechanical behavior of the solder joint. Thermomechanical fatigue occurs as a result of strain imposed as the temperature changes in solder-joining materials of different coefficients of thermal expansion. This has increased in complexity due to the legislative requirements of eliminating Pb from solders to become more environmentally benign.

All Sn-based solders form interfacial intermetallic with the typically used Cu (Cu_3Sn/Cu_6Sn_5) or Ni (Ni_3Sn_4) metallizations. The higher Sn content, Pb-free, solders do not significantly increase the thickness of the interfacial intermetallic layers. Under thermomechanical fatigue conditions, the brittle intermetallic layers have no impact on the deformation behavior or lifetime of the solder joints. The lack of an interfacial intermetallic impact on solder joint behavior is due to the good time-dependent deformation behavior of the solders that allow the damage during thermal cycling to be accommodated in the solder rather than at the brittle interfacial intermetallics.

The microstructure of the solder joints defines the thermomechanical behavior. Eutectic Sn-Pb solder has a lamellar structure of interfacial Pb-rich and Sn-rich phases that are grouped into colonies of similarly oriented lamella. Under thermomechanical deformation conditions, the eutectic Sn-Pb microstructure undergoes heterogeneous coarsening with deformation concentrated at the cell boundaries. The lifetime of the solder is reduced due to the concentration of the strain.

The thermomechanical fatigue behavior of Sn-3.5Ag solder and Sn-3.8Ag-0.7Cu alloy do not undergo significant microstructural evolution with some phase coarsening but minimal grain-size evolution. Crack initiation and propagation at the highest strain region of the solder joint. Cracks can occur through the interfacial intermetallic, but this not what initiates the crack – the crack initiation/propagation is associated with regions of high strain

in the join. Sn-Ag-Cu has a longer thermomechanical fatigue lifetime than near-eutectic Sn-Pb solders and is due to the limited coarsening but enhanced compliance due to the added Cu. Eutectic Sn-3.5Ag solder has a somewhat shorter thermal fatigue lifetime than the other Pb-free alloys and this appears to be due to the higher strength of this alloy that reduces the compliance of the solder and shortens the thermal fatigue life.

The eutectic Sn-0.7Cu solder has the fastest steady-state creep behavior of the Pb-free solders and deforms by grain-boundary sliding/rotation. No microstructural evolution is observed so strain is no concentrated in the joint leading to a longer thermomechanical fatigue lifetime. Fracture of the Sn-Cu solder in thermomechanical fatigue is by grain-boundary cracking.

References

1. Directive 2002/95/EC of the European Parliament and the Council of Jan.27, 2003, Official J. of the European Union, 13.2.2003, L 37/19-38, (2003)
2. Management Methods for Prevention and Control of Pollution form Production of Electronic and Information Products, English translation of draft comments for China ROHS (July 2003).
3. Frear, D.R., Jones, W.B., and Kinsman, K.R. (1990) *Solder Mechanics: A State of the Art Assessment*, TMS, Warrendale, PA, pp. 47–74.
4. Frear, D.R. (1990) Microstructural evolution during thermomechanical fatigue of 62Sn-36Pb-2Ag and 60Sn-40Pb solder joints. *IEEE Trans. Compon. Hybrids Manufact. Technol.*, **13**, 718–726.
5. Frear, D.R., Grivas, D., and Morris, J.W. Jr. (1988) Microstructural study of the thermal fatigue failures in 60Sn-40Pb solder joints. *J. Electron. Mater.*, **17**, 171–180.
6. Frear, D.R., Grivas, D., and Morris, J.W. Jr. (1989) Parameters affecting thermal fatigue behavior of 60Sn-40Pb solder joints. *J. Electron. Mater.*, **18**, 671–680.
7. Glazer, J. (1995) Metallurgy of low temperature Pb-free solder for electronic assembly. *Int. Mat. Rev.*, **40**, 65–93.
8. 'Lead-free solder project', National Center for Manufacturing Sciences, August 1997.
9. Miric, A.Z. and Grusd, A. (1998) Lead-free Alloys. *Solder Surf. Mount Technol.*, **10**, 19–25.
10. McCormack, M. and Jin, S. (1993) Progress in the design of new lead-free solder alloys. *JOM*, **45**, 36–40.
11. Vianco, P.T. and Frear, D.R. (1993) Issues in the replacement of lead-bearing solders. *JOM*, **45**, 14–19.
12. Frear, D.R. and Vianco, P.T. (1994) Intermetallic growth behavior of low and high melting temperature solder alloys. *Metall. Trans.*, **25**, 1509–1523.
13. Boettinger, W.J. *et al.* (1993) Reactive wetting and intermetallic formation, in *The Mechanics of Solder Alloy Wetting & Spreading*(eds F.G. Yost, F.M., Hosking, and D.R. Frear), Van Nostrand, Reinhold New York.
14. Yost, F.G., Hosking, F.M., and Frear, D.R. (1993) *The Mechanics of Solder Alloy Wetting and Spreading*, Van Nostrand, Reinhold New York.
15. Frear, D.R., Grivas, D., and Morris, J.W. Jr. (1988) Microstructural study of the thermal fatigue failures in 60Sn-40Pb solder joints. *J. Electron. Mater.*, **17**, 171–180.
16. Kim, H.K., Tu, K.N., and Totta, P.A. (1996) Ripening-assisted asymmetric spalling of Cu-Sn compound spheroids in solder joints on Si wafers. *Appl. Phys. Lett.*, **68**, 2204–2206.
17. Roesner, B., Baraton, X., Guttmann, K., and Samin, C. (1998) Thermal fatigue of solder flip-chip assemblies. Proc. 48th Electron. Comp. Tech. Conf., pp. 872–877.

18. Stephens, J.J. and Frear, D.R. (1999) Time dependent deformation behavior of near eutectic 60Sn-40Pb solder. *Metall. Trans*, **30**, 1301–1313.
19. Liang, J. *et al.* (1997) Creep study for fatigue life assessment of two Pb-free high temperature solder alloys. *Mater. Res. Soc. Symp. Proc.*, **445**, 307–312.
20. Dutta, I. *et al.* (2005) Effect of thermo-mechanically induced microstructural coarsening on the evolution of creep response of SnAg-based microelectronic solders. *Mater. Sci. Eng. A*, **410–411**, 48–52.
21. Dutta, I., Park, C., and Choi, S. (2004) Impression creep characterization of rapidly cooled Sn-3.5Ag solders. *Mater. Sci. Eng. A*, **A379**, 401.
22. Lu, H.Y., Balkan, H., and Ng, K.Y.S. (2006) Effect of Ag content on the microstructure development of Sn-Ag-Cu interconnects. *J. Mater. Sci.: Mater. Electron.*, **17**, 171–188.
23. Song, H.G., Morris, J.W., and Hua, F. (2002) The creep properties of lead-free solder joints. *JOM*, **6**, 30–32.
24. Mathew, M.D. *et al.* (2005) Creep deformation characteristics of tin and tin-based electronic solder alloys. *Metall. Mater. Trans. A.*, **36**, 99–105.
25. Rist, M.A., Plumbridge, W.J., and Cooper, S. (2006) Creep-constitutive behavior of Sn-3.8Ag-0.7Cu solder using an internal stress approach. *J. Electron. Mater.*, **35**, 1050—2058. 1050.
26. Shin, S.W. and Yu, J. (2005) Creep deformation of Sn-3.5Ag-xCu and Sn-3.5Ag-xBi solder joints. *J. Electron Mater.*, **34**, 188–195.
27. Guo, Z., Pao, Y.H., and Conrad, H. (1995) Plastic deformation kinetics of 95.5Sn4Cu0.5Ag solder joints. *Trans. ASME J. Electron. Packag.*, **117**, 100.
28. Neu, R.W., Scott, D.T., and Woodmansee, M.W. (2001) Thermomechanical behavior of 96Sn-4Ag and castin alloy. *ASME Trans. J. Electron. Packag.*, **123**, 238.
29. Kerr, M. and Chawla, N. (2004) Creep deformation behavior of Sn–3.5Ag solder/Cu couple at small length scales. *Acta Mater.*, **52**, 4527–4535.
30. Mei, Z. and Morris, J.W. (1992) Characterization of eutectic Sn-Bi solder joints. *J. Electron. Mater.*, **21**, 599–607.
31. Frear, D.R. (1997) Constitutive Behavior of Pb-free Solder alloys Sandia National Labs Report #SAND96-0037.
32. Liang, J. *et al.* (1997). Creep study for fatigue life assessment of two Pb-free high temperature solder alloys. *Mater. Res. Soc. Symp. Proc*, **445**, 307–312.
33. Grusd, A. (1999) Integrity of Solder Joints from Pb-free Solder Paste. *Proc. NEPCON West'99*, p. 57.
34. Grusd, A. (1998) Lead Free Solders in Electronics. Proc. Surface Mount Int. Conf., pp. 648–661.
35. Glazer, J. (1994) Microstructure and mechanical properties of Pb-free solder alloys for low-cost electronic assembly: A review. *J. Electron. Mater.*, **23**693–700.
36. Frear, D.R., Grivas, D., and Morris, J.W. Jr. (1989) Parameters affecting thermal fatigue behavior of 60Sn-40Pb solder joints. *J. Electronic Mater.*, **18**, 671–680.
37. Frear, D.R. (1992) Microstructural evolution during the thermomechanical fatigue of solder joints, in *The Metal Science of Joining*(eds M.J. Cieslak, M.E. Glicksman, S. Kang, and J.H. Perepezko), TMS Publications, Warrendale, PA USA, pp. 191–200.

10

Electromechanical Coupling in Sn-Rich Solder Interconnects

Q.S. Zhu[1], *H.Y. Liu*[1], *L. Zhang*[1], *Q.L. Zeng*[1], *Z.G. Wang*[1], *and J.K. Shang*[1,2]
[1] *Shenyang National Laboratory for Materials Science, Institute of Metal Research, Chinese Academy of Sciences, Shenyang 110016, China*
[2] *Department of Materials Science and Engineering, University of Illinois, Urbana IL 61801, USA*

Abstract

Electromechanical coupling in Sn-based solder interconnects was investigated by examining the effects of the electromigration on the mechanical behavior of microsized Sn-3.5Ag-0.7Cu, pure Sn and single-crystal Sn solder interconnects. Prior to mechanical loading, electromigration induced grain-boundary grooving, Sn hillock formation, Cu_6Sn_5 formation, and the wave-like surface relief on the solder surface. The tensile tests following electromigration showed that the strength of the pure Sn and Sn-3.5Ag-0.7Cu interconnects rapidly decreased with the electromigration time, while the strength of the Sn single-crystal interconnects remained relatively stable. From the stress-relaxation tests, it is shown that the stress-relaxation rate of the Sn-Ag-Cu and pure Sn solder interconnects were enhanced by the electromigration, as the stress-relaxation rate increased with the electromigration time. In the polycrystalline pure Sn, the reduced resistance to deformation was related to the Sn grain tilting or sliding as evident from the grain-boundary grooving. Such a grain-boundary effect disappeared in the single-crystal Sn sample. For the Sn-3.5Ag-0.7Cu solder interconnect, the current-induced softening and the enhanced stress-relaxation rate is explained in terms of the dislocation interaction with excess vacancies produced by electromigration.

Lead-free Solders: Materials Reliability for Electronics, First Edition. Edited by K. N. Subramanian.

10.1 Introduction

In microelectronic devices, solder joints serve as both electric and mechanical connections and therefore must withstand both electrical and mechanical loads. As the packaging density continues to increase, the dimension of the solder joint becomes smaller and smaller so that failures of a solder joint may occur by mechanical loading, electrical loading or combined electromechanical loading [1–8]. Under mechanical loading, solder joints may suffer from creep, fatigue, and impact failures, all of which have been extensively studied [9–11]. Recent work on electric loading of solder joints has also clearly shown the susceptibility of Pb-free solders to electromigration damage, which may appear as voids, hillocks, solute segregation, growth and dissolution of the intermetallic compounds at the electrodes [1–3]. When electrical and mechanical loads are combined, potential complications from the Joule heating and the sensitivity of the solder alloys to thermal loading make it difficulty to sort out the contributions from individual loads. Consequently, the coupling between electrical and mechanical loads has not been well understood in solder interconnects.

It is known that the electromigration is the directional diffusion process of the atom and vacancy driven by the electron wind force. Because of their low melting temperatures, Sn-based solder alloys tend to undergo time-dependent deformation when subject to mechanical loading, where diffusion also plays a significant role. When the two processes of electromigration and time-dependent deformation are combined, the overall response of a solder joint to electromechanical loading is expected to rely strongly on the underlying diffusion mechanisms, which, in solder alloys, may be closely related to the solder microstructures, such as alloying phases, grain boundary and crystal orientation. In the polycrystalline pure Sn, diffusivity is directionally dependent and is larger along the grain boundary than through the interior of the grain. Consequently, the electromechanical coupling should be strongly dependent on grain-boundary processes. The previous studies on the conductive metal film has shown that the atomic diffusion under an electrical current was dominated by the grain-boundary diffusion. In the Al or Cu wire, a bamboo-structure grain boundary or single-crystal structure was proposed to slow down the damage induced by the electromigration [12, 13]. Recently, it was reported that the twin-modified grain boundaries in copper could block the atomic migration under the current stress [14]. Compared to the high melting metal film conductor, the solder normally operates at a high homologous temperature where both lattice and grain-boundary diffusion may play important roles. The contribution of two diffusion mechanisms in solders during the electromechanical loading would be strongly dependent on the grain size or whether the solder joints contain polycrystalline or single-crystal Sn.

In the Sn-based solder alloys, the alloying element may have different atomic diffusivities compared to the Sn. In the eutectic SnPb solder interconnect, above 100 °C, the Pb is the faster-moving species and the diffusivity differential may lead to the phase separation [15]. Such a phase-separation phenomenon also occurred in the eutectic SnBi solder interconnect after electromigration [16]. In the Sn-9Zn/Cu interconnect, because the backstress induced by the Sn electromigration promoted Zn migration to the cathode, an abnormal polarity effect occurred where the intermetallic compound layer at the cathode was thicker than that at the anode [17]. For the eutectic SnAgCu solder interconnects, since the amount of the

alloying elements is not high enough, the migration of Ag and Cu is insignificant as compared with the self-diffusion of Sn. The massive migration of Sn may result in excess vacancies so that vacancies may play a significant role in the deformation and failure processes under electromechanical loading.

In this study, polycrystalline pure Sn, single-crystal Sn and Sn-3.5Ag-0.7Cu alloy were subject to electrical and mechanical loading to investigate the interaction of electromigration damage process with mechanical deformation process. To avoid potential complications from the Joule heating, electrical and mechanical loads were applied to solder interconnects in sequence. The elecctromigration damages were first observed on the sample surfaces to provide evidence of atomic migration in the solder interconnects. In the pure Sn interconnects, it was the grain-boundary process that dominated the electromechanical response of the solder joints. By contrast, for Sn-Ag-Cu alloy, the mechanisms based on the vacancy and atomic diffusion are suggested for the surface morphology occurrence and mechanical performance after electromigration.

10.2 Experimental

The Sn-Ag-Cu and normal pure Sn solder interconnects in this study were made by reflow soldering using a Sn-3.8Ag-0.7Cu solder and pure Sn. Two copper cubes were ground and carefully polished to obtain clean surfaces before coating by the soldering flux. For the Sn-Ag-Cu interconnect, the copper wires were placed between the two adjoining surfaces to control the solder bond thickness to 300 μm. For the pure Sn interconnect, the molybdenum wires were used to control the solder thickness and to prevent the elements from dissolving into the Sn solder. After the two cubes were aligned and fixed, the assembly was heated in an oven where the solder was reflowed at 250 °C for 40 s. After air cooling, the bulk solder joints were cut by electric discharge machining into $300 \times 300\ \mu m^2$ square bars.

The single-crystal Sn plate was grown from the tin of 99.999% purity by the Bridgman method in a horizontal furnace. A thin sheet was cut vertically to the growth direction using electric discharge machining and was polished to a thickness of 400 μm. The crystal orientation of the thin sheet was determined by an XRD method, as shown in Figure 10.1. The thin sheet was clamped by two Cu bars to form a sandwich structure and then was mounted into a steel mold where a certain compressive stress can be produced along the axis direction of the Cu bar. Then the mold was put into a vacuum furnace where the pressure was reduced to 10^{-3} Pa and the temperature was controlled at 130 °C that is much lower than the melting point (232 °C) of pure tin. After the thermocompression process, the Sn single-crystal interconnects were created. The bar samples were further polished to about $300 \times 300\ \mu m^2$ in cross section.

Before the electromigration test, the microsized solder interconnects samples were carefully polished to obtain a mirror-like surface. Electromigration tests were carried out by applying a constant direct current at a current density of 3×10^4 A/cm^2. During the test, the electromigration samples were immersed in a heat-conducting oil to minimize oxidation of the sample surface and to dissipate the Joule heating, as shown in Figure 10.2. Select samples were cleaned to remove the oil during and after testing and then were examined by scanning electron microscopy (SEM).

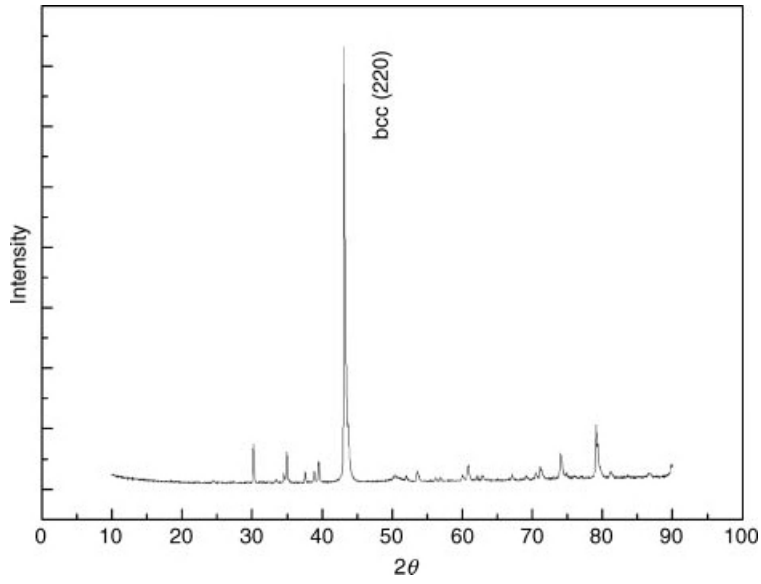

Figure 10.1 *XRD patterns of Sn single-crystal sheet.*

The tensile strengths of the microsized solder joints with and without electromigration were measured on a micromechanical testing system. The load range for the testing machine was 50 N, with a load control accuracy of better than 1% and a displacement resolution of 1 nm. The tensile tests were performed at a constant displacement control of 3.0×10^{-4} mm s^{-1}. For the stress relaxation tests, the sample was first installed in the micromechanical testing system. Then, a tensile strain of 10% was imposed on the samples at a constant strain rate of 10^{-3}/s prior to the stress-relaxation process. The strain was maintained through the constant strain-controlling mode of the machine, and the response curves between the stress and time were monitored and recorded by the computer.

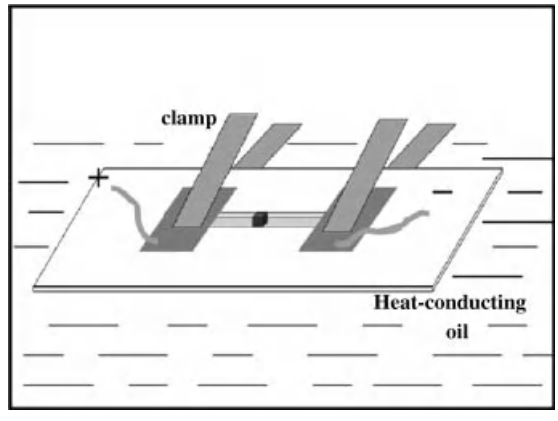

Figure 10.2 *Schematic diagram of electromigration testing.*

10.3 Results

10.3.1 Surface Morphology of Sn-3.5Ag-0.7Cu Interconnects after Electromigration

As shown in Figures 10.3a and b [18], the smooth surface of the interconnect had turned rough after electromigration for 150 h. The surface protuberances with different shapes and sizes were clearly observed. From the EDS analysis, the relatively higher and bright protuberances were identified as pure tin and thus as 'Sn hillocks', while the relatively lower and dark protuberances were identified as the Cu_6Sn_5 IMC phases. From the *in-situ* observation results, it was found that the number and size of the Sn hillocks significantly increased after extending the electromigration time, as shown in Figures 10.3c and d [18]. It was also noted that the Sn-hillock growth was generally accompanied by the appearance of additional Cu_6Sn_5 IMC on the surface during electromigration. When the sample surface was further polished into the core of solder, EPMA analysis results in Figure 10.4 showed that the Cu content was nearly zero at the center of the sample but sharply increased near the surface, indicating the Cu atoms migrated to the surface. The Cu_6Sn_5 phases resulting from

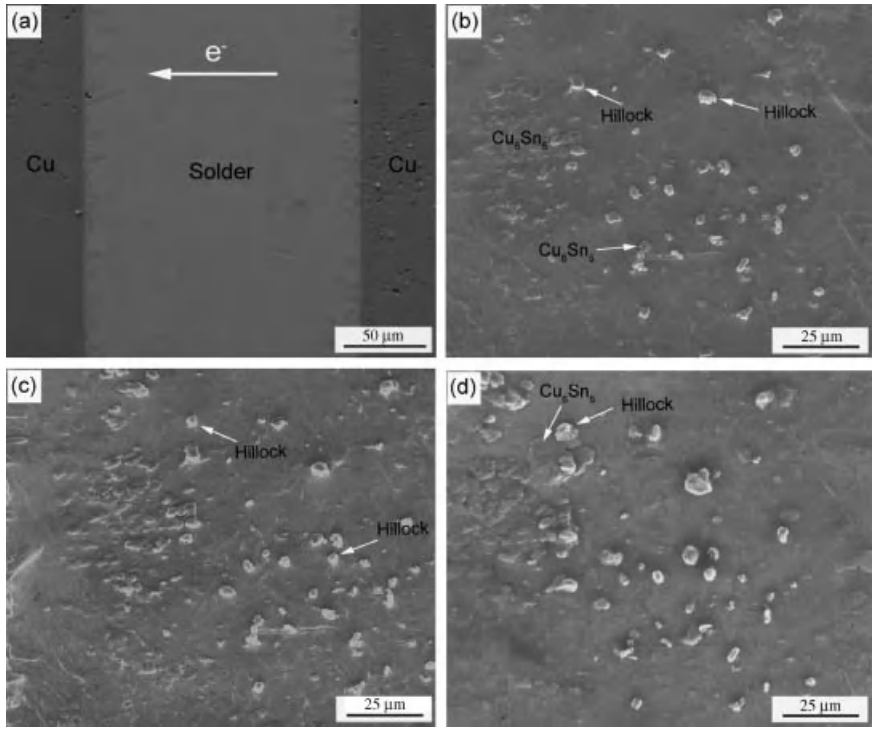

Figure 10.3 *Surface morphology of the Sn-3.8Ag-0.7Cu solder interconnect: (a) before electromigration, (b) electromigration for 150 h, (c) electromigration for 190 h, (d) electromigration for 250 h. (Reproduced from J. Electron. Mater., Surface morphology of Sn-rich solder interconnects after electrical loading by Q. S. Zhu, H. Y. Liu, Z. G. Wang and J. K. Shang, in press).*

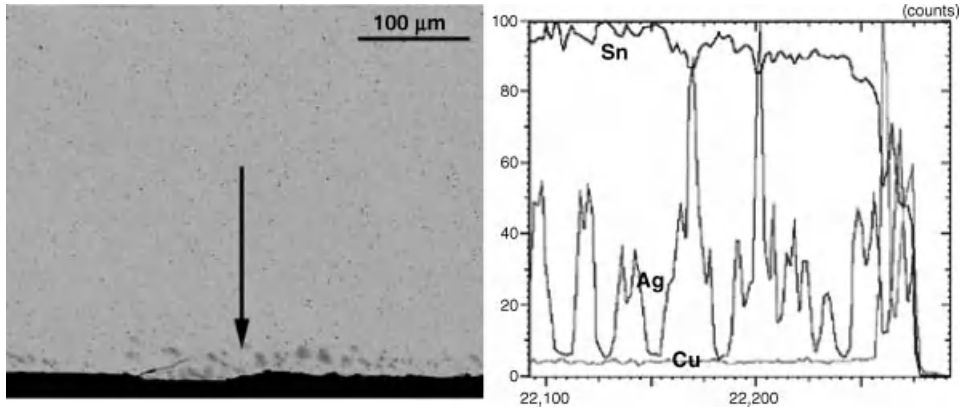

Figure 10.4 *EPMA results of the Sn-3.8Ag-0.7Cu solder interconnect as marked by arrow.*

the Cu migration can be clearly distinguished from the Sn hillocks by changing the SEM-SE image mode into the SEM-BSD image mode, as shown in Figure 10.5. In addition, the cone-like shape of the hillocks was also different from that of the Cu_6Sn_5 IMC phase. Such a current stressing-induced Sn-hillock growth was similar to that which occurred on electrodeposited pure Sn layer [19].

10.3.2 Surface Morphology of Pure Sn Interconnect after Electromigration

For the pure Sn interconnect, the Sn hillocks and Cu_6Sn_5 segregation were hardly observed after electromigration, as shown in Figure 10.6a [18]. Instead, the Sn grain-boundary grooves occurred on the surface. As shown in Figure 10.6b [18], the formation of the grain-boundary groove may be related to the grain motion, such as grain-boundary sliding or tilting. The grain rotation occurred during the electromigration of Sn solder interconnects [8] where one side of the grain rose while the other side sank, as shown in Figure 10.6c [18]. After prolonging electromigration time, the grain rotation continued and the grain-boundary

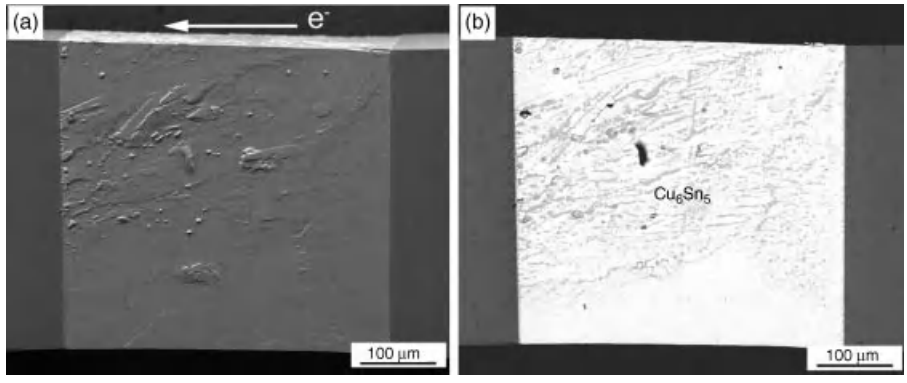

Figure 10.5 *Hillock growth and Cu_6Sn_5 IMC phase segregation on the surface after electromigration: (a) SEM-SE image mode, (b) SEM-BSD image mode.*

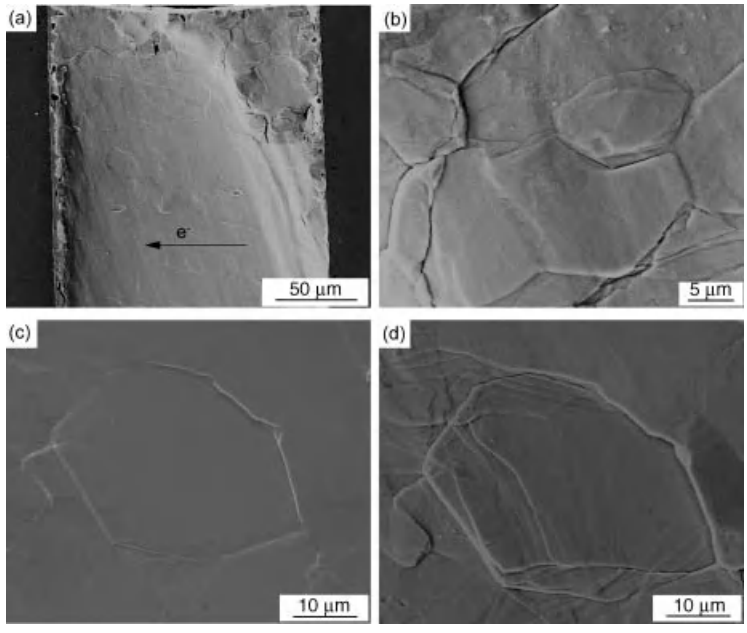

Figure 10.6 *Surface morphology of the pure Sn interconnect: (a) electromigration for 180 h, (b) magnified image of grain-boundary groove morphology, (c) grain rotation after electromigration for 130 h, (d) further grain rotation after electromigration for 180 h. (Reproduced from J. Electron. Mater., Surface morphology of Sn-rich solder interconnects after electrical loading by Q. S. Zhu, H. Y. Liu, Z. G. Wang and J. K. Shang, in press).*

grooves were further deepened, as shown in Figure 10.6d [18]. The similar surface-grooving phenomena was also reported on the pure Sn strip after electromigration [20]. In contrast to the Sn hillock, the occurrence of the grain-boundary groove did not change the original grain shape and size.

In a Cu/SnCu interconnect, electromigration may force the Cu atom to diffuse from the Cu metallization at the cathode to the anode. For a microscale interconnect, the Cu atom diffusion on the surface should be much faster than either lattice diffusion or grain boundary. However, the Cu_6Sn_5 was hardly visible on the surface of Sn interconnect after electromigration. From this case, it was concluded that the migration of Cu to the surface in the Sn-3.5Ag-0.7Cu interconnect surface should come from the inside of the solder rather than the Cu substrate at the electrode.

10.3.3 Surface Morphology of Single-Crystal Sn Interconnect after Electromigration

For the polycrystalline Sn, the current stressing created deep grooves along the Sn grain boundary. When the single-crystal Sn interconnects were subjected to the same current stressing, it was observed that the interconnects had a smooth surface for a long time (a zone was produced by surface polish), as shown in Figure 10.7a [18]. After very long electromigration, a wave-like relief that traversed the surface was observed, as shown in

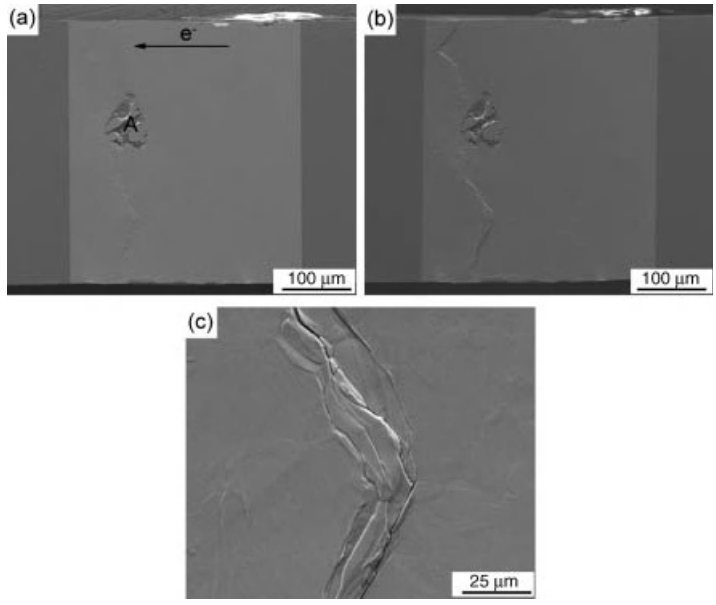

Figure 10.7 *Surface morphology of the single-crystal interconnects: (a) electromigration for 130 h, (b) electromigration for 250 h, (c) magnified image of the relief. (Reproduced from J. Electron. Mater, Surface morphology of Sn-rich solder interconnects after electrical loading by Q. S. Zhu, H. Y. Liu, Z. G. Wang and J. K. Shang, in press).*

Figure 10.7b [18]. The relief line became wider with current stressing time, as shown in Figure 10.7c [18]. From other single-crystal samples after electromigration, it was known that the occurrence of this wave-like relief was situated at a different location. These features implied that the formation of the wave-like relief may be associated with the current-induced Sn diffusion on the surface where the current-density distribution was erratic.

10.3.4 Tensile Strength of Solder Interconnects after Electromigration

When the microsized interconnects were tested in tension at a constant strain rate under the microforce measurement system, the engineering stress–strain curves shown in Figure 10.8 were obtained; before and after electromigration, the Sn-3.5Ag-0.7Cu solder interconnects displayed a ductile stress–strain behavior. The strains at fracture were comparable but the tensile strengths differed between the samples before and after electromigration. Therefore, the application of the electric current reduced the deformation resistance of the solder interconnects. In addition, the strength drop increased with the prolonging electromigration time. Although the tensile strength reached a rather low value, the fracture of the solder interconnects remained in a ductile mode, which suggested that the softening of the interconnect was associated with the deformed solder rather than the brittle IMC interface. In these regards, the current-induced softening of the Sn-3.5Ag-0.7Cu solder interconnects in this case was quite different from the severe strength drop phenomena resulting from the brittle fracture at the cathode in the previous studies [4] where the flip-chip samples were employed.

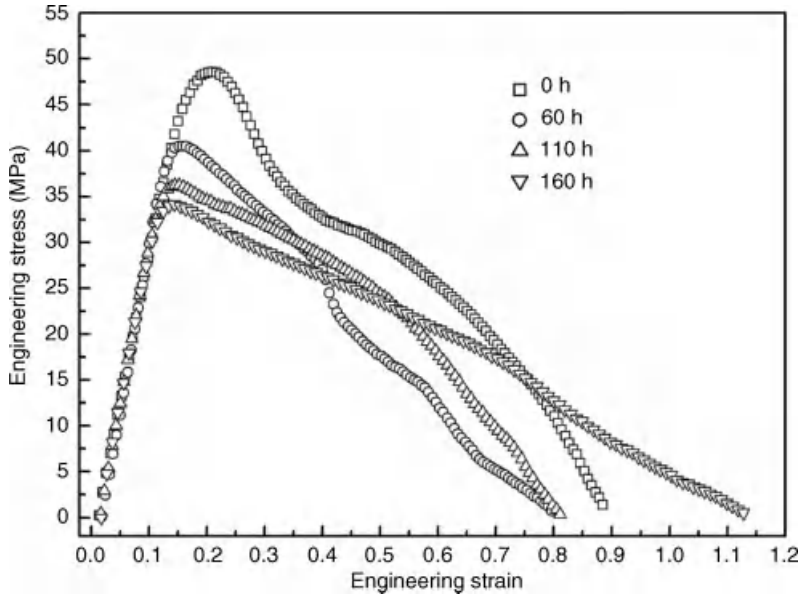

Figure 10.8 *Tensile curves of Sn-3.8Ag-0.7Cu solder interconnects after electromigration for different time.*

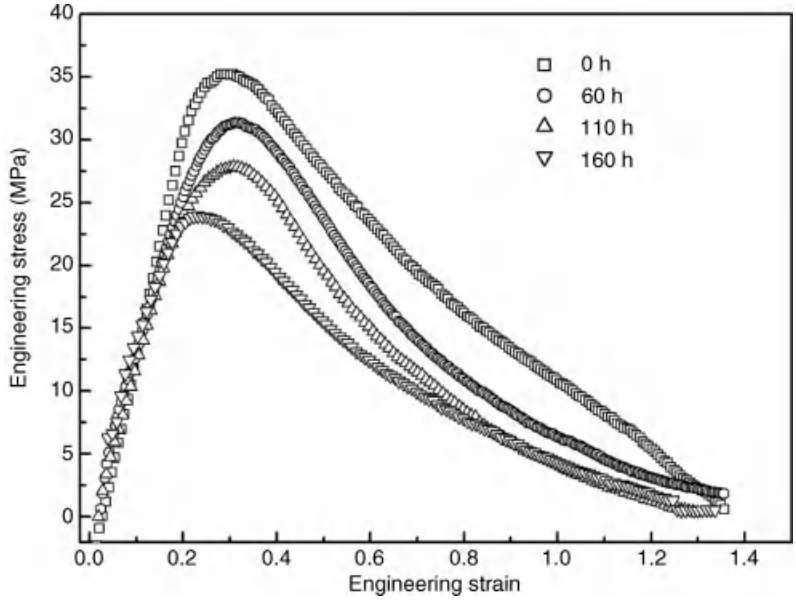

Figure 10.9 *Tensile curves of pure Sn interconnects after electromigration for different times.*

Similarly, the pure Sn solder interconnects also exhibited a considerable reduction in the tensile strength after electromigration, as shown in Figure 10.9. The reduction was greater at a longer electromigration time. The strengths of the pure Sn interconnects were generally lower than those of Sn-3.5Ag-0.7Cu solder interconnects, which is in accordance with the strength comparison between the bulk pure Sn and Sn-3.5Ag-0.7Cu alloys. For the single-crystal Sn interconnects, without the grain-boundary and alloying-strengthening effects, the strengths were much lower compared to those of the pure Sn and Sn-3.5Ag-0.7Cu solder interconnects, as shown in Figure 10.10. However, it was interesting to note that the strength of the single-crystal Sn interconnects had changed very little after the electromigration. The strength reduction of the single-crystal Sn interconnects was much lower than those of the pure Sn and Sn-3.5Ag-0.7Cu solder interconnects.

10.3.5 Stress-Relaxation Behavior of Solder Interconnects after Electromigration

At a fixed strain, the stress-relaxation process may be regarded as a transition of the elastic strain into the plastic strain so that the stress-relaxation rate can be expressed as below,

$$\frac{\mathrm{d}\sigma}{\mathrm{d}t} = E\frac{\mathrm{d}\varepsilon_\mathrm{e}}{\mathrm{d}t} = -E\frac{\mathrm{d}\varepsilon_\mathrm{p}}{\mathrm{d}t} \tag{10.1}$$

where ε_p is plastic strain, ε_e is elastic strain, σ is stress at any time, and E is Young's modulus. Stress relaxation describes a time-dependent deformation process of a material, that is, the stress relaxes with time under a given constant strain [21].

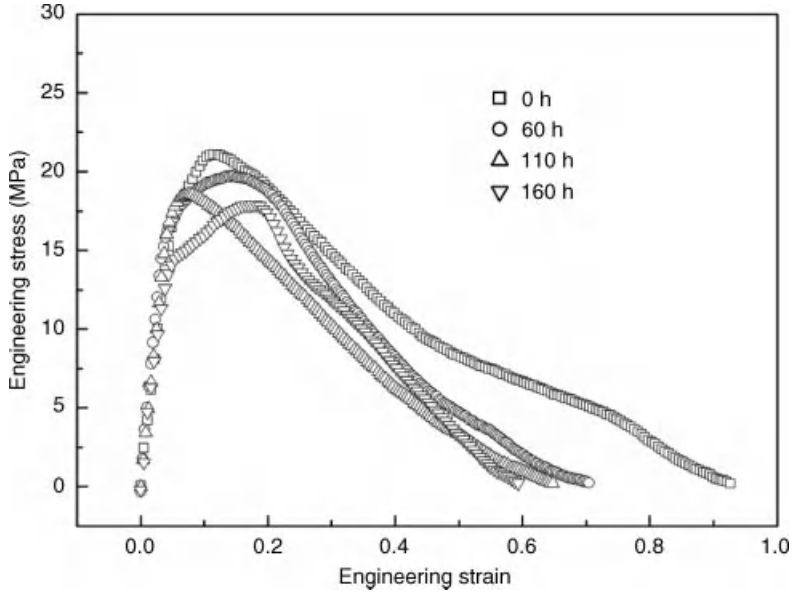

Figure 10.10 *Tensile curves of single-crystal interconnects after electromigration for different times.*

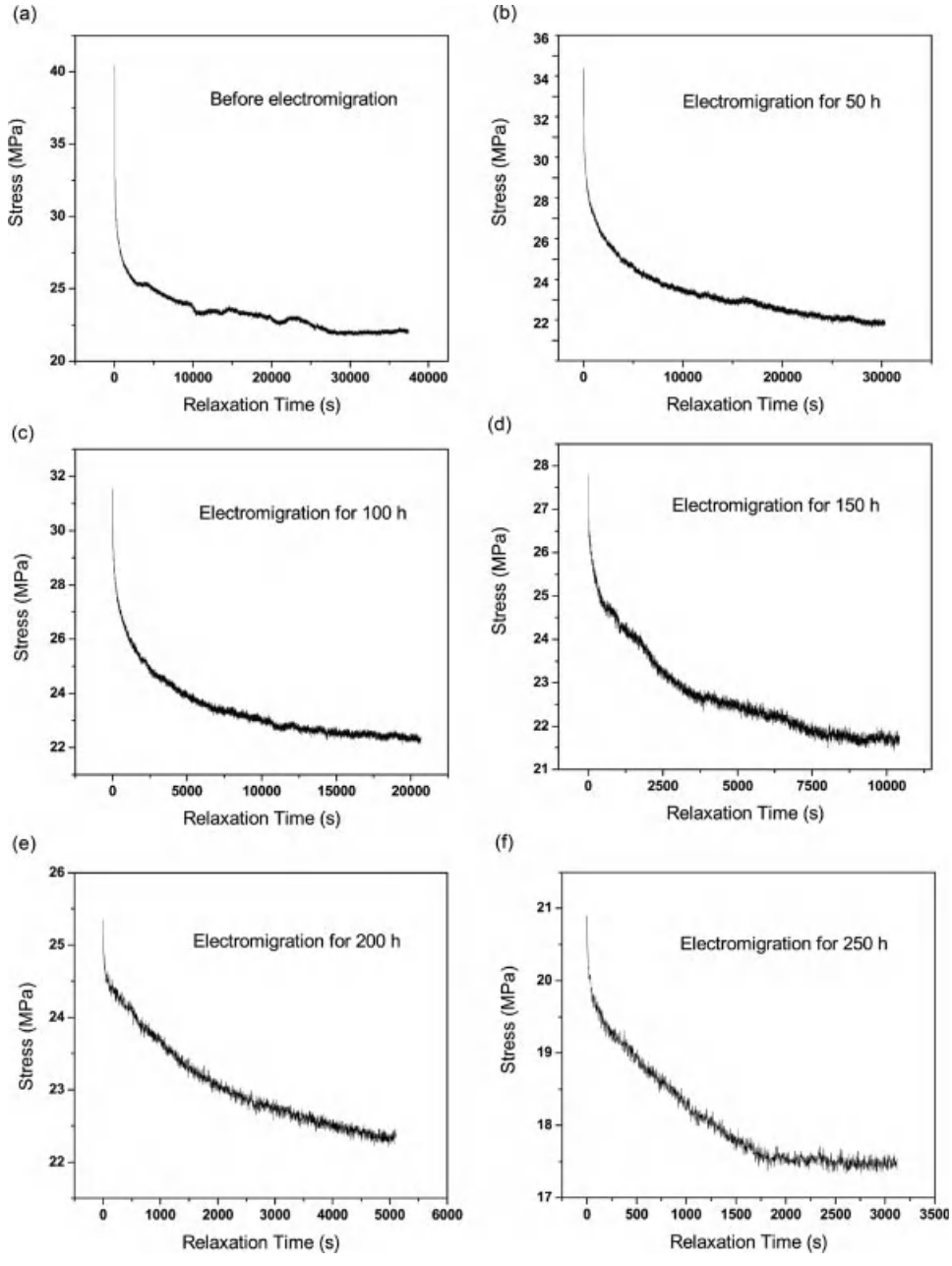

Figure 10.11 *Stress-relaxation rates of the solder joint after current stressing: (a–c) electrical current for 0 h, 50 h and 100 h, (d–f) electrical current for 150 h, 200 h and 250 h. (Reproduced from J. Mater. Res., Enhanced stress relaxation of Sn–3.8Ag–0.7Cu solder by electrical current by H.Y. Liu, Q.S. Zhu, L. Zhang, Z.G. Wang, J.K. Shang, 25, 6, 1172 Copyright (2010) Cambridge University Press).*

The stress-relaxation curves of the samples after electric current stressing from 0 to 250 h are shown in Figure 10.11 [7]. The stress-relaxation curves showed two different types of behavior. The first type, exemplified by Figures 10.11a–c, consisted of two regimes, the initial rapid drop, followed by a slow gradual decay to the final plateau. The second type, represented by Figures 10.11d–f, included a middle section, where substantial reduction in the stress persisted over a long time. The latter type was observed in the solder joints exposed to long-time applications of electric current, presumably with heavier electromigration damage.

From the above stress-relaxation curves, the stress-relaxation rate is shown in Figure 10.12 in terms of the strain rate as a function of the stress. In all cases, the stress-relaxation rate slowed down as the stress decreased. At a certain stress, the stress-relaxation rate after longer current exposures was always notably higher. For example, at the stress value of 25 MPa, the strain rate was 4.1E–7, 2.1E–6, 9.0E–5/s after current stressing for 0, 100, and 200 h, respectively. For electromigration times less than 100 h, the stress exponent n obtained from each test was almost the same, as shown in Figure 10.12a, and the value was very close to the results in the previous reports of tin-rich solders [22, 23]. At more

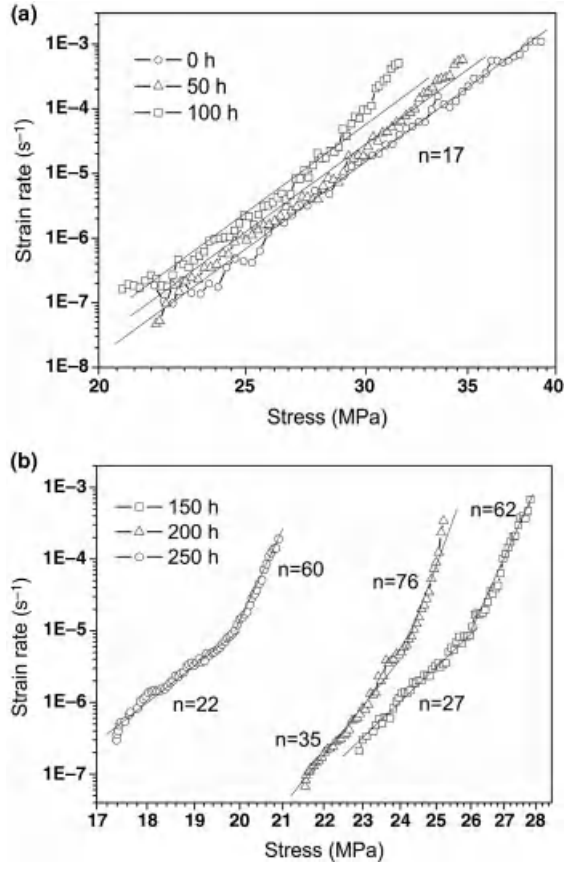

Figure 10.12 *Stress-relaxation time vs. electromigration time for the solder joints.*

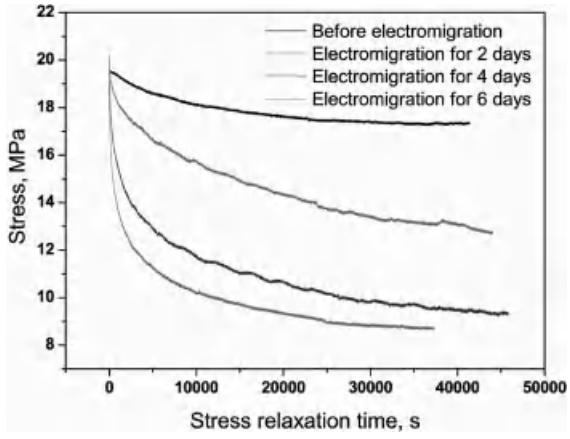

Figure 10.13 *Stress relaxation of the tin solder joint as a function of current stressing time. (Reproduced from Mater. Sci. Eng. A., Stress relaxation behavior of Cu/Sn/Cu micro-connect after electrical current by H.Y. Liu, Q.S. Zhu, Z.G. Wang, J.K. Shang, 528, 3, 1467–1471 Copyright (2011) Elsevier Ltd).*

than 100 h, there was a significant difference in the low-stress region and the high-stress region, as shown in Figure 10.12b.

For the pure Sn interconnects, the stress-relaxation plots as a function of time are shown in Figure 10.13 [8]. The same initial stress was applied to the samples, but the stress decreased faster when the sample was electrically loaded for a longer time. As the stress-relaxation time was prolonged to 10 000 s, the residual stresses of the samples were 18.1, 15.7, 11.7 and 10.2 MPa, respectively, for samples after electromigration for 0, 48, 96 and 144 h. As shown in Figure 10.14 [8], at a given electromigration time, the strain rate decreased significantly as the

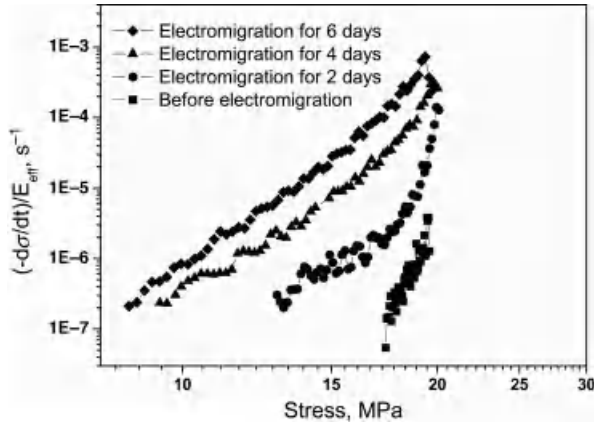

Figure 10.14 *Stress-relaxation rates of the tin solder joint after current stressing. (Reproduced from Mater. Sci. Eng. A., Stress relaxation behavior of Cu/Sn/Cu micro-connect after electrical current by H.Y. Liu, Q.S. Zhu, Z.G. Wang, J.K. Shang, 528, 3, 1467–1471 Copyright (2011) Elsevier Ltd).*

stress decreased. At the beginning of the stress relaxation, the strain rate of Sn interconnects without current stressing was only 1.3E–6/s. In contrast, after electromigration for 48 h, it was increased to 1.3E–4/s, about 10^2 times higher than that without current stressing. From the plots, the value of the stress exponent, n, was obtained to be 24 for the sample without current stressing, while the value was only 9 for the sample after current stressing.

10.4 Discussion

10.4.1 Stress Induced by Vacancy Concentration at the Grain Boundary

The electromigration is often taken as a directional motion of metal atoms under electrical fields. For common metals, the driven force of electromigration comes from the impinging of electrons to the atoms. As a result, the atoms move from the cathode to the anode with the electron flux and accordingly a flux of vacancies diffuse in the opposite direction. Thus, there will be a vacancy-concentration gradient occurring in the metals, forming a tensile-stress region near the cathode side and a compressive-stress region near the anode side [2, 24]. It is usually found that a high concentration of vacancies accumulate to form voids at the cathode side, while the excess atoms result in the expansion of the interfacial intermetallic compound at the anode side [25].

During the electromigration, the grain boundary acted as the dominant diffusion channel of metal atoms where the atom diffusivity may be about 10^6 times that of lattice diffusion at room temperature. The schematic diagram in Figure 10.15 shows the atom diffusion at the triple junction of the grain boundaries under the driving force of the electron wind. When the number of atoms flowing out are more than those flowing in, vacancies occur to bring about a tensile stress. Conversely, when the number of atoms flowing in are more than those flowing out, the excessive atoms produce a compressive stress. At a very low stress level, the stress is related to the equilibrium vacancy concentration as [19],

$$\sigma = \frac{kT}{\Omega}\frac{\Delta C_V}{C_V^0} \tag{10.2}$$

where Ω is the atom volume, k is the Boltzmann constant, T is the temperature, ΔC_V is the vacancy concentration, and C_V^0 is the initial vacancy concentration. The equation states that

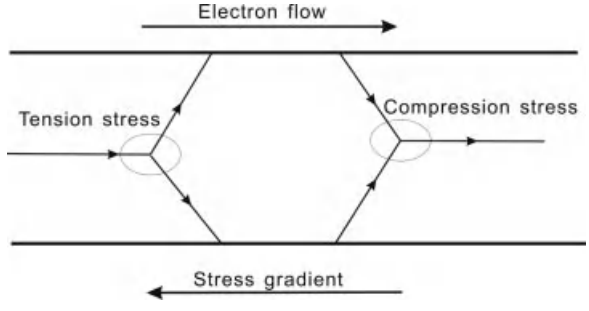

Figure 10.15 *Stress generation at the trigeminal grain boundary by electromigration.*

the stress at the grain boundary increases with the vacancy concentration during electromigration.

The stress at the grain boundary during electromigration can promote the Coble creep in which the atoms diffuse along grain boundaries onto the free surface and the grain-boundary sliding accommodates this diffusional flow. On the other hand, if there is a divergence of vacancy concentration occurring at the grain boundaries, the divergence can generate a torque. This torque imposed on one grain, especially the surface free grain, can rotate the grain. The grain-rotation phenomena had been directly observed in the previous study where the Sn strips were used in electromigration tests [20]. It was also reported that the rotated grain had a favorable crystallization orientation for electrical resistance [26]. In the present case, as the coupling results of the grain rotation and grain-boundary sliding, the typical morphologies of the grain-boundary grooves were observed on the surfaces of the Sn interconnects after electromigration. With increasing electromigration time, the vacancy concentration at the grain boundaries rose, which resulted in a larger stress and torque. In consequence, the depth of grain-boundary grooves increased with the electromigration time.

10.4.2 Compression Stress Induced by the Cu_6Sn_5 Formation on the Surface

During electromigration, the solder interconnect samples were immersed in heat-conducting oil to dissipate the Joule heating. It is measured that the heat-conducting oil near the sample surface had a constant temperature range of 60–70 °C. For comparison, the core temperature of the solder interconnect may be higher than 100 °C that was roughly estimated from the temperature of electromigration sample in air as reference. Thus, in the distance between the core and the surface, a thermal gradient above 1000 °C/cm was created, which was sufficient to induce thermomigration according to the previous studies [27, 28]. In thermomigration, the Cu atom had the tendency to move to the cold end. When the Cu atoms migrated from the core onto the free surface with the lowest-energy state, Cu_6Sn_5 IMC formed on the surface.

The equilibrium solubility of Cu in solid Sn is very small, that is, 6×10^{-3} mass fraction Cu at 227 °C and 10^{-7} mass fraction Cu at room temperature [19]. The Cu diffusion in Sn matrix is extremely fast, especially driven by large thermal gradient. For the fast diffusion of Cu in Sn, it can be presumed that the Cu is dissolved interstitially in Sn [29]. When the precipitation of Cu_6Sn_5 occurred from a saturated Sn(Cu) solid solution, there was a difference between the molar volume of the saturated solution and the volume of an equilibrium mixture of Sn and Cu_6Sn_5 of the same composition. The volume of the saturated solution expanded when it was transformed into the equilibrium phases of Cu_6Sn_5 and Sn. Thus, the volume strain would produce an inplane compressive stress near the surface grain layer.

Like the Sn whiskers, the hillock growth is often treated as a localized diffusional creep/grain-boundary sliding phenomenon that relieves the compressive stress [19]. For the Sn-rich solders with a low melting temperature, the grain-boundary diffusion is expected to be the dominant self-diffusion mechanism. The inplane compressive stress is assumed to drive the flux of Sn towards the hillock or whisker. Tu *et al.* [30] have proposed a model for whisker or hillock growth based on an imposed constant inplane compressive stress and grain-boundary diffusion to the base of the hillock or whisker. Based on the model, it can be concluded that the growth of hillocks was strongly dependent on the compressive stress.

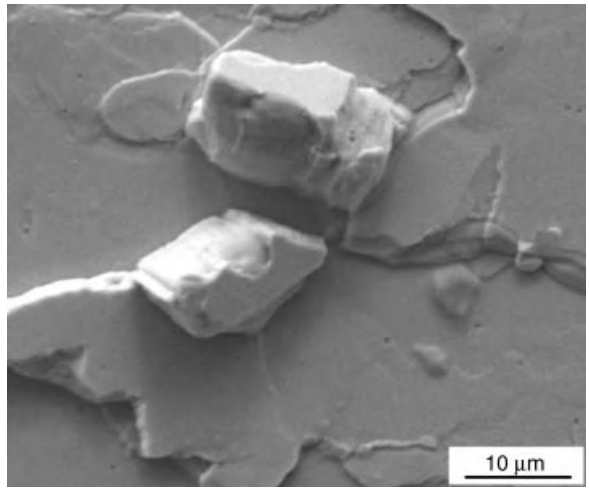

Figure 10.16 *The growing Sn hillocks with a flat top during electromigration. (Reproduced from J. Electron. Mater., Surface morphology of Sn-rich solder interconnects after electrical loading by Q. S. Zhu, H. Y. Liu, Z. G. Wang and J. K. Shang, in press).*

As shown in Figure 10.16 [18], it was noted that the hillock appeared to have a small flat top at the center, indicating the original location of the hillock grain prior to the migration of its boundaries. For the pure Sn interconnects, under the low stress at the grain boundary, the surface grains can only slightly tilt or slide but can not grow up into the hillocks for the lack of a large compressive stress. In contrast, for the Sn-3.5Ag-0.7Cu solder interconnect, as the schematic diagram in Figure 10.17 [18] illustrates, when the sufficient compressive stress was derived from the volume strain, the motivated grain would grow into the hillocks and the hillocks become larger with increasing electromigration time. The *in-situ* observation results also confirmed that the hillocks rapidly grew at the beginning stage of electromigration when the Cu_6Sn_5 first formed on the surface and then the growth rate decreased after the Cu_6Sn_5 formation slowed down.

10.4.3 Vacancy-Concentration Distribution after Current Stressing

During electromigration, driven by the electron wind force, the Sn atoms transported from cathode to anode and accordingly a flux of vacancies diffused in the opposite direction. The vacancy flux caused by electromigration in one dimension is described by the following:

$$J = -D\frac{\partial C}{\partial x} - \frac{DZ^* e\rho j}{kT}C \tag{10.3}$$

where ρ is the electrical resistivity of the metal, C is the vacancy concentration, D is the diffusivity, Z^* is the effective charge number, e is the electric charge, j is the electrical density, k is the Boltzmann constant, and T is the absolute temperature. For the initial condition, $C(x, 0) = C_0$, and the boundary conditions, $J(0, t) = 0, J(l, t) = 0$. At the cathode, where $x = 0$, the approximate solution is, when $n = 1$, given by Eq. (10.4) obtained by Clement [31],

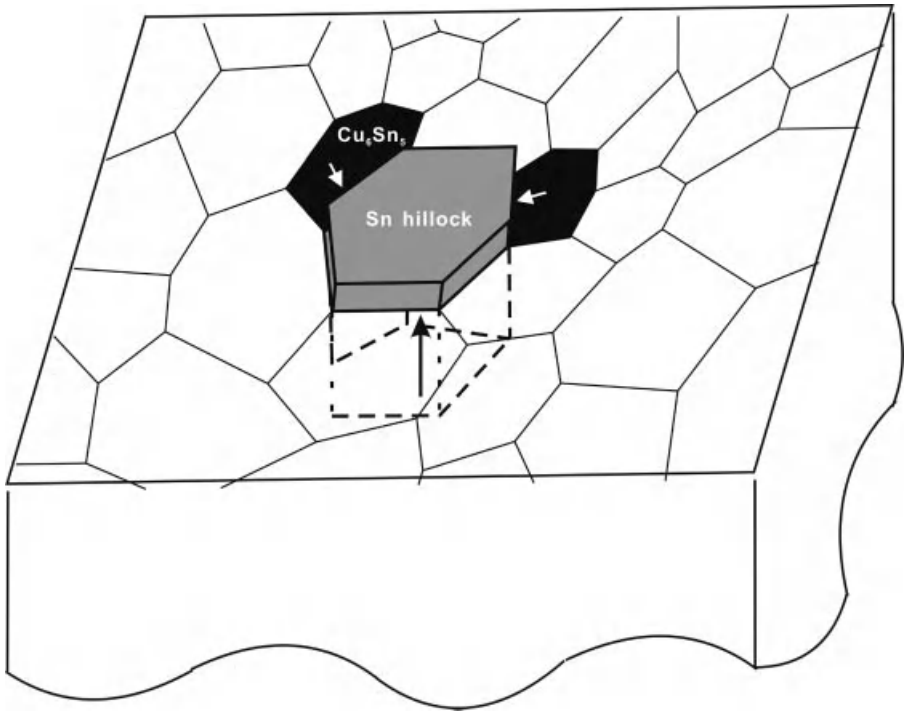

Figure 10.17 *Schematic diagram of the Sn hillock growth under inplane compressive stress from Cu_6Sn_5 segregation. (Reproduced from J. Electron. Mater., Surface morphology of Sn-rich solder interconnects after electrical loading by Q. S. Zhu, H. Y. Liu, Z. G. Wang and J. K. Shang, in press).*

$$\frac{C(0,t)}{C(0)}\Big|_{n=1} = \frac{\gamma}{1-e^{-\gamma}} - \frac{2\gamma\left(1+e^{\frac{\gamma}{2}}\right)}{\pi^2} e^{\left(-\pi^2\zeta\right)} \tag{10.4}$$

where $\xi = \frac{x}{l}$, $\eta = \frac{C}{C_0}$, $\zeta = \frac{Dt}{l^2}$, $\gamma = \frac{Z^* e\rho jl}{kT}$, and l is the conductor length. In the study [7], the calculations of the vacancy concentration ratio c/c_0 with electromigration time t from 50 h to 250 h were made based on the relationship of ζ and electromigration time t. At the cathode, the vacancy concentration linearly increased with an increase in electromigration time on a semilog plot. The concentration calculated here is the case at the cathode where the vacancy concentration was the largest. The vacancy flux changed the equilibrium vacancy concentration into a positive concentration gradient from the anode to the cathode. On the other hand, the Sn hillocks on the surface indicated that there were a large number of Sn atoms that moved onto the surface and accordingly the same number of vacancies were created in the interior of the solder. Based on the effect of the vacancy concentration gradient and vacancy creation, a high vacancy concentration should be generated in the cathode side after electromigration.

10.4.4 Effect of High Vacancy Concentration on Strength

In metals, when the vacancy concentration is supersaturated, the vacancies tend to move to the dislocation line and apply a force on the dislocation that promotes dislocation climb. The

climb force per unit length of dislocation that is perpendicular to the gliding plane is given by [32, 33]:

$$F_{os} = \frac{kTb}{\Omega} \ln \frac{c}{c_0} \tag{10.5}$$

where c_0 is the equilibrium vacancy concentration, c is vacancy concentration at any time, Ω is the atomic volume, F_{os} is the climb force on dislocation, b is the Burgers vector, k is the Boltzmann constant, and T is the absolute temperature. Based on this expression, the accumulation of the vacancy concentration produced a greater dislocation climb force. The driving stress for dislocation motion σ_0 may be written as the sum of the climb stress and the external stress σ_t, which can be expressed as,

$$\sigma_0 = \sigma_t + F_{os}/b \tag{10.6}$$

By combing Eqs. (10.5) and (10.6), the external stress σ_t can be expressed as a function of the vacancy concentration,

$$\sigma_t = \sigma_0 - \frac{kT}{\Omega} \ln \frac{c}{c_0} \tag{10.7}$$

It is apparent that the external stress required for dislocation motion is reduced with increasing vacancy concentration. During the tensile deformation of the interconnect, the strength was determined by the solder deformation. The ductile deformation occurred in the solder near the cathode where the vacancy concentration was high enough to produce a force on the dislocation that promotes dislocation climb. Therefore, the tensile strength of the pure Sn and Sn-3.5Ag-0.7Cu solder interconnects exhibited a notable drop with increasing electromigration time. In polycrystalline Sn and alloy, the grain boundary acted as the dominant transport path of the atom or vacancy so that the softening effect was strong. However, in the Sn single-crystal interconnects, the high vacancy concentration was difficult to form and the effect of electromigration on the tensile strength became inappreciable.

10.4.5 Effect of High Vacancy Concentration on Stress-Relaxation Rate

In the climb-assisted dislocation-glide process, the process of glide and climb are sequential. Consequently, the stress-relaxation rate is limited by the slower of the two steps. Since the climb rate is notably lower than that of the dislocation glide, the stress-relaxation rate is determined by the dislocation climb. For a single dislocation loop, the strain rate due to dislocation climb can be expressed as [34],

$$d\varepsilon/dt = \frac{ML^3}{h^2} v_c \tag{10.8}$$

where L is the average dislocation loop diameter, h is the vertical distance between two parallel slip planes, v_c is the climb rate, and M is a microstructural constant. When $c \gg c_0$, the climb rate v_c is

$$v_c = \frac{8D}{b} \frac{c}{c_0} \tag{10.9}$$

where c_0 is the equilibrium vacancy concentration, c is vacancy concentration at any time, Combining Eq. (10.8) with Eq. (10.9), which showed a proportional relationship of v_c and vacancy concentration c/c_0, the stress-relaxation rate can be simply expressed as,

$$d\varepsilon/dt = Ac/c_0 \tag{10.10}$$

where A is a constant. It is apparent that the strain rate due to dislocation climb was promoted by a higher vacancy concentration.

For the Sn-Ag-Cu and polycrystalline Sn solder interconnects, as discussed in Section 10.4.2, the vacancy concentration was greatly increased on the cathode side after electromigration. Therefore, the stress-relaxation rate based on the climb-assisted dislocation-glide process would be promoted by the high vacancy concentration. According to the calculated stress exponent value of the Sn-Ag-Cu interconnect, it was estimated that a time-dependent deformation during the stress-relaxation process was dominated by the climb-assisted dislocation-glide mechanism. Based on this model, the theoretical relaxation time decreased linearly with an increase in the electromigration time on a semilog plot, which agreed well with the experimental results [7].

For the pure Sn solder interconnects, the stress exponent value of 24 for the samples without electromigration decreased to 9 after electromigration for 100 h, and the activation energy value of 86.4 kJ/mol before electromigration was also modified into a value of 42.9 kJ/mol after electromigration, which suggested that the grain-boundary diffusion also played an important role during stress-relaxation process for the electromigration samples [35]. As sources and sinks of vacancies, the grain boundary may facilitate grain-boundary deformation including grain-boundary diffusion or sliding. With the increase in the vacancy concentration at a grain boundary, the atomic diffusion rate along the grain boundary is faster, leading to a higher stress-relaxation rate. Therefore, besides assisting climb-assisted dislocation glide, the accumulation of a high vacancy concentration also enhanced the stress-relaxation rate by accelerating grain-boundary diffusion and sliding.

10.5 Conclusions

1. After electromigration, the grain-boundary grooves appeared on the surface of the pure Sn solder interconnects, while the Sn hillocks and additional Cu_6Sn_5 IMC appeared on the surface of the Sn-3.5Ag-0.7Cu interconnects. For comparison, the surface of the Sn single-crystal interconnects was relatively smooth after the same electromigration time; for longer electromigration time, the wave-like surface relief occurred in the single-crystal joint.
2. For the pure Sn interconnect, the grain-boundary grooves resulted from the grain tilting or sliding due to the divergence of vacancy concentration and the Coble creep; the occurrence of the wave-like relief on the Sn single-crystal interconnects was related to the Sn surface diffusion. For the Sn-Ag-Cu connect, the formation of Cu_6Sn_5 IMC on the surface produced a large inplane compressive stress in the surface grain layer, which supported the growth of the motivated grains into the hillock.
3. During electromigration, the vacancy-concentration gradient occurred from the anode to the cathode and the vacancies were created behind the Sn diffusion onto the surface. On

the cathode side, the increased vacancy concentration produced a force on the dislocation that promotes dislocation climb; as a result, the strength of the Sn and Sn-3.5Ag-0.7Cu interconnects decreased significantly with increasing electromigration time.

4. After electromigration, the stress-relaxation rates of the Sn-Ag-Cu and pure Sn solder interconnects were increased. The increase of the stress-relaxation rate was related to the high vacancy concentration that promoted the climb-assisted dislocation-glide process. For the pure Sn interconnects after electromigration, the grain-boundary diffusion and sliding was enhanced by a higher vacancy concentration at the grain boundary, leading to an increase of the stress-relaxation rate.
5. The Sn single-crystal interconnects exhibited only a slight decrease in the strength after the electromigration, largely because it was difficult to establish a vacancy gradient in the single-crystal interconnect.

Acknowledgments

This study was financially supported by the National Basic Research Program of China, under the Grant No.2010CB631006 and the National Natural Science Foundation of China (NSFC), under the Grant No.51101161.

References

1. Zeng, K. and Tu, K.N. (2002) *Mater. Sci. Eng. R*, **38**, 55.
2. Tu, K.N. (2003) *J. Appl. Phys.*, **94**, 5451.
3. Chan, Y.C. and Yang, D. (2010) *Prog. Mater. Sci.*, **55**, 428.
4. Ren, F., Nah, J.W., Tu, K.N. *et al.* (2006) *Appl. Phys. Lett.*, **89**, 141914.
5. Wang, X.J., Zhu, Q.S., Wang, Z.G., and Shang, J.K. (2010) *J. Mater. Sci. Technol.*, **26**, 737.
6. Zhang, L., Wang, Z.G., and Shang, J.K. (2007) *Scr. Mater.*, **56**, 381.
7. Liu, H.Y., Zhu, Q.S., Zhang, L. *et al.* (2010) *J. Mater. Res.*, **5**, 1172.
8. Liu, H.Y., Zhu, Q.S., Wang, Z.G., and Shang, J.K. (2011) *Mater. Sci. Eng. A*, **528**, 1467.
9. Song, H.G., Morris, JW., and Hua, F. (2002) *J. Met.*, **54**, 30–32.
10. Shang, J.K., Zeng, Q.L., and Zhang, L. (2007) *J. Mater. Sci.: Mater. in Electronics*, **18**, 211–227.
11. Lai, Y., Chang, H.C., and Yeh, C.L. (2007) *Microelectron. Reliab.*, **47**, 2179–2187.
12. Pierce, J.M. and Thomas, M.E. (1981) *Appl. Phys. Lett.*, **39**, 165.
13. Heurle, F. and Ames, I. (1970) *Appl. Phys. Lett.*, **16**, 80.
14. Chen, K.C., Wu, W.W., Liao, C.N. *et al.* (2008) *Science*, **321**, 1066.
15. Branderburg, S. and Yeh, S. Electromigration studies of flip chip bump solder joints (1998) Proceeding of Surface Mount International Conference and Exposition, San Jose, CA.
16. Yang, Q.L. and Shang, J.K. (2005) *J. Electron. Mater.*, **34**, 1363.
17. Zhang, X.F., Guo, J.D., and Shang, J.K. (2007) *Scr. Mater.*, **57**, 513.
18. Zhu, Q.S., Liu, H.Y., Wang, Z.G., and Shang, J.K., *J. Electron. Mater.*, under review (JEMS-3022).
19. Boettinger, W.J., Johnson, C.E., Bendersky, L.A. *et al.* (2005) *Acta Mater.*, **53**, 5033.
20. Wu, A.T. and Hsieh, T.C. (2008) *Appl. Phys. Lett.*, **92**, 121921.
21. Sinha, N.K. and Sinha, S. (2005) *Mater. Sci. Eng. A*, **393**, 179.
22. Kerr, M. and Chawla, N. (2004) *Acta Mater.*, **52**, 4527.
23. Wiese, S. and Wolter, K.J. (2004) *Microelectron. Reliab.*, **44**, 223.

24. Blench, I.A. (1976) *J. Appl. Phys.*, **47**, 1204.
25. Gan, H. and Tu, K.N. (2005) *J. Appl. Phys.*, **97**, 063514.
26. Wu, A.T., Tu, K.N., Lloyd, J.R. *et al.* (2004) *Appl. Phys. Lett.*, **85**, 2490.
27. Hsiao, H.Y. and Chen, C. (2007) *Appl. Phys. Lett.*, **90**, 152105.
28. Huang, A.T., Gusak, A.M., Tu, K.N., and Lai, Y.S. (2006) *Appl. Phys. Lett.*, **88**, 141911.
29. Dyson, B.F., Anthony, T.R., and Turnbull, D. (1967) *J. Appl. Phys.*, **38**, 3408.
30. Tu, K.N. (1994) *Phys. Rev. B Condens. Matter*, **49**, 2030.
31. Clement, J.J. (1999) *J. Appl. Phys.*, **71**, 4264.
32. Yu, Y.N. and Mao, W.M. (2001) The elastic properties of dislocation, in *Structure of Material* (eds W. Zhangand L. Mei), Beijing, China Machine Press.
33. Yu, Y.N. and Mao, WM. (2001) Dislocation climb, in *Structure of Material* (eds W. Zhang and L. Mei), Beijing, China Machine Press.
34. Courtney, T.H. (2004) High-temperature deformation of crystalline materials, in *Mechanical Behavior of Materials* (ed. Z.F. Zhang), Beijing, Metallurgical Industry Press.
35. Chen, T. and Dutta, I. (2008) *J. Electron. Mater.*, **37**, 347.

11

Effect of Temperature-Dependent Deformation Characteristics on Thermomechanical Fatigue Reliability of Eutectic Sn-Ag Solder Joints

Andre Lee, Deep Choudhuri, and K.N. Subramanian
Department of Chemical Engineering and Materials Science, Michigan State University, East Lansing MI. 48824, USA

Abstract

Deformation responses of different entities in the eutectic Sn-Ag joints during simple shear monotonic loading at different temperatures and strain rates were investigated. Results from these monotonic tests were then used to explore the thermomechanical fatigue, TMF, of these same joints with different temperature extremes. To understand the effects of temperature on the deformation isothermal monotonic loading of single shear-lap solder joints were performed with temperature ranging from -55 to $150\,^{\circ}\mathrm{C}$ with a simple shear strain rate of $10^{-3}\ \mathrm{s}^{-1}$. The effects of strain rate were probed using three different simple shear strain rates, 10^{-3}, 10^{-2}, and $10^{-1}\ \mathrm{s}^{-1}$ at -15 and $0\,^{\circ}\mathrm{C}$. In the subzero temperature extremes, the load bearing characteristics of eutectic Sn-Ag solder joints were controlled by the adhesion between the interfacial layer of Cu_6Sn_5 intermetallic compound and the Sn matrix. However, as the temperature increases, at higher-temperature extremes the failure mode was dominated by the Sn-Sn grain-boundary sliding/decohesion within the solder matrix. Furthermore, the deformation mode at faster strain rates/higher temperature was comparable to that of slower strain rates/lower temperatures. These findings justify the observed differences in surface damage features and residual mechanical properties of

Lead-free Solders: Materials Reliability for Electronics, First Edition. Edited by K. N. Subramanian.

solder joints exposed to the *low-temperature regime* TMF between −55 and 125 °C, and *high-temperature regime* TMF between −15 to 150 °C. In the *low-temperature regime* TMF, fracture between interfacial Cu_6Sn_5 intermetallics and Sn, and between Sn grains, without any significant plastic deformation within Sn grains were the dominant modes of damage, such damage causes significant reduction in the residual shear strength from the very early stages of the *low-temperature regime* TMF. The increases of solder matrix compliance at 150 °C enables plastic deformation to take place and delay the reduction of residual shear strength to later stage of TMF.

11.1 Introduction

Sn-based, Pb-free alloys are widely utilized to fabricate solder joints in microelectronics applications. A typical joint consists of a solder region sandwiched between interfacial intermetallic compound (IMC) layer/s, and several distributed IMC phases (e.g., Ag_3Sn, Cu_6Sn_5) within the solder matrix, making it a heterogeneous, multiconstituent system. Hence, the consideration of different microstructural entities is important as those entities would contribute to the load-bearing capacity of joints subjected to stresses. For example, during service, stresses are generated within solder joints when subjected to thermal excursions, resulting in their thermomechanical fatigue (TMF) [1, 2]. Consequently, the mechanical reliability of those joints will depend on the mode of deformation to accommodate imposed stresses and strains by different microstructural entities. Several studies have shown that TMF of Sn-based, Pb-free solder joint results in Sn-grain-boundary damage [1–6] and plastic deformation of the solder matrix [7]. A few studies have also indicated that the interface between IMC layer and solder matrix are also susceptible during TMF [8, 9]. These studies indicate that various microstructural entities present within a solder joint contribute to its mechanical response during TMF. Furthermore, the extent of such contributions may also vary with temperature and strain rate that will depend on the heating and cooling rates.

The temperature profile existing during thermal excursions consists of difference in temperature extremes (ΔT), heating and cooling rates, dwell times at the temperature extremes, among other service parameters [10, 11]. Strains resulting from CTE mismatches would result in generation of stresses within the joint, which will further depend on temperature extremes as the mode to accommodate the imposed stress may change. In a typical TMF profile, at a given ΔT, solder joints experience strains due to mismatches in coefficient of thermal expansion (CTE) between various microstructural entities, strain-rate effects are realized from imposed ramp rates, and the extent of stress relaxation that occurs in various entities is a consequence of the duration time at the temperature extremes. Hence, for characterizing the mechanical response of solder joints subjected TMF one needs to decouple temperature and strain-rate effects, in addition to influences from various microstructural entities.

Microstructural and mechanical response observations based on isothermal monotonic loading of solder joints can be utilized for characterization purposes. Flow stress resulting from monotonic loading depends on both temperature and strain rate [12]. Individual effects of temperature and strain rate can be isolated by holding either one constant [12]. Rhee *et al.* [13] had utilized this technique to determine the influences of temperature and strain

rate on the mechanical response of eutectic Sn-Ag. However, in that study the lowest test temperature utilized was 25 °C [13]. Solder joints are regularly subjected to subzero temperatures during service [3, 8–10, 14, 15]. Since the deformation behavior of materials is strongly depending on temperature, at subzero temperatures mechanical response of Sn-based solders may be different as compared to that prevalent at higher temperatures.

The objectives of this study were: (1) to investigate the influence of different temperatures and strain rates, on the deformation behavior of eutectic Sn-Ag shear-lap solder joints by monotonically loading them under isothermal conditions, and (2) to utilize those results to understand the TMF behavior of solder joints that underwent thermal excursions in two different temperature regimes, while maintaining similar differences between temperature extremes (ΔT).

11.2 Experimental Details

Eutectic Sn-Ag solder was used in this study to reduce the complexities that could arise from multiple microstructural entities to the mechanical response. Monotonic simple shear tests were carried out on solder joints made with this solder through isothermal deformation over a broad range of temperatures (−55 and 150 °C), since these were the extreme temperatures encountered in the TMF test temperature profiles. Additional tests were also carried out using various strain rates at 0 and −15 °C to clearly identify changes in deformation modes as a result of imposed strain rate. Such studies provide information regarding the deformation modes of different entities within the solder at various imposed temperature ramp rates. Understandings gained from the isothermal, monotonic loading tests provided the basis for justifying the TMF responses of the same eutectic Sn-Ag solder joints of the same joint geometry subjected to thermal cycling between two different temperature ranges, −55 °C/125 °C and −15 °C/150 °C, with similar dwell times at temperature extremes and ramp rates.

11.2.1 Test-Specimen Preparation

Commercially available eutectic Sn-Ag paste was utilized for fabricating single shear-lap solder-joint specimens. Machined quartz spacers with well-defined thickness were used during fabrication of joints that helped to maintain a relatively constant joint thickness of about $100 \pm 5\ \mu$m. The exact thickness of joints was measured with an optical microscope for determining the displacement rates and shear strains needed for mechanical characterization. The temperature profile used in the reflow process, as well as other fabrication details of solder-joint specimens, are described in earlier publications [9].

11.2.2 Thermal Cycling

All solder joints were thermally cycled using a bench-top model of MicroClimate® test chambers by Cincinnati Sub-Zero with a programmable controller. Two different temperature regimes were used. For the *low-temperature regime*, test specimens were placed in the environmental chamber that was initially at −55 °C. It was then heated with an average rate of 3.9 °C per minute to 125 °C, and held at this temperature for 10 min. Following this high-temperature dwell specimens were cooled to −55 °C at an average cooling rate of about

2.4 °C per minute. The dwell time at −55 °C was set for 45 minutes. For the *high-temperature regime*, test specimens were placed in the environmental chamber that was initially at −15 °C. It was then heated at an average rate of 3.9 °C per minute to 150 °C, and held at this temperature for 10 min. Following this high-temperature dwell specimens were cooled to −15 °C at an average cooling rate of about 2.4 °C per minute. The dwell time at −15 °C was set for 45 min.

11.2.3 Microstructural Characterization

A scanning electron microscope (SEM) was used to carry out microstructural characterization. To monitor the effect of thermal cycling, representative solder joints were metallographically polished on one side using an established procedure, prior to placing them in the environmental chamber. These specimens were taken out of the chamber at periodic intervals and the resultant surface damage was documented using SEM. For specimens deformed at different temperatures and strain rates, one side of the joint was metallurgically polished prior to deformation. The polished side of mechanically failed joints was examined to determine the mode of deformation.

11.2.4 Mechanical Testing

Mechanical characterization was carried out using a mechanical solids analyzer from TA Instruments, RSA-III, equipped with a forced-convection air oven for uniformity of temperature within the chamber. To evaluate the effect of thermal cycling on mechanical properties, batches of eutectic Sn-Ag solder joints exposed to 1, 10, 25, 50, 100, 200, 300, 400, and 500 TMF cycles, were strained to failure at 25 °C with a simple shear strain rate of $10^{-3}\,s^{-1}$. For each condition, eight to ten specimens were tested so that the results obtained provide realistic trends. The fractured surfaces of the mechanically tested specimens were examined to identify the facture path, and to obtain the actual joint area that contributed to the strength of the joint. This methodology is well documented in prior publications [3–7, 13, 16]. To examine the effect of temperature on deformation mode, batches of eutectic Sn-Ag solder joints were assessed by monotonically loading the specimens isothermally at −55, −40, −15, 0, 25, 75, and 150 °C at a constant simple shear strain rate of $10^{-3}\,s^{-1}$. The effect of strain rates were examined by monotonically loading the solder joints at simple shear rates of $10^{-3}\,s^{-1}$, $10^{-2}\,s^{-1}$, and $10^{-1}\,s^{-1}$ at −15 and 0 °C, since changes in modes of deformation were expected to be strain-rate sensitive in this temperature range. Three to four specimens were tested for each chosen temperature and strain rate. Most of the specimens were strained to failure. However, in order to preserve the deformation features few of the specimens were strained beyond the peak shear stress without complete detachment.

11.3 Results and Discussion

The following subsections explain the influences of temperature and strain rate on the mechanical response of eutectic Sn-Ag single shear-lap solder joints on the basis of mechanical and microstructural characterization.

11.3.1 Effects of Temperature

Figure 11.1a shows the shear stress vs. simple shear strain plot of joints monotonically loaded under shear with a simple shear strain rate of 10^{-3} s^{-1} at different temperatures. It is evident from Figure 11.1a that the shear flow stress of eutectic Sn-Ag is a strong function of temperature. To further emphasize the influence of temperature, the average peak shear stress is plotted as a function of temperature in Figure 11.1b. For comparison, data from a similar study conducted by Rhee *et al.* [13] at higher temperatures on eutectic Sn-Ag single

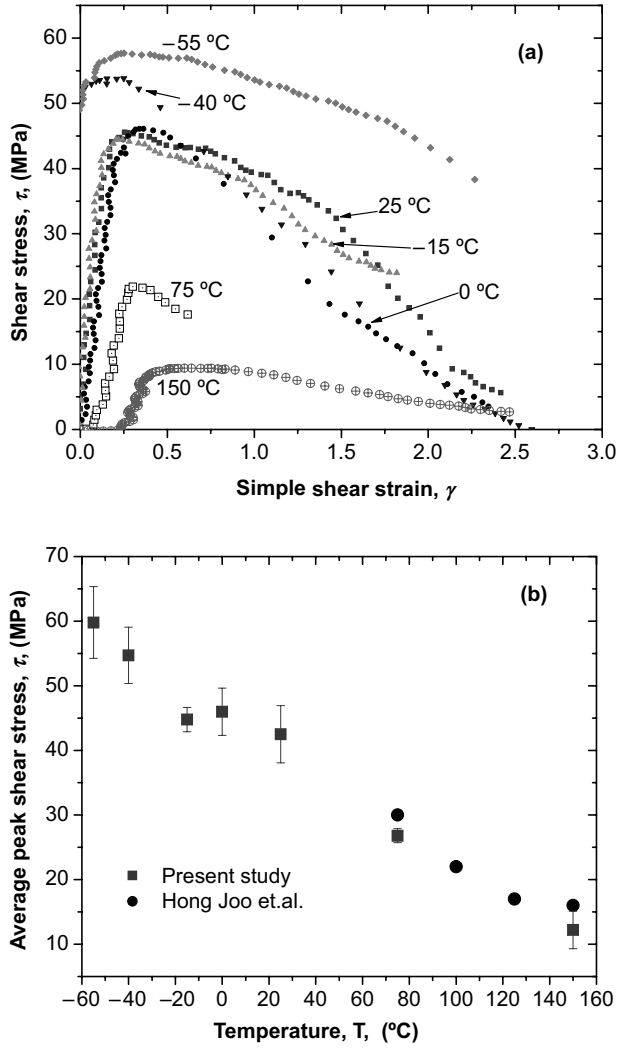

Figure 11.1 *Plots showing (a) mechanical response of eutectic Sn-Ag solder joints subjected to monotonic shear loading at a simple shear strain rate of 10^{-3} s^{-1} at different temperatures as indicated, and (b) effect of temperature on the peak shear stress.*

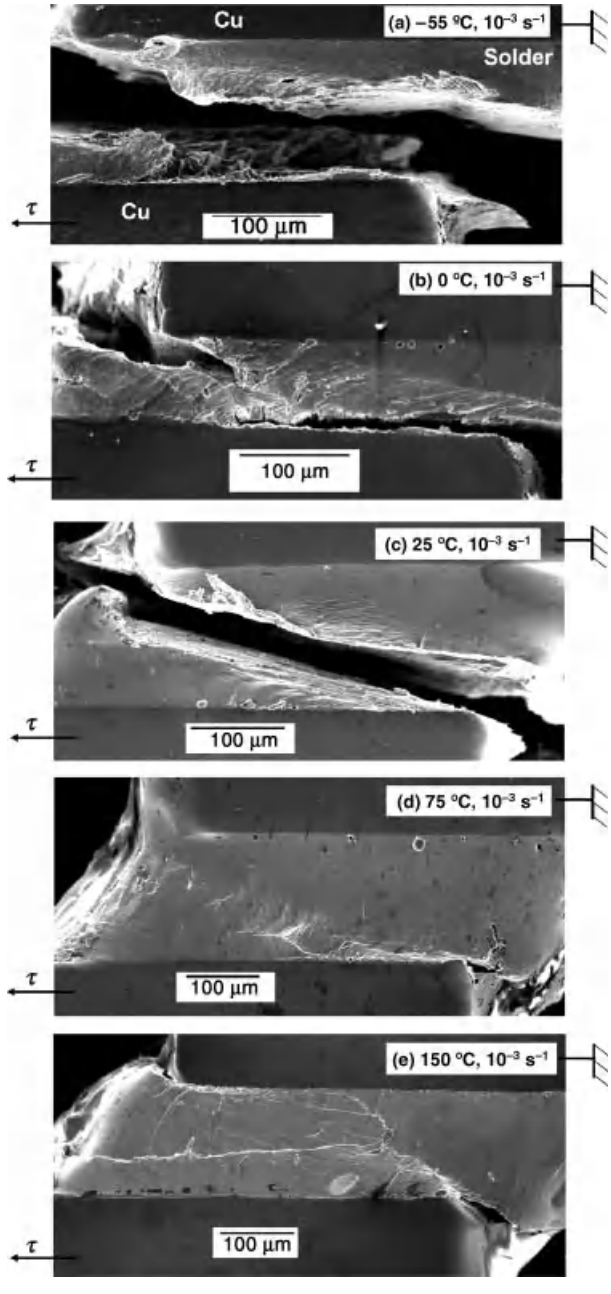

Figure 11.2 *SEM micrographs showing failure crack paths in specimens monotonically loaded at (a) −55°C, (b) 0°C, (c) 25°C, (d) 75°C, and (e) 150°C. All the specimens were strained beyond the peak shear stress at a simple shear strain rate of 10^{-3} s^{-1}. The bottom copper strip was attached to the moving crosshead of the machine, while the one at the top strip was fixed.*

shear lap joints is also shown. Figure 11.1b suggests that the dependence of peak shear stress on temperatures can be categorized into three distinct regions (identified with dotted, broken and solid lines). The peak shear stress increases with decrease in temperature, although it remains relatively stable in the temperature range of 25 and −15 °C. These observations indicate that, depending on the temperature, different modes of deformation contribute to failure of solder joints subjected to monotonic shear loading. Microstructural features resulting from the observed mechanical response (Figure 11.1) of eutectic Sn-Ag solder joints are presented in the following section.

Figure 11.2 shows the failure crack path as observed on the polished side of the solder joints, which were monotonically strained beyond the peak shear stress at different temperatures. SEM micrographs presented in Figures 11.2a and b suggest that between −55 and 0 °C failure occurs though crack propagation primarily along the Cu_6Sn_5 layer/solder interfacial region. However, above 25 °C, failure seems to have occurred though crack propagation within the solder region, as shown in Figure 11.2c–e. It was also noted that at 150 °C, Figure 11.2e, the crack seems to have propagated along the length of the solder region, instead of diagonally propagating to opposite corners of the solder joints as in specimens deformed at 25 and 75 °C shown in Figures 11.2c and d. Such influences of temperature on the mode of failure crack propagation are summarized by overlaying schematics of the crack path on SEM micrographs of a typical joint as shown in Figures 11.3a and b. Typical specimens that monotonically loaded at −55 and 0 °C are given in Figure 11.3a, while those loaded at 25, 75, and 150 °C were presented in Figure 11.3b. These figures suggest that the solder region is stiffer at temperatures below 0 °C than at temperatures above 25 °C, since at lower temperatures (below 0 °C) a failure crack is observed at the Cu_6Sn_5 layer/solder interfacial region, rather than within the solder region. This also implies that mode of deformation behavior of the solder region within the joint would also depend on the temperature.

Figure 11.2 also indicates the differences in the deformation behavior with temperature. The specimen strained at 0 °C (Figure 11.2b) appears to have more surface features than those strained at −55 °C (Figure 11.2a). Variations in the surface features can be observed in specimens deformed at higher temperatures (Figures 11.2c–e). Such effects of temperature on the deformation behavior were further systematically examined through SEM micrographs of the interfacial and solder regions.

The Cu_6Sn_5 layer/solder interfacial region of the solder joints deformed at −55 °C are presented in micrographs provided in Figure 11.4. The micrograph shown in Figure 11.4a is a higher magnification view of region marked 'X' in Figure 11.2a, while the one in Figure 11.4b is a higher magnification view of region marked 'Y' in Figure 11.2a. These SEM images indicate that monotonic shear straining at −55 °C causes decohesion between the Cu_6Sn_5 layer and the solder matrix, and cleaving of interfacial Cu_6Sn_5 scallops. Both of these features can be noted in Figure 11.4a, while only unbroken Cu_6Sn_5 scallops are obvious in Figure 11.4b. Cu_6Sn_5 scallops in the interfacial region in both the SEM micrographs are marked with arrows. Damage due to monotonic shear loading at −55 °C was further examined though observation of the fracture surface of the solder joint (Figure 11.5). SEM micrographs in Figure 11.5a and b illustrate cleaved and unbroken Cu_6Sn_5 scallops, respectively. Cu_6Sn_5 layer/solder interfacial damage was also observed in the solder joint deformed at 0 °C (Figure 11.6a). Additionally, at the same temperature a large number of shear bands within the solder region have also been observed, as compared

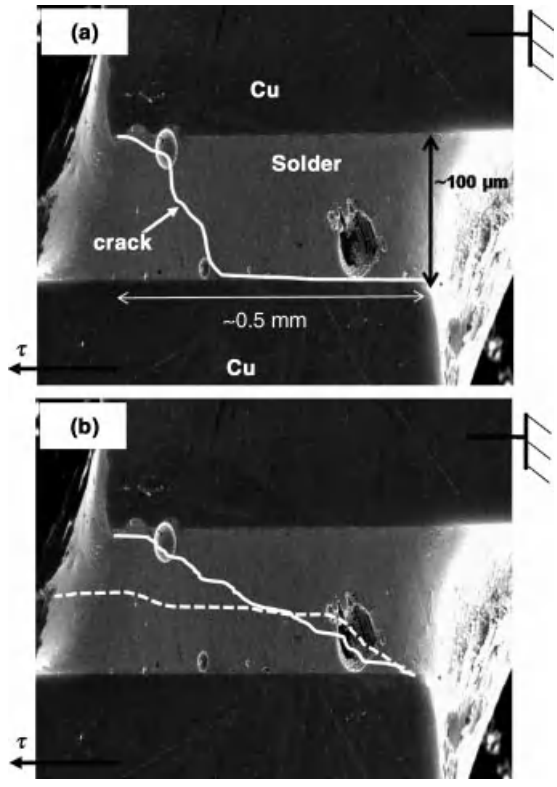

Figure 11.3 *Schematics showing the temperature dependence of failure crack paths (overlaid on an SEM micrograph of a typical joint cross section). Crack paths at temperatures (a) −55 °C and 0 °C, and (b) 25 °C, 75 °C, and 150 °C. In (b) crack path indicated by the solid line is for failure at 25 °C and 75 °C, while the broken line is for 150 °C.*

to the specimen deformed at −55 °C. Figures 11.7a and b further illustrate the differences between the solder matrices of the specimens deformed at −55 and 0 °C, respectively. These micrographs indicate that imposed strains are dissipated through different deformation mechanisms at these two temperatures. At −55 °C relatively less deformation occurs within the solder matrix as compared to that at 0 °C, further indicating increased stiffness of the solder matrix at lower temperatures. As a result, imposed strains are accommodated through Cu_6Sn_5 layer/solder interfacial damage at −55 °C rather than by the solder region. However, at 0 °C the solder matrix becomes more compliant, and as a consequence imposed strains are accommodated through damage at the Cu_6Sn_5 layer/solder interfacial region and plastic deformation of the solder matrix through formation of shear bands.

At higher temperatures (above 25 °C) increased compliance of the solder matrix results in different modes of deformation. Such features are presented in the SEM micrographs of the interfacial region of specimens deformed at 25, 75, and 150 °C in Figures 11.6b–d, respectively. These images show the presence of shear bands in specimens deformed at 25 and 75 °C, while Sn-Sn grain-boundary sliding/decohesion is noted in specimens strained at 75 and 150 °C. Such temperature-dependent mode of deformation in eutectic

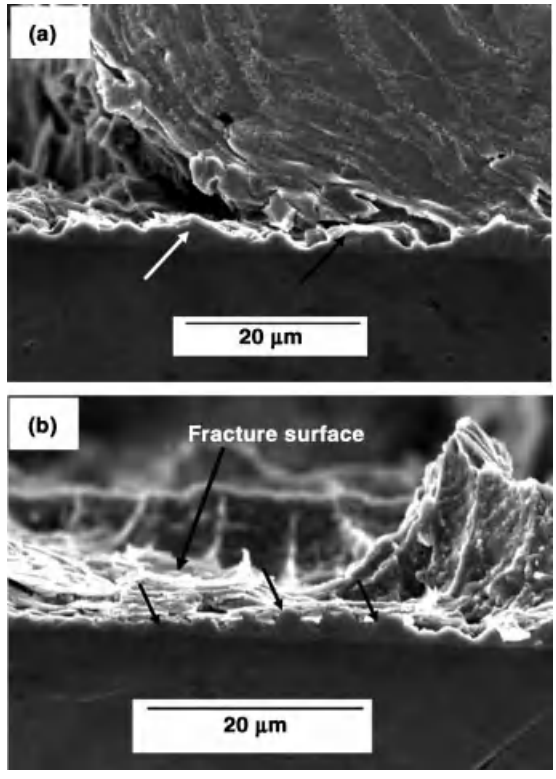

Figure 11.4 *SEM micrographs of the interfacial region of a solder joint monotonically strained at simple shear strain rate of 10^{-3} s^{-1} at −55 °C. The Cu_6Sn_5 layer is marked with arrows in the images. (a) Cleaved Cu_6Sn_5 scallop and crack between the interfacial Cu_6Sn_5 layer and solder (corresponding to 'X' in Figures 11.2a), and (b) fracture surface and Cu_6Sn_5 layer attached to the Cu substrate (corresponding to 'Y' in Figure 11.2a).*

Sn-Ag solder joints at a temperature range of 25–150 °C has been previously reported by Rhee *et al.* [9]. Nonetheless, irrespective of the differences in the deformation modes (Figures 11.6b and c) at temperatures above 25 °C, imposed strain due to monotonic loading is accommodated through deformation within the solder matrix instead of at the Cu_6Sn_5 layer/solder interface. This is further highlighted in the SEM images (Figures 11.7c and d) of the solder region of the joints deformed at 25, 75, and 150 °C.

Based on the SEM micrographs presented in Figures and the mechanical response (Figure 11.1) of eutectic Sn-Ag the following effects of temperature on the deformation behavior emerge. At higher temperatures (25, 75, and 150 °C) the solder is more compliant than at lower temperatures (−55 and 0 °C). Consequently, imposed strains during monotonic loading at 25, 75, and 150 °C, are dissipated through deformation of the solder matrix. Such dissipation occurs through either shear banding or grain-boundary sliding/decohesion. At 75 and 150 °C interfacial grain-boundary damage results in lower peak stress in solder joints (Figure 11.1b) as compared to solder joints deformed through the formation of shear bands (at 25 °C). However, at lower temperatures, as a result of increased stiffness of the

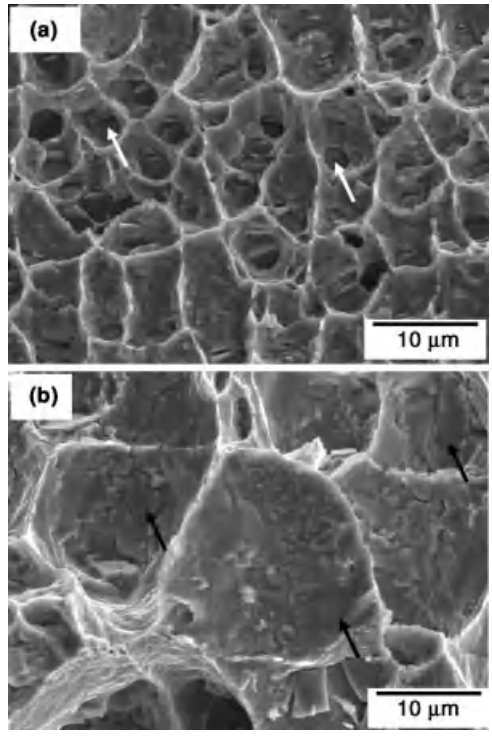

Figure 11.5 *SEM micrographs of fracture surfaces of the specimen monotonically strained to failure at a simple shear strain rate of $10^{-3}\,s^{-1}$ at −55 °C. Arrows within the images indicate cleaved Cu_6Sn_5 scallops in (a), and Cu_6Sn_5 scallops embedded within the solder matrix in (b).*

solder matrix, the Cu_6Sn_5 layer/solder interface becomes more susceptible to failure under monotonic loading. Moreover, such a transition is not abrupt, as indicated by deformation features in the specimen deformed at 0 °C (Figures 11.6a and 11.7b). At that temperature both Cu_6Sn_5 layer/solder interfacial damage and shear bands within the solder matrix are observed, suggesting the presence of two competing modes of deformation during monotonic loading. Furthermore, upon comparing with Figure 11.1b, it seems that the transition between Cu_6Sn_5 layer/solder interfacial damage to shear banding occurs in the range of −15 and 0 °C, since the peak shear stress stabilizes within that range. In other words, at subzero temperatures stress required to cause deformation of the solder matrix is larger than that required to accommodate deformation at the Cu_6Sn_5 layer/solder interface. This is further supported by the deformed microstructures of the joint failed at −55 °C (Figures 11.4 and 11.7a) where one can observe relatively fewer shear bands within the solder matrix as compared to a specimen failed at 0 °C. As a result at −55 °C imposed monotonic loading is accommodated primarily through Cu_6Sn_5 layer/solder interfacial decohesion rather than by plastic deformation of the solder matrix.

The results presented thus far demonstrate only the effects of temperature at a constant simple strain rate on the deformation behavior of eutectic Sn-Ag. The influence of different simple strain rates during monotonic shear loading have been examined in the following section.

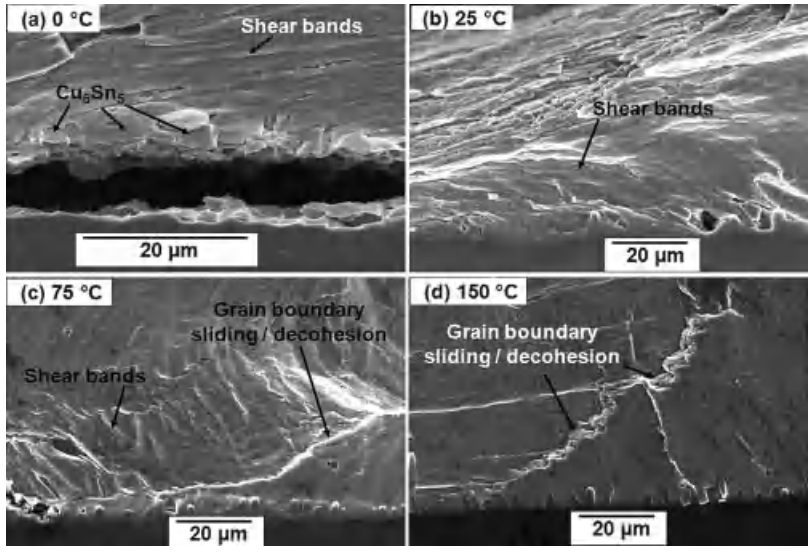

Figure 11.6 *SEM micrographs of the interfacial region of solder joints monotonically strained at a simple shear strain rate of $10^{-3}\,s^{-1}$ at (a) 0°C, (b) 25°C, (c) 75°C, and (d) 150°C.*

11.3.2 Effects of Strain Rate

Figures 11.8a and b show the variation of peak shear stress (τ) with simple shear strain rate ($d\gamma/dt$) at -15 and 0 °C, respectively. This plot indicates that deformation behavior of eutectic Sn-Ag is sensitive to strain rates. Similar effects of strain rate on eutectic Sn-Ag at higher temperature (above 25 °C) has also been shown by Rhee *et al.* [13] and Lee *et al.* [17]. The present and prior studies [13, 17] show that eutectic Sn-Ag is highly stain-rate sensitive over a broad range of temperatures, that is, between -15 and 150 °C.

Additionally, the creep-stress exponent 'n' was also obtained for the temperatures employed in this study by using Norton's equation [13].

$$d\gamma/dt = A\tau^n \exp\left(-Q/8.314\,T\right) \tag{11.1}$$

where A, Q and T are a constant, activation energy and temperature in Kelvin, respectively. The creep-stress exponent 'n' is obtained from the natural logarithmic plots of $d\gamma/dt$ vs. τ, as shown in Figure 11.8b. A similar method has also been utilized in prior studies [13, 17] for determining 'n'. Table 11.1 compares the value of 'n' at different temperatures. Higher 'n' values at subzero temperatures suggest a change in mode of deformation under the influence of monotonic loading under shear. Additionally, the rise in 'n' seems to have occurred in the neighborhood of 0 °C. Consequently, microstructures of the polished side of solder joints deformed with simple shear strain rates of $10^{-3}\,s^{-1}$, $10^{-2}\,s^{-1}$, and $10^{-1}\,s^{-1}$ at 0 °C were examined. Figures 11.9a and b show failure crack propagation paths of solder joints monotonically loaded at $10^{-2}\,s^{-1}$, and $10^{-1}\,s^{-1}$, respectively. These specimens were examined after deforming them beyond the peak shear stress. Both the SEM micrographs shown in Figure 11.9 suggest that failure has occurred at the Cu_6Sn_5 layer/solder interfacial region. To ascertain the reason for the observed failure crack propagation

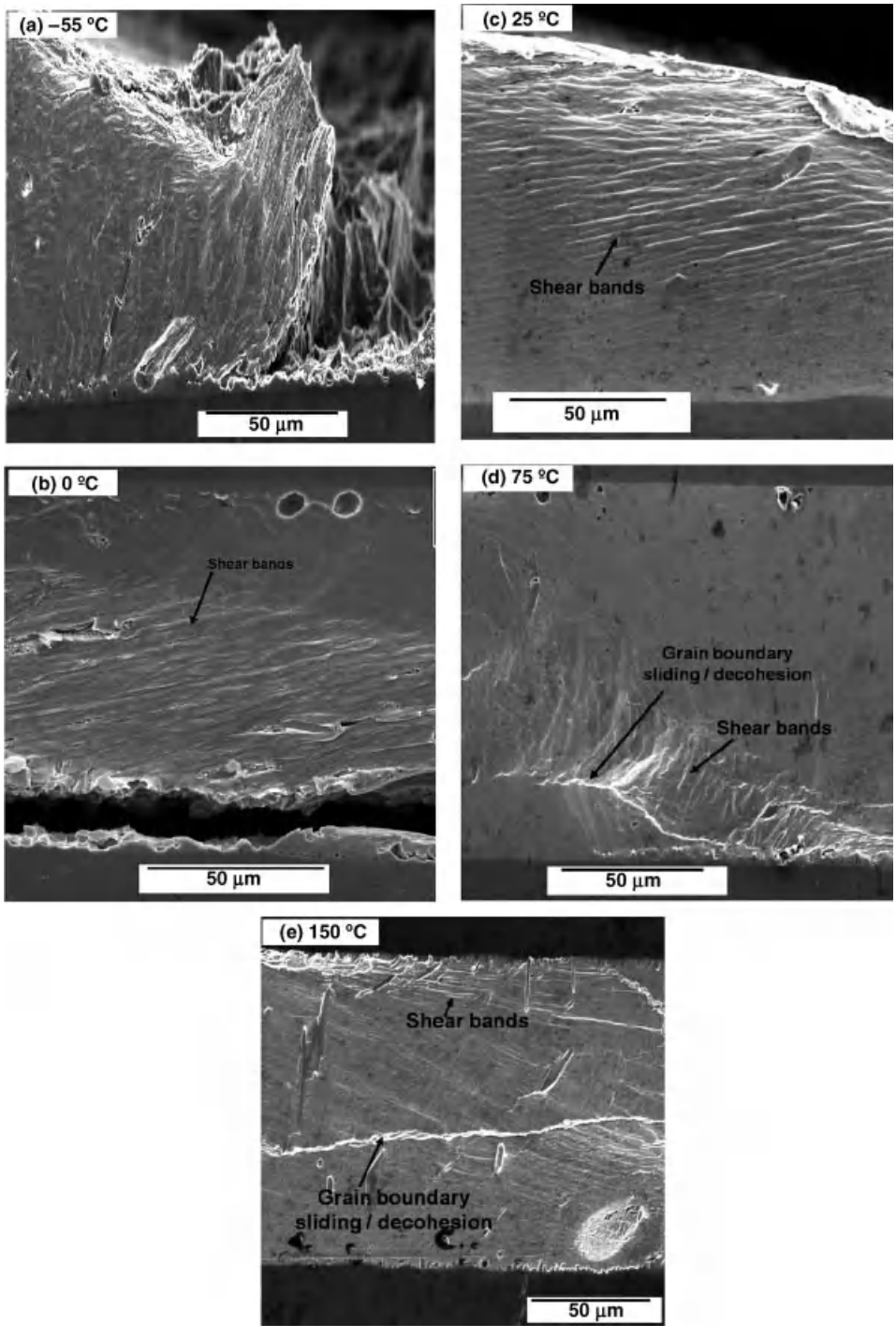

Figure 11.7 *SEM micrographs of the interfacial region of solder joints monotonically strained at a simple shear strain rate of $10^{-3}\ s^{-1}$ at (a) −55°C, (b) 0°C, (c) 25°C, (d) 75°C, and (e) 150°C.*

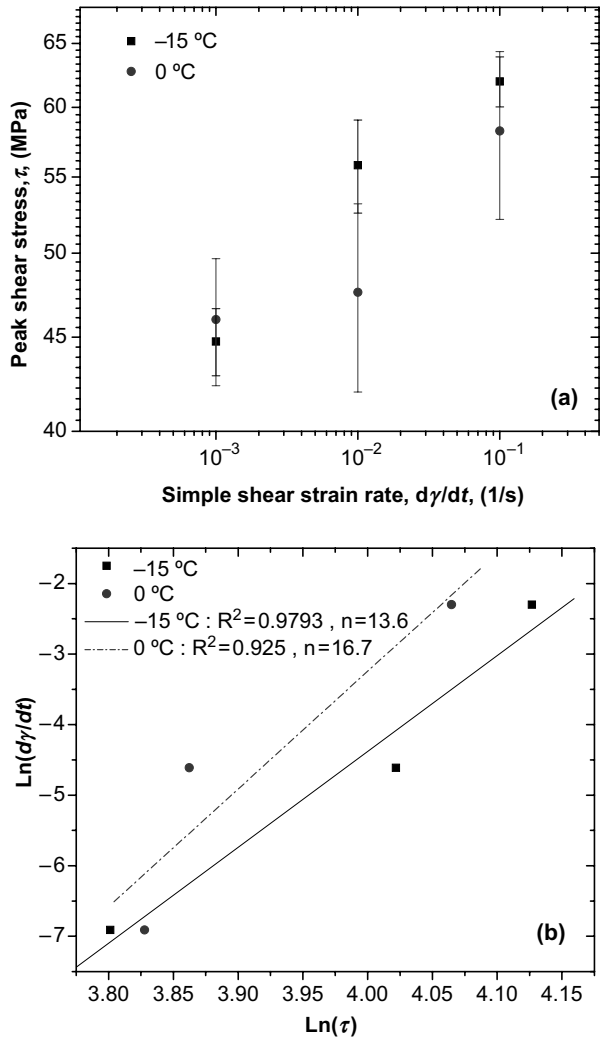

Figure 11.8 *Plots showing simple shear strain rate ($d\gamma/dt$) vs. peak shear stress (τ) at (a) −15°C, (b) 0°C, and (b) natural logarithmic plots for $d\gamma/dt$ vs. τ for determining creep-stress exponent 'n'. The slope of the regression line provides 'n'.*

Table 11.1 *Creep-stress exponent 'n'* (Eq. (11.1)) at different temperatures.

Temperature (°C)	*n*	Reference
−15	13.6	Present study
0	16.7	
25	10.0	Rhee *et al.* [13]
100	10.5	
150	11.7	

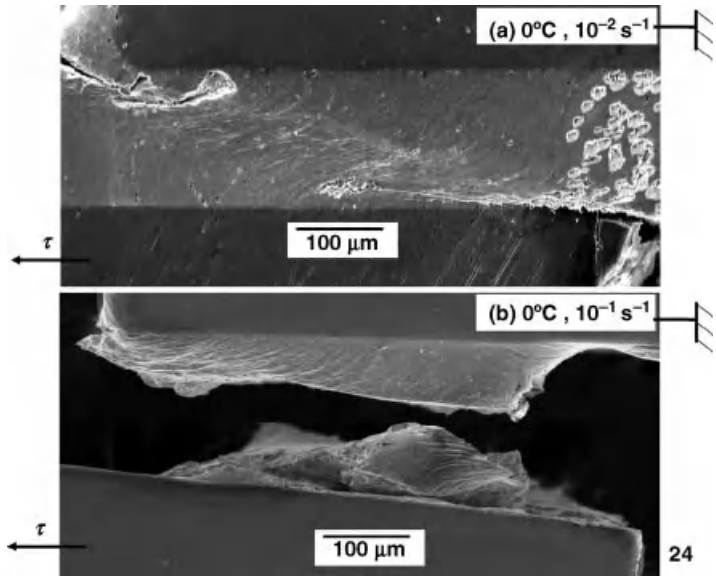

Figure 11.9 *SEM micrographs showing failure crack paths in specimens monotonically loaded at a simple shear strain rate of (a) $10^{-2}\,s^{-1}$ and (b) $10^{-1}\,s^{-1}$. Both the specimens were deformed at 0°C.*

path higher-magnification SEM images of the solder and interfacial region were obtained and are presented in Figure 11.10.

Comparison of the joint cross section of specimens deformed with $10^{-3}\,s^{-1}$ as shown in Figure 11.10a, and $10^{-2}\,s^{-1}$, as shown in Figure 11.10b, revealed significant numbers of shear bands within the solder matrix at lower strain rate. However, at higher strain rate ($10^{-2}\,s^{-1}$) shear bands seem to concentrate within the solder matrix near the Cu_6Sn_5 layer. This is further supported by the high-magnification SEM image of the interfacial region presented in Figure 11.11a. These observations indicate that at higher strain rates, the deformation is confined to the regions adjacent to the Cu_6Sn_5 layer, whereas at lower strain rates the deformation is accommodated by the entire solder region. Micrographs of the specimen deformed at $10^{-2}\,s^{-1}$ do not show any indication of Cu_6Sn_5 layer/solder interfacial decohesion. However, such decohesion was apparent in high-magnification SEM of the interfacial region of the specimen deformed at $10^{-1}\,s^{-1}$, as shown in Figure 11.11b. Such observations indicate that strains generated during faster rates of deformation are accommodated by Cu_6Sn_5 layer/solder interfacial decohesion.

11.3.3 Influence of Temperature Regime of TMF on the Residual Mechanical Properties

The effect of low-temperature regime TMF on the residual mechanical strength is shown in Figure 11.12. The residual shear strength of joints was found to drop rapidly by about 35% within the first 100 cycles, and by about 50% after 500 cycles, as compared to the initial shear strength. This drastic decrease in the residual shear strength can be attributed to the

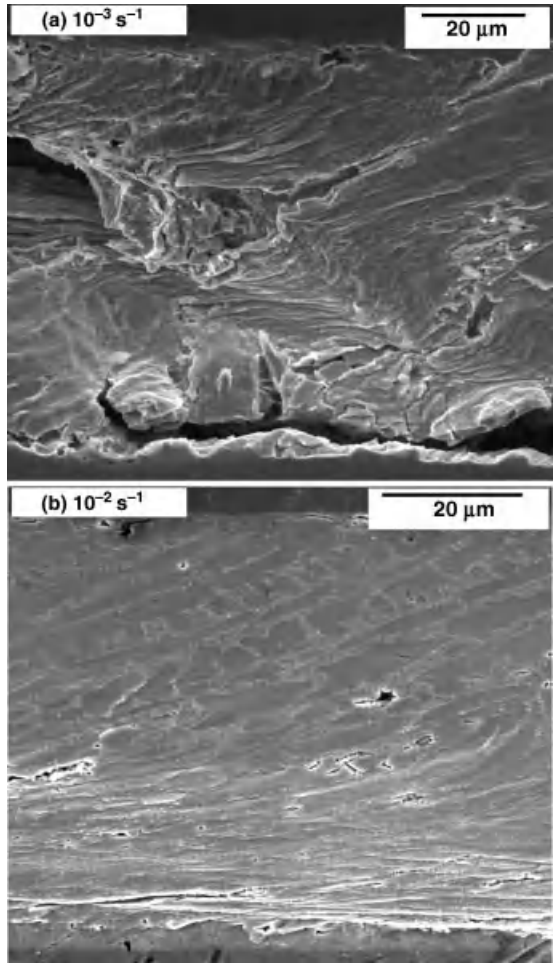

Figure 11.10 *SEM micrographs comparing deformation within the solder region of specimen subjected to monotonic loading at simple shear strain rates of (a) 10^{-3} s^{-1} and (b) 10^{-2} s^{-1}. Both the specimens were deformed at 0°C.*

appearance of cracks at the interface of the IMC layer and solder matrix in the very early stages of TMF. Evidence of such interfacial debonding on mechanical properties comes from the fracture features in a mechanically sheared specimen, as shown in Figure 11.13. The fracture path of this Eutectic Sn-Ag solder joint, subjected to 500 cycles of TMF in the low-temperature regime, is initiated along the IMC layer and solder interface near the corner, as marked on Figure 11.13, and proceeds predominantly along the interface. The Sn-Sn grain-boundary decohesion observed may cause some deviations of the crack path. This finding suggests that these interfacial cracks, developed at interfaces during TMF cycles, had caused the failure to take place at those locations during mechanical testing. Since the imposition of thermal stresses arising from this low-temperature regime TMF are not accommodated by plastic deformation within Sn grains, relaxation of thermal stresses

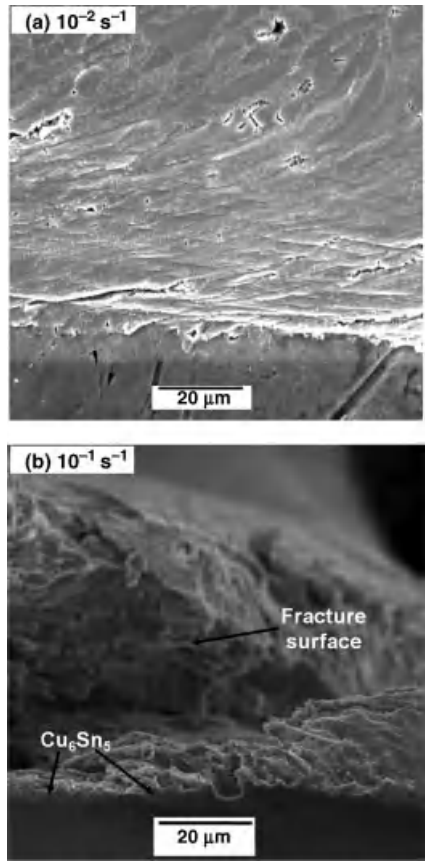

Figure 11.11 *SEM micrographs comparing the interfacial region of specimens deformed at simple strain rates of (a) 10^{-2} s^{-1} and (b) 10^{-1} s^{-1}. Both the specimens were deformed at 0°C.*

that one normally expects during dwell times at extreme temperatures will not be a contributing factor.

Figure11.14 compares the effect of *low-* and *high-temperature regime* TMF on the residual strength of eutectic Sn-Ag solder joints after 500 cycles. This plot also shows the influence of other service parameters such as dwell times and heating rate on residual strength of solder joints subjected to *high-temperature regime* TMF. Evidently, *low-temperature regime* TMF has a more detrimental effect on the residual mechanical properties of solder joints as compared to *high-temperature regime* TMF. These results, in conjunction with microstructural observations, suggest that interfacial and grain-boundary fractures, with lack of observable plastic deformation within the Sn grains during low-temperature TMF, may be the major contributing factors for the significant drop in strength under such conditions. Under these conditions cracks continue to form and propagate with each successive cycle of TMF. Hence, residual strength does not seem to stabilize even after 500 cycles of low-temperature TMF. This is in contrast with findings of *high-temperature*

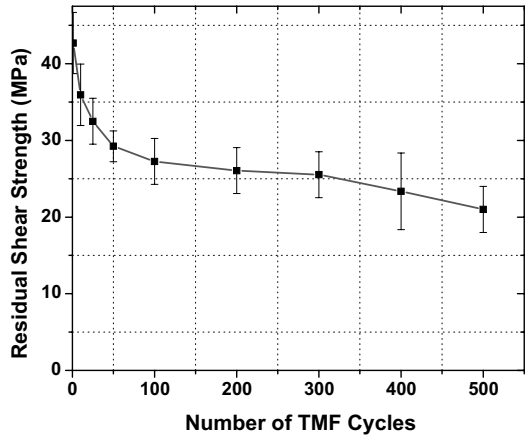

Figure 11.12 *Plot showing the variation of residual shear strength of eutectic Sn-3.5Ag solder joints as a function of TMF cycles.*

regime TMF studies, wherein residual mechanical properties seem to stabilize after 250 TMF cycles [4–6].

11.3.4 Effect of Temperature Regime of TMF on Surface-Damage Accumulation

Surface-damage features resulting from *high-temperature regime* TMF are similar, irrespective of whether it was from TMF with long dwell at the low-temperature extreme (−15 °C) or with long dwell at the high-temperature extreme (150 °C). Under such conditions, microstructural damage is localized to Sn matrix present in regions closer to the solder/substrate interface IMC layer as shown in Figures 11.15a and b. Microstructural damages resulting from *high-temperature regime* TMF consists of surface manifestations of grain-boundary sliding and/or relief, and grain-boundary decohesion, all of which are associated with significant extents of deformation within the Sn matrix. Illustrations of these manifestations are presented in Figure 11.16. In Figure 11.16a, Sn grain-boundary

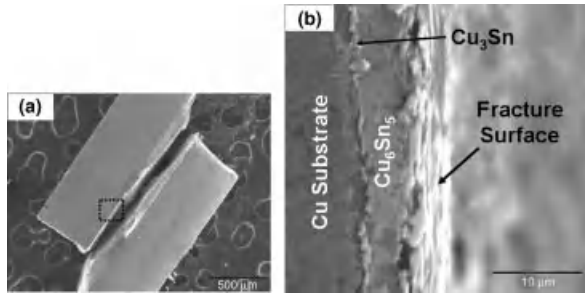

Figure 11.13 *(a) Side view of a mechanically failed eutectic Sn-3.5Ag solder joint; (b) Enlarged view on the of the region inside the dotted rectangle in (a). This joint had undergone 500 cycles of low-temperature regime TMF prior to mechanical testing.*

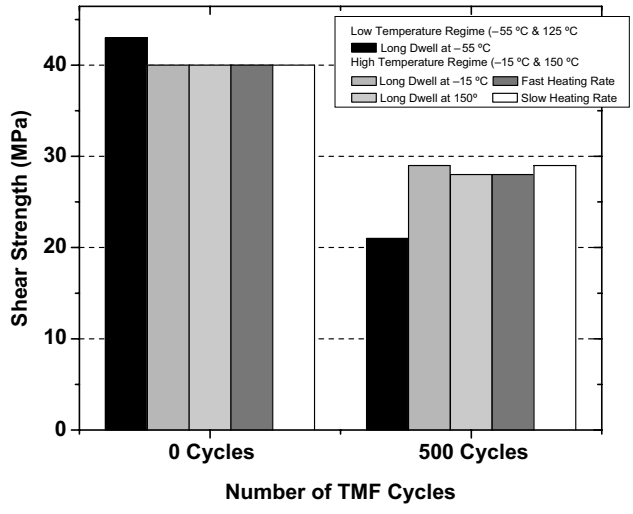

Figure 11.14 *Plot comparing the effect of high- and low-temperature regime TMF on average shear strength of eutectic Sn-3.5Ag single shear-lap solder joints after 500 cycles.*

decohesion is observed at approximately one grain diameter away from the IMC layer and solder interface, while Figure 11.16b presents surface damage due to grain-boundary sliding and/or relief.

On the other hand, microstructural damage due to *low-temperature regime* TMF is marked by the lack of any observable plastic deformation within Sn regions. This is consistent with the observation reported by Rhee *et al.* [13] that mechanical strength of Sn is strongly dependent on temperature. As a consequence, at the low temperatures encountered in low-temperature regime TMF absence of significant plastic deformation within the Sn grains plays an important role. The thermal stresses arising from TMF basically cause grain-boundary debonding within Sn, and interfacial debonding between IMCs and Sn grains.

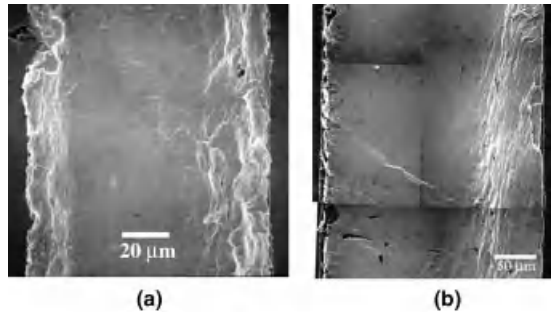

Figure 11.15 *SEM images showing surface damage on eutectic Sn-3.5Ag solder joints after 1000 cycles of high-temperature regime TMF with long dwell at (a) high-temperature extreme, and (b) low-temperature extreme.*

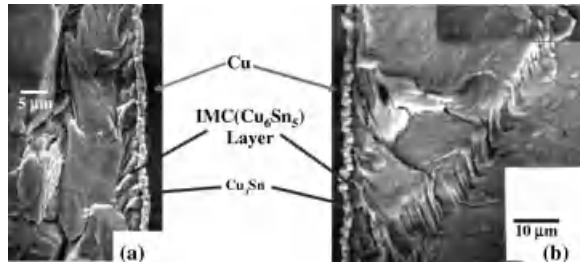

Figure 11.16 *SEM images showing the effect of high-temperature regime TMF on surface damage features within the solder near the IMC layer/solder interface, (a) Sn-Sn grain decohesion and (b) grain-boundary sliding/relief and shear banding.*

11.3.5 Evolution of Microstructural Damages during Low-Temperature Regime TMF

To asses the evolution of surface damage, three regions were chosen on the polished side of the representative solder joint. The schematic provided in Figure 11.17 indicates the locations of these regions, which, hereafter will be referred to as regions 1, 2 and 3. Microstructural evolution in these regions with increased number of TMF cycles is presented in Figures 11.18–11.20. All these images reveal that damage accumulates from very early stages of TMF, that is, within the first 50 cycles, unlike in specimens subjected to TMF in −15 to 150 °C range [4, 6]. In that *high-temperature regime* TMF, surface manifestation of damage was first noted only after about 250 cycles [4, 6].

The surface manifestation of damage noted in the low-temperature regime TMF occurs in two ways. The first type of surface manifestation is in the form of relief features within the

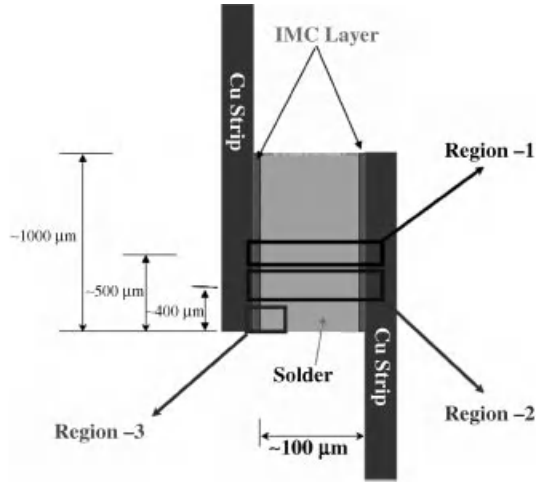

Figure 11.17 *Schematic of the regions on the solder joint observed for microstructural evolution. Region 1 is at the middle, region 2 is ∼100 μm below region 1 and region 3 is at the edge of the joint.*

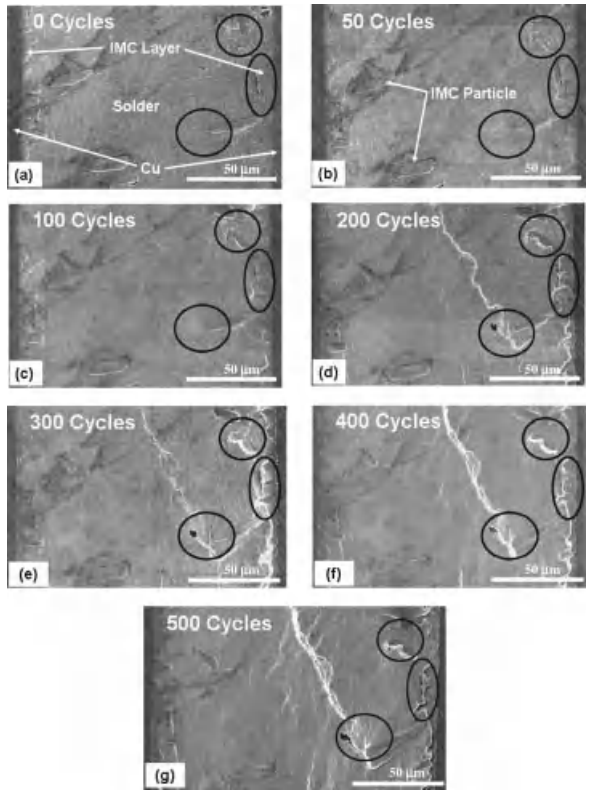

Figure 11.18 *SEM images of region 1 showing the evolution of surface damage within the solder and near the IMC layer, and at the IMC/solder interface, after (a) 0, (b) 50, (c) 100, (d) 200, (e) 300, (f) 400, and (g) 500 cycles of TMF.*

solder region. Such features were observed in regions 1, and 2 (Figure 11.18 and 11.19). In region 3, which is very near the corner of the joint, this feature was absent throughout the entire duration of this study (Figure 11.20). In region 1, such damage appears to proceed from the center of the joint towards the IMC/solder interface at an angle of approximately 30° with the IMC layer, whereas in region 2, damage runs almost parallel to the IMC/solder interface. These observations suggest that surface-relief features within the solder matrix may be due to thermal stresses that arise from the anisotropy of Sn during TMF, and the inability to dissipate these stresses by plastically deforming the Sn grains. Hence, grains move relative to each others by mode-II or mode-III types of fracture.

The second type of surface manifestation noted is the debonding between the IMC and Sn grains. Such debonding occurs both at the solder matrix and the IMC layer it forms with the substrate, as well as within the solder matrix and the IMC particles embedded in it. This type of surface manifestation is observed prominently after 100 cycles in all three regions of the joint.

The micrographs shown in Figures 11.18–11.20 depict the progression of interfacial debonding between IMCs and Sn matrix with increased number of thermal cycles. High-magnification SEM micrographs of these interfaces after 500 TMF cycles suggest that

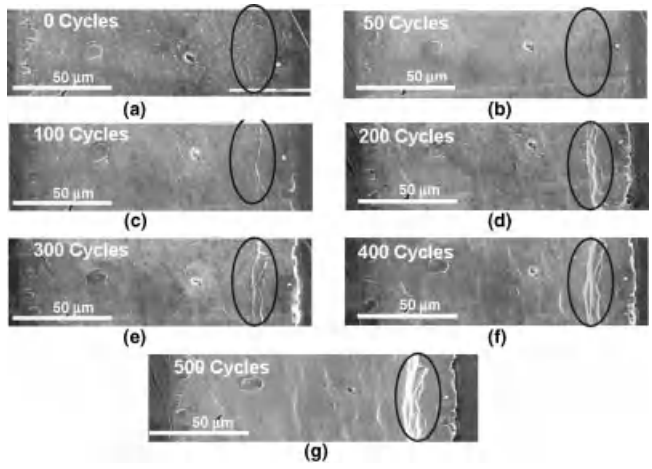

Figure 11.19 *SEM images of region 2 showing the evolution of surface damage within the solder near the IMC layer, and at the IMC/solder interface, after (a) 0, (b) 50, (c) 100, (d) 200, (e) 300, (f) 400, and (g) 500 cycles of TMF.*

failures occur in two different modes. In one case, Sn grains protrude over the surface of IMCs by mode-II or mode-III type of fracture at their interface, while in other case cracks form in between solder and IMCs by mode-I type fracture and open up. It is important to note that there are no indications of plastic deformation in the Sn grains adjacent to these IMCs. These features can be observed in the micrographs presented in Figure 11.21. Such observations are indicative that the thermal stresses generated between the IMC and the adjoining Sn grains could not be accommodated by deformation within the Sn grains prior to crack formation, unlike in *high-temperature regime* TMF.

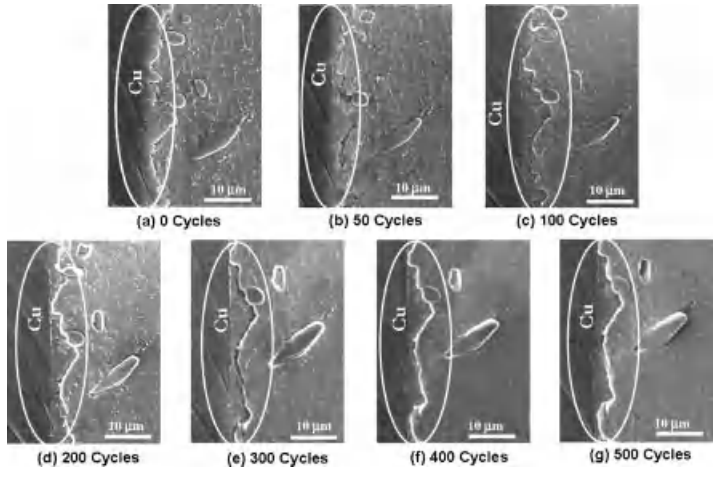

Figure 11.20 *SEM images of region 3 showing the evolution of surface damage at the IMC/solder interface after (a) 0, (b) 50, (c) 100, (d) 200, (e) 300, (f) 400, and (g) 500 cycles of TMF.*

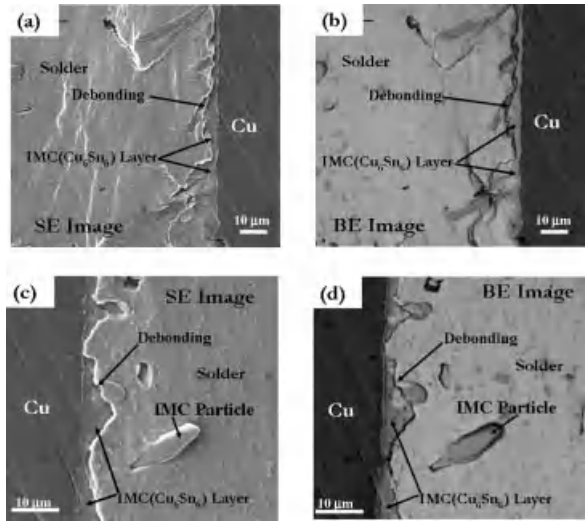

Figure 11.21 *High-magnification images showing debonding at the IMC layer/solder interface at two different regions after 500 cycles (a) Location near region 1 and (b) is the corresponding BE image. SEM image of region 3 is shown in (c) and its corresponding BE image in (d).*

11.4 Summary and Conclusions

The mechanical response of various microstructural entities within the solider joint of eutectic Sn-Ag solder and copper substrate subjected to a simple shear deformation at different temperatures and strain rates was investigated. The results of monotonic deformation provide a better understanding of solder-joint reliability when they are subjected to thermomechanical fatigue cycles with different temperature profiles. Deformation modes of Sn-Ag solder joints subjected to isothermal simple monotonic shear loading over a broad range of temperatures of interest in the range of −55 to 150 °C with a constant simple shear strain rate of $10^{-3}\,s^{-1}$ indicated that, depending on the temperature, different microstructural entities control the strength of the solder joint. Shear failure of solder joints at lower temperatures, −55 to 0 °C, is dominated by the decohesion of the substrate/matrix interfacial Cu_6Sn_5 layer, while at higher temperatures, 75 to 150 °C, Sn grain-boundary interfaces that are within the solder matrix become weaker leading to failure by grain--boundary sliding or decohesion. In another words, the compliance of different entities at a specific temperature determines the location of failure.

Microstructural observations of specimens deformed at 0 °C with different strain rates reveled that as the strain rate increases the deformation becomes more concentrated at regions within the solder matrix adjacent to the substrate/matrix interfacial Cu_6Sn_5 layer. It appears that the mechanical response of eutectic Sn-Ag solder joints at lower temperatures for a constant deformation rate is similar to that of at higher temperatures but at a faster deformation rate.

During *lower-temperature regime* TMF, thermal cycling between −55 and 125 °C, surface damage is mainly in the form of debonding between IMCs and solder, and with

some Sn grain-boundary fractures, without any observable deformation within the Sn grains. These observations are completely different from those grain-boundary events with extensive deformation within Sn grains at regions close to solder and substrate interface noted under *high-temperature regime* TMF, cycling between −15 and 150 °C. Residual mechanical properties continued to drop drastically during the early stages of *low-temperature regime* TMF, without stabilizing even after 500 cycles, whereas in *high-temperature regime* TMF the residual shear strength of solder joints stabilizes after 250 cycles. In addition, magnitude of the loss in mechanical shear strength is much greater for *low-temperature regime* TMF.

References

1. Lee, J.G., Telang, L., Subramanian, K.N., and Bieler, T.R. (2002) Modeling thermomechanical fatigue behavior of Sn-Ag solder joints. *J. Electron. Mater.*, **31**, 1152–1159.
2. Subramanian, K.N. (2007) Role of anisotropic behaviour of Sn on thermomechanical fatigue and fracture of Sn-based solder joints under thermal excursions. *Fatigue Fract. Eng. Mater. Struct.*, **30**, 420–431.
3. Lee, J.G. and Subramanian, K.N. (2005) Microstructural features contributing to enhanced behaviour of Sn-Ag based solder joints. *Solder. Surf. Mount Technol.*, **17**, 33–39.
4. Lee, J.G. and Subramanian, K.N. (2007) Effects of TMF heating rates on damage accumulation and resultant mechanical behavior of Sn-Ag based solder joints. *Microelectron. Reliab.*, **47**, 118–131.
5. Subramanian, K.N. and Lee, J.G. (2006) Effects of internal stresses on the thermomechanical behavior of Sn-based solder joints. *Mater. Sci. Eng. A Struct.*, **421**, 46–56.
6. Lee, J.G. and Subramanian, K.N. (2003) Effect of dwell times on thermomechanical fatigue behavior of Sn-Ag-based solder joints. *J. Electron. Mater.*, **32**, 523–530.
7. Choi, S., Lee, J.G., Subramanian, K.N. *et al.* (2002) Microstructural characterization of damage in thermomechanically fatigued Sn-Ag based solder joints. *J. Electron. Mater.*, **31**, 292–297.
8. Nousiainen, O., Kangasvieri, T., Rautioaho, R., and Vahakangas, J. (2009) Thermal fatigue endurance of lead-free composite solder joints over a temperature range of −55 °C to 150 °C. *J. Electron. Mater.*, **38**,843–851.
9. Kobayashi, T., Lee, A., and Subramanian, K.N. (2009) Impact behavior of thermomechanical fatigue Sn-based solder joints. *J. Electron. Mater.*, **38**, 2659–2667.
10. Subramanian, K.N. (2007) Assessment of factors influencing thermomechanical fatigue behavior of Sn-based solder joints under severe service environments. *J. Mater. Sci.: Mater. Electron.*, **18**, 237–246.
11. Subramanian, K.N. (2005) A parametric approach for assessment of thermomechanical fatigue performance of Sn-based solder joints. *J. Electron. Mater.*, **34**, 1313–1317.
12. Deiter, G. (1998) *Mechanical Metallurgy*, McGraw-Hill Book Company, London.
13. Rhee, H., Subramanian, K.N., Lee, A., and Lee, J.G. (2003) Mechanical characterization of Sn-3.5Ag solder joints at various temperatures. *Solder. Surf. Mount Technol.*, **15**, 21–26.
14. Matin, M.A., Vellinga, W.P., and Geers, M.G.D. (2007) Thermomechanical fatigue damage evolution in SAC solder joints. *Mater. Sci. Eng. A- Struct.*, **445**, 73–85.
15. Suhling, J.C., Gale, H.S., Johnson, R.W. *et al.* (2004) Thermal cycling reliability of lead-free chip resistor solder joints. *Solder. Surf. Mount Technol.*, **16**, 77–87.
16. Lee, J.G., Guo, F., Choi, S. *et al.* (2002) Residual-mechanical behavior of thermomechanically fatigued Sn-Ag based solder joints. *J. Electron. Mater.*, **31**, 946–952.
17. Lee, A. and Subramanian, K.N. (2005) Development of nano-composite lead-free electronic solders. *J. Electron. Mater.*, **34**, 1399–1407.

Thematic Area VI

Whisker Growth Issues Affecting Reliability

12

Sn Whiskers: Causes, Mechanisms and Mitigation Strategies

Nitin Jadhav and Eric Chason
School of Engineering, Brown University, Providence, Rhode Island, USA

12.1 Introduction

SnPb coatings have been used heavily in the electronics industry as protective layers due to their excellent resistance to oxidation and corrosion, superior electrical conductivity and ductility [1]. In addition, their low melting temperature makes them an ideal candidate for use as a solder material. But increasing concerns about environmental effects are moving the electronics industry towards Pb-free electronics. Aside from the pull of the market, governments of many countries [2] are passing regulations restricting the use of Pb. In 2006 the European Union passed the 'Waste Electrical and Electronic Equipment (WEEE) and Restriction of Hazardous Substances (RoHS)' legislation that banned the use of Pb in most electronics products. Similar legislation prohibiting the future use of Pb in electronics equipment has been passed in several other countries including Japan, China and some states of the USA.

Because pure Sn has similar properties to SnPb alloys it is being considered as a replacement material, but there are significant concerns regarding its usage. One of the biggest challenges with using pure Sn is the growth of Sn whiskers, that is conductive filaments of crystalline Sn that grow out of the surface of pure Sn coatings and solder balls over time. These whiskers are known to cause system failures and thus represent a huge reliability issue. An example of a whisker from a 1-micrometer thick electroplated layer is shown in Figure 12.1. The whiskers can be a few micrometers in diameter, up to millimeters in length and grow spontaneously over a period of months to years [3, 4]. Various

Lead-free Solders: Materials Reliability for Electronics, First Edition. Edited by K. N. Subramanian.

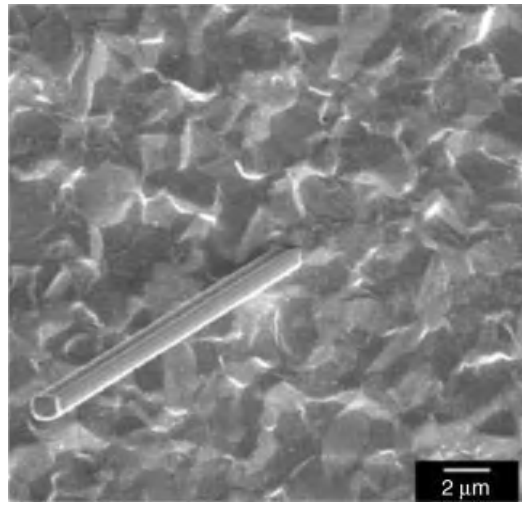

Figure 12.1 *SEM image of Sn whisker growing from Sn surface.*

environmental parameters (temperature, humidity, electric field and contamination) may speed up their formation and whiskers have been found to form under numerous service environments.

There have been many failures in the past attributed to Sn whisker formation [5–11] and a useful compendium of whisker examples and whisker-related failures is maintained by NASA [5]. Some examples of whiskers found on components taken from this site are shown in Figure 12.2a of Sn whiskers growing on a Sn-plated Cu lead frame after 3 years of ambient storage and Figure 12.2b of a whisker bridging across nearby hook terminals. If a whisker forms in an electronic component it can result in inferior performance as it may act as an antenna emitting electromagnetic radiations [6]. More severe damage may result if a Sn whisker forms and comes in contact with a nearby conducting surface as it may then result in an electrical short circuit. The damage that the short circuit may cause depends on the power available and the atmosphere. At ambient pressure, high currents may lead to melting of the whisker so that there is only a temporary glitch before the whisker is destroyed. If the

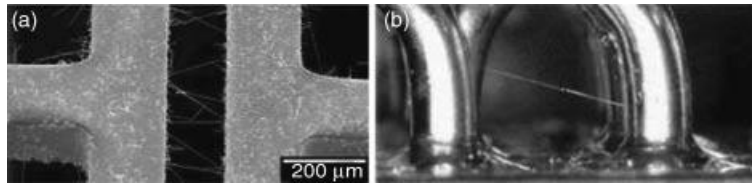

Figure 12.2 *Examples of failures attributed to Sn whiskers. (a) Sn whiskers growing on a tin-plated copper lead frame after 3 years of ambient storage (Photos Courtesy of Peter Bush (State University New York at Buffalo)). (b) Sn whisker forming on a hook terminal of a Sn-plated relay. (Reprinted with permission from the NASA Electronic Parts and Packaging (NEPP) Program [5]).*

Figure 12.3 *A hermetic relay whose failure is suspected to be caused by Sn whisker-induced metal vapor arc. (Reprinted with permission from the NASA Electronic Parts and Packaging (NEPP) Program [5]).*

available current is insufficient to melt the whisker, it may persist and result in permanent damage to the component. This situation can be more severe if it happens in outer space where the whisker can cause even more destructive phenomenon (see an example in Figure 12.3). In the absence of oxygen, the whisker can vaporize and initiate plasma that can conduct over 200 amps of current, leading to the melting of the components. Apart from the whisker growing to form a bridge between two components, it may also break loose and form short circuits between electric terminals at other sites or it may interfere with sensitive surfaces of optoelectronics equipments and thus may result in poor performance of the electronic components [7].

So far, whiskers have been implicated in over one billion dollars of damage by the electronic industry. Examples can be found in both terrestrial and space environments including satellite, defense, medical and other critical components (details of these failures can be found at the NASA Web site [5]). A particularly significant example is found in the HS 601 type of satellite (Galaxy IV, Galaxy VII, Galaxy IIIR and Soloidaridad 1) manufactured by Hughes Space and Communications Company (HSC) (now Boeing). Four of these satellites have suffered complete failure due to short circuits by Sn whisker in their satellite control processors (SCP). In all of these cases, whiskers grew on pure Sn that was plated on electromagnetic relays of the SCP. Although these satellites were designed with a redundant SCP, failures in both of them resulted in complete loss of the satellites. There are currently four more satellites that have had failures in the SCP due to whiskers in their relays and are now running on their redundant SCPs. Similar failures have been seen in relays in military planes used by the air force of several countries [8]. A huge batch of Swatch watches were recalled at an estimated cost of $1bn due to reliability issues caused by whisker formation [9]. Whisker-related issues have also resulted in recall of several models of pacemaker (devices that act as an artificial heart) [10] and there have been incidents of failures in relay used in many nuclear power plants [11] due to whisker formation in them.

Apart from the long whiskers, other features known as hillocks have also been observed to form on pure Sn surfaces. Hillocks are generally shorter and thicker than whiskers

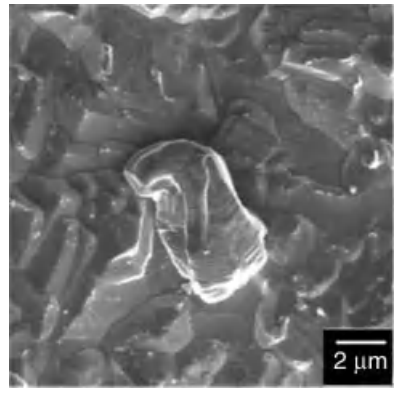

Figure 12.4 *SEM micrograph of hillock growing out of Sn plating on Cu surface.*

(Figure 12.4) but they are believed to have a similar driving force controlling their formation. A feature is generally called a whisker if its diameter remains the same over time, whereas a feature is termed a hillock if the diameter changes as it grows (consistent with subsurface grain growth as the features grow out of the surface). As whiskers and hillocks grow, they may both have changes in their growth direction that will result in kinking, as shown in Figure 12.5.

The phenomenon of Sn whiskers has been known for a long time. They were first reported by Bell laboratories researchers in 1951 [12] with respect to failures found on channel filters used for multichannel transmission lines. Investigation revealed failure due to shorting by Sn whisker formation. Addition of Pb as proposed by Arnold [13] was seen as the most promising solution and has been adopted as an industry standard. Consequently, SnPb alloys have been used in the electronics industry for six decades that effectively eliminated whisker formation. Only the increasing awareness of the harmful effects of Pb and regulations against its use has prompted the need for electronic component manufactures to move toward pure Sn coating systems, causing the re-emergence of the whisker problem.

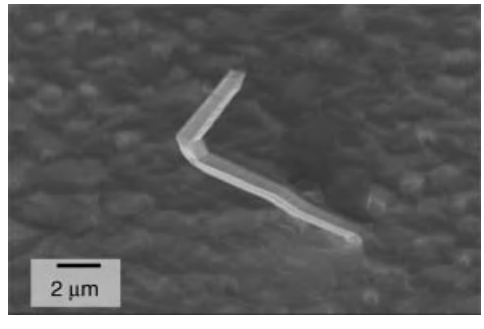

Figure 12.5 *Kinking of whisker growing out of a Sn surface.*

12.2 Features of Whisker Formation

Over the ensuing 60 years, numerous studies have been done to understand Sn whisker formation (an extensive bibliography of studies can be found in [14]). Nevertheless, there are still many unanswered questions that need to be addressed before the mechanisms of whisker nucleation and growth can be fully understood. The many different experimental studies have used a wide range of experimental parameters and processing conditions (e.g. plating solution, substrate, film thickness, plating temperature, rate of deposition, other pre- and postplating conditions and treatments, usage environment) which makes quantitative comparison among them difficult. Furthermore, many features of individual systems are not well characterized (e.g. grain size, texture, microstructure) and these can play an important role in whisker formation. The complexity in the system and lack of comprehensive studies has been one of the key reasons that the whisker phenomenon is not completely understood even after six decades of research. Despite this, there are many features of whisker growth that have been seen across a number of systems and for which there is general consensus. This chapter will focus on whiskers that grow from substrate in the absence of any Sn vapor phase. Following is a summary of some of the key understanding that has been developed:

a. Whiskers grow with the addition of atoms at the base of the whiskers.

   In 1953 Koonce and Arnold of Bell Laboratories [15] showed that whiskers form by the addition of material to the base of a whisker rather than its tip. Their finding was based on observation of whisker growth monitored in an electron microscope over a period of several weeks. This core idea has been verified by various other research groups [16–18] and is well accepted. For illustration, Figure 12.6 shows whisker growth monitored continuously in an SEM, where it can be clearly seen that the top part of the whisker remain unchanged while the whisker grows through addition of more material at its base. Videos of whisker nucleation and growth made from these SEM images (taken every 10 min over a period of several days) can be seen at our research Web site [18].

b. Compressive stress enhances whisker growth:

   Although several other driving forces have been proposed (oxidation [19], surface contamination, scratches), stress is generally believed to be the primary driving force for whisker formation [20, 21]. Various experiments have been performed to investigate the effect of stress on whisker growth and all of them have concluded that compressive stress accelerates the rate of whisker growth. In the early 1950s researchers from US Steel [22] did experiments in which they applied clamping forces (up to

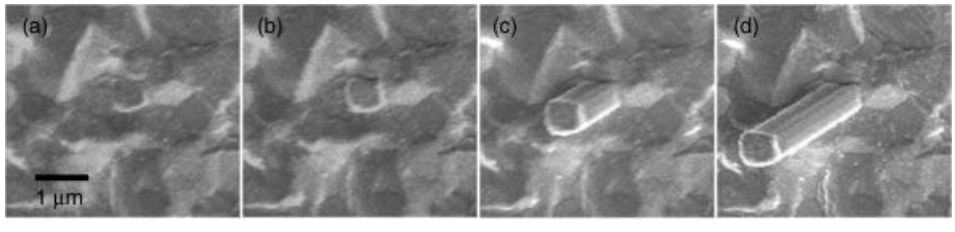

Figure 12.6 *Sequence of SEM images showing nucleation and growth of same whisker for different periods after deposition (a) 14 h 20 min, (b) 14 h 40 min, (c) 17 h and (d) 21 h.*

7500 psi) on Sn films electrodeposited onto steel substrates and found the whisker growth rate increased from 1 Å/s to 10 000 Å/s. These were the first experiments to establish the principle that the whisker formation can result from compressive stresses in the Sn films.

The Sn films may develop stress due to various reasons and some potential causes are listed below. An important consideration is whether the stress is a one-time event that can be removed by relaxation processes or whether it is continuously generated and can lead to long whisker growth.

I. Residual stress due to plating: A film may have stress formation during the electroplating process. The nature (compressive or tensile) and magnitude of the stress depends on plating conditions (such as rate of deposition and temperature) and the electrochemical solution used (additives and electrolytes). This stress formation is a one-time event and therefore does not get regenerated if it is relaxed.
II. Mechanical stress: Stress can be generated in Sn layers due to mechanical operations such as trimming, forming, clamping, and so on, on the electronic component. Similar to plating stress, mechanical processes are typically one-time events and are not expected to regenerate if they are removed.
III. Thermal mismatch: Thermal mechanical stress can form due to the difference in the coefficient of thermal expansion between the Sn layer and the substrate. Although relaxation processes can remove this stress, if the system is thermally cycled the stress can be regenerated over multiple cycles.
IV. Electromigration: Electromigration in the Sn layer can result in the accumulation of atoms at the anode side (vacancy at the cathode) resulting in compressive stress build up at the anode that may lead to whisker formation. This stress can persist if the current flow is maintained.
V. Intermetallic (IMC) formation: Stress can also be developed due to IMC formation in Sn-Cu system. IMC grows by diffusion of Cu into the Sn layer, resulting in a volume expansion that leads to stress in the Sn layer. IMC growth can continue for long periods of time.

Unlike the one-time stress due to some of the sources, thermal cycling, electromigration and IMC formation can all lead to repeated or continuous application of stress to the Sn layer and hence long whisker growth. In particular, the IMC formation is a slow and continuous process that extends over a long period of time and is the result of a thermodynamically driven reaction between the Cu and Sn. Once plated, its growth cannot be externally controlled and thus it is one of the biggest concerns in pure-Sn components leading to whisker formation.

c. IMC formation:

One of the key developments in understanding whisker formation phenomena is the role of IMC formation. In Sn layers electroplated over brass or Cu substrates, the Cu diffuses into the Sn layer and starts reacting with Sn atoms to form Cu_6Sn_5 which is the preferred intermetallic phase at room temperature. The FIB cross section (Figure 12.7) shows the morphology of a Sn-Cu bilayer and the IMC formation. Most of the IMC forms near the interface of Sn and Cu and grows preferentially into the Sn grain boundary (referred to as triple junctions). Tu [23] has shown in marker studies that Cu is the dominant diffusing species, which is consistent with the observation that the IMC generally grows on the Sn side of the interface.

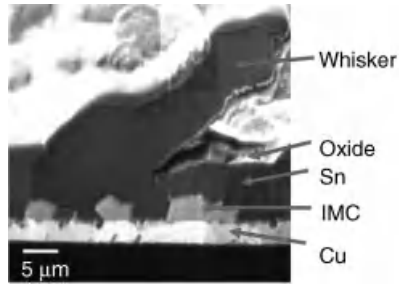

Figure 12.7 *FIB cross section of a Sn layer plated over Cu. The arrows indicate the presence of whisker, oxide layer, Sn, IMC and Cu, respectively.*

In order to see the morphology of the IMC, the Sn layer can be selectively removed using an etchant, leaving behind the IMC and Cu layers. The SEM images (Figure 12.8) of the interface after Sn removal confirm that most of the IMC forms at the Sn grain boundary especially at the triple junctions. Higher-resolution AFM images of the IMC particles at the triple junction reveal that they have facetted morphology [24]. Cross-sectional TEM (Figure 12.9) images of the SnCu interface shows that fine-grained IMC

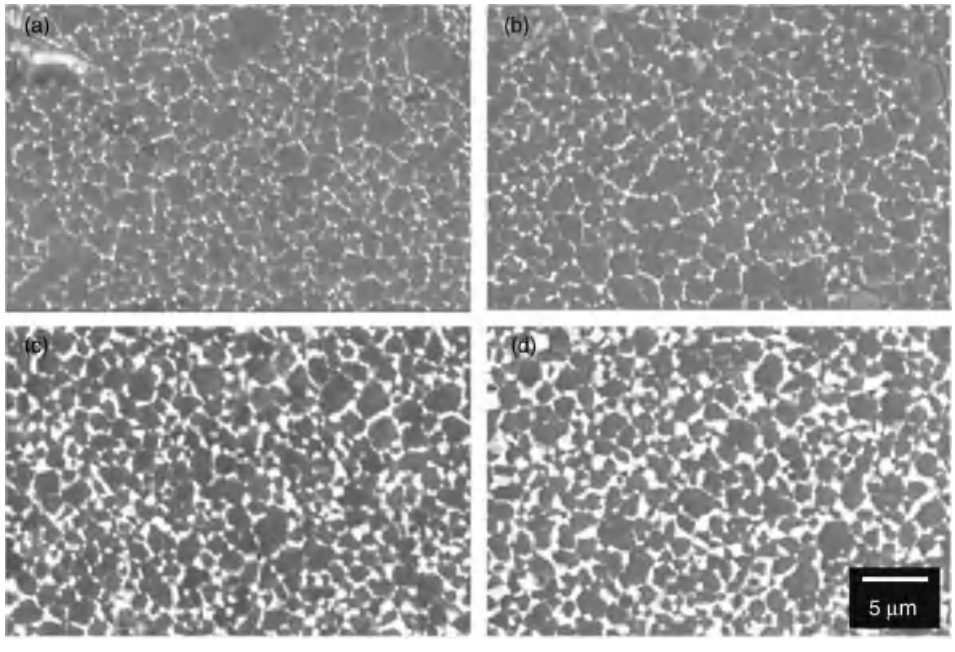

Figure 12.8 *SEM images of intermetallic at Sn/Cu interface after removal of unreacted Sn by selective etching. The samples were prepared with an initial Sn layer thickness of 1450 nm and held for (a) 2 h, (b) 8 h, (c) 18 h, and (d) 48 h before etching. The bright spots correspond to particles of IMC.*

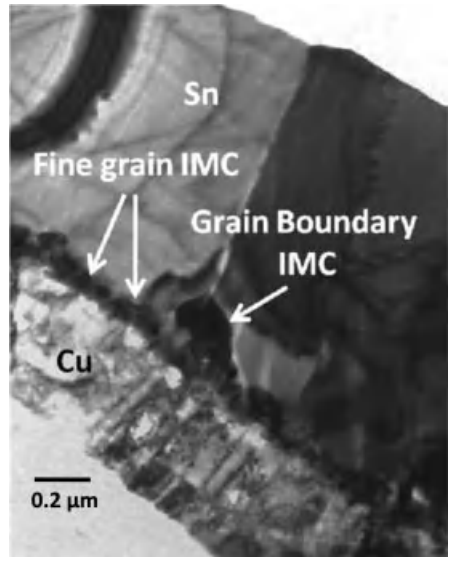

Figure 12.9 *TEM micrograph of SnCu cross section taken five days after deposition. IMC particles grow at the SnCu interface with two morphologies. Coarse-facetted particles are observed at the Sn grain triple junction and fine-grain particles are observed in the interior of the Sn grain.*

forms at the Sn grain interior, in addition to the facetted particles that nucleate at the Sn grain boundary. Over time, as the overall IMC volume increases the fine-grained IMC in the grain interior forms a continuous layer at the Cu/Sn interface.

The IMC growth kinetics can be determined by measuring the weight of the sample after deposition and again after etching to remove the unreacted Sn in the layer [16, 25, 26]. Figure 12.10a shows the IMC growth over time in a sample that has a 1.4-micrometer layer of Sn electrodeposited on top of 0.6 micrometers of Cu. It can be seen that the IMC starts forming very quickly after the Sn is deposited on Cu and its volume increases with a rate that decrease over time. Measurements over longer periods of time indicate a square root of time dependence, which suggests that diffusion of Sn across the IMC layer becomes the rate limiting step in the IMC growth. This is consistent with the formation of a continuous IMC layer at the Sn/Cu interface, as seen in the TEM.

d. IMC formation and stress

In 1973 Tu [27] suggested that the stress buildup due to IMC formation at the Sn/Cu interface is the main driving force for whisker growth. Since the volume of the intermetallic compound is larger than the volume of the same number of Sn atoms in the metallic beta-Sn phase, the growth of IMC within the Sn is expected to create compressive stress in the Sn layer. In 1998 Lee and Lee [20] measured the stress in Sn layers on top of Cu using a beam-deflection method. Although the as-deposited Sn initially had tensile stress, over time the layer developed compressive stress in it, attributed to the growth of Cu-Sn intermetallic at the Sn grain boundaries. These were the first experiments that directly correlated the internal compressive stress evolution with

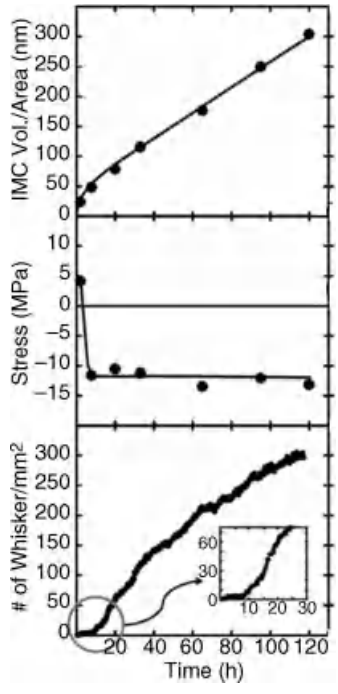

Figure 12.10 *Measurements of the evolution of IMC volume, Sn stress and whisker density from samples with Sn thickness of 1450 nm electroplated over 600 nm of copper layer.*

the whisker formation. More recently, X-ray diffraction techniques have also been used to quantify the stress evolution in the Sn layer [28–30]. Microdiffraction experiments using synchrotron radiation have the potential for quantifying the stress in individual grains within the Sn microstructure [31].

e. Correlation between IMC formation, stress and whisker formation

To directly study the correlation between IMC growth, stress and whisker formation, we have made measurements of these quantities on a series of samples grown under identical conditions and measured after different time intervals [17]. The results are shown in Figure 12.10. As discussed above, the IMC grows continuously at a rate that slows over time. The corresponding stress evolution shows a rapid transition from the as-deposited tensile state to a compressive stress (Figure 12.10b). Most significantly, the stress saturates at a value of approximately 12 MPa even though the IMC volume continues to increase. The whisker density was measured optically and nondestructively in real time on a single sample over the same period. We see that there is an incubation time before the whiskers start to emerge, which is equivalent to the time that it takes for the stress to reach its saturation compressive value (Figure 12.10c). Similar measurements have been done on samples with different Sn layer thickness and grain size. These have enabled us to see how the structure of the Sn layer modifies the IMC growth and stress relaxation in the Sn layer. In all these studies, however, we find that the whiskers don't start to grow until the stress reaches its saturation value. We also find that a larger

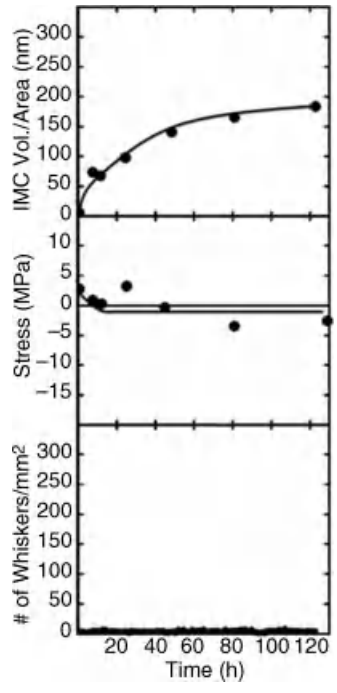

Figure 12.11 *Measurements of the evolution of IMC volume, SnPb stress and whisker density from samples with SnPb thickness of 1450 nm electroplated on top of 600 nm of copper layer.*

compressive stress in the Sn layer corresponds to a higher nucleation rate for the whiskers.

We have also performed annealing experiments that leave the layers with tensile stress in them even after 100 days and we find that these layers don't develop whiskers. Similarly, the use of Ni interlayers between the Cu and Sn leads to tensile stress in the Sn layers and these layers also don't develop whiskers [32]. Finally, measurements of IMC growth, stress and whisker formation in Sn-Pb alloy layers (Figure 12.11) shows that the presence of Pb in the Sn layer leads to enhanced stress relaxation (Figure 12.11b) so that the Sn layer remains nearly stress free even though the amount of IMC growth (Figure 12.11a) is similar to the pure Sn layers. These results are all consistent with the conclusion that compressive stress is the key driving force for whisker formation and that whiskers tend to grow in an attempt to relax the stress.

12.3 Understanding the Relationship between IMC Growth, Stress and Whisker Formation

The previous discussion demonstrates a connection between IMC growth, stress evolution and growth of whiskers. The resurgence of interest due to the advent of Pb-free manufacturing has enabled these issues to be revisited with modern characterization techniques and

modeling capabilities. Due to this new focus, many aspects of the mechanisms underlying whisker growth are beginning to be understood. In the following sections we discuss recent experiments and models that help to elucidate the underlying mechanisms of whisker formation. The section is organized in terms of outstanding questions that are currently being studied:

- How does the stress arise from the IMC growth?
- How does stress lead to whisker formation?

1. How does the stress arise from the IMC growth?

   As Cu diffuses into Sn and reacts with it, the volume of the IMC created is 44% larger than the volume of the same number of Sn atoms in the parent phase. This expansion is expected to generate compressive stress in the surrounding Sn matrix, but the strain is clearly too large to be accommodated by purely elastic deformation of the Sn. Also, the stress in Sn (as shown in Figure 12.10b) saturates at a very early stage of IMC growth and doesn't change significantly even though the IMC continues to grow. These results indicate that there is significant stress relaxation going on in the Sn layer as the IMC grows. The resulting steady-state stress in the Sn layer is a balance between the increase in stress due to IMC formation and relaxation due to various relaxation processes. (e.g. by diffusion of Sn atoms and dislocation emission). In this section we describe results of experiments designed to shed light on these relaxation processes and the results of FEA models of the stress evolution based on these mechanisms.

   Although whisker formation is a result of stress, it does not mean that whisker formation is the only stress-relaxation process occurring. The melting temperature of Sn is only 505 K, so room temperature is more than 50% of the melting temperature. Therefore, Sn creeps readily at room temperature both by dislocation and grain-boundary diffusional creep [33, 34]. In cross-sectional TEM measurements (Figure 12.12) [35] near the Sn/Cu interface, subgrain boundaries and individual dislocations are observed due to the emission of dislocations around large IMC grains, confirming the occurrence

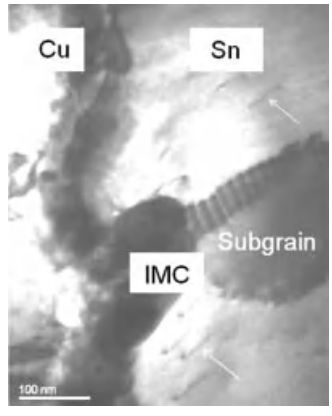

Figure 12.12 *TEM micrograph of SnCu cross section taken five days after deposition. Arrows point to dislocations that are emitted from the IMC region. A subgrain boundary can also be seen forming from aggregation of dislocations.*

of plastic deformation in the Sn. The role of Sn diffusion on stress evolution was confirmed by an experiment in which half of a pure Sn layer was covered with Cu and monitored over time [36]. After a few days, whiskers were observed growing out of the Sn away from the Cu layer without the presence of any Cu observed. This result was interpreted to show that the stress around the IMC could induce long-range diffusion of Sn atoms and create stress (and hence whisker growth) far from where the IMC is produced. The importance of long-range stress-driven Sn diffusion is also confirmed by the experiments in which mechanical clamping leads to whisker formation even in the absence of IMC growth [22]. Furthermore, since the length of the Sn whiskers can be many orders of magnitude greater than the Sn thickness it clearly indicates that there is long-range Sn atom diffusion along the Sn grain boundary.

The presence of the tenacious Sn-oxide layer at the surface also plays a very important role in the stress evolution. TEM measurements indicate that dislocations pile-up under the oxide layer and aren't able to pass through it [35]. When the oxide is removed, however, dislocation annihilation at the free surface is observed. The oxide similarly suppresses relaxation by diffusion of atoms to the surface. Indeed, we find that removal of the surface oxide by etching [37] or sputtering [38] leads to rapid relaxation of the stress in the layer.

These experimental results suggest the following mechanisms need to be considered in order to understand the stress evolution in a Sn layer on Cu. The growth of IMC particles by incorporation of Cu leads to compressive strain in the Sn layer. The strain is too large to be accommodated by elastic deformation alone so that stress relaxation due to dislocation-mediated plasticity and stress-induced grain-boundary diffusion must be considered. The presence of an oxide layer must be included because of its role in preventing the stress relaxation at the surface.

To model the stress evolution, these mechanisms have been incorporated into a simulation using finite element analysis (FEA) (a full description of the model can be found in [39]). The microstructure in the model consists of a periodic array of columnar hexagonal Sn grains (with grain size equal to the thickness) bonded to a Cu substrate (Figure 12.13). Cu is modeled as an elastic layer and the Sn grains as elastic perfectly plastic solids with a von Mises yield surface (modulus = 50 GPa and yield stress = 14.5 MPa) and flow potential. Stress-driven mass transport in the Sn grain boundaries is also explicitly incorporated in the simulation with a diffusion coefficient in the grain boundary of 4.8×10^{-9} cm^2/s [40]. Since the Sn-oxide layer on the surface prevents diffusion of the Sn atoms there, we assume that there is no flux out of the Sn grains. In order to simulate the IMC formation at the Sn/Cu interface a localized 44% transformation strain is applied at the base along the Sn/Sn grain boundaries. This model does not include whisker growth and is therefore intended to examine the stress evolution that is the cause of whisker formation and provide insight into how the stress spreads throughout the Sn layer due to IMC formation. One of the key advantages of the numerical simulations is that it allows us to explore the effect of various material behaviors explicitly in ways that are not possible through experimental measurement alone.

Figure 12.13 shows the simulated stress distribution that develops in a Sn film due to expanding IMC particles, while including the effects of elasticity, plastic deformation due to ideal plasticity and stress relaxation due to grain-boundary diffusion. The volume

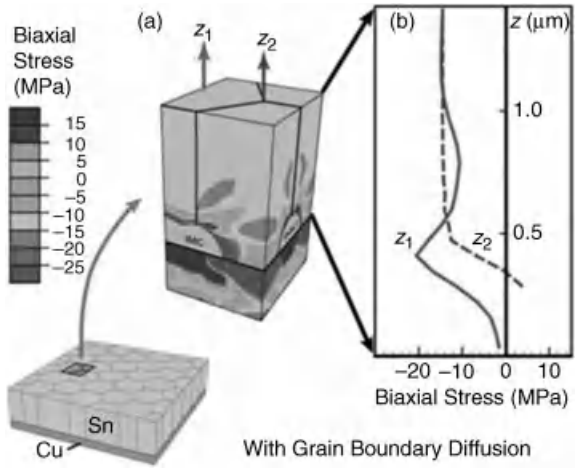

Figure 12.13 *Result of FEA simulations for the evolution of stress in a Sn film with columnar microstructure due to IMC growth. The model includes stress relaxation by both elastic-plastic behavior and grain-boundary diffusion in the Sn. The contour plots (a) show the three-dimensional distribution of stress through the film; the legend relates the color to the stress state. (b) Show the corresponding stress distributions along the lines Z1 and Z2 indicated on the contour plots.*

element (Figure 12.13a) shows the distribution of mean biaxial stress with the colors representing different ranges of stress. The graph in Figure 12.13b shows the distribution of stress along the lines z1 and z2 indicated in the volume element. As the IMC grows, the stress spreads throughout the layer, spread primarily by the stress-induced diffusion along the grain boundaries. The average stress in the Sn quickly reaches a maximum compressive value of approximately −12 MPa, and then remains relatively constant throughout the thickness. This finding is consistent with TEM observations that observed dislocations across the entire film and near to the Sn surface [35].

Figure 12.14 shows the evolution of the average stress in the Sn film as the IMC volume increases with time. The IMC volume is assumed to increase with a growth rate similar to that found in our experiments (Figure 12.10a); the corresponding experimental measurement of the average stress is shown by the symbols in the figure. The two lines correspond to calculations by the FEA simulations with two different sets of relaxation mechanisms. The solid line represents results from the simulation described above that include ideal plasticity and grain-boundary diffusion. Rapid diffusion along the grain boundary spreads the stress throughout the layer until it reaches the saturation value, similar to what is seen experimentally. The dashed line represents the result of simulations where the grain-boundary diffusion has been excluded but all other mechanisms remain the same. When grain-boundary diffusion is not included, the stress rises more slowly than seen experimentally and takes a long time to reach saturation. In addition, the stress remains confined to a small region localized near the growing IMC layer and thus the stress averaged through the thickness of the film is small (few MPa).

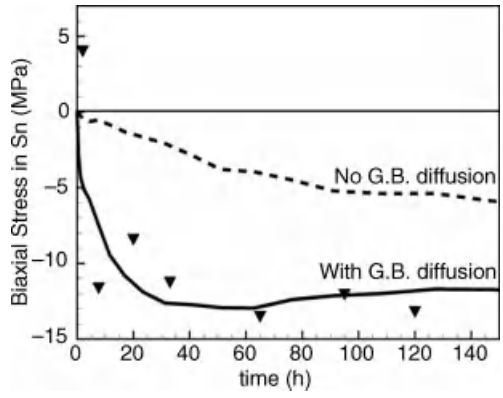

Figure 12.14 *A comparison between the time variations of the average stress in the Sn layer predicted by FEA simulations and experiment. The dashed line shows FEA predictions for a film that relaxes only by ideal plastic flow in the grain interiors. The solid line shows results for a film that relaxes by both grain-boundary diffusion and plastic flow (same as in Figure 12.13). The symbols represent the corresponding experimental stress measurements (for 1450 nm Sn). (Reprinted with permission from IEEE Transactions on Electronics Packaging Manufacturing vol. 33, no. 3, pp. 189, July 2010 (© 2010 IEEE) [18]).*

From the simulation results we conclude that both dislocation-mediated plasticity and grain-boundary diffusion play an important role in the stress evolution in the Sn layer as the IMC forms. These two mechanisms spread the stress throughout the Sn layer and bring it to saturation with relatively small amounts of IMC formation.

2. How does stress lead to whisker formation?

   From the FEA model described above, it can be seen that various stress-relaxation mechanisms active in the Sn layer can explain the steady-state stress as observed in experiments even in the absence of whisker formation. To develop further insight into how the stress leads to whisker growth, the finite element simulations described in the previous section have been extended to account for whisker nucleation and growth [26].

   A key element of the model is how it accounts for whisker nucleation, that is why do whiskers form where they do? In the model we assume that the whisker forms at specific sites that we refer to as 'weak' grains that will deform at lower stress than their neighbors. The presence of a 'weak' grain may occur by several mechanisms. The whiskering grain may be oriented in a particular way so that it has a lower yield stress than its neighbors. Or, as suggested by Smetana [41], there may be horizontal grain boundaries at which atoms can be accommodated into the grain and force it out of the film. A similar mechanism can occur if there is recrystallization [42] leading to deformation of a whiskering grain driven by strain energy density.

   An alternative model for nucleation is the possibility that the whiskers grow where the oxide is weak and can allow stress relaxation to occur. To determine if weakness in the oxide controls whisker nulceation, we monitored Sn surfaces in a FIB/SEM after we selectively removed the oxide from a small region using the focused ion beam [17]. We did not observe any change of the Sn in the region where the oxide was removed, which clearly indicated that it is not sufficient to only remove the oxide in order for

whiskers to nucleate. The underlying grain structure clearly plays an important role in whisker nucleation, so we therefore invoke the concept of nucleation at a 'weak' grain.

The FEA model contains the same processes of stress relaxation by plastic flow within individual grains and stress-driven diffusion of material along grain boundaries as described above. The Sn layer was modeled as a polycrystalline film with columnar microstructure and an impenetrable surface except at the weak grain. The IMC growth is simulated by applying a uniform volumetric expansion at a steady rate (de/dt) in all the grains. In order to simulate the whisker formation and growth, a periodic distribution of 'soft' grains are added whose yield stress is lower than that of the other grains.

The model shows that any microstructural feature that reduces the stress in one grain (soft grain) relative to its surrounding will result in local stress gradients around the grain. Even if the average stress in the film may be low due to other relaxations processes, large stress gradients can develop around the whisker or hillocks. The formation of surface features will relax the stress locally but in the presence of the stress source (like IMC formation) the stress gradient will be maintained by continuous stress generation. These stress gradients will provide the driving force for Sn atoms to diffuse from the high-stress area toward the root of the whisker that is a relatively low-stress (almost stress-free) region. The Sn atoms that diffuse to the root of the whisker are then incorporated into the whisker.

Figure 12.15 shows the result of the FEA model of stress evolution around a growing whisker (details can be found in [43]). The colors correspond to different stress values as shown in the key alongside the image; the red color corresponds to the saturation yield stress in the material. Since the whisker grain has been assigned a lower yield stress, this 'weak grain' undergoes plastic deformation before its neighboring grains

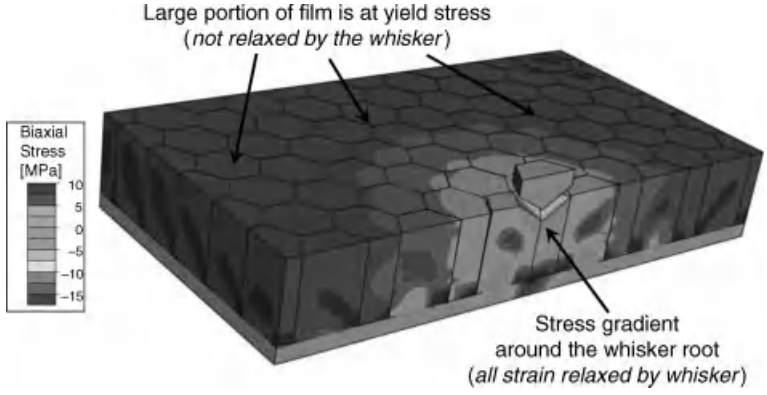

Figure 12.15 *FEA model results of stress evolution in the SnCu system with whisker growth showing a periodic cell surrounding a single 'weak' grain that forms a whisker. The grains in the immediate vicinity of the whiskering grain are relaxed while the grains further away reach their yield stress (colors correspond to stress levels shown in the legend). The weak grain has 0.2 times the yield stress of the surrounding grains and the total volumetric strain is 0.25% with an applied volumetric strain rate of* 8.3×10^{-7}*/s.*

and thus deforms outward, creating a whisker. This localized relaxation creates a stress gradient that acts as the driving force for the Sn atom of the surrounding grains and drives them to the root of the whisker, driving the whisker's growth. As we go further away from the whiskering grain the effect of the stress relaxation (due to the whisker) decreases. The stress in grains far away from the whisker may reach higher stress leading to its yield point (relaxing only by plastic deformation). The area of this relaxation zone near the whisker depends on two factors, the rate of whisker growth (additional medium of relaxation) and the rate of IMC (source of stress) formation. Buchovecky *et al.* [39] have developed a model relating the whisker growth rate, IMC formation rate and whisker density. Depending on these parameters, the whisker may either play a large part in stress relaxation of the layer or most of the relaxation may occur by plastic deformation without whiskering. Comparison of this model with measurements [26] suggests that in many cases, whiskers are not the dominant stress-relieving mechanism in the Sn layer.

12.4 Summary Picture of Whisker Formation

From the many experimental and computational studies done by various research groups, including ours, we believe that a general understanding of the overall processes taking place in whisker formation is beginning to emerge. Although they are not really separated, we have broken the process down into two stages. The first stage consists of the stress development in the Sn layer leading to the second stage of whisker nucleation and growth. These stages themselves consist of various steps, which are explained in the following section using simple schematics to illustrate them (Figures 12.16 and 12.17). We emphasize that this description leaves out many details and is not necessarily universal, but we believe it does provide a useful picture of how whiskers grow.

- **Stage 1:** Stress build up in SnCu system
  a. As-deposited Sn has a microstructure that depends on the deposition technique:
  As Sn is electroplated on top of Cu it forms a columnar structure (as shown in Figure 12.16a) with a grain size depending on plating conditions (bath chemistry,

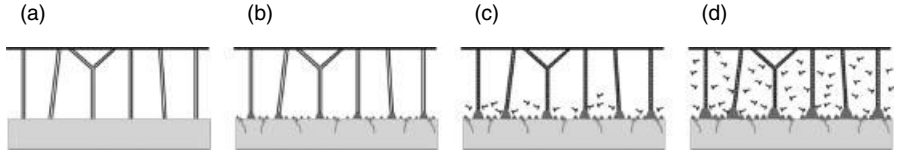

Figure 12.16 *Schematic diagram summarizing the processes controlling stress evolution in Sn layers on Cu. (a) Sn is electroplated on Cu and forms a layer with columnar grains. (b) Cu diffuses into the Sn layer and forms an intermetallic at the interface, growing preferentially at the Sn grain boundaries. (c) The IMC formation creates compressive stress in the Sn adjacent to the growing IMC leading to dislocation emission and grain-boundary diffusion. (d) As the IMC grows, the compressive stress spreads throughout the Sn layer and saturates.*

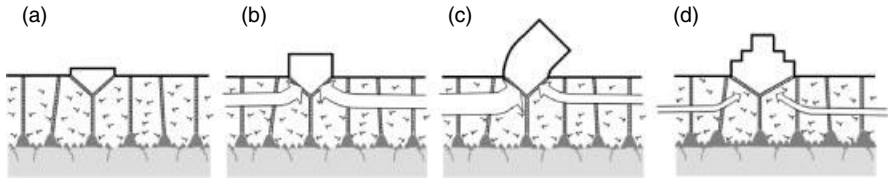

Figure 12.17 *Schematic summarizing the processes of whisker nucleation and growth in Sn layers under compressive stress. (a) With the compressive stress build-up, a whisker nucleates at a weak grain. (b) The stress relaxation due to whisker formation creates a stress gradient that drives diffusion of Sn atoms from the nearby region (through grain-boundary diffusion) to the root of the whiskering grain. (c) A nonuniform flow of Sn atoms may lead to a tilt in a whisker. (d) Whiskering grain may undergo lateral grain growth, increasing its diameter and resulting in hillock formation.*

current density, sample surface, etc.) and composition. Electroplating, which has been the preferred route for Sn deposition, may result in residual tensile stress due to plating.

b. Diffusion of Cu into Sn leads to the formation of an intermetallic (IMC) in the Sn layer:

Soon after the Sn deposition, Cu starts diffusing into the Sn layer (as shown in Figure 12.16b). The amount of Sn that diffuses into the Cu layer is negligible compared to Cu diffusion into Sn. The diffused Cu reacts with the Sn and forms Cu_6Sn_5, nucleating preferentially at the Sn grain boundaries (triple junctions).

c. Intermetallic formation generates compressive stress, leading to relaxation by dislocation emission and grain-boundary diffusion:

The formation of IMC coincides with a large volume increase, creating stress that exceeds Sn's yield stress. Thus, the region surrounding the IMC particles undergoes plastic deformation. In the presence of an active source of strain (IMC formation), the region under the plastic regime creeps both by emitting dislocations and by driving Sn atom diffusion along the grain boundary from an area of high stress toward the stress-free region (Figure 12.16c). The oxide layer on top of the Sn prevents relaxation of the stress at the surface.

d. Stress spreads throughout the Sn layer and saturates:

Over time, as Cu diffuses into Sn and forms more IMC, a larger region reaches its yield stress due to the accommodation of dislocations emitted around the IMC and stress-driven diffusion along the grain boundaries. Ultimately, the entire Sn layer reaches its yield stress and the average stress in the Sn layer reach a steady state (Figure 12.16d). Further IMC formation has no effect on the stress level. However, the microstructure and composition of the layer can affect its mechanical properties so that, for instance, thicker films may have a lower yield stress.

- **Stage 2:** Whisker nucleation and growth.

a. Nucleation of whiskers from a 'weak' grain:

As the compressive stress builds up in the Sn layer, 'weak' grains that deform at lower stresses than the average Sn grains, undergo plastic deformation, as shown in Figure 12.17a. The grain can be weak due to the presence of horizontal grain boundaries

(as shown in Figure 12.17a) or other reasons such as recrystallization or a lower yield stress (as discussed in the previous section).

b. Stress gradient from surrounding grains to 'weak' grain drives diffusion to whisker base:

As the weak grain undergoes plastic deformation, the stress in the grain relaxes, which results in a gradient of stress relative to the surrounding grains. This stress gradient drives diffusion along the grain boundaries, transporting Sn atoms from the surrounding region to the weak grain, as shown by horizontal arrows in Figure 12.17b. Incorporation of the arriving atoms into the weak grain leads to growth of the grain outward in the form of a whisker. Since the maximum stress at the weak grain is lower than the average stress, the stress gradient persists as the whisker grows, feeding Sn atoms to its base continuously.

c. Nonuniformities in the flow field and incorporation into the grain leads to different morphologies:

If the arriving atoms are incorporated uniformly into the base of the growing whisker, then it will most likely grow in the form of a long, thin whisker. However, there are various reasons why the flow of Sn atoms being accommodated into different sides of the growing whisker may not be the same, which can lead to other growth morphologies. The flow may be nonuniform because the stress field is inhomogeneous, or because the different growth planes at the base of the whisker may grow at different rates. The horizontal grain boundaries at the base of the whisker may rotate due to growth of the whisker into neighboring grains. For whatever reason, if the flow of Sn into the whiskering grain is not homogeneous, it may result in a tilt or twist in the whisker, as represented in Figure 12.17c and observed in many whiskers. In addition, the whiskering grain may grow laterally [44] by consuming its neighboring grains (as shown in Figure 12.17d), resulting in hillock-like features that have increasing diameters as they grow.

12.5 Strategies to Mitigate Whisker Formation

Finally, we describe various mitigation strategies that have been proposed to suppress whisker formation. Though numerous mitigation strategies have been proposed [45–47] there isn't yet any single strategy that works reliably and has been universally adopted. Almost all of these strategies are still in the development phase and are based on either eradicating the cause for the stress build-up or applying barriers to impede whiskers from coming in contact with conductive surfaces.

1. **Conformal Coatings:** The idea behind conformal coatings is to put a layer of another material over the Sn surface to suppress the growth of whiskers and also make it difficult for the whisker to contact a conducting surface if it does form. The effectiveness of conformal coatings has been studied by various research groups [48–50] using various polymer and other materials including: acrylic, silicone, polyurethane, parylene, urethane acrylates, para-xylene, uralane. Even with conformal coatings, whiskers are often found at the edge of the sample or at places with thinner film. Though thicker conformal films perform better, the coatings do not always inhibit the whisker formation. In some cases, whiskers were observed to puncture the film so they could grow out, and even

puncture the coating on the adjacent side to cause failure. Touw [51] has performed a survey of different users regarding coating effectiveness and found the following consensus: parylene C and epoxy (>3 mil) seem to be strong mitigators; uralane (>1 mil), urethane (1–2 mil), epoxy (1–3 mil), arcylic (2>mil), silicon (>3 mil) and ALD coatings are reasonable mitigators and silicone (2–3 mil) and arcylic (1–2 mil) are ineffective mitigators. Nevertheless, conformal coatings are attractive, first because of their ease of use (they can be sprayed on old parts) and their potential for preventing short circuits, especially if the adjacent surfaces are both coated. On the negative side, the conformal coating doesn't eliminate the driving force for whisker formation and coating the parts makes it difficult to rework the board when repairs are needed.

2. **Surface Treatment:** Various research groups are working on modifying the Sn surface by depositing various materials on top of it. Surface treatment could be an effective method of whisker prevention if it can assist the Sn layer in stress relaxation and thus eliminate the driving force for whisker formation or by inhibiting whisker nucleation. Suganuma *et al.* [52] demonstrated that various surface treatments on Sn plating could prevent whisker formation. Two different thicknesses of nickel layer (0.05 micrometers and 0.2 micrometers) were plated and it was found that whereas the thin nickel layer may facilitate the whisker formation the thicker nickel films were effective in suppressing the whisker formation. Plating with other materials like Au and Pd (both 0.05 micrometers and 0.2 micrometers) has been shown [53] to be an effective mitigator for whisker formation.
3. **Microstructure modification:** Another approach to whisker mitigation is to modify the Sn microstructure (and hence the stress-relaxation kinetics) by processes such as alloying [54–56], using different electroplating chemistry [54] or varying the plating techniques [57, 58]. Various research groups are studying alloying with Bi, Ag, Mg, and so on [54–56, 59]. Although Bi and Ag have been shown to assist in resisting whisker formation, Mg has not been shown to help in whisker mitigation. Hillman *et al.* [58] evaluated the effectiveness of Sn-Bi alloy surface finish and found that no whiskers were observed with 0.3–3% of Bi, however some whiskers were observed on areas with less than 0.3% Bi. Sandnes *et al.* [59] have demonstrated that pulsed deposition of Sn-Bi alloys results in equiaxed grains similar to the microstructure that is found in Sn-Pb layers. It has been suggested that the presence of horizontal grain boundaries in this case can enhance stress relaxation by providing sinks for the diffusing Sn atoms [38, 44], however, this has not yet been demonstrated for these alloys. Moon *et al.* [60] have shown that electroplating with high current density or with plating solution with lower Sn^{2+} concentration, results in fewer hillocks forming. The higher current density or lower Sn^{2+}concentration result in smaller columnar grains diameter and rotation of preferred orientation of the deposit toward the [001] direction, for which the intergranular shear due to the anisotropy of Sn is minimum, consistent with an elastic-strain argument [20].
4. **Underlayers:** Another strategy that has been proposed for whisker mitigation is to insert an additional layer between the Sn and Cu to stop the IMC formation and therefore suppress stress buildup in the Sn. The interlayer material can be chosen so that it forms an intermetallic at the interface but induces less stress than the Sn-Cu intermetallic. Various materials have been tried as a protective barrier for Cu diffusion to Sn, with Ni and Ag appearing to be the most promising [61–64]. Although this process seems to be an

effective method for mitigation, the underlayer may break during the forming or service of the part, allowing the Cu to diffuse into the Sn and cause whiskers to form.

5. **Heat treatment:** Annealing and various other heat treatments have been proposed as a way to stop whiskers and various research groups [61, 62, 65] are working on optimizing the exact heat-treatment conditions (i.e. heating temperature, holding time, rate of cooling and rate of heating). Heat treatments are easy to implement and seem to be useful in multiple ways. The accelerated kinetics at high temperature may enhance relaxation of stress due to other processes (chemical and mechanical). It may also enhance the growth of the IMC and create a uniform layer that can act as a diffusion barrier to slow the formation of additional IMC. Contraction of the Sn layer during cooling can also remove any compressive stress that develops due to the growth of the IMC at elevated temperature.

12.6 Conclusion

To conclude, Pb-free Sn will be the preferred choice of the electronics industry over Pb-containing alloys because of environmental concerns and recent government regulations. As the industry switches to Pb-free manufacturing, spontaneous formation of Sn whiskers has once again became a key reliability issue. In this chapter, an attempt has been made to describe the current understanding of whisker formation and various mitigation strategies that have been proposed by various groups. The Sn layer, when deposited on top of a Cu layer, reacts with it and forms an IMC at the Sn/Cu interface. The IMC formation results in an increase in volume in the Sn layer resulting in compressive stress. In the presence of compressive stress, weak grains deform and nucleate a whisker as a means of relieving the local stress. The stress relaxation creates a stress gradient that drives Sn diffusion along the grain boundaries to the whiskering grain. There are multiple mitigation strategies based on stopping whisker growth, suppressing IMC formation or assisting Sn relaxation. Though many key steps leading to whisker formation are understood, there is still not sufficient knowledge to develop a predictive model of whisker formation.

Acknowledgments

The authors gratefully acknowledge the support of the Brown MRSEC (DMR0079964) and NSF (DMR0856229) and would like to thank Jae Wook Shin, Wai Lun Chan, Eric Buchovecky, Lucine Reinbold, Sharvan Kumar, Allan F. Bower, Lambert Ben Freund and Gordon Barr for their helpful contributions.

References

1. Lyon, S.B. (2009) Corrosion of Tin and Its alloys, in *Shreir's Corrosion* (eds T. Richardson *et al.*), Elsevier, Amsterdam; Oxford, pp. 2068–2077.
2. Herat, S. (2008) Green electronics through legislation and lead free soldering. *CLEAN – Soil, Air, Water*, **36**, 145–151.

3. Hampshire, B. and Hymes, L. (2000, September 2000) Shaving Tin Whiskers. Circuits Assembly. 50–53. Available http://circuitsassembly.com/cms/images/stories/pdf/0408/0408nemi.pdf.
4. Dunn, B.D. (1987) A laboratory study of Tin whisker growth, in *European Space Agency (ESA) STR-223*, vol., ed. ESA STR-223 September 1987, http://esmat.esa.int/Publications/Published_papers/ESA-STR-223.pdf
5. NASA, Multiple examples of whisker-induced failures are documented on the NASA website Available http://nepp.nasa.gov/whisker/.
6. Galyon, G.T. and Gedney, R. (2004) Avoiding Tin Whisker Reliability Problems. Circuits Assembly. 26–31. Available http://circuitsassembly.com/cms/images/stories/pdf/0408/0408nemi.pdf.
7. H. Leidecker and J. BrusseTin, whiskers: A history of documented electrical system failures—A briefing prepared for the Space Shuttle program office, April, 2006. https://nepp.nasa.gov/whisker/reference/tech_papers/2006-Leidecker-Tin-Whisker-Failures.pdf
8. Nordwall, B.D. (1986) Air force links radar problems to growth of tin whiskers. *Aviation Week Space Technology.* June 20, 1986, pp. 65–70.
9. Jacobsen, K. (2008) Within a whisker of failure: Removing lead from solder may seem a smart idea environmentally, but the resulting microscopic growths called tin whiskers could be just as problematic, in The Guardian, ed. on Wednesday 2nd April 2008, http://www.guardian.co.uk/technology/2008/apr/03/research.engineering
10. FDA ITG Page (March, 14 1986) *Tin Whiskers – Problems, Causes, and Solutions*, http://www.fda.gov/ no. 42.
11. Daddona, P. (2005) Reactor shutdown: Dominion learns big lesson from a tiny tin whisker, in *The Day*, ed. New London, Connecticut. 4 July 2005.
12. Compton, K.G. *et al.* (1951) Filamentary growths on metal surfaces – Whiskers. *Corrosion*, **7**, 327–334.
13. Arnold, S.M. (1959) The Growth of Metal Whiskers on Electrical Components. IEEE Electronic Components Technology Conference, pp. 75–82.
14. Galyon, G.T. (2005) Annotated tin whisker bibliography and anthology. *IEEE Trans. Electron. Packag. Manuf.*, **28**, 94–122.
15. Koonce, S.E. and Arnold, S.M. (1953) Growth of metal whiskers. *J. Appl. Phys.*, **24**, 365–366.
16. Lindborg, U. (1975) Observations on growth of whisker crystals from zinc electroplate. *Metall Mater Trans A* **6**, 1581–1586.
17. Jadhav, N. *et al.* (2010) Real-time SEM/FIB Studies of whisker growth and surface modification. *JOM*, **62**, 30–37.
18. Chason, E. and Jadhav, N. (2010) Research activities in Prof. Eric Chason's Laboratory. Available http://www.engin.brown.edu/faculty/Chason/research/whisker.html.
19. Barsoum, M.W. *et al.* (2004) Driving force and mechanism for spontaneous metal whisker formation. *Phys. Rev. Lett.*, **93**, 4.
20. Lee, B.Z. and Lee, D.N. (1998) Spontaneous growth mechanism of tin whiskers. *Acta Mater.*, **46**, 3701–3714.
21. Tu, K.N. (1994) Irreversible-processes of spontaneous whisker growth in bimetallic Cu-Sn thin-film reactions. *Phys. Rev. B*, **49**, 2030–2034.
22. Fisher, R.M. *et al.* (1954) Accelerated growth of Tin whiskers. *Acta Metall.*, **2**, 368–369, 371–373.
23. Tu, K.N. and Thompson, R.D. (1982) Kinetics of interfacial reaction in bimetallic Cu-Sn thin-films. *Acta Metall.*, **30**, 947–952.
24. Zhang, W. *et al.* (2005) Investigation of Sn-Cu intermetallic compounds by AFM: New aspects of the role of intermetallic compounds in whisker formation. *IEEE Trans. Electron. Packag. Manuf.*, **28**, 85–93.

25. Oberndorff, P. *et al.* (2003) Intermetallic Formation in Relation to Tin Whiskers. presented at the IPC/Soldertec International Conference on Lead-Free Electronics "Towards Implementation of the RHS Directive". Brussels.
26. Jadhav, N. *et al.* (2010) Understanding the correlation between intermetallic growth, stress evolution, and Sn whisker nucleation. *IEEE Trans. Electron. Packag. Manuf.*, **33**, 183–192.
27. Tu, K.N. (1973) Interdiffusion and reaction in bimetallic Cu-Sn thin films. *Acta Metall.*, **21**, 347–354.
28. Sobiech, M. *et al.* (2008) Driving force for Sn whisker growth in the system Cu-Sn. *Appl. Phys. Lett.*, **93**, 3.
29. Sobiech, M. *et al.* (2009) Local, submicron, strain gradients as the cause of Sn whisker growth. *Appl. Phys. Lett.*, **94**.221901:1–3
30. Choi, W.J. *et al.* (2003) Tin whiskers studied by synchrotron radiation scanning X-ray micro-diffraction. *Acta Mater.*, **51**, 6253–6261.
31. Ice, G.E. *et al.* (2005) X-ray microbeam measurements of subgrain stress distributions in polycrystalline materials. *Mater. Sci. Eng. A Struct.*, **399**, 43–48.
32. Zhang, Y. *et al.* (2004) Tin Whisker Growth-Substrate Effect: Understanding CTE mismatch and IMC formation. presented at the IPC Printed Circuits Expo SMEMA Council APEX Designers Summit.
33. Weertman, J. and Breen, J.E. (1956) Creep of Tin single crystals. *J. Appl. Phys.*, **27**, 1189–1193.
34. Shin, J.W. and Chason, E. (2009) Compressive stress generation in Sn thin films and the role of grain boundary diffusion. *Phys. Rev. Lett.*, **103**.056102:1–4
35. Kumar, K.S. *et al.* (2008) Plastic deformation processes in Cu/Sn bimetallic films. *J. Mater. Res.*, **23**, 2916–2934.
36. Reinbold, L. *et al.* (2009) Relation of Sn whisker formation to intermetallic growth: Results from a novel Sn-Cu "bimetal ledge specimen". *J. Mater. Res.*, **24**, 3583–3589.
37. Shin, J.W. and Chason, E. (2009) Stress behavior of electroplated Sn films during thermal cycling. *J. Mater. Res.*, **24**, 1522–1528.
38. Chason, E. *et al.* (2008) Whisker formation in Sn and Pb-Sn coatings: Role of intermetallic growth, stress evolution, and plastic deformation processes. *Appl. Phys. Lett.*, **92**.171901:1–3
39. Buchovecky, E. *et al.* (2009) Finite element modeling of stress evolution in Sn films due to growth of the Cu_6Sn_5 intermetallic compound. *J. Electron. Mater.*, **38**, 2676–2684.
40. Lange, W. and Bergner, D. (1962) Messung der Korngrenzenselbstdiffusion in polykristallinem Zinn. *Phys. Status Solidi B*, **2**, 1410–1414.
41. Smetana, J. (2007) Theory of tin whisker growth: "The end game". *IEEE Trans. Electron. Packag. Manuf.*, **30**, 11–22.
42. Vianco, P.T. and Rejent, J.A. (2009) Dynamic recrystallization (DRX) as the mechanism for Sn whisker development. Part I: A model. *J. Electron. Mater.*, **38**, 1815–1825.
43. Buchovecky, E.J. *et al.* (2009) A model of Sn whisker growth by coupled plastic flow and grain boundary diffusion. *Appl. Phys. Lett.*, **94**, 3.
44. Boettinger, W.J. *et al.* (2005) Whisker and hillock formation on Sn, Sn-Cu and Sn-Pb electrodeposits. *Acta Mater.*, **53**, 5033–5050.
45. Mathew, S. *et al.* (2007) Tin whiskers: How to mitigate and manage the risks. High Density packaging and Microsystem Integration, 2007. HDP '07. International Symposium on, pp. 1–8.
46. Osterman, M. (2002) Mitigation strategies for tin whiskers. Available http://www.calce.umd.edu/lead-free/tin-whiskers/TINWHISKERMITIGATION.pdf.
47. Brusse, J.A. *et al.* (2002) Tin whiskers: Attributes and mitigation. Proceedings of 22nd Capacitor and Resistor Technology Symposium, pp. 67–80.
48. Woodrow, T. and Ledbury, E. (2006) Evaluation of Conformal Coatings as a Tin Whisker Mitigation Strategy, Part 2. SMTA International Conference Rosemont IL.

49. Doornik, J. *et al.* (2007) Effectiveness of EPM conformal coatings as a mitigation against Tin whiskers. CALCE International Symposium on Tin Whiskers, 2007. Proceedings. 1st, UMCP, College Park, MD.
50. Hunt, C. and Wickham, M. (2010) Mitigation of tin whiskers with polymer coatings. Advanced Packaging Materials: Microtech, 2010. APM '10. International Symposium on, pp. 78–87.
51. Touw, A.E. (2010) Results of mitigation effectiveness survey and plans for GEIA-STD-0005-2 revision. CALCE International Symposium on Tin Whiskers, 2010. CALCE 2010. 4th UMCP, College Park, MD.
52. Suganuma, K. *et al.* (2007) Prevention of Sn whisker formation by surface treatment off Sn plating. presented at the 136th TMS Annual Meeting & Exhibition, Orlando, FL.
53. Kim, K.-S. *et al.* (2008) Prevention of Sn whisker formation by surface treatment of Sn plating part II. presented at the 137th TMS Annual Meeting, 2008 New Orleans, Louisiana.
54. Wickham, M. *et al.* (2001) Processability of lead-free component termination materials, National Physical laboratory, Teddington, Middlesex, United Kingdom.
55. Chen, K. and Wilcox, G.D. (2005) Observations of the spontaneous growth of tin whiskers on tin-manganese alloy electrodeposits. *Phys. Rev. Lett.*, **94**, 066104. Feb 18 (Epub 2005 Feb 2005).
56. Kim, K.S. *et al.* (2006) Tin whisker formation of lead-free plated leadframes. *Microelectron. Reliab.*, **46**, 1080–1086.
57. Lal, S. and Moyer, T.D. (2005) Role of intrinsic stresses in the phenomena of tin whiskers in electrical connectors. *IEEE Trans. Electron. Packag. Manuf.*, **28**, 63–74.
58. Hillman, D. *et al.* (2007) The use of Tin/Bismuth plating for Tin whisker mitigation on fabricated mechanical parts. CALCE International Symposium on Tin Whiskers, 2007. Proceedings. 1st, UMCP, College Park, MD.
59. Sandnes, E. *et al.* (2008) Equi-axed grain formation in electrodeposited Sn-Bi. *J. Electron. Mater.*, **37**, 490–497.
60. Moon, K.W. *et al.* (2010) Effect of current density and electrolyte concentration on hillock growth from pure bright Sn electrodeposits. *J. Appl. Electrochem.*, **40**, 1671–1681.
61. Dittes, M. *et al.* (2003) Tin Whisker formation – results, test methods and countermeasures. Electronic Components and Technology Conference, 2003. Proceedings. 53rd, pp. 822–826.
62. Whitlaw, K. *et al.* (2004) Preventing whiskers in electrodeposited Tin for semiconductor lead frame applications. *Circuit World*, Vol. **30**Iss: 2, 20–24.
63. Xu, C. *et al.* (2005) Driving force for the formation of Sn whiskers: Compressive stress – Pathways for its generation and remedies for its elimination and minimization. *IEEE Trans. Electron. Packag. Manuf.*, **28**, 31–35.
64. Panashchenko, L. and Osterman, M. (2009) Examination of nickel underlayer as a tin whisker mitigator. Electronic Components and Technology Conference, 2009. ECTC 2009. 59th, pp. 1037–1043.
65. Zhang, Y. *et al.* (2002) Understanding Whisker Phenomenon: Whisker Index and Tin/Copper, Tin/Nickel Interface. IPC SMEMA Council Apex.

13

Tin Whiskers

Katsuaki Suganuma
Institute of Scientific and Industrial Research, Osaka University, Japan

13.1 Low Melting Point Metals and Whisker Formation

Whiskers are thin filaments that sometimes grow on plating metals and even on solder fillets at room temperature or below 100 °C. These metals are typically, tin, cadmium and zinc, which are typical low melting temperature metals. Such metals have been widely used as plating and interconnection materials in the electronics industries for many decades. They are indispensable both for protecting substrates and electrodes from contamination and oxidation and for forming excellent metallic interconnection among electrodes by a melting reaction at suitable low temperatures, which results in a good quality of interconnections. Nevertheless, due to their low melting temperatures, several drawbacks concerning with interconnection reliability exist. There are concerns about heat-exposure resistance, creep/fatigue properties and electromigration sensitivity. Whiskering is one of the most serious issues among them and, in fact, numbers of electronic failures have been reported in history [1–3].

So, why do low melting point metals cause whiskering? It is well understood that the basic mechanism of whiskering is in fast diffusion of atoms. To realize the fast diffusion, typical values of self-diffusion coefficients of the major metals used in electronics are compared with typical transition metals in Table 13.1. The diffusion constants of tin, cadmium, and zinc at room temperature are quite large as compared with the other metals with higher melting points. Room temperature, 25 °C, is half of the melting temperatures of tin, cadmium and zinc, at which diffusion becomes very fast. In addition, grain boundaries play a the key role of the fast diffusion path at such low temperature and the grain-boundary diffusion is much faster than the lattice diffusion listed in Table 13.1. By the fast diffusion of

Lead-free Solders: Materials Reliability for Electronics, First Edition. Edited by K. N. Subramanian.

Table 13.1 *Self-diffusion coefficients of various metals at room temperature.*

Metal	Diffusion coefficient D (25 °C, cm^2/s)	Melting point T_m (°C)
Sn	1.8×10^{-18}	232
Zn	2.4×10^{-18}	420
Cd	1.0×10^{-15}	321
Cu	1.4×10^{-37}	1084
Au	7.0×10^{-33}	1064
Ag	7.5×10^{-34}	962
Cr	2.5×10^{-75}	1903
Pt	6.2×10^{-52}	1768

atoms along grain boundaries, whiskers nucleate at some points, which have not been clarified yet in any cases, and grow from the surface of the metals.

In addition, the grain structure of a plating layer is believed to be the other feature. Figure 13.1 shows typical grain structure of tin-plating as-plated conditions. A tin-plating layer has typical columnar structure, in which grains of tin stand on a copper substrate. Because diffusion along grain boundaries is very fast at room temperature, this columnar structure apparently enhances whisker growth by supplying tin atoms into growing whiskers, if there is enough driving force for diffusion.

Whiskers from metal plating of low melting temperatures grow at the root of whiskers [4]. This is different from most of the whiskers of the other metals and ceramics of high melting temperatures, where whiskers grow at the top of whiskers. The latter whisker growth mechanism is called the vapor–liquid–solid (VLS) mechanism [5]. In early times, tin

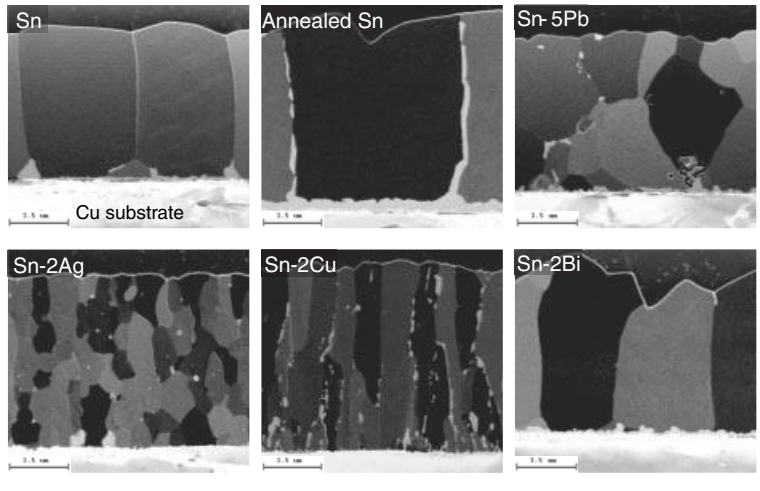

Figure 13.1 *Typical as-plated grain and interface microstructures of Sn, annealed Sn at 150 °C for 30 min, and alloy platings (SIM).*

whisker mechanisms were discussed in terms of dislocation theory [6, 7]. None of them succeeded to explain the real growth of whiskers. Nowadays, the whisker growth is believed to be controlled by compressive-stress-induced recrystallization of grains with accelerated atom diffusion under certain kinds of stress gradient [8, 9]. The essential driving force of whisker growth is compressive stress in metals. In the practical applications of electronic products, five different environments become the origins of compressive stress. These are listed as follows [10]:

- room-temperature whiskers;
- thermal-cycling whiskers;
- oxidation/corrosion whiskers;
- mechanical-compression whiskers;
- electromigration whiskers.

Thus, in the present chapter, tin whisker growth is mainly discussed because intensive studies have been reported only on tin whiskers as compared with cadmium and zinc. Whisker growth mechanisms of tin in the five different environments are briefly summarized and some mitigation methods are introduced in a later section.

13.2 Room-Temperature Tin Whiskers on Copper Substrate

Tin whiskers spontaneously grow straight and long on copper substrates in room-temperature storage. Figure 13.2 shows a typical room-temperature whisker. Tin plating on a copper substrate forms Cu_6Sn_5intermetallic compound (IMC) grains at their interface, even at room temperature. The IMC growth is very fast. These IMC grains locate at the grain-boundary lines of tin plating on a substrate and, at the triple junctions of grain boundaries, the IMC growth becomes extremely fast. Figure 13.3 shows the example of IMC grains on a copper substrate before and after room-temperature exposures [11]. This inhomogeneous IMC

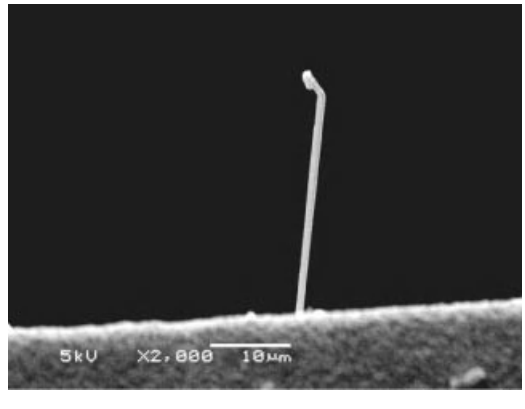

Figure 13.2 *Tin whisker grown on Sn-Cu plated copper lead-frame at room temperature (SEM).*

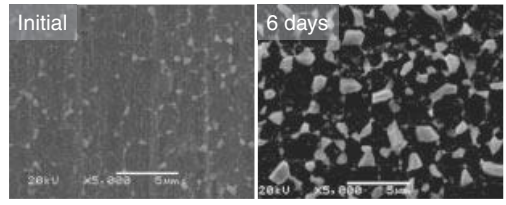

Figure 13.3 *Morphology change of IMC at interface of pure Sn plating just after plating and after 6 days at room temperature (SEM).*

growth produces a compressive stress gradient in a tin plating layer resulting in whisker growth [9]. It is also pointed out that the IMC grain shape has a great influence on whisker growth. Pyramid-shaped IMC growth enhances whisker growth by a large stress gradient across the plating layer, while platelet-shape IMC does not [12].

Thus, the room-temperature whisker growth can be schematically shown as in Figure 13.4.

It is known that the other substrate such as brass, 42 alloy and nickel underlayer plated substrates are immune to whisker formation. The IMC growth on brass and 42 alloy substrate is very slow as compared with copper and it is believed that compressive-stress development is negligible for these substrates. Although a nickel underlayer forms IMC grains, the IMCs grow as platelets and compressive stress is very low.

Heat treatment of tin plating on copper can reduce whisker formation drastically. Typical heat-treatment conditions are 150 °C for 30 or 60 min. By this heat treatment, a uniform IMC layer covers the interface retarding the supply of copper atoms into the tin. So, a reflow treatment also forms a uniform IMC layer, resulting in the mitigation of room-temperature whiskers.

13.3 Thermal-Cycling Whiskers on 42 Alloy/Ceramics

Thermal-expansion mismatch between tin plating and substrates induces compressive stress during thermal cycling, resulting in whisker growth. Figure 13.5 shows typical whisker microstructure of tin-plated electrode on a ceramic chip component after thermal cycling. The thermal-cycling whiskers grow dense and winding as compared with the room-

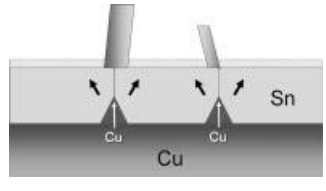

Figure 13.4 *Room-temperature whisker growth on Cu substrate. Fast diffusion of Cu atoms forms pyramid shape IMCs at the grain boundaries from the substrate.*

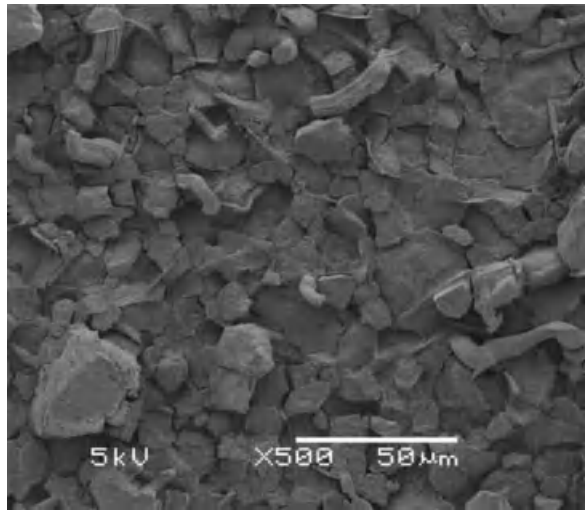

Figure 13.5 *Thermal-cycling whiskers on Sn after 1500 cycles between −40°C and 125°C (SEM).*

temperature whiskers shown in Figure 13.2. During thermal cycling, especially at elevated temperature, tin expands more than the substrate and compressive stress arises, resulting in whisker initiation. The thermal-cycling whisker growth mechanism is schematically shown as Figure 13.6.

Recently, the author showed the growth mechanism of thermal-cycling whiskers in detail [13]. Figure 13.7 shows an enlarged image of a thermal-cycling whisker. It shows the clear striation rings on the surface that corresponding to one cycle growth in thermal cycling and the deep root groove. Figure 13.8a shows a backscattered secondary electron image (BSE) of the cross section of the root groove. In the groove, a thick SnO film grows from both sides of the gap. The SnO thick film will contact at elevated temperature because of compressive stress, resulting in severe friction against the whisker growth from the bottom of the whisker. This can provide the reason why thermal-cycling whiskers grow winding, as schematically shown in Figure 13.8b. In addition, thermal-cycling whiskers

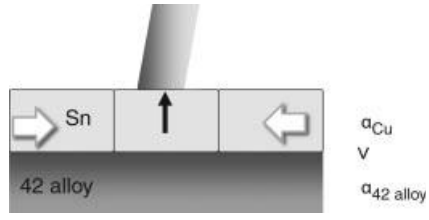

Figure 13.6 *Thermal-expansion mismatch causes compressive stress in Sn plating layer resulting in whisker initiation from surface.*

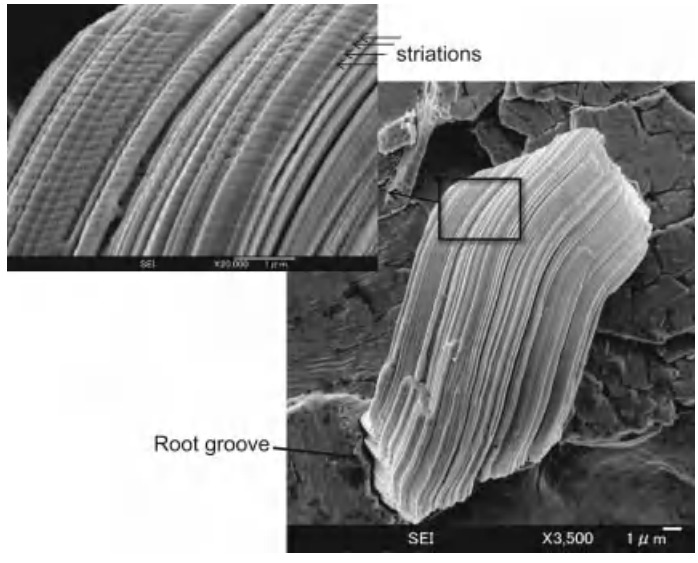

Figure 13.7 *Striations and root groove observed on thermal-cycling whisker of Sn plated on ceramic chip component (SEM, 1500 cycles between −40 and 125°C).*

grow thick due to the presence of surface oxide films that must be broken for the initiation of whiskers.

It is easily understood that a nickel underlayer cannot prevent thermal-cycling whiskers, in contrast to the room-temperature whiskers because nickel underlayer cannot relax the thermal expansion mismatch between tin plating and the substrates [13].

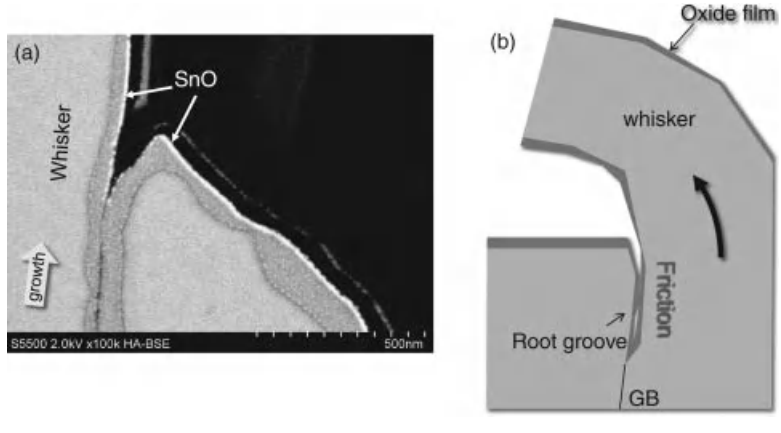

Figure 13.8 *(a) BSE image of cross section of root groove showing SnO surface contacting inside the groove (1500 cycles between −40 and 125°C). (b) Schematic drawing of thermal-cycling whisker growth [13].*

Figure 13.9 *SEM photograph of tin whiskers from Sn-3Ag solder fillet on a Cu pad exposed at 85 C/85%RH for 1000 h. ((Image kindly supplied courtesy of JEITA Whisker Mitigation Project).*

13.4 Oxidation/Corrosion Whiskers

Oxidation or corrosion of tin forms whiskers not only from plating but also from solder fillets on circuit boards. Figure 13.9 shows typical oxidation whiskers [14]. The oxidation whiskers are much localized and are thick and straight. In high humidity, tin is easily corroded from the surface and along grain boundaries. The formation of tin oxides, SnO and SnO_2, induces compressive stress around these oxides. The growth mechanism is schematically shown in Figure 13.10. When tin contains active alloying elements such as zinc, zinc atoms segregate to grain boundaries of tin to form ZnO [15]. ZnO also induces compressive stress resulting in the formation of tin whiskers.

iNEMI reported the occurrence conditions for oxidation whiskers by changing humidity/temperature [15]. Table 13.2 summarizes the results. Beyond 60% humidity, corrosion whiskers appear. Oxidation/corrosion whiskers have a relatively long incubation period for whisker imitation. For example, at 85 °C/85% RH, tin whisker appear after 1000 h. The latest work reported that flux composition has a great influence on the oxidation/corrosion

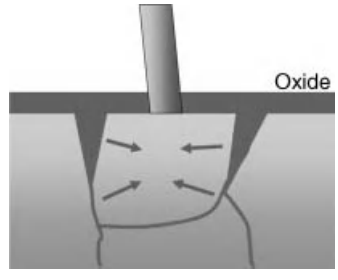

Figure 13.10 *Oxidation of Sn/alloying elements induces compressive stress resulting in whisker growth.*

Table 13.2 *iNEMI assessment for corrosion whisker.*

	Humidity (% RH)			
Temperature (°C)	10	40	60	85
30	N	—	N	C W
45	—	—	C W	—
60	N	N	C W	C W
85	—	—	—	C W
100	—	—	C W	—

N: Neither corrosion nor whisker, CW: Corrosion and whisker.

whisker growth [14]. High addition of halogen in flux enhances corrosion of tin resulting in severe whisker growth.

Zinc whisker growth from zinc plating on steels can be explained by the oxidation/corrosion mechanism [16, 17]. Zinc plating on steels exposed in air for a long period forms oxides as well as Zn-Ni IMC. These oxides and IMCs induce compressive stress resulting in dense, thin and long zinc whiskers as shown in Figure 13.11.

13.5 Mechanical-Compression Whiskers in Connectors

Connectors have serious problems with externally applied force forming mechanical connections. The mechanical-compression whiskers have been known since the early times [8]. After 2000, the mechanically induced tin whiskers in various types of connectors appeared again in the market.

Externally applied force induces tin whiskers instantly though compressive deformation and recrystallization of a tin-plating layer. Whiskers grow in a few seconds around the indentation mark by the external force, as shown in Figure 13.12. Under indentation, recrystallization of tin grains occurs immediately after deformation, which indicates the occurrence of massive transport of atoms. The growth mechanism is shown in Figure 13.13.

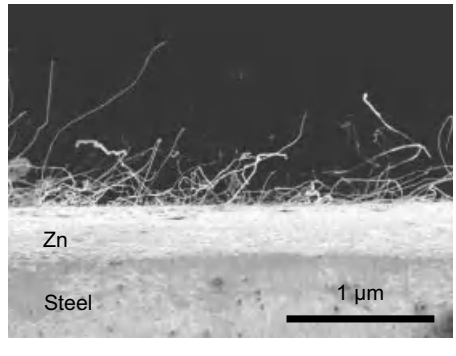

Figure 13.11 *Zn whiskers from Zn plating on steel after room-temperature exposure for long period in a computer room (SEM) [17].*

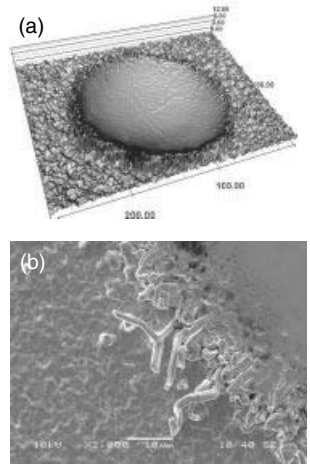

Figure 13.12 *(a) Mechanically induced indentation mark measured by laser microscope and (b) tin whiskers around a edge after 168 h (SEM).*

Recently, the effect of externally applied force on whisker formation was analyzed by a finite element method with various parameters [18]. It was proved that IMC blocking has a great influence on whisker initiation and growth.

13.6 Electromigration Whiskers

Intense current density sometimes causes massive diffusion of metal atoms in the direction of electron flow, namely, electromigration (EM). The miniaturization trend of line space/width of circuits has brought a new failure phenomenon for soldered interconnections. The directional atomic migration can induce significant microstructural changes at solder-joint areas such as voids formation, massive IMC growth, crack propagation, whiskers/solder extrusion, and dissolution of under bump metallization. All of these severe microstructural changes will result in failures of solder interconnections.

There have been only limited numbers of reports on EM whiskers [19–22]. Figure 13.14 shows one of the typical examples of EM whiskers grown from tin plating [21]. Due to the massive migration of tin atoms in the plated layer from the anode side, right, to the cathode side, left, a depleted zone of tin was formed on the anode side. Long whiskers, which were apparently pushed out by fast tin atom accumulation, grew on the cathode side. In another

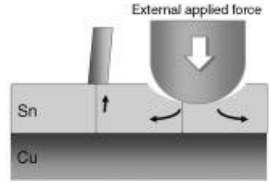

Figure 13.13 *Schematic illustration of mechanical-compression-induced whisker growth.*

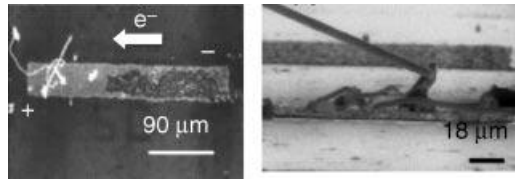

Figure 13.14 *Electromigration tin whiskers on Si observed at the cathode side after a current density of 1.5×10^5 A/cm^2 for 280 h at 50°C [20]. (Reproduced with permission from Journal of Applied Physics, Some aspects of bonding-solder deterioration observed in long-lived semiconductor lasers: Solder migration and whisker growth by K. Mizuishi, 55, 2, 289–295 Copyright (1983) American Institute of Physics).*

report of a power die attach application [20], indium atoms can easily migrate in gold solder matrix, resulting in the formation of indium whiskers.

Thus, there is still lacking information on EM whiskers. One needs the detailed mechanism with the whiskering conditions such as trigger current/temperature, alloying effects, and compressive-stress measurements at nucleation sites. An acceleration testing method should be also required to be established for the EM whisker growth.

13.7 Whisker Mitigation

In this section, some whisker-mitigation methods are introduced although there have been a limited numbers of studies carried out on whisker mitigation. One needs to understand several points in designing the whisker-mitigation strategy. They are 1) stopping directional diffusion of atoms towards plating surface, 2) relaxation of compressive stress gradient, and 3) grain and surface modification of plating layers. These three routes are essential path ways and practical methods will be provided from these routes. In addition, it is very important to understand the five categories of whiskers, with which the researcher is dealing, because the origin of compressive stress is different from one to the others. Here, some mitigation examples are introduced.

For room-temperature whiskers, the annealing/reflow treatment is quite effective, as mentioned in the earlier section. By annealing, a uniform IMC layer covers the interface and it modifies the stress state in a plating layer. In fact, stress does not change into negative, as shown in Figure 13.15 [23]. This effect comes from the retardation of rapid pyramid like IMC growth at the interface.

Insertion of a nickel underlayer between a tin plating layer and a copper substrate can prevent the room-temperature whisker growth. A nickel layer modifies the pyramid-like IMC growth along tin grain boundaries on a copper substrate into the randomly dispersed platelet IMC growth [24]. Such platelet IMC formation also occurred on chromium-alloyed copper substrate [12].

Alloying bismuth into tin has a great effect to modify large IMC pyramids into fine IMC dispersion, resulting in mitigation of whisker growth just as well as lead addition to tin [14, 24, 25]. Such IMC morphology changes by alloying are shown in Figure 13.1.

Alloying silver to tin also has an excellent effect on whisker mitigation in a different mechanism from the bismuth addition. Although the mechanism has not been understood

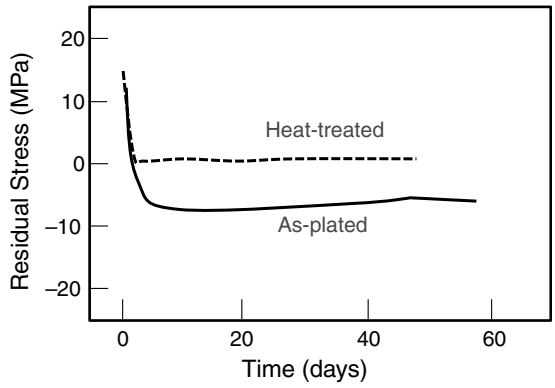

Figure 13.15 *Residual stress in Sn plating on Cu as a function of time after plating [21]. (Reproduced with permission from Journal of Applied Physics, Tin whisker growth driven by electrical currents by S. H. Liu, Chih Chen, P. C. Liu and T. Chou, 95, 12, 7742-7747 Copyright (2004) American Institute of Physics).*

well, silver alloying modifies grain microstructure from columnar to uniaxial type, while the bismuth addition does not change the columnar grain microstructure.

Surface coating with organic or inorganic/metal layers are excellent methods for whisker mitigation. The conventional conformal coatings with polymers such as urethane and silicone cover the entire surface including component electrodes and electrode pads of printed circuit boards. The conformal coating can stop most room-temperature whiskers and thermal-cycling whiskers effectively. Some room-temperature whiskers, however, still break though a conformal coating layer. Even though whiskers penetrate a conformal coating layer, short circuits to the neighboring circuits can be avoided by the covering polymer layer on the neighboring circuits. Uniformity of the conformal coating, especially on edges of electrodes, should be controlled to secure coverage.

A thin metal layer over a tin plating layer has excellent mitigation effect for all types of whiskers [26]. Figure 13.16 shows the surface microstructure of thin gold overplated tin plating.

Other whisker mitigation methods have been also proposed [27, 28].

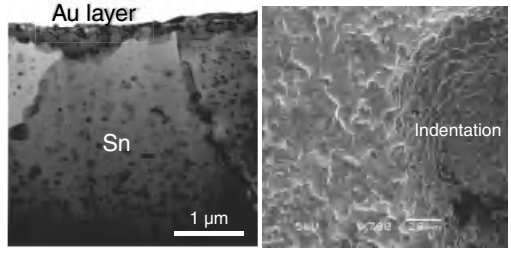

Figure 13.16 *(a) Au nano-overcoating on Sn plating (TEM) and (b) indentation edge microstructure in the same condition shown in Figure 13.12 (SEM).*

13.8 Future Work

In the present chapter, the current understanding of whisker phenomenon especially for tin plating and solders was briefly summarized. In addition, the previous section introduced possible mitigation methods. As pointed in the beginning, the whisker issue has a long history and still we need time to understand the whole story from the theoretical basis to practical mitigations and to related reliability-evaluation methods. There have been already several guidelines for whiskers from industrial associations [29–31]. Unfortunately, none of these guidelines are perfect for a wide range of practical applications. People can use these guidelines with careful consideration, especially, by understanding what kind of environments they are dealing with.

Nevertheless, by a lot of scientific studies carried out after 2000, it is believed that we are approaching very close to the real understanding of the whisker phenomenon. It will be possible to make a precise prediction of whisker initiation and growth based on the established mechanisms. That could also lead us to the perfect mitigation of whiskers.

References

1. Cobb, H.L. (1946) Cadmium whiskers. *Monthly Rev. Am. Electroplaters Soc.*, **33**, 28–30.
2. NASA Tin Whisker (and Other Metal Whisker) Homepage: http://nepp.nasa.gov/whisker/.
3. Brusse, J. and Sampson, M. (2005) Zinc whiskers: Hidden cause of equipment failure. *IT Pro*, **6**, 43–47.
4. Koonce, S.E. and Arnold, S.M. (1953) Growth of metal whiskers. *J. Appl. Phys.*, **24**, 365–366.
5. Wagner, R.S. and Ellis, W.C. (1964) Vapor-liquid-solid mechanism of single crystal growth. *Appl. Phys. Letters*, **4**, 89–90.
6. Eshelby, J.D. (1953) A tentative theory of metallic whisker growth. *Phys. Rev. Lett.*, **91**, 755–756.
7. Franks, J. (1958) Growth of whiskers in the solid phase. Acta Metallurgica, **6**, 103–109.
8. Fisher, R.M., Darken, L.S., and Carroll, K.G. (1954) Accelerated growth of tin whiskers. *Acta Metal.*, **2**, 368–372.
9. Terasaki, T., Iwasaki, T., Okura, Y. *et al.* (2009) Evaluation of tin-whisker growth during thermal-cycle testing using stress- and mass-diffusion analysis. 59th Electronic Components and Technology Conference (ECTC2009), pp. 277–284.
10. Suganuma, K. (2005) *Introduction of Lead-Free Soldering Reliability*, Kogyo-Chosakai, Tokyo.
11. Suganuma, K. (April 25–26 2007) Tin whisker formation on fine pitch connectors. 1st International Symposium on Tin Whiskers, University of Maryland.
12. Kato, T., Akahoshi, H., Nakamura, M. *et al.* (2010) Correlation between whisker initiation and compressive stress in electrodeposited Tin–Copper coating on copper leadframes. *IEEE Trans. Electron. Packag. Manuf.*, **33**, 165–176.
13. Suganuma, K. (2010) Tin whisker growth in vacuum thermal cycling. Presented at 2010 TMS Annual Meeting & Exhibition, February 14–18, Seattle.
14. Suganuma, K. (2010) JEITA tin whisker mitigation project. Presented at 4th International Symposium on Tin Whiskers, June 23–24, Maryland.
15. Jiang, J., Lee, J.-E., Kim, K.-S., and Suganuma, K. (2008) Oxidation behavior of Sn–Zn solders under high-temperature and high-humidity conditions. *J. Alloys Compd.*, **462**, 244–251.
16. Wei, C.C., Liu, P.C., Jeffrey, C.C. *et al.* (2007) Relieving Sn whisker growth driven by oxidation on Cu leadframe by annealing and reflowing treatments. *J. Appl. Phys.*, **102**, 043521.

17. Baated, A., Kim, K.-S., and Suganuma, K. (2010) Whisker growth from an electroplated zinc coating. *J. Mater. Res.*, **25**, 2175–2182.
18. Shibutani, T., Yu, Q., Shiratori, M., and Pecht, M.G. (2008) Pressure-induced tin whisker formation. *Microelectron. Reliab.*, **48**, 1033–1039.
19. Blech, I.A. and Meieran, E.S. (1969) Electromigration in thin Al film. *J. Appl. Phys.*, **40**, 485–491.
20. Mizuishi, K. (1984) Some aspects of bonding-solder deterioration observed in long-lived semiconductor lasers: Solder migration and whisker growth. *J. Appl. Phys.*, **55**, 389–395.
21. Liu, S.H., Chen, C., Liu, P.C., and Chou, T. (2004) Tin whisker growth driven by electrical currents. *J. Appl. Phys.*, **95**, 7742–7747.
22. Ouyang, F.Y., Chen, K., Tu, K.N., and Lai, Y.-S. (2007) Effect of current crowding on whisker growth at the anode in flip chip solder joints. *Appl. Phys. Lett.*, **91**, 231919.
23. Lee, B.Z. and Lee, D.N. (1998) Spontaneous growth mechanism of tin whiskers. *Acta Metal.*, **46**, 3701–3714.
24. Suganuma, K. (2010) Effects of alloying on tin whisker growth and some finding on fatigue mechanism. Presented at 6th Lead-Free Solder and Technology Workshop: 139th Annual Meeting & Exhibition, February 14, Seattle.
25. Suganuma, K., Kim, K.-S., Kim, S.-S. *et al.* (2009) Whisker growth behavior of tin and tin alloy lead-free finishes. Presented at 2009 TMS Annual Meeting & Exhibition, February 15–19, San Francisco.
26. Yorikado Y, Kim G.-S., Suganuma K., Tsujimoto M., and Yanada I. (2006), Effect of Ni flash coating on Sn whisker growth, 16th Microelectronics Symposium, Japan Institute of Electronics Packaging Society, pp. 207–210.
27. Takeuchi M., Kamiyama K. and Suganuma K. (2006), Tin whisker prevention for fine pitch connectors by surface roughening, *J. Electronic. Mater.*, **35**, 1918–1925.
28. Baated, A., Kim, K.-S., Suganuma, K. *et al.* (2010) Effects of reflow atmosphere and flux on Sn whisker growth of Sn–Ag–Cu solders. *J Mater. Sci.: Mater. Electron.*, **21**, 1066–1075.
29. JEDEC JESD201, (2008), Environmental Acceptance Requirements for Tin Whisker Susceptibility of Tin and Tin Alloy Surface Finishes.
30. ANSI-GEIA-STD-0005-2 Standard, (2010), Standard for mitigating the effects of tin whiskers in aerospace and high performance electronics systems, Government Electronics & Information Technology Association.
31. JEITA ET-7305, (2011), Guidline for selection of lead-free materials for tin-whisker mitigation, Japan Electronics and Information technology Industrial Association.

Thematic Area VII

Electromigration Issues Affecting Reliability

14

Electromigration Reliability of Pb-Free Solder Joints

Seung-Hyun Chae, Yiwei Wang, and Paul S. Ho
Microelectronics Research Center, The University of Texas at Austin, TX 78758, USA

14.1 Introduction

Trends in semiconductor devices and packages are moving toward higher performance, multifunctionality, smaller form factor, and ecofriendliness. This leads to demands for higher input/output (I/O) and power density, finer interconnection pitch, and implementation of new materials such as Pb-free solder. The transistor count has increased by $\sim 10^7$ fold over the past 30 years. Over the same period, the microprocessor die size has grown approximately 7% annually, which has been accompanied by doubling the chip speed every two years, and power increased at an exponential rate [1]. These trends have a significant impact on packaging technology. As the transistor count and speed increase, the required number of interconnects between the die and package has to increase to accommodate increased signal counts as well as to support the increased demand for power and ground. According to Rent's rule, the number of terminal pins, T, follows a power-law relationship of $T = tg^p$, where g is the number of logic gates, t and p are constants ($p < 1.0$, and generally $0.5 < p < 0.8$) [2]. To accommodate the wiring demand the flip-chip solder pitch is projected to continuously decrease according to the International Technology Roadmap for Semiconductors (ITRS) [3], as seen in Figure 14.1.

With decreasing solder bump pitch, the current density carried by the solder continues to increase, raising serious reliability concern due to electromigration (EM). EM describes the mass transport driven by momentum transfer from conducting electrons to metal ions under

Lead-free Solders: Materials Reliability for Electronics, First Edition. Edited by K. N. Subramanian.

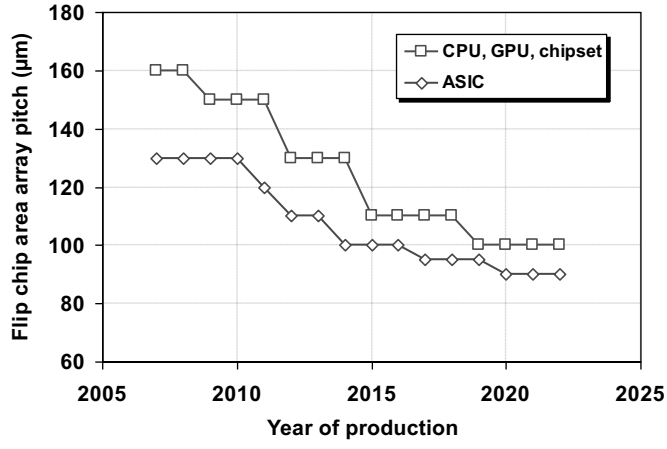

Figure 14.1 *Flip-chip area array pitch projected by ITRS in 2007.*

an electric current. The atomic flux, J_{EM}, induced by EM can be expressed as:

$$J_{EM} = Cv_d = C\frac{D}{kT}Z^* e\rho j \tag{14.1}$$

where C is the concentration of atoms per unit volume, v_d is the drift velocity, D is the diffusivity, k is Boltzmann's constant, T is the absolute temperature, Z^* is the effective charge number, ρ is the resistivity, and j is the current density. Even though the current density in the solder bumps is still about two orders of magnitude lower than that for back-end-of-line (BEOL) interconnects, EM becomes a serious reliability issue in solder bumps because solder alloys have a low melting point, a high diffusivity, and a large effective charge number [4, 5].

In addition to EM, the large current density can generate a significant amount of Joule heat from the metal trace connected to the bump, which can build a large temperature gradient in the solder bump to induce thermomigration (TM). TM, also known as the Ludwig–Soret effect or Soret effect, is also a mass-transport phenomenon induced by momentum transfer between diffusing atoms and electrons [6, 7]. Under TM, the mass transport can induce damage formation in the solder and become another reliability concern. The flux equation for TM is described as

$$J_{TM} = -C\frac{D}{kT}\frac{Q^*}{T}\frac{dT}{dx} \tag{14.2}$$

Here, $-(Q^*/T)(dT/dx)$ is the driving force induced by the thermal gradient dT/dx. Q^* is defined as the heat of transport, which has a unit of (heat) energy and can be interpreted as the difference between the heat carried by the migrating atom and the heat of the atom at the initial state (the hot end or the cold end depending on the sign of Q^*) [7].

To comply with RoHS (Restriction of Hazadous Substances) requirements for environmental safety, Pb-free solder alloys have been introduced and widely implemented by the industry. The major constituent of Pb-free solder alloys is Sn, which tends to react with

under bump metallurgy (UBM) to form more Sn-containing intermetallic compounds (IMCs) compared with Pb-based solders. An IMC layer is essential for good solder wetting and adhesion at the interface. On the other hand, excessive IMC growth should be avoided for mechanical reliability and electrical performance since IMCs are generally brittle and have a higher electrical resistivity than the solder material. Also, IMC growth can generate Kirkendall voids that deteriorate drop impact reliability [8]. Under current stressing, IMC growth can be accelerated by EM. In addition, IMCs may grow until UBM or substrate pad depletes completely due to the abundant Sn supply. Therefore, it is important, especially for Pb-free solder joints, to characterize IMC growth enhanced by current stressing and to examine its role in EM reliability.

The noble and near-noble elements such as Cu, Ni, Ag, and Au are known as 'fast diffusers' in Pb and Sn by diffusing via an interstitial mechanism [9–13]. They play an important role in solder-joint reliability since not only do they diffuse extremely fast compared to other elements, but also form IMCs with solder constituents. Sn acts similarly to Pb as a host for fast diffusers. However, an important difference stems from the different lattice structure. Diffusivity in Pb is independent of the crystalline orientation because Pb has a face-centered cubic (FCC) structure. In contrast, in metallic Sn (β-Sn) that has a body-centered tetragonal (BCT) structure with lattice parameters of $a = b = 5.83$ Å and $c = 3.18$ Å, the diffusivity is remarkably different between parallel and perpendicular direction to the c-axis of the Sn lattice. This is also true for self-diffusion [14]. For fast diffusers in Sn, the ratio of the diffusivity typically varies by a factor of 30–40 at 200 °C [15]. In particular, Ni diffusion in Sn exhibits the highest anisotropy. Diffusion in the direction perpendicular to the c-axis is not very different from the other fast diffusers. In contrast, diffusion along the c-axis is extraordinarily fast with very low activation energy of less than 0.2 eV [13]. In fact, the ratio of diffusivity in the direction parallel and perpendicular to the c-axis is more than 10^5 at 120 °C. This yields distinctly different rates of IMC formation and impacts EM reliability. Recently, the effect of Sn grain structure on EM reliability has generated extensive interests for Sn-based solder joints, particularly for UBM containing Ni.

In this chapter, we review EM reliability of Pb-free solder joints focusing on the IMC formation and growth kinetics and their effects on EM performance and failure mechanisms. We include a discussion on TM as compared with EM and the recent results on the effect of Sn grain structure on EM lifetime. In Section 14.2, we review failure mechanisms related to mass transport that are directly or indirectly induced by current stressing. The effects of solder alloy (Pb-containing solder vs. Pb-free solder) and UBM structure (thick Cu UBM vs. thin Ni UBM) on EM failure mode are highlighted. This is followed by an assessment of the relative strength of TM against EM. TM may accompany EM when a large enough temperature gradient is created in solder joints under current stressing or in the adjacent solder joints. Here, the effect of EM and that of TM on morphological changes are compared. Section 14.3 addresses IMC growth kinetics in Pb-free solder joints both under thermal aging and under current-stressing conditions. A useful correlation between EM failure and IMC growth can be reached by considering EM failure kinetics. In Section 14.4, the effect of Sn grain structure on EM reliability is investigated. Different failure modes depending on Sn grain orientation are discussed. Lastly, the influence of multiple solder reflows on Sn grain structure and EM lifetime is presented.

14.2 Failure Mechanisms of Solder Joints by Forced Atomic Migration

14.2.1 EM

EM failure in solder joints can be correlated to the mass transport of the constituents: (1) the major constituents of solder alloys such as Pb and Sn; (2) the minor constituents such as fast diffusers from UBM or substrate. The mass transport of Pb or Sn under EM can lead to voids or extrusions, which eventually cause open or short circuits [16–19]. Fast diffusion of Cu or Ni in UBM can induce the dissolution of UBM resulting in the formation of interfacial IMC layers. This can lead to circuit failures by dewetting of the solder from the contact or by interfacial fracture [20].

Phase separation was observed in eutectic Sn-Pb solder joints under EM [7, 17, 19, 21]. Figure 14.2 shows the microstructure of eutectic Sn-Pb solder bumps after current stressing of 2.25×10^4 A/cm^2 at 150 °C. A Pb-rich phase accumulated at the anode side, while a Sn-rich phase accumulated at the cathode side. This is because the diffusivities of the two components are different. It has been reported that under current stressing, Pb was found to be the dominant diffusion species at temperatures above 100 °C, while Sn became dominant at temperatures below 100 °C [22]. Eutectic Sn-Bi solder exhibits similar characteristics under current stressing, where Bi migrates along the electron flow to accumulate at the anode side of a joint [23, 24].

Figure 14.3 shows a time sequence of IMC formation in composite solder joints (high-Pb solder on the die side and eutectic Sn-Pb solder on the substrate side) with 5 μm Cu UBM under current stressing [25]. At the upper left corner of the UBM, IMC grew and UBM depleted under EM, followed by void formation. This was attributed to the current crowding that occurred where the metal trace with a small cross section meets the solder joint with a large cross section. This led to a 'pancake-type' void propagation as illustrated in Figure 14.4. As voids form, the current crowding region moves toward the void front, where the subsequent void propagation takes place. In this way, voids propagate through the interface to track the current crowding. This is a common failure mode by EM especially when UBM is relatively thin [25–27]. The current density at the current-crowding region was found to be about one order of magnitude higher than the

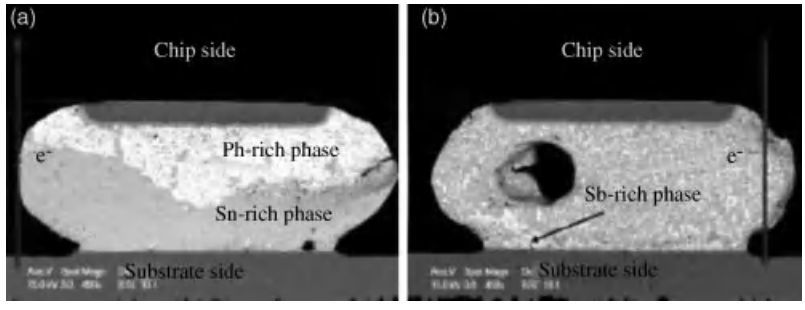

Figure 14.2 *Cross-sectional SEM images of the current stressed eutectic Sn-Pb solder bumps at 150°C for 6 h [21]. (Reproduced with permission from Microelectron. Eng., Effects of electromigration on microstructural evolution of eutectic SnPb flip chip solder bumps by D.-G. Kim, W.-C. Moon and S.-B. Jung, 83, 11–12, 2391–2395 Copyright (2006) Elsevier Ltd).*

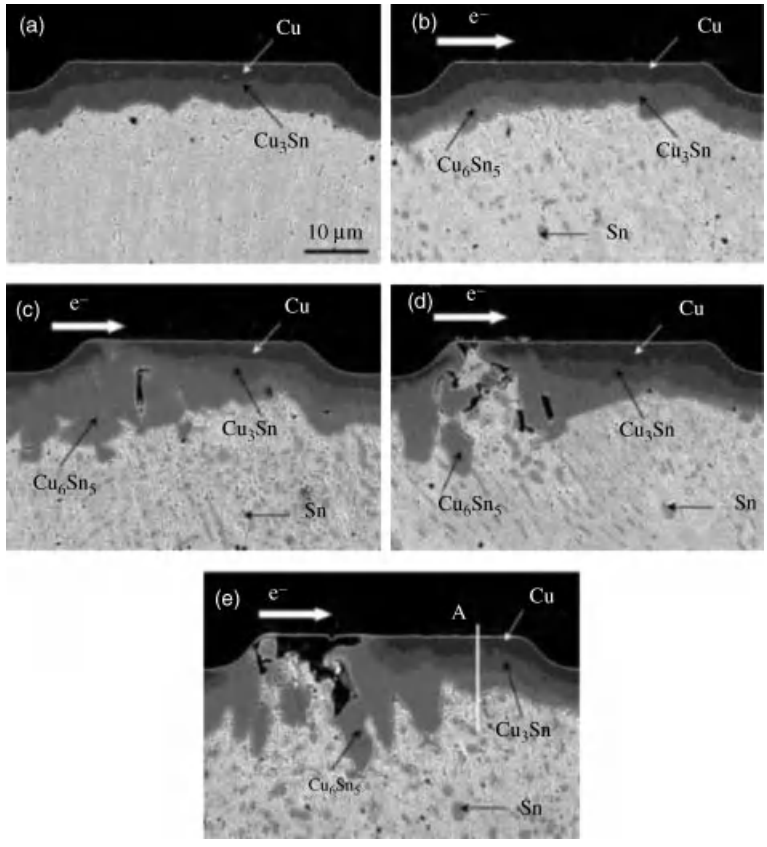

Figure 14.3 *SEM images of cathode side of composite (97Pb-3Sn on the die side and 63Sn-37Pb on the substrate side) bumps after current stressing of 2.25×10^4 A/cm^2 at 155 °C. (a) Before current stressing, (b) after 3 h, (c) after 12 h, (d) after 18 h, and (e) after 20 h [25]. (Reproduced with permission from J. Appl. Phys., Mechanism of electromigration-induced failure in the 97Pb–3Sn and 37Pb–63Sn composite solder joints by J. W. Nah, K. W. Paik, J. O. Suh and K. N. Tu, 94, 12, 7560–7566 Copyright (2003) American Institute of Physics).*

average current density at the interface [28]. This enhances the local damage formation under EM in solder joints. Current crowding can also cause the EM failure rate to be different depending on the current polarity. Typically, solder joints with electrons passing toward the substrate side fail much faster than those with electrons moving toward the die side.

In Sn-based Pb-free solder joints, the phase segregation of the alloying elements (typically Ag and/or Cu) is negligible because their concentration is minuscule. Instead, faster IMC growth and dissolution of UBM play an important role in controlling the EM failure of Pb-free solder joints. Figure 14.5 shows EM damage evolution in Sn-Ag solder joints where the UBM stacks consist of TiW (0.25 μm)/Cu (18 μm) [29]. At Stage I, IMC layers grew by consuming Cu UBM. The resistance increase was negligible at this stage. At Stage II, EM-induced voids were initiated at the Cu_6Sn_5/solder interface. These voids grew

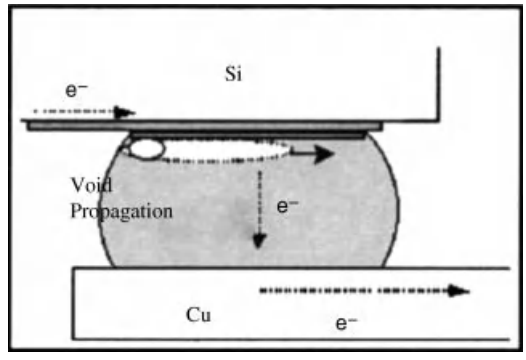

Figure 14.4 *Schematic illustration depicting the cross section of a solder joint with pancake-type void formation and propagation in eutectic Sn-Pb solder [26]. (Reproduced with permission from Appl. Phys. Lett., Current-crowding-induced electromigration failure in flip chip solder joints by E. C. C. Yeh et al., 80, 4, 580–582 Copyright (2002) American Institute of Physics).*

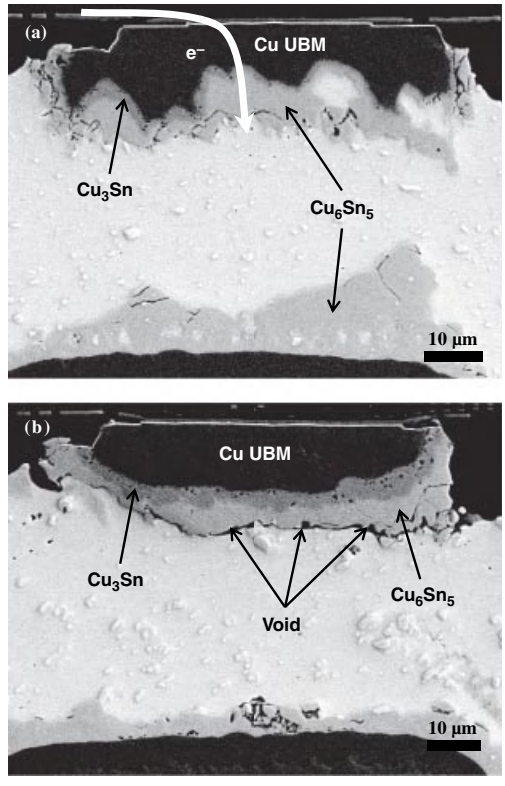

Figure 14.5 *EM damage evolution in Sn-Ag solder joints with Cu UBM. (a) Stage I, (b) Stage II, (c) Stage III, and (d) final open failure [29]. (Reproduced from J. Mater. Sci: Mater. Electron., Electromigration Statistics and Damage Evolution for Pb-Free Solder Joints with Cu and Ni UBM in Plastic Flip-Chip Packages by S.-H. Chae et al., 18, 247–258 Copyright (2007) Springer Science + Business Media).*

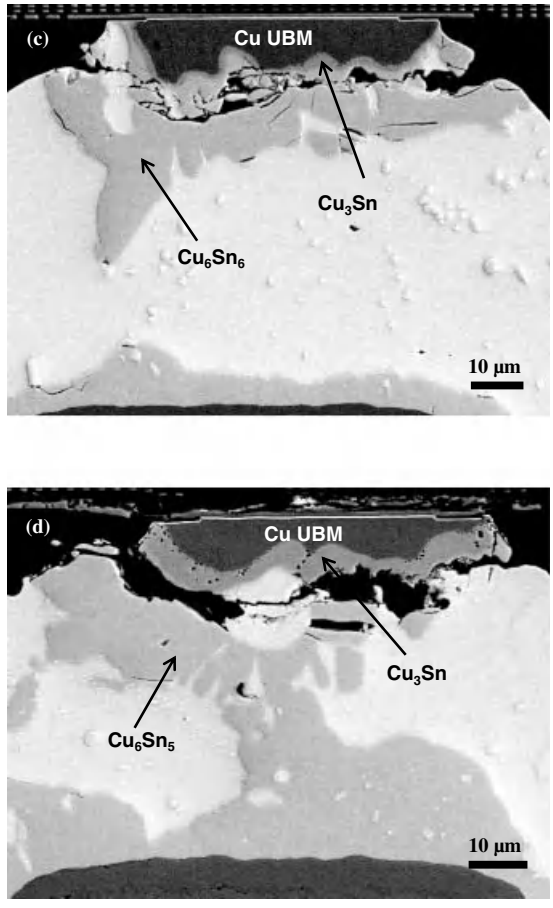

Figure 14.5 *(Continued)*

independent of Kirkendall voids formed in the Cu_3Sn layer. At this point, the resistance increase (ΔR) was still small, only several mΩ. Also, the current-crowding effect on UBM consumption and void initiation was found to be weak owing to the thick Cu UBM structure. Crowding of the electron flow at the entrance of Cu UBM could be relaxed or spread out through the thick UBM before they reached the IMC/solder interface. Figure 14.5c depicts a solder joint at Stage III after ΔR jumped to ~80–100 mΩ. At this stage, substantial Cu_6Sn_5 growth was observed, and EM voids were widespread in the Cu_6Sn_5 layer near the Cu_3Sn/Cu_6Sn_5 interface, making the joint almost open. The void location moved from the Cu_6Sn_5/solder interface to the vicinity of the Cu_3Sn/Cu_6Sn_5 interface. Before discrete voids were connected to each other, the ligament between the voids had a high current density, which further enhanced Cu_6Sn_5 growth with simultaneous void enlargement. Simultaneously, vacancies were driven toward the die side to compensate for the mass flux imbalance. Chao *et al.* [30–32] developed a 1D vacancy transport model using a finite difference method and showed that vacancies were accumulated in the Cu_6Sn_5 layer near the Cu_3Sn/Cu_6Sn_5 interface in a Cu-Sn diffusion couple under current stressing. Thus voids continued to form in the Cu_6Sn_5 layer near the Cu_3Sn/Cu_6Sn_5 interface. This was partly attributed to the fact

that the diffusivity (D) and the effective charge number (Z^*) of Cu in the Cu_6Sn_5 layer was found to be larger than those in the Cu_3Sn layer. At this stage, Cu_6Sn_5 grew preferentially through the limited region where solder was still connected. Increased local current density in this region could accelerate IMC growth until failure. When an open failure finally occurred, an extensive formation of Cu_6Sn_5 was observed spanning out from the die side to the substrate side. Gan *et al.* [33] observed a polarity effect in V-groove samples where IMC growth was retarded at the cathode side of a joint, while the growth was enhanced at the anode side. However, this effect was not clearly observed in flip-chip solder joints, as seen in Figure 14.5.

When UBM is comprised of Ti (0.1 μm)/Ni (2 μm), the EM damage evolution is depicted in Figure 14.6. At Stage I where ΔR was negligible, initial voids were found at the current-crowding location. Some part of Ni UBM was dissolved into solder to form Ni_3Sn_4. At Stage

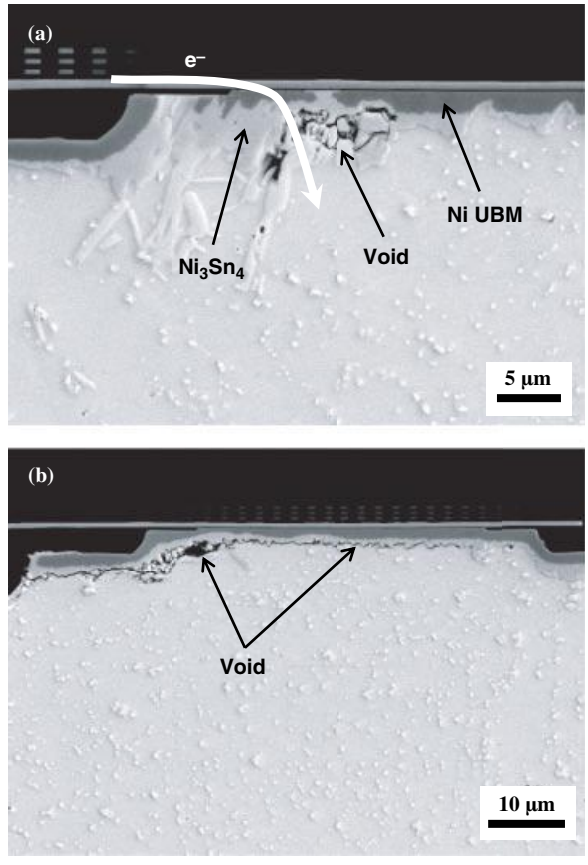

Figure 14.6 *EM damage evolution in Sn-Ag solder joints with Ni UBM. (a) Stage I, (b) Stage II, (c) Stage III, and (d) Stage IV [29]. (Reproduced from J. Mater. Sci: Mater. Electron., Electromigration Statistics and Damage Evolution for Pb-Free Solder Joints with Cu and Ni UBM in Plastic Flip-Chip Packages by S.-H. Chae et al., 18, 247–258 Copyright (2007) Springer Science + Business Media).*

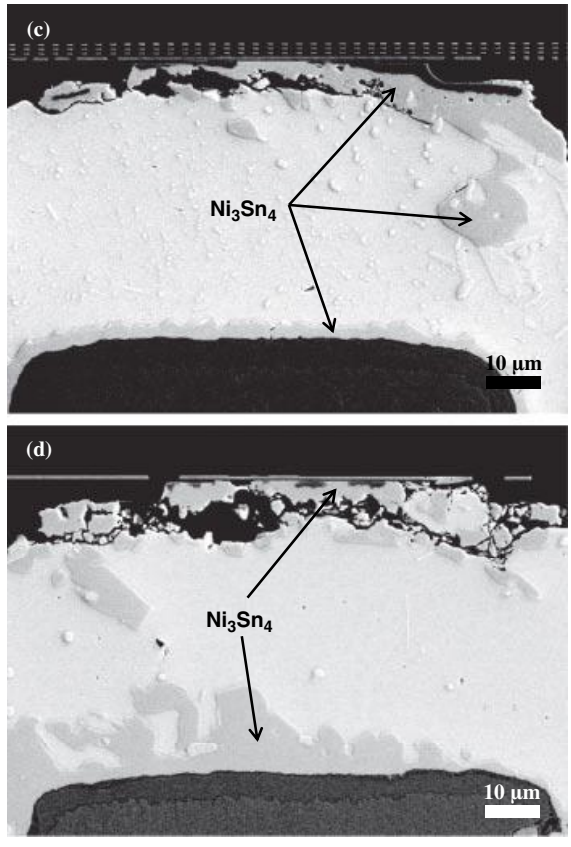

Figure 14.6 *(Continued)*

II the void propagated through the Ni_3Sn_4/solder interface leading to a pancake-type void. The IMC growth was not substantial yet and ΔR was in the range of several mΩ only, although the voiding area covered more than a half of the interface. Numerical analyses revealed that ΔR followed a near-exponential pattern with respect to voiding fraction in solder bumps [29, 34]. Thus, the resistance change is not significant unless a solder joint becomes almost open. Further void growth increased the local current density, leading to accelerated IMC and void growth, as seen in Figure 14.6c. The polarity effect was not observed since IMC growth occurred predominantly at the UBM side. Figure 14.6d shows a solder joint that was nearly open. At this stage, a large amount of IMC accumulated on the substrate side, while the solder joint became almost open. Solder-joint melting often occurred after this stage due to the substantial increase of Joule heat prior to the final open failure.

14.2.2 TM

TM in flip-chip solder joints was first reported by Ye *et al.* [35]. They found voids on the die side in eutectic Sn-Pb solder joints where electrons flowed from the substrate side to the die side. This could not be explained by EM, and they attributed that to TM that accompanied

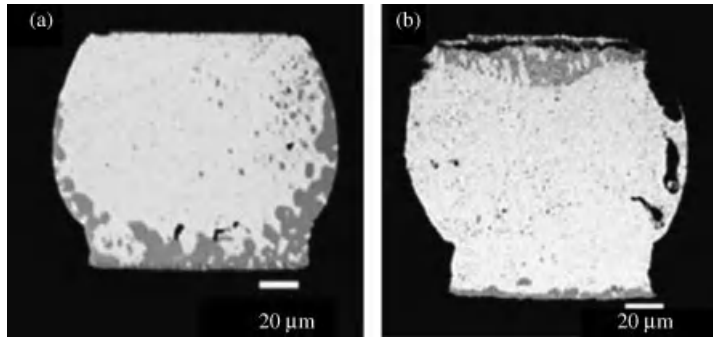

Figure 14.7 *Composite (97Pb-3Sn with eutectic Sn-Pb) solder joints (a) before testing, and (b) after TM [36]. (Reproduced with permission from Appl. Phys. Lett., Thermomigration in SnPb composite flip chip solder joints by A. T. Huang et al., 88, 141911 Copyright (2006) American Institute of Physics).*

EM. The major heat source that makes the die side of solder joints hotter than the substrate side is known to be the thin metal trace on the die carrying the electric current into the solder. Also, due to the current crowding, the current density distribution in solder joints is not uniform. This can also play a role in setting up the temperature gradient in the solder. Using a finite element method (FEM), Ye estimated the temperature gradient in the solder to be $\sim$1500 °C/cm.

Because Si is a good thermal conductor, the unpowered solder joints adjacent to powered solder joints can experience a similar thermal effect. Figure 14.7 shows a damaged unpowered bump due to TM at an ambient temperature of 150 °C. The adjacent powered solder joints were under 1 A of current stressing. TM induced a redistribution of Pb-rich and Sn-rich phases where the Pb-rich phase moved toward the cold end, while the Sn-rich phases moved toward the hot end [36].

Chuang and Liu created a temperature gradient of 1000 °C/cm in a bulk eutectic SnPb solder without current stressing [37]. The Pb phase was found to deplete from the hot end, although voiding was not observed. The heat of transport was estimated to be 22.16 kJ/mol or 0.23 eV. TM was also studied by Hsiao and Chen [38] using an alternating current at 45 Hz. The same amount of Joule heating was expected to be created while EM-induced damage was retarded. The temperature gradient in eutectic SnPb solder joints was measured directly to be 2143 °C/cm at 100 °C by infrared microscopy. The flux by TM was calculated by the marker motion, and the heat of transport was obtained to be 26.8 kJ/mol or 0.28 eV.

For Pb-free solders, Chen *et al.* found that in Sn-3.5Ag solder joints Cu atoms from UBM migrated from the hot end (die side) to the cold end (substrate side) leading to dissolution of the 5-µm thick UBM and void formation at the UBM/IMC interface [39]. The temperature gradient for TM required to overwhelm EM under the current density of 9.7×10^3 A/cm^2 was estimated to be 400 °C/cm. A study by Hsiao and Chen [40] showed that Sn migrated toward the hot end in Sn-3.5Ag solder bumps under a temperature gradient of 2829 °C/cm generated by AC. On the other hand, no damage was reported in the 5 µm Cu/3 µm Ni UBM in this study. Q^* of Sn was calculated to be -0.014 eV from measurements of marker movements.

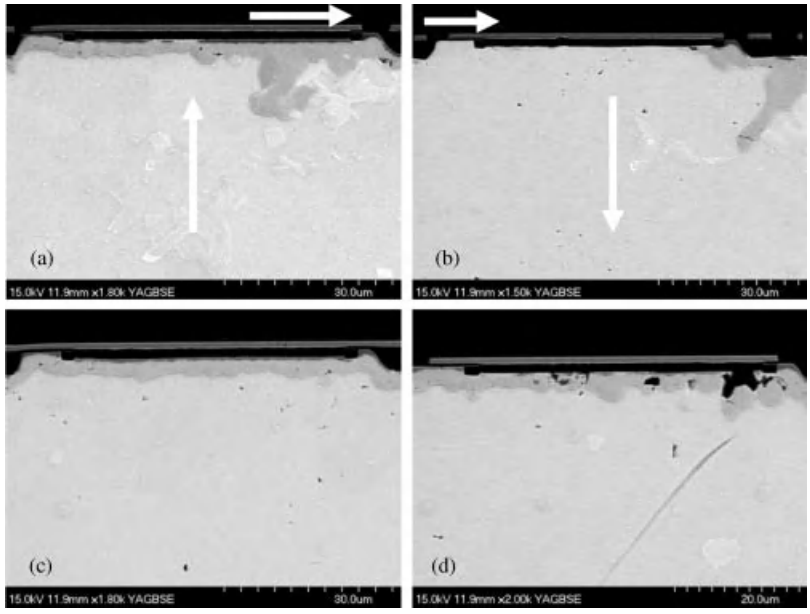

Figure 14.8 *Solder bumps with Ni UBM subject to (a), (b) TM + EM, and (c), (d) TM only.*

In a recent study, Chae and Ho [41] compared TM against EM in Sn-2.5Ag solder bumps in flip-chip packages. To increase thermal gradient the backside of the die was heated while the bottom of the substrate was cooled. In this experiment, only 4 bumps were current stressed with 0.8 A among 31 solder bumps in the same row. Thus, only the TM force was applied to 27 bumps, while 4 bumps were subject to both EM and TM driving forces.

Figure 14.8 shows solder bumps with 1-μm thick Ni UBM with and without current stressing. Current stressing was stopped after 6 days when a current-stressed bump became open, while the TM force was maintained for 69 days. The average temperature gradient in solder bumps under current stressing was determined to be 980 °C/cm by FEM. Without current stressing the temperature gradient was 950 °C/cm. Under current stressing, most of the UBM was depleted in an anode bump (Figure 14.8b) while Ni_3Sn_4 accumulated at the UBM side in a cathode bump (Figure 14.8a). Even though current stressing was applied only for 6 days, the UBM depletion was likely to be dominated by EM because it did not occur in a bump with opposite polarity. Solder bumps subjected to TM force only are shown in Figure 14.8c and d. TM damage was not identified in the rest 20 bumps as seen in Figure 14.8c, although voiding occurred in 7 bumps, as seen in Figure 14.8d.

Figure 14.9 shows solder bumps with 18-μm thick Cu UBM with and without current stressing. Current stressing was interrupted after 12 days before current-stressed bumps failed. The TM force was still kept applied until 48 days. The average temperature gradient in solder bumps with and without current stressing was determined to be 700 °C/cm using FEM. When electrons flowed to the die side, IMCs were accumulated on the die side, as seen

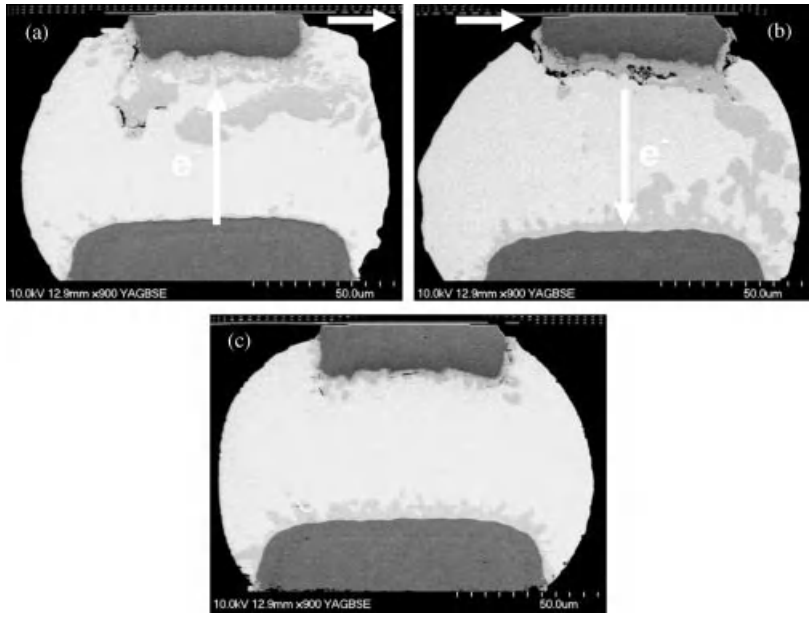

Figure 14.9 *Solder bumps with Cu UBM subject to (a), (b), (d) TM + EM, and (c) TM only.*

in Figure 14.9a. In solder joints in which electrons passed toward the substrate side (Figure 14.9b), voids were found at the Cu_6Sn_5/solder interface, while Cu_6Sn_5 grew on both die and substrate sides. These phenomena are similar to those in typical EM tests without a large temperature gradient [29]. Also, in all the other solder bumps without current stressing, morphology changes were minimal without significant TM damage, as shown in Figure 14.9c. Such morphology changes indicate that the effect of TM was not significant compared with EM in this case.

In general, the relative atomic flux by EM and TM can be compared using the following flux relations:

$$\frac{J_{\mathrm{EM}}}{(CD_0/k)} = \frac{Z^* e \rho j}{T} \exp\left(-\frac{Q}{kT}\right) \tag{14.3}$$

and

$$\frac{J_{\mathrm{TM}}}{(CD_0/k)} = \frac{Q^*}{T^2}\left|\frac{\mathrm{d}T}{\mathrm{d}x}\right| \exp\left(-\frac{Q}{kT}\right) \tag{14.4}$$

In this study, $j = 4 \times 10^4$ A/cm^2 and $\mathrm{d}T/\mathrm{d}x \sim 10^3$ K/cm. For solder joints, it is also reasonable to take $Z^* \sim 10$, $\rho \sim 10^{-7}\,\Omega$ m, and $Q^* \sim 0.25$ eV. Figure 14.10 plots Eqs. (14.3) and (14.4), and $F_{\mathrm{TM}}/F_{\mathrm{EM}}$ $(=J_{\mathrm{TM}}/J_{\mathrm{EM}})$ as a function of temperature using the above parameters. The EM flux was always predominant over the TM flux even with the very

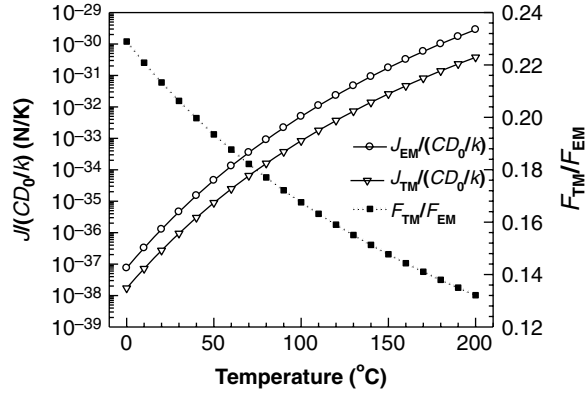

Figure 14.10 *Estimated atomic flux driven by EM and TM, and the ratio of corresponding driving forces as a function of temperature for solder joints.*

large temperature gradient. The relative effect of TM increased with decreasing temperature. Still, the ratio was less than 0.25 at 0 °C. Since the typical current density and temperature gradient for solder joints in a field condition are $\leq 10^4$ A/cm^2 and $\leq$300 K/cm, respectively [42], the relative ratio shown in Figure 14.10 will still hold at the field condition, as long as the above parameters used in the estimate are relevant.

14.3 IMC Growth

14.3.1 Under Thermal Aging

IMC growth is driven by the concentration gradient or the chemical potential gradient. The mass flux is governed by Fick's first law:

$$J = -D\frac{\partial C}{\partial x} \tag{14.5}$$

where D is the diffusivity, and C is the concentration. The scallop-shaped morphology of Cu_6Sn_5 and Ni_3Sn_4 became flattened as they were thickened. This is because Cu atoms can diffuse faster into and react with Sn through the region where Cu_6Sn_5 is thinner [8]. The flattening of Ni_3Sn_4 can be understood with the same explanation. This flattening process is also controlled by thermodynamics because the surface energy of the IMC grains in the solid solder is higher than that in the liquid solder [8, 43]. The layer-type Cu_3Sn also grew with aging time. During IMC growth, the number and the size of Kirkendall voids in the Cu_3Sn layer increased due to the diffusion of Cu into Sn. For Ni-Sn diffusion couples, however, Kirkendall voids were not observed.

The IMC layer growth can be expressed by an equation of the usual form [44]:

$$x = x_0 + kt^n \tag{14.6}$$

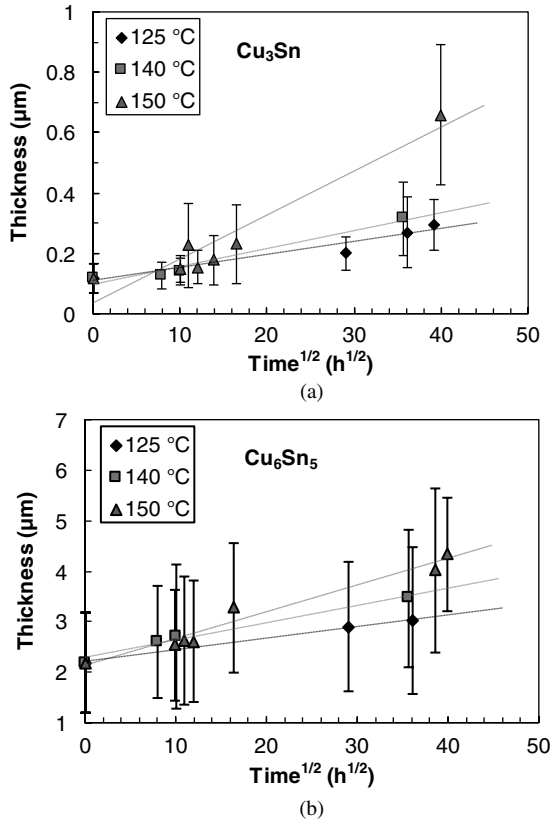

Figure 14.11 *IMC thickness as a function of aging time without current stressing. (a) Cu_3Sn, (b) Cu_6Sn_5, (c) total Cu-Sn IMCs, and (d) Ni_3Sn_4.*

where x is the thickness at time t, x_0 is the initial thickness at $t = 0$, k is the growth rate constant, and n is the time exponent and its value reflects the IMC growth mechanism. The exponent, n, is 0.5 if bulk (lattice) diffusion is the rate-controlling mechanism, while $n = 1$ if the growth is controlled by interfacial reaction. Other n values ranging from 0.21 to 0.37 have been reported for interfacial solid-liquid reactions [45–51]. Schaefer *et al.* observed a $t^{1/4}$ dependence of the IMC growth between Cu and liquid Sn-Pb solder, and proposed a grain-boundary diffusion-controlled mechanism for thin IMC layers with the predicted $n = 1/3$ [52]. They explained that the discrepancy could be due to the transition of the predominant transport mechanism from grain-boundary diffusion to slower volume diffusion. For $n = 1/3$, a mechanism similar to grain coarsening was also proposed [49]. Vianco *et al.* found that $n = 0.5$ for lower temperatures (70, 100, and 135 °C) and $n = 0.42$ for higher temperatures (170 and 205 °C) from their study on IMC growth of pure Sn, Sn-3.5Ag, and Sn-5Sb solders [53].

Figure 14.11 shows the thickness changes of each IMC as a function of $t^{1/2}$ at different temperatures. Relatively large error bars for Cu_6Sn_5 and Ni_3Sn_4 were attributed to the large variance of thickness over the irregular scallop morphology. Obviously, the growth rate increased with increasing temperature. The thickness was found to be a linear function of

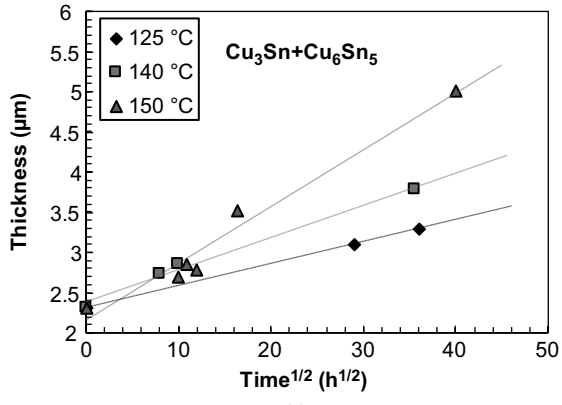

(c)

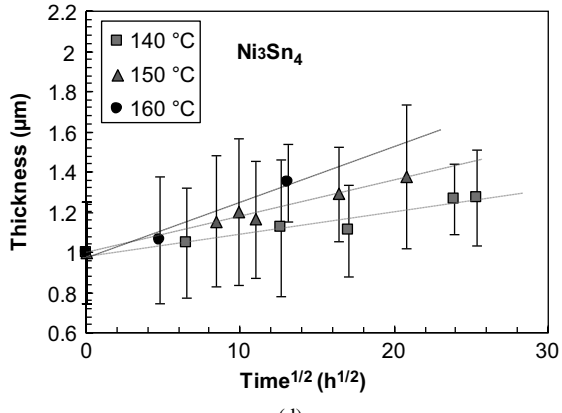

(d)

Figure 14.11 *(Continued)*

$t^{1/2}$, confirming that the growth kinetics of the IMCs followed the parabolic diffusion-controlled growth kinetics under thermal aging. Cu_6Sn_5 showed the fastest growth rate and Cu_3Sn the slowest of three IMCs. The growth rate constant, k, is summarized in Table 14.1.

The ratio of k for the ε-phase (Cu_3Sn) to the η-phase (Cu_6Sn_5) increased with aging temperature, as can be seen in Table 14.1. This was also predicted by Mei *et al.* in their

Table 14.1 *IMC growth rate constant, k (in nm/h$^{1/2}$), under thermal aging only [54]. (Reproduced with permission from the dissertation of S.-H. Chae, The University of Texas at Austin, Copyright (2010) S.-H. Chae).*

Solder Temperature (°C)	Cu_3Sn	Cu_6Sn_5	Total Cu-Sn IMCs	Ni_3Sn_4
125	4	23	27	–
140	6	34	40	11
150	15	53	71	18
160	–	–	–	28

multiphase diffusion model for Cu-Sn diffusion couples [55]. The effect of isothermal aging on Cu-Sn diffusion couples can be analyzed in three temperature ranges: low ($T < 70\,^{\circ}C$), intermediate ($70\,^{\circ}C < T < 170\,^{\circ}C$), and high ($T > 170\,^{\circ}C$) temperatures. It has been observed that, upon thermal aging of a Cu-solder diffusion couple with η-phase layer at the interface at low temperatures, the η-phase grew in thickness without forming the ε-phase [56–59], while at high temperatures the ε-phase formed immediately [56–58, 60]. For annealing at intermediate temperatures, the formation of the ε-phase started after an incubation time [57, 60, 61]. This incubation time decreased with increasing temperature. The ε-phase has been shown to grow at the expense of the η-phase and has a higher activation energy of formation. Thus, the growth of the ε-phase becomes more dominant at higher temperatures [58, 59]. The absence of ε-phase at low temperatures and the presence of the incubation time at intermediate temperatures were also explained with Cu-Sn equilibrium phase diagram [62]. The η-phase is in equilibrium with Sn saturated with Cu, while the ε-phase is in equilibrium with Cu saturated with Sn. During solder reflow, Cu may not have a chance to be saturated with Sn even at the reflow temperature because Cu dissolves into the molten solder. This means the initial phase formed at the interface is likely to be the η-phase. Moreover, the diffusivity of Sn in Cu ($\sim 10^{-24}\,m^2/s$ at $220\,^{\circ}C$) is very low compared with that of Cu in Sn ($\sim 10^{-11}\,m^2/s$ at $220\,^{\circ}C$). Therefore, during annealing the ε-phase would not appear until Cu becomes saturated with Sn. Harrison *et al.* found both η- and ε-phases when Sn0.7Cu solder was reflowed on a Cu-Sn metallization, whereas they found only η-phase when the metallization was pure Cu [63].

Also, IMC growth characteristics are influenced by the interdiffusion mechanism of Cu and Sn. Previous studies [12, 59, 64–66] suggest that interstitial diffusion of Cu is dominant at lower temperatures ($<170\,^{\circ}C$), while vacancy diffusion of Sn becomes dominant at higher temperatures ($>170\,^{\circ}C$). These mechanisms were consistent with the observation that inert markers in a Cu-Sn diffusion couple moved toward the Cu side at low temperature ($<170\,^{\circ}C$) [59], but toward the Sn side at high temperature ($>170\,^{\circ}C$) [64–66].

From the temperature-dependent growth-rate constants, the apparent activation energy for IMC growth can be calculated. In the case of $n = 0.5$ in Eq. (14.6), k^2 has the same units, m^2/s, as the diffusivity. Accordingly, the apparent activation energy for IMC growth can be determined by the following Arrhenius equation [64, 67–75]:

$$k^2 = k_0^2 \exp\left(-\frac{Q}{RT}\right) \tag{14.7}$$

where k^2 is the square of the growth rate constant, k_0^2 is the pre-exponential factor, Q is the apparent activation energy, R is the gas constant, and T is the aging temperature. Figure 14.12 plots ln k^2 vs. $1/T$ for Cu-Sn and Ni-Sn IMCs. The apparent activation energies were determined to be 1.1 ± 0.3 eV for ($Cu_3Sn + Cu_6Sn_5$), 1.3 ± 0.6 eV for Cu_3Sn, 0.9 ± 0.2 eV for Cu_6Sn_5, and 1.41 ± 0.04 eV for Ni_3Sn_4. As discussed above, the activation energy for the ε-phase was larger than that for the η-phase. The apparent activation energy for the growth of the total Cu-Sn IMCs is in good agreement with EM activation energy of 1.0 ± 0.3 eV for Cu UBM solders [29]. This indicates that the Cu-Sn IMC growth plays a critical role in controlling the EM reliability. For the Ni_3Sn_4 growth, the apparent activation energy is higher than the EM activation energy of 0.9 ± 0.2 eV for Ni UBM solders [29]. This will be discussed further in the following section.

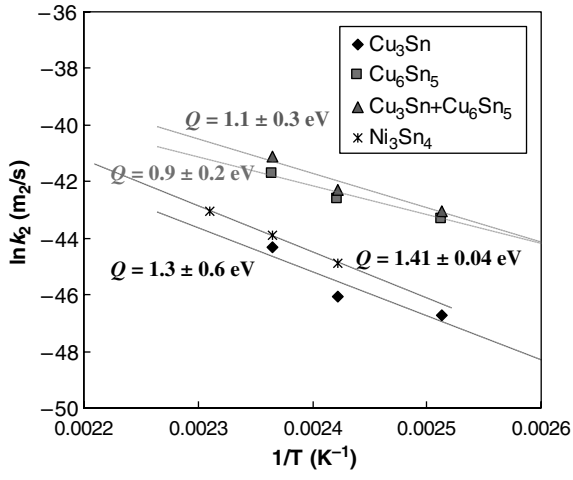

Figure 14.12 *Arrhenius plot for the growth rates of Cu-Sn and Ni-Sn IMCs.*

Tables 14.2 and 14.3 summarize the apparent activation energies reported by various researchers for the growth of Cu-Sn IMCs and Ni_3Sn_4, respectively. The temperature dependency of the activation energy was also studied in [53, 56, 74, 76, 77], which suggested different interdiffusion characteristics of Cu and Sn, or Ni and Sn, as discussed earlier. Overall, the apparent activation energies vary significantly among the experiments. They have been ascribed to the differences in the microstructure of the metallization (UBM or substrate) layer as well as IMC layers due to the differences in processing of the diffusion couples. The different grain size and the morphology of the layers can have a substantial effect on the IMC growth kinetics [62].

Addition of minor elements can also change the growth kinetics. Pinizzotto *et al.* added 4.5 wt% of Ni particles in eutectic SnPb solder on Cu substrate and found that the resulting activation energies increased from 0.8 eV to 2.17 eV for the η-phase [78]. Choi *et al.* added 20 vol% η-phase particles to eutectic SnPb and eutectic SnAg solders and found that Q for the ε-phase growth increased from 1.15 to 1.67 eV for eutectic SnPb and 1.20 eV to 2.10 eV for eutectic SnAg [69]. For the test module used in this work, Ni atoms from the Ni-P substrate finish layer was expected to saturate the molten solder during the second solder reflow. Therefore, relatively high activation energies for the Cu-Sn and Ni-Sn reactions in this work are to be expected.

Another common approach used to obtain apparent activation energies is based on an empirical power-law equation [43, 53, 57, 60, 62, 79–81]:

$$x = x_0 + A \exp\left(-\frac{Q}{RT}\right) t^n \tag{14.8}$$

where A is a constant. It is clear that the activation energy calculated from Eqs. (14.6) and (14.7) is half that from Eq. (14.8). This discrepancy is also responsible for the large variation in the activation energy.

Table 14.2 *Apparent activation energy for the Cu-Sn IMC growth.*

Solder Alloy	Soldering Method	Metallization	Temperature Range (°C)	Apparent Activation Energy (eV)			Ref.
				Cu_3Sn	Cu_6Sn_5	Total	
Sn		Cu	180–210	1.34	1.39	—	[82]
60Sn-40Pb	Hot dipping	Cu	100–175	—	—	0.25	[83]
Sn	Electroplating	Cu	70–170	—	—	0.29	[84, 85]
60Sn-40Pb	Electroplating	Cu	70–170	—	—	0.34	
Sn		Cu	190–220	0.63	0.55	0.60	[64]
Sn	Electroplating	Rolled Cu	70–170	—	—	0.30	[86]
Sn	Electroplating	Phosphor bronze	22–140	—	—	0.27	[76]
			140–220	—	—	0.51	
Sn	Hot dipping	Cu tab	70–205	0.45	—	0.68	[57]
			70–135	—	—	1.09	
			170–205	—	—	0.26	
63Sn-37Pb	Hot dipping	Cu tab	70–170	0.22	—	0.47	
Sn-3.5Ag	Hot dipping	Cu tab	70–205	0.52	—	0.61	[53]
			70–135	—	—	1.05	
			170–205	—	—	0.44	
Sn-5Sb	Hot dipping	Cu tab	70–205	0.52	—	0.63	
			70–135	—	—	0.83	
			170–205	—	—	0.40	
63Sn-37Pb	Reflow	Cu pad	70–170	—	—	1.09	[87]
63Sn-37Pb	Reflow	Cu strip	50–150	—	1.15	—	[69]
Composite 63Sn-37Pb	Reflow	Cu strip	50–150	—	1.67	—	
Sn-3.5Ag	Reflow	Cu strip	70–180	—	1.20	—	
Composite Sn-3.5Ag	Reflow	Cu strip	70–180	—	2.10	—	
Sn-1.2 at% Cu	Hot dipping	Cu (3.5 at% Sn)	100–170	0.87	0.59	0.80	[60]
63Sn-37Pb	Reflow	Electroless Cu/Au	80–160	—	—	0.31	[58]
63Sn-37Pb	Electroplating	Sputtered Cu	85–150	—	—	0.78–1.14	[70]
63Sn-37Pb	Reflow	Electroplated Cu	125–170	—	—	1.25	[88]
Sn-3.5Ag	Reflow	Electroplated Cu	125–170	—	—	1.19	
Sn-3.8Ag-0.7Cu	Reflow	Electroplated Cu	125–170	—	—	0.94	

Sn-0.7Cu	Reflow	Electroplated Cu	125–170	—	—	1.00	
Sn-3.2Ag-0.8Cu			70–150	—	—	0.74	[89]
Sn-3.5Ag	Reflow	Cu pad	70–170	0.92	0.50	0.67	[90]
Sn-58Bi	Reflow	Cu sheet	70–120	—	1.33	—	[91]
Sn-58Bi	Reflow	Cu sheet	70–200	0.94	1.02	1.11	[92]
Sn-3.5Ag	Reflow	Cu sheet	70–200	0.78	0.57	0.68	[93]
Sn-3.5Ag-0.75Cu	Reflow	Cu sheet	100–200	0.83	0.51	0.65	[94]
Sn-3.5Ag	Hot dipping	Cu coupon	70–170	—	0.61	0.78	[73]
Sn	Electroplating	Electroplated Cu	100–150	—	—	0.66	[74]
			150–175	—	—	1.43	
Sn	Reflow	Electroplated Cu	125–180	—	—	0.57	[75]

Table 14.3 *Apparent activation energy for the Ni_3Sn_4 growth.*

Solder Alloy	Soldering Method	Metallization	Temperature Range (°C)	Apparent Activation Energy (eV)	Ref.
Sn	Electroplating	Electroplated Ni	100–150	0.60	[77]
			150–175	0.94	
Sn		Electroless Ni	75–160	0.31	[68]
		Electroless Ni/Au	75–160	0.19	
		Electroless Ni/Pd	75–160	0.25	
Sn-3.5Ag		Electroless Ni	75–160	0.13	
		Electroless Ni/Au	75–160	0.55	
		Electroless Ni/Pd	75–160	0.07	
63Sn-37Pb		Electroless Ni	75–160	0.29	
		Electroless Ni/Au	75–160	0.41	
		Electroless Ni/Pd	75–160	0.19	
Sn-58Bi	Hot dipping	Ni slab	85–120	0.93	[95]
63Sn-37Pb	Reflow	Electroplated Ni/Au	80–160	0.47	[79]
SnPbAg	Reflow	Electroplated Ni/Au	125–175	1.62	[96]
SnAg	Reflow	Electroplated Ni/Au	125–175	1.61	
Sn-3.5Ag	Reflow	Electroless Ni-P/Au	70–170	0.75	[90]
Sn-58Bi	Reflow	Electroless Ni-P	70–120	0.85	[91]
Sn-3.5Ag-5Bi	Reflow	Electroless Ni-P	100–170	0.55	[97]
Sn-3.5Ag	Reflow	Electroless Ni-P	100–170	0.51	[72]
Sn-37Pb	Reflow	Electroless Ni-P	130–190	1.46	[80]
Sn-3.5Ag	Reflow	Electroless Ni-P	130–190	1.14	[71]
		Sputtered Ni	130–190	0.94	
Sn-3.5Ag	Reflow	Electroplated Ni/Au	150–200	0.17	[43]
Sn	Electroplating	Electroplated Ni	100–150	0.60	[74]
			150–175	0.94	

14.3.2 Under Current Stressing

Figure 14.13a shows cross-sectional SEM images of IMC growth in Cu UBM solders under current stressing. The effect of the electric current on IMC formation was found to be significant. The enhanced growth of the η-phase (Cu_6Sn_5) was especially apparent during an extended time period of current stressing. Gan and Tu [33] observed a polarity effect in solder joints where the IMC growth was enhanced on the anode side, while it was retarded on the cathode side. In this study, the IMC growth on both sides was enhanced under current stressing. The nonuniform growth of the η-phase appeared to reflect the electron flow distribution in the solder. As a result, the extensively grown η-phase from the UBM side was often observed to bridge to the substrate finish layer. Figure 14.13a also shows the emergence of the ε-phase (Cu_3Sn) after an extended period of current stressing. Nevertheless, the ε-phase maintained its layer-like morphology, meaning that the layer was quite conformal. This finding supports the view that the ε-phase grows at the expense of the η-phase [58, 59, 98]. The current-enhanced Ni_3Sn_4 growth is shown in Figure 14.13b. It is clear that the Ni_3Sn_4 growth was not as extensive as the Cu_6Sn_5 growth.

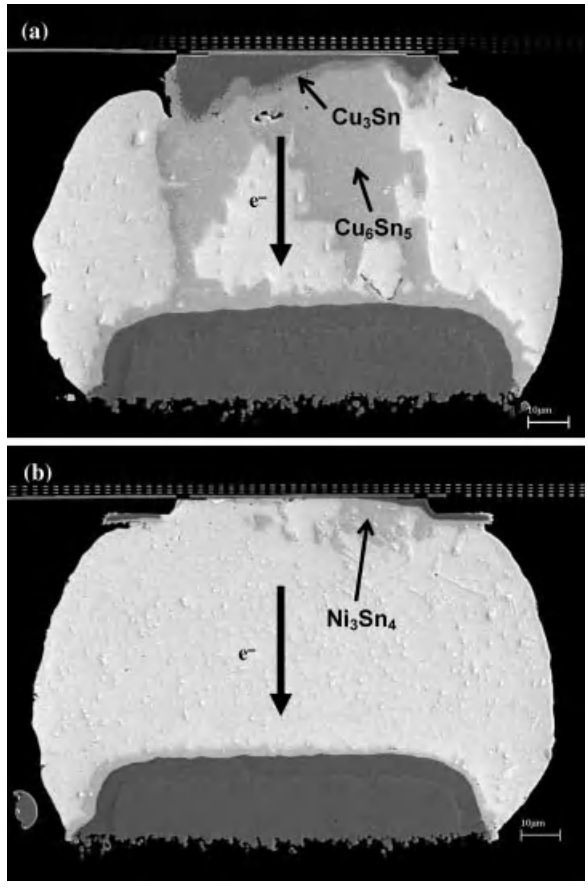

Figure 14.13 *IMC growth under current stressing of 1 A. (a) Solder bump with Cu UBM after 1536 h at 130°C, and (b) solder bump with Ni UBM after 121 h at 155°C.*

The nominal thickness changes of the IMCs in the anode solder joints are shown in Figure 14.14. With the passage of an electric current, Gan *et al.* [33] reported parabolic growth kinetics for IMC growth. In this study, however, the current-enhanced IMC growth was found to follow linear growth kinetics except for the ε-phase. Figure 14.14a plots the thickness of the Cu_3Sn layer as a function of $\sqrt{\text{time}}$. Although its temperature dependence was not clearly understood, the growth of Cu_3Sn was more likely to follow the parabolic growth law under the EM condition. This suggests the Cu_3Sn growth was a diffusion-controlled process. Yet the growth rate constant, k, was more than 10 times larger than that without current stressing. Figures 14.14b–d plot the other IMC thicknesses versus time. The growth of both Cu_6Sn_5 and Ni_3Sn_4 were well described by the linear time dependence. The total Cu-Sn IMC thickness also closely followed the t dependence because Cu_6Sn_5 was the dominant phase in the IMC growth. The IMC growth-rate constants for the case of $n = 1$, w, are summarized in Table 14.4.

To understand the IMC growth phenomena under current stressing it is important to solve the flux equation including the current-induced mass transport. Under current

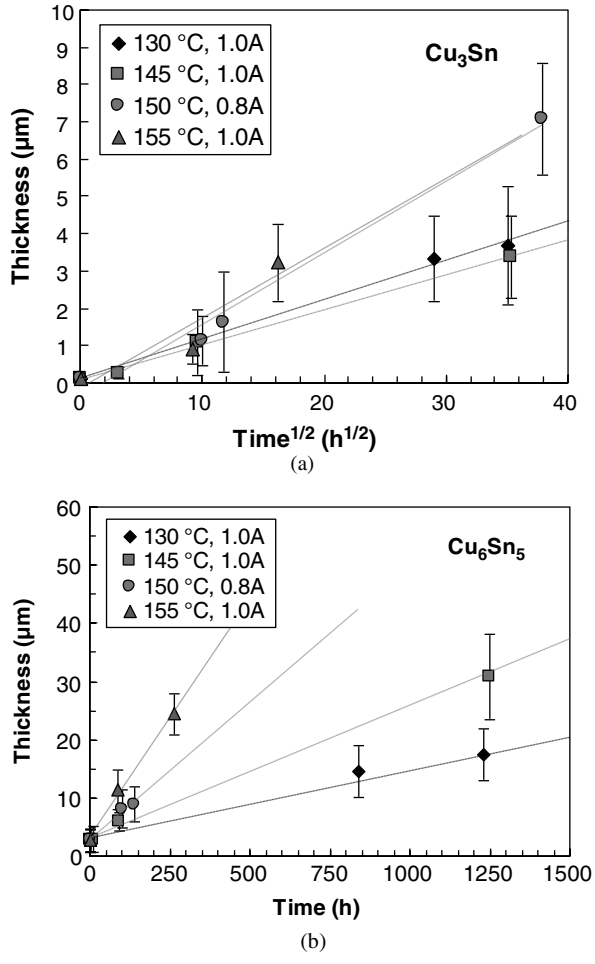

Figure 14.14 *IMC thickness as a function of aging time with current stressing. (a) Cu_3Sn, (b) Cu_6Sn_5, (c) total Cu-Sn IMCs, and (d) Ni_3Sn_4.*

stressing, both the chemical potential gradient and the electron momentum transfer contribute to the diffusion of atoms. Accordingly, the mass transport can be expressed by a general form:

$$J = J_{\text{chem}} + J_{\text{EM}} = -D\frac{\partial C}{\partial x} + C\frac{D}{kT}Z^* e\rho j \tag{14.9}$$

where J_{chem} is the mass flux driven by the chemical potential gradient and J_{EM} is the mass flux driven by the electron momentum transfer. Obtaining a general solution of Eq. (14.9) for Cu-Sn diffusion couples is not trivial. Chao *et al.* developed a multiphase diffusion model for a Cu-Sn diffusion couple under current stressing, and deduced material properties in the IMC phases from the experimental data using a finite difference method

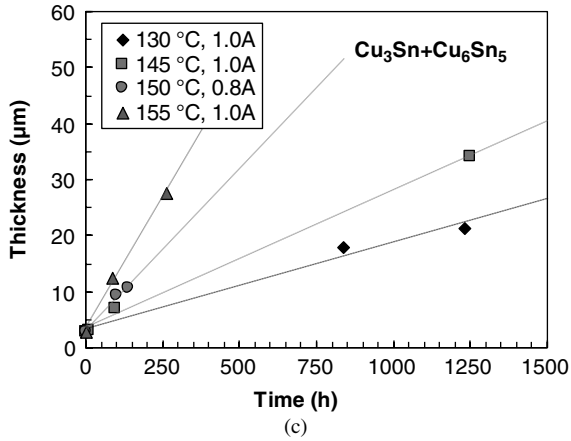

(c)

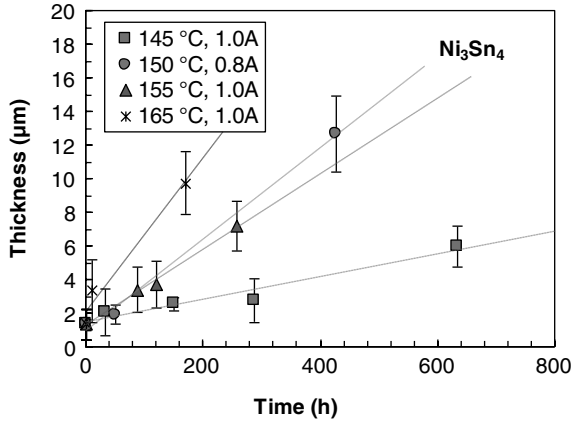

(d)

Figure 14.14 *(Continued)*

based on the simulated annealing technique [30–32]. The analysis predicted the growth kinetics of Cu_6Sn_5 changed from parabolic to linear as the current density increased. This is because the second term on the right side of Eq. (14.9) becomes dominant under a higher current density.

Table 14.4 *IMC growth-rate constant, w (in nm/h), with current stressing [54]. (Reproduced with permission from the dissertation of S.-H. Chae, The University of Texas at Austin, Copyright (2010) S.-H. Chae).*

Solder Temperature (°C)	Applied Current (A)	Cu_6Sn_5	Total Cu-Sn IMCs	Ni_3Sn_4
130	1.0	12	16	—
145	1.0	22	25	6.8
150	0.8	47	58	27
155	1.0	81	93	23
165	1.0	—	—	46

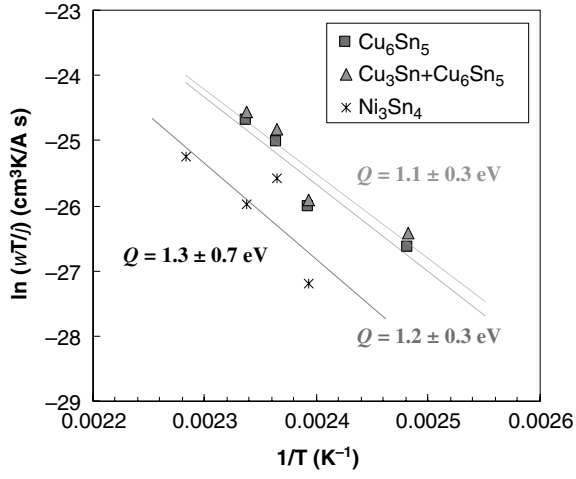

Figure 14.15 *Arrhenius plot of wT/j, where w is the growth rate constant under current stressing.*

In order to analyze the temperature dependency of the EM-enhanced IMC growth in this condition, Eq. (14.6) can be applied with $n = 1$:

$$x = x_0 + wt \tag{14.10}$$

Here, the growth-rate constant k in Eq. (14.6) is replaced by w, which has the units of velocity. Since the IMC growth is accomplished by atomic migration to a phase boundary, the IMC growth rate is proportional to the velocity of the net atomic movement, which is called the EM drift velocity [99]. From Eq. (14.9), the drift velocity is defined as

$$v_{\mathrm{d}} = \frac{D}{kT} Z^* e\rho j = \frac{D_0}{kT} \exp\left(-\frac{Q}{kT}\right) Z^* e\rho j \tag{14.11}$$

Therefore, the temperature dependence or apparent activation energy can be determined from an Arrhenius plot of $v_{\mathrm{d}}T/j$. Figure 14.15 plots the parameter wT/j as a function of temperature for Cu_6Sn_5, ($Cu_3Sn + Cu_6Sn_5$), and Ni_3Sn_4. The activation energies were found to be 1.2 ± 0.3 eV, 1.1 ± 0.3 eV, and 1.3 ± 0.7 eV, respectively. The values for the Cu-Sn IMCs were slightly larger than those determined from the thermal aging experiments, while that for Ni_3Sn_4 was smaller. Although the differences were not statistically significant, the errors could be attributed to the outliers in Figure 14.15. In fact, although the cross-sectioning of solder joints was conducted before they failed, EM voids were already developed in some solder joints under current stressing. This could increase the local current density distribution, subsequently leading to the change in the growth rate.

The activation energies determined from different types of experiments in this study are summarized in Table 14.5. As discussed in the previous section, the EM reliability of solder joints with Cu UBM was found to be closely related to the IMC growth. The fact that the activation energies determined from three different measurements were in good agreement supports this finding. In contrast, for Ni UBM solders the activation energy for EM is lower than those associated with the IMC growth. The difference in the activation energy can be attributed to the diffusion characteristics of Ni in Sn matrix, particularly that correlating to

Table 14.5 *Summary of activation energies for Cu-Sn and Ni-Sn systems obtained from different experiments [54]. (Reproduced with permission from the dissertation of S.-H. Chae, The University of Texas at Austin, Copyright (2010) S.-H. Chae).*

Pb-Free Solder Joint	IMC	Type of Measurement		
		EM Failure Lifetime (from [29])	IMC Growth w/o Current Stressing	IMC Growth w/Current Stressing
Cu UBM solder	Cu_6Sn_5	1.0 ± 0.3 eV	0.9 ± 0.2 eV	1.2 ± 0.3 eV
	Cu_3Sn		1.3 ± 0.6 eV	–
	Total Cu-Sn IMCs		1.1 ± 0.3 eV	1.1 ± 0.3 eV
Ni UBM solder	Ni_3Sn_4	0.9 ± 0.2 eV	1.41 ± 0.04 eV	1.3 ± 0.7 eV

the Sn grain orientation. First, Sn grain orientation was reported to have a significant effect on the EM failure mode or damage evolution in Ni UBM solders because the diffusivity of Ni along the *c*-axis of Sn is $\sim 10^5$ times faster than along the *a*-axis. According to Lu *et al.* [100], when the Ni diffusion path was aligned with the *c*-axis of Sn, Ni UBM dissolved fast without significant IMC growth under EM. Under this circumstance, the mass transport should be dominated by interstitial diffusion of Ni in Sn matrix, not by the interdiffusion driving IMC growth. The different diffusion mechanisms could lead to different activation energies determined from EM and IMC growth. Although the Sn grain orientation in the solder joints is expected to be random, those with grains oriented along or close to the *c*-axis will dominate the EM statistics. The effect of Sn grain structure on EM reliability is further discussed in the following section. Secondly, in addition to EM of Ni atoms, EM of Sn atoms at the IMC/solder interface toward the substrate side is expected to be more prominent in the thin UBM structure than in the thick UBM structure due to the current-crowding effect. This mass transport will contribute to EM damage evolution, whereas it is not accounted for in the IMC growth measurements. Thirdly, the thickness variation of the Ni UBM used in this study was ± 0.5 μm. Thus, the UBM may deplete faster in a region where the UBM thickness is thinner than other regions. All the above-mentioned factors can result in EM failure kinetics different from the interdiffusion-driven IMC growth kinetics.

14.4 Effect of Sn Grain Structure on EM Reliability

EM degradation mechanisms depending on Sn grain structure were first reported by Lu *et al.* [100] using electron backscatter diffraction (EBSD). Rapid depletion of UBM and IMCs was observed when the *c*-axis of Sn grains was aligned with the current direction. When the *c*-axis of Sn grains is not aligned with the current direction EM voiding was observed at the IMC/solder interface leaving UBM and IMCs less damaged. The latter damage mode was defined as mode I and the former as mode II. Figure 14.16 represents these two failure modes. In mode I, EM damage was dominated by Sn self-diffusion. The mode II type of mechanism, dominated by fast interstitial diffusion process, was often found

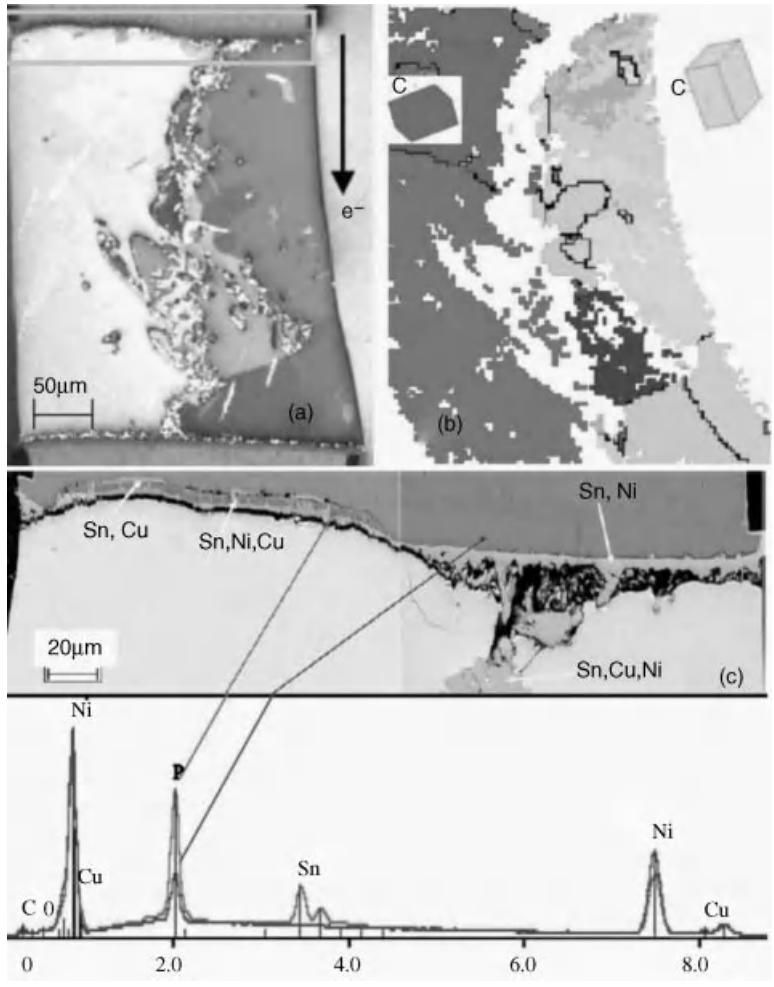

Figure 14.16 *A solder joint after 555 h EM test, (a) crosspolarized image, (b) EBSD map, and (c) SEM image and EDX spectrums of the boxed region in (a) [100]. (Reproduced with permission from Appl. Phys. Lett., Effect of Sn grain orientation on electromigration degradation mechanism in high Sn-based Pb-free solders by M. Lu, D.-Y. Shih, P. Lauro et al., 92, 21, 211909 Copyright (2008) American Institute of Physics).*

in samples failing early. SnCu solder exhibited the mode-II damage more than SnAg and SnAgCu solders. Owing to the stable Ag_3Sn IMC network in SnAg(Cu) solders, Sn grain reorientation was prevented due to the presence of cyclic twinning structures. This resulted in randomness of Sn grain orientation and thus lower propensity of the mode-II mechanism. They also found that minor Zn doping in SnAg solder improved the stability of the interface, bulk microstructure, and Ag_3Sn and Cu_6Sn_5 IMC networks [101]. Although Zn doping could not control Sn grain orientation, strong binding of Zn with Cu effectively slowed down

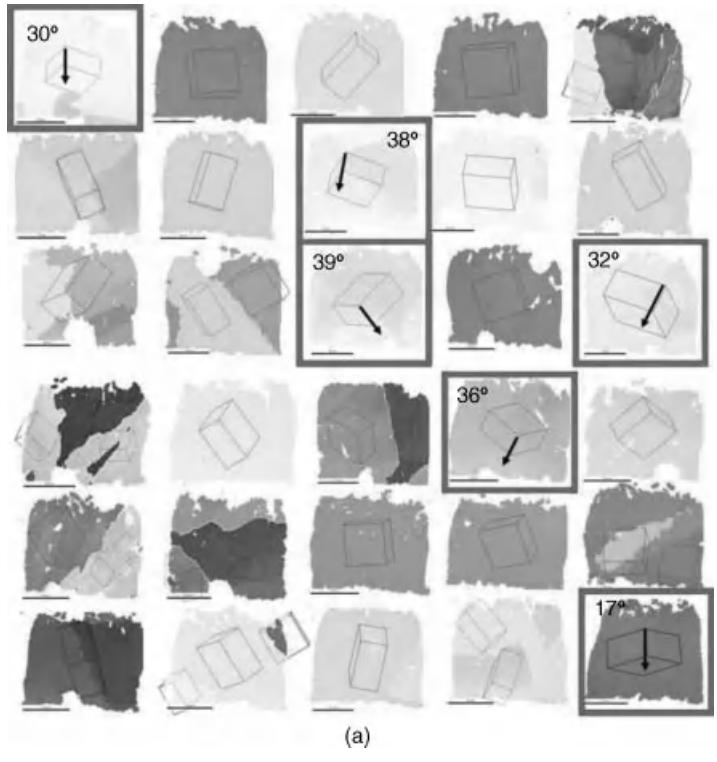

Figure 14.17 *EBSD mapping of as-reflowed solder bumps (a) after a single reflow process, and (b) after multiple reflow processes.*

EM damage. This helped suppress the mode-II type early failure and also improved the mode-I type lifetime.

For a given solder alloy (Sn-2.5Ag), Wang *et al.* [102] found that the Sn grain structure was altered by different preconditioning history. Samples were divided into two groups, one underwent a single solder reflow and the other multiple reflows. Figure 14.17 compares Sn grain structures characterized by the EBSD technique of pristine solder bumps between single- and multiple-reflow groups. Solder bumps with a single reflow showed a few large grains, while multiple reflows rendered finer grain sizes. The latter made the Sn grain orientation statistically more random. In Figure 14.17a, many bumps exhibit a single large grain. Highlighted with boxes are grains with the *c*-axis aligned with low angles about the vertical axis. According to Lu *et al.* [100], this case is prone to early failure induced by fast depletion of UBM under current stressing. In contrast, large grains with the low-angle alignment were not as often observed in the multiple-reflow group (Figure 14.17b) as in Figure 14.17a. This suggests that the multiple-reflow process could result in a less anisotropic grain structure. The effect of thermal aging on Sn grain structure is shown in Figure 14.18. Isothermal aging was conducted at 150 °C for over 450 h. The group with multiple reflows revealed that the majority of solder bumps were

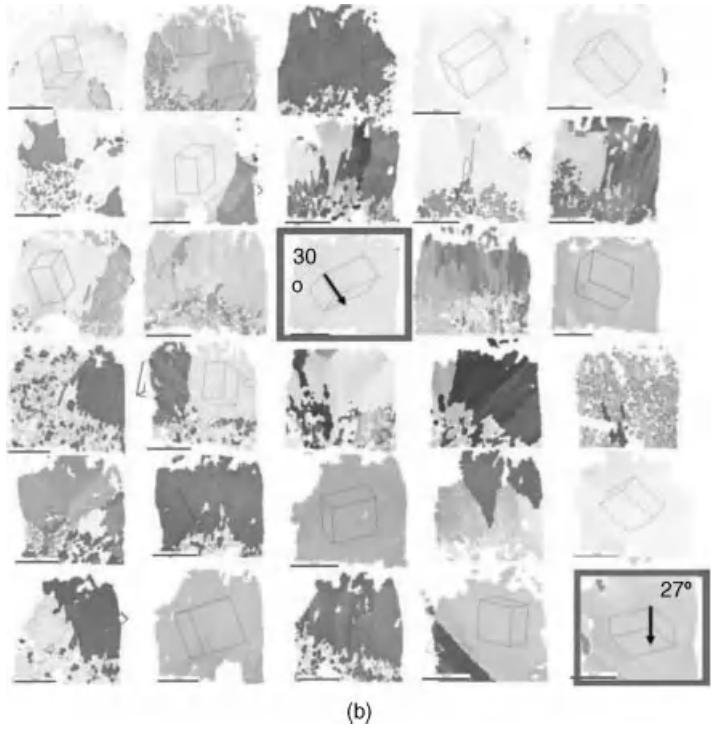

Figure 14.17 *(Continued)*

composed of multiple grains. Although fine Sn grains could coarsen after thermal aging, cyclic twinning structures were observed as in the previous study to prevent the grain realignment. The group with single reflow still showed single large grains dominating the grain structure.

EM test results from these two groups are depicted in Figure 14.19. Solder bumps after a single reflow showed more scattered failure distribution (larger σ) than solder bumps after multiple reflows. This was attributed to the fact that when solder bumps consisted of only a few grains the effect of the grain orientation became predominant. A single grain with the *c*-axis perpendicular or parallel to the electron flow direction would be two extreme cases that could exhibit a large difference in lifetime. On the other hand, solder bumps with a multigrain structure could be essentially isotropic because of the statistical distribution of each grain orientation. These findings suggest that optimizing thermal history of solder joints can yield optimized Sn grain structures to improve EM reliability.

14.5 Summary

This chapter has addressed several important issues controlling EM reliability of Pb-free solder joints. Section 14.2 described common EM failure mechanisms of Pb-free solder

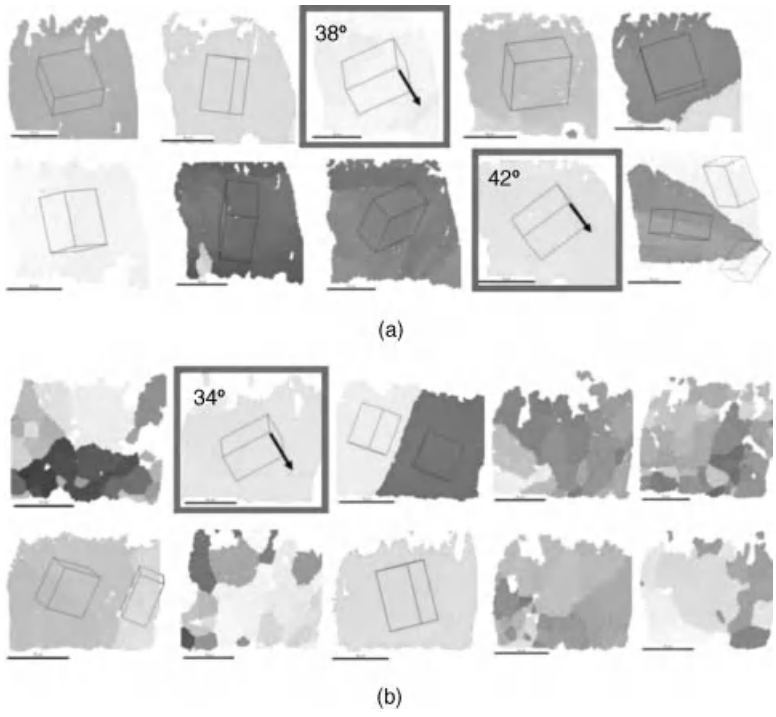

Figure 14.18 *EBSD mapping of solder bumps subjected to an isothermal aging process at 150°C for over 450 h. (a) Single-reflow group, and (b) multiple-reflow group.*

joints as well as Pb-containing solder joints. Damage evolution in Pb-free solder joints with Cu UBM and Ni UBM was compared. Damage by TM was also reviewed, followed by direct comparison between EM-induced damage and TM-induced damage. EM flux was found to be dominant against TM flux in typical circumstances.

Extensive IMC growth under current stressing is one of the important characteristics of Pb-free solder joints. IMC growth kinetics was investigated with and without current stressing in Section 14.3. With thermal aging only, IMC growth followed the parabolic growth kinetics. Under high current stressing, linear growth kinetics was observed for Cu_6Sn_5 and Ni_3Sn_4 IMCs, which was consistent with a kinetic model. Apparent activation energies obtained from IMC growth under thermal aging, IMC growth under current stressing, and EM experiments were then compared. For solder joints with Cu stud UBM, all of these activation energies were consistent, which indicates that IMC growth plays an important role in controlling EM reliability.

Noble and near-noble metals diffuse interstitially in Sn matrix, and their diffusivities significantly depend on the Sn grain orientation due to the anisotropic nature of BCT lattice of Sn. Among them, Ni shows the highest anisotropic diffusion behavior in Sn. This causes different EM failure mechanisms depending on Sn grain structure. Section 14.4 discussed this issue. When the *c*-axis of Sn grain was aligned with the current flow direction early failure was observed due to the fast depletion of UBM. Ag_3Sn IMC in Ag-containing Pb-free

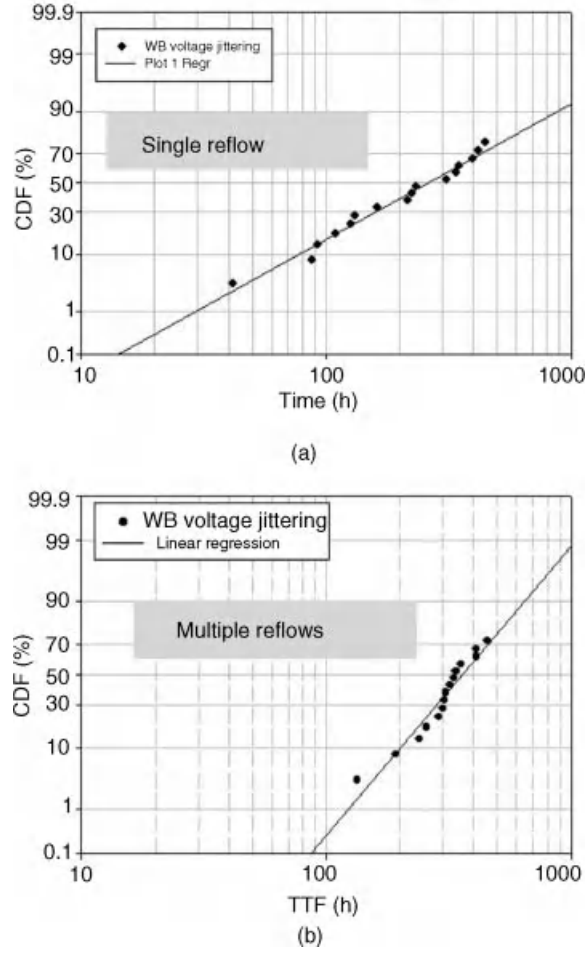

Figure 14.19 *EM failure distribution of the group (a) with a single reflow process, and (b) with multiple reflow processes.*

solders was found to improve the stability of Sn grain structure, which provided SnAg(Cu) solder joints with better EM reliability compared with SnCu solder joints. Zn doping to solder alloy was also found to improve EM reliability of Pb-free solders. In addition, randomly oriented fine grain structure of Sn matrix was presented to enhance EM reliability by tightening failure distribution. This was achieved by multiple solder reflow processes. Fine polycrystalline structure could effectively cancel out the highly anisotropic nature of Sn grains, which in turn can lower the probability of low-angle alignment of the *c*-axis with the current flow direction. This finding suggests a potential approach to optimize Sn grain structures for improving EM reliability.

Acknowledgments

The authors would like to acknowledge Semiconductor Research Corporation (SRC), Freescale Semiconductor, and Texas Instruments for their financial support.

References

1. International SEMATECH (Mar 2003) Critical Reliability Challenges for The International Technology Roadmap for Semiconductors (ITRS), *Technology Transfer #03024377A-TR*.
2. Landman, B.S. and Russo, R.L. (1971) On a pin versus block relationship for partitions of logic graphs. *IEEE Trans. Comp.*, **C-20**, 1469.
3. *Assembly and Packaging in International Technology Roadmap for Semiconductors, 2007 Edition.*
4. Tu, K.N. (2003) Recent advances on electromigration in very-large-scale-integration of interconnects. *J. Appl. Phys.*, **94**, 5451.
5. Tu, K.N. (2003) Physics and materials challenges for lead-free solders. *J. Appl. Phys.*, **93**, 1335.
6. Jost, W. (1952) *Diffusion in Solids, Liquids, and Gases*, Academic Press, New York.
7. Tu, K.-N. (2007) *Solder Joint Technology – Materials, Properties, and Reliability*, Springer, New York.
8. Zeng, K., Stierman, R., Chiu, T.-C. *et al.* (2005) Kirkendall void formation in eutectic SnPb solder joints on bare Cu and its effect on joint reliability. *J. Appl. Phys.*, **97**, 024508.
9. Decker, D.L. (1975) Diffusion of copper in lead. *Phys. Rev. B*, **11**, 1770.
10. Dyson, B.F. (1966) Diffusion of gold and silver in tin single crystals. *J. Appl. Phys.*, **37**, 2375–2377.
11. Dyson, B.F., Anthony, T., and Turnbull, D. (1966) Interstitial diffusion of copper and silver in lead. *J. Appl. Phys.*, **37**, 2370–2374.
12. Dyson, B.F., Anthony, T., and Turnbull, D. (1967) Interstitial diffusion of copper in tin. *J. Appl. Phys.*, **38**, 3408.
13. Yeh, D.C. and Huntington, H.B. (1984) Extreme fast-diffusion system: Nickel in single-crystal tin. *Phys. Rev. Lett.*, **53**, 1469–1472.
14. Sun, P.H. and Ohring, M. (1976) Tracer self-diffusion and electromigration in thin tin films. *J. Appl. Phys.*, **47**, 478–485.
15. Lloyd, J.R., Tu, K.-N., and Jaspal, J. (2004) The physics and materials science of electromigration and thermomigration in solders, in *Handbook of Lead-Free Solder Technology for Microelectronic Assemblies* (eds K.J. Puttlitzand K.A. Stalter), Marcel Dekker, New York, pp. 827–850.
16. Liu, C.T., Chen, C., and Tu, K.N. (2000) Electromigration in Sn-Pb solder strips as a function of alloy composition. *J. Appl. Phys.*, **88**, 5703.
17. Brandenburg, S. and Yeh, S. (1998) Electromigration studies of flip chip bump solder joints. *Proc. Surface Mount International Conference and Exposition*, San Jose, CA, pp. 337–344.
18. Huynh, Q.T., Liu, C.Y., Chen, C., and Tu, K.N. (2000) Electromigration in eutectic SnPb solder lines. *J. Appl. Phys.*, **89**, 4332.
19. Lee, T.Y., Tu, K.N., Kuo, S.M., and Frear, D.R. (2001) Electromigration of eutectic SnPb solder interconnects for flip chip technology. *J. Appl. Phys.*, **89**, 3189.
20. Lee, T.Y., Tu, K.N., and Frear, D.R. (2001) Electromigration of eutectic SnPb and $SnAg_{3.8}Cu_{0.7}$ flip chip solder bumps and under-bump metallization. *J. Appl. Phys.*, **90**, 4502.

21. Kim, D.-G., Moon, W.-C., and Jung, S.-B. (2006) Effects of electromigration on microstructural evolution of eutectic SnPb flip chip solder bumps. *Microelectron. Reliab.*, **83**, 2391.
22. Gupta, D., Vieregge, K., and Gust, W. (1998) Interface diffusion in eutectic Pb-Sn solder. *Acta Mater.*, **47**, 5.
23. Yang, Q.L. and Shang, J.K. (2005) Interfacial segregation of Bi during current stressing of Sn-Bi/Cu solder interconnect. *J. Electron. Mater.*, **34**, 1363–1367.
24. Chen, L.T. and Chen, C.M. (2006) Electromigration study in the eutectic SnBi solder joint on the Ni/Au metallization. *J. Mater. Res.*, **21**, 962–969.
25. Nah, J.W., Paik, K.W., Suh, J.O., and Tu, K.N. (2003) Mechanism of electromigration-induced failure in the 97Pb-3Sn and 37Pb-63Sn composite solder joints. *J. Appl. Phys.*, **94**, 7560.
26. Yeh, E.C.C., Choi, W.J., Tu, K.N. *et al.* (2002) Current-crowding-induced electromigration failure in flip chip solder joints. *Appl. Phys. Lett.*, **80**, 580.
27. Zhang, L. *et al.* (2006) Effect of current crowding on void propagation at the interface between intermetallic compound and solder in flip chip solder joints. *Appl. Phys. Lett.*, **88**, 012106.
28. Shao, T.L., Liang, S.W., Lin, T.C., and Chen, C. (2005) Three-dimensional simulation on current-density distribution in flip-chip solder joints under electric current stressing. *J. Appl. Phys.*, **98**, 044509.
29. Chae, S.-H. *et al.* (2007) Electromigration statistics and damage evolution for Pb-free solder joints with Cu and Ni UBM in plastic flip-chip packages. *J. Mater. Sci.: Mater. Electron.*, **18**, 247–258.
30. Chao, B., Chae, S.-H., Zhang, X. *et al.* (2006) Electromigration enhanced intermetallic growth and void formation in Pb-free solder joints. *J. Appl. Phys.*, **100**, 084909.
31. Chao, B., Chae, S.-H., Zhang, X. *et al.* (2007) Investigation of diffusion and electromigration parameters for Cu-Sn intermetallic compounds in Pb-free solders using simulated annealing. *Acta Mater.*, **55**, 2805.
32. Chao, B., Zhang, X., Chao, S.-H., and Ho, P.S. (2009) Recent advances on kinetic analysis of electromigration enhanced intermetallic growth and damage formation in Pb-free solder joints. *Microelectron. Reliab.*, **49**, 253–263.
33. Gan, H. and Tu, K.N. (2005) Polarity effect of electromigration on kinetics of intermetallic compound formation in Pb-free solder V-groove samples. *J. Appl. Phys.*, **97**, 063514.
34. Yamanaka, K., Tsukada, Y., and Suganuma, K. (2007) Studies on solder bump electromigration in Cu/Sn-3Ag-0.5Cu/Cu system. *Microelectron. Reliab.*, **47**, 1280–1287.
35. Ye, H., Basaran, C., and Hopkins, D. (2003) Thermomigration in Pb-Sn solder joints under joule heating during electric current stressing. *Appl. Phys. Lett.*, **82**, 1045.
36. Huang, A.T., Gusak, A.M., and Tu, K.N. (2006) Thermomigration in SnPb composite flip chip solder joints. *Appl. Phys. Lett.*, **88**, 141911.
37. Chuang, Y.C. and Liu, C.Y. (2006) Thermomigration in eutectic SnPb alloy. *Appl. Phy. Lett.*, **88**, 174105.
38. Hsiao, H.-Y. and Chen, C. (2007) Thermomigration in flip-chip SnPb solder joints under alternating current stressing. *Appl. Phys. Lett.*, **90**, 152105.
39. Chen, H.-Y., Chen, C., and Tu, K.N. (2008) Failure induced by thermomigration of interstitial Cu in Pb-free flip chip solder joints. *Appl. Phys. Lett.*, **93**, 122103.
40. Hsiao, H.-Y. and Chen, C. (2009) Thermomigration in Pb-free SnAg solder joint under alternating current stressing. *Appl. Phys. Lett.*, **94**, 092107.
41. Chae, S.-H. and Ho, P.S., Comparison of Electromigration and Thermomigration in Pb-Free Solder Joints, in preparation.
42. Giacomo, G.D. and Oggioni, S. (2002) Reliability of flip chip applications with ceramic and organic chip carriers. *Microelectron. Reliab.*, **42**, 1541.
43. Alam, M.O. and Chan, Y.C. (2005) Solid-state growth kinetics of Ni_3Sn_4 at the Sn-3.5Ag solder/Ni interface. *J. Appl. Phys.*, **98**, 123527.

44. Circhenall, C.E. (1959) *Physical Metallurgy*, McGraw-Hill, New York, pp. 216–217.
45. Frear, D.R. (1991) in *Solder Mechanics: A State of the Art Assessment* (eds D.R. Frear, W.B. Jones, and K.R. Kinsman), TMS, Warrendale, PA, p. 191.
46. Schaefer, M., Laub, W., Sabee, J.M., and Fournelle, R.A. (1993) A numerical method for predicting intermetallic layer thickness developed during the formation of solder joints. *J. Electron. Mater.*, **25**, 992.
47. Bader, S., Gust, W., and Hieber, H. (1995) Rapid formation of intermetallic compounds interdiffusion in the Cu-Sn and Ni-Sn systems. *Acta Met.*, **43**, 329.
48. Bartels, F., Morris, J.W. Jr., Dalke, G., and Gust, W. (1994) Intermetallic phase formation in thin solid-liquid diffusion couples. *J. Electron. Mater.*, **23**, 787.
49. Kim, H.K. and Tu, K.N. (1996) Kinetic analysis of the soldering reaction between eutectic SnPb alloy and Cu accompanied by ripening. *Phys. Rev. B*, **53**, 16027.
50. Schaefer, M., Laub, W., Fournelle, R.A., and Liang, J. (1997) in *Design & Reliability of Solders and Solder Interconnections* (eds R.K. Mahidhara *et al.*), TMS, Warrendale, PA, p. 247.
51. London, J. and Ashall, D.W. (1986) Some properties of soldered joints made with a tin/silver eutectic alloy. *Brazing Soldering.*, **10**, 17.
52. Schaefer, M., Rournelle, R.A., and Liang, J. (1998) Theory for intermetallic phase growth between Cu and liquid Sn-Pb solder based on grain boundary diffusion control. *J. Electron. Mater.*, **27**, 1167.
53. Vianco, P.T., Erickson, K.L., and Hopkins, P.L. (1994) Solid state intermetallic compound growth between copper and high temperature Tin-Rich solders - part I: Experimental analysis. *J. Electron. Mater.*, **23**, 721.
54. Chae, S.-H. (2010) Ph. D. Dissertation, The University of Texas at Austin.
55. Mei, Z., Sunwoo, A.J., and Morris, J.W. Jr. (1992) Analysis of low-temperature intermetallic growth in copper-tin diffusion couples. *Metall. Trans. A.*, **23**, 857.
56. Sunwoo, A.J., Morris, J.W. Jr., and Lucey, G.K. Jr. (1992) The growth of Cu-Sn intermetallics at a pretinned copper-solder interface. *Metall. Trans. A.*, **23**, 1323.
57. Vianco, P.T., Hlava, P.F., and Kilgo, A.C. (1994) Intermetallic compound layer formation between copper and hot-dipped 100In, 50In-50Sn, 100Sn and 63Sn37Pb coatings. *J. Electron. Mater.*, **23**, 583.
58. Tu, K.N. (1973) Interdiffusion and reaction in bimetallic Cu-Sn thin films. *Acta Metall.*, **21**, 317.
59. Tu, K.N. and Thompson, R.D. (1982) Kinetics of interfacial reaction in bimetallic Cu-Sn thin films. *Acta Metall.*, **30**, 947.
60. Lee, Y.G. and Duh, J.G. (1999) Interfacial morphology and concentration profile in the unleaded Solder/Cu joint assembly. *J. Mater. Sci. - Mater. Electron.*, **10**, 33.
61. Prakash, K.H. and Sritharan, T. (2003) Effects of solid state annealing on the interface intermetallics between tin-lead solders and copper. *J. Electron. Mater.*, **32**, 939.
62. Pang, J.H.L., Prakash, K.H., and Low, T.H. (2004) Isothermal and thermal cycling aging on IMC growth rate in Pb-free and Pb-based solder interfaces. *Proc. Inter Society Conference on Thermal Phenomena*, pp. 109–115.
63. Harrison, M.R., Vincent, J.H., and Steen, H.A.H. (2001) Lead-free reflow soldering for electronics assembly. *Solder Surf. Mount. Technol.*, **13**, 21.
64. Onishi, M. and Fujibuchi, H. (1975) Reaction-diffusion in Cu-Sn system. *Trans. Jpn. Inst. Met.*, **16**, 539.
65. Oikawa, H. and Hosoi, A. (1975) Interdiffusion in Cu-Sn solid solutions – confirmation of anomalously large Kirkendall effect. *Scr. Metall.*, **9**, 823.
66. Hoshino, K., Iijima, Y., and Hirano, K. (1980) Interdiffusion and Kirkendall effects in Cu–Sn alloys *Trans. Jpn. Inst. Met.*, **21**, 674.
67. Flanders, D.R., Jacobs, E.G., and Pinizzotto, R.F. (1997) Activation energies of intermetallic growth of Sn-Ag eutectic solder on copper substrates. *J. Electron. Mater.*, **26**, 883.

68. Blair, H.D., Pan, T., and Nicholson, J.M. (1998) Intermetallic compound growth on Ni, Au/Ni and Pd/Ni substrates with Sn/Pb, Sn/Ag and Sn solders. *Proc. IEEE 48th Electronic Components and Technology Conference*, pp. 259–267.
69. Choi, S., Bieler, T.R., Lucas, J.P., and Subramanian, K.N. (1999) Characterization of the growth of intermetallic interfacial layers of Sn-Ag and Sn-Pb eutectic solders and their composite solders on Cu substrate during isothermal long-term aging. *J. Electron. Mater.*, **28**, 1209.
70. Xiao, G.-W. *et al.* (2001) Effect of Cu stud microstructure and electroplating process on intermetallic compounds growth and reliability of flip-chip solder bump. *IEEE Trans. Comp. Packag. Technol.*, **24**, 682.
71. Chen, Z., He, M., and Qi, G. (2004) Morphology and kinetic study of the interfacial reaction between the Sn-3.5Ag solder and electroless Ni-P metallization. *J. Electron. Mater.*, **33**, 1465.
72. Yoon, J.W. and Jung, S.B. (2004) Growth kinetics of Ni_3Sn_4 and Ni_3P layer between Sn-3.5Ag solder and electroless Ni-P substrate. *J. Alloys Compd.*, **376**, 105.
73. Yu, D.Q. *et al.* (2005) Intermetallic compounds growth between Sn-3.5Ag lead-free solder and Cu substrate by dipping method. *J. Alloys Compd.*, **392**, 192.
74. Labie, R., Ruythooren, W., and Humbeeck, J.V. (2007) Solid state diffusion in Cu-Sn and Ni-Sn diffusion couples with flip-chip scale dimensions. *Intermetallics.*, **15**, 396.
75. Lim, G.-T. *et al.* (2009) Temperature effect on intermetallic compound growth kinetics of Cu Pillar/Sn bumps. *J. Electron. Mater.*, **38**, 2228.
76. Haimovich, J. (1993) Cu-Sn intermetallic compound growth in hot-air-levelled tin at and below 100 °C. *AMP J. Technol.*, **3**, 46.
77. Olsen, D., Wright, R., and Berg, H. (1978) Effects of intermetallics on the reliability of tin coated Cu, Ag, and Ni parts. *Proc. Reliability Phys. Symp., Las Vegas, NV*, pp. 80–86.
78. Pinizzotto, R.F. *et al.* (1993) The dependence of the activation energies of intermetallic formation on the composition of composite Sn/Pb solders. *Proc. IEEE 31st Annual International Reliability Physics Symposium*, pp. 209–216.
79. Tu, P.L., Chan, Y.C., Hung, K.C., and Lai, J.K.L. (2001) Growth kinetics of internetallic compounds in chip scale package solder joint. *Scr. Mater.*, **44**, 317.
80. He, M., Chen, Z., and Qi, G. (2004) Solid state interfacial reaction of Sn-37Pb and Sn-3.5Ag solders with Ni-P under bump metallization. *Acta Mater.*, **52**, 2047.
81. Ghosh, G. (2000) Interfacial microstructure and the kinetics of interfacial reaction in diffusion couples between Sn-Pb solder and Cu/Ni/Pd metallization. *Acta Mater.*, **48**, 3719.
82. Starke, E., Wever, H. (1964) *Z. Metallk.*, **55**, 107.
83. Zakraysek, L. (1972) Intermetallic growth in Tin-rich solders. *Welding J.*, **51**, 536.
84. Unsworth, D.A. and Mackay, C.A. (1973) Preliminary report on growth of compound layers on various metals bases plated with tin and its alloys. *Trans. Inst. Met. Finish.*, **51**, 85.
85. Stephens, J.(Mar. 2 1989) in *Internal Memorandum*, Sandia National Laboratories.
86. Kay, P.J. and Mackay, C.A. (1976) The growth of internetallic compounds on common basis materials coated with tin and tin-lead alloys. *Trans. Inst. Met. Finish.*, **54**, 68.
87. Chan, Y.C., So, A.C.K., and Lai, J.K.L. (1998) Growth kinetic studies of Cu-Sn intermetallic compound and its effect on shear strength of LCCC SMT solder joints. *Mater. Sci. Eng.*, **B55**, 5.
88. Lee, T.Y. *et al.* (2002) Morphology, kinetics, and thermodynamics of solid-state aging of eutectic SnPb and Pb-free solders (Sn-3.5Ag, Sn-3.8Ag-0.7Cu and Sn-0.7Cu) on Cu. *J. Mater. Res.*, **17**, 291.
89. Siewert, T.A., Madeni, J.C., and Liu, S.(Apr 2003) Formation and growth of intermetallics at the interface between lead-free solders and copper substrates. *Proc. APEX Conference on Electronics Manufacturing*.
90. Lee, C.B. *et al.* (2003) Intermetallic compound layer formation between Sn–3.5 mass% Ag BGA solder ball and (Cu, immersion Au/electroless Ni–P/Cu) substrate. *J. Mater. Sci.: Mater. Electron.*, **14**, 487.

91. Yoon, J.W., Lee, C.B., and Jung, S.B. (2002) Interfacial reactions between Sn-58 mass% Bi eutectic solder and (Cu, electroless Ni-P/Cu) substrate. *Mater. Trans.*, **43**, 1821.
92. Yoon, J.W. and Jung, S.B. (2003) Investigation of interfacial reactions between Sn-5Bi solder and Cu substrate. *J. Alloys Compd.*, **359**, 202.
93. Yoon, J.W., Lee, C.B., Kim, D.U., and Jung, S.B. (2003) Reaction diffusions of Cu_6Sn_5 and Cu_3Sn intermetallic compound in the couple of Sn-3.5Ag eutectic solder and copper substrate. *Met. Mater. Int.*, **9**, 193.
94. Yoon, J.W. and Jung, S.B. (2004) Effect of isothermal aging on intermetallic compound layer growth at the interface between Sn-3.5Ag-0.75Cu solder and Cu substrate. *J. Mater. Sci.*, **39**, 4211.
95. Chen, C. *et al.* (2000) Long-term aging study on the solid-state reaction between 58Bi42Sn solder and Ni substrate. *J. Electron. Mater.*, **29**, 1200.
96. Li, M. *et al.* (2002) Microstructure, joint strength and failure mechanisms of SnPb and Pb-free solders in BGA packages. *IEEE Trans. Electron. Packag.*, **25**, 185.
97. Yoon, J.W., Lee, C.B., and Jung, S.B. (2003) Growth of an intermetallic compound layer with Sn-3.5Ag-5Bi on Cu and Ni-P/Cu during aging treatment. *J. Electron. Mater.*, **32**, 1195.
98. Deng, X., Piotrowski, G., Williams, J.J., and Chawla, N. (2003) Influence of initial morphology and thickness of Cu_6Sn_5 and Cu_3Sn intermetallics on growth and evolution during thermal aging of Sn-Ag solder/Cu joints. *J. Electron. Mater.*, **32**, 1403.
99. Huntington, H.B. and Grone, A.R. (1961) Current-induced marker motion in gold wires. *J. Phys. Chem. Solids.*, **20**, 76–87.
100. Lu, M., Shih, D.-Y., Lauro, P. *et al.* (2008) Effect of Sn grain orientation on electromigration degradation mechanism in high Sn-based Pb-free solders. *Appl, Phys. Lett.*, **92**, 211909.
101. Lu, M., Shih, D.-Y., Kang, S.K. *et al.* (2009) Effect of Zn doping on SnAg solder microstructure and electromigration stability. *J. Appl. Phys.*, **106**, 053509.
102. Wang, Y., Lu, K.H., Gupta, V. *et al.* (May 2011) Effect of Sn Grain Structure on Electromigration Reliability of Pb-Free Solders. *Proc. 61st IEEE Electronic Components and Technology Conference (ECTC), Lake Buena Vista, FL.*

15

Electromigration in Pb-Free Solder Joints in Electronic Packaging

Chih Chen[1], *Shih-Wei Liang*[1], *Yuan-Wei Chang*[1], *Hsiang-Yao Hsiao*[1], *Jung Kyu Han*[2], *and K.N. Tu*[2]

[1] *Department of Materials Science and Engineering, National Chiao Tung University, Hsin-chu 30010, Taiwan, Republic of China*

[2] *Department of Materials Science and Engineering, University of California at Los Angeles, Los Angeles, California 90095-1595, USA*

Abstract

Pb-free solders have been adopted to replace Pb-containing SnPb solders in the electronic packaging industry due to environmental concerns. Electromigration is one of the critical reliability issues for fine-pitch Pb-free solder bumps. This chapter reviews the unique features of electromigration in flip-chip solder bumps, emphasizing the effects of current crowding and Joule heating. It also describes the changes in the physical properties of the solder bumps during electromigration, such as bump-resistance changes, the redistribution of temperature, and the enhanced brittle mechanical behavior. In addition, the challenges for a better understanding of electromigration in Pb-free solder microbumps are discussed. As the dissolution rates of Ni and Cu in Pb-free solders are much higher than those in Pb-containing solders, fast dissolution of Cu and Ni from the under-bump metallization into the solder bump under electromigration may endanger the solder bump reliability because of the anisotropic nature of Sn microstructure in Pb-free solder microbumps.

Lead-free Solders: Materials Reliability for Electronics, First Edition. Edited by K. N. Subramanian.

15.1 Introduction

Electromigration (EM) has been the most persistent reliability issue in the interconnect and packaging technology of microelectronic devices [1]. It is the mass transport of atoms driven by momentum exchange between a high density of moving charge carriers and diffusing atoms. The drifting electrons collide with atoms, causing the atoms to exchange positions with neighboring vacancies during current stressing. This results in the accumulation of atoms on the anode end and void formation on the cathode end of interconnects in large-scale integrations of circuits on Si chips, as well as in flip-chip solder joints of the packaging technology that connects the Si chips to their substrates. This can eventually lead to short and open failures. Due to the relentless drive for the miniaturization of microelectronic devices, the flip-chip solder joints in the packaging technology for these devices are being scaled down, whereas the required performance continues to increase. Flip-chip solder bumps with a nominal diameter of 25 to 10 μm have been fabricated [2]. In particular, tiny solder bumps of tens of micrometers are needed to connect Cu vias with through-Si-via (TSV) technology in the 3-dimensional integrated circuits (3D IC) of stacking chips [3]. As a result, the current density in the interconnect and packaging technology rises continuously with each generation, making EM in solder joints a critical reliability issue [4–7]. In addition, with environmental concerns, the microelectronics industry is moving toward Pb-free solder alternatives. Because most of the mainstream Pb-free solders are Sn-based alloys, electromigration in Sn-based solders has attracted much attention because very little field data are available [8]. Thus, the test standard for electromigration in solder joints has been emended [9].

In general, the atomic flux of electromigration 'J_{EM}' in a conductor driven by a constant current density 'j' can be expressed by the following equation [10]:

$$J_{EM} = C\frac{D}{kT}Z^{*}eE = C\left(\frac{D_0}{kT}\right)\exp\left(-\frac{E_a}{kT}\right)Z^{*}e\rho j \tag{15.1}$$

where J_{EM} is the electromigration flux, C is the concentration of atoms per unit volume of the conductor, D is the effective diffusivity of the conductor at the testing temperature, Z^{*} is the effective charge number, E is the electric field, D_0 is the prefactor of the diffusivity, E_a is the activation energy of diffusion in the electromigration, ρ and j are resistivity and current density of the conductor, respectively, k is Boltzmann's constant, and T is the absolute temperature.

The EM behavior of flip-chip solder joints becomes more complicated by interfacial chemical reactions that also take place at the cathode and at the anode during EM, in addition to the atomic transport driven by an electric field accompanied by thermal gradients. This chapter reviews the unique features of EM in solder bumps, the changes in physical properties of solder bumps during EM, and the challenges encountered from EM in Pb-free solder microbumps.

15.2 Unique Features for EM in Flip-Chip Pb-Free Solder Joints

Due to the unique layout of the line-to-bump structure in flip-chip solder joints, two prominent effects take place during electromigration. One is the effect of current

crowding [11–16], and the other is the effect of Joule heating [13, 17–20]. The former plays a crucial role in void nucleation and propagation [16, 21–24], and the latter may create a hot spot in the solder [18, 25], which can accelerate electromigration damage. In addition, it may trigger thermomigration to accompany the electromigration [17, 26–29].

15.2.1 Serious Current-Crowding Effect

The distribution of current density inside a flip-chip solder joint is not uniform due to the current-density transition from the on-chip thin metal traces to the solder bump. Finite element analysis has been carried out to simulate the 3D current density distribution in flip-chip solder joints [13–16]. As shown in Figure 15.1, when a pair of solder bumps was subjected to a current stressing of 0.6 A, the current crowded as it entered the solder bump from the Al trace on the chip side. A simplified under-bump metallization (UBM) structure with a contact opening of 270 μm in diameter was adopted. The contact opening on the substrate side was 300 μm in diameter. The Al trace on the chip side was 400 μm wide and 1.2 μm thick, whereas the Cu line on the substrate side was 400 μm wide and 30 μm thick. The diameter of the solder bump was 350 μm. Because the cross-sectional area of the Al trace is generally about two orders of magnitude smaller than that of the solder bump, the current density in the Al trace reaches 5.6×10^5 A/cm^2, and it is about two orders of magnitude higher than the average current density in the solder joint. However, once the current enters the contact opening of the bumps, the majority of the current will no longer drift along the thin horizontal Al trace because its resistance is much higher than that of the bumps. Instead, most of the currents drift into the bump vertically to flow in a lower-resistance path. Thus, an extremely nonuniform current distribution occurs at the contact opening of the solder bump. Current crowding occurs in the solder joint much more seriously than that in the Al and Cu interconnects.

The current-crowding effect is illustrated in detail by simulation in Figure 15.2.

A 3D thermoelectrical coupled simulation was performed for solder joints of about 180 μm in diameter. The model used was a SOLID69 8-node hexahedral coupled field element with Ansys software. The electrical and thermal resistivities of the materials, as

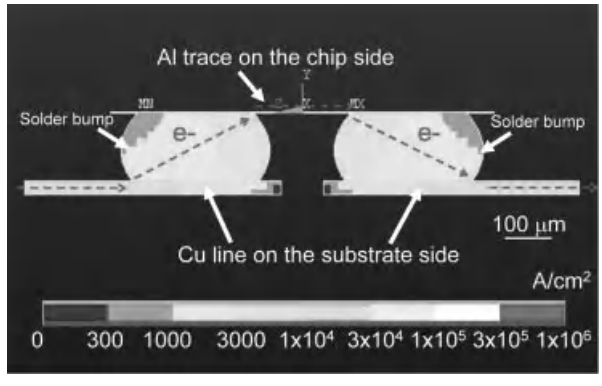

Figure 15.1 *Cross-sectional view showing the current-crowding effect in solder bumps. Peak current density occurs at the current entrances of the Al trace into the solder bump.*

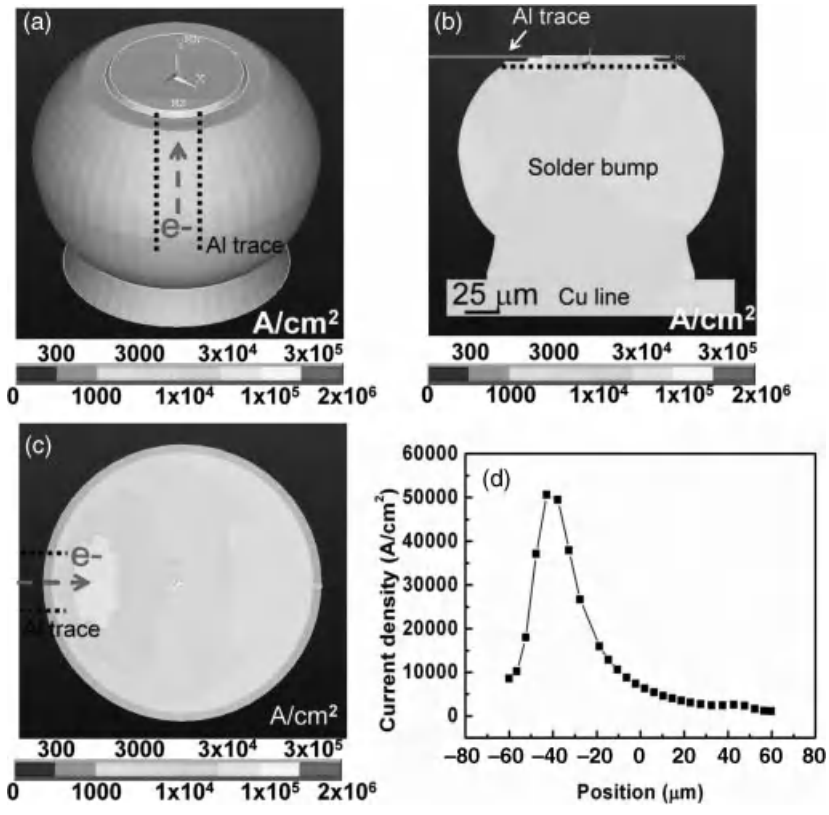

Figure 15.2 *(a) Tilt-view of the simulated current-density distribution in a whole solder bump when the joint is stressed at 0.6 A and 100°C. Current-density distribution from (b) a cross-sectional view and (c) a top view. (d) The values of the current density along the dashed line in (b).*

well as the boundary conditions used in this modeling, followed those used in a previous study [18]. The diameter of the passivation opening and the UBM opening were 85 μm and 120 μm, respectively. Figure 15.2a shows the current distribution in the solder bump only. The cross-sectional view and top view are depicted in Figures 15.2b and c, respectively. A significant portion of the current entered the bump through a small area in the contact opening adjacent to the Al trace. The values of current density along the dashed line in Figure 15.2b are plotted in Figure 15.2d. It indicates that the peak current density occurs at the entrance point of the solder bump, and its value is 5.1×10^4 A/cm^2. On the other hand, the value was as low as 1.1×10^3 A/cm^2 on the other end of the contact opening. Thus, the current-crowding effect is very serious in flip-chip solder joints.

15.2.2 Joule Heating and Nonuniform Temperature Distribution During EM

Joule heating is waste heat generated by entropy production, which is given as [30]

$$\frac{T\mathrm{d}S}{V\mathrm{d}t} = j^2\rho \tag{15.2}$$

where T, S, V, and t are temperature, entropy, volume, and time, respectively, and dS/dt is the rate of entropy production. Thus, j and ρ are, respectively, the current density (A/cm^2) and resistivity ($\mu\Omega$ cm). Usually, the heating power, P, is described by the Joule-heating relationship:

$$P = I^2R = j^2\rho V \tag{15.3}$$

where I is the applied current, $I/A = j$, A is the cross-sectional area of the sample, R is the resistance of the entire sample, $R = \rho l/A$, where l is the length of the sample, and $V = Al$. Thus, $P = I^2R$ is Joule heating per unit time of the entire sample, and $j^2\rho$ is the Joule heating per unit volume of the sample per unit time. The units of P are J/s or W.

To compare the Joule heating in Al interconnects and solder bumps, as described above, the resistance of the Al trace is typically hundreds of milliohms [15]. In contrast, it is about 7 milliohms for a solder bump [24] and tens of milliohms for the Cu lines on the substrate side. Considering Joule heating per unit volume for Al, with $j = 10^6$ A/cm^2 and $\rho = 10^{-6}\,\Omega$ cm, the Joule heating is $\rho j^2 = 10^6$ J/cm^3 s. In solders, with $\rho = 10^{-5}\,\Omega$ cm, $j = 10^4$ A/cm^2 will result in Joule heating of $\rho j^2 = 10^3$ J/cm^3 s. Therefore, the Al trace on the chip side serves as the major contributor to Joule heating, causing the solder bump to be hotter at the chip side than at the substrate side.

Nonsymmetrical Joule heating takes place during electromigration tests due to current crowding. As shown in Figure 15.3, the temperature distribution in the solder joints can be obtained using thermoelectrical finite element simulation [15, 17]. In the two solder bumps stressed by 0.59 A through the circuit shown in the figure the Al trace is the hottest component in the joint. Figure 15.4a shows the simulated temperature distribution in the solder joints only. It is clear that a hot spot exists at the entrance point of the current from the Al trace. Figure 15.4b illustrates the cross-sectional view of the temperature distribution inside the solder, showing the existence of the hot spots in the solder adjacent to the entrance points of the current from the Al trace into the solder at the contact opening. The temperature at these spots was 95.6 °C, which was 4.5 °C higher than the average value in the solder. A

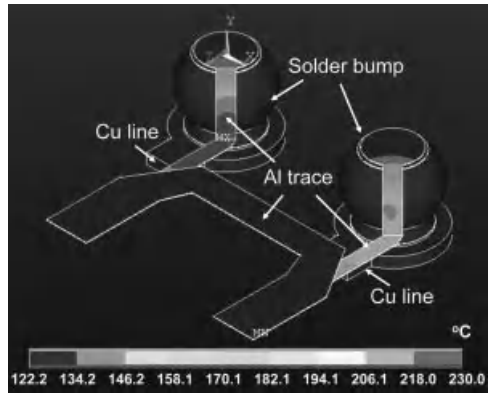

Figure 15.3 *Three-dimensional simulation of the temperature distribution for two solder joints subjected to 0.59-A current stressing. The peak temperature occurs at the Al trace because it has a higher resistance.*

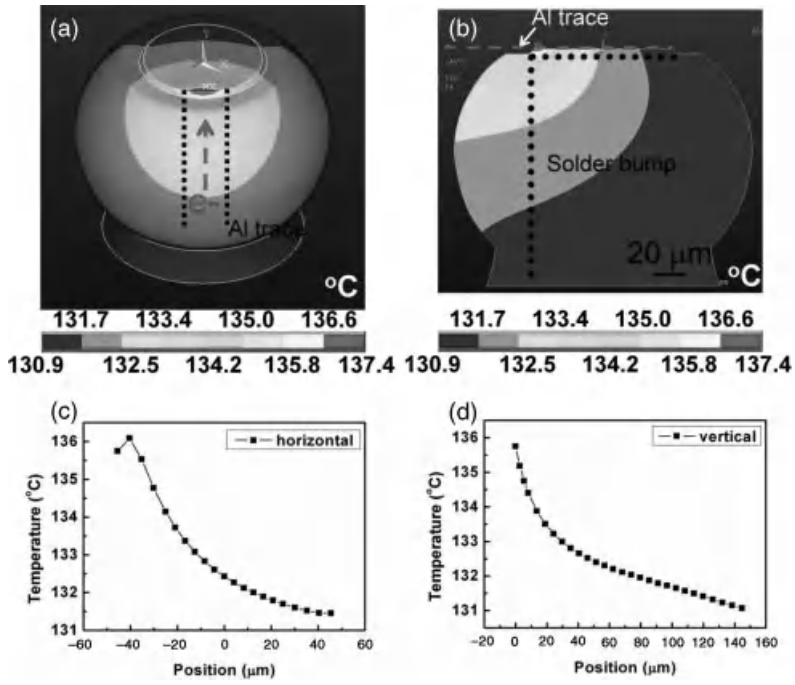

Figure 15.4 *(a) Tilt-view of the simulated temperature distribution within a whole solder bump when the joint is stressed at 0.59 A and 100 °C. (b) Cross-sectional view showing the temperature distribution. A hot spot was observed at the current entrance from the Al trace. The temperature profile along (c) the horizontal dashed line, and (d) along the vertical dashed line in (b).*

hot spot can be observed clearly in the figure. The temperature on the chip side was higher than that on the substrate side. Figure 15.4c illustrates the temperature profile along the horizontal dashed line in Figure 15.4b; whereas Figure 15.4d illustrates the temperature profile along the vertical dashed line in Figure 15.4b. The thermal gradient here is denoted as the subtraction of the temperature in the hot spot by the temperature at the opposite end of the solder, and it is then divided by the distance between the two locations. In this stressing condition, the vertical thermal gradient was calculated to be 276 °C/cm, whereas the horizontal thermal gradient was calculated to be 634 °C/cm. The current density in the Al trace was 1.1×10^6 A/cm^2. The average current density in the solder joint was 5.2×10^3 A/cm^2 based on the contact opening. In the hot spot, the maximum current density was 1.7×10^5 A/cm^2, whereas the average current density involved in a volume of 5 μm × 5 μm × 5 μm was estimated to be 1.4×10^5 A/cm^2. The existence of the hot spot may be attributed to two factors. First, it may be due to the local Joule heating inside the solder itself, as described in Eq. (15.2). In this simulation model, the total resistance of the Al trace was about 900 mΩ, and the resistance of the solder bump was about 10 mΩ. Therefore, the Al trace generated most of the heat. Due to the serious current crowding in the solder joint, local Joule heating occurred there. Because the Al trace has higher Joule heating effect, the hot spot is closer to the Al trace.

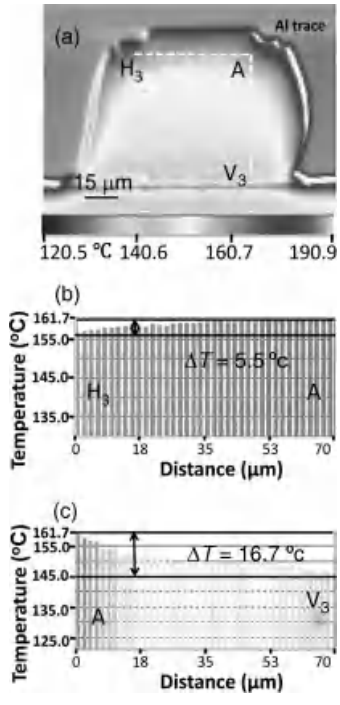

Figure 15.5 *(a) The measured temperature map by infrared microscopy when the joint was stressed by 0.6 A. A hot spot is clearly observed in the upper right of the bump. (b) The temperature profile along the horizontal line in (a), and (c) The temperature profile along the vertical line in (a). A huge thermal gradient of 2392 °C/cm developed across the solder bump.*

Experimental measurements by infrared microscopy have been reported recently to verify the simulation results of the hot spot [31]. One half of an array of solder bumps were polished to their centers approximately. The diameter of the solder bumps was about 150 μm. The solder bumps were joined to a FR5 substrate. Figure 15.5a shows the measured temperature map when the stressing current was 0.6 A. A hot spot can be clearly noted. The temperature difference is 5.5 °C and 16.7°C along the horizontal and vertical lines in Figure 15.5a, respectively, as illustrated in Figures 15.5b and c. The origin of Figure 15.5b was set at point H_3, whereas the origin of Figure 15.5c was set at point A. A huge thermal gradient of 2392 °C/cm developed across the solder bump. The thermal gradient is defined here as the temperature difference between the two ends of the dashed line divided by the length of the line, which was 70 μm for both the horizontal and vertical lines. The Joule-heating effect also established a horizontal thermal gradient of 786 °C/cm.

Figure 15.6a shows the plot of average and hot-spot temperatures as a function of applied current densities or applied current with a 5-μm Cu/3-μm Ni UBM. The applied current ranges from 0.1 to 0.6 A. With currents larger than 0.6 A, the solder bump tended to melt. The curve shows a parabolic behavior, which follows the Joule-heating relationship as described in Eq. (15.2). Therefore, the Joule-heating effect is very significant at higher stressing currents. The built-in thermal gradient as a function of applied current is shown in

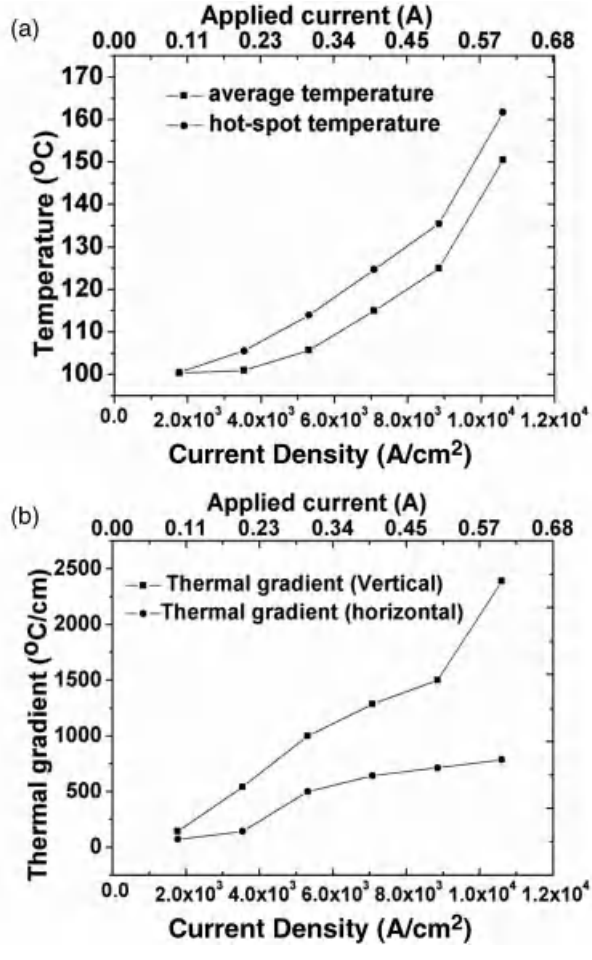

Figure 15.6 *(a) Plot of average and hot-spot temperatures as a function of applied current densities/current with a 5-μm Cu/3-μm Ni UBM. (b) thermal gradient as a function of applied current. The thermal gradient may be over 200 °C/cm when the applied current density is larger than 1×10^4 A/cm^2.*

Figure 15.6b. A thermal gradient over 2000 °C/cm can be established if the applied current density is large enough.

15.2.3 Effect of Current Crowding and Joule Heating on EM Failure

15.2.3.1 Pancake-Type Void Formation in Solder Joints with Thin-Film UBM

Current crowding and Joule heating play crucial roles in electromigration failure. Several studies have been carried out to investigate the associated failure mechanisms in flip-chip solder joints [4, 11–29, 33–51]. As illustrated in Figures 15.1 and 15.2, the local current density at the current-crowded region is much higher than that in the rest of the solder joint,

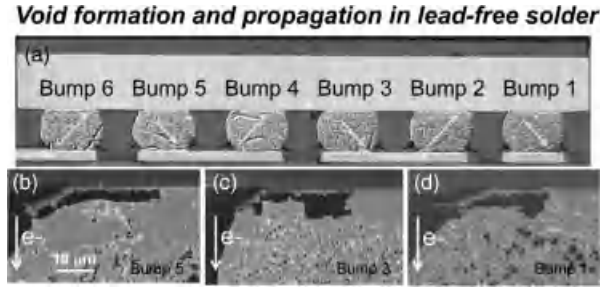

Figure 15.7 *(a) SEM of cross sections of solder bumps showing the location of void formation (odd numbered bumps, upper left corner). The electron flow is indicated by the arrows. (b) Enlarged SEM image for the voids in Bump 5. (c) Enlarged SEM image for the voids in Bump 3. (d) Enlarged SEM image for the voids in Bump 1.*

and electromigration damage starts to appear near the entrance point of the Al trace. Because solders are more susceptible to electromigration than the rest of the metallization materials in the joints [1], such as Al, Ti, Cu, Ni and intermetallic compound (IMC), electromigration damage generally starts to occur first in solders because the critical product of electromigration for solder is two orders of magnitude smaller than that of Al and Cu interconnects.

For solder joints with a thin-film UBM, voids start to nucleate at the interface between the solder bump and the IMC on the chip side [19, 21, 33]. Figure 15.7 shows the void formation in eutectic SnPb solder joints with a thin-film UBM of 1-μm Al/0.32-μm Ni(V)/0.8-μm Cu [33]. The applied current density was about 3.5×10^3 A/cm^2 at an ambient temperature of 50 °C. The direction of electron flow in Bumps 1 to 6 is indicated by the arrows in Figure 15.7a. Pancake-type voids form near the entrance of the Al trace on the chip side, as can be observed in the enlarged scanning electron micrographs provided in Figure 15.7b–d. The void formation may be attributed to two factors. First, the local current density is much larger there than it is in the rest of the bump, resulting in a larger electron wind force and thus higher electromigration rate. Secondly, the local temperature in this region may be higher than that encountered in the rest of the bump, causing the faster diffusion or electromigration rate of the solder. Thus, voids start to form at the current-crowding/hot-spot region. Once the voids form, the location of current-crowding/hot-spot region may shift to the front of the void in order for the current to enter into the solder bump along a low-resistance path [21, 22]. The migration of the current-crowding/hot-spot region will lead the void to propagate laterally until the void depletes the entire contact opening and causes open failure of the joint.

15.2.3.2 UBM Dissolution in Solder Joints with Thick-Film UBM

Because the electronic packaging industry adopted Pb-free solders due to environmental concerns, Sn-based alloys are being used as the mainstream solders. These Pb-free solders possess higher melting points (over 210 °C) than those of the eutectic SnPb solders (183 °C), causing a higher dissolution rate and higher solubility of Cu and Ni in the molten solder as well as a higher rate of IMC formation between the solder and Cu and Ni. For example, the saturation solubility of Cu in the molten eutectic SnPb at 220 °C is estimated to be about 0.18 wt%, but that in the molten eutectic SnAgCu at 260 °C is about 1.54 wt% [9].

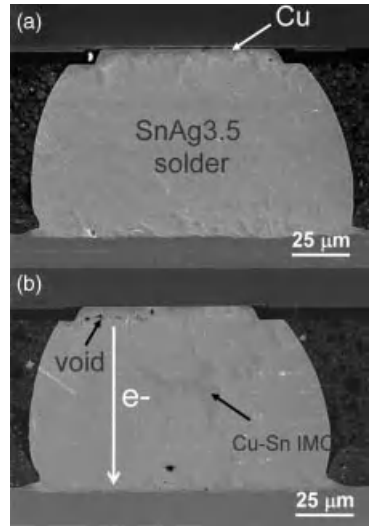

Figure 15.8 *Cross-sectional SEM images for Pb-free SnAg solder joints with a 5-μm Cu UBM (a) before current stressing and (b) after stressing by a constant current of 0.8 A at 150°C for 55 h. Voids formed at the current crowding region and Cu-Sn IMC formed in the solder bumps.*

Thicker Ni or Cu layers have been adopted as the UBM for Pb-free solder bumps. Hence, the EM failure mechanism for solder joints with thick-film UBMs becomes very important. Current stressing may enhance IMC formation at the solder/UBM interface [52–57]. While the microelectronic industry adopts a thicker Cu UBM to reduce current crowding, the applied current accelerates the dissolution of the Cu UBM, causing extensive Cu-Sn IMC formation [16, 54, 55]. Figure 15.8a shows the SEM images for Pb-free eutectic SnAg solder joints with a 5-μm Cu UBM before current stressing. The joint was stressed by a constant current of 0.8 A at 150 °C. Current-crowding and Joule-heating effects have once again played critical roles in the failure mechanism. At the earlier stage of electromigration, the Cu layer near the current-crowding/hot-spot region was consumed first due to the higher current density and higher local temperature there, forming some Cu-Sn IMC at the solder/Cu interface, as shown in Figure 15.8b. When the Cu UBM was consumed completely, the adhesion of the solder/Ti (or Al) interface became very weak because the solder did not wet the Ti or Al surface. Voids formed easily at the interface during subsequent current stressing.

For solder joints with a Ni UBM, the failure mechanism appears to be slightly different from that in solder joints with a Cu UBM. In some stressing conditions, voids may form in the interface of the Ni-Sn IMC and solder at the earlier stage of EM because Ni UBM dissolves much more slowly than Cu UBM during current stressing [24]. The saturation solubility of Ni is 0.28 at% in the eutectic SnAg solder at its reflow temperature of 250 °C [9], which is much lower than the Cu solubility. In addition, Ni has a lower consumption rate than Cu by the molten solder [58, 59]. Due to the slow dissolution of Ni in solders, voids may form in solder bumps in the early stages of EM. Figure 15.9a shows the SEM image for a SnAg solder bump before current stressing. The UBM was 0.5-μm

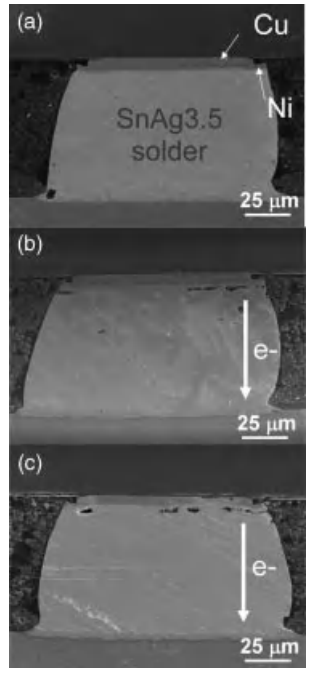

Figure 15.9 *(a) Cross-sectional SEM image for a Pb-free SnAg bump with 5-μm Cu/3-μm Ni UBM (a) before current stressing and (b) after the current stressing by 0.9 A at 150 °C for (b) 121 h and (c) 193 h. Voids formed at initial stages without obvious dissolution of the Ni UBM. After stressing for 193 h, Ni and Cu UBM dissolved into the solder bumps.*

Ti/0.5-μm Cu/5-μm Cu/3-μm Ni. The Ti layer and the 0.5-μm Cu seed layer were sputtered, whereas the 5-μm Cu and the 3-μm Ni layers were electroplated. After the fabrication process, a thin layer of Ni_3Sn_4 was formed between the Ni and the solder layer. After current stressing by 0.9 A at 150 °C for 121 h with a downward electron flow, voids started to form under the IMC layer in the upper-right corner of the contact opening, where current crowding occurred most seriously. Yet, the Ni and Cu UBMs may dissolve at later stages of EM, as illustrated in Figure 15.9c, which was stressed by 0.9 A at 150 °C for 193 h. The Ni and the Cu UBMs on the right-hand side were transformed into IMCs. In addition to the voids in the original interface of the solder and the Ni_3Sn_4 layers, voids were also formed at the Ti/solder interface.

15.2.4 Thermomigration in Solder Joints

Thermomigration (TM) is covered in another chapter in this book, so it will not be addressed here. As described above, EM generates Joule heating, and when the heat is conducted away, it has to have a temperature gradient. When the temperature gradient is large, of the order of 1000 °C/cm, thermomigration in solder alloys can be significant [60, 61]. For a microbump of 10 μm in diameter with a temperature difference of 1 °C across it, the temperature gradient is 1000 °C/cm, and thus thermomigration cannot be ignored.

15.3 Changes of Physical Properties of Solder Bumps During EM

Several physical properties of solder bumps may be changed during current stressing, including electrical resistance, temperature distribution, and mechanical strength.

15.3.1 Electrical Resistance

Microstructural changes during EM may influence the electrical resistance of the solder bump, including void formation, IMC formation, phase redistribution, and grain rotation of Sn. Three kinds of test patterns may be used to monitor the resistance changes during EM: daisy chains [14, 62], Kelvin probes [2, 24, 33, 49, 63], and Wheatstone bridges [64]. A daisy chain consists of a single series of bumps in a chain with current flow alternatively between die and substrate, as shown in Figure 15.10a. The daisy chains can detect early failures due to processing defects and provide better statistics of the lower tail of the failure distribution. However, it is difficult to separate failures from each current stressing without a detailed failure analysis. In addition, most of the chain resistance is due to the wiring metal lines in the die and in the substrate rather than due to the bump, and thus it is difficult to identify the failed bump without cross-sectional or X-ray tomography inspection. On the other hand, the Kelvin probes and Wheatstone bridges are able to measure single bump resistance change accurately, and thus a slight resistance change due to microstructure change induced by EM can be detected using these two test structures.

15.3.1.1 Effect of Void Formation on Bump Resistance

As voids form and propagate along the contact interface of IMC and solder, electrons need to drift longer in the wiring trace on the chip side [21, 22]. In addition, the cross section of contact opening available for electron conduction decreases as voids grow bigger [2, 24, 49]. The bump resistance increases less than 0.1 mΩ in the initial stage of void formation using Kelvin probes. The Kelvin probes of solder bumps are shown schematically in Figure 15.10b. An Al trace connects four bumps together. Six Cu lines on the substrate were connected to the four bumps, and the lines were labeled as Nodes 1 through 6, as shown

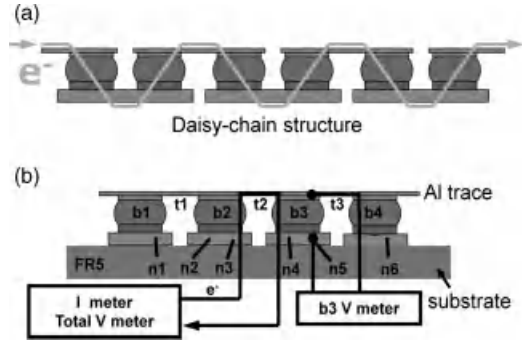

Figure 15.10 *(a) Schematic of daisy-chain configuration. It consists of a single series of bumps in a chain with current flow alternating between the die and substrate. (b) Schematic diagram for the Kelvin bump probes. The bump resistance for Bump 3 can be measured by applying current through Node 3 and 4 and by measuring voltage through Node 5 and 6.*

in the figure. With these six Cu lines, various experimental setups can be performed to measure the bump resistance for Bump 2 or Bump 3 or the resistance for the middle segment of the Al trace. In this study, current was applied through Nodes 3 and 4, that is, electrons flowing from the chip side to the substrate side for Bump 3 but in the opposite direction for Bump 2, as illustrated in Figure 15.10b. The voltage change in Bump 2 was monitored through Nodes 1 and 2, whereas the voltage change in Bump 3 was monitored through Nodes 5 and 6. Therefore, the change in bump resistance during electromigration for the two bumps, Bumps 2 and 3, with opposite direction of electron flow can be monitored simultaneously. In general, a void is formed on the chip side of Bump 3 due to the serious current-crowding effect. Hence, the results for Bump 3 are reviewed here.

As shown in Figure 15.11, the resistance of Bump 3 can be monitored by the Kelvin probes. The solder joint is the same as that shown in Figure 15.9a, and it is stressed under 0.8 A at 150 °C with electron flow from the chip side to the substrate side. The initial bump resistance was only 0.6 mΩ. As the stressing time increased, the bump resistance continued to increase slowly up to 80% of the failure time, and the bump failed when the resistance rose abruptly at around 756 h. The inset in Figure 15.11 shows the data in Figure 15.12 up to 80% of the stressing time. The bump resistance started to increase after 20 h. The time for the resistance to reach 1.03 times of the initial value was 29.8 h, which was 4% of the failure time.

The Kelvin probes can detect different stages of void formation and propagation, and Figures 15.12a–f show the void formation and propagation at different stages [24]. Figure 15.12a shows the cross-sectional SEM image for the bump before current stressing. The stages in Figures 15.12b–f are denoted as Stage 1 through 5 here, and the corresponding stressing time, normalized time, and normalized resistance are tabulated in Table 15.1 Figure 15.12b shows the SEM image for another bump stressed by 0.8 A at 150 °C for 29.8 h. The bump resistance increased from 0.60 mΩ to 0.62 mΩ after the current stressing, which is an increase of 1.03 times the initial value. The direction of the electron flow is indicated by

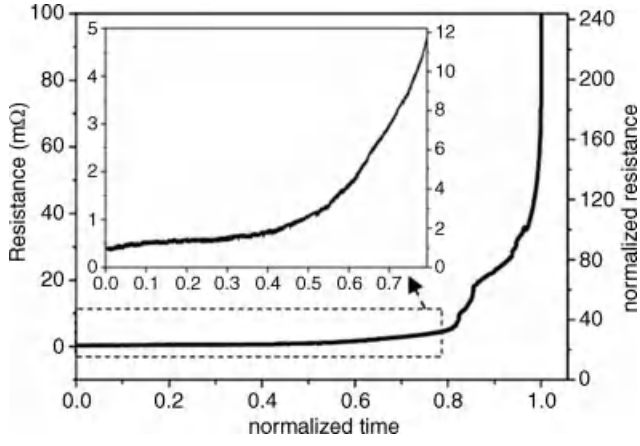

Figure 15.11 *The resistance changes versus normalized stressing time for Bump 3 monitored by Kelvin probes under 0.8 A at 150°C. with downward electron flow. The inset in this figure shows the resistance changes up to 80% of the stressing time.*

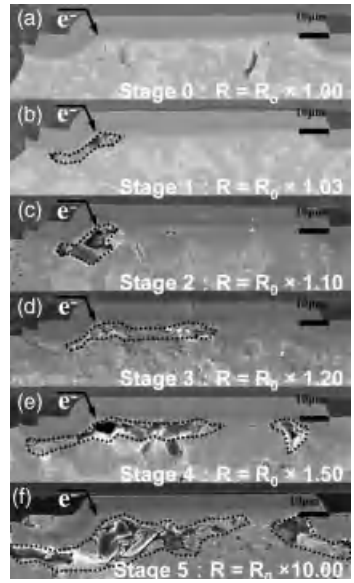

Figure 15.12 *Void formation at different stages of EM when the joints were stressed by 0.8 A at 150°C. (a) before current stressing, (b)–(f) correspond to stages when the bump resistance reached (b) 1.03×, (c) 1.10×, (d) 1.20×, (e) 1.50×, and (f) 10.00× of its original value.*

the arrow in the figure. Small voids started to form under the IMC layer in the left corner of the contact opening, where current crowding occurred most vigorously. Due to the slower IMC formation rate between Ni and Sn, no clear IMC formation was observed in the initial stages. Another bump was stressed at the same condition for 101 h, and the current stressing was terminated when the bump resistance reached 1.10 times the initial value. The cross-sectional image is shown in Figure 15.12c, which shows larger voids at the interface of the solder and the IMC. This condition is denoted as Stage 2. Under the stressing conditions, voids started to form at approximately 5% of the failure time, and they grew continuously for the rest of the stressing time. The incubation time for void formation is relatively short compared with the failure time, which may be attributed to the fact that the cross section of the UBM opening is quite large, and thus it takes time for the voids to propagate and deplete

Table 15.1 *The resistivity for the possible bump components.*

Materials	Resistivity (μΩ) cm at 20°C)
Al	3.2
Cu	1.7
Cu_6Sn_5 IMC	17.5
Ni_3Sn_4 IMC	28.5
Eutectic Sn63Pb37	14.6
Electroless Ni	~70
Electroplated Ni	~6
Sn-based Pb-free solders	~12

the entire UBM opening. It is interesting that voids start to form at approximately 5% of the failure time, and they propagate along the contact opening for the rest of time. This behavior is quite different from that of Al and Cu interconnects, where the failure time is limited by void nucleation. Once voids form, they grow fast, and the interconnect fails soon after that.

As voids grow toward the rest of the contact opening, the resistance continues to increase. The increase in bump resistance during various stages of stressing can be measured precisely using Kelvin bump probes, and it can be employed to monitor the void formation and microstructure change during EM.

15.3.1.2 Effect of IMC Formation on Bump Resistance

Formation of Cu-Sn or Ni-Sn IMC may also contribute to the resistance increase of solder bumps. Table 15.2 shows the resistivity for the possible bump components [65]. Because the resistivity of Pb-free solders ($\sim$12 $\mu\Omega$ cm) is lower than that of SnPb eutectic solder ($\sim$14.6 $\mu\Omega$ cm), the percentage increase of resistance due to IMC formation will be higher for Pb-free solder. In addition, as pointed out above, an extensive amount of IMC may form during the electromigration in Pb-free solders [55, 66–68]. Thus, it is expected that the IMC formation may also have an effect on the bump resistance. Yet, there are no studies published on this issue so far.

15.3.1.3 Effect of Phase Redistribution on Bump Resistance

Phase redistribution occurs in electromigration in Pb-containing flip-chip solder bumps [16, 69–71]. Because the SnPb solder is a binary alloy, including the Pb-rich and Sn-rich phases, the diffusion behavior in the solder during electromigration is complicated. It was reported that the dominant diffusion species was Sn atoms in a thin SnPb stripe when stressed at room temperature [6, 72]. On the other hand, Huynh *et al.* conducted another electromigration study at 150 °C using V-groove samples and found that Pb atoms were the dominant diffusion species [7] because Pb atoms have higher diffusivity than Sn atoms at high temperatures around 150 °C [73]. It was found that the redistribution of the Pb-rich and the Sn-rich phases may alter the resistance of the solder [74]. The resistance difference may be up to 6.5% for a thin solder stripe. For flip-chip solder bumps, the Pb-rich phase migrates to the anode at high stressing temperatures, and a complete phase separation between the Pb-rich and Sn-rich phases may take place [69, 70]. How the microstructure redistribution changes the bump resistance is unclear at the moment. For Sn-based Pb-free solder joints, there may be no obvious phase redistribution because Sn grains are the dominant microstructure in the solders except for grain rotation.

Table 15.2 *The normalized resistance, real stressing time, and normalized time for the five stages during current stressing.*

Stage	Normalized Resistance	Real Stressing Time (h)	Normalized Time ($\times 10^{-2}$)
0	1.00	0.0	0.0
1	1.03	29.8	3.94
2	1.10	101.5	13.4
3	1.20	140.0	18.5
4	1.50	155.3	20.5
5	10.00	383.0	50.6
final	open	756.6	100.0

15.3.1.4 Effect of Sn-Grain Rotation on Bump Resistance

Several studies points out that the beta-Sn grains rotate during current stressing [75–77]. The grain rotation may decrease the resistance of a Sn line up to 10% because beta-Sn has a body-center tetragonal crystal structure. Its lattice parameters are $a = b = 0.583$ nm and $c = 0.318$ nm, and its electrical conductivities are 13.25 and 20.27 $\mu\Omega$ cm, respectively. The c-axis of Sn grains may have a tendency to align with the current direction during current stressing to lower the total resistance of the structure. For Sn-based Pb-free solder bumps, Sn grains are the major phase. The grain rotation may have an effect on their electrical resistance. Lloyd [75] reported a voltage drop of up to 10% in 1 day while applying a current density of 6.25×10^3 A/cm^2 at 150 °C to a Sn stripe. This stressing condition is close to the test condition of electromigration of flip-chip solder joints. Yet, grain rotation has not been observed in Pb-free flip-chip solder joints during current stressing as yet. This deserves further study.

It is noteworthy that the wiring traces in the chip side may also degrade during the EM process [42, 44]. The degradation of the Al or Cu traces may cause a substantial resistance increase and Joule heating because the original resistance of the wiring traces is typically a few hundred milliohms.

15.3.2 Temperature Redistribution

As voids form and propagate during EM, the temperature in the solder bump may be redistributed, causing a shift of the hot spot. In addition, as voids deplete the contact area, the local electrical resistance increases, resulting in a higher local Joule heating effect. Thus, the solder near the hot spots may melt during the EM tests [20, 29, 46, 50, 78]. Because the solder bumps are completely surrounded by the Si chip, underfill, and the substrate, it is very hard to measure the temperature redistribution in the solder bumps at various stages of EM. Three-dimensional thermoelectrical simulations have been performed to predict the temperature redistribution in the bump at various stages of void formation in electromigration [22]. The temperature redistribution that occurs when voids deplete 0, 15.5, 19.5, 50.0, 80.5, and 96.0% of the contact opening on the chip side are given in Figure 15.13a through f. The joint was subjected to a constant current stressing of 0.6 A at 100 °C. The electrons entered the solder bump from the upper left-hand side. Before the current stressing, the hot-spot temperature was 137.4 °C, and it was located at the current crowded region. As the voids formed and depleted 15.5% of the contact opening, as shown in Figure 15.13b, electrons might drift farther along the Al trace, passing the void before entering the solder. In addition, the electrons might drain down to the solder through the surrounding UBM/IMC layer, resulting in two distinguishable hot regions at this stage. The hot-spot temperature did not increase appreciably as the voids depleted 80% of the contact opening because the remaining contact area is still quite large. There was no significant increase in hot-spot temperature until the voids depleted 96% of the contact opening when the temperature increased to 134.6 °C. Although the hot-spot temperature did not increase much in the stage before the voids depleted 80.5% of the contact opening, it still played an important role in void propagation. The atom diffusion rate near the hot spot is faster than that in the rest of the region. At the final stage illustrated in Figure 15.13F, the dramatic temperature increase was due to the very small conducting area that remained.

The temperature evolution during various stages of electromigration has been measured by placing a thermocouple on the chip surface [78]. No obvious temperature increase was

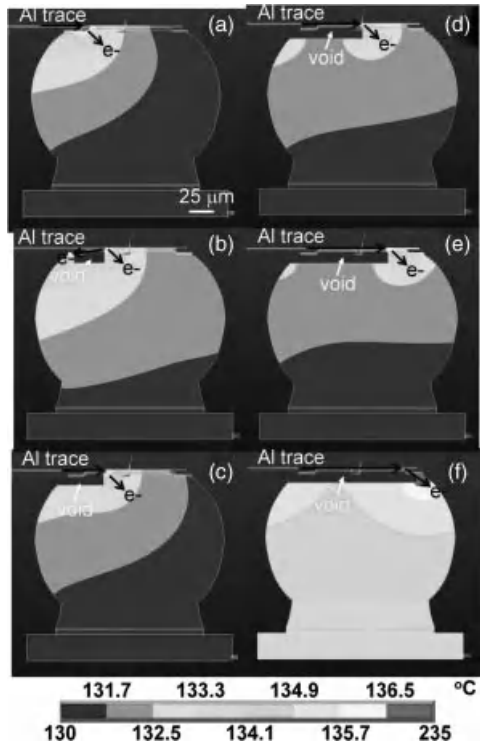

Figure 15.13 *Three-dimensional simulation showing the temperature redistribution when voids depleted (a) 0%, (b) 15.5%, (c) 19.5%, (d) 50.0%, (e) 80.5%, and (f) 96.0% of the passivation opening on the chip side.*

detected before reaching 50% of the failure time. A slight temperature increase occurred after that, and an abrupt increase in temperature at the very final stage took place. The behavior is similar to the simulation results. The effect of void propagation on the temperature increase was also analyzed with X-ray microscopy, Kelvin probes, and infrared microscopy [79]. It was found that the temperature rise due to void formation was less than 1.3 °C when the voids depleted about 75% of the contact opening, even though the bump resistance increased to 10.40 times its initial value. However, the temperature rose abruptly after an increase of up to 8.0 °C when the voids depleted 96.2% of the contact opening. Therefore, it seems that the temperature did not increase obviously in the early stage of void formation. However, the Joule-heating effect may become more significantly in later stages of void formation.

15.3.3 Mechanical Properties: Electromigration-Induced Brittleness in Solder Joints

Electromigration can have a significant influence on the mechanical properties of solder joints [80–84]. After electromigration, voids may form at the cathode interface between solder and IMCs, resulting in the degradation of fracture toughness in terms of the tensile, shear, and fatigue properties. Figure 15.14 shows the fracture modes of tensile tests for

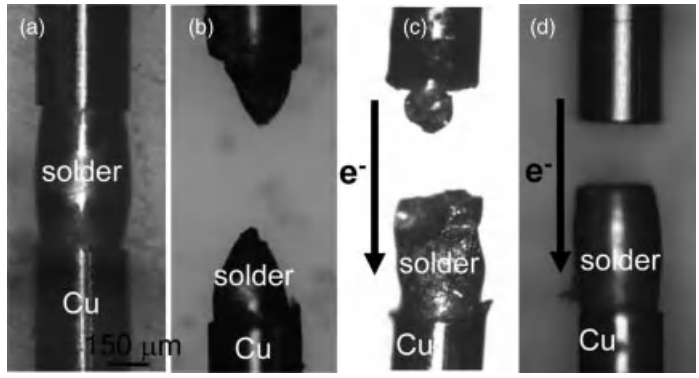

Figure 15.14 *Fracture images of tensile test after EM: (a) optical picture of original sample, (b) fracture image without EM, (c) fracture image after EM, 5×10^3 A/cm^2 at 145°C for 96 h, (d) fracture image after EM, 5×10^3 A/cm^2 at 145°C for 144 h.*

solder joints without and with electromigration testing. To combine the electromigration test and mechanical test, a Cu(wire)–solder bump(Sn97.5Ag3.8Cu0.7)–Cu(wire) sample was fabricated, as shown in Figure 15.14a. One of the samples underwent the tensile test without an applied current. The strain rate was 10^{-2}/s. Ductile fracture of necking was observed inside solder bump, as shown in Figure 15.14b. Other samples were subjected to an applied current for electromigration before tensile testing. The current density was 5.03×10^3A/cm^2 at 145 °C for 96 h and 144 h. Tensile testing with the same strain rate followed. It was found that brittle fractures occurred at the cathode interface of the solder joints. Figure 15.15 compares the stress–strain curves before and after electromigration, and

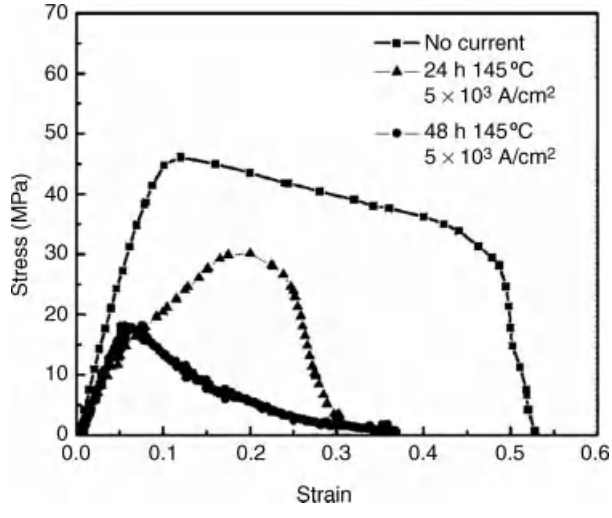

Figure 15.15 *Stress–strain curves before and after electromigration. The tensile strength decreases with increasing electromigration time when the samples are stressed by 5×10^3 A/cm^2 at 145°C.*

it shows that the tensile strength decreased with increasing electromigration time. The curve with closed square symbols is a tensile test result without current stressing. The curves with closed triangle and closed circle symbols are, respectively, the sample stressed by 5×10^3 A/cm^2 for 24 and 48 h at 145 °C. The tensile strength decreased from 46 MPa for 0 h to 30 MPa for 24 h and to 18 MPa for 48 h. These results demonstrate that electromigration has a profound effect on the mechanical properties of solder joints, especially on the cathode side of the joint.

15.4 Challenges for Understanding EM in Pb-Free Solder Microbumps

At the moment, the microelectronic industry is moving from 2D IC to 3D IC. The packaging technology of 3D IC requires vertical interconnects using TSV and microbumps. There are many challenges for understanding EM in Pb-free microsolder bumps, as discussed below.

15.4.1 Fast Dissolution of Cu and Ni under EM

As stated in Section 3.1.2, extensive IMC formation may occur during electromigration of Pb-free solders with Cu UBM. In particular, for solder joints with Cu columns or with TSV, the height of the solder microbump may be as low as 10 to 20 μm. As a result, the entire solder bump may be transformed completely into Cu-Sn IMCs during current stressing, which may induce brittle fracture [55]. The EM behavior of the IMCs may become important. However, this issue has not been addressed as yet. In addition, because a large number of Cu or Ni atoms are dissolved into solder bumps to form IMCs, how they affect the mechanical properties is of interest. In addition, how the IMCs affect the Sn diffusion due to EM is unclear, especially near the anode where IMCs form.

15.4.2 Effect of Grain Orientation on Electromigration

It was reported recently that extra-fast Cu and Ni dissolution may take place along a specific orientation. Lu *et al.* [85] found that rapid depletion of IMCs and Cu UBMs occurs along the *c*-axis of Sn crystals, resulting in significant damage to the joints because the Cu diffusivity is 500 times faster along the *c*-axis than that along the *a*- or *b*-axis of Sn crystals at 25 °C [86], and the diffusivity of Ni along the tetragonal (*c*-) axis is $\sim 7 \times 10^4$ times that at right angles (*a*- or *b*-axis) at 120 °C [87]. Therefore, in a microbump with lower number of grains, Sn grain orientation plays an important role in Sn-based Pb-free solder EM. More studies are needed to provide better understanding of this interesting phenomenon of anisotropy.

15.4.3 Stress in Solder Bumps

Several researchers proposed that there exists stress in solder joints during current stressing [88–90]. The built-in stress may be related to the current-crowding effect. Figures 15.16a–e shows the surface morphology of whisker formation at the anode in a solder bump after stressing by 1.4×10^4 A/cm^2 at 150 °C for (a) 0 h, (b) 38.5 h, (c) 68.5 h, (d) 99.5 h, and (e) 248.5 h, respectively. The electrons went up into the solder bump and escaped from the upper-right corner. What is important to note here is that it shows the very

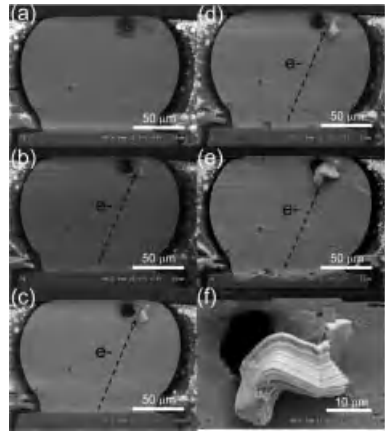

Figure 15.16 *SEM images of the cross section of eutectic SnAgCu solder joints after (a) 0 h, (b) 38.5 h, (c) 68.5 h, (d) 99.5 h, and (e) 248.5 h and (f) an enlarged image of the whisker.*

beginning of the initiation of a whisker from a cracked surface. In the enlarged image provided in Figure 15.16f, a rack of lines on the whisker surface is seen. The results indicate that high stress has been established during current stressing in flip-chip solder joints at relatively high temperatures. The back stress in SnAgCu is larger than that in the eutectic SnPb solder [90]. In a microbump, whether the backstress potential gradient is large enough to retard EM is unclear.

15.5 Thermomigration of Cu and Ni in Pb-Free Solder Microbumps

As described in Section 2.4, we expect a large temperature gradient in microbumps even if there is only 1 °C temperature difference across the microbump. Given the high solubility of Cu and Ni in Pb-free solders and the fast diffusion rates of Cu and Ni along the c-axis of Sn crystals, the effect of thermomigration on microbumps cannot be ignored. It is possible that the dissolution of the Cu and Ni atoms may occur under a thermal gradient produced during EM process [91].

15.6 Summary

The behaviors of EM in flip-chip solder joints were reviewed, emphasizing the effects of current crowding and Joule heating. Serious current-crowding and Joule-heating effects play critical roles in the EM failure mechanisms of solder joints. For solder joints with thin-film UBMs, voids are initiated at the location with the peak current density and with the peak temperature in the solder. For solder joints with thick-film UBMs, while the current crowding and peak temperature are in the UBM and far from the solder, the dissolution of UBM materials starts at a similar location and then gradually consumes the rest of the UBM. It merely takes a longer time to fail. Electromigration-enhanced dissolution of UBM

materials will be the main challenge for TSV and microbumps. The bumps may become brittle when they are transformed completely into IMCs.

Acknowledgments

The authors at NCTU would like to thank the National Science Council of R.O.C. for the financial support through grant No. NSC96-2628-E-009-010-MY3. The authors at UCLA would like to thank the support from SRC contract #1772.

References

1. Tu, K.N. (2003) Recent advances on electromigration in very-large-scale-integration of interconnects. *J. Appl. Phys.*, **94**, 5451–5473.
2. Wright, S.L., Polastre, R., Gan, H. *et al.* (2006) Characterization of micro-bump C4 interconnects for Si-carrier SOP applications. Proc. of the Electronic Components and Technology Conference, 56th, San Diego, 15, pp. 633–640.
3. Tsui, Y.K. and Lee, S.W.R. (2005) Design and fabrication of a flip-chip-on-chip 3-D packaging structure with a through-silicon via for underfill dispensing. *IEEE Trans. Adv. Packag.*, **28**, 413–420.
4. Brandenburg, S. and Yeh, S. (1998) Electromigration studies of flip chip solder bump solder joints. Proc. of Surface Mount International Conference and Exhibition, San Jose, pp. 337–344.
5. Liu, C.Y., Chen, C., Liao, C.N., and Tu, K.N. (1999) Microstructure-electromigration correlation in a thin stripe of eutectic SnPb solder stressed between Cu electrodes. *Appl. Phys. Lett.*, **75**, 58–60.
6. Liu, C.Y., Chen, C., and Tu, K.N. (2000) Electromigration in Sn-Pb solder strips as a function of alloy composition. *J. Appl. Phys.*, **88**, 5703–5709.
7. Chen, C., Tong, H.M., and Tu, K.N. (2010) Electromigration and thermomigration in Pb-free flip-chip solder joints. *Ann. Rev. Mater. Res.*, **40**, 531.
8. Zeng, K. and Tu, K.N. (2002) Six cases of reliability study of Pb-free solder joints in electronic packaging technology. *Mater. Sci. Eng. Rep.*, **R38**, 55–105.
9. JEDEC Test standard (2008): JEP154 guideline for charactering solder bump electromigration under constant and temperature stress. JEDEC SOLID STATE TECHNOLOGY ASSOCIATION, Arlington, USA.
10. Huntington, H.B. and Grone, A.R. (1961) Current-induced marker motion in gold wires. *J. Phys. Chem. Solids.*, **20**, 76–87.
11. Yeh, E.C.C. and Tu, K.N. (2000) Numerical simulation of current crowding phenomena and their effects on electromigration in very large scale integration interconnects. *J. Appl. Phys.*, **88**, 5680–5686.
12. Yeh, E.C.C., Choi, W.J., Tu, K.N. *et al.* (2002) Current-crowding-induced electromigration failure in flip chip solder joints. *Appl. Phys. Lett.*, **80**, 580–582.
13. Shao, T.L., Liang, S.W., Lin, T.C., and Chen, C. (2005) Three-dimensional simulation on current-density distribution in flip-chip solder joints under electric current stressing. *J. Appl. Phys.*, **98**, 044509.
14. Lai, Y.S. and Kao, C.L. (2006) Characteristics of current crowding in flip-chip solder bumps. *Microelectron. Reliab.*, **46**, 915–922.

15. Liang, S.W., Chang, Y.W., and Chen, C. (2006) Effect of Al-trace dimension on Joule heating and current crowding in flip-chip solder joints under accelerated electromigration. *Appl. Phys. Lett.*, **88**, 172108.
16. Nah, J.W., Paik, K.W., Suh, J.O., and Tu, K.N. (2003) Mechanism of electromigration-induced failure in the 97Pb-3Sn and 37Pb-63Sn composite solder joints. *J. Appl. Phys.*, **94**, 7560–7566.
17. Ye, H., Basaran, C., and Hopkins, D. (2003) Thermomigration in Pb-Sn solder joints under joule heating during electric current stressing. *Appl. Phys. Lett.*, **82**, 1045–1047.
18. Chiu, S.H., Shao, T.L., Chen, C. *et al.* (2006) Infrared microscopy of hot spots induced by joule heating in flip-chip SnAg solder joints under accelerated electromigration. *Appl. Phys. Lett.*, **88**, 022110.
19. Shao, T.L., Chen, Y.H., Chiu, S.H., and Chen, C. (2004) Electromigration failure mechanisms for SnAg3.5 solder bumps on Ti/Cr-Cu/Cu and Ni(P)/Au metallization pads. *J. Appl. Phys.*, **96**, 4518–4524.
20. Alam, M.O., Wu, B.Y., Chan, Y.C., and Tu, K.N. (2006) High electric current density-induced interfacial reactions in micro ball grid array (μ BGA) solder joints. *Acta Mater.*, **54**, 613–621.
21. Zhang, L.Y., Ou, S.Q., Huang, J. *et al.* (2006) Effect of current crowding on void propagation at the interface between intermetallic compound and solder in flip chip solder joints. *Appl. Phys. Lett.*, **88**, 012106.
22. Liang, S.W., Chang, Y.W., Shao, T.L. *et al.* (2006) Effect of 3-dimensional current and temperature distribution on void formation and propagation in flip-chip solder joints during electromigration. *Appl. Phys. Lett.*, **89**, 022117.
23. Lin, Y.H., Hu, Y.C., Tsai, C.M. *et al.* (2005) In situ observation of the void formation-and-propagation mechanism in solder joints under current-stressing. *Acta Mater.*, **53**, 2029–2035.
24. Chang, Y.W., Liang, S.W., and Chen, C. (2006) Study of void formation due to electromigration in flip-chip solder joints using Kelvin bump probes. *Appl. Phys. Lett.*, **89**, 032103.
25. Liang, S.W., Chang, Y.W., and Chen, C. (2007) Three-dimensional thermoelectrical simulation in flip-chip solder joints with thick underbump metallizations during accelerated electromigration testing. *J. Electron. Mater.*, **36**, 159–167.
26. Huang, A.T., Gusak, A.M., and Tu, K.N. (2006) Thermomigration in SnPb composite flip chip solder joints. *Appl. Phys. Lett.*, **88**, 141911.
27. Liu, C.Y., Chen, J.T., Chuang, Y.C. *et al.* (2007) Electromigration-induced Kirkendall voids at the Cu/Cu_3Sn interface in flip-chip Cu/Sn/Cu joints. *Appl. Phys. Lett.*, **90**, 112114.
28. Hsiao, H.Y. and Chen, C. (2007) Thermomigration in flip-chip SnPb solder joints under alternating current stressing. *Appl. Phys. Lett.*, **90**, 152105.
29. Huang, A.T., Tu, K.N., and Lai, Y.S. (2006) Effect of the combination of electromigration and thermomigration on phase migration and partial melting in flip chip composite SnPb solder joints. *J. Appl. Phys.*, **100**, 033512.
30. Thomas, C.C. (1995) *Introduction to Thermodynamics of Irreversible Processes*, Springfield, Prigogine. IL, Chap. I.
31. Hsiao, H.Y., Liang, S.W., Ku, M.F. *et al.* (2008) Direct measurement of hot-spot temperature in flip-chip solder joints under current stressing using infrared microscopy. *J. Appl. Phys.*, **104**, 033708.
32. Black, J.R. (1969) Electromigration – a brief survey and some recent results. *IEEE Trans. Electron Devices*, **ED-16**, 338.
33. Gee, S., Kelkar, N., Huang, J., and Tu, K.N. (2005) Lead-free and SnPb bump electromigration testing. Proc. of InterPACK, San Francisco, IPACK2005-73417.
34. Ding, M., Wang, G., Chao, B., and Ho, P.S. (2006) Effect of contact metallization on electromigration reliability of Pb-free solder joints. *J. Appl. Phys.*, **99**, 094906.
35. Lin, Y.L., Lai, Y.S., Tsai, C.M., and Kao, C.R. (2006) Effect of surface finish on the failure mechanisms of flip-chip solder joints under electromigration. *J. Electron. Mater.*, **35**, 2147–2153.

36. Nah, J.W., Suh, J.O., and Tu, K.N. (2005) Effect of current crowding and Joule heating on electromigration-induced failure in flip chip composite solder joints tested at room temperature. *J. Appl Phys.*, **98**, 013715.
37. Lee, T.Y., Tu, K.N., Kuo, S.M., and Frear, D.R. (2001) Electromigration of eutectic SnPb solder interconnects for flip chip technology. *J. Appl. Phys.*, **89**, 3189–3194.
38. Miyazaki, T. and Omata, T. (2006) Electromigration degradation mechanism for Pb-free flip-chip micro solder bumps. *Microelectron. Reliab.*, **46**, 1898–1903.
39. Eaton, D.H., Rowatt, J.D., and Dauksher, W.J. (2006) Geometry effects on the electromtgration of eutectic Sn/Pb flip-chip solder bumps. Proc. IEEE International Reliability Physics Symposium, San Jose, pp. 243–249.
40. Wu, J.D., Zheng, P.J., Lee, C.W. *et al.* (2006) A study in flip-chip UBM/bump reliability with effects of SnPb solder composition. *Microelectron. Reliab.*, **46**, 41–52.
41. Jang, J.W., Ramanathan, L.N., and Frear, D.R. (2008) Electromigration behavior of lead-free solder flip chip bumps on NiP/Cu metallization. *J. Appl. Phys.*, **103**, 123506.
42. Ouyang, F.Y., Tu, K.N., Kao, C.L., and Lai, Y.S. (2007) Effect of electromigration in the anodic Al interconnect on melting of flip chip solder joints. *Appl. Phys. Lett.*, **90**, 211914.
43. Chiu, S.H. and Chen, C. (2006) Investigation of void nucleation and propagation during electromigration of flip-chip solder joints using X-ray microscopy. *Appl. Phys. Lett.*, **89**, 262106.
44. Liang, S.W., Chiu, S.H., and Chen, C. (2007) Effect of degradation of Al line on Joule heating of flip-chip solder joints. *Appl. Phys. Lett.*, **90**, 082103.
45. Yamanaka, K., Tsukada, Y., and Suganuma, K. (2007) Studies on solder bump electromigration in Cu/Sn-3Ag-0.5Cu/Cu system. *Microelectron. Reliab.*, **47**, 1280–1287.
46. Hsu, Y.C., Shao, T.L., Yang, C.J., and Chen, C. (2003) Electromigration study in SnAg3.8Cu0.7 solder joints on Ti/Cr-Cu/Cu under bump metallization. *J. Electron. Mater.*, **32**, 1222–1227.
47. Choi, W.J., Yeh, E.C.C., and Tu, K.N. (2003) Mean-time-to-failure study of flip chip solder joints on Cu/Ni(V)/Al thin-film under-bump-metallization. *J. Appl. Phys.*, **94**, 5665–5671.
48. Lin, Y.L., Chang, C.W., Tsai, C.M. *et al.* (2006) Electromigration-induced UBM consumption and the resulting failure mechanisms in flip-chip solder joints. *J. Electron. Mater.*, **35**, 1010–1016.
49. Chang, Y.W., Chiang, T.H., and Chen, C. (2007) Effect of void propagation on bump resistance due to electromigration in flip-chip solder joints using Kelvin structure. *Appl. Phys. Lett.*, **91**, 132113.
50. Yang, D., Chan, Y.C., and Tu, K.N. (2008) The time-dependent melting failure in flip chip lead-free solder interconnects under current stressing. *Appl. Phys. Lett.*, **93**, 041907.
51. Lin, Y.L., Lai., Y.S., Lin, Y.W., and Kao, C.R. (2008) Effect of UBM thickness on the mean time to failure of flip-chip solder joints under electromigration. *J. Electron. Mater.*, **37**, 96–101.
52. Chen, C.M. and Chen, S.W. (2001) Electromigration effect upon the Sn-0.7 wt% Cu/Ni and Sn-3.5 wt% Ag/Ni interfacial reactions. *J. Appl. Phys.*, **90**, 1208–1214.
53. Lin, C.T., Chuang, Y.C., Wang, S.J., and Liu, C.Y. (2006) Current density dependence of electromigration-induced flip-chip Cu pad consumption. *Appl. Phys. Lett.*, **89**, 101906.
54. Liu, C.Y., Ke, L., Chuang, Y.C., and Wang, S.J. (2006) Study of electromigration-induced Cu consumption in the flip-chip Sn/Cu solder bumps. *J. Appl. Phys.*, **100**, 083702.
55. Xu, L.H., Han, J.K., Liang, J.J. *et al.* (2008) Electromigration induced high fraction of compound formation in SnAgCu flip chip solder joints with copper column. *Appl. Phys. Lett.*, **92**, 262104.
56. Gan, H. and Tu, K.N. (2005) Polarity effect of electromigration on kinetics of intermetallic compound formation in Pb-free solder V-groove samples. *J. Appl. Phys.*, **97**, 063514.
57. Orchard, H.T. and Greer, A.L. (2005) Electromigration effects on compound growth at interfaces. *Appl. Phys. Lett.*, **86**, 231906.
58. Kim, P.G., Jang, J.W., Lee, T.Y., and Tu, K.N. (1999) Interfacial reaction and wetting behavior in eutectic SnPb solder on Ni/Ti thin films and Ni foils. *J. Appl. Phys.*, **86**, 6746–6751.

59. Kim, H.K. and Tu, K.N. (1995) Rate of consumption of Cu soldering accompanied by ripening. *Appl. Phys. Lett.*, **67**, 2002–2004.
60. Shewmon, P.G. (1989) *Diffusion in Solids*, TMS, Warrendale, Chap. 7.
61. Ragone, D.V. (1995) *Thermodynamics of Materials*, vol. **2** John Wiley & Sons, New York, Chap. 8.
62. Ebersberger, B., Bauer, R., and Alexa, L. (2005) Reliability of lead-free SnAg solder bumps: influence of electromigration and temperature. Proc. of the Electronic Components and Technology Conference, 55th, Orlando, 32, pp. 1407–1415.
63. Liang, S.W., Chang, Y.W., and Chen, C. (2006) Geometrical effect of bump resistance measurement by Kelvin structure. *J. Electron. Mater.*, **35**, 1647–1654.
64. Chae, S.H., Zhang, X., Chao, H.L. *et al.* (2006) Electromigration lifetime statistics for Pb-free solder joints with Cu and Ni UBM in plastic flip-chip packages. Proc. of the Electronic Components and Technology Conference, 56th, San Diego, 15, pp. 650–657.
65. http://www.nist.gov/.
66. Yang, P.C., Kuo, C.C., and Chen, C. (2008) The effect of pre-aging on the electromigration of flip-chip snag solder joints. *JOM.*, **60**, 77–80.
67. Chen, Y.H., Shao, T.L., Liu, P.C. *et al.* (2005) Microstructure evolution during electromigration in eutectic SnPb solder bumps. *J. Mater. Res.*, **20**, 2432–2442.
68. Chao, B., Chae, S.H., Zhang, X.F. *et al.* (2006) Electromigration enhanced intermetallic growth and void formation in Pb-free solder joints. *J. Appl. Phys.*, **100**, 084909.
69. Glenn, A.R. (2003) Issues in accelerated electromigration of solder bumps. *Microelectron. Reliab.*, **43**, 1975–1980.
70. Lai, Y.S., Chen, K.M., Kao, C.L. *et al.* (2007) Electromigration of Sn-37Pb and Sn-3Ag-1.5Cu/Sn-3Ag-0.5Cu composite flip-chip solder bumps with Ti/Ni(V)/Cu under bump metallurgy. *Microelectron. Reliab.*, **47**, 1273–1279.
71. Liu, Y.H. and Lin, K.L. (2005) Damages and microstructural variation of high-lead and eutectic SnPb composite flip chip solder bumps induced by electromigration. *J. Mater. Res.*, **20**, 2184–2193.
72. Chou, C.K., Hsu, Y.C., and Chen, C. (2006) Electromigration in Eutectic SnPb Solder Stripes. *J. Electron. Mater.*, **35**, 1655–1659.
73. Gupta, D., Vieregge, K., and Gust, W. (1999) Interface diffusion in eutectic Pb-Sn solder. *Acta Mater.*, **47**, 5–12.
74. Chou, C.K., Chen, C.A., Liang, S.W., and Chen, C. (2006) Redistribution of Pb-rich phase during electromigration in eutectic SnPb solder stripes. *J. Appl. Phys.*, **99**, 054502.
75. Lloyd, J.R. (2003) Electromigration induced resistance decrease in Sn conductors. *J. Appl. Phys.*, **94**, 6483–6486.
76. Wu, A.T., Tu, K.N., Lloyd, J.R. *et al.* (2004) Electromigration-induced microstructure evolution in tin studied by synchrotron X-ray microdiffraction. *Appl. Phys. Lett.*, **85**, 2490–2492.
77. Wu, A.T., Gusak, A.M., Tu, K.N., and Kao, C.R. (2005) Electromigration-induced grain rotation in anisotropic conducting beta tin. *Appl. Phys. Lett.*, **86**, 241902.
78. Tsai, C.M., Lin, Y.L., Tsai, J.Y. *et al.* (2006) Local melting induced by electromigration in flip-chip solder joints. *J. Electron. Mater.*, **35**, 1005–1009.
79. Chang, Y.W., Chiu, S.H., and Chen, C.,(2010) Investigation of void nucleation and propagation on the Joule heating effect during electromigration in flip-chip solder joint. *J. Electron. Mater*, **39** (11), 2489–2494.
80. Liu, C.Y., Chen, C., and Tu, K.N. (1999) Direct correlation between mechanical failure and metallurgical reaction in flip chip solder joints. *J. Appl. Phys.*, **85**, 3882–3886.
81. Jang, J.W., Silva, A.P.D., Lee, T.Y. *et al.* (2001) Direct correlation between microstructure and mechanical tensile properties in Pb-free solders and eutectic SnPb solder for flip chip technology. *Appl. Phys. Lett.*, **79**, 482–484.

82. Ren, F., Nah, J.W., Tu, K.N. *et al.* (2006) Electromigration induced ductile-to-brittle transition in lead-free solder joints. *Appl. Phys. Lett.*, **89**, 141914.
83. Zhang, L., Wang, Z.G., and Shang, J.K. (2007) Current-induced weakening of Sn3.5Ag0.7Cu Pb-free solder joints. *Scr. Mater.*, **56**, 381–384.
84. Nah, J.W., Ren, F., Paik, K.W., and Tu, K.N. (2006) Effect of electromigration on mechanical shear behavior of flip chip solder joints. *J. Mater. Res.*, **21**, 698–702.
85. Lu, M., Shih, D.Y., Lauro, P. *et al.* (2008) Effect of Sn grain orientation on electromigration degradation mechanism in high Sn-based Pb-free solders. *Appl. Phys. Lett.*, **92**, 211909.
86. Dyson, B.F., Anthony, T.R., and Turnbull, D. (1967) Interstitial diffusion of copper in tin. *J. Appl. Phys.*, **38**, 3408.
87. Yeh, D.C. and Huntington, H.B. (1984) Extreme fast-diffusion system – nickel in single-crystal tin. *Phys. Rev. Lett.*, **53**, 1469–1472.
88. Xu, L.H., Pang, J.H.L., and Tu, K.N. (2006) Effect of electromigration-induced back stress gradient on nanoindentation marker movement in SnAgCu solder joints. *Appl. Phys. Lett.*, **89**, 221909.
89. Wu, B.Y., Chan, Y.C., Zhong, H.W. *et al.* (2007) Study of the thermal stress in a Pb-free half-bump solder joint under current stressing. *Appl. Phys. Lett.*, **90**, 232112.
90. Ouyang, F.Y., Chen, K., Tu, K.N., and Lai, Y.S. (2007) Effect of current crowding on whisker growth at the anode in flip chip solder joints. *Appl. Phys. Lett.*, **91**, 231919.
91. Chen, H.Y., Chen, C., and Tu, K.N. (2008) Failure induced by thermomigration of interstitial Cu in Pb-free flip chip solder joints. *Appl. Phys. Lett.*, **93**, 122103.

16

Effects of Electromigration on Electronic Solder Joints

Sinn-wen Chen[1], *Chih-ming Chen*[2], *Chao-hong Wang*[3], *and Chia-ming Hsu*[1]
[1] *Department of Chemical Engineering, National Tsing Hua University, #101, Sec. 2, Kuang-Fu Rd., Hsin-Chu 300, Taiwan*
[2] *Department of Chemical Engineering, National Chung Hsing University, #250, Kuo Kuang Rd., Taichung 402, Taiwan*
[3] *Department of Chemical Engineering, National Chung Cheng University, #168, University Road, Chiayi 621, Taiwan*

Abstract

A unique characteristic of electronic solder joints is the passage of electric currents. In addition to the Joule heating, the passage of electric currents causes electromigration. Electromigration is the mass transport of metal atoms induced by current stressing, and it affects the microstructures of solders and the interfacial reactions at solder joints. Phase segregation, void formation and Sn extrusion in the solder matrix and other microstructural evolutions of solders have been observed. It has also been reported that the growth of intermetallic compounds would be either enhanced or retarded with the passage of electric currents. This chapter reviews the current understanding and observation of electromigration on electronic solder joints. In addition to experimental investigations, mathematical model descriptions of electromigration effects are summarized as well.

16.1 Introduction

Soldering is a very important joining technology in the electronic packaging industry [1]. Owing to health and environmental concerns [2], the conventional Sn-Pb solders are being

Lead-free Solders: Materials Reliability for Electronics, First Edition. Edited by K. N. Subramanian.

replaced by Pb-free solders [3–5]. In addition to the challenges of bringing new Pb-free solder alloys into electronic manufacturing, various emerging soldering techniques, such as ball-grid array (BGA), flip-chip and through-silicon via (TSV), have all together made soldering technology very critical to electronic products [6].

Electromigration is the mass transport of metal atoms induced by current stressing [7]. In general, the atomic flux due to electromigration can be expressed as the product of mobility and force, as suggested by Huntington and Grone [8]:

$$J = CV_{\mathrm{EM}} = CmF_{\mathrm{total}} = C\left(\frac{D_{\mathrm{eff}}}{kT}\right)Z^{*}e\rho j$$

where J is the atomic flux, C is the concentration of migrating species, D is the diffusivity of migrating species, V_{EM} is the drift velocity of the conductor, m is the mobility, D_{eff} is the effective diffusivity, k is Bolzmann's constant, T is the absolute temperature, Z^{*} is the effective charge, e is electronic charge, ρ is the metal resistivity, and j is the current density.

With the reducing scale and higher current density of solder joints, the electromigration effect has become much more significant. The reliability concern of solder joints caused by electromigration can be categorized in two main parts: microstructural changes of solders and the suppression or enhancement of growth of intermetallic compounds (IMCs) at the interfaces. The microstructural changes of solder alloys induced by electromigration include void formation, hillock formation, and phase segregation.

This chapter reviews the current understanding of the two main effects of electromigration on electronic solder joints. Section 16.2 focuses on the effects of electromigration on microstructural changes of solder matrix. Section 16.3 describes the various phenomena observed regarding effects of electromigration on interfacial reactions, such as symmetric and asymmetric layer growth. In addition toexperimental observations, the mathematical modeling of electromigration effects is also discussed in Section 16.4.

16.2 Effects of Electromigration on Solders

Most of the elements used in solder alloys have negative effective charges [7]. When only electromigration is considered, the atoms with negative effective charges move along with the flow of electrons, and the atoms migrate from the cathode side to the anode side. Atomic accumulation could generate compressive stress at the anode side, and voids might form at the cathode side.

It needs attention that there are confusions about the terms of cathode and anode in the literature. Cathode is the electrode that electric current flows out of and the anode is the one that electrons flow into. Since the structure of solder joint is usually substrate/solder/substrate, and the cathode is the side where the electrons flow in from the substrate toward the solder, the anode is the one that electrons flow out from the solder to the substrate. However, the structure setups in some experimental designs are solder/substrate/solder, the cathode and anode would have opposite flowing directions of electrons from the solder toward substrate or vice versa. In order to avoid confusion, unless it is very clear, the terms 'substrate to solder' and 'solder to substrate' should be used instead of cathode and anode.

Most solder alloys comprise two elements or more. The passage of electric current through alloys provides driving forces of electromigration on atomic fluxes. However, different elements have different diffusivities and effective charges [7]. The dominant migrating element, which is the one of the highest product of diffusivity and effective charge ($D_{\text{eff}} \times Z^*$), moves toward the anode. The dominant migrating flux could generate and impose stress on other kinds of atoms in the solders, and the stress could have an effect on the atomic fluxes of other elements. The microstructural evolution of solders depends on the atomic fluxes of all constituent elements, and the interactions of the constituent elements should be considered in the discussion concerning the effects of electromigration upon solders.

Electromigration effects on solders can be classified into three types. The first type of effect is observed in solders whose constituent elements, except the dominant moving species, show high resistance against electromigration and remain nearly immobile. The second type of effect is seen in solders with elements moving along with the electrons in addition to the migration of the element of highest $D_{\text{eff}} \times Z^*$, leading to more severe void and hillock formation. However, if the compressive stress cannot be efficiently released by hillock formation, reversed fluxes of the other elements from the anode to the cathode occur in the third type of effect to release the stress, leading to phase separation.

16.2.1 Solder Joints with Primarily Only One Moving Species

The Sn-9 wt%Zn solder shows an electromigration effect of the first type. Figure 16.1 is a schematic diagram of the sample configuration for the electromigration study [9], and the solder fills in the middle trench of the Cu. After current stressing (10^5 A/cm^2 density) at 80 °C for 240 h, the solder experiences a microstructural change as seen in Figure 16.2. Sn is extruded out of the solder surface (as indicated by the dotted circle), indicating that Sn is the dominant migrating species in the Sn-9 wt%Zn solder under electromigration [9–11]. In contrast, the other element, Zn, is nearly immobile under electromigration because the shape and orientation of the Zn-rich precipitates remain almost the same before and after current stressing.

It is found that the microstructure of the solder also has a significant effect on the electromigration behavior [9]. For the fan-cooled solder with finer Zn precipitates, the

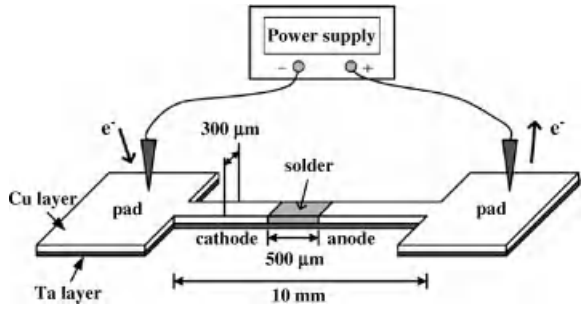

Figure 16.1 *A schematic showing one type of sample configuration for the electromigration study.*

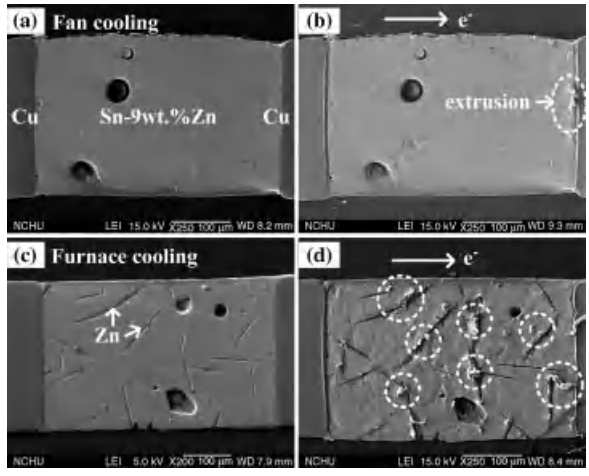

Figure 16.2 *(a) The fan-cooled Sn-9 wt%Zn solder stripe before current stressing. (b) The fan-cooled Sn-9 wt%Zn solder stripe after current stressing of 10^5 A/cm^2 at 80°C for 240 h. (c) The furnace-cooled Sn-9 wt%Zn solder stripe before current stressing. (d) The furnace-cooled Sn-9 wt%Zn solder stripe after current stressing of 10^5 A/cm^2 at 80°C for 240 h.*

surface microstructure of the solder is almost unaffected, except for the formation of some Sn-rich extrusion sites at the anode end, as shown in Figure 16.2b. In contrast, in the furnace-cooled solder with coarse needle-like Zn-rich precipitates, many Sn-rich extrusion sites are formed not only at the anode end but also within the solder, principally near the Zn-rich precipitates, as shown in Figure 16.2d. The above results suggest that a rapid cooling rate of the reflow process may be a good strategy to improve the electromigration resistance of the Sn-9 wt%Zn solder.

The most popular Pb-free solder alloys, Sn-3 wt%Ag-0.5 wt%Cu [12], Sn- 4 wt%Ag-0.5 wt%Cu [13], and Sn-0.7 wt%Cu [14], all show an electromigration effect of the first type. In these Sn-rich solders, Sn is the dominant migrating species. Voids are usually formed at the cathode, the substrate to solder side, of the solder joints due to the electromigration-induced atomic departure of Sn. No noticeable movement of the Cu_6Sn_5 and Ag_3Sn precipitates is reported, which may be attributed to the higher resistance of the intermetallic compounds against electromigration. In comparison with the conventional eutectic Sn-Pb solder, the Sn-Ag-Cu-based solders exhibit higher resistance against electromigration [15–17].

16.2.2 Solder Joints with Significant Hillock and Void Formation

The following Sn-Bi solder is an example of solder exhibiting an electromigration effect of the second type. Figure 16.3a shows another sample configuration for electromigration study [18]. The sample is prepared by depositing a patterned Sn-Bi solder thin film of 20 μm thickness on a Cu trace. The plan-view SEM image of the as-prepared sample is shown in Figure 16.3b. After current stressing (1.3×10^4 A/cm^2) at 85 ± 3 °C for 240 h, solder depletion and mass accumulation of Bi are observed at both the cathode and anode, as shown in Figures 16.3c and d, respectively. Mass accumulation of Bi at the anode and solder depletion at the cathode reveals that electromigration drives both Bi and Sn to depart from the cathode.

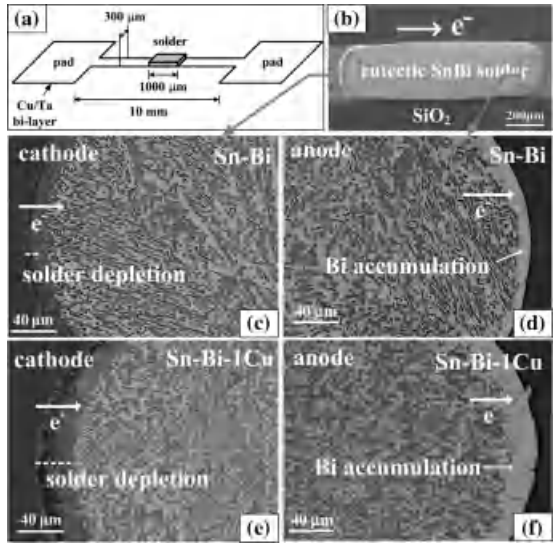

Figure 16.3 *(a) A schematic of the thin-film-type solder sample used for the electromigration study. (b) The plan-view scanning electron microscope image of a real sample. (c) The cathode end of the eutectic SnBi solder after current stressing (1.3×10^4 A/cm^2, 85 ± 3 °C) for 240 h. (d) The anode end of the eutectic SnBi solder after current stressing. (e) The cathode end of the SnBi-1Cu solder after current stressing. (f) The anode end of the SnBi-1Cu solder after current stressing.*

Even with the same alloys, their responses to electromigration could vary with temperatures. The Sn-8 wt%Zn-3 wt%Bi solder alloy at 80 °C shows the first type of electromigration effect. Upon current stressing with a density of 10^5 A/cm^2 at 80 °C, the Bi atoms in the fan-cooled solder migrate to the anode end, but Sn and Zn are relatively immobile [19]. The amount of Bi is only 3 wt%; hence, its migration does not cause any noticeable change in the microstructure of solder. However, when the temperature is raised to 125 °C, the effect of electromigration is enhanced and not only Bi but also Sn migrates. Excess migration of Sn results in the formation of Sn extrusion and voids near the anode and cathode, respectively, as shown in Figure 16.4. The Sn-8 wt%Zn-3 wt%Bi solder at 125 °C thus exhibits an electromigration effect of the second type.

16.2.3 Solder Joints with Phase Segregation

In some sample configurations, the effects of electromigration on the eutectic Sn-Bi solder are of the third type [20–22]. By passing a direct current with a density of 6.5×10^3 A/cm^2 through the solder ball sandwiched between two Ni bond pads, as shown in Figure 16.5a, the initial eutectic microstructure as shown in Figure 16.5b changes gradually and phase segregation appears. Bi atoms segregate to the anode, while a Sn-rich layer forms at the cathode, as shown in Figures 16.5c and d, respectively. This phenomenon is more pronounced in the bulk-type Sn-Bi eutectic solder, as shown in Figure 16.6 [22]. Bi atoms migrates to the anode under electromigration, while Sn atoms are passively pushed back to fill the vacancies at the cathode caused by the departure of

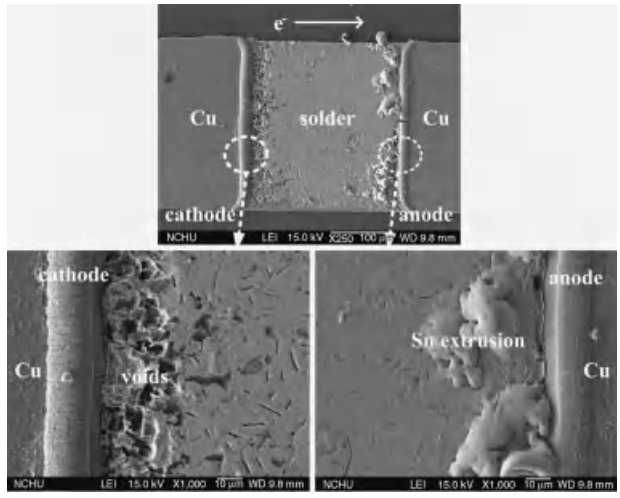

Figure 16.4 *The fan-cooled Sn-8 wt%Zn-3 wt%Bi solder stripe after current stressing of 10^5 A/cm^2 at 125°C.*

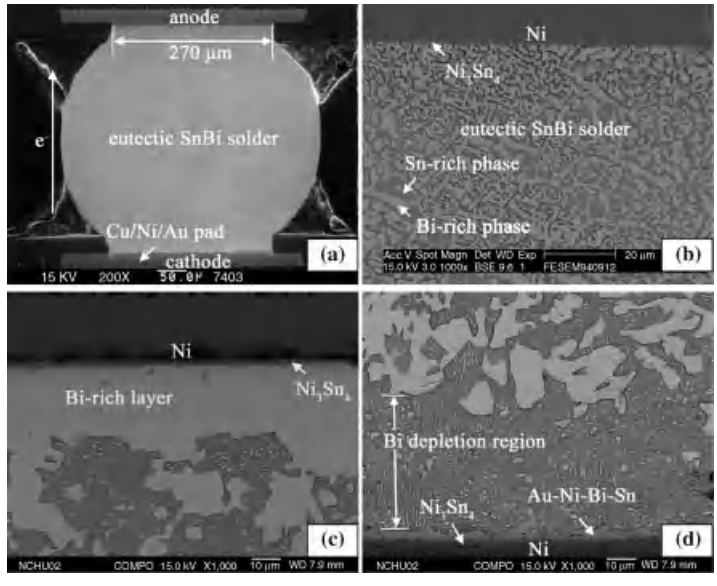

Figure 16.5 *Microstructural evolution of the eutectic SnBi solder under current stressing of 6.5×10^3 A/cm^2 at 70°C. (a) The eutectic SnBi solder ball sandwiched between two Ni bond pads as the sample for the electromigration study. (b) The initial eutectic microstructure of the eutectic SnBi solder before current stressing. (c) The microstructure at the anode side after 15 days of current stressing of 6.5×10^3 A/cm^2 at 70°C. (d) The microstructure at the cathode side after 15 days of current stressing of 6.5×10^3 A/cm^2 at 70°C.*

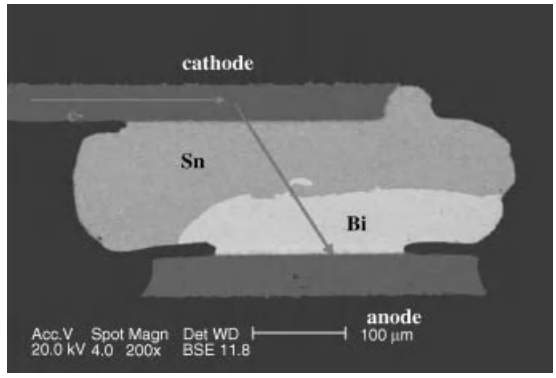

Figure 16.6 *Pronounced phase separation in a bulk-type Sn-Bi solder joint under a current density of* 5×10^3 *A/cm*^{2} *at 75°C.*

the Bi atoms [20, 22]. As a result, no voids are formed at the cathode due to the refilling of the Sn atoms.

Phase separation is also observed in the eutectic Sn-Pb [16, 23, 24] and in Sn-In solders [25]. Similar to Bi atoms, Pb atoms migrate along with the electrons and move to the anode, while Sn atoms are pushed back to the cathode, as shown in Figure 16.7 [16]. However, in the eutectic Sn-In solder, Sn is the dominant migrating species under electromigration. Sn atoms accumulate at the anode, while In atoms are displaced along the opposite direction.

In the thin-film-type solder sample, the surface-to-volume ratio is large, and the compressive stress can be released by the formation of solder hillocks or extrusion out of the film surface. However, in the ball-type solder sample, the surface-to-volume ratio is relatively small. The compressive stress cannot be completely released from the limited ball surface. Thus, in order to release the compressive stress, reversed Sn migration from the anode to the cathode occurs. As a result, phase separation develops gradually. In the solder joint of commercial products, phase separation is easier to develop. This is because the solder ball is encapsulated within the underfill, no free surface is provided for the formation of hillocks and extrusion, so that the reversed Sn migration is the most efficient way to release the compressive stress.

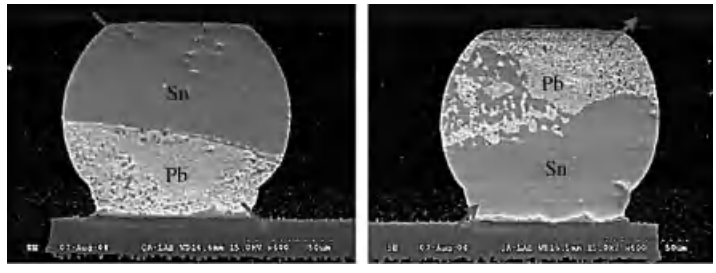

Figure 16.7 *Pronounced phase separation in a bulk-type Sn-Pb solder joint under a current of 0.6 A at 135°C for 306 h. The arrows indicate the flow direction of electrons.*

16.3 Effects of Electromigration on Interfacial Reactions

When solder and substrates are brought into contact at the solder joints, diffusion of atoms and interfacial reactions usually occur. In most situations, IMCs form at the interface [26, 27]. The mechanical properties of IMCs are different from those of solders and substrates. Formation and growth of IMCs are thus important to the reliabilities of solder joints, and there have been many investigations on the interfacial reactions at the solder joints [27–30]. The passage of electric current at a solder joint causes Joule heating, thus raising the temperature of the joint, and accelerating interfacial reactions [31, 32].

In addition to the effects of Joule heating, passage of electric current also causes other effects, such as the electromigration effect and the Peltier effect [31–34]. As mentioned previously, electromigration is the mass transport of metal atoms induced by current stressing [7]. Since the growth of IMCs is a result of the interfacial atomic fluxes, the atomic fluxes caused by electromigration should play a role in interfacial reactions. Ever since the first paper published in 1998 addressing the polarization effect of interfacial reactions caused by electromigration [35], the effects of electromigration on interfacial reactions in solders have attracted very intensive investigations [36–63].

The effects of electromigration on interfacial reactions vary with materials systems as well as current densities. It has been observed that the passage of electric currents could either have no effect on the thickness of the reaction layer [48, 49], or enhance the layer growth in one current direction and retard the growth at the opposite direction [39–47], or enhance the layer growth in both directions [35, 48]. Most studies on effects of electromigration found that only the growth rates of the IMCs were changed but not the types of reaction products. However, different reaction phases are observed in some samples with the passage of electric current [50, 52].

16.3.1 Asymmetric IMC Layer Growth (Electron from Solder to Substrate: Enhancement, Electron from Substrate to Solder: Suppression)

The earliest paper on asymmetric IMC growth in solder samples is about the effects of electromigration on interfacial reaction of the Sn/Ag system [39]. The reaction specimen shown in Figure 16.8 is a sandwich-type configuration of solder/substrate/solder [40]. The flow direction of electrons at interface I is from Sn to Ag but is reversed at interface II, which is from Ag to Sn. The reaction phase at 120–200 °C is the Ag_3Sn phase at both interfaces with and without passage of electric current [39]. However, the passage of electric current significantly affects the growth rate of the Ag_3Sn phase. As shown in Figure 16.9, in the

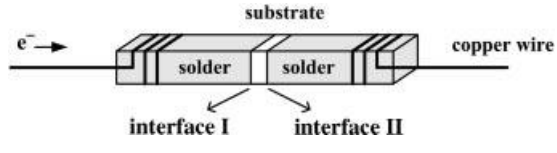

Figure 16.8 *A schematic of the reaction couple designed for the study of the electromigration effects upon the interfacial reactions.*

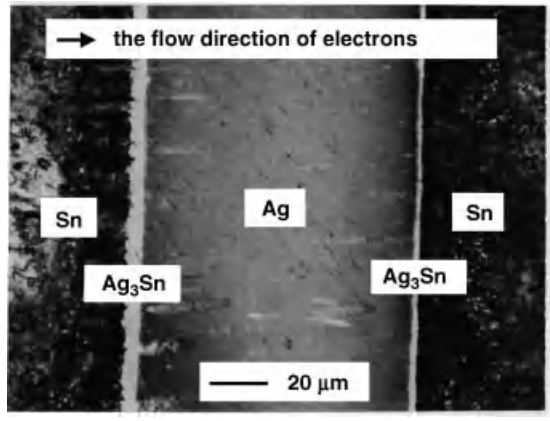

Figure 16.9 *The Sn/Ag/Sn reaction couple after current stressing of 500 A/cm^2 at 140°C for 480 h.*

reaction couple reacted at 140 °C for 480 h, the growth of the Ag_3Sn phase is enhanced at interface I but retarded at interface II.

This polarity effect caused by electromigration was also observed in Sn/Ni/Sn reaction specimens [41, 42]. For the Sn/Ni/Sn specimens reacted at 160 °C with the passage of 500 A/cm^2 electric current, the Ni_3Sn_4 phase at interface I is thicker than that at interface II. This polarity effect of reaction enhancement at the 'solder to substrate' side and suppression at the 'substrate to solder' side has been observed in various other systems [43–45]. For example, the Cu-Zn compound is also thicker at the 'solder to substrate' side in the Sn-9 wt% Zn/Cu system [43]. In all these above-mentioned samples, the reaction is enhanced when the electromigration-induced flux is in the same direction as the dominant migrating flux caused by chemical potential gradients, and the reaction is retarded when the two fluxes are in opposite directions.

Figure 16.10 is the IMC layer thickness in the Cu/Sn-3.8 wt%Ag-0.7 wt%Cu/Cu couple reacted at 180 °C with the passage of current of 3.2×10^4 A/cm^2 density [46]. The IMC is thicker at the interface where electrons are from the Sn-3.8 wt%Ag- 0.7 wt%Cu solder to the Cu substrate, and the phenomenon is similar to those mentioned previously. However, it is revealed that Cu is the dominant diffusion species in their experimental conditions [46], and the results cannot be simply explained by addition or subtraction of diffusion fluxes and electromigration fluxes. The effect of 'back stress' on the magnitudes of fluxes has been proposed to be the primary mechanism [46].

16.3.2 Asymmetric IMC Layer Growth (Electron from Solder to Substrate: Suppression, Electron from Substrate to Solder: Enhancement): Peltier Effect

Figure 16.11 is the micrograph of the Sn/Co/Sn couple reacted at 180 °C for 24 h with passing an electric current of 5000 A/cm^2 density [47]. It can be observed that the $CoSn_3$ layer at the 'substrate to solder' side, the interface II, was 40% thicker than that at the 'solder to substrate' side, the interface I. The electric current enhances the growth of IMC at the side

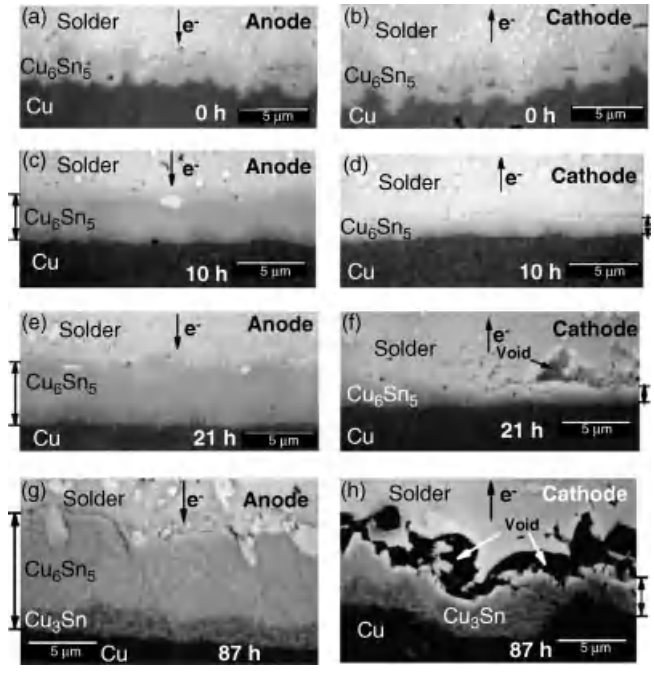

Figure 16.10 *The IMC layer thickness in the Cu/Sn-3.8 wt%Ag-0.7 wt%Cu/Cu couple reacted at 180°C with the passage through of current of 3.2×10^4 A/cm^2 density.*

where electrons are from substrate to solder and retards the growth of IMC at the other side, and the results are different from those mentioned in Section 16.3.1 The asymmetric effect in the Sn/Co/Sn is caused by the Peltier effect. The Peltier effect is the liberation or absorption of heat at the junction of the metals with the passage of electric current, and is a result of the fact that carriers also carry heat when they flow through a conductor. It has been

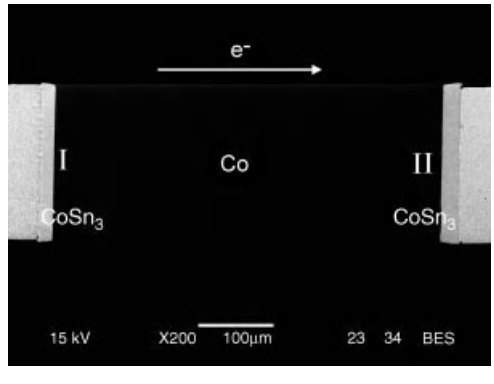

Figure 16.11 *The Sn/Co/Sn reaction couple after current stressing of 5000 A/cm^2 at 180°C for 24 h.*

demonstrated that the growth difference between the both interfaces results from the temperature difference of about 4.5 °C caused by the Peltier effect [47].

16.3.3 Symmetric IMC Layer Growth (Cathode and Anode: Enhancement or Suppression)

In the Al/Ni couple reacted at 400 °C [35] with and without the passage of electric current, Al_3Ni_2 and Al_3Ni phases are formed. The reaction layers at both the cathode and anode in the couple with the passage of electric current of 500 A/cm^2 density are thicker than those in the couples without passage of electric currents. This symmetric enhancement of layer growth by electromigration at both the cathode and anode is as interesting as the above-mentioned asymmetric effect. It is likely that the current enhances the nucleation of reaction phases, and the layer thickness is not only controlled by the accumulation of atomic fluxes [35]. Similar symmetric enhancement of IMC layer growth has also been found in the Bi/Ni couple [48], but the mechanism remains unclear.

16.3.4 No Effect with Passage of Electric Current

It has also been found that the passage of electric currents had no effect on the thickness of the reaction layer in various samples [48, 49]. For example, no polarity effect was observed in the Zn/Ni couple reacted at 200 °C with the passage of a 300-A/cm^{2}current [48]. No effect in the Sn/Cu/Sn specimen at 200 °C with the passage of a 500-A/cm^2 current [49] can be observed either. It is likely that the electromigration-induced flux is much smaller than the atomic fluxes driven by chemical potential gradients. The relatively small electromigration flux could be the result of small effective charge of Z^* of the dominant migration atoms, or small electric current.

16.3.5 Effects of Electromigration on Reaction Phases: Evolution of Reaction Phase and Alternating Layer Formation

For most of the experiments with the passage of electric current, the reaction phase is the same but the growth rates are different. However, different reaction products have also been observed in the samples with and without passage of electric currents. In the Sn/Ni couples reacted at 120 °C, in addition to the Ni_3Sn_4 phase, a metastable $NiSn_4$ phase is also formed [50, 51]. However, with the passage of an electric current of 5000 A/cm^2 density, only the Ni_3Sn_4 phase is formed at both interfaces, but the $NiSn_4$ phase is found only at the 'substrate to solder' side, the interface II. The electron current flow alters the reaction phase, that is, the formation of $NiSn_4$ phase is suppressed at the 'solder to substrate' side.

Figure 16.12 is the micrograph of the Sn-0.7 wt%Cu/Ni couple reacted at 180 °C with 2000 A/cm^2 current stressing for 240 h [52]. Different reaction products are observed at the cathode and the anode sides. The Cu_6Sn_5 phase is found at interface I, while the Cu_6Sn_5 and Ni_3Sn_4 are formed at interface II. In the Sn-0.7 wt%Cu/Ni couples without current stressing, the initial reaction product is Cu_6Sn_5 [52]. With longer reaction time, the Ni_3Sn_4 would form due to the depletion of Cu element. It has been found that the reaction products are sensitive to the Cu concentration [53, 54]. The difference of the reaction products observed in the cathode and anode sides in the Sn-0.7 wt%Cu/Ni couples [55] are likely caused by the

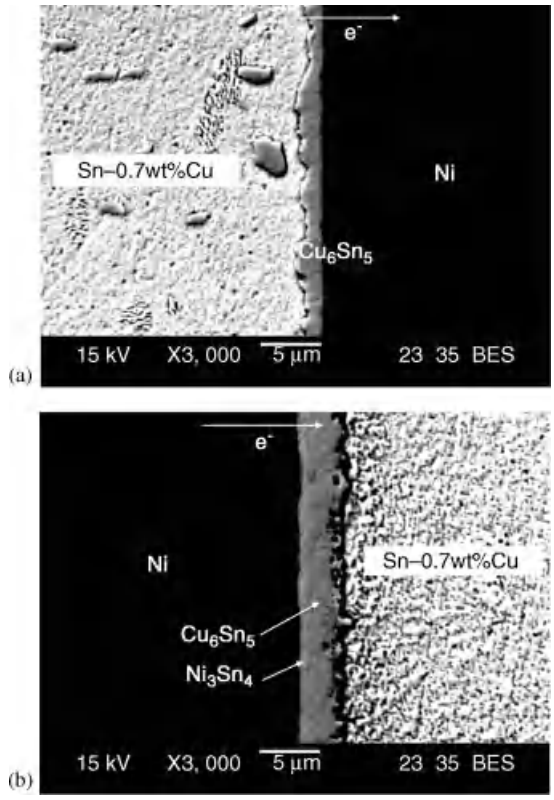

Figure 16.12 *The Sn-0.7 wt%Cu/Ni/Sn-0.7 wt%Cu reaction couple after current stressing of 2000 A/cm^2 at 180°C for 240 h. (a) Interface I and (b) Interface II.*

asymmetric effects of reaction phase growth. The difference in the reaction products is in fact only the shift in the time frame of reaction-phase evolution, and the reaction products would all become Ni_3Sn_4 phase with longer reaction time.

The evolution of phase formation is also found in the Sn/Ni-7 wt%V couples [56]. Ni-7 wt% V is one of the UBM (under-bump metallization) materials. Without current stressing, the initial product is T phase, and then it becomes T/Ni_3Sn_4. Finally, the interesting phenomenon, T/Ni_3Sn_4/T/Ni_3Sn_4, is found. As shown in Figure 16.13, the alternating T/Ni_3Sn_4/T/Ni_3Sn_4 is formed after reaction at 200 °C for 168 h with passage of electric current of 500 A/cm^2 density. The overall reaction layers are thicker at interface I, which is attributed to the Sn flux induced by electromigration. It was also found that the alternating layer formed at the interface I was earlier than that at interface II under current stressing. This indicates that the effect of electric currents causes the different evolution time of reaction phases.

16.3.6 Microstructural Changes Caused by Electromigration

Figure 16.14 is the micrograph of the Sn/Cu/Sn couple reacted at 170 °C for 120 h with passage of 5000 A/cm^2 current [57]. Both Cu_6Sn_5 and Cu_3Sn phase layers are formed at the

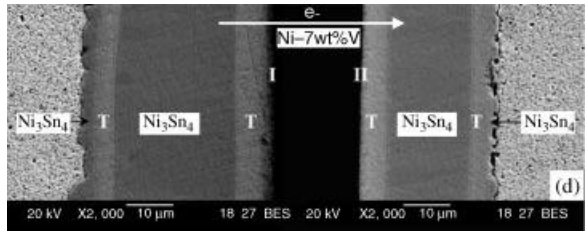

Figure 16.13 *The Sn/Ni-7 wt%V/Sn couple reacted at 200°C for 168 h with the passage of an electric current of 500 A/cm^2.*

'solder to substrate' side, and the results are similar to those reacted in the same condition for shorter reaction time. However, very different microstructure is observed at the 'substrate to solder' side: very thin IMC layers are observed at the interface, while abnormally large and nonplanar Cu_6Sn_5 phase is found in the solder matrix. The asymmetric microstructure is more significant with longer reaction time and higher reaction temperatures. Similar microstructural change phenomena are found in various samples, especially in the solder/Cu systems [51, 57–63]. The diffusion of Cu is greatly enhanced with the passage of electric currents, and the substantial Cu atom accumulation results in the formation of extremely large Cu_6Sn_5 phases.

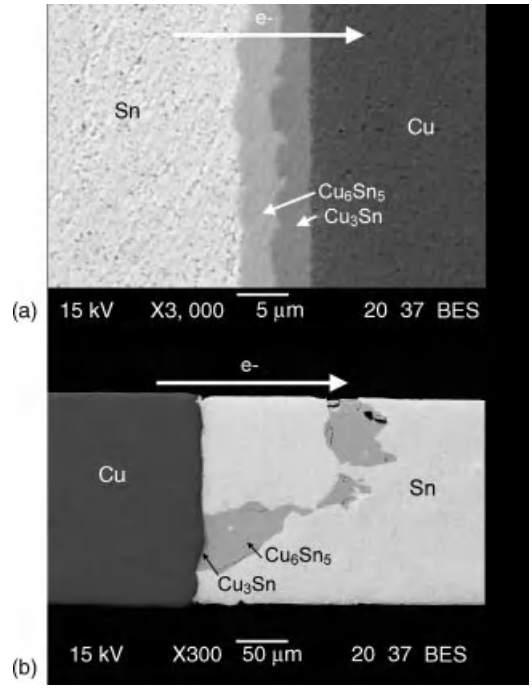

Figure 16.14 *The Sn/Cu/Sn reaction couple reacted at 170°C for 120 h with the passage of an electric current of 5000 A/cm^2. (a) Interface I and (b) Interface II.*

16.4 Modeling Description of Effects of Electromigration on IMC Growth

According to these experimental results mentioned above, there are several kinds of growth modes regarding the effects of electromigration on IMC growth. In some cases, the current has no effect on the growth of IMC layers [48, 49]. In other cases, a direct current induces asymmetric effects, enhancement at one interface and suppression at the other, or symmetric effects, a symmetrical enhancement or suppression of growth at both cathode and anode sides [39–48, 64, 65, 76–83]. Several mathematical models have been proposed to describe the effects of electromigration on the growth of IMCs [67–71]. These models could be grouped into three major kinds: atomic flux summation model, atomic flux summation with stress modification model, and a generalized model considering the changes in reaction and mechanism [72]

16.4.1 The Atomic Flux Summation Model

With the passage of electric current, the atomic fluxes at the solder joints are driven both by the chemical potential gradient and electromigration effect, and the atomic fluxes are the sum of diffusion flux and electromigration flux. The atomic fluxes could be described by the Nernst–Einstein equation [66] if the two fluxes are in the same direction:

$$J = -D\nabla C + C\left(\frac{D_{\text{eff}}}{kT}\right)Z^* e\rho j \tag{16.1}$$

If the directions of two fluxes are opposite, the flux equation is written as:

$$J = -D\nabla C - C\left(\frac{D_{\text{eff}}}{kT}\right)Z^* e\rho j \tag{16.2}$$

With reference to the concept of the Nernst–Einstein equation, kinetic analysis of the electromigration effect on growth of the IMC layer is developed [67–71]. According to the law of mass conservation, the flux of solute crossing the interface equals the flux summation of the two adjoining phases α and β [67, 68]. The velocity of the interface movement can be expressed as:

$$\begin{aligned} v &= \frac{\mathrm{d}x}{\mathrm{d}t} = v_{\text{chem}} + v_{\text{EM}} \\ &= \frac{1}{C_{\alpha\beta} - C_{\beta\alpha}}\left\{\left(\tilde{D}_\beta \frac{\partial C_\beta}{\partial x} - \tilde{D}_\alpha \frac{\partial C_\alpha}{\partial x}\right) + j\left[C_{\beta\alpha}\left(C_0 - C_{\beta\alpha}\right)\tilde{\phi}_\beta - C_{\alpha\beta}\left(C_0 - C_{\alpha\beta}\right)\tilde{\phi}_\alpha\right]\right\} \end{aligned} \tag{16.3}$$

where $\tilde{\phi}_i$ is the effective interdiffusion electromigration coefficient of phase i. The calculated results and the experimental measurements of the IMC growth are shown in Figure 16.15. A relationship between reaction time and thickness of IMC layer for the

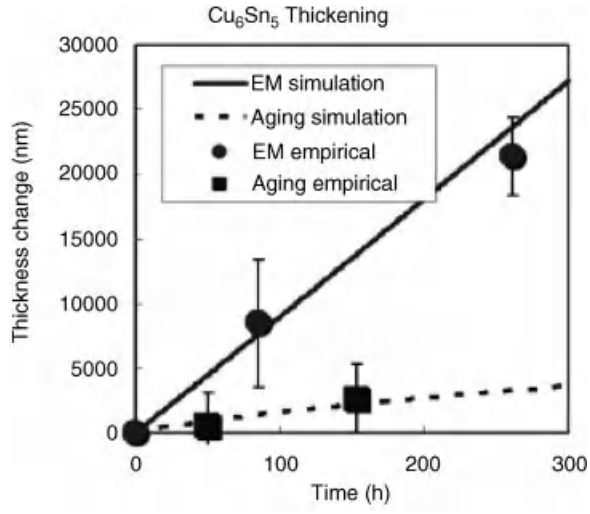

Figure 16.15 *The thickness change of Cu_6Sn_5 plotted as a function of time (experimental data [74, 75]).*

reaction couples with passage of current was developed [39] on the basis of a similar concept:

$$t = \frac{\Delta x}{U} - \frac{M}{U^2}\ln\left(1 + \frac{U}{M}\Delta x\right) \tag{16.4}$$

where M corresponds to the chemical potential gradient term and U corresponds to the electromigration term. The results shown in Figure 16.15 and derived by Eq. (16.3) indicate that the IMC layer grows linearly with reaction time when electromigration is dominant, while its growth follows the parabolic law when the chemical diffusion is dominant.

These models [67–71] illustrate successfully the observations that the reaction layer is thicker at the 'solder to substrate' side where the electromigration-induced flux is in the same direction as the chemical-potential gradient-induced flux, while the layer is thinner at the 'substrate to solder' side where the two kinds of fluxes are of opposite directions. These models are valid in cases of the diffusion-controlled growth and consider the significant electromigration effect on diffusion of a main diffusing species. However, the results of symmetric growth as mentioned in Section 16.3.3 and some others in the literature [36–38, 64, 65, 76–83] cannot be reasonably explained. The reaction mechanisms in this kind of models are assumed to be inert to electromigration, and thus are not applicable to the cases where mechanisms might be altered.

16.4.2 The Atomic Flux Summation with Stress Modification Model

In recent years, the effects of current on IMC growth on Cu/Sn-3.8 wt%Ag-0.7 wt% Cu solder have been examined. Although the suppression at the 'substrate to solder' side and the enhancement at the 'solder to substrate' side induced by current were observed, it is demonstrated that Cu is the dominant diffusion species in the experimental conditions [47].

This phenomenon cannot be reasonably explained by any one of the equations mentioned above. Hence, the other driving force for atom migration called 'back stress' has been taken into account [47]. A model considering the effect of diffusion, electromigration and back stress has been developed to explain the growth rates of IMCs with the current in the couple. It is shown as follows:

$$\frac{\mathrm{d}(\Delta x)}{\mathrm{d}t} = \frac{a + a^*}{\Delta x} + b \tag{16.5}$$

Where $a/\Delta x$, $a^*/\Delta x$ and b, represent the chemical potential gradient term, back stress gradient and electromigration, respectively. It has been concluded that the growth rate of an IMC is larger at the 'solder to substrate' side since a^* is positive, and smaller at the 'substrate to solder' side due to the negative a^*, compared with that in the no-current case.

16.4.3 Generalized Modeling for Growth of IMC Layer

In view of the lack of a general model for explaining the majority of these experimental results, a comprehensive phenomenological model [72], which takes into account the reaction and diffusion of 'two' species, was developed from the mathematical reaction-diffusion model derived by Dybkov [73], to interpret the current effect on IMC layer growth was developed. The growth of the two IMC layers was given by

$$\begin{aligned}
\frac{\delta \tilde{x}_\mathrm{c}}{\delta \tau} &= \frac{1}{1 + \dfrac{1}{\dfrac{\alpha_\mathrm{A}}{\tilde{x}'} + \beta_\mathrm{A}}} + \frac{\mu H\left(\dfrac{\alpha_\mathrm{B}}{\tilde{x}} - \beta_\mathrm{B}\right)}{1 + \dfrac{1}{\dfrac{\alpha_\mathrm{B}}{\tilde{x}'} - \beta_\mathrm{B}}} \\
\frac{\delta \tilde{x}_\mathrm{a}}{\delta \tau} &= \frac{H\left(\dfrac{\alpha_\mathrm{A}}{\tilde{x}} - \beta_\mathrm{A}\right)}{1 + \dfrac{1}{\dfrac{\alpha_\mathrm{A}}{\tilde{x}} - \beta_\mathrm{A}}} + \frac{\mu}{1 + \dfrac{1}{\dfrac{\alpha_\mathrm{B}}{\tilde{x}} + \beta_\mathrm{B}}}
\end{aligned} \tag{16.6}$$

With $H(x)$ being the Heaviside function:

$$H(y) = \begin{cases} 1 & y \geq 0 \\ 0 & \text{otherwise} \end{cases}$$

where $\tilde{x}_\mathrm{a}$ is the dimensionless form of thickness of layer on the 'substrate to solder' side, $\tilde{x}_\mathrm{c}$ is the dimensionless form of thickness of layer on the 'solder to substrate' side. α_A and α_B are the ratios of characteristic diffusion rates to interfacial reaction rates of species A and B, respectively; β_A and β_B are the ratios of characteristic electromigration rates to interfacial reaction rates of species A and B, respectively.

Figure 16.16 shows the time dependency of changes in thickness under different conditions [72]. As can be seen, with only one major diffusion species and a relatively small diffusion barrier, if the electromigration effect on the major diffusion species is more important, 'solder to substrate' side enhancement and 'substrate to solder' side suppression will be observed. On the other hand, if the electromigration effect on the minor diffusion species is more important, the IMC growth will undergo 'solder to substrate' side suppression

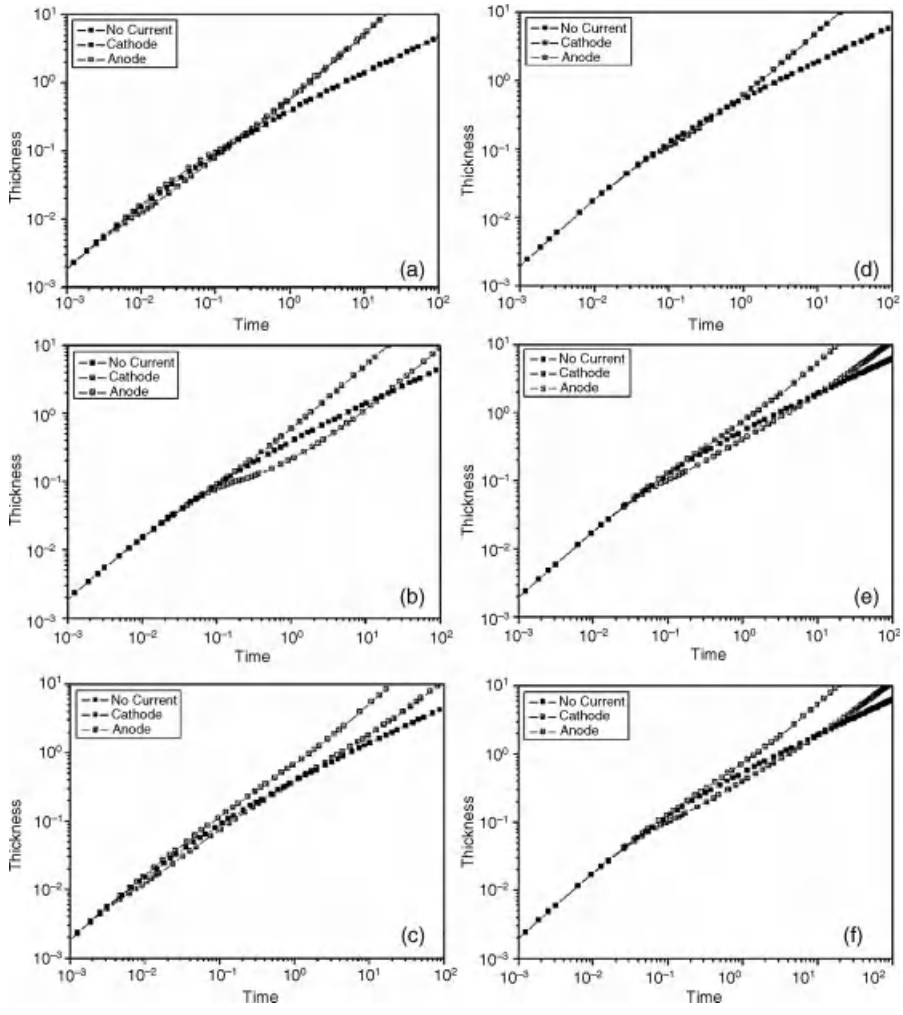

Figure 16.16 *The thickness of the intermetallic layer of AB reaction couple with and without the passage of electric current. (a) ($\mu = 1$, $\alpha_A = 0.1$, $\alpha_B = 0.01$, $\beta_A = 1$, $\beta_B = 1$); (b) ($\mu = 1$, $\alpha_A = 0.1$, $\alpha_B = 0.01$, $\beta_A = 1$, $\beta_B = 0.1$); (c) ($\mu = 1$, $\alpha_A = 0.1$, $\alpha_B = 0.01$, $\beta_A = 0.1$, $\beta_B = 1$); (d) ($\mu = 1$, $\alpha_A = 0.1$, $\alpha_B = 0.1$, $\beta_A = 1$, $\beta_B = 1$); (e) ($\mu = 1$, $\alpha_A = 0.1$, $\alpha_B = 0.1$, $\beta_A = 1$, $\beta_B = 0.1$); (f) ($\mu = 1$, $\alpha_A = 0.1$, $\alpha_B = 0.1$, $\beta_A = 0.1$, $\beta_B = 1$).*

and 'substrate to solder' side enhancement. The other case is that when the diffusion barrier is insignificant and both species have comparable diffusion rates, the effects of electromigration on both species will be crucial, and the current will cause suppression at both sides. Finally, if the diffusion barrier is significant, simultaneous cathode and anode enhancements will be observed because electromigration will become the dominant mass-transfer mechanism.

The generalized model is likely to be employed to interpret the majority of the experimental results. However, acquisition of the parameters used in the models, such as

the effective charges of atoms for β term, is usually difficult and not reliable, unless very accurate experimental data are available. Furthermore, this model is still not applicable to some special cases. For example, the thickness of the IMC layer at the substrate to solder side 'shrinks' after the passage of current in the Cu/Sn-3.8 wt%Ag-0.7 wt%Cu/Cu diffusion couple at 120 and 150 °C [47]. In addition to the diffusion and electromigration fluxes, other mass-transfer mechanisms might be considered and need to be verified with experimental determinations.

16.5 Conclusions

The experimental investigations have clearly indicated that the effects of electromigration on electronic solder joints are significant, affecting both the microstructures of the solder matrix and the interfacial reactions. The effect of electromigration further mingles with the diffusion driven by chemical-potential gradients, thus making the results much more complicated. Although the effects of electromigration are obvious, the detailed mechanisms involved especially the interaction of electromigration with chemical-potential-driven diffusion remains unclear. However, without fundamental understanding, it is not possible to develop a good mathematical modeling description for predicting and illustrating the effects of electromigration. In order to really understand and further control such effects, it is crucial that more investigations should focus on the fundamental understanding and participation of researchers of different academic backgrounds would be very helpful.

Acknowledgments

The authors acknowledge the financial support of National Science Council of Taiwan.

References

1. Klein Wassink, R.J. (1989) *Solder in Electronics*, 2nd edn, Electrochemical Publications, Isle of Man, UK.
2. Official Journal of the European Union, L 37/19-L 37/23, 13.2.2003.
3. Abtew, M. and Selvaduray, G. (2000) Lead-free solder in microelectronics. *Mater. Sci. Eng. R*, **27**, 95–141.
4. Bath, J., Handwerker, C., and Bradley, E. (2000) Research update: lead-free solder alternatives. *Circ. Assembly*, **5**, 31–40.
5. Laurila, T., Vuorinen, V., and Kivilahti, J.K. (2005) Interfacial reactions between lead-free solders and common base materials. *Mater. Sci. Eng.*, **49**, 1–60.
6. Lassig, S. (2007) Manufacturing integration considerations of through-silicon via etching. *Solid State Technol*, **50**, 48.
7. Huntington, H.B. (1975) Electromigration in metals, in *Diffusion in Solids: Recent Developments* (eds A.S. Nowick and J.J. Burton), Academic Press, New York.
8. Huntington, H.B. and Grone, A.R. (1961) Current-induced marker motion in gold wires. *J. Phys. Chem. Solids*, **20**, 76–81.

9. Hung, Y.M. and Chen, C.M. (2008) Electromigration of Sn-9 wt.%Zn solder. *J. Electron. Mater.*, **37**, 887–893.
10. Zhang, X.F., Guo, J.D., and Shang, J.K. (2007) Abnormal polarity effect of electromigration on intermetallic compound formation in Sn-9Zn solder interconnect. *Scr. Mater.*, **57**, 513–516.
11. Kuo, S.M. and Lin, K.L. (2007) Microstructure evolution during electromigration between Sn–9Zn solder and Cu. *J. Mater. Res.*, **22**, 1240–1249.
12. Yamanaka, K., Tsukada, Y., and Suganuma, K. (2006) Electromigration effect on solder bump in Cu/Sn-3Ag-0.5Cu/Cu system. *Scr. Mater.*, **55**, 867–870.
13. Chen, C., Tong, H.M., and Tu, K.N. (2010) Electromigration and thermomigration in Pb-free flip-chip solder joints. *Annu. Rev. Mater. Res.*, **40**, 531–555.
14. Lu, C.C., Wang, S.J., and Liu, C.Y. (2003) Electromigration studies on Sn(Cu) alloy lines. *J. Electron. Mater.*, **32**, 1515–1522.
15. Lee, T.Y., Tu, K.N., and Frear, D.R. (2001) Electromigration of eutectic SnPb and SnAg3.8Cu0.7 flip chip solder bumps and under-bump metallization. *J. Appl. Phys.*, **90**, 4502–4508.
16. Lai, Y.S., Chen, K.M., Kao, C.L. *et al.* (2007) Electromigration of Sn-37Pb and Sn-3Ag-1.5Cu/Sn-3Ag-0.5Cu composite flip-chip solder bumps with Ti/Ni(V)/Cu under bump metallurgy. *Microelectron. Reliab.*, **47**, 1273–1279.
17. Ha, S.S., Kim, J.W., Yoon, J.W. *et al.* (2009) Electromigration behavior in Sn-37Pb and Sn-3.0Ag-0.5Cu flip-chip solder joints under high current density. *J. Electron. Mater.*, **38**, 70–77.
18. Chen, C.M., Huang, C.C., Liao, C.N., and Liou, K.M. (2007) Effects of copper doping on microstructural evolution in eutectic SnBi solder stripes under annealing and current stressing. *J. Electron. Mater.*, **36**, 760–765.
19. Chen, C.M., Hung, Y.M., and Lin, C.H. (2009) Electromigration of Sn-8 wt.% Zn-3 wt.% Bi and Sn-9 wt.% Zn-1 wt.% Cu solders. *J. Alloys Compd.*, **475**, 238–244.
20. Chen, L.T. and Chen, C.M. (2006) Electromigration study in the eutectic SnBi solder joint on the Ni/Au metallization. *J. Mater. Res.*, **21**, 962–969.
21. Yang, Q.L. and Shang, J.K. (2005) Interfacial segregation of Bi during current stressing of Sn-Bi/Cu solder interconnect. *J. Electron. Mater.*, **34**, 1363–1367.
22. Chan, Y.C. and Yang, D. (2010) Failure mechanisms of solder interconnects under current stressing in advanced electronic packages. *Prog. Mater. Sci.*, **55**, 428–475.
23. Brandenburg, S. and Yeh, S. (1998) Proc. Surface Mount International Conference and Exhibition, Electromigration Studies of Flip Chip Bump Solder Joints. SMI 98.
24. Rinne, G.A. (2003) Issues in accelerated electromigration of solder bumps. *Microelectron. Reliab.*, **43**, 1975–1980.
25. Daghfal, J.P. and Shang, J.K. (2007) Current-induced phase partitioning in eutectic indium-tin Pb-free solder interconnect. *J. Electron. Mater.*, **36**, 1372–1377.
26. Zeng, K. and Tu, K.N. (2002) Six cases of reliability study of Pb-free solder joints in electronic packaging technology. *Mater. Sci. Eng. R.*, **38**, 55–105.
27. Wang, C.H. and Chen, S.W. (2006) Sn-0.7 wt%Cu/Ni interfacial reactions at 250 °C. *Acta Mater.*, **54**, 247–253.
28. He, M., Chen, Z., and Qi, G. (2004) Solid state interfacial reaction of Sn-37Pb and Sn-3.5Ag solders with Ni-P under bump metallization. *Acta Mater.*, **52**, 2047–2056.
29. Yoon, J.W., Kim, S.W., and Jung, S.B. (2005) IMC morphology interfacial reaction and joint reliability of Pb-free Sn-Ag-Cu solder on electrolytic Ni BGA substrate. *J. Alloys Compd.*, **392**, 247–252.
30. Chuang, C.M., Hung, H.T., Liu, P.C., and Lin, K.L. (2004) The interfacial reaction between Sn-Zn-Ag-Ga-Al solders and metallized Cu substrates. *J. Electron. Mater.*, **33**, 7–13.
31. Tsai, C.M., Lin, Y.L., Tsai, J.Y. *et al.* (2006) Local melting induced by electromigration in flip-chip solder joints. *J. Electron. Mater.*, **35**, 1005–1009.

32. Liang, S.W., Chang, Y.W., and Chen, C. (2006) Effect of Al-trace dimension on Joule heating and current crowding in flip-chip solder joints under accelerated electromigration. *Appl. Phys Lett.*, **88**, 172108.
33. Fukushima, A., Yagami, K., Tulapurkar, A.A. *et al.* (2005) Peltier Effect in sub-micron-size metallic junctions. *Jpn. J. Appl. Phys.*, **44**, 12–14.
34. Liao, C.N., Chen, K.C., Wu, W.W., and Chen, L.J. (2005) In situ transmission electron microscope observations of electromigration in copper lines at room temperature. *Appl. Phys Lett.*, **87**, 141903.
35. Liu, W.C., Chen, S.W., and Chen, C.M. (1998) The Al/Ni interfacial reactions under the influence of electric current. *J. Electron. Mater.*, **27**, L5–9.
36. Kumar, A., He, M., Chen, Z., and Teo, P.S. (2004) Effect of electromigration on interfacial reactions between electroless Ni-P and Sn–3.5% Ag solder. *Thin Solid Films*, **462–463**, 413–418.
37. Bertolino, N., Garay, J.E., Anselmi-Tamburini, U., and Munir, Z.A. (2002) High flux current effects in interfacial reactions in Au-Al multilayers. *Philos. Mag. B*, **82**, 969–985.
38. Garay, J.E., Anselmi-Tamburini, U., and Munir, Z.A. (2003) Enhanced growth of intermetallic phases in the Ni-Ti system by current effects. *Acta Mater.*, **51**, 4487–4495.
39. Chen, C.M. and Chen, S.W. (1999) Electric current effects on Sn/Ag interfacial reactions. *J. Electron. Mater.*, **28**, 902–906.
40. Chen, S.W. and Chen, C.M. (2003) Electromigration effects upon interfacial reactions. *JOM*, **55**, 62–67.
41. Chen, C.M. and Chen, S.W. (2002) Electromigration effect upon the Sn/Ag and Sn/Ni interfacial reactions at various temperatures. *Acta Mater.*, **50**, 2461–2469.
42. Chen, S.W., Chen, C.M., and Liu, W.C. (1998) Electric current effects upon the Sn/Cu and Sn/Ni interfacial reactions. *J. Electron. Mater.*, **27**, 1193–1998.
43. Zhang, X.F., Guo, J.D., and Shang, J.K. (2007) Abnormal polarity effect of electromigration on intermetallic compound formation in Sn–9Zn solder interconnect. *Scr. Mater.*, **57**, 513–516.
44. Kuo, S.M. and Lin, K.L. (2008) Polarity effect of electromigration on intermetallic compound formation in a Cu/Sn–9Zn/Cu sandwich. *J. Mater. Res.*, **23**, 1087–1094.
45. Gu, X., Yang, D., Chan, Y.C., and Wu, B.Y. (2008) Effects of electromigration on the growth of intermetallic compounds in Cu/SnBi/Cu solder joints. *J. Mater. Res.*, **23**, 2591–2596.
46. Wang, C.H. and Chen, S.W. (2009) Peltier effect on Sn/Co interfacial reactions. *J. Electron. Mater.*, **38**, 655–662.
47. Gan, H. and Tu, K.N. (2005) Polarity effect of electromigration on kinetics of intermetallic compound formation in Pb-free solder V-groove samples. *J. Appl. Phys.*, **97**, 063514.
48. Chen, C.M. and Chen, S.W. (2000) Electromigtration effect upon the Zn/Ni and Bi/Ni interfacial reactions. *J. Electron. Mater.*, **29**, 1222–1228.
49. Chen, S.W., Chen, C.M., and Liu, W.C. (1998) Electric current effects upon the Sn/Cu and Sn/Ni interfacial reactions. *J. Electron. Mater.*, **27**, 1193–1998.
50. Chen, C.M. and Chen, S.W. (2003) Electromigration effect upon the low- temperature Sn/Ni interfacial reactions. *J. Mater. Res.*, **18**, 1293–1296.
51. Wang, C.H. Kuo, C.Y., Chen, H.H. and Chen, S.W. (2010) Effect of current density and temperature on Sn/Ni interfacial reactions under current stressing. *Intermetallics*, **19**, 75–80.
52. Wang, C.H. (2008) Interfacial reactions and microstructural evolutions of the solder joints in electronic and thermoelectronic devices, Ph.D. Dissertation, National Tsing Hua University.
53. Wang, C.H. and Chen, S.W. (2008) Interfacial reactions in Sn-(Cu)/Cu_6Sn_5/Ni couples at 210 °C. *Intermetallics*, **16**, 531–537.
54. Luo, W.C., Ho, C.E., Tsai, J.Y. *et al.* (2005) Solid-state reactions between Ni and Sn-Ag-Cu solders with different Cu concentrations. *Mater. Sci. Eng. A*, **396**, 385–391.
55. Chen, C.M. and Chen, S.W. (2001) Electromigration effect upon the Sn-0.7 wt%Cu/Ni and Sn-3.5 wt%Ag/Ni interfacial reactions. *J. Appl. Phys.*, **90**, 1208–1214.

56. Chen, C.C., Chen, S.W., and Chang, C.H. (2008) Electromigration effects upon the Sn/Ni–7 wt% V interfacial reactions. *J. Appl. Phys.*, **103**, 063518.
57. Chen, S.W. and Wang, C.H. (2007) Effects of electromigration on interfacial reactions in cast Sn/Cu joints. *J. Mater. Res.*, **22**, 695–702.
58. Hu, Y.C., Lin, Y.H., Kao, C.R., and Tu, K.N. (2003) Electromigration failure in flip chip solder joints due to rapid dissolution of copper. *J. Mater. Sci.*, **18**, 2544–2548.
59. Lin, Y.H., Hu, Y.C., Tsai, C.M. *et al.* (2005) In situ observation of the void formation-and-propagation mechanism in solder joints under current-stressing. *Acta Mater.*, **53**, 2029–2035.
60. Liu, C.Y., Ke, L., Chuang, Y.C., and Wang, S.J. (2006) Study of electromigration-induced Cu consumption in the flip-chip Sn/Cu solder bumps. *J. Appl. Phys.*, **100**, 083702.
61. Chao, B., Chae, S.H., Zhang, X. *et al.* (2006) Electromigration enhanced intermetallic growth and void formation in Pb-free solder joints. *J. Appl. Phys.*, **100**, 084909.
62. Nah, J.W., Suh, J.O., Tu, K.N. *et al.* (2006) Electromigration in flip chip solder joints having a thick Cu column bump and a shallow solder interconnect. *J. Appl. Phys.*, **100**, 123513.
63. Lin, C.T., Chung, Y.C., Wang, S.J., and Liu, C.Y. (2006) Current density dependence of electromigration-induced flip-chip Cu pad consumption. *Appl. Phys. Lett.*, **89**, 101906.
64. Bertolino, N., Garay, J.E., Anselmi-Tamburini, U., and Munir, Z.A. (2001) Electro- migration effects in Al-Au multilayers. *Scr. Mater.*, **44**, 737–742.
65. Friedman, J.R., Garay, J.E., Anselmi-Tamburini, U., and Munir, Z.A. (2004) Modified interfacial reactions in Ag-Zn multilayers under the influence of high DC currents. *Intermetallics*, **12**, 589–597.
66. Huntington, H.B. (1975) Effect of diving force on atom motion. *Thin Solid Film*, **25**, 265–280.
67. Chao, B., Chae, S.H., Zhang, X. *et al.* (2006) Electromigration enhanced intermetallic growth and void formation in Pb-free solder joints. *J. Appl. Phys.*, **100**, 084909.
68. Chao, B.H.L., Zhang, X.F., Chae, S.H., and Ho, P.S. (2009) Recent advances on kinetic analysis of electromigration enhanced intermetallic growth and damage formation in Pb-free solder joints. *Microelectron Reliab.*, **49**, 253–263.
69. Gurov, K.P. and Gusak, A.M. (1981) On the theory of phase growth in the diffusion zone during mutual diffusion in an external electric field. *Phys. Met. Metallogr.*, **52**, 75–81.
70. Gosele, U. and Tu, K.N. (1982) Growth kinetics of planar binary diffusion couples: "thin-film case" versus "bulk cases". *J. Appl. Phys.*, **53**, 3252–3260.
71. Orchard, H.T. and Greer, A.L. (2005) Electromigration effects on compound growth at interfaces. *Appl. Phys. Lett.*, **86**, 231906.
72. Hsu, C.M., Wong, D.S.H., and Chen, S.W. (2007) Generalized phenomenological model for the effect of electromigration on interfacial reaction. *J. Appl. Phys.*, **102**, 023715.
73. Dybkov, V.I. (1986) Reaction diffusion in heterogeneous binary systems. *J. Mater. Sci.*, **21**, 3078–3084.
74. Siewert, T.A., Madeni, J.C., and Liu, S. (2003) Formation and growth of intermetallics at the interface between lead-free solders and copper substrates. *Proceedings of the APEX Conference on Electronics Manufacturing*.
75. Chae, S.H., Zhang, X., Chao, H.-L. *et al.* (2006) Electromigration lifetime statistics for Pb-free solder joints with Cu and Ni UBM in plastic flip-chip packages. *Proceedings of the 56th Electronic Components and Technology Conference*, pp. 650–656.
76. Chen, L.D., Huang, M.L., and Zhou, S.M. (2010) Effect of electromigration on intermetallic compound formation in line-type Cu/Sn/Cu interconnect. *J. Alloys Compd.*, **504**, 535–541.
77. Wu, W.H., Chung, H.L., Chen, C.N., and Ho, C.E. (2009) The influence of current direction on the Cu-Ni cross-interaction in Cu/Sn/Ni diffusion couples. *J. Electron. Mater.*, **38**, 2563–2572.
78. Kim, D.G. and Jung, S.B. (2005) Intermetallic compound formation and growth kinetics in flip chip joints using Sn-3.0Ag-0.5Cu solder and Ni-P under bump metallurgy. *Mater. Trans.*, **46**, 1295–1300.

79. Yu, C., Yang, Y., Lu, H., and Chen, J.M. (2010) Effects of current stressing on formation and evolution of Kirkendall voids at Sn-3.5Ag/Cu interface. *J. Electron. Mater.*, **39**, 1309–1314.
80. Yang, Q.L., Shang, P.J., Guo, J.D. *et al.* (2009) Current-induced growth of P-rich phase at electroless nickel/Sn interface. *J. Mater. Res.*, **24**, 2767—2774.
81. Lu, Y.D., He, X.Q., En, Y.F. *et al.* (2009) Polarity effect of electromigration on intermetallic compound formation in SnPb solder joints. *Acta Mater.*, **57**, 2560–2566.
82. Zhang, X.F., Guo, J.D., and Shang, J.K. (2009) Effects of electromigration on interfacial reactions in the Ni/Sn-Zn/Cu solder interconnect. *J. Electron. Mater.*, **38**, 425–429.
83. Chiu, T.C. and Lin, K.L. (2008) Electromigration behavior of the Cu/Au/SnAgCu/Cu solder combination. *J. Mater. Res.*, **23**, 264–273.

Thematic Area VIII

Thermomigration Issues Affecting Reliability

17

Thermomigration in SnPb and Pb-Free Flip-Chip Solder Joints

Tian Tian[1], *K.N. Tu*[1], *Hsiao-Yun Chen*[2], *Hsiang-Yao Hsiao*[2], *and Chih Chen*[2]
[1] *Department of Materials Science and Engineering, University of California, Los Angeles, CA 90095-1595, USA*
[2] *Department of Materials Science and Engineering, National Chiao Tung University, Hsinchu, Taiwan, 30010, ROC*

17.1 Introduction

When an inhomogeneous binary solid solution or alloy is annealed at a constant temperature and a constant pressure, it will become homogenous in order to lower the free energy. On the contrary, when a homogeneous binary alloy is annealed at constant pressure but under a temperature gradient, the opposite will happen, and the alloy will show phase separation and become inhomogeneous so the free energy increases [1–12]. This dealloying phenomenon is called Soret effect, which is due to thermomigration (TM) or mass migration driven by a temperature gradient. Since the inhomogeneous alloy has higher free energy than the homogeneous alloy does, thermomigration is an energetic process that transforms a phase from a low-energy state to a high-energy state. It is different from a conventional phase transformation that tends to lower Gibbs free energy. TM could occur in a pure metal, too.

It is noteworthy that TM in Al and Cu interconnects has seldom been studied, yet TM is now recognized as a serious reliability problem in flip-chip solder joints. In comparison, it is much easier to have TM in solder alloys than in Al and Cu interconnects, especially in flip-chip solder joints. We can have a temperature gradient of 1000 °C/cm in the joint, which is large enough to cause TM. Also, at the device working temperature of 100 °C, lattice diffusion in solder joints is fast.

Lead-free Solders: Materials Reliability for Electronics, First Edition. Edited by K. N. Subramanian.

The temperature gradient in a flip-chip solder joint comes from Joule heating of the Al or Cu interconnects and the unique geometry of flip-chip system. Figure 17.1 shows the flip-chip test vehicle in our study. Figure 17.1a is the schematic diagram of a flip-chip on a substrate. Those small squares on the edges of the substrate are the electrical contact pads. Figure 17.1b reveals the array of solder bumps between the chip and the substrate in Figure 17.1a by a nondestructive X-ray tomography technique.

If we test one pair of solder bumps, we can have, as depicted in Figure 17.2a, a schematic diagram of their cross section. On the top or the chip side, there is a short Al thin-film interconnect connecting the two bumps, whereas on the bottom side, each bump has a thick Cu line connecting it to other bumps or to the outside circuit. Figure 17.2b is a three-dimensional schematic diagram depicting the unique line-to-bump configuration of the Al thin film and one of the solder bumps. As a point of reference to better understand Joule heating in an Al interconnect and a solder bump in a flip-chip device, the resistance of an Al trace is typically hundreds of milliohms, whereas it is approximately 7 mΩ for a solder bump and tens of milliohms for the Cu lines on the substrate side. Considering Joule heating per unit volume for Al, if we take $j = 10^6\,\mathrm{A\,cm^{-2}}$ and $\rho = 10^{-6}\,\Omega\,\mathrm{cm}$, then Joule heating per unit volume is $\rho j^2 = 10^6\,\mathrm{J\,cm^{-3}\,s^{-1}}$. For the solder, if we take $j = 10^4\,\mathrm{A\,cm^{-2}}$ and $\rho = 10^{-5}\,\Omega$ cm, then Joule heating is $\rho j^2 = 10^3\,\mathrm{J\,cm^{-3}\,s^{-1}}$. Therefore, the Al trace on the chip side serves as the major contributor to Joule heating, causing the side of the solder bump at the chip side to be hotter than that on the substrate side. Additionally, the cross section of the Al line on the chip side is at least two orders of magnitude smaller than that of the solder bump. Thus, there is a very large current-density change at the contact between the bump and the line because the same current is passing through them, resulting in current crowding. This current crowding will contribute an additional nonsymmetrical Joule-heating distribution to the solder.

3D Finite element analysis (FEA) could provide us a clearly simulation picture of the temperature distribution inside solder bumps. Figure 17.3a shows the simulated temperature distribution in a single solder bump which is powered by 0.6 A current. Figure 17.3b illustrates a cross-sectional view of the temperature distribution inside the solder, showing the existence of the hot spot in the solder adjacent to the entrance point where the electrons flow from the Al trace enters the solder at the contact opening. The temperature at the spot is

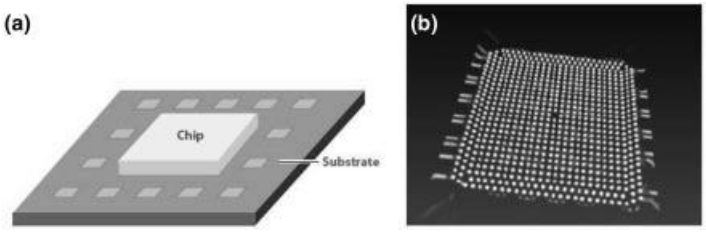

Figure 17.1 *(a) Schematic diagram of a flip-chip on a substrate. The small squares on the substrate are the electrical contact pads. (b) Synchrotron radiation X-ray tomographic image of the sample, showing an array of solder bumps. The synchrotron radiation X-ray tomographic image is courtesy of Miss Tian Tian at University of California, Los Angeles and Dr. Alastair Macdowell at the Advanced Light Source/Lawrence Berkeley National Laboratory. The flip-chip sample is courtesy of Dr. Yi-Shao Lai at Advanced Semiconductor Engineering, Taiwan, ROC.*

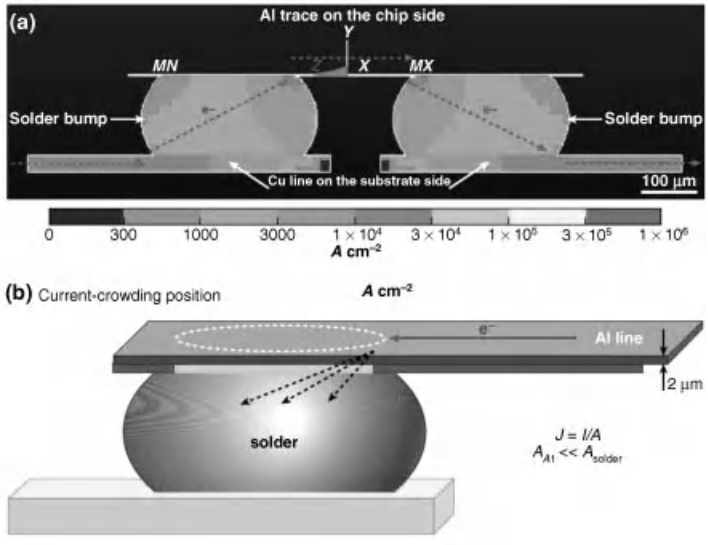

Figure 17.2 *(a) Cross-sectional view showing the current-crowding effect in solder bumps during current stressing. Peak current density occurs at the current entrances of the Al trace into the solder bump. (b) Three-dimensional schematic diagram depicting the unique line-to-bump configuration of the Al thin film and one of the solder bumps.*

137.4 °C, which is 5.6 °C higher than the average value in the solder. A hot spot is evident. The temperature on the chip side is higher than that on the substrate side. Figure 17.3c illustrates the temperature profile along the horizontal dashed line in Figure 17.3b and d illustrates the temperature profile along the vertical dashed line in Figure 17.3b.

Historically, eutectic SnPb solder is most widely used in the semiconductor packaging industry. Intensive studies on TM in SnPb solder joints have been done in recent decades. One big advantage of SnPb solder is the large contrast of optical and SEM images between Sn and Pb so that we can observe their phase separation under TM easily. In Section 17.2, we will give a brief review on TM in flip-chip solder joints of SnPb.

In Section 17.3, TM in Pb-free flip-chip solder joints will be presented. In Section 17.4, the fundamental of TM will be presented and the driving force of TM and heat of transport will be discussed. In Sections 17.5 and 17.6, the interaction between TM and creep and that between TM and EM will be given, respectively.

17.2 Thermomigration in SnPb Flip-Chip Solder Joints

17.2.1 Thermomigration in Unpowered Composite SnPb Solder Joints

Figures 17.4a and b show, respectively, the schematic diagram of the cross section of a composite flip-chip solder joint of 97Pb3Sn and 37Pb63Sn, and the corresponding SEM images. The composite solder joints have been used to study TM. As a control experiment to begin with, a constant-temperature heating of the composite flip-chip samples was

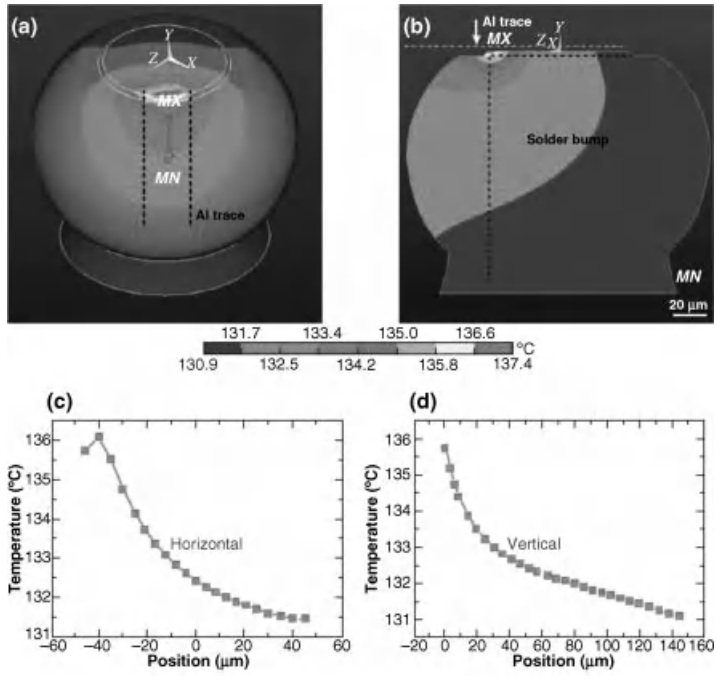

Figure 17.3 *(a) Tilt view of the simulated temperature distribution over an entire solder bump when the joint is stressed by 0.6 A at 100 °C. (b) Cross-sectional view showing the temperature distribution. A hot spot is observed at the current entrance from the Al trace. (c, d) The temperature profiles along (c) the black horizontal dashed line and (d) the black vertical dashed line in panel b. The red horizontal dashed line denotes the position of the Al trace in panel b.*

performed in an oven at constant temperature of 150 °C and at constant atmospheric pressure for a period of 1, 2 and 4 weeks. The microstructures of the cross section were examined under optical microscope (OM) and scanning electron microscope (SEM). No mixing between the high-Pb and the eutectic SnPb was observed, and the image was

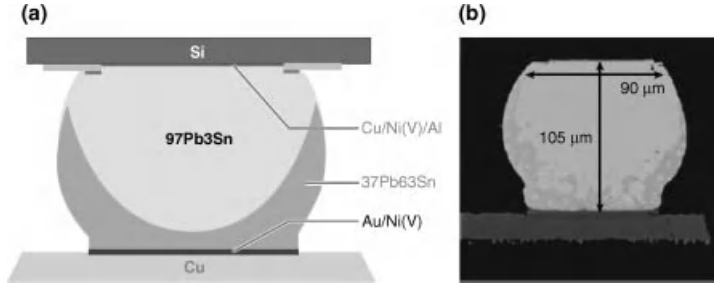

Figure 17.4 *(a) A cross section of a composite 97Pb3Sn and 37Pb63Sn flip-chip solder joint. (b) Scanning electron microscopy (SEM) image of the cross section. The darker region at the bottom is the eutectic SnPb. The brighter region is the 97Pb3Sn phase.*

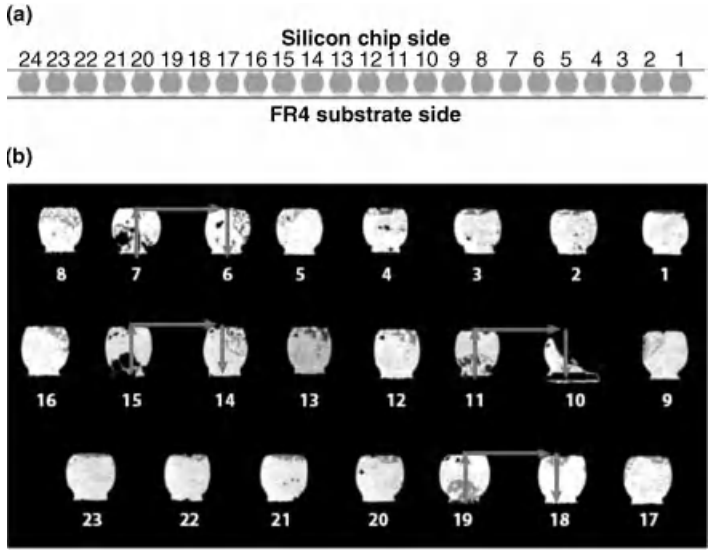

Figure 17.5 *(a) Schematic diagram depicting 24 bumps on the periphery of a Si chip. Each bump has its original microstructure, as shown in Figure 17.4(b), before EM stressing. EM was conducted at 1.6×10^4 A cm^{-2} at 150°C through only four pairs of bumps on the chip's periphery: pairs 6/7, 10/11, 14/15, and 18/19. (b) TM affected all the unpowered solder joints: The darker eutectic phase moved to the hot Si side.*

essentially unchanged, just as in Figure 17.4b. The observation of no phase mixing can be explained by the negligible chemical potential difference between the high-Pb and the eutectic SnPb at a constant temperature of 150 °C on the basis of the binary phase diagram of Sn-Pb. In other words, there is neither a chemical potential gradient nor a driving force to move the phases.

To induce TM in the composite solder joints, we used the temperature gradient induced by Joule heating in EM. A set of flip-chip samples is depicted in Figure 17.5a, wherein there are 24 bumps on the periphery of a Si chip, and all the bumps had their original microstructure, as shown in Figure 17.4b, before EM stressing. After EM was conducted through only four pairs of bumps–pairs 6/7, 10/11, 14/15, and 18/19 in Figure 17.5a–TM affected all the unpowered solder joints, as shown in Figure 17.5b. All the Sn (the darker image) migrated to the hot Si side, whereas the Pb migrated to the cold substrate side. The redistribution of Sn and Pb was caused by the temperature gradient across the solder joints because no current was applied to them. Since Si has a very good thermal conductivity, the Joule heating of Al interconnects on the chip side of the four pairs of powered bumps has heated the entire Si chip to induce a temperature gradient and in turn the TM across all the unpowered bumps.

17.2.2 *In-Situ* Observation of Thermomigration in Composite SnPb Solder Joints

In-situ observation of TM was conducted with flip-chip composite SnPb samples (Figure 17.6a). The chip was cut, and only a thin strip of Si was retained. The strip had one row of solder bumps connecting it to the substrate. The bumps were polished to

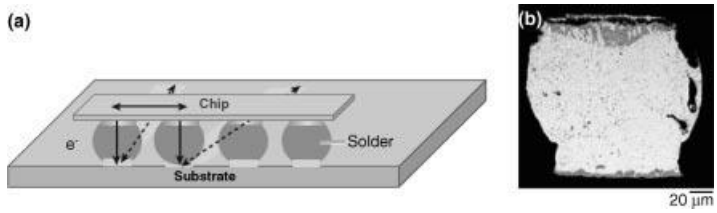

Figure 17.6 *(a) A schematic diagram of the Si stripe and a row of four of the cross-sectioned bumps. The chip was cut, and only a thin stripe of Si was retained. The stripe has one row of solder bumps connecting it to the substrate. The bumps were cut in the middle so that the cross section of the bump was exposed for in-situ observation during EM. The pair of joints on the left was powered at 2×10^4 A cm^{-2} for 20 h at 150 °C. The pair of joints on the right had no electric current. All joints showed composition redistribution and damage. (b) An SEM image of one of these joints.*

the middle so that the cross section of each bump was exposed for in-situ observation during TM. Figure 17.6a is a schematic diagram of the Si strip and a row of four cross-sectioned bumps. The pair of joints depicted on the left side of Figure 17.6a was powered at 2×10^4 A cm^{-2} at 150 °C for 20 h. The pair of joints on the right had no electric current. Interestingly, both pairs of joints exhibited composition redistribution and damage after the EM stressing. The unpowered pair showed a uniform void formation at the interface on the top side, that is, the Si side, which is also the hot side. Figure 17.6b shows an SEM image of one of these joints. In the bulk of the joint, some phase redistribution can be recognized. The redistribution of Sn and Pb can be measured by an electron microprobe from the cross sections of the unpowered pair, as depicted on the right side of Figure 17.6a, where Sn has migrated to the hot side and Pb has moved to the cold side. The void formation indicates that TM can cause failure in flip-chip solder joints.

When an electron microprobe was used to measure the composition distribution across a polished cross section of the flip-chip sample after TM, a highly irregular or stochastic composition distribution of three scans was observed, as shown in Figure 17.7; no smooth concentration profile was observed.

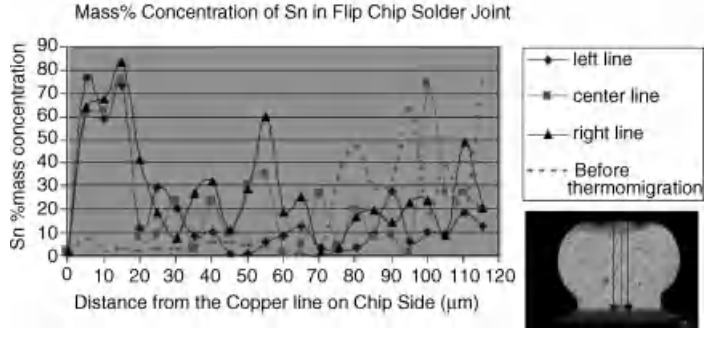

Figure 17.7 *Electron microprobe measurement of composition redistribution across a polished cross section of the flip-chip sample after TM. A highly irregular or stochastic composition distribution was found; no smooth concentration profile was observed.*

17.2.3 Thermomigration in Unpowered Eutectic SnPb Solder Joints

The eutectic 37Pb63Sn flip-chip solder joints, without the high-Pb, used for TM test were arranged similarly to that shown in Figure 17.6a. The under-bump metallurgy (UBM) thin films on the chip side were Al (~0.3 μm)/Ni(V) (~0.3 μm)/Cu (~0.7 μm) deposited by sputtering. The bond-pad metal layers on the substrate side were Ni (5 μm)/Au (0.05 μm) prepared by electroplating. The bump height between the UBM and the bond-pad is 90 μm. The contact opening on the chip side has a diameter of 90 μm.

Figure 17.8a shows an enlarged SEM picture of an unpowered bump after TM. The redistribution of Sn and Pb is shown by the accumulation of a large amount of Pb (lighter color) to the substrate side (the cold side), yet there is no accumulation of Sn to the chip side (the hot side) and the Sn distribution is quite uniform across the bump. The very surprising finding is not only that the microstructure in the bulk of the bump is quite uniform (except the accumulated Pb-rich phase), but also the lamellar structure is much finer, indicating the existence of many more interfaces in the microstructure after the phase separation, in turn a higher-energy state. We recall that when a eutectic two-phase microstructure is annealed at constant temperature, coarsening, instead of refinement, of the two-phase lamellar microstructure should occur to reduce the surface energy.

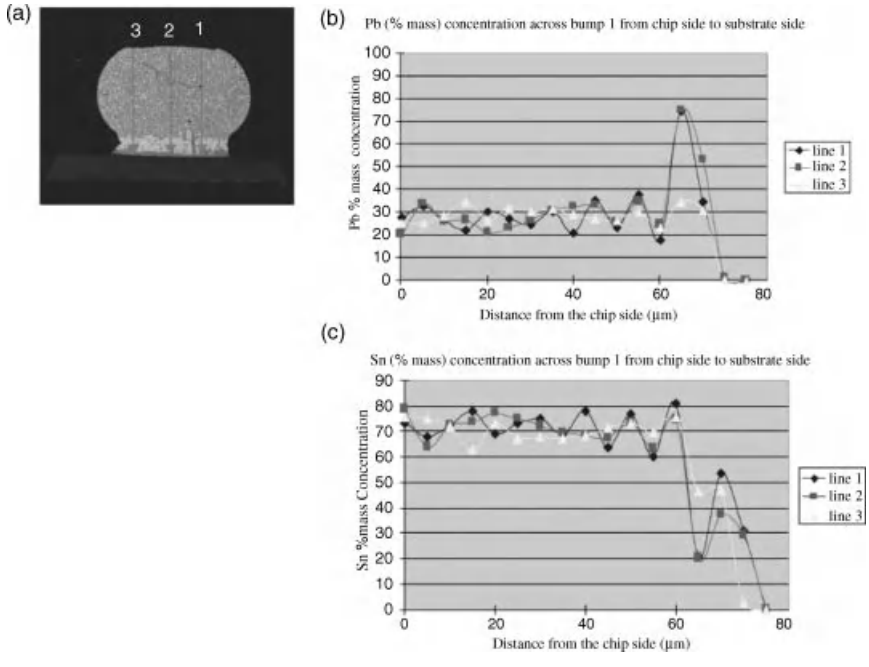

Figure 17.8 *(a) Enlarged SEM image of bump No. 11. The redistribution of Sn and Pb can be seen. It shows the migration of a large amount of Pb to the substrate side (the cold side), yet there is no accumulation of Sn to the chip side (the hot side). (b, c) Concentration profiles across the bump by EPMA of Pb and Sn, respectively. Three profile lines across the bumps were scanned and every line is the average of three sets of data points. Each point was taken at each 5-μm step from the chip side to the substrate side.*

The concentration profiles across the bump by microprobe are shown in Figures 17.8b and c. Three profile lines across the bumps were scanned and every line is the average of three sets of data points. Each point was taken at every 5-μm step from the chip side to the substrate side. The results shows that the concentration of Pb on the substrate side is about 73% and that of Sn on the chip side is around from 70 to 80%. However, the concentration distribution reveals that there is no linear concentration gradient. Near the cold end, the accumulation of Pb and depletion of Sn occurred. However, away from the cold end, the average distribution of Pb and Sn in the rest of the sample is quite uniform, except for some minor local fluctuations due to the two-phase microstructure. Clearly, Pb moves with the temperature gradient and is the dominant diffusing species in the TM because it accumulates at the cold end, but there is no concentration gradient of Pb served as the driving force for the diffusion of Pb, unlike precipitation. If Sn were the dominant diffusing species, the concentration profile of Pb would have increased uniformly in the bulk of the sample, but not a pile-up at the cold side. The higher concentration of Sn at the end of the substrate side is due to the formation of Cu_6Sn_5 IMC.

17.3 Thermomigration in Pb-Free Flip-Chip Solder Joints

Because of concerns about the environment impact of Pb-containing solders, the electronic packaging industry is replacing them by Pb-free solders, most of which have a high Sn content of approximately over 96 wt%. Besides studying the TM in flip-chip solder joints by powering direct current (DC) through neighboring solder bumps to generate the temperature gradient, passing alternating current (AC) directly is an excellent approach to study TM in a pair of solder bumps because there is no electromigration under AC. This is a good way to decouple TM from EM in the powered bumps.

Figure 17.9 shows the schematic diagram of a Pb-free solder bump used in the TM study. Solder joints were polished approximately to their centers. Figure 17.10a displays the SEM

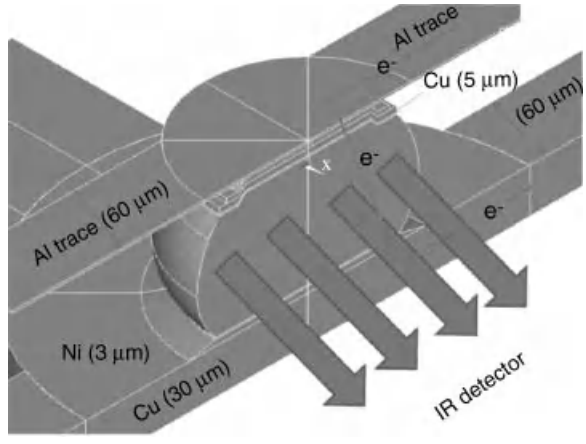

Figure 17.9 *Schematic diagram of the Pb-free solder in the TM study. The red arrows indicate the electron flow directions. The blue arrows indicate the direction of IR measurement.*

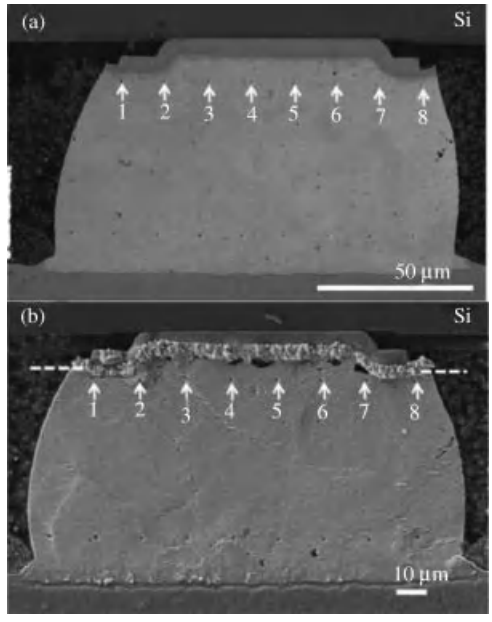

Figure 17.10 *SEM images of cross-sectioned bump with markers before and after TM test at a current of 0.57 A or current density of 1.01 × 10^4 A cm^{-2} and 100 °C. (a) Before TM, and (b) After 800 h of the TM test. The markers moved toward the substrate end.*

image of the cross section of the solder before current stressing. A focused ion beam was employed to etch eight markers in the solder bump, as labeled by 1–8 in the figure. AC stressing was employed to introduce a temperature gradient but without EM damage. The thermal gradient created by current stressing is measured using infrared microscopy, as depicted schematically in Figure 17.9. Cross-sectioned solder joints were employed to facilitate the measurement of the thermal gradient inside the solder bumps. The solder joints comprise eutectic SnAg3.5 solder bumps with electroplated 5-μm Cu/3-μm Ni under-bump metallization (UBM). To observe the TM in-situ, solder joints were cross sectioned into halves, polished laterally until the contact openings were exposed, leaving about 50% of the mass of the bump. The flip-chip packages were heated at a temperature of 100 °C on a hot plate. An AC current of 0.57 A was passed through the joints, producing a nominal current density of 1.01 × 10^4 cm^2. Before the current stressing, the emissivity of the specimen was calibrated at 100 °C, after which the joint was powered. The temperature was then measured to map the temperature distribution after the temperature reached a steady state. The temperatures in the solder joints were mapped by QFI thermal infrared microscopy, with a temperature resolution of 0.1 °C and a spatial resolution of 2 μm. Figure 17.11a presents the temperature distribution in the bump before current stressing. The temperature distribution across the solder bump was quite uniform. When current stressing commences at 0.57 A, the temperature distribution in the bump changes in response to Joule heating, as shown in Figure 17.11b. The average increase in temperature in the bump due to current stressing was as high as 40 °C. Figure 17.11c shows the temperature profile along the dashed line in Figure 17.11b. The thermal gradient was measured to be 2829 °C/cm. After 800 h of current

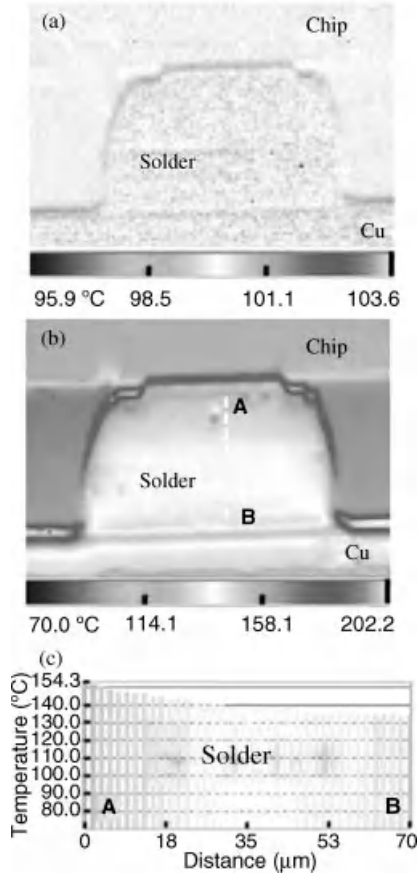

Figure 17.11 *(a) Temperature map of SnAg bump before current stressing, indicating a uniform temperature distribution in solder; (b) temperature map of bump powered by 0.57 A; (c) temperature profile along dashed line in (b); a huge thermal gradient of 2829°C/cm is generated.*

stressing, hillocks are present on the chip side, as shown in Figure 17.10b. The hillocks are formed by the mass transfer in the solder bump caused by TM. The hillocks comprised of almost pure Sn using a SEM energy-dispersive spectrum. The results reveal that Sn atoms are driven from the cold side to the hot side under TM. In addition, it is found that the markers moved toward the substrate end, which also indicated atoms transported from the substrate end to the chip end.

The formation of hillocks at the hot end in Figure 17.10b indicates that the hot end was under compression. Both stress and temperature have effects on the vacancy concentration in the hot end in this case. According to the Nabarro–Herring creep model, the vacancy concentration in the compressive region is below the equilibrium concentration in the unstressed region. Then, from the temperature effect the hot end should have a higher concentration of vacancies than the cold end. Since TM has occurred and marker motion indicated that mass flux had moved to the hot end, the net vacancy flux was to move to the

cold end, so the temperature effect may be larger than the stress effect. The interaction between TM and creep will be presented in Section 17.5.

17.3.1 Thermomigration of Cu and Ni in Pb-Free Flip-Chip Solder Joints

The dissolution rate of Cu and Ni in Pb-free solders is quite high. In addition, the diffusion rate along the *c*-axis of Sn crystals is much faster than that in the *a*- and *b*-axis. The dissolution of Cu and Ni atoms may occur under a thermal gradient. Figure 17.12a shows a eutectic SnAg solder bump with a 5-μm UBM on the chip side before a TM test. This bump was next to a bump that was under EM stressing at 0.55 A and 150 °C. This joint had no current passing through it but possessed a thermal gradient of 1143 °C/cm, as illustrated in Figure 17.12b. After 60 h of the TM test, the Cu-Sn IMC migrated to the cold (substrate) end, as shown in Figure 17.12c. Although this bump was unpowered, the damage is clear near the upper left corner, as indicated in Figure 17.12c. The Cu UBM dissolved almost completely into the solder. This dissolution can be attributed to the TM of Cu atoms by fast interstitial diffusion and the reaction with Sn atoms to form Cu-Sn IMCs inside the solder bump. Therefore, the TM of Cu enhances Cu dissolution during the EM process, accelerating EM failure in Pb-free solder joints with the dissolution of Cu UBMs. How to mitigate this effect deserves further study.

The damage caused by TM can be observed more clearly after longer stressing times. Figures 17.13a–d show the void formation in the chip end of four bumps after the current was applied only through Bumps 2 and 3 for 76 h. Bumps 1 and 4 had no current passing through. We expect that the electromigration force should push the Cu and Sn atoms to the chip end for Bump 2 as indicated by the arrow. Hillocks might be formed in the chip end if EM was the only driving force. However, voids formed in the anode/chip end, as shown in Figure 17.13b. Therefore, it infers that the TM force overwhelms the EM force in this case. To conduct a quantitative comparison of these driving forces, we shall present a brief review of the driving force of TM below.

17.4 Driving Force of Thermomigration

In the thermoelectric effect, a temperature gradient can move electrons. Similarly in thermomigration, a temperature gradient can drive atoms. In essence, the electrons in the high-temperature region have higher energy in scattering or stronger interaction with diffusing atoms, hence atoms move down the temperature gradient. On the driving force of atomic diffusion, we recall that the atomic flux driven by chemical potential can be given as,

$$J = C < v >= CMF = C\frac{D}{kT}\left(-\frac{\partial \mu}{\partial x}\right) \tag{17.1}$$

where C is atomic concentration, $<v>$ is drift velocity, $M = D/kT$ is mobility, F is driving force, and μ is chemical potential energy. Considering temperature gradient as the driving force, we have

$$J = C\frac{D}{kT}\frac{Q^*}{T}\left(-\frac{\partial T}{\partial x}\right) \tag{17.2}$$

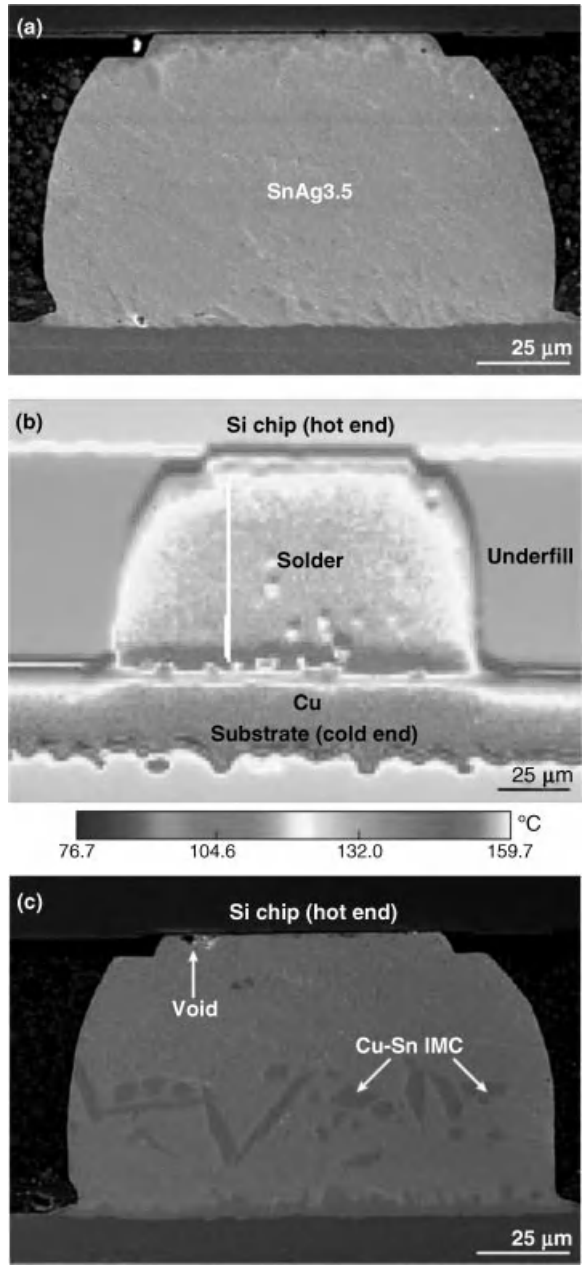

Figure 17.12 *(a) Cross-sectional SEM images representing the microstructure for an unpowered bump before a TM test. (b) Temperature distribution measured by an infrared microscope when the neighboring bumps were stressed by 0.55 A at 150°C. The built-in thermal gradient was 1143°C cm^{-1} across the solder bump. (c) After the TM test for 60 h. The Cu UBM was dissolved and the CuSn IMCs migrated toward the cold end.*

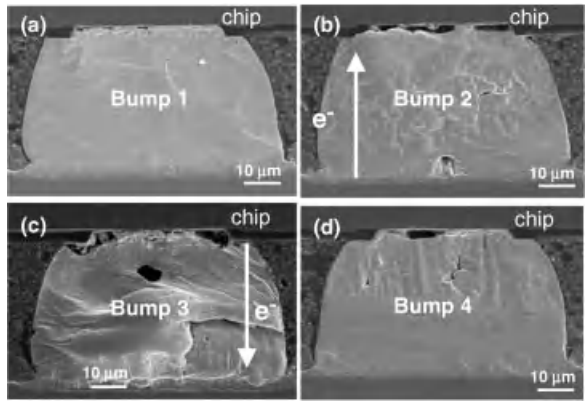

Figure 17.13 *Cross-sectional SEM images showing the microstructures of the four bumps after the current stressing of 0.55 A through Bump 2 and Bump 3 at 150° C for 76 hours. (a) Bump 1, no current passing through. (b) Bump 2 with an upward electron flow., (c) Bump 3 with a downward electron flow, (d) Bump 4, no current passing through. Voids formed in the chip side in all the four bumps.*

where Q^* is defined as the heat of transport. Comparing the last two equations, we see that Q^* has the same meaning and dimension as μ, so it is the heat energy per atom. The definition of Q^* is the difference between the heat carried by the moving atom and the heat of the atom at the initial state (the hot end or the cold end). On the basis of Eq. (17.2) and the sign of the temperature gradient, for the flux of an element which moves from the hot end to the cold end, Q^* is positive. For an element moving from cold to hot, Q^* is negative.

The driving force of thermomigration is given as

$$F = -\frac{Q^*}{T}\left(\frac{\partial T}{\partial x}\right) \tag{17.3}$$

To make a simple estimation of the magnitude of the driving force, we take $\Delta T/\Delta x =$ 1000 °C/cm, and consider the temperature difference across an atomic jump and take the jump distance to be $a = 3 \times 10^{-8}$ cm. We have a temperature change of 3×10^{-5} K across an atomic spacing. So the thermal energy change will be.

$$3k\Delta T = 3 \times 1.38 \times 10^{-23}(\text{J/K}) \times 3 \times 10^{-5}\text{K} \approx 1.3 \times 10^{-27}\text{J}$$

As a comparison, we shall consider the driving force, F, of EM at a current density of 1×10^4 A/cm^2 or 1×10^8 A/m^2 which we know has induced EM in solder alloys.

$$F = Z^*eE = Z^*e\rho j$$

We shall take $\rho = 10 \times 10^{-8}$ Ω m, Z^* of the order of 10, and e $= 1.602 \times 10^{-19}$ C, and we have $F = 10 \times 1.6 \times 10^{-19}$ (C) $\times 10 \times 10^{-8}$ (Ω m) $\times 10^8$ A/m$^2 = 1.6 \times 10^{-17}$ C V/m $= 1.6 \times 10^{-17}$ N.

The work done by the force in a distance of atomic jump of 3×10^{-10} m will be $\Delta \mathbf{w} = 4.8 \times 10^{-27}$ N m $= 4.8 \times 10^{-27}$ J. This value is close to the thermal energy change we have calculated in the above for TM. Thus, if a current density of 10^4 A/cm^2 can induce EM in a solder joint, a temperature gradient of 1000 °C/cm will induce TM in a solder joint.

We can apply the above procedure of calculation to obtain a quantitive comparison of TM and EM in the samples shown in Figures 17.12 and 17.13. We assume that Cu atoms are the diffusion species for the migration of the Cu-Sn IMCs. The effective charge number of Cu is taken as 6.4, resistivity as $1.67 \times 10^{-8}\,\Omega$ m, and the current density as 9.7×10^{7} A/m^2. Thus, the electromigration force is 1.66×10^{-18} N. The work done by the force in an atomic jump distance of 3×10^{-10} m is 4.98×10^{-28} J. We note that we have taken the resistivity of pure Cu in the above calculation. On the other hand, if we use the resistivity of the solder, it will be much higher.

When the TM force balances the EM force, we have $3k\Delta T = 4.98 \times 10^{-28}$ J, which yields $\Delta T = 1.2 \times 10^{-5}$ K across an atomic jump, so the thermal gradient is 400 °C/cm. In other words, when the thermal gradient is greater than the critical value of 400 °C/cm, the TM force on Cu atoms is bigger than the EM force. Therefore, voids would form in the chip/anode end in Bump 2. Otherwise, voids would not be present in the chip/anode end for Bump 2. Instead, hillocks would form there. As shown in Figure 17.12b, the thermal gradient in Bump 2 reached 1643 °C/cm, which is greater than the calculated critical gradient. Therefore, as Cu atoms dissolved from the UBM and driven by TM to migrate toward the substrate side, which was against the direction of electrical current in Bump 2, vacancies were left at the interface between the UBM and the solder to form voids there. Therefore, the TM of Cu enhances Cu dissolution during the EM process, accelerating EM failure in Pb-free solder joints with the dissolution of Cu UBMs. How to mitigate this effect deserves further study.

Similar electromigration tests were performed in eutectic SnAg solder joints with an additional 3-μm Ni UBM on the 5-μm Cu UBM. It is interesting to find that there were no damages nor voids observed in Bumps 1, 2, and 4, except that the thickness of Ni-Sn IMCs grew. Voids formed only in Bump 3, which had a downward electron flow. Thus, no TM of Cu and Ni was found in the joints with Ni UBMs. The results also suggest that the dissolution of Ni UBM is much slower than that of Cu, so Ni can serve as a diffusion barrier for Cu TM.

17.4.1 Irreversible Processes of Thermomigration

In terms of the irreversible processes, the heat flow and mass flow in TM can be expressed by the temperature gradients and chemical potential gradients as below. We note that the latter has temperature as a variable.

$$\begin{aligned} J_Q &= -L_{QQ}\frac{1}{T}\frac{\mathrm{d}T}{\mathrm{d}x} - L_{QM}T\frac{\mathrm{d}}{\mathrm{d}x}\left(\frac{\mu}{T}\right) \\ J_M &= -L_{MQ}\frac{1}{T}\frac{\mathrm{d}T}{\mathrm{d}x} - L_{MM}T\frac{\mathrm{d}}{\mathrm{d}x}\left(\frac{\mu}{T}\right) \end{aligned} \tag{17.4}$$

When a material is held in a temperature gradient until a concentration gradient is established to balance the temperature gradient, it comes to a steady state that the mass flow J_M will be zero. Taking $J_M = 0$, we have from the last equation,

$$L_{MQ}\frac{1}{T}\frac{\mathrm{d}T}{\mathrm{d}x} = -L_{MM}T\frac{\mathrm{d}}{\mathrm{d}x}\left(\frac{\mu}{T}\right)$$

Eliminating $T/\mathrm{d}x$, we have

$$d\left(\frac{\mu}{T}\right) = -\frac{L_{MQ}}{L_{MM}}\frac{\mathrm{d}T}{T^2}$$

Now, by differentiation we have

$$d\left(\frac{\mu}{T}\right) = \frac{1}{T}\mathrm{d}\mu + \mu\mathrm{d}\left(\frac{1}{T}\right) = \frac{1}{T}\mathrm{d}\mu - \mu\frac{1}{T^2}\mathrm{d}T$$

Using the thermodynamic relations,

$$\mathrm{d}\mu = -SdT + Vdp \text{ and } m = \mathrm{H} - \mathrm{TS}$$

and substituting them into the previous equation, we obtain

$$\mathrm{d}\left(\frac{\mu}{T}\right) = \frac{V\mathrm{d}p}{T} - H\frac{\mathrm{d}T}{T^2} = -\frac{L_{MQ}}{L_{MM}}\frac{\mathrm{d}T}{T^2}$$

thus

$$\frac{V\mathrm{d}p}{T} = \left(H - \frac{L_{MQ}}{L_{MM}}\right)\frac{\mathrm{d}T}{T^2}$$

To gain an understanding of the meaning of $L_{\mathrm{MQ}}/L_{\mathrm{MM}}$, we consider the ratio of heat flow to mass flow under isothermal conditions, that is, when $\mathrm{d}T/\mathrm{d}x = 0$. We have

$$\frac{J_Q}{J_M} = \frac{L_{QM}}{L_{MM}} = \frac{L_{MQ}}{L_{MM}}$$

by using Onsager's relation that $L_{QM} = L_{MQ}$.

The term L_{MQ}/L_{MM} represents the energy flow associated with a mass flow. Defining $Q' = L_{MQ}/L_{MM}$, we have

$$\frac{V\mathrm{d}p}{T} = (H - Q')\frac{\mathrm{d}T}{T^2} = Q^*\frac{\mathrm{d}T}{T^2} \tag{17.5}$$

where we define the heat of transport, $Q^* = H - Q'$. It represents the difference between the energy associated with the materials that flows (Q') and the enthalpy of the materials (H) in the reservoir from which the flow starts.

17.5 Coupling between Thermomigration and Creep

In the following, we shall couple TM and creep. The coupling between EM and creep has been analyzed. Both EM and creep are constant-temperature processes, but TM is not. To couple TM and creep in the following analysis, we assume first that the Pb-free solder composition is pure Sn, so that there is no concentration gradient. This is a reasonable assumption since in the SnAg solder, Ag diffuses interstitially in Sn so most Ag will be driven to the cold end in the early stage of TM. In the large part of the period of 800 h of TM reported before, it was basically Sn diffusion in pure Sn. Secondly, we should consider creep under a temperature gradient in order to couple it to TM. For simplicity, while we have

temperature as a variable, we shall use the concept of constant-temperature creep since the temperature difference across the solder joint is only a few degrees centigrade, so $\Delta T/T_{\mathrm{m}}$ is very small where T_{m} is the melting point of the solder.

By replacing the chemical potential, μ, by the stress potential, $\sigma\Omega$, we couple creep and TM by the following pair of equations.

$$J_M = C\frac{D}{kT}\left[-T\frac{\mathrm{d}}{\mathrm{d}x}\left(\frac{\sigma\Omega}{T}\right)\right] - C\frac{D}{kT}\frac{Q^*}{T}\frac{\mathrm{d}T}{\mathrm{d}x} \tag{17.6}$$

$$J_Q = L_{QM}\left[-T\frac{\mathrm{d}}{\mathrm{d}x}\left(\frac{\sigma\Omega}{T}\right)\right] + \kappa\frac{\mathrm{d}T}{\mathrm{d}x} \tag{17.7}$$

We can rewrite the last two equations as,

$$J_M = C\frac{D}{kT}\left[-\frac{\mathrm{d}\sigma\Omega}{\mathrm{d}x} + \left(\frac{\sigma\Omega - Q^*}{T}\right)\frac{\mathrm{d}T}{\mathrm{d}x}\right] \tag{17.8}$$

$$J_Q = L_{QM}\left(-\frac{\mathrm{d}\sigma\Omega}{\mathrm{d}x}\right) + \left(L_{QM}\frac{\sigma\Omega}{T} + \kappa\right)\frac{\mathrm{d}T}{\mathrm{d}x} \tag{17.9}$$

In Eq. (17.8), only Q^* is unknown. This is because experimentally, we can measure J_M from marker motion, we can assume σ to be the elastic limit so we have $\mathrm{d}\sigma/\mathrm{d}x$, and we know $\mathrm{d}T/\mathrm{d}x$ and T. On marker motion, we have

$$\Omega J_M A t = A\Delta x$$

Where Ω is atomic volume of Sn, A is cross-sectional area of the sample, t is stressing time, Δx is the average displacement of markers. We found Q^* to be 7.4 kJ/mole.

In Eq. (17.8), if we let $J_M = 0$, it means the back stress will balance the TM, and there is no net atomic flux at a steady state, we have,

$$\frac{\mathrm{d}\sigma\Omega}{\mathrm{d}x} = \left(\frac{\sigma\Omega - Q^*}{T}\right)\frac{\mathrm{d}T}{\mathrm{d}x} \tag{17.10}$$

By rearrangement, we have

$$\frac{\mathrm{d}T}{T} = \frac{\mathrm{d}\sigma\Omega}{\sigma\Omega - Q^*}$$

By integration, we obtain

$$\frac{T_1}{T_2} = \frac{\sigma_1\Omega - Q^*}{\sigma_2\Omega - Q^*}$$

Then,

$$\frac{\Delta T}{\Delta\sigma} = \frac{T_1 - T_2}{\sigma_1 - \sigma_2} = \frac{T_2\Omega}{\sigma_2\Omega - Q^*} \tag{17.11}$$

We note that both σ and Q^* can be positive and negative. The above equation indicates the condition under which TM can be balanced by creep or by stress migration. We recall that in

EM by stress short strips of Al, a critical length was found below which there will be no EM. But in TM in a flip-chip solder joint under backstress, no critical length is found.

17.6 Coupling between Thermomigration and Electromigration: Thermoelectric Effect on Electromigration

In the schematic diagram in Figure 17.2a, Joule heating of the Al interconnect on the chip side induces a temperature gradient across both the solder bumps. At the same time, electromigration occurs in both of them. As depicted by the arrows that indicate the electron flow direction, atoms will be driven upward in the left-hand side solder bump, but downward in the right-hand side bump. Thus, the temperature gradient, from hot to cold, is in the same direction in the right-hand side solder bump, but they are opposite in the left-hand side bump. EM and TM interact differently in them. Experimentally, as shown in Figure 17.5, among the four pairs of bumps, No. 6–7, 10–12, 14–15, and 18–19, the combined effects of TM and EM are shown by the images that in the left-hand side bump, the darker Sn-rich phase has moved to the bottom, but in the right-hand side bump, it moved to the top, indicating that the effect of EM is larger than that of TM. Bump No. 10 has shown melting in the upper part.

To analyze the interaction between EM and TM, we could write the following equation that

$$J_{\mathrm{m}} = C\frac{D}{kT}\frac{Q^*}{T}\frac{\mathrm{d}T}{\mathrm{d}x} \pm C\frac{D}{kT}Z^*eE \tag{17.12}$$

where the first term on the right-hand side is the atomic flux caused by thermomigration and the second term by electromigration. However, we note that as discussed in the previous section on the interaction between TM and creep; while creep is typically a constant temperature process, TM is a nonconstant-temperature process. We encounter the same issue here that EM is usually a constant-temperature process.

In considering creep in a solder joint, we assume that the effect of $\Delta T/T_{\mathrm{m}}$ on the stress-potential gradient, the driving force of creep, is small, so we can analyze the creep as a constant temperature process. But this may not be true in EM due to the thermoelectric effect, and the temperature gradient will cause a voltage drop in the solder joint, which in turn will affect the driving force of electromigration. How big is this thermoelectric effect is unclear and a detailed analysis and calculation is needed. If we assume steady-state processes, the analysis will become simpler.

17.7 Summary

In this chapter, we have briefly reviewed the behavior of thermomigration in flip-chip solder joints of SnPb and Pb-free solders. Due to Joule heating of the interconnect on the chip side, a temperature gradient of 1000 °C/cm can exist in the flip-chip solder joint and it is large enough to cause thermomigration. The thermomigration can interact with stress migration as well as electromigration in the solder joint to cause failure. Thus, thermomigration is a reliability concern in flip-chip technology and can lead to void and hillock formation.

Acknowledgments

The authors at UCLA would like to acknowledge the support by SRC contract # NJ-1772.

References

1. Shewmon, P. (1989) Chapter 7 on Thermo- and electro-transport in solids, *Diffusion in Solids*, TMS, Warrendale, PA.
2. Ragone, D.V. (1995) Chapter 8 on Nonequilibrium thermodynamics, *Thermodynamics of Materials*, vol. **II**, Wiley, New York.
3. Balluffi, R.W., Allen, S.M., and Carter, W.C. (2005) Chapter 2 on Irreversible thermodynamics: Coupled forces and fluxes, *Kinetics of Materials*, Wiley-Interscience, Hoboken, NJ.
4. Roush, W. and Jaspal, J. (1982) Thermomigration in Pb-in solder. IEEE Proceedings, CH1781, pp. 342–345.
5. Campbell, D.R., Tu, K.N., and Robinson, R.E. (1976) Interdiffusion in a bulk couple of Pb-PbIn alloy. *Acta Met.*, **24**, 609.
6. Ye, H., Basaran, C., and Hopkins, D.C. (2003) Thermomigration in Pb-Sn solder joints under joule heating during electric current stressing. *Appl. Phys. Lett.*, **82**, 1045–1047.
7. Chuang, Y.C. and Liu, C.Y. (2006) Thermomigration in eutectic SnPb alloy. *Appl. Phys. Lett*, **88**, 174105.
8. Hsiao, H.-Y. and Chen, C. (2009) Thermomigration in Pb-free SnAg solder joint under alternating current stressing. *Appl. Phys. Lett.*, **94**, 092107.
9. Huang, A., Gusak, A.M., Tu, K.N., and Lai, Y.-S. (2006) Thermomigration in SnPb composite flip chip solder joints. *Appl. Phys. Lett.*, **88**, 141911.
10. Chen, H.Y., Chen, C., and Tu, K.N. (2008) Failure induced by thermomigration of interstitial Cu in Pb-free flip-chip solder joints. *Appl. Phys. Lett.*, **93**, 122103.
11. Tian, T. and Tu, K.N. (2009) Thermomigration in flip chip solder joints. *ASE Technol. J.*, **2**(2), 132–136.
12. Chen, C., Tong, H.M., and Tu, K.N. (2010) Electromigration and thermomigration in Pb free flip chip solder joints. *Annu. Rev. Mater. Res.*, **40**, 531–555.

Thematic Area IX

Miniaturization Issues Affecting Reliability

18

Influence of Miniaturization on Mechanical Reliability of Lead-Free Solder Interconnects

Golta Khatibi[1], *Herbert Ipser*[2], *Martin Lederer*[1], *and Brigitte Weiss*[1]
[1] *University of Vienna, Physics of Nanostructured Materials, Boltzmanngasse 5, Vienna A-1090, Austria*
[2] *University of Vienna, Department of Inorganic Chemistry/Materials Chemistry, Waehringerstr. 42, Vienna A-1090, Austria*

18.1 Introduction

The electronics industry is among the most dynamic and challenging industry sectors covering a wide variety of products ranging from telecommunication to automotive, aviation and traction applications. Market and consumer requirements include innovative products of higher performance, reliability and market availability. The number of applications under harsh environmental conditions increases, and the integration of new functions into products with higher efficiency and packing density leads to the implementation of new materials and rapid downscaling (*miniaturization*) of the devices.

New generations of microsystems and of microelectronic devices require the application of new materials and material combinations. The miniaturization of such systems is intimately connected with the thermomechanical performance of the used materials that determines their reliability and functionality. Due to their application purposes microsystems are manufactured as a combination of various materials, and it is well known that solder and solder joints are the critical links in such systems. With an estimate of some 10^{13}

Lead-free Solders: Materials Reliability for Electronics, First Edition. Edited by K. N. Subramanian.

joints per annum [1] the solder joints may be regarded as a critical feature for future development of electronics.

The political decision to replace lead-containing solders by lead-free ones has caused enormous efforts in technical investigations of solder joints based on lead-free solder materials, and numerous detailed results have been published.

Although the development of solder materials and soldering techniques reaches back several thousand years it is only in the last few decades that the performance of soldered joints in electronic devices has received detailed attention. A lot of work has been done since Engelmaier [2] stated that the electronic industry continues to struggle with reliable solder attachments, as well as with the soldering process itself, and the behavior of solder joints under changing thermal and mechanical loading conditions. He suggested that not just the reliability of the isolated solder joints should be considered but the reliability of the solder joint system in the context of individual elements that are connected via the solder joints to the printing wiring board (PWB). The characteristics of these three elements – component, substrate, and solder joint – together with the conditions of use, the design life, and the acceptable failure probability for the electronic assembly determine the reliability of any surface-mount solder attachment [3].

This complex system consists of the solder and the base material through which the solder is metallurgically bonded to the PWB; it contains one or more thin layers of intermetallic compounds (IMCs) with various grain sizes and, in addition, numerous phases in the solder material itself. As a consequence of the complexity of such a material system, solder-joint failures may occur during operation that is, in fact, one of the major problems affecting the reliability. Hence, the structural integrity of the joints and thus the mechanical behavior of solders and joints have gained considerable importance.

An additional complicating factor is that the solder under typical temperatures of operation behaves more like a viscoplastic than a typical structural material [4–6]. It is subjected to creep and stress relaxation and can be considered as a system having a load-bearing capability on a strictly temporary basis. Furthermore, the IMCs forming an interface between solder and a particular plating material are considered to resemble a good metallurgical bond, however, it is known that – depending on the operational conditions – the microstructure and the geometrical stability of IMCs may change, possibly resulting in a reduced lifetime [6–8].

Alloys used as solders in the electronics industry require a low melting temperature, and the variety of such alloys is enormous, however, the traditional tin-lead alloys have dominated in the past and are currently being replaced by lead-free solders due to the toxicity of lead [9]. This required new attempts for selecting solder alloys with properties comparable to those of the conventional lead-based solders, following well-defined performance characteristics of solder alloys in electronic devices. In general, the alloy should meet the electrical and mechanical performance and must also have the desired melting temperature. The major performance characteristics are manufacturability and reliability, where the *reliability* of a solder alloy seems to be mainly dependent on the mechanical properties of the resulting joints such as: Young's modulus, yield strength, shear strength, fatigue and creep behavior under operational loading conditions.

In the meantime, numerous lead-free alloy systems have been presented, and various literature data, reviews, conference reports and data banks [4–6, 10–15] are now available reporting a great variety of microstructure characteristics as well as physical, chemical,

mechanical and some fatigue data. Most studies were concentrating on the performance of solder materials and/or solder joints under thermal loading conditions because the majority of failures arose due to the development of cyclic strains induced by thermal fluctuations and due to a mismatch in the coefficients of thermal expansion (CTE) of the materials used for the substrate and of the solder connection itself. The thermomechanical response of solder joints has been the subject of numerous studies, and several models have been presented to predict their thermomechanical fatigue (TMF) life [3, 16–18]. The results of investigations have been compiled and discussed in detail in several overview articles [19, 20].

Investigations on isothermal fatigue response and crack-growth properties of solder joints are still limited [21–23] although the intrinsic vulnerability to cyclic deformation, associated with the localization and concentration of damage giving rise to early crack initiation, is well known. A shortcoming of most of the earlier data on mechanical properties of solder joints used for modeling is that testing was carried out on bulk samples with a volume of about ($10^{-6}\,m^3$) [24]. In this context one has to consider that modern technology has been reducing the soldered volume from several $10^{-9}\,m^3$ for soldering foils down to flip-chip (solder ball) joints of the order of $<10^{-12}\,m^3$ [25, 26]. This miniaturization reduces the solder gap and simultaneously also the typical diameter of solder area. The reduction of the solder gap decreases the volume ratio between the ductile solder region and the brittle IMC zone at the interface and may thus change the mechanical strength of the solder interconnect. The decrease of the diameter of the solder area down to 100 µm and below could very likely be the cause of enhanced crack probability.

From materials-science considerations in small dimensions [27] it is well known that, in general, the relevant data for bulk materials cannot be used for small cross-sectional areas due to dimensional constraints known as the 'size effect'. Literature data on the mechanical influence of the reduced solder volume of solder joints and even the solder materials themselves are scarce and contradictory.

In the case of solder joints, the size and/or constraint effect is a more complex issue. Due to their reduced size and their structural conditions, solder joints are not only subject to dimensional but also to geometrical constraints. The free plastic deformation of the soft and highly viscoplastic solder alloy that acts as interconnect between two substrates with a much higher rigidity is highly restricted. The degree of the restriction of the deformation depends on the size and geometry of the solder joint and on physical and mechanical properties of the solder and the substrate material. In addition, due to the reduced volume of the solder joints, which is in the range of a few mm^3 to μm^3, microstructural constraints also play a major role in their mechanical performance.

The present chapter aims to give an overview of recent investigations on the effect of miniaturization on mechanical properties of lead-free solder joints with respect to microstructural and mechanical constraints with a focus on their static response, that is, tensile, shear, stress relaxation and creep. In order to arrive at a better understanding of the mechanical response of solder joints, it was attempted to divide, as far as possible, this complex topic that comprises several parameters into single factors and treat them individually. The study includes idealized joints (model joints) as well as actual solder joints. First, the pure *constraint effect* in idealized solder joints with small volume/gap size ratio is discussed and subsequently the studies on the dependence of the mechanical response of solder joints on their microstructural features are treated. A summary of these

results shall provide an overview of some of the most important parameters affecting the reliability of miniaturized lead-free solder joints.

18.2 Effect of Miniaturization on Static Properties of Solder Joints (Tensile and Shear)

18.2.1 Constraint and Geometry Effects in Model Joints

It is well known that, besides size-dependent microstructural effects in solder joints, future reliability will greatly depend on the occurrence of size effects or dimensionally induced constraints that can dramatically change the mechanical properties of solder joints in small dimensions. Already in earlier studies on geometrically constrained brazed and soldered joints it was observed that the tensile strength increases drastically with decreasing size of the solder gap, and this effect can reach several orders of magnitude in comparison with the bulk properties. In analogy to constrained thin films, this effect was related to the geometric aspect ratio of the joint and was explained by the build-up of a triaxial stress state in the thin joint when the joint is subjected to a perpendicular strain at the substrate interface [24, 28–31]. All the earlier studies on constraint effects in solder joints concerned mainly investigations on Pb-Sn solders [29, 30, 32]. On the contrary, very few systematic experimental studies are available in the literature dealing with the effect of the geometry and the reduced size of lead-free solder joints on their mechanical performance. A series of investigations by Zimprich *et al.* [33, 34] on *model joints (idealized joints)* were performed in tensile and shear mode using rectangular-shaped specimens, mainly because of the simple geometry and the simpler physical interpretation of a principally constrained situation. The solder was Sn3.5Ag and the substrate was usually Cu; the gap sizes varied between 25 and 850 μm. The joints were prepared by reflow soldering to achieve near-industrial processing conditions.

Shear loading is, of course, the more critical and more important situation in real solder joints but its interpretation is not so straightforward compared to tensile testing; therefore, this systematic investigation focused at first on the tensile behavior of constrained joints. The situation in real solder joints, as used in microelectronics, is obviously much more complex but, nevertheless, it can be assumed that constraining effects in tensile and shear loading will play an important role in the understanding of the mechanical behavior of interconnects.

To assess the bonding strength of the joints with varying gap sizes, tensile tests were performed at room temperature using a commercial 5-kN tensile testing machine and a fixed cross head speed of 0.5 mm/min for all tests. After soldering, the samples were dumb-bell shaped to achieve a solder joint with a soldered area of $3 \times 2\,\text{mm}^2$; afterwards they were polished and subsequently annealed at 80 °C for 3 h (stress relief) and 120 °C for 6 h (aging), respectively. For each gap size results were obtained as the average from at least six specimens; the reproducibility of the data was found to be of the order of 10%.

A pronounced increase in tensile strength and simultaneously a decrease in fracture strain were observed with decreasing gap size for these model solder joints (Figure 18.1). The ultimate tensile strength (UTS) for solder joints with a gap size of about 25 μm showed values similar to that of the Cu base material (300 MPa), while for a gap size of 850 μm a

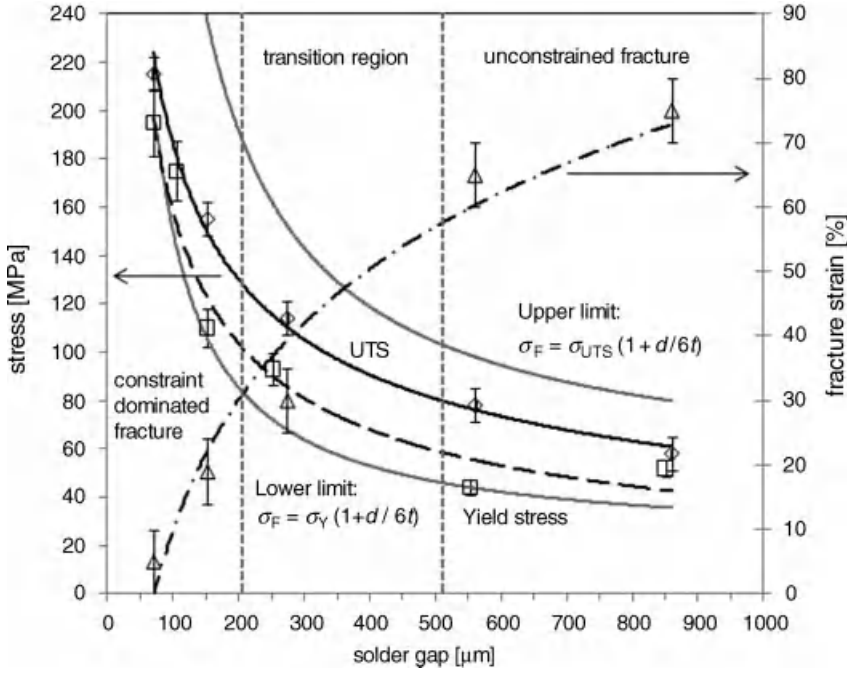

Figure 18.1 *Ultimate tensile strength (UTS) and fracture strain of Sn3.5Ag/Cu solder joints with various gap sizes [33]. (Reprinted from Journal of Materials Science: Materials in Electronics, Size effects in small scaled lead-free solder joints by P. Zimprich, A. Betzwar-Kotas, G. Khatibi, B. Weiss and H. Ipser, 19, 4, 383–388 Copyright (2008) Springer Science + Business Media).*

clear trend was found towards the tensile strength of the solder material itself (experimentally determined to be 50 MPa for the Sn3.5Ag solder) [33]. Figure 18.1 shows that Sn3.5Ag/Cu solder joints with varying gap sizes exhibited a clear evidence of the effect of mechanical constraints. The observed behavior can be explained qualitatively with the well-established model for brazed joints, first pointed out by Orowan *et al.* [35], owing to the development of triaxial stresses in the thinner joints, depending on diameter and thickness of the solder joint. Qualitatively, the tensile behavior of solder joints was found to be similar to that of brazed joints (down to about 100 µm), and the influence of the IMC seemed to be negligible. This behavior could be described by a relatively simple equation where the stress of the joint σ_F is proportional to the stress of the substrate and to geometrical factors with d being the diameter of the sample and t the joint thickness:[1]

$$\sigma_F(\text{joint}) = \sigma_{UTS/yield}(\text{braze or solder})\, x\, (1 + d/6t) \qquad (18.1)$$

Based on the Orowan equation (Eq. (18.1)), curves predicted for the upper and lower limits of the solder joint strength as a function of gap size are shown in Figure 18.1 together with experimental data points.

[1] This equation was originally derived for round bar-shaped specimens and was adapted to rectangularly shaped specimens in this study.

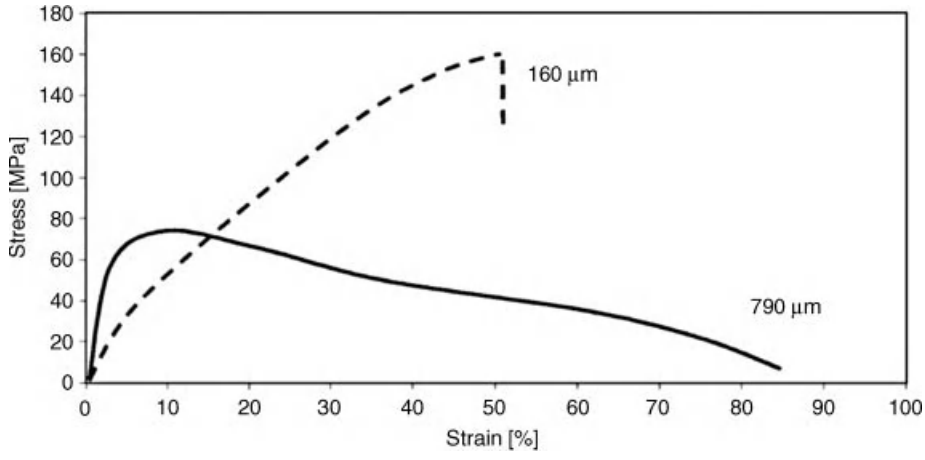

Figure 18.2 *Typical stress–strain curves of Sn-3.5Ag/Cu solder joints with gap size of 160 and 790 µm [33]. (Reprinted from Journal of Materials Science: Materials in Electronics, Size effects in small scaled lead-free solder joints by P. Zimprich, A. Betzwar-Kotas, G. Khatibi, B. Weiss and H. Ipser, 19, 4, 383–388 Copyright (2008) Springer Science + Business Media).*

Additional evidence for the development of dimensional constraints could be found in a significant change of the fracture mode with joint thickness. Increasing the thickness of the solder gap led to enhanced plastic deformation in the solder volume that in most cases resulted in fracture inside the solder instead of cracking at the IMC/solder interface (Figures 18.2 and 18.3).

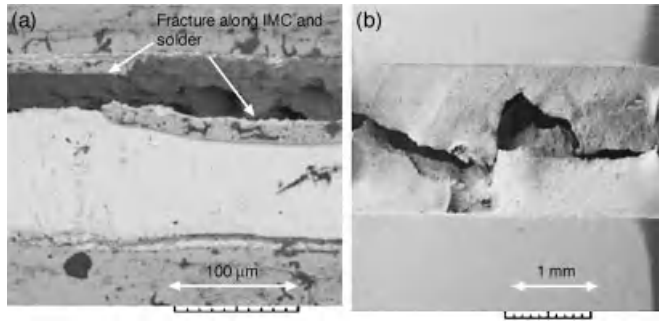

Figure 18.3 *(a) SEM image of a Sn-3.5Ag/Cu solder joint with gap size 160 µm after fracture at 650 N and strain of 50%; the fracture occurs at the interface between IMC and the solder material; (b) SEM image of a solder joint with gap size 790 µm after loading at 90 N and 40% strain; the fracture occurs inside the solder [33, 34]. (Reprinted from Journal of Electronic Materials, Mechanical Size Effects in Miniaturized Lead-Free Solder Joints by P. Zimprich, U. Saeed, A. Betzwar-Kotasi, B. Weiss and H. Ipser, 37, 1, 102–109 Copyright (2008) Springer Science + Business Media). (Reprinted from Journal of Materials Science: Materials in Electronics, Size effects in small scaled lead-free solder joints by P. Zimprich, A. Betzwar-Kotas, G. Khatibi, B. Weiss and H. Ipser, 19, 4, 383–388 Copyright (2008) Springer Science + Business Media).*

Table 18.1 *Experimentally determined material data for Cu substrate.*

Material	σ_y [MPa]	σ_{UTS} [MPa]
Cu (80 °C/3 h)	250	310
Cu (170 °C/500 h)	50	223

Using the Orowan model, as the solder-joint thickness decreases and reaches an infinitesimal value, the theoretical value of the joint strength increases towards infinity. This is due to the assumption that the base material behaves perfectly rigid. However, due to the actual compliance of the base material, the strength of the joint approaches a finite value for thin solder gaps.

This behavior was investigated by FEM simulations performed with ANSYS 11.[2] In this study (details are being published elsewhere), solder and Cu were both simulated with elastoplastic material models using multilinear hardening. The cross section of the solder gaps was 2 mm × 3 mm. Based on material data presented in Table 18.1 for Cu substrate and on literature values for Sn-3.5Ag solder [1], the calculated curve for the joint stress versus gap size showed good agreement with the experimental data (Figure 18.4). After an aging treatment of 500 h at 170 °C, calculated UTS versus solder gap size showed reduced values, however with a smaller constraining effect. Preliminary experiments on samples with this heat treatment indicated a good correlation with the calculated values.

The constraining effect leads to different types of fracture depending on the thickness of solder gaps, as already shown in Figures 18.2 and 18.3: gaps with large thickness broke due to necking at the midsection of the solder, whereas thin gaps exhibited brittle fracture of the solder near the interface. This experimental observation was confirmed by FEM simulations.

In Figures 18.5 and 18.6 a comparison of plastic von Mises strain is shown for two different gap sizes. In both samples the stress along the tensile axis was 59 MPa. These figures refer to samples heat treated for 3 h at 80 °C. While the specimen with a gap size of 900 μm is already close to rupture, the plastic strain in the solder with 300 μm thickness is overall below 0.2%. The thicker solder joint broke due to necking in the middle of the gap. In contrast, rupture of the thinner solder joint was assumed for that load step where the local plastic strain at the edges of the solder exceeded 50%. However, the longitudinal fracture strain along the tensile direction averaged over the volume of the solder gap was less than 5% for gap sizes smaller than or equal to 300 μm.

The fracture criterion used in the FEM simulations is further illustrated in Figure 18.7. Fracture was assumed when the maximum of local plastic von Mises strain exceeded 50%. This value agrees with experimental observations of tensile tests for bulk solders that reached a maximum local strain of approximately 50% at the position of necking. These calculations resemble the actual experimental findings. Similar calculations were performed for all gap sizes (Figure 18.4).

Recently, a similar study on size and volume effects on the strength of microscale lead-free Sn-3.0Ag-0.5Cu solder joints with a gap size of 75 to 525 μm on Cu rods with diameters

[2] http://www.ansys.com/.

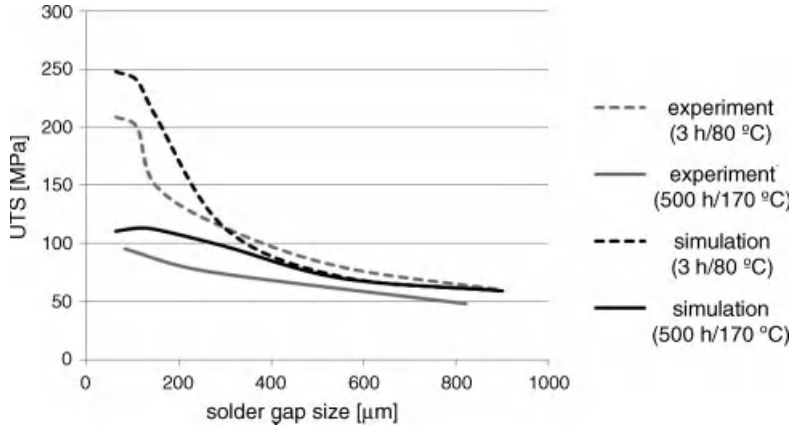

Figure 18.4 *The experimental values for the constraining effect are compared with results of simulations: the UTS of solder joints clearly exceeds the tensile strength of 40 MPa for bulk solder.*

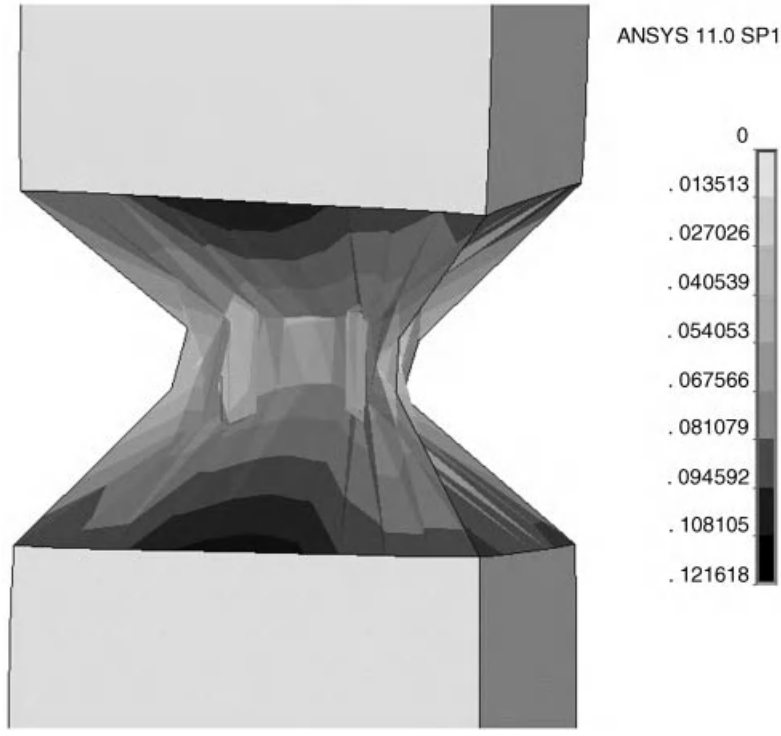

Figure 18.5 *Plot of the plastic von Mises strain for the initially 900-µm thick solder gap at a tensile stress of 59 MPa. A pronounced necking is observed. The maximum value of von Mises strain is 12.2%.*

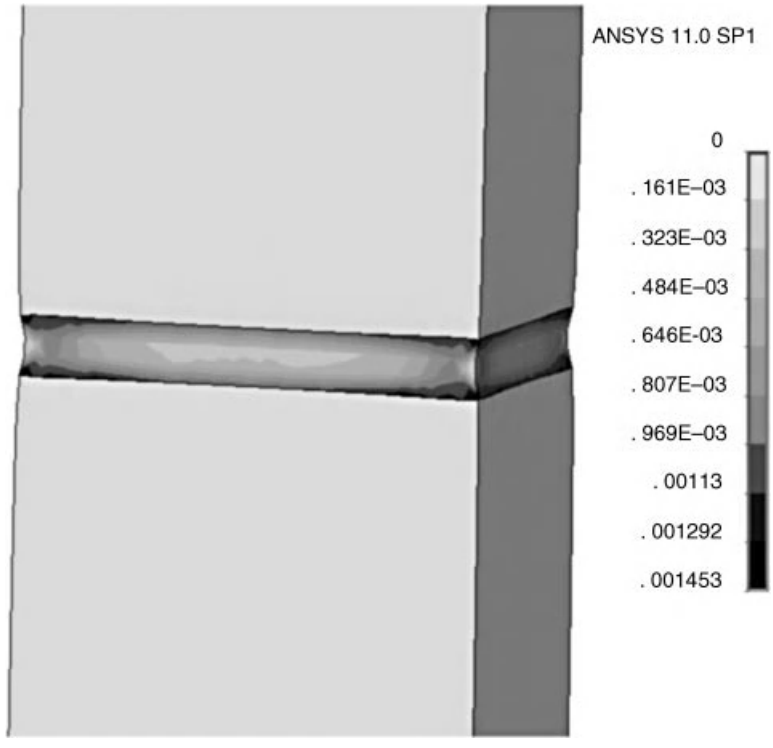

Figure 18.6 *Plot of the plastic von Mises strain for the sample with 300-μm solder gap at a tensile stress of 59 MPa. The maximum of von Mises strain is found at the corners. The plastic strain is everywhere below 0.2%.*

of 200 to 575 μm was performed by Yin *et al.* [36] and arrived at similar results, as reported by Zimprich *et al.* [33, 34].

Cugnoni *et al.* performed similar studies on size and constraining effects in lead-free (Sn-4.0Ag-0.5Cu) solder joints under tension [37]. They used rectangular specimens with cross sections of 20×1 mm^2, and the gap sizes were varied in the range from 0.25 to 2.4 mm. The experimental results showed a constraining effect that was somewhat smaller than expected on the basis of von Mises plasticity. The authors attributed this result to a high amount of porosity within the solder gaps, whereby porosity increased with decreasing gap sizes. This was probably due to the thermal profile of the soldering process that included rapid cooling in water. Therefore, the authors developed an inverse numerical identification procedure using the FEM code ABAQUS[3] in order to determine the material properties of solder joints with varying porosity. The results for the material properties obtained from nonlinear fitting are depicted in Figure 18.8. Furthermore, one can calculate the contribution of the constraining effect to the measured UTS of solder joints, as shown in the diagram (Figure 18.8).

[3] http://www.simulia.com/products/unified_fea.html.

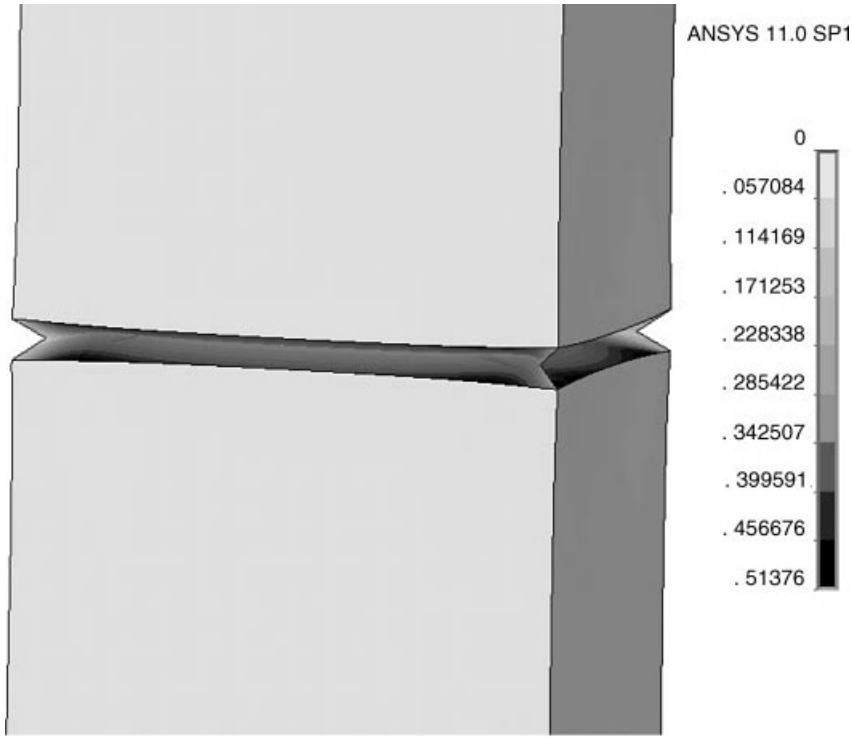

Figure 18.7 *Illustration of the fracture criterion for a sample with gap size of 64 μm. Here, the local plastic von Mises strains depicted in red exceeded a value of 50%. Therefore, the sample was considered as broken at this load step of the simulation.*

An increase of porosity on decreasing the solder volume/size has also been observed by other investigators [30, 38]. The presence of internal defects such as oxide particles, microvoids and transverse grain boundaries has also been reported to reduce the joint strength [30]. The significance of voids on the reliability of solder joints is variable. Three-dimensional voids may be sufficiently large to reduce the actual soldered area, they may accelerate growth or act as crack deflectors or blunters [1, 39].

Furthermore, to investigate the influence of the gap size on the shear strength of solder joints at 25 °C, single-lap shear specimens of Sn-3.5Ag solder were prepared using Cu and Ni plates as reported in Ref. [34]. The soldered area of the joints was 4 mm^2, which is larger than the soldered areas used in electronic systems (about 1 mm^2); the higher area was found to achieve better joint reproducibility. Shear-stress–displacement curves of such joints for gap sizes between 80 and 450 μm show a clear constraining effect (Figure 18.9). A minimal effect of substrate material on the shear strength of solder joints prepared with Cu or Ni substrates was observed. A comparison of shear strength with tensile data for gap sizes from 330 down to 150 μm shows a strong increase of shear strength, which is approximately three times larger than the increase of the UTS in the same gap-size region (Figure 18.10). The present experiments provide comparative values of the shear stress without evaluation of the shear strain.

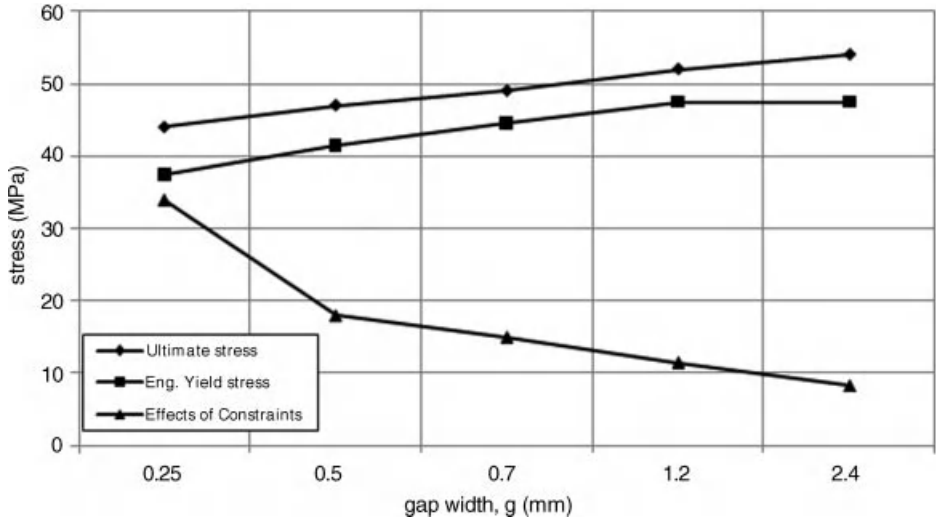

Figure 18.8 *Constitutive properties and constraining effects in Sn-4.0Ag-0.5Cu/Cu joints as a function of solder gap [37]. (Reproduced with permission from Fatigue & Fracture of Engineering Materials & Structures, Experimental and numerical studies on size and constraining effects in lead-free solder joints by J. Cugnoni, J. Botsis, V. Sivasubramanian and J. Janczak-Rusch, 30, 5, 387–399 Copyright (2007) John Wiley & Sons).*

An interpretation of shear stress–strain response of solder joints is known to be a difficult task. Few studies have examined the effects of geometry on the elastic and plastic behavior of solder joints tested using the lap-shear technique [40, 41]. Using numerical models and experimentally determined shear stress–strain curves for Cu/Sn–3.5Ag/Cu solder joints, the effect of solder joint thickness and of the geometry of the joint and the substrate on the shear-strain response of miniaturized solder joints were studied [41]. Shen *et al.* pointed out that during shear loading of solder joints the transmission of shear strain into the solder is very ineffective when the solder is in the elastic state [41]. It could be shown that the shear strain

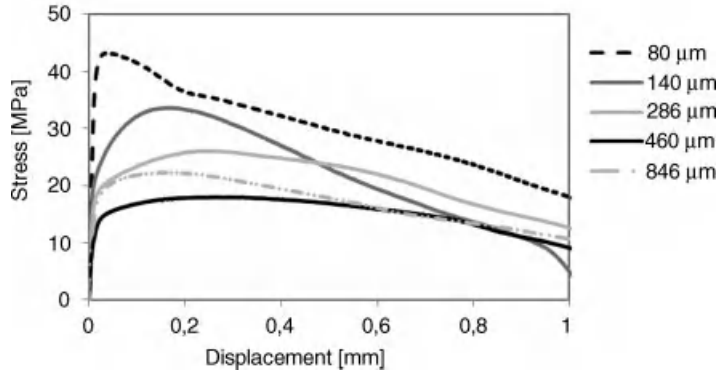

Figure 18.9 *Shear-stress–displacement curves for Sn-3.5Ag solder joints of different gap sizes.*

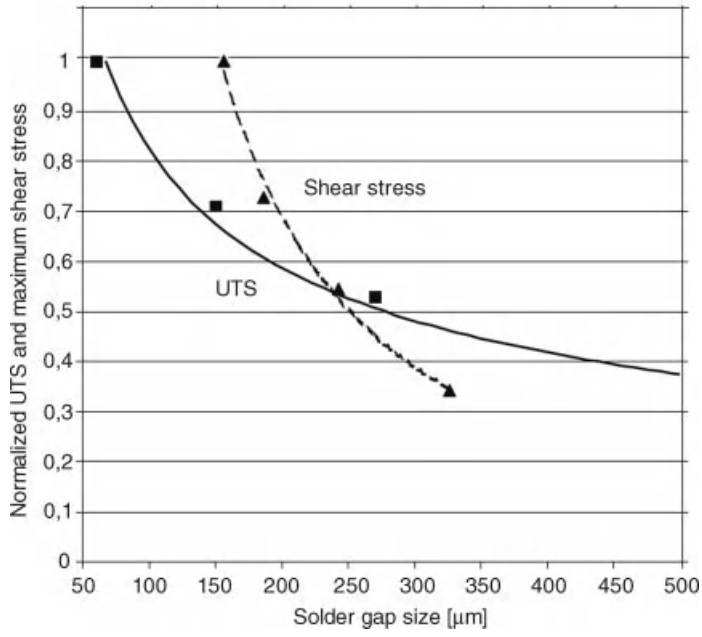

Figure 18.10 *Comparison of normalized UTS and normalized maximum shear stress of Sn-3.5Ag solder joints. The rate of increase in shear strength in a certain range of joint size (150–350 lm) was found to be approximately three times higher than that measured for tensile specimens [34]. (Reprinted from Journal of Electronic Materials, Mechanical Size Effects in Miniaturized Lead-Free Solder Joints by P. Zimprich, U. Saeed, A. Betzwar-Kotas, B. Weiss and H. Ipser, 37, 1, 102–109 Copyright (2008) Springer Science + Business Media).*

of the solder approaches progressively the 'true' shear value with increasing joint thickness. A comparison of the nominal strain in the joint as measured by a clip gage and the actual strain as measured by a direct optical method is shown in Figure 18.11. By correction of the far-field strain for the amount of shear strain of the Cu substrate the curves show that, after an initial delayed build-up of strain in the solder joint, the actual and apparent (far-field) curves are parallel and show the same trend. Thus, the shear strain in a joint is initially induced in the substrate and, depending on the joint thickness, is then transferred into the solder joint. Subtraction of the deformation of the Cu substrate provides a reasonable approximation of the solder strain in the elastic regime but not in the plastic regime. In most cases the Cu substrate is at least an order of magnitude thicker than the solder but it is not a rigid solid and will participate in the deformation process during loading. Thus, for a reliable evaluation of shear strain response of miniaturized solder joints the above-mentioned considerations should be taken into account.

The root cause for the increased tensile strength of the constrained joint geometry is illustrated in Figure 18.12: Due to the lower yield strength of the solder material, a plastic deformation occurs in the solder joint, while the copper base material is behaving almost elastically. Furthermore, the solder material has the lower elastic modulus and higher Poisson ratio compared to Cu, and therefore the crosscontraction in the solder is higher than

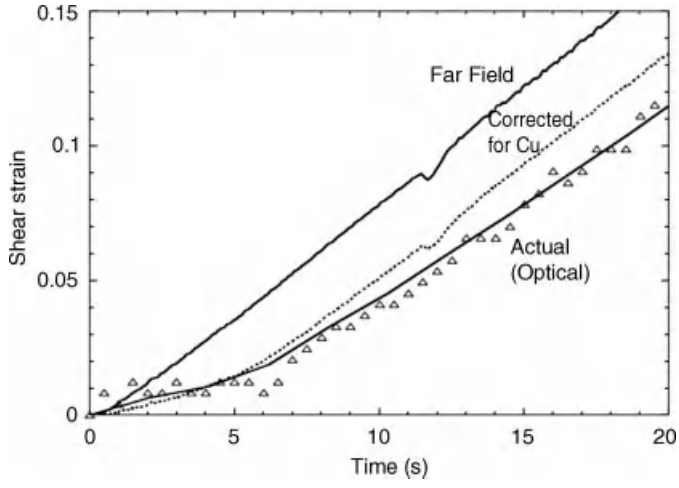

Figure 18.11 *Shear strain versus time plot of a Sn-3.5Ag/Cu joint at a strain rate of about 10^{-2}/s. The actual strain in the solder was measured by direct optical sensing. Correcting the nominal (far-field) strain for the elastic deformation of copper yields a closer response to the actual one [41]. (Reproduced with permission from Acta Materialia, Deformation analysis of lap-shear testing of solder joints by Y. L. Shen, N. Chawla, E. S. Ege and X. Deng, 53, 9, 2633–2642 Copyright (2005) Elsevier Ltd).*

in copper. In the case of a thick solder joint, the crosscontraction in the solder leads to pronounced necking. In the middle of such a joint the material behaves similar to a tensile specimen consisting of solder material only. Hence, the tensile strength of a thick joint will be similar to that of bulk solder material. In the case of a thin joint, however, the crosscontraction of the solder material is more suppressed by the boundary conditions along the interface. As a consequence, the solder material is exposed to triaxial tensile stress caused by the proximity to the interface. Following the principles of von Mises plasticity, the hydrostatic component of the stress is subtracted from the stress tensor in order to obtain the deviatoric stress. Further, the von Mises stress equivalent $\sigma_{\mathrm{vM}} = \sqrt{3 \cdot J_2}$ is calculated with the use of the second invariant J_2 of the deviatoric stress. Therefore, the von Mises stress equivalent within a thin solder joint is reduced in comparison to a thick joint subjected to the same tensile load. Consequently, plastic yielding of a thin joint is shifted to higher loads. This explains why thinner joints show higher tensile strengths. The sample depicted in Figure 18.12 carries a tensile load that is approximately 2.7 times higher than the tensile strength of bulk solder, and even higher strengths are possible for thinner solder gaps.

18.2.1.1 Influence of the Microstructure

Besides the mere constraining effect, some authors attempted to include the influence of the microstructure and the geometry on the mechanical response of miniaturized solder joints. Solder joints display a particular microstructure with features that are considerably different from those in the bulk solder alloys. They are mechanically constrained and metallurgically bonded between the substrate materials due to formation of interfacial IMCs. However, such IMCs are not only present in the interface of solder joints but also as a dispersed phase

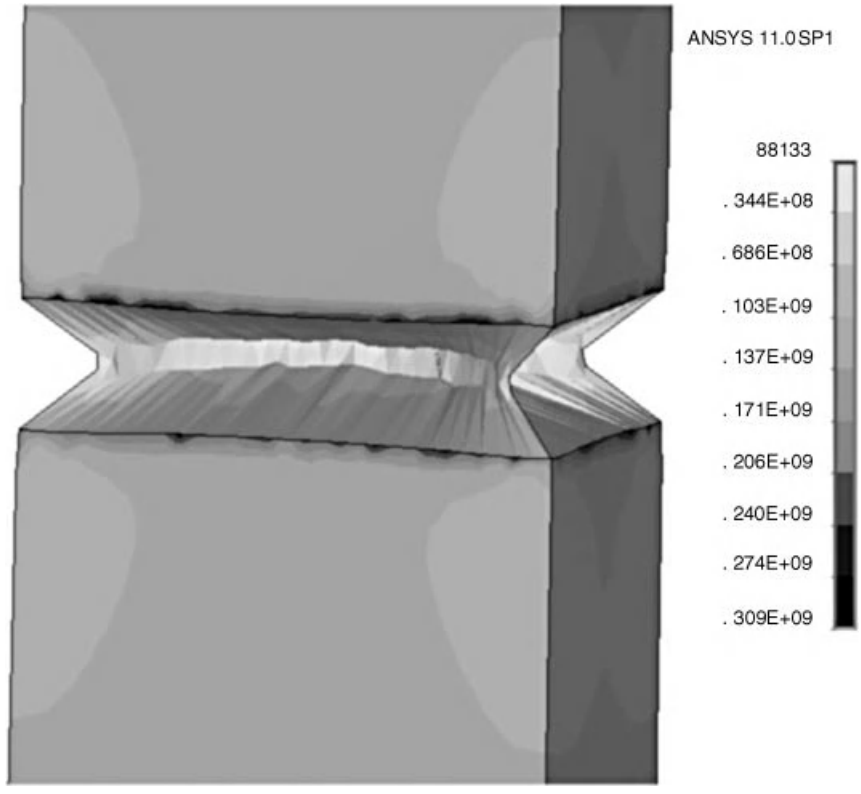

Figure 18.12 *FEM simulation for a solder joint with 300 μm gap size. A plot of the von Mises stress equivalent is shown. Due to triaxial tensile stress the stress equivalent within the solder is less than the stress equivalent in the base material.*

throughout the entire joint. Since the microstructure of the alloy of a joint is often difficult to reproduce in the bulk it has been suggested to use realistic specimen geometries to study the microstructural and/or size effects in solder joints [42–48]. The specific microstructural features of the solder joints include primarily the microstructure of the solder bulk as well as thickness, morphology and properties of the interfacial IMC layers. In addition, the strength of the joint may depend on the size, number, and texture of the grains of the bulk solder alloy and also on the location and percentage of various defects like voids, pores, and cracks, and so on, in the joint.

In a study by Hegde *et al.* [49], the effect of microstructure and size of the joint on stress–strain properties of Sn-3.8Ag-0.7Cu solder joints was investigated and compared with bulk solder of the same alloy. Their experimental results confirmed the previous findings on the strengthening effect of the constrained joints [28–37]. The authors suggested that this strengthening is a contribution of solder joint aspect ratio, state of the stress, and microstructure. The relationship between the solder aspect ratio (g/t) (gap size to thickness),

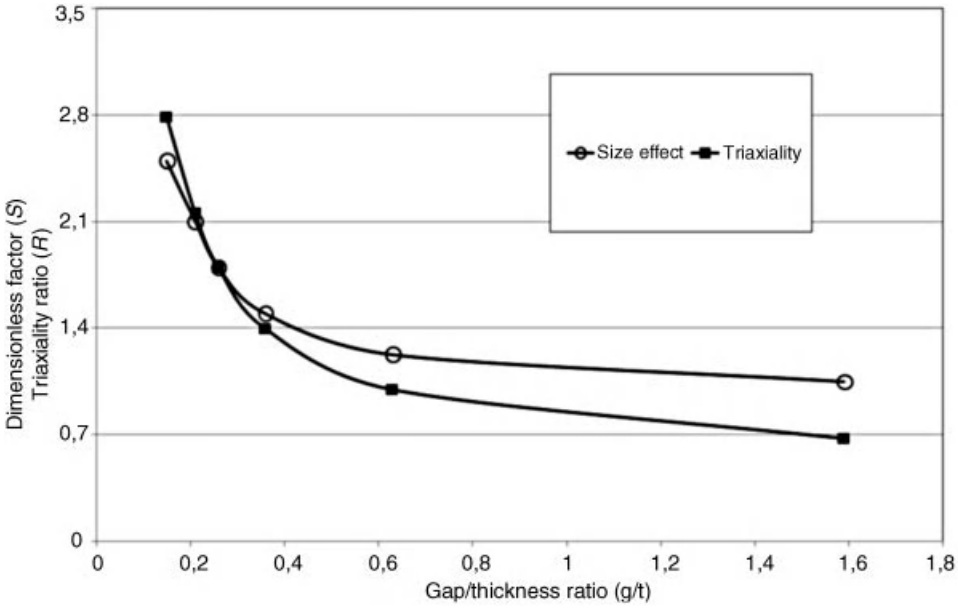

Figure 18.13 *Size effect, $S = \sigma_n/\sigma_e$ (normal stress/equivalent stress) and triaxiality ratio, $R_t = \sigma_h/\sigma_m$ (volume average of hydrostatic stress/volume average of von Mises or equivalent stress) as functions of gap length to thickness ratio [49]. (Reproduced with permission from Microelectronics and Packaging Conference, 2009. EMPC 2009, Size and Microstructure Effects on the Stress-Strain Behaviour of Lead-Free Solder Joints by P. Hegde, D. C. Whalley and V. V. Silberschmidt, 1–9 Copyright (2009) IEEE).*

size effect and the triaxiality ratio is shown in Figure 18.13. The size effect is defined in terms of $S = \sigma_n/\sigma_e$ (normal stress/equivalent stress) and the effect of hydrostatic stress is defined as the triaxiality ratio with $R_t = \sigma_h/\sigma_m$ (volume average of hydrostatic stress/volume average of von Mises or equivalent stress). An increase in both parameters S and R, which is analogous to an increase in the normal stress and hydrostatic stress, respectively, results in an increased apparent tensile strength in the thinner joints. In this study the experimentally determined tensile strengths of the solder joints showed higher values that the theoretically determined values. The authors explain this discrepancy by the contribution of the fine microstructure of the miniaturized solder joints to the further strengthening of the joints as a function of the gap size. The contribution of the microstructure was approximated to be about 30% for the smaller joint size.

The influence of the cooling rate on microstructure and mechanical properties of lead-free solders has been the subject of various studies [43–48, 50]. The microstructure of a system in thermodynamic equilibrium can be obtained with a very slow cooling rate providing sufficient diffusion time. In solder joints, due to their very small volume, even natural air cooling can significantly cause a deviation of the microstructure from its equilibrium state. Comparative studies of the microstructures of bulk solder alloys with solder joints of the same alloys show distinctive differences [46, 51–54].

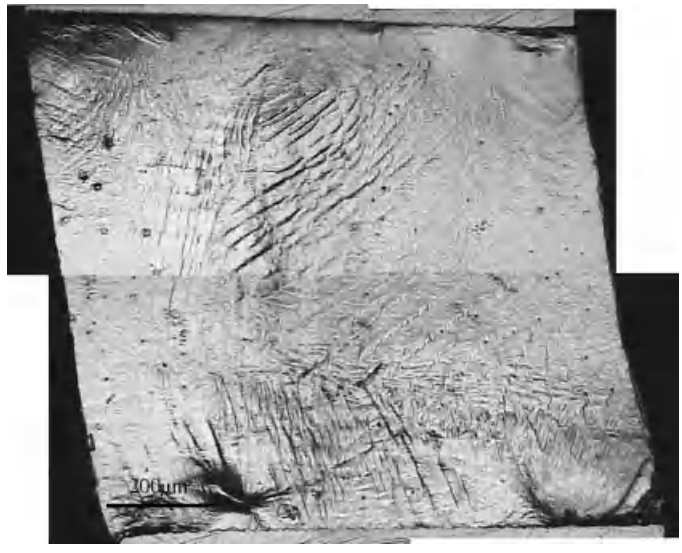

Figure 18.14 *Deformation of a large Sn-3.8Ag-0.7Cu/Cu joint after shear deformation $\gamma = 19\%$ (Reproduced from Proceedings - Electronic Components & Technology Conference, 56th (Vol. 1), Grain Features of SnAgCu Solder and their Effect on Mechanical Behaviour of Micro-joints by J Gong et al., 250–257 Copyright (2006) IEEE). [48]*

The microstructure of typical Sn-Ag-Cu near-eutectic alloys consists usually of a eutectic network of Ag_3Sn fibrous precipitates and a β-Sn matrix surrounded by primary β-Sn grains [43, 45, 47, 50–56]. The eutectic structure coarsens by decreasing the cooling rate and by increasing the Ag content [50]. In the above-mentioned study by Hegde *et al.* the microstructure of Sn-3.8Ag-0.7Cu bulk solder specimens and of corresponding solder joints with a gap size of 0.35 mm were compared [49]. Both were prepared from the same solder paste and reflowed under identical conditions. Apart from the fact that the IMC layers between solder and substrate exist only in the solder joint, clear differences could be observed in the solder alloy of both specimen types: although the cooling rate of both specimen types was similar, the microstructure of the solder joint was found to be finer than that of the bulk solder. The main differences were the larger size of the Sn dendrites, larger size of the β-Sn grains and also the higher fraction of the eutectic phase in the bulk solder. Furthermore, Ag_3Sn IMC particles were more abundant in the solder joints, and Cu_6Sn_5 IMC particles were mainly observed in the solder joints, probably due to the diffusion of Cu from the substrate into the solder. These results show that the microstructure and the related mechanical properties of solder joints with a very small volume differ from those with a larger volume even if prepared under the same process conditions.

Due to the considerable anisotropic behavior of β-Sn with a contracted body-centered tetragonal (BCT) structure, crystal features, such as grain size and orientation, may become key factors for the reliability of a microjoint. With further miniaturization, the effect of the local lattice of β-Sn on the mechanical response of solder joints could be more significant [48, 55, 56]. Based on these facts, Gong *et al.* [48] studied the relationship between the joint size and the microstructure of a Sn-3.8Ag-0.7Cu alloy. Solder joints with gap sizes

between 10 and 1000 μm were prepared under various cooling rates. *In-situ* shear experiments that simulated the condition of shear loading in BGAs were conducted to correlate the mechanical behavior of the solder joint to their microstructural features. They found that decreasing the dimensions of the joint resulted in the reduction of the number of grains, and higher cooling rates resulted in a finer microstructure. The grain size was not significantly sensitive to the cooling rate in the range between 0.13 and 4.5 K/s. The shear response of the miniaturized joints, based on the observation of slip-band formation in the individual grains of solders with different thicknesses, showed that mostly a few and not all the grains in the multicrystalline solder joints are plastically deformed. The direction of the slip in the individual grains was strongly anisotropic and lattice-orientation dependent. The grains did not necessarily deform in the most suitable slip system with respect to the loading direction (Figure 18.14). It was concluded that, as the joint size is reduced, the structure and thus the mechanical behavior of the Sn-Ag-Cu microjoints move from a polycrystalline to a single-crystalline behavior and that the nonthermally activated inelastic behavior of Sn-3.8Ag-0.7Cu grains in a microjoint is considerably lattice dependent.

18.2.1.2 Effect of IMC, Aging Effects and Fracture Morphology

In the following, a selection of studies on the effect of thickness, morphology, and the ratio of the interfacial IMC layer to the joint size on the mechanical performance of solder joints are briefly presented and discussed.

Investigations on a variety of lead-free solder alloys and substrates showed that, depending on the microstructure of the solder joints, decreasing the stand-off height may lead to an improvement or a degradation of tensile and shear properties. One of the main objectives of these investigations was to establish a relationship between the thickness of the IMC interfacial layer and the solder gap size (defined as stand-off height) [57–59].

In a study by Wang *et al.* [57] solder joints of Cu/Sn/Cu and Cu/Sn/Ni with small thicknesses between 10 and 100 μm were prepared by soldering pure Sn foils between two Cu or Ni/Cu flat bars. It was found that by reducing the gap size from 100 to 10 μm, the concentration of Cu (substrate material) in the solder joint alloy was increased. Assuming a constant dissolution rate of the substrate materials in the solder during the reflow process, a smaller solder volume is earlier saturated than a larger one. Consequently, in solder joints with smaller volume, the percentage of the dissolved substrate material is higher but its absolute amount is lower than in joints with a larger volume [57]. The dissolved Cu forms a solid solution and Cu-rich particles in the solder, resulting in different microstructures depending on the solder volume. In the cooling period of the reflow process, the dissolved base materials will react with the solder alloy, to form an interfacial IMC layer. Therefore, as the gap size of the solder joint, and consequently its volume, decreases, the ratio of IMC thickness to gap size increases although a thinner interfacial IMC layer can be formed (Figure 18.15). Tensile tests performed with these solder joints showed an increase of the UTS with decreasing gap size of Cu/Sn/Cu joints down to 10 μm. The same trend was observed for Cu/Sn/Ni joints down to 20 μm, with an even more prominent effect. A degradation of the UTS was observed for the Cu/Sn/Ni joint with a 10-μm gap size. Similar to other studies, a transition from ductile to brittle fracture with decreasing gap size was observed. In the case of Cu/Sn/Ni joints, fracture occurred at the interface between solder and Ni. The $(Cu,Ni)_6Sn_5$ IMC showed a layer-type morphology with irregular protruding parts that is different from the scallop type of the single-phase Cu_6Sn_5 for Cu/Sn/Cu joints. At the Ni side of the Cu/Sn/Ni joint, two layers of IMCs

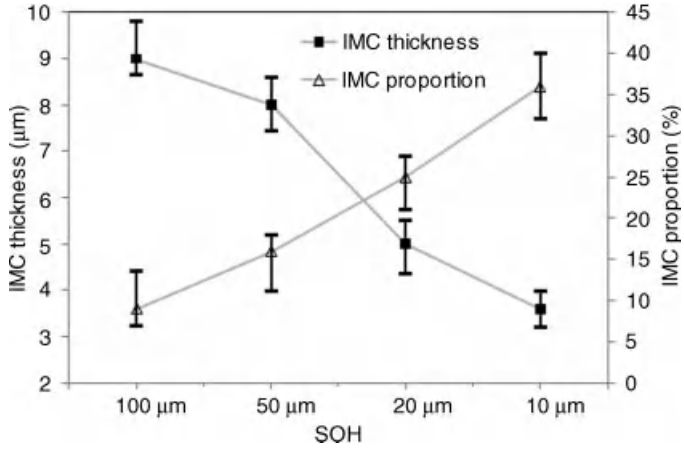

Figure 18.15 *IMC thickness and proportion changes in the Cu/Sn/Cu solder joints with 100, 50, 20, and 10 μm stand-off height [57]. (Reproduced with permission from Solder. Surface Mount Technology, Effect of stand-off height on the microstructure and mechanical behavior of solder joints by B. Wang et al., 22, 1, 11–18 Copyright (2010) Emerald Group Publishing Ltd).*

were observed: next to Ni a thin layer of an Ni-Cu-Sn IMC, identified as a transient phase from Ni_3Sn_4 to Cu_6Sn_5, adhered to $(Cu,Ni)_6Sn_5$. Formation of these IMC layers at the Ni side was found to be responsible for the occurrence of brittle-type fracture between the two IMC layers. Solder joints with a gap size of 10 μm failed mainly by a cleavage type of fracture. The drop of UTS for Cu/Sn/Ni joint with a thickness of 10 μm was also related to the reduction of the number of grains to just one single one across the thickness of the solder joint (Figure 18.16).

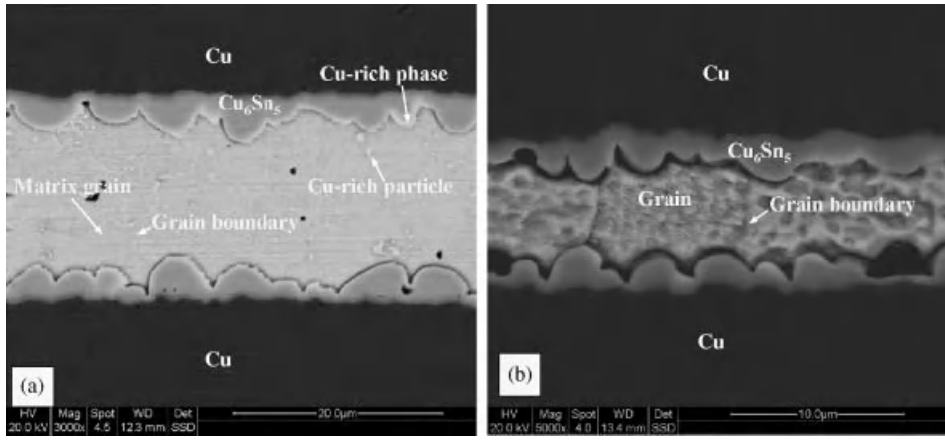

Figure 18.16 *Cross-sectional backscattered electron (BSE) images of the Cu/Sn/Cu solder joints with stand-off heights of (a) 20 μm and (b) 10 μm [57]. (Reproduced with permission from Solder. Surface Mount Technology, Effect of stand-off height on the microstructure and mechanical behavior of solder joints by B. Wang et al., 22, 1, 11–18 Copyright (2010) Emerald group Publishing Ltd).*

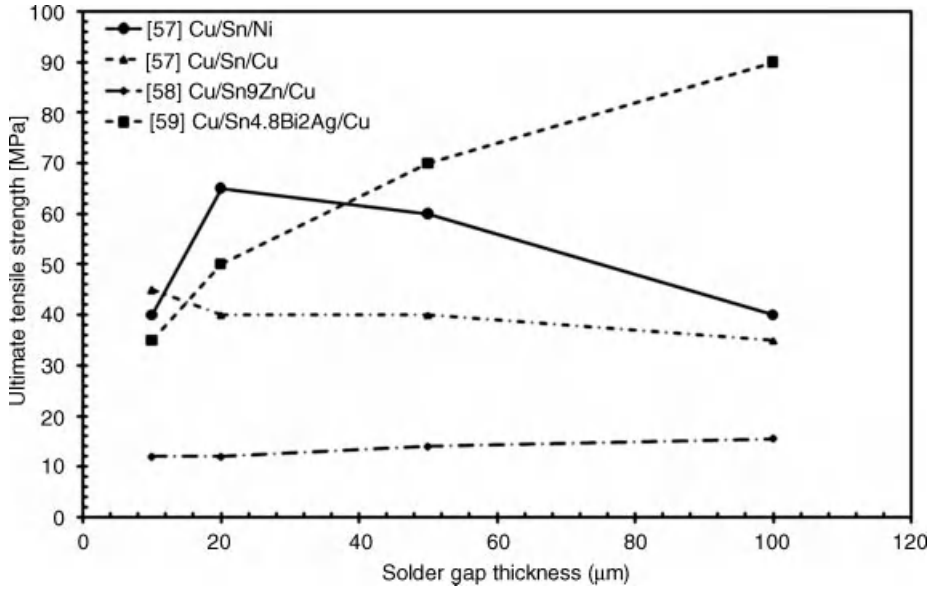

Figure 18.17 *Dependence of tensile strength on the gap size (stand-off height) for different solder/substrate combinations [57–59].*

An inverse relationship between the reduction of gap size and tensile strength was also found for Cu/Sn-9Zn/Cu solder joints [58]. The reduction of tensile strength was explained by a significant change of the microstructure of the solder bulk in the thinner joints due to diffusion of Zn and Cu from and into the bulk of the solder. The transformation of the composition and microstructure of the solder bulk on reducing the gap size from a eutectic Sn-9Zn to a hypoeutectic structure with a higher percentage of *dissociative intermetallic compounds* were correlated to a change in the fracture morphology of the solder joints and a strong drop in the tensile strength. A summary of the results of these studies is presented in Figure 18.17 [57–59]. The figure demonstrates that an improvement (i.e. an increase) of the mechanical strength of solder joints with decreasing gap size cannot be generalized for all types of joints and also depends strongly, among other factors, on the composition of the solder and the microstructure of the joint.

Though the influence of isothermal aging on the evolution of the microstructure of solder joints has been studied extensively work done on the dependence of these specific microstructural features on mechanical properties of the solder joints is scarce [13–15, 60]. Lee *et al.* [61] correlated the tensile and shear strength of Cu/Sn-3.5 Ag/Cu solder joints with a thickness of about 300 μm to the thickness and morphology of their interfacial IMC layers. They observed a significant decrease of tensile and shear strength of the solder joints by increasing the aging time and/or temperature (Figures 18.18 and 18.19). Degradation of the solder-joint properties was related to the growth of the interfacial IMC layers, increased roughness of the solder/Cu_6Sn_5 interface and the mode of fracture. The interface of solder/substrate was identified as a location of high stress concentration and thus considered decisive for the reliability of the solder joint. The residual stresses in the interface of the solder/IMC layers, induced during the cooling phase of the soldering process, may originate from the

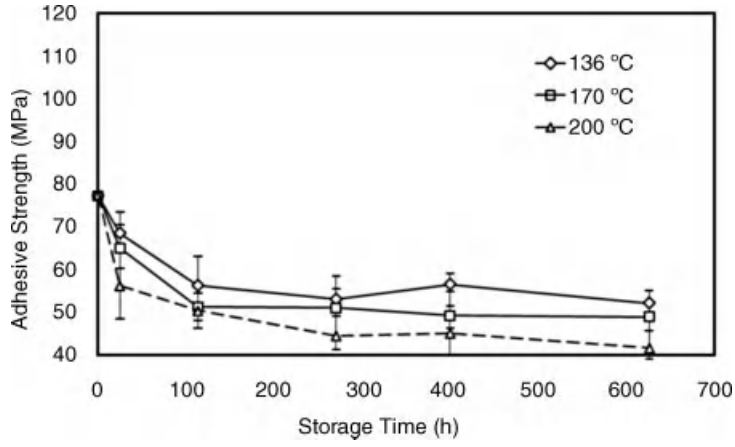

Figure 18.18 *The degradation of adhesive strength of Sn-3.5Ag solder joints with aging time [61]. (Reproduced with permission from Materials Science and Engineering A, Influence of interfacial intermetallic compound on fracture behavior of solder joints by H. Lee et al., 358, 1–2, 134–141 Copyright (2003) Elsevier Ltd).*

phase-transformation-induced stresses in the solder/substrate interface and the stress induced by the difference of CTEs of substrate and solder alloy. The geometry of the IMC interfacial layer, especially the protruding regions of scallop-shaped IMCs like the Cu_6Sn_5 phase, count as another source of stress concentration (see Figure 18.16).

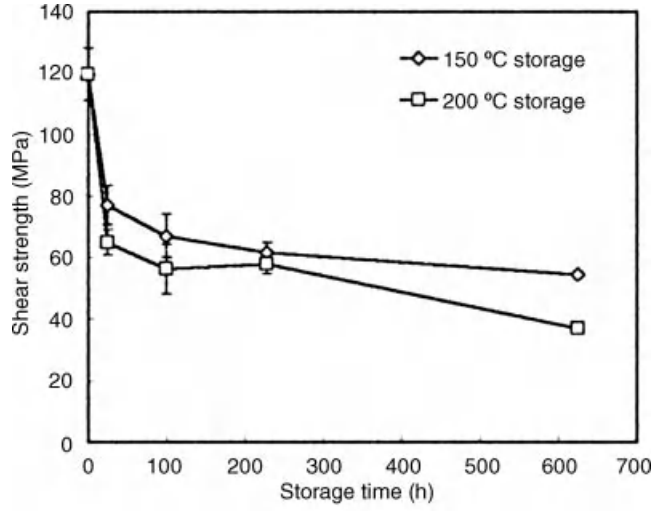

Figure 18.19 *The shear strength degradation of Sn-4.11Ag-1.86Sb solder joints with aging time [61]. (Reproduced with permission from Materials Science and Engineering A, Influence of interfacial intermetallic compound on fracture behavior of solder joints by H. Lee et al., 358, 1–2, 134–141 Copyright (2003) Elsevier Ltd).*

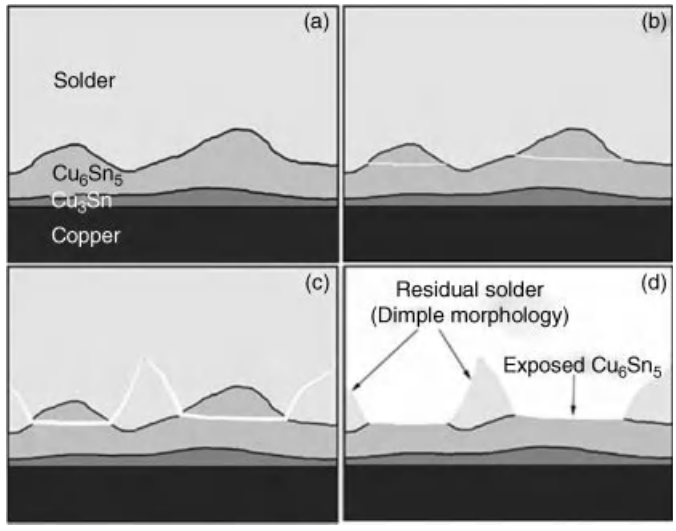

Figure 18.20 *The evolution of dimple morphology. (a) Unloaded; (b) protruded Cu_6Sn_5 starts to break; (c) the crack propagates toward the solder; (d) dimple morphology forms [61]. (Reproduced with permission from Materials Science and Engineering A, Influence of interfacial intermetallic compound on fracture behavior of solder joints by H. Lee et al., 358, 1–2, 134–141 Copyright (2003) Elsevier Ltd).*

The authors suggest that, although the stress intensity within the softer regions of the solder joint is lower than in the IMC layer, fracture does not necessarily occur in the IMC layers and the fracture mode depends to the thickness of the interfacial IMC layer.

Fracture in solder joints with a thin IMC layer (<1 μm) tends to occur along the interface of solder/Cu_6Sn_5 due to stress-concentration effects. As the thickness and, consequently, the roughness of the solder/Cu_6Sn_5 interface increases, the accumulated residual stress and the stress concentration factor are also increased. The protruding region of the Cu_6Sn_5 layer are intrinsically weakened by residual transformation-induced stress and are subjected to the highest concentrated stress due to both multiphase and geometry condition. These stresses lead to the fracture of the protruding region of the Cu_6Sn_5 layer. Fracture of the joint originates in this region and then propagates into the solder causing the formation of dimple morphology (Figure 18.20). As the total thickness of the interfacial IMC layers grows beyond 10 μm and the interface becomes much rougher, the origin of the fracture moves further into the interior of this layer. The crack propagates laterally through the Cu_6Sn_5 layer and finally results in the formation of cleavage morphology (Figure 18.21). Accordingly, increased IMC layer growth is accompanied by a gradual decrease in joint strength [61].

Though this investigation concerns Cu_6Sn_5 and Cu_3Sn phases in interfacial Cu-Sn IMC layers the corresponding findings may also be applied also to other solder/substrate systems in Sn-rich solder joints [60].

It can be summarized that the formation of IMCs in solid/liquid reaction couples is primarily controlled by the dissolution processes of the base metals and is highly dependent on the solder volume and the concentration of the required elements for interface phases. The microstructure of the solder and the interfacial IMC layers can drastically change

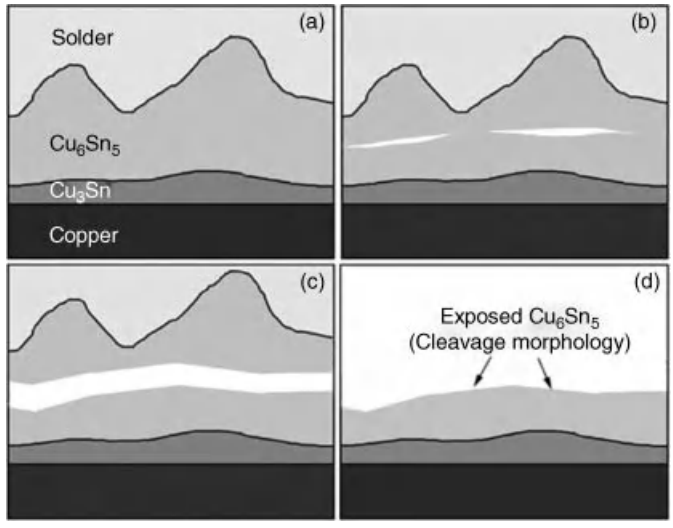

Figure 18.21 *The evolution of cleavage morphology, (a) unloaded; (b) the crack forms inside the protruded Cu_6Sn_5; (c) the crack propagated laterally; (d) cleavage morphology forms [61]. (Reproduced with permission from Materials Science and Engineering A, Influence of interfacial intermetallic compound on fracture behavior of solder joints by H. Lee et al., 358, 1–2, 134–141 Copyright (2003) Elsevier Ltd).*

during solid-state aging. It is generally accepted that during the *aging process* the growth of interfacial IMC layers tends to weaken the solder joints due to their brittleness that results in a decreased reliability. This negative effect may even be intensified by the simultaneous presence of different IMCs, originating from two different substrate materials, due to the weakening effect of the interface between two brittle materials [13]. Kirkendall voiding and massive spalling in the interfacial layers subjected to isothermal aging are severe reliability concerns of solder joints. A typical case of Kirkendall voiding in the IMC layer of a Cu/Ag-3.5Sn/Cu joint is shown in Figure 18.22. Massive spalling has been observed in several solder/substrate systems including Sn-Ag-Cu over Ni substrate and is more a reliability issue in solder joints with smaller volume due to their limited availability of substrate material and a faster concentration drop [62].

18.2.2 Constraining Effects in Actual Joints

18.2.2.1 Influence of Solder Volume, Pad Size, Microstructure

All studies described in Section 18.2.-1. were conducted on model joints soldered between two flat surfaces of rectangular or round bars of Cu or Ni substrate. In actual joints a large variety of geometries and compositions of the solder and pad metallization is possible. The actual joints include leadless and leaded solder attachments like Flip-Chip C4 (controlled collapse chip connection) solder joints, BGAs with C5 (ball grid array) solder attachments and CGAs (column grid arrays) with high-temperature solder columns, and solder joints with fillets, for example, chip components [3]. The following section deals with exemplary

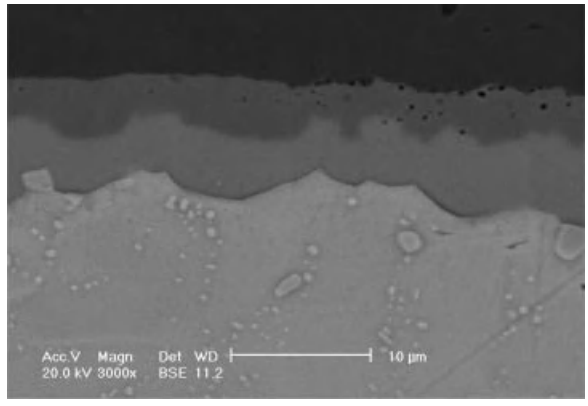

Figure 18.22 *Kirkendall voiding in the interfacial IMC layer of an aged Cu/Ag-3.5Sn/Cu solder joint.*

studies that were performed on actual solder ball bonds, such as BGAs and flip-chips under different production conditions.

In a comprehensive study by Darveaux *et al.* solder ball bonds (BGAs) of various volume, aspect ratios and pad metallizations were investigated by different testing procedures [44].

In general, it was found that for solder balls with different volumes but a similar aspect ratio (solder height/pad diameter) independent of the solder alloy, susceptibility to interface failure increases on increasing the solder volume, aging time and temperature.

Taking only ductile fracture type into consideration, an increase of tensile strength with increase in solder volume was also observed, except of those with a 0.050-mm^3 solder volume (Figure 18.23). (The deviation of the strength for 0.05-mm^3 samples was not

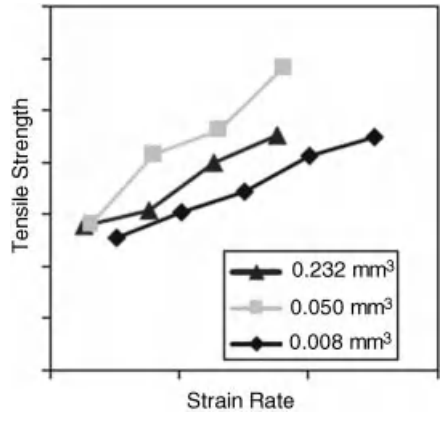

Figure 18.23 *Effect of joint size on the tensile strength of Sn-3.0Ag-0.5Cu solder joints: Ni/Au metallization, 22C, (0.4 mm, 0.8 mm, and 1.27 mm pitch samples). (Reproduced from 58th IEEE Electronic Components and Technology Conference (Vol. 1), Effect of joint size and pad metallization on solder mechanical properties by R. Darveaux et al., 113–122 Copyright (2008) IEEE). [44]*

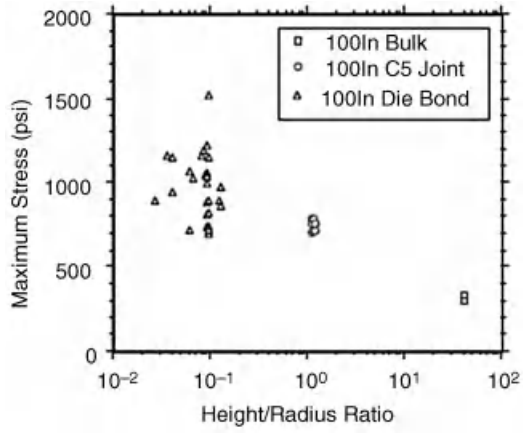

Figure 18.24 *Effect of sample aspect ratio on solder strength under tensile loading: indium solder, 25°C, $1.0 \times 10^{-3}\ s^{-1}$ strain rate. (Reproduced from 58th IEEE Electronic Components and Technology Conference (Vol. 1), Effect of joint size and pad metallization on solder mechanical properties by R. Darveaux et al., 113–122 Copyright (2008) IEEE). [44]*

discussed further.) Analysis of the size dependency of the fracture mode of specimens tested by different strain rates showed that the larger joints have a lower ductile-to-brittle transition strain rate compared to smaller joints. Results of creep tests for SAC solder joints showed a very slight increase of creep resistance for the larger joints as well as higher susceptibility to interface failure for SAC105 and SAC305 on Ni/Au metallization and Cu metallization.

A clear example of the influence of the solder joint geometry size on tensile strength is shown in Figure 18.24 for indium solder joints and bulk specimens. Bulk specimens with a very high aspect ratio show a significantly less creep resistance (lower strength) than C5 (BGA) joints and the die bond joints. The die bond joints (die attach) show the highest average tensile stress that is most likely due to the constraining effect of interfaces between the In solder and the Si die. It can be concluded that for solder ball bonds with a similar aspect ratio (0.84 to 1.20), the variation of joint size by a factor of five did not show a noticeable effect on their mechanical properties. A change in the solder volume mainly resulted in a change of the fracture mode that certainly has an impact on the reliability of the joints. An obvious increase of solder strength could then clearly be demonstrated where not only the volume was reduced but the geometry and shape of the solder significantly varied. This result is more or less in agreement with the notion that the aspect ratio of a constrained joint is the more sensible factor in view of evaluation of the size effect in solder joints.

Depending on the alloy system the microstructure of the solder joint can be modified as a consequence of the degree of undercooling, where features such as fine grains, supersaturated solid solutions, and anomalous eutectic structures can be observed. Due to their small volume, solder ball bonds are, even under normal process conditions, subjected to a rapid solidification and thus to a high degree of undercooling. Kinyanjui *et al.* [52] studied the solidification behavior of solder balls prepared from high-purity Sn (99.99%) and different Sn-Ag-Cu alloys in relationship with the degree of undercooling of the alloy during rapid solidification. The study included ball grid array (BGA) joints of Sn-3.0Ag-0.8Cu solder,

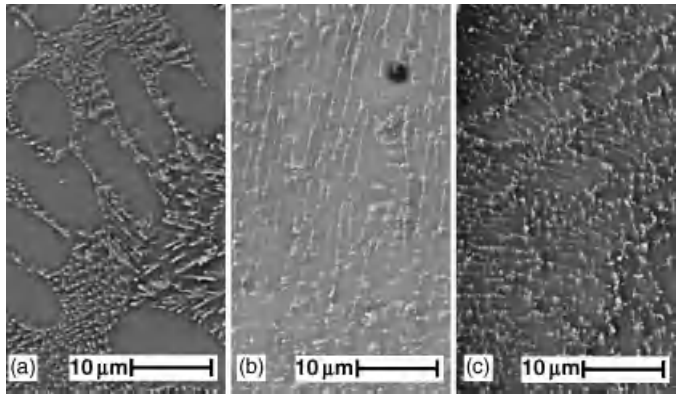

Figure 18.25 *The effect of Sn-Ag-Cu sample size on microstructure; (a) BGA (ball diameter 760 µm), (b) WL/CSP (ball diameter 265 µm), (c) Flip-chip (ball diameter 125 µm) [52]. (Reproduced with permission from Journal of Materials Research, Effect of sample size on the solidification temperature and microstructure of SnAgCu near eutectic alloys by R. Kinyanjui et al., 20, 11, 2914–2918 Copyright (2005) Cambridge University Press).*

wafer-level chip-scale package (WL/CSP) joints, and flip-chip (FC2) joints of Sn-3.5Ag-1.0Cu solder, with diameters of 760, 265, and 125 µm, respectively. All the joints were in the as-reflowed condition, without subsequent aging or thermomechanical treatments. The solidification temperature of the samples was determined by differential scanning calorimetry. It was found that, with a cooling rate of 1 °C/s from the melt, an inverse linear relationship exists between solder volume and degree of undercooling. The Sn dendrite arm width was observed to increase monotonically with the ball diameter (Figure 18.25). The authors concluded that the mechanical response of solder balls will depend upon the degree of undercooling, and therefore upon the solder ball size.

Madeni *et al.* [43] investigated the microstructure of bulk solders and solder droplets of Sn-3.5Ag, Sn-0.7Cu, Sn-3.2Ag-0.8Cu on Cu substrates with three different cooling rates. All solder droplets displayed a dendritic substructure with the size of the dendrite arms increasing as the cooling rate decreased. The relationships between size of the secondary dendritic arms of the solder droplets and cooling rate and between microhardness and cooling rate shows an increase in dendritic arm size, that is, a coarser microstructure, which leads to lower hardness values and consequently to less favorable mechanical properties of the solder.

Mueller *et al.* [53] conducted solidification experiments to investigate the phase sizes, shapes and grain orientations in Sn-3.0Ag-0.5Cu solder balls with diameters in the range of 130 to 1100 µm. Similar to previous investigations it was found that the microstructure becomes finer and the formation of small, randomly oriented grains becomes more frequent with smaller solder volumes. The analysis of the microstructures showed that the formation of large primary IMCs increases with slower cooling rates and smaller ball sizes. The authors reported that there was no significant influence of the cooling rate on the grain orientation and dendritic growth of β-Sn found in these small solder bumps. Unexpected results were obtained on the influence of the cooling rate on the grain size and orientation of the solder balls with different volumes. Solder balls solidified under similar conditions

could also exhibit completely different grain-size distributions and orientations (Figure 18.26).

Huang *et al.* [63, 64] found that the microstructure is highly affected by both size and geometry of the solder joint. Solder pads with diameters of 80 and 1500 μm with a coating of electroless Ni immersion gold (ENIG) were used to produce Sn-3.5Ag solder bumps with stand-off heights of 20 and 200 μm, respectively [63]. The microstructure of both types of solder bumps consisted of a considerable amount of primary Sn phase, β-Sn and Ag_3Sn eutectic [64]. These structures have been observed in Sn-Ag-Cu alloys due to the suppression of β-Sn nucleation (see for example [13, 56]). A statistical evaluation of the particle size of Ag_3Sn IMCs showed a trend to finer particles in the smaller solder joints. A further refinement of the structure is obtained by reducing the joint size and by a faster cooling rate. The heat-sinking effects of the surrounding material in the smaller solder joints is more effective than for larger joints, resulting in steeper thermal gradients and higher heat-extraction rates and leading to a finer structure. A more pronounced size dependency of the microstructure was observed in the interface layer between solder bumps and substrate that was studied under various reaction times. The formation kinetics of the interfacial IMC layer, especially at the interface near the bump edge, was faster in small solder joints compared to the larger bumps, resulting in a difference in thickness, morphology and number of IMC layers (Figure 18.27). Further investigations were conducted on different solder bump geometries with pad sizes, ranging from 1 mm down to 25 μm, prepared by different bumping techniques, that is, solder dipping and stencil printing [64]. For an accurate prediction of the solder–pad interactions and hence the growth kinetics of the

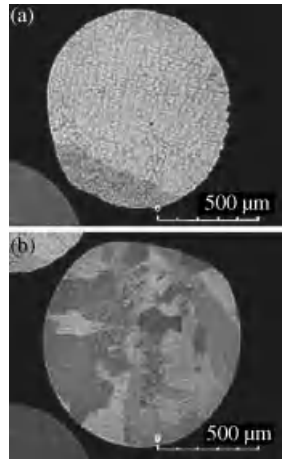

Figure 18.26 *(a) and (b), Sn-3.0Ag-0.5Cu solder balls with a diameter of 1100 μm and cooling rate of 0.33 K/s; (c) and (d), Sn-3.0Ag-0.5Cu solder balls with a diameter of 130 μm and cooling rate of 1.1 K/s [53]. (Reproduced from International Conference on Thermal, Mechanical and Multi-Physics Simulation Experiments in Microelectronics and Micro-Systems, 2007. EuroSime 2007, The Dependence of Composition, Cooling Rate and Size on the Solidification Behaviour of SnAgCu Solders by M. Mueller, 1, 197–206 Copyright (2007) IEEE).*

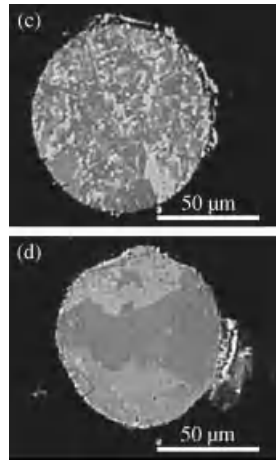

Figure 18.26 *(Continued)*

IMCs, the influence of the pad size on the dissolution of Cu in the solder alloy was calculated. The example provided in Figure 18.28 shows the consumed thickness of Cu pad in the liquid solder in dependence of time. According to this, the dissolution rate of Cu in Sn-3.5Ag solder is faster than in pure Sn and more than twice as fast as in Sn-3.8Ag-0.7Cu solder in the axial direction. For all solders the dissolution rate increases as the pad size decreases, which means that the smaller pad sizes are consumed faster than the larger ones. The authors note that these calculations are based on simplified conditions (without

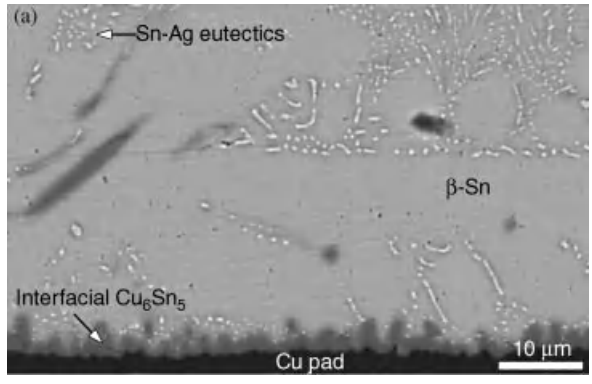

Figure 18.27 *SEM cross-sectional microstructure of SPR (stencil printing followed by reflow) Sn-3.5Ag on (a) 1-mm diameter Cu pad at 240°C for 90 s, and (b) 0.1-mm diameter Cu pad at 240°C for 90 s [63]. (Reproduced with permission from Microelectronics Reliability, Microstructural considerations for ultrafine lead free solder joints by Z. Huang et al., 47, 12, 1997–2006 Copyright (2007) Elsevier Ltd).*

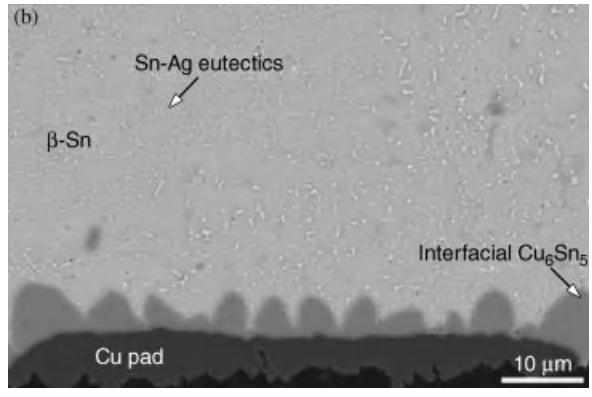

Figure 18.27 *(Continued)*

considering the possible convection), thus the consumption rate of Cu under real conditions can be higher than the values presented in this study.

The size-dependent reaction rate between the pad and the solder plays a major role for the subsequent microstructure of the solder joint and the IMC interface layer, and thus for the mechanical properties and the reliability of the joint. Microstructural investigations of solder bumps prepared under the same reflow conditions showed clear differences between the small and large solder bumps (Figure 18.27). The main finding concerning the

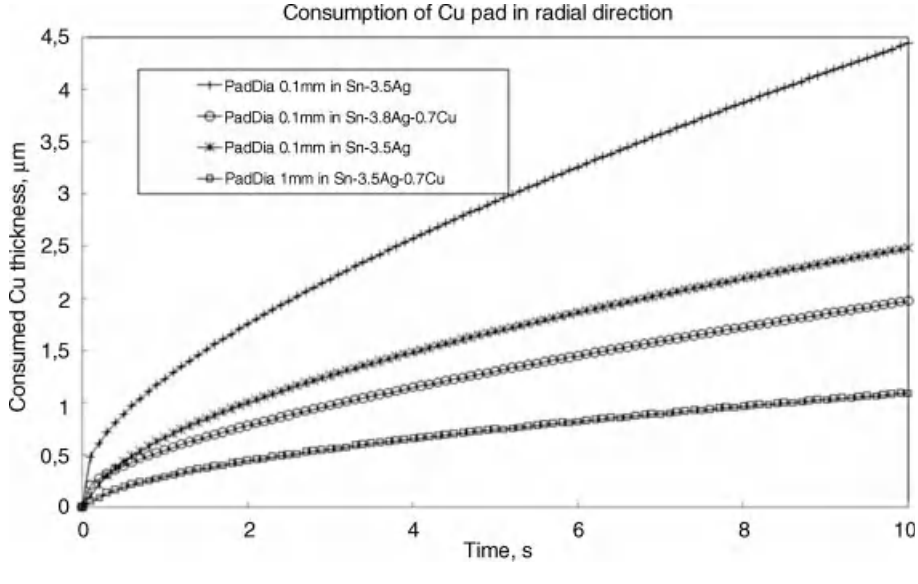

Figure 18.28 *Dissolution of Cu pad into liquid solder at 240°C in the axial direction [63]. (Reproduced with permission from Microelectronics Reliability, Microstructural considerations for ultrafine lead free solder joints by Z. Huang et al., 47, 12, 1997–2006 Copyright (2007) Elsevier Ltd).*

relationship between solder size/geometry and microstructure is that, in general, the smaller volume results in a faster cooling rate and thus in a finer structure with improved mechanical properties. The formation of interfacial IMCs in the solder joints is also highly dependent on the solder volume and the concentration of the elements in the solder that are required for interface phase formations. The thickness of the IMC layer increases if the solder joint is subjected to high-temperature storage. The strength of the joints is related to the properties of the IMC layer in the interface, especially their brittleness. It has been shown that the relative percentage of IMC has an inverse relationship with the volume of the solder [31, 57, 58]. The proportional increase of the thickness of the IMC layer with a decrease of the solder-joint volume results in a higher affinity to brittle fracture, as well as a higher rate of degradation, cracking and voiding of the interface, and with this to a higher probability of failure.

18.2.3 Fracture Mechanics Considerations of Solder Joints

Understanding the crack-growth behavior in solder joints and thus the expected fracture mode under various loading conditions has been recognized to be an important task for prediction of their lifetime and reliability. Stress intensity factors (SIF) K_I and K_{II} which define the state of stress at the crack tip in tensile and shear mode, depend on different factors such as composition and materials properties of the solder alloy, solder joint thickness and volume, location of the crack with respect to its distance from the interface and strain rate [65, 66].

Using a fracture-mechanics approach, Alam *et al.* [65, 66] attempted to describe the crack-growth behavior of solder joints in the interfacial IMC layers using FEM simulations. They calculated the variation of stress intensity factors in modes I and II under tensile loading in dependence of the solder-joint thickness, IMC layer thickness, crack size and distance of the crack from the interface, including the effect of strain rate [65]. In a homogeneous elastic material subjected to tensile loading the value of K_I is more relevant, while the value of K_{II} is negligible. This investigation showed that tensile loading of a solder joint, constrained between a rigid substrate, leads to a contraction of the viscoplastic solder material in the direction perpendicular to the loading direction and generates a strong shear contraction near the interface that contributes to the shear stress in the solder/IMC interface and is responsible for higher K_{II} values at the IMC crack tip. This study showed that if the location of the crack approaches the interface, the values of stress intensity factors, in particular the K_{II} value, increases (Figure 18.29). Thus, it may be expected that a thicker IMC layer in fact increases the reliability of a solder joint for a cracked IMC.

Increased thickness of the solder joint also leads to higher values of the SIFs (Figure 18.30). This effect is considered to be related to the mass effect of solder alloys: Thicker solder layers exert higher viscoplastic deformation that contributes to higher stresses and strain near the crack tip at the solder interfaces. In comparison with Pb-Sn solder joints, SAC solder showed higher values of K_I and K_{II}. At higher strain rates solders undergo less deformation as well as less contraction, thus a lower stress intensity at the crack tip is expected if solders are loaded at higher loading rates.

An earlier study on the fracture behavior of brass/solder/brass joints provides a detailed analysis of the failure mechanism and toughness of a constrained ductile layer between stiff substrates [67]. The major mechanism of ductile fracture, which is the near crack-tip void

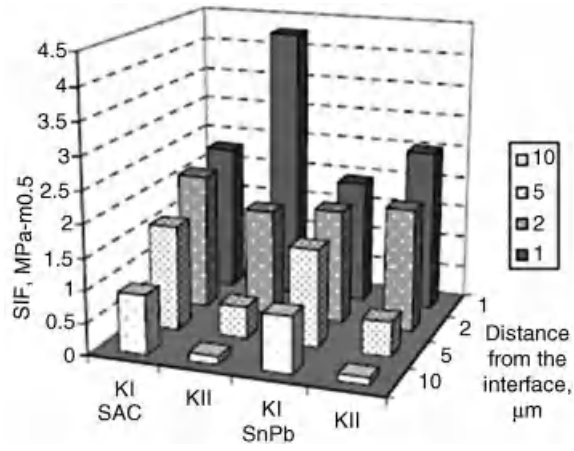

Figure 18.29 *The variation of K_I and K_{II} values of lead-free and Sn-Pb solders with the crack locations. (Reproduced from Electronics System-Integration Technology Conference, 2008. ESTC 2008. 2nd, Fracture mechanics analysis of cracks in solder joint Intermetallic Compounds by M. O. Alam et al., 757–762 Copyright (2008) IEEE). [65]*

growth and coalescence, is directly related to the intensity of stress triaxiality near the crack tip. In analogy to reduction in ductility, fracture toughness is decreased in thinner, highly constrained joints. Generally, voids in any material grow in proportion to the stress triaxiality. Higher degrees of stress triaxiality result in a rapid growth of voids leading to unstable cavitation and fracture of the joint [67]. A comparison of Sn-3.8Ag-0.7Cu solder

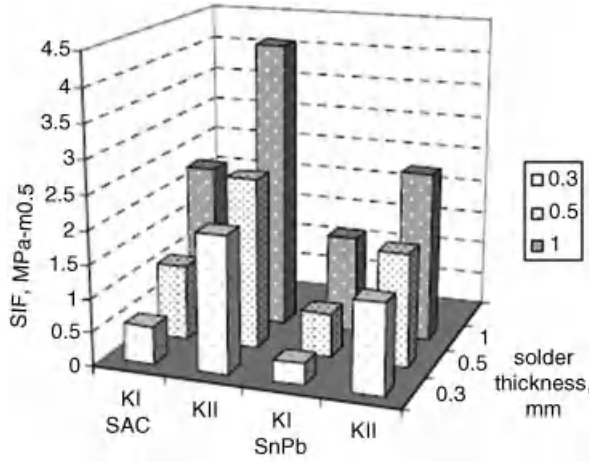

Figure 18.30 *The variation of K_I and K_{II} values of lead-free and Sn-Pb solders with the solder layer thickness at a loading rate of 0.8 MPa/s. (Reproduced from Electronics System-Integration Technology Conference, 2008. ESTC 2008. 2nd, Fracture mechanics analysis of cracks in solder joint Intermetallic Compounds by M. O. Alam et al., 757–762 Copyright (2008) IEEE). [65]*

joints with thicknesses of 0.3 and 0.8 mm showed higher impact energy for thicker solder joints, indicating increased fracture toughness [68].

18.3 Creep and Relaxation of Solder Joints

Wiese *et al.*, conducted creep experiments on Sn-Ag and SAC solders of several types of solder-joint specimens in comparison with bulk solder specimens [69]. The authors referred to the remarkable scatter in the data available on creep response of solder joints and attempted to establish a correlation between creep data obtained from bulk specimens, flip-chips, and solder bumps in the range of 200 to 1100 μm diameter. The scatter in creep data in the literature was related to the differences between microstructure and the methodology that vary strongly among different investigations. These variations include the type of test (constant-load test, load-stepping test, constant-strain-rate test, strain-rate-change test), the chosen stress or strain-rate range, the test temperatures and the method of determination of steady-state strain rate. Thus, in order to compare creep data between bulk specimens and microsolder balls it was suggested to choose parameters that are relatively independent of test conditions. Taking into account the dependency of activation energy on the test temperature, the activation energy (Q) and the stress exponents (n) were introduced as suitable parameters.

It was found that the creep behavior of bulk solder specimens followed a simple power law, with a stress exponent between $n = 11$–12, independent of temperature and alloy type. The creep curves of microsolder ball specimens were best fitted using a sinh-law. The stress exponent was found to be between $n = 12$–14 at room temperature and decreased to $n = 7$–8 at 125 °C. Flip-chip specimens demonstrated very high stress exponents in the range of $n = 11$–20. Due to the small range of test temperatures used in these investigations no fit-function could be established.

For solder joints with a very small volume (flip-chip joints) the metallization material not only changed the absolute creep strength but also the stress sensitivity of the creep response. These effects were not detected in bulk specimens. The impact of activation energy on the creep strength of solder joints was not straightforward.

The different creep behavior between bulk solder specimens and miniaturized solder joints was mainly attributed to the effect of microstructure. It was found that in the small solder joints, due to a limited dendritic growth, a higher number of grain boundaries exist in the smaller joints in comparison with the bulk solder. In addition to the intrinsic strengthening of the solder by Ag_3Sn and/or Cu_5Sn_6 intermetallic particles dispersed within the β-Sn matrix, the presence of certain IMCs such as $AuSn_4$ originating from Au metallization may provide an additional strengthening mechanism. These IMCs accumulate preferably at the grain-boundary triples and can serve as additional effective barriers for dislocation movement. This investigation demonstrates the complexity of the creep behavior of miniaturized solder joints and the large number of variables that might have an impact on the creep response of actual joints.

In a recent study, stress-relaxation tests in tensile mode were performed with model solder joints consisting of eutectic Sn-3.5Ag solder and Cu substrates, with gap sizes between 150 and 750 μm [70]. A simple geometry was chosen to minimize the number of variables that

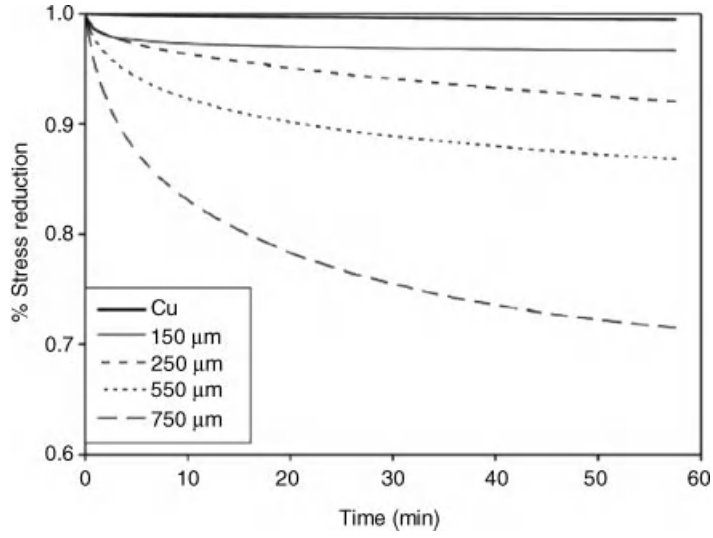

Figure 18.31 *Normalized stress drop (in %) of solder joints with varying gap sizes at 25 °C [70]. (Reprinted with permission from Journal of Electronic Materials, Contraining effects of lead-free solder joints during stress relaxation by P. Zimprich, U. Saeed, B. Weiss, and H. Ipser, 38, 3, 392–399 Copyright (2009) Springer Science + Business Media).*

might affect the time- and temperature-dependent behavior of miniaturized lead-free solder joints. The stress-relaxation experiments were performed under tensile loading with constant strain rate of 1.2×10^{-4} at 25 and 120 °C. The samples were loaded to some initial load of about 0.25% strain in the plastic range between yield strength and UTS and then the load drop was recorded as a function of time. The relaxation in the Cu was measured at both temperatures and found to be negligible for the load levels encountered in this study. It was not necessary to account for machine compliance because strain rather than crosshead displacement was controlled [71].

The normalized stress-relaxation response of all solder joints measured at 25 and 120 °C is demonstrated in Figures 18.31 and 18.32, respectively. These results show that the stress drop in solder joints is size and temperature dependent. Figure 18.31 shows a stress drop of 30% for a solder joint with a gap size of 750 µm after one hour, whereas for a 150-µm gap size the stress drop was only 5%. The stress drop in pure Cu was measured to be 0.5% at this temperature. The dependency of stress drop on the testing temperature is shown in Figure 18.32. In the case of a 750-µm gap size, the stress drop at 120 °C was 45%, while the stress drop for a 150-µm gap size was only 10%. The present data indicate that constraints imposed on the solder joint hinder a complete relaxation, leading to the presence of residual stresses. These residual stresses, particularly in thin joints, may be large enough to cause further damage during service because of the lack of ductility in comparison with thick joints. This result can be understood by taking into account the results for the stress–strain behavior of various gap sizes as shown in Figures 18.31 and 18.32. Due to the higher mobility of dislocations, thick joints show a higher ductility than thin joints and therefore in comparison with the highly constrained thin joints a higher rate of relaxation drop may be expected.

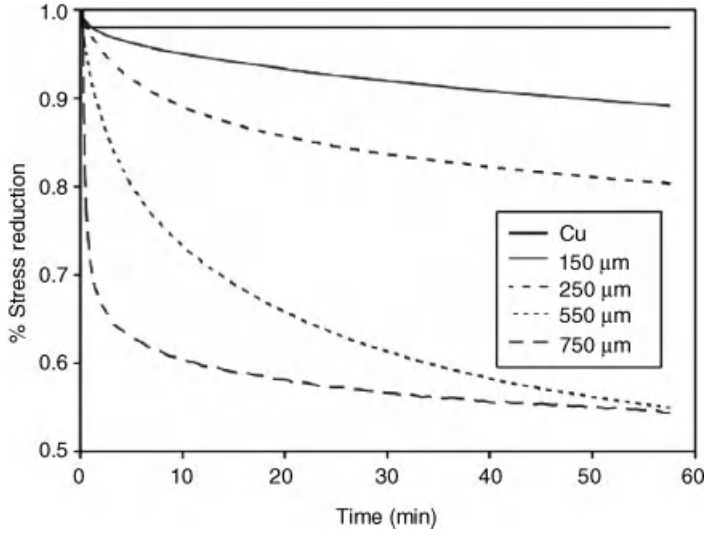

Figure 18.32 *Normalized stress drop (in %) of solder joints with varying gap sizes at 120°C [70]. (Reprinted with permission from Journal of Electronic Materials, Contraining effects of lead-free solder joints during stress relaxation by P. Zimprich, U. Saeed, B. Weiss, and H. Ipser, 38, 3, 392–399 Copyright (2009) Springer Science + Business Media).*

The increase of the stress-exponent values with decreasing gap size is thought to be largely due to the constraint effect.The obtained stress exponent values for thick joints (750 µm) are similar to those for bulk Sn-Ag solders (negligible constraint effect), whereas in the case of 150-µm joints, stress exponents are considerably larger, that is, $n > 7$. These stress exponent values for thin joints are in good agreement with Jadhav *et al.* [72] who also found values between 6 and 11 for gap sizes between 100 and 250 µm. The high stress exponent values for small solder gaps are – to a large extent – most probably due to a much more pronounced constraint effect. In addition, part of it can also be attributed to the higher density of Ag_3Sn particles or precipitates. It is well known that an intermetallic Cu_6Sn_5 layer forms at the interface of the Cu substrate with the Sn-3.5Ag solder. The thinner the joint, the larger becomes the relative amount of Sn that is consumed by the formation of Cu_6Sn_5 that increases the volume fraction of Ag_3Sn particles in the solder. These Ag_3Sn particles act as obstacles creating additional internal stress or backstresses, that resists the motion of dislocations. Despite the range of reported stress exponent, dislocation climb is still thought to be the predominant mechanism controlling creep deformation; indeed the dislocation–precipitate interactions have been used to rationalize the very high-stress exponent [73].

Thus, it can be concluded that increasing the gap size (or height of the joint) results in a better compliance and improved creep resistance of the joint.

The influence of solder gap size on shear creep response of Sn-3.5Ag solder joints was also studied by Jiang *et al.* [74]. Single shear lap specimens with gap sizes between 50 and 500 µm and a cross section of 1 mm^2 were prepared using Cu strips as substrate. Figure 18.33

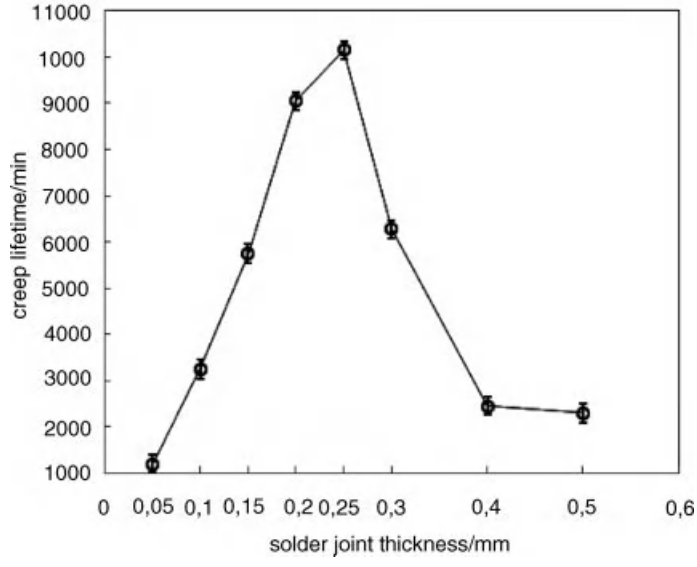

Figure 18.33 *Creep lifetime of Cu/Sn-3.5Ag/Cu model joints with different thicknesses [74]. (Reprinted from Journal of Physics D: Applied Physics, Size effects of lead-free solder joint thickness under shear creep based on micro-electrical-resistance strain by L. Jiang et al., 41, 16, 165412 Copyright (2008) Institute of Physics).*

shows an increase of creep life of the solder joints up to a gap size of 0.25 mm and a subsequent drop with a further increase of the gap size.

The results of this study, concerning an optimal solder-joint thickness, were explained partly by microstructural considerations. It was suggested that increasing the solder volume results in an increase in the probability of the presence of defects and voids in the bulk of a solder joint. Defects and voids in a solder joints were not only found to be sites of stress concentration, causing inferior mechanical properties, but also to be overheating points that result in a reduced reliability of the solder joints. Thus, the higher percentage of defects in the larger joints results in a reduction of creep life. On the other hand, the increase in the life of solder joints with increasing solder gap size in the range up to 0.25 mm can be related to a reduction of constraint effects and the gradual increased compliance in thicker joints. Reduction of creep life is not clearly argued. An increase in voids and defects with larger solder volumes is in contrast to the finding of other investigators [30, 37].

18.4 Summary and Conclusions

A summary of the results of various investigations on the effect of miniaturization on the strength of lead-free solder joints is presented in Figures 18.34 and 18.35. These results include tensile and shear strength of model joints of Sn-rich alloys soldered on

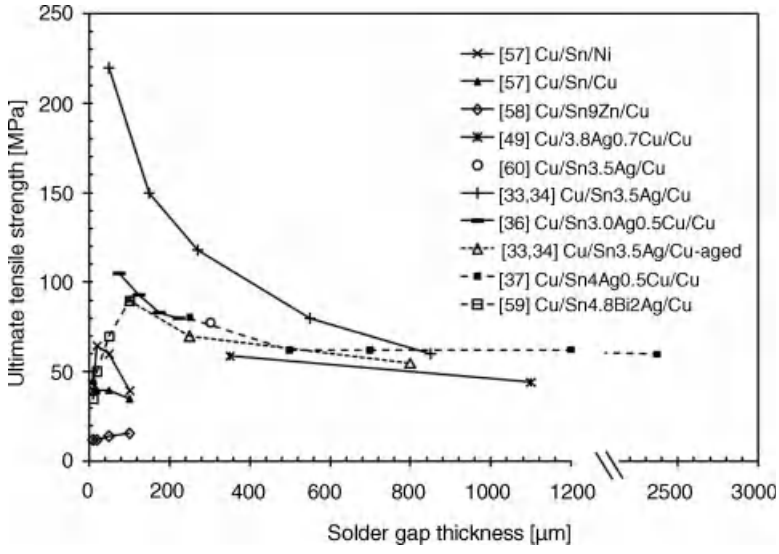

Figure 18.34 *Tensile strength of various solder joints as a function of gap size.*

Cu and Ni rod- or plate-shaped substrates. Independently of the absolute values of the strength, the curves show three main trends:

- An increase in strength down to a certain joint thickness followed by a decrease of strength or occurrence of an optimum joint thickness: this case is mainly related to the ratio of the

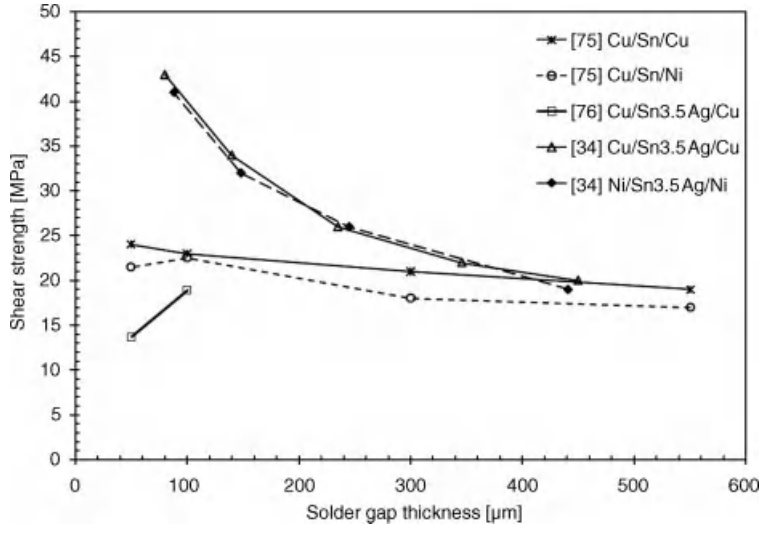

Figure 18.35 *Shear strength of various solder joints as a function of gap size.*

IMC thickness to solder gap size that has a higher impact on the strength of the thin joints; thin joints with a thin IMC layer seem to show the highest joint strengths.

- A decrease in strength with decreasing joint thickness was observed mainly in the thickness range below 100 μm. Several investigations showed that this is mainly due to the quality of the joint and to an increased porosity with reduced joint thickness. Increase of the ratio of IMC to solder gap thickness and also a change in composition of the solder alloy with decreasing solder volume were also reported as possible factors.
- Depending on the metallurgical systems, aspect ratio and quality of the joints moderate to high degrees of solder-joint strengthening with decreasing gap size were found; this was accompanied by a continuous reduction of ductility.

Due to the complexity of the studies on the effect of miniaturization on solder joints it was attempted to summarize the results of these investigation into two categories: *microstructural effects and constraining effects.*

The focus of the studies on the microstructure of miniaturized joints has been either the relationship between the reduction of the solder volume and the cooling rate or the relationship between the reduction of the solder gap size or diameter of the solder ball bonds and the related variation of concentration of the substrate material in the joint. As a general rule, solidification of a specific alloy with a smaller volume results in a faster cooling rate and a subsequent finer microstructure. For example, in lead-free solder alloys a faster cooling rate is usually connected with a refinement of Sn grains and of the lamellas of the eutectic phases. But it is not only the volume of solder itself but also the rate of heat transfer through the attached components (primarily the substrate) that determines the actual cooling rate and the resulting microstructure. A reduction of the solder volume leads to shorter diffusion paths between the substrate and the solder material and an increased concentration of the substrate material in the solder [42–53]. This variation of the elemental concentration in the solder alloys then leads to drastic changes in the microstructure of the joints, especially to the formation of IMC particles within the bulk of the solder joint and the interfacial IMC layers [54, 60, 63, 64].

Among other microstructural features, the reduction of joint size or volume might also result in a reduction of the number of grains in the joint. A transformation of the solder alloy from a polycrystalline material to a multicrystalline material should be followed by a shift of the material performance as well. The properties and the texture of individual grains that form a multicrystalline material, play an important role in the mechanical response of the solder joints [24, 53, 56]. A schematic representation of the relationship between solder gap size, microstructure and strength of solder joints is shown in Figure 18.36.

It is generally accepted that a reduction of the thickness of a solder joint results in a high strengthening effect. With a decrease of the gap size, the strength of the joint is expected to approach that of the substrate material; on the other hand, if the gap size is increased properties similar to that of the bulk solder alloy are expected. Ductility has an inverse relationship with the strength of the joint, and it was shown that this behavior is mainly related to development of hydrostatic stresses in constraint joints [28–37, 67, 70].

The strength of the joint and the constraining effect can be decisively altered by the quality and microstructure of the solder joint. The presence of defects like voids, pores or

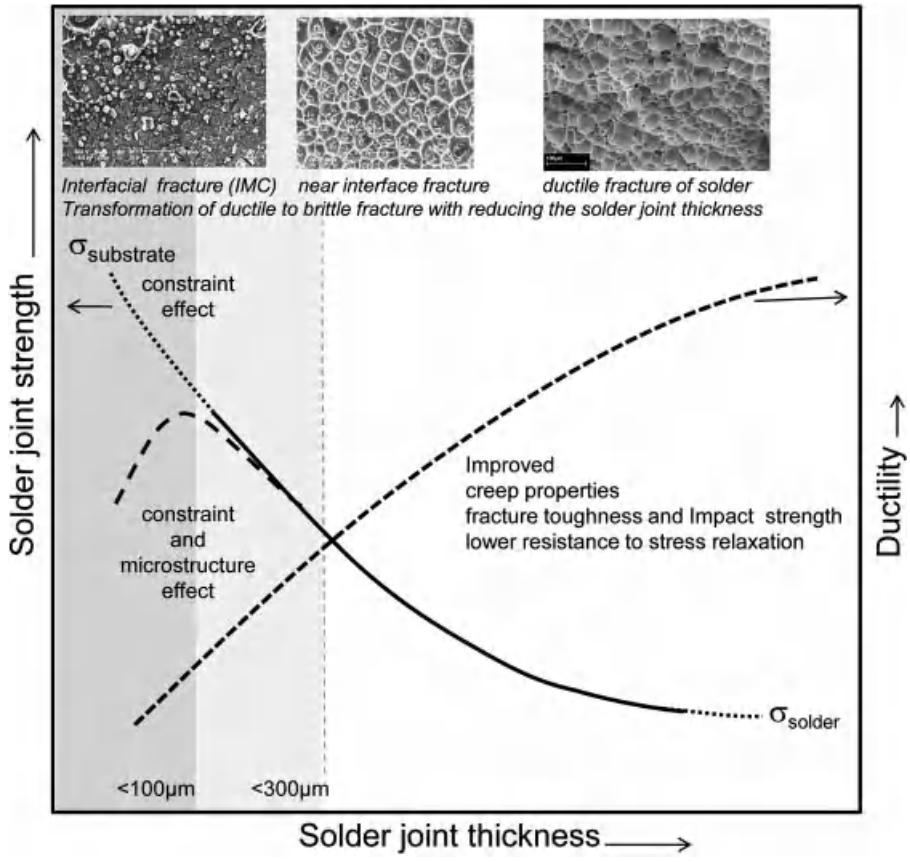

Figure 18.36 *Constraint and microstructural effects on the relationship between gap size and strength of a solder joint.*

nonwetted regions in the joint might reduce the joint strength, whereas finer microstructures, which are commonly observed in thinner joints, might lead to a higher joint strength. The thickness of the interfacial IMC and its ratio to the solder gap thickness leads to a change of the fracture mode, which is more prominent in thinner solder joints. A transition of ductile to brittle fracture mode results in an earlier fracture and a decrease in the strength of the joint.

Aging generally causes a decrease of solder joint strength. This is a result of the degradation of the interface due to voiding, spalling or cracking, which is again more effective in thinner joints. Coarsening of the microstructure as a result of thermal aging and reduction of the number of grains is among the factors that affect the mechanical response of solder joints.

Experimental parameters that modify the constraining effect on tensile and shear response of the solder joints are *strain rate*, *specimen geometry* and *aspect ratio*. During testing, strain rate in solder joints of different sizes should be equivalent. In the case of a fixed far-field strain rate for different gap sizes, a stronger apparent constraining effect would be expected. Increased gap thickness results in a reduction of hydrostatic stresses in

the constraint joint and a higher compliance. Thus, improved creep properties, higher stress-relaxation rates and better fracture toughness values are expected.

Acknowledgments

The authors gratefully acknowledge the financial support of Austrian Research Agency and Technology Agency of the City of Vienna in the frame of Comet program.

References

1. Plumbridge, W.J. and Kariya, Y. (2004) Structural integrity in electronics. *Fatigue Fract. Eng. Mater. Struct.*, **27**, 723–734.
2. Engelmaier, W. (1997) Soldering: Why we are still struggling. *Circuits Assembly* (2), 68–72.
3. Engelmaier, W. (1997) Solder joints in electronics: design for reliability. *Design & Reliability of Solders and Solder Interconnections, Proceedings of a Symposium held during the TMS Annual Meeting, Orlando, Fla., Feb. 10–13*, pp. 9–19.
4. Plumbridge, W.J., Matela, R.J., and Westwater, A. (2003) *Structural Integrity and Reliability in Electronics*, Kluwer Academic Publishers, London.
5. Tu, K.N. (2007) *Solder Joint Technology: Materials, Properties, and Reliability*, Springer, New York.
6. Evans, J.W. and Engelmeier, W. (2007) *A Guide to Lead-free Solders: Physical Metallurgy and Reliability*, Springer, New York.
7. Zeng, K. and Tu, K.N. (2002) Six cases of reliability study of Pb-free solder joints in electronic packaging technology. *Mater. Sci. Eng.*, **R38**, 55–105.
8. Chromik, R.R., Vinci, R.P., Allen, S.L., and Notis, M.R. (2003) Mechanical properties of Pb-free solder and Sn-based intermetallics measured by nanoindendation. *JOM*, **55**(6), 66–69.
9. Directive 2002/95/EC of the European Parliament and of the Council of 27 January 2003 on the restriction of the use of certain hazardous substances in electrical and electronic equipment (RoHS), Official Journal of the European Union L37, 19-23 2003; Directive 2003/96/EC of the European Parliament and of the Council of 27 January 2003 on Waste Electrical and Electronic Equipment (WEEE), Official Journal of the European Union L37, 24–38, 2003.
10. National Institute of Standards & Technology and Colorado School of Mines (2002) Database for Solder Properties with Emphasis on New Lead-free Solders, Release, 4.0, http://www.boulder.nist.gov/div853/lead_free/solders.html.
11. Sievert, T., Smith, D., and Madeni, J.C. (eds) (2002) *Database for Solder Properties with Emphasis on New Lead-Free Solders*, National Institute of Standards and Technology and the Colorado, School of Mines, Colorado, US.
12. Schmetterer, C., Ipser, H., and Pearce, J. (eds) (2008) *Handbook of Properties of SAC Solders and Joints*, ELFNET-COST 531, vol. **2**, COST Office, Brussels.
13. Subramanian, K.N. (ed.) (2007) *Lead-free Electronic Solders: A Special Issue of the J. Mater. Sci. Mater. Electron.*, vol. **18**(1–3), Springer, New York.
14. Bath, J. (2007) *Lead-Free Soldering*, Springer, New York.
15. Shangguan, D. (ed.) (2005) *Lead-Free Solder Interconnect Reliability*, ASM International, Materials Park, OH.
16. Solomon, H.D. (1986) Fatigue of 60/40 solder. *IEEE Trans. Compon. Hybrids Manufact. Technol.*, **9**, 423–432.

17. Clech, J.-P., Manock, J.C., Noctor, D.M. *et al.* (1993) A comprehensive surface mount reliability model: background, validation and applications. In *Proc. 40th Electronic Components and Technology conference*, pp. 62–70.
18. Darveaux, R. (1997) Solder joint fatigue life model. In *Proc.TMS Annual Meeting, Orlando, FL*, pp. 213–218.
19. Lee, W.W., Nguyen, L.T., and Selvaduray, G.S. (2000) Solder joint fatigue model: review and applicability to chip scale packages. *Microelectron. Reliab.*, **40**, 231–244.
20. Clech, J.-P. (2004) Lead-free and mixed assembly solder joint reliability trends. *Proceedings (CD-ROM), IPC/SMEMA Council APEX 2004 Conference, Anaheim, CA, Feb. 23–26*, pp. S28-3-1 through S28-3-14.
21. Andersson, C., Lai, Z., Liu, J. *et al.* (2005) Comparison of isothermal mechanical fatigue properties of lead-free solder joints and bulk solders. *Mater. Sci. Eng.*, **A394**, 20–27.
22. Andersson, C., Sun, P., and Liu, J. (2006) Low cycle fatigue of Sn-based lead-free solder joints and the analysis of fatigue life prediction uncertainty. *IEEE Proceedings of, HDP'06*, pp. 19–26.
23. Dušek, M. and Hunt, C.P. (2006) Test Approach to Isothermal Fatigue Measurements for Lead-free Solders, National Physical Laboratory, UK, report No., DEPC-MPR 048, March, ISSN: 1744- 0270.
24. Bonda, N.R. and Noyan, I.C. (1992) Deformation inhomogeneity and representative volume in Pb/Sn solder alloys. *Metal. Mater. Trans. A*, **23**, 479–484.
25. Villain, J. (2003) Structures in microsections of small solder volumes. *Micromater. Nanomater.*, (2), 50.
26. Gomez, J. and Basaran, C. (2005) A thermodynamics based damage mechanics constitutive model for low cycle fatigue analysis of microelectronics solder joints incorporating size effects. *Int. J. Solids Struct.*, **42**, 3744–3772.
27. Arzt, E. (1998) Size effects in materials due to microstructural and dimensional constraints: Comparative Review. *Acta Mater.*, **46**, 5611–5626.
28. Saxton, H.J., West, A.J., and Barrett, C.R. (1971) Deformation and failure of Brazed Joints-macroscopic considerations. *Metal. Trans.*, **2**, 999–1007.
29. Almond, E.A., Brown, D.K., Davies, G.J., and Cottenden, A.M. (1983) Theoretical and experimental interlayered butt joints tested in tension. *Intern. J. Mech. Sci.*, **25**, 175–189.
30. Ranieri, J., Lauten, F., and Avery, D. (1995) Plastic constraint of large aspect ratio solder joints. *J. Electron. Mater.*, **24**, 1419–1423.
31. Takeshita, K. and Terakura, Y. (1998) A novel approach for predicting the tensile strength of brazed joints. *Metal. Mater. Trans. A*, **29**, 587–592.
32. Bonda, N.R. and Noyan, I.C. (1996) Effect of the specimen size in predicting the mechanical properties of PbSn solder alloys. *IEEE Trans. Compon., Packag., Manufact. Technol.*, **19**.
33. Zimprich, P., Betzwar Kotas, A., Khatibi, G., Weiss, B., Ipser, H. (2008) Size effects in small scaled lead-free solder joints. *J. Mater. Sci.: Mater. Electron.*, **19**, 383–388.
34. Zimprich, P., Saeed, U., Betzwar-Kotas, A. *et al.* (2008) Mechanical size effects in miniaturized lead-free solder joints. *J. Electron. Mater.*, **37**, 102–109.
35. Orowan, E., Nye, J., and Cairns, W.J. (1945) *MOS Arm. Res. Dept. Rept.*, **16**, 35.
36. Yin, L.M., Zhang, X.P., and Lu, C. (2009) Size and volume effects on the strength of microscale lead-free solder joints. *J. Electron. Mater.*, **38**, 2179–2183.
37. Cugnoni, J., Botsis, J., Sivasubramaniam, V., and Janczak-Rusch, J. (2006) Experimental and numerical studies on size and constraining effects in lead-free solder joints. *Fatigue Fract. Engng. Mater. Struct.*, **30**, 387–399.
38. Vianco Lead, P. (2000) (Pb)-Free Solder Application, Report No. SAND2006-2066C, published by Office of Scientific and Technical Information 15 Sep.

39. Lauten, F., Ranieri, J., and Avery, D. (1995) Development of a solder material process to relieve the plastic constraint associated with thin joints. *J. Electron. Mater.*, **24**, 1425–1428.
40. Chawla, N., Shen, Y.-L., Deng, X., and Ege, ES. (2004) An evaluation of the lap-shear test for Sn-rich solder/Cu couples: experiments and simulation. *J. Electron. Mater*, **33**, 1589–1595.
41. Shen, Y.-L., Chawla, N., Ege, E.S., and Deng, X. (2005) Deformation analysis of lap-shear testing of solder joints. *Acta Mater*, **53**, 2633–2642.
42. Mei, Z., Morris, J.W. Jr., Shine, M.C., and Summers, T.S.E. (1991) Effects of cooling rate on mechanical properties of near-eutectic tin-lead solder joints. *J. Electron. Mater.*, **20**, 599–608.
43. Madeni, J., Liu, S., and Siewert, T. (2002) Casting of lead-free solder bulk specimens with various solidification rates. *Proceedings of the ASM International Conference, Indianapolis, IN*.
44. Darveaux, R., Reichman, C., Berry, C.J. *et al.* (2008) Effect of joint size and pad metallization on solder mechanical properties. *58th IEEE Electronic Components and Technology Conference* (Vol. 1), pp. 113–122.
45. Wiese, S., Roellig, M., Mueller, M., and Wolter, K.-J. (2008) The effect of downscaling the dimensions of solder interconnects on their creep properties. *Microelectron. Reliab.*, **48**, 843–850.
46. Sidhu, R.S. and Chawla, N. (2008) Microstructure characterization and creep behavior of Pb-free Sn-rich solder alloys: Part I. microstructure characterization of bulk solder and solder/copper joints. *Metal. Mater. Trans. A*, **39**, 340–348.
47. Sidhu, R.S., Deng, X., and Chawla, N. (2008) Microstructure characterization and creep behavior of Pb-free Sn-rich solder alloys: Part II. creep behavior of bulk solder and solder/copper joints. *Metal. Mater. Trans. A*, **39**, 349–362.
48. Gong, J., Liu, C., Conway, P., and Silberschmidt, V. (2006) Grain features of SnAgCu solder and their effect on mechanical behaviour of micro-joints. *Proceedings - Electronic Components & Technology Conference, 56th* (Vol. 1), pp. 250–257.
49. Hegde, P., Whalley, D.C., and Silberschmidt, V.V. (2009) Size and microstructure effects on the stress-strain behaviour of lead-free solder joints. *Microelectronics and Packaging Conference*, EMPC 2009, pp. 1–9.
50. Kim, K.S., Huh, S.H., and Suganuma, K. (2002) Effects of cooling speed on microstructure and tensile properties of Sn-Ag-Cu alloys. *Mater. Sci. Eng. A*, **333**, 106–114.
51. Chada, S., Herrmann, A., Laub, W. *et al.* (1997) Microstructural investigation of Sn-Ag and Sn-Ag solder joints. *Solder. Surface Mount Technol.*, **9**, 9–13.
52. Kinyanjui, R., Lehman, L.P., Zavalij, L., and Cotts, E. (2005) Effect of sample size on the solidification temperature and microstructure of SnAgCu near eutectic alloys. *J. Mater. Res.*, **20**, 2914–2918.
53. Mueller, M., Wiese, S., Roellig, M., and Wolter, K.-J. (2007) The dependence of composition, cooling rate and size on the solidification behaviour of SnAgCu solders. *International Conference on Thermal, Mechanical & Multi-Physics Simulation and Experiments in Microelectronics & Micro System, London, United Kingdom*, Apr. 15–18 2007, 1, pp. 197–206.
54. Huang, Z., Conway, P., and Liu, C. (2005) Effect of solder bump geometry on the microstructure of Sn-3.5 wt% Ag on electroless nickel immersion gold during solder dipping. *J. Mater. Res.*, **20**, 649–658.
55. Gong, J., Liu, C., Conway, P., and Silberschmidt, V. (2009) Formation of Sn dendrites and SnAg eutectics in a SnAgCu solder. *Scr. Mater.*, **61**, 682–685.
56. Lalonde, A., Emelander, D., Jeannette, J. *et al.* (2004) Quantitative metallography of β-Sn dendrites in Sn-3.8Ag-0.7Cu ball grid array solder balls via electron backscatter diffraction and polarized light microscopy. *J. Electron. Mater.*, **33**, 1545.
57. Wang, B., Wu, F., Wu, Y. *et al.* (2010) Effect of stand-off height on the microstructure and mechanical behavior of solder joints. *Solder. Surface Mount Technol.*, **22**, 11–18.
58. Wu, F., Wang, B., Du, B. *et al.* (2009) Effect of stand-off height on microstructure and tensile strength of the Cu/Sn9Zn/Cu solder joint. *J. Electron. Mater.*, **38**, 860–865.

59. Liu, H., Zhou, L., Li, J. *et al.* (2009) Effect of stand-off height on the reliability of Cu/Sn-4.8Bi-2Ag/Cu solder joint. *International Conference on Electronic Packaging Technology & High Density Packaging (ICEPT-HDP)*.
60. Laurila, T., Vuorinen, V., and Kivilahti, J.K. (2005) Interfacial reactions between lead-free solders and common base materials. *Mater. Sci. Eng.*, **R49**, 1–60.
61. Lee, H.-T., Chen, M.-H., Jao, H.-M., and Liao, T.-L. (2003) Influence of interfacial intermetallic compound on fracture behavior of solder joints. *Mater. Eng.*, **A358**, 134–141.
62. Yang, S.C. and Kao, C.R. (2007) Massive spalling of intermetallics in solder joints: a general phenomenon that can occur in multiple solder-substrate systems. *Electronic Components and Technology Conference*.
63. Huang, Z., Conway, P., and Thomson, R. (2007) Microstructural considerations for ultrafine lead free solder joints. *Microelectron. Reliab.*, **47**, 1997–2006.
64. Huang, Z., Conway, P., Jung, E. *et al.* (2006) Reliability issues in Pb-free solder joint miniaturization. *J. Electron. Mater.*, **35**(9), 1761–1772.
65. Alam, M.O., Lu, H., and Bailey, C. (2008) Fracture mechanics analysis of cracks in solder joint intermetallic compounds. *IEEE, 2nd Electronics Systemintegration Technology Conference*.
66. Alam, M.O., Lu, H., and Bailey, Chris. (2009) Fracture mechanics analysis of solder joint intermetallic compounds in shear test. *Comput. Mater. Sci.*, **45**, 576–583.
67. Choi, S.-H., Song, B.-G. Kang, K.-J., and Fleck, N.A. (2001) Fracture of a ductile layer constrained by stiff substrates. *Fatigue Fract. Eng. M.*, **24**(1), 1–13.
68. Loo, S., Lee, P., Lim, Z. *et al.* (2010) Interface fracture toughness assessment of solder joints using double cantilever beam test. *Int. J. Mod. Phys. B*, **24**(1 & 2), 164–174.
69. Wiese, S., Roellig, M., Mueller, M., and Wolter, K.-J. (2008) The effect of downscaling the dimensions of solder interconnects on their creep properties. *Microelectron. Reliab.*, **48**, 843–850.
70. Zimprich, P., Saeed, U., Weiss, B., and Ipser, H. (2009) Constraining effects of lead-free solders joint during stress relaxation. *J. Electron. Mater.*, **38**(3), 392–399.
71. Mavoori, H., Chin, J., Vaynman, S. *et al.* (1997) Creep, stress relaxation, and plastic deformation in Sn-Ag and Sn-Zn eutectic solders. *J. Electron. Mater*, **26**(7), 783–790.
72. Jadhav, S.G., Bieler, T.R., Subramanian, K.N., and Lucas, J.P. (2001) Stress relaxation behavior of composite and eutectic sn-Ag solder joints, *J. Electron. Mater.*, **30**, 1197.
73. Murty, K.L., Yang, H., Deane, P., and Magill, P.,EEP-Vol. 19-1, *Advanced Electronic Packaging (ASME, Philadelphia, PA, 1997)*.
74. Li, J., Zhang, G., and Zhou, J. (2008) Size effects of lead-free solder joint thickness under shear creep based on micro-electrical-resistance strain. *J. Phys. D: Appl. Phys.*, **41**, 165412.
75. Lee, G., Song, J., Lai, Y. *et al.* (2009) Size and substrate effects on microstructure and shear properties of solder joints, *International Conference on Electronic Materials and Packaging (EMAP 2008)*, 187–190.
76. Wu, F., He, M., Wu,Y. *et al.* (2006) Effect of Interfacial IMCs Proportion on the Reliability of Miniature Lead-Free Solder Joint, 7th *International Conference on Electronics Packaging Technology (ICEPT 2006)*, 1–5.

Index

3DIC *see* three-dimensional integrated circuits
activators 182
ADAMIS database 54
additives 182
adhesive layers 221–2
Ag_3Sn precipitates
  microstructure 198–202, 204–7, 209, 225, 238, 243, 247
  miniaturization 470, 477
  minor alloying additions 122, 125, 129–33, 146, 150
  nanocomposite solder 166
  see also silver; tin–silver alloys; tin–silver–copper alloys
aging effects
  electromigration 351–58, 365–6
  microstructure 200–202, 216–19, 227
  miniaturization 461–6, 481
  minor alloying additions 139–40
alloy development
  computational thermodynamics 48–51
  historical context 45–48
  modeling other properties 65–68
  modeling thermodynamic properties using SOLDERS database 58–65
  phase diagrams 45–70
  SOLDERS database 56–68
  thermodynamic databases 51–68
alternating layer formation 411–12
alumina 170
aluminum–copper–zinc alloys 54
aluminum hydroxide fillers 186–9
aluminum interconnects 425–6
annealing processes 318, 361
antimony doping 123–4, 126–8
  see also tin–antimony alloys
arc discharge 163
aspect ratios 458–9, 467–8, 481–2
asymmetric IMC layer growth
  enhancement and suppression 408–11, 416–17
  Peltier effect 409–11
atomic flux
  electromigration 340, 350–1, 376, 402, 414–16
  summation model 414–15
  summation with stress modification model 415–16
  thermomigration 440
Au *see* gold

back stress 409, 416, 440–42
backend-of-line (BEOL) interconnects 340
backscattered electron (BSE) imaging 200–201, 327–8, 462
  see also electron backscatter diffraction
ball grid arrays (BGA)
  chemical effects on reliability 182–4
  electromigration 402
  microstructure 211–12
  miniaturization 461, 466–70
  minor alloying additions 125, 129–31, 134, 146, 151, 154
  phase diagrams 72
barrel cracks 187–8
BEOL *see* backend-of-line
BGA *see* ball grid arrays
Bi *see* bismuth doping; tin–bismuth alloys
binary phase diagrams 14–28, 47, 60–6, 73–85
bismuth doping 123–4, 126–8
  see also tin–bismuth alloys; tin–silver–bismuth alloys
bisphenol A 186, 191
bivariant equilibria 17
brittleness 391–3, 395
BSE *see* backscattered electron

Lead-free Solders: Materials Reliability for Electronics, First Edition. Edited by K. N. Subramanian.

C4NP process 134–5
CAF *see* conductive anodic filament
CALPHAD method
  nickel–phosphorus systems 94, 99, 111–12
  phase diagrams 22–3, 48, 52
carbon nanotubes (CNT) 165, 168, 170
catetic phase reactions 16–17
CBGA *see* ceramic ball grid arrays
CDCA *see* consumable-electrode direct current arc
ceramic ball grid arrays (CBGA) 125, 129–31, 134
ceramic substrates 326–8
cerium doping 148
CGA *see* column grid arrays
Charpy-type impact tests 6
chemical effects on reliability 181–94
  cleaning chemicals and equipment 185
  conductive anodic filament formation 189–93
  fluxes and pastes 181–5
  laminates 185–9
chemical reduction methods 163
chemical vapor deposition (CVD) 163
cleaning chemicals and equipment 185
CMM *see* compact mixed mode
CNT *see* carbon nanotubes
coarsening kinetics *see* precipitate coarsening
cobalt doping
  effective undercooling reduction 32–3
  minor alloying additions 135–6
  see also tin–cobalt alloys
coefficient of thermal expansion (CTE) 5, 6
  chemical effects on reliability 186–8, 193
  microstructure 233–4
  miniaturization 447, 464
  nanocomposite solder 168, 170–71
  temperature-dependent deformation 274
column grid arrays (CGA) 466
compact mixed mode (CMM) specimens 220–21, 227
composite SnPb solder joints 427–30
compound formation 33–4
compressive stress
  electromigration 407
  whisker growth 303–4, 306–16, 325–7, 329, 332
computational thermodynamics
  calculation for multicomponent systems 48–50
  critical assessment of thermodynamic properties 51
  modeling Gibbs energies 50–51
  phase diagrams 48–51
conductive anodic filament (CAF) formation 189–93
conformal coatings 316–17, 333
consistency conditions 52–4
constraint effect 447, 448–73, 480–2
consumable-electrode direct current arc (CDCA) 163
cooling rates 459
copper doping 135–6, 152–3
  see also tin–copper alloys; tin–silver–copper alloys
copper–indium alloys 27
copper interconnects 425–6
copper metallization
  electromechanical coupling 257
  electromigration 354, 356–7
  microstructure 238–43, 246–7
  miniaturization 468
  minor alloying additions 137–8, 144
copper–nickel alloys 14–19
copper–silver alloys 47–8
copper/tin–copper/nickel sandwich structures 13
corrosion whiskers 329–30
crack propagation
  chemical effects on reliability 187–8
  microstructure 197–98, 219–27, 236–7, 246, 248–9
  miniaturization 450, 461–6, 473–5, 481–2
  minor alloying additions 130
  nanocomposite solder 173–4
  temperature-dependent deformation 278–80, 286–8
creep
  microstructure 197–8, 206–19, 227, 244–5, 247, 249
  miniaturization 446, 475–78, 482
  nanocomposite solder 170, 175
  thermomigration 427, 434–5, 439–41
creep-stress exponent 282–6
crystallographic data 50–51, 52
CS *see* current stressing
CTE *see* coefficient of thermal expansion
Cu *see* copper
current-crowding effect
  electromigration 377–8, 382–5, 393–4
  thermomigration 426–7

current stressing (CS) 5
  electromigration 358–63, 384, 387–9, 393–4, 405, 412
  thermomigration 433–4, 437
CVD *see* chemical vapor deposition
cyclic twinning morphology 146

daisy chains 386
decomposition 188–9
defects 478
delamination 187–9
density function theory (DFT) 136
density of nanocomposite solder 169
dicyandiamide (DICY) 186
differential scanning calorimetry (DSC) 132–4
differential thermal analysis (DTA) 74, 77–82, 86, 89, 92
diffusion-controlled phenomena 199
diffusion couples 360–61
dimple morphology 465
dioxins 186
dislocation climb 268–9
dislocation glide 268–9
dislocation theory 325
dissociative intermetallic compounds 463
double shear-lap geometry 211–12
drop impact resistance 150
DSC *see* differential scanning calorimetry
DTA *see* differential thermal analysis
ductility
  electromechanical coupling, stress 268
  electromigration 392–3
  microstructure 220
  miniaturization 467–8, 473–4, 476, 480
  nanocomposite solder 170, 175

EBSD *see* electron backscatter diffraction
EDS *see* energy-dispersive spectroscopy
EDX *see* energy-dispersive X-ray
effective undercooling reduction 32–3
elastic deformation 310–11
elastic modulus 456–7
electrical failures 183–4
electrical resistance 386–90
electrician's solder 60–6
electroless Ni immersion gold (ENIG)
  electromigration 358
  microstructure 200, 207
  miniaturization 470
  phase diagrams 72
electromechanical coupling 251–71
  compression stress due to IMCs 265–7
  context 252–3
  discussion 264–69
  electromigration 251, 252, 253–70
  experimental procedure 253–4
  grain-boundary grooving 251, 256–7
  grain-boundary vacancy concentration 264–5, 266–70
  hillock growth 251, 255–6, 265–7
  polycrystalline pure tin 251–4, 256–7, 260, 268–70
  results 255–64
  single-crystal tin 251–4, 257–8, 260, 268–70
  stress-relaxation tests 251, 254, 260–4, 268–70
  surface morphology 255–8
  tensile strength 258–60, 267–8
  tin–silver–copper alloys 251–6, 268–70
electromigration (EM) 5, 7–9, 339–73
  asymmetric IMC layer growth 408–11, 416–17
  atomic flux 340, 350–51, 376, 402, 414–16
  back stress 409, 416
  brittleness 391–3, 395
  challenges 393–4
  compressive stress 407
  context 339–41, 375–6, 401–2
  current-crowding effect 377–8, 382–5, 393–4
  current stressing 358–63, 384, 387–9, 393–4, 405, 412
  dissolution of UBM in solder joints 383–5
  electrical resistance 386–90
  electromechanical coupling 251, 252, 253–70
  electronic packaging 375–99
  electronic solder joints 401–22
  failure mechanisms 341, 342–51, 363–6, 382–3
  fast dissolution of Cu and Ni 393
  flip-chip technology 339–40, 342–4, 347–8, 375–85, 389, 402
  grain rotation 390, 393
  grain structure 363–6
  hillock formation 404–5, 407
  interfacial reactions 408–13
  intermetallic compounds 341, 345–8, 351–65, 367, 383–5, 388–9, 393, 402, 404, 408–18
  Joule heating 378–5, 394

electromigration (EM) (*Continued*)
microstructure 355, 386, 402–7, 412–13
minor alloying additions 151–3
models of IMC growth 414–18
no effect of electric current 411
Peltier effect 409–11
phase redistribution 389
phase segregation 405–7
physical properties of solder bumps 386–93
primarily one moving species 403–4
reaction phase effects 411–12
resistance 403–4
symmetric IMC layer growth 411
temperature distribution/ redistribution 378–85, 390–1
thermal aging 351–8, 365–6
thermomigration 340, 347–51, 385, 394, 427, 429, 437–8, 441
under bump metallization 341, 342–50, 354, 358–9, 362–3, 367–8, 375, 377–8, 381–5, 388–9, 393–4, 412
void propagation 342–7, 351, 382–3, 386–91, 404–5
whisker growth 304, 331–2
electron backscatter diffraction (EBSD) 147–8, 363–7
electron probe microanalysis (EPMA)
electromechanical coupling 255–6
nickel–phosphorus systems 77–8, 80, 87, 91–2
thermomigration 430–1
electroplating
electromigration 356–58
whisker growth 304, 314–15, 324–34
EM *see* electromigration
energy dispersive spectroscopy (EDS) 200–1, 255
energy-dispersive X-ray (EDX) spectroscopy 142
ENIG *see* electroless nickel gold
enthalpy of formation 95, 109–10
environmental parameters 3–4
epichlorhydrin 191
EPMA *see* electron probe microanalysis
epoxy laminates 185–89
eutectic colonies 234–5
eutectic phase reactions
nickel–phosphorus systems 79–82, 84–5, 87, 91
phase diagrams 16–17, 47, 58
eutectic Sn–Ag *see* tin–silver alloys
eutectoid phase reactions
nickel–phosphorus systems 80, 87, 92
phase diagrams 16–17

fan-cooled solders 403–6
fast diffusers 341
fast dissolution 393
fatigue cracking
chemical effects on reliability 187–8
microstructure 197–8, 219–27, 236–7, 246, 248–9
miniaturization 450, 461–6, 473–5, 481–2
minor alloying additions 130
nanocomposite solder 173–4
temperature-dependent deformation 278–80, 286–8
FEA *see* finite element analysis
FEM *see* finite element modeling
FIB *see* focused ion beam
finite element analysis (FEA) 310–14, 426–7
finite element modeling (FEM)
electromigration 348–9, 379–80
microstructure 221
miniaturization 451, 453, 458, 473
flip-chip technology
current-crowding effect 377–8, 382–5
dissolution of UBM in solder joints 383–5
electromigration 339–40, 342–4, 347–8, 375–85, 389, 402
Joule heating and temperature distribution 378–85
microstructure 200
miniaturization 469
minor alloying additions 122, 131–5, 151–4
phase diagrams 38, 72
thermomigration 425–42
void propagation 382–3
fluxes 181–5
focused ion beam (FIB) technique 142–4
FR-4 epoxy 185–6
fracture
mechanics 473–5
morphology 461–6
toughness 222–5, 227, 391–3
see also fatigue cracking

generalized IMC layer growth model 416–18
germanium doping 148

Gibbs energies
  computational thermodynamics 48–51
  nickel–phosphorus systems 104, 109–11
  phase diagrams 17–21, 46–55
Gibbs phase rule 17
glass/polymer interface 189–3
glass-transition temperatures 237
gold alloys 4
gold–copper alloys 48–49
gold metallization 467–68, 475
gold overplating 333
gold/tin/copper sandwich structures 13
grain-boundaries
  decohesion 273, 279–82, 286–7, 289–91, 294–5
  diffusion 305–6, 310–12, 314–15, 323–4
  grooving 251, 256–7
  microstructure 246–7, 249
  sliding 246–7, 249, 273, 280–2, 290–91, 294–5
  temperature-dependent deformation 273, 279–82, 286–7, 289–1, 294–5
  vacancy concentration 264–5, 266–70
  whisker growth 7, 305–6, 310–12, 314–15, 323–4
grain rotation 390, 393
grain size 166
grain structure 363–6
graping 183–4
growth rates 34–6

halogen-free (HF) laminates 186–89
head-on-pillow (HOP) defects 182–4
heat capacity 95
heat treatment 318
HF *see* halogen-free
high strain rate fractures 197–8, 219–27
hillock growth
  electromechanical coupling 251, 255–6, 265–7
  electromigration 404–5, 407
  thermomigration 434–5, 438
  whisker growth 301–2, 313
homotetic phase reactions 16–17
HOP *see* head-on-pillow
hot dipping 356–8

I/O *see* input/output
IMC *see* intermetallic compounds
impact loading 6
impact strength 139–40
imposed fields 5
in-service parameters 3–4
indium doping 123–4, 126–28
  see also tin–indium alloys
indium–nickel–antimony alloys 53–4
indium whiskers 332
input/output (I/O) demands 339
Interconnect Stress Test (IST) 187
interfacial reactions
  asymmetric IMC layer growth 408–11
  electromigration 408–13
  minor alloying additions 122, 136–45
  nickel–phosphorus systems 79–2, 84–7, 90–92
  no effect of electric current 411
  Peltier effect 409–11
  phase diagrams 15–17, 28–32, 33–4, 38–41, 47, 58
  reaction phase effects 411–12
  symmetric IMC layer growth 411
interfacial void formation 143–5
intermediate phases 15–17
intermetallic compounds (IMC)
  asymmetric IMC layer growth 408–11
  current stressing 358–63, 384, 388–89
  electromechanical coupling 252–3, 255–6, 265–7, 269
  electromigration 341, 345–48, 351–65, 367, 383–5, 388–9, 393, 402, 404, 408–18
  grain structure 363–5
  material design 3–4
  microstructure 198–200, 220, 222–5, 237–8, 240–43, 246–9
  miniaturization 446–7, 449–50, 457–58, 460–6, 469–73, 475–7, 480–81
  minor alloying additions 125, 131–3, 136–46, 148–50
  models of IMC growth 414–18
  nanocomposite solder 162, 167, 174
  nickel–phosphorus systems 78, 111
  Peltier effect 410–11
  phase diagrams 13–14, 30–2, 34, 62, 65, 72, 86
  spalling of Ni-Sn intermetallics 144–5
  symmetric IMC layer growth 411
  temperature-dependent deformation 273–4, 279–82, 286–7, 289–94
  thermal aging 351–8
  thermomechanical fatigue 6

intermetallic compounds (IMC) (*Continued*)
thermomigration 432, 435–6, 438
whisker growth 7, 304–15, 317–18, 325–6, 330–32
intermittent electrical failures 183–4
International Technology Roadmap for Semiconductors (ITRS) 339–40
invariant equilibria 17
isopiestic methods 80–4, 94, 99–100, 102–103, 105–11
isoplethal sections
nickel–phosphorus systems 89–90
phase diagrams 37, 59, 62
isothermal aging 200–202, 216–19
isothermal sections
nickel–phosphorus systems 94
phase diagrams 29, 31, 35–6, 39–39
IST *see* Interconnect Stress Test
ITRS *see* International Technology Roadmap for Semiconductors

J-integrals 220–1
Joule heating (JH) 5, 8
electromigration 378–85, 394
minor alloying additions 151
thermomigration 426–7

Kelvin probes 386–89, 391
KEML *see* Knudsen effusion mass loss
KEMS *see* Knudsen effusion mass spectrometry
kinking 302
Kirkendall voids 345, 351, 466–7
knee cracks 187–88
Knudsen effusion mass loss (KEML) 102, 106–8
Knudsen effusion mass spectrometry (KEMS) 94, 102

laminates 185–89
lanthanum doping 148
lap-shear technique 454–5, 457
lead *see* tin–lead alloys
lever rule 15–16
limited tin supply 40–1
liquidus projections
alloy development 60–1
nickel–phosphorus systems 89
undercooling 32
low temperature cofiring ceramic (LTCC) devices 36–7

Ludwig–Soret effect *see* thermomigration

magnesium hydroxide fillers 186–7
manganese doping 140
material design 3–4
mean effective diffusion distances 205–6
mechanical-compression whiskers 330–31, 333
mechanical integrity 5–6
mechanical milling 163
mechanical strength
nanocomposite solder 170, 175
temperature-dependent deformation 286–9
melting points
microstructure 237–8
nanocomposite solder 168, 175
phase diagrams 36–8
metal alloy reinforced nanocomposite solder 165
metallic-oxide-reinforced nanocomposite solder 165
microalloying *see* minor alloying additions; nanocomposite solder
microemulsion methods 163
microhardness
minor alloying additions 149–50
nanocomposite solder 169–70, 175
microstructure 197–231
aging effects 200–202, 216–19, 227
coarsening 8
context 197–9, 233–4
creep 197–8, 206–19, 227, 244–5, 247, 249
electromigration 355, 386, 402–7, 412–13
eutectic colonies 234–5
high strain rate fractures 197–8, 219–27
intermetallic compounds 237–8, 240–43, 246–9
isothermal aging 200–202
mechanical metallurgy of lead-free solders 243–5
mechanistic basis for creep constants 211–16
miniaturization 447, 457–61, 466–73, 480–1
minor alloying additions 145–49, 151
nanocomposite solder 166–7
precipitate coarsening 199–6, 209, 227, 236, 247
quantitative characterization 197, 202–6
reflow parameters 223–4

steady-state creep 207–209, 212–16, 247, 249
temperature-dependent deformation 274–5, 276, 278–84, 286–94
thermomechanical behavior 233–50
thermomechanical cycling 199, 200–202
thermomechanical fatigue 246–49
thermomigration 436–7
tin–lead alloys 234–7, 240–41, 244–49
unified creep model 197–8, 209–19, 227
whisker growth 312–13, 317, 324, 333
miniaturization 445–85
aging effects 461–6, 481
aspect ratios, volume and pad size 458–59, 466–73, 481–2
constraint effect 447, 448–73, 480–82
context 445–48
creep and relaxation 446, 475–8, 482
fracture mechanics 473–5
fracture morphology 461–6
intermetallic compounds 446–7, 449–50, 457–8, 460–6, 469–73, 475–7, 480–1
microstructure 447, 457–61, 466–73, 480–1
modeling constraint and geometry effects 448–66
shear loading 448, 453–6
size effect 447, 448–66
static properties of solder joints 448–66
tensile strength 448–9, 451–7, 461–3, 476, 479
thermomechanical behavior 445–6
see also nanocomposite solder
minor alloying additions 121–59
Ag_3Sn plate formation 122, 125, 129–33, 146, 150
context 122–5
drop impact resistance 150
electromigration 151–3
interfacial reactions 122, 136–45
interfacial void formation 143–5
intermetallic compounds 125, 131–3, 136–46, 148–50
mechanical properties 149–51
microelectronic applications 122
microstructure 145–49, 151
spalling of Ni-Sn intermetallics 144–5
strength and hardness 149–50
surface finishes 137–38
thermal fatigue resistance 150–2
under bump metallization 134–38
undercooling 122, 129–30, 132–6, 146
US patents issued 123–4, 126–28
mixed mode fracture behavior 220–21, 227
monolithic metal-reinforced nanocomposite solder 165
monotectic phase reactions 16–17
monovariant equilibria 17
multiwall carbon nanotubes (MWCNT) 168

Nabarro–Herring creep model 434–5
nanocomposite solder 161–77
challenges and solutions 171–74
context 162
fabrication processes 162–5
grain size 166
intermetallic compounds 162, 167, 174
mechanical properties 169–70, 175
microstructure 166–7
nanoparticle fabrication 162–3
physical properties 167–9, 174–5
reinforcement types 165
necking 451–3, 457
nickel alloys 7
see also tin–nickel alloys
nickel doping 135–7, 139–40, 148, 152–3
nickel metallization
microstructure 240–3, 246–7
miniaturization 467–8
minor alloying additions 137–8
thermomigration 433–4
nickel–copper alloys 14–19
nickel–phosphorus systems 71–118
binary phase equilibria 73–85
experimental results 77–85, 86–94, 99–11
homogeneity ranges and compositions 78–80, 85–7
interaction with tin-based solders 71–118
interfacial reactions 79–82, 84–7, 90–2
isopiestic methods 80–4, 94, 99–100, 102–103, 105–11
literature overviews 73–7, 85–6, 95–9
minor alloying additions 135, 138, 145, 150–3
nickel–phosphorus phase diagrams 73–6, 77–82, 95–8, 102–5
nickel–tin phase diagrams 73–4
phase diagrams 56–7, 73–6, 77–82, 95–8, 102–5
phase-field designations 90, 92, 94

nickel–phosphorus systems (*Continued*)
phosphorus–tin phase diagrams 76–7, 82–5, 99, 105–11
relevance of results 111–13
space groups and compositions 85–6, 93
ternary phase equilibria 85–94
thermochemical data 94–111
nickel–tin phase diagrams 73–4
nickel underlayers 328, 332
nonmetallic reinforced nanocomposite solder 165
normalized stress-relaxation curves 476–7
nucleation density 166
nucleation and growth 303–4, 311–12, 314–16

optical microscopy (OM) 428–29
Orowan model 450–51
Ostwald ripening 199
overplating 333
oxidation/corrosion whiskers 329–30

pancake-type void propagation 342–4, 382–3
pastes
chemical effects on reliability 181–5
nanocomposite solder 167
Pb *see* tin–lead alloys
Peltier effect 409–11
peritectic phase reactions
nickel–phosphorus systems 79–81, 84, 91–2
phase diagrams 16–17
peritectoid phase reactions 16–17
PF *see* plastic flow and fracture
phase diagrams
alloy development 45–70
applications in lead-free soldering 13–45
binary systems 14–28, 47, 60–6, 73–85
CALPHAD method 22–3, 48, 53, 94, 99, 111–12
computational thermodynamics 49–51
effective undercooling reduction 32–3
historical context 45–48
homogeneity ranges and compositions 78–80
interfacial reactions 15–17, 28–34, 38–41, 47, 58, 79–82, 84–7, 90–2
intermediate phases 15–17
isopiestic methods 80–4, 94, 99–100, 102–3, 105–11
isoplethal sections 37
isothermal sections 29, 31, 35–6, 39–41
lever rule 15–16
limited tin supply 40–1
modeling other properties 65–68
modeling thermodynamic properties using SOLDERS database 58–5
multicomponent systems 48–50
nickel–phosphorus systems 56–7, 71–118
phase equilibria 15–17, 28–32, 33–4, 38–41, 47, 58
SOLDERS database 56–68
ternary systems 22, 26–7, 29–40, 53–4, 58–62, 85–94
thermodynamic databases 51–58
unexpected compound formation 33–4
unexpected growth rates 34–6
unexpected melting of solder 36–8
uphill diffusion 38–40
phase redistribution 389
phase segregation 405–7
phenolic novolac (PN) resins 186, 193
phosphorus-doped epoxy 186–7
phosphorus–nickel systems *see* nickel–phosphorus systems
phosphorus–tin phase diagrams 76–7, 82–5, 99, 105–11
plastic deformation
miniaturization 450–4, 457–59
minor alloying additions 149
whisker growth 310–12, 314, 316
plastic flow and fracture (PF) 5
platelet IMC growth 326, 332
PN *see* phenolic novolac
polycrystalline pure tin
electromechanical coupling 251–4, 256–7, 260, 268–69
whisker growth 299–300
polyhedral oligomeric silsesquioxanes (POSS) 168, 170–71, 175
polymorphism of tin 8
porosity 454, 480–1
POSS *see* polyhedral oligomeric silsesquioxanes
Pourbaix diagrams 191
precipitate coarsening 199–6, 209, 227, 236, 247
primary creep curves 212, 214–16
printed wiring boards (PWB)
chemical effects on reliability 186, 187–93
miniaturization 446
punch-stress dependence 207–9

PWB *see* printed wiring boards
pyramidal IMC growth 326, 332

quad flat pack no leads (QFN) 182

reflow soldering
  electromigration 356–8, 365–8
  miniaturization 471–2
  parameters 223–4
Restriction of Hazardous Substances (RoHS) 122, 233, 340–1
room-temperature whiskers 325–6, 332–3
root grooves 327–8

SAC *see* tin–silver–copper
satellite control processors (SCP) 301
Sb *see* antimony doping; tin–antimony alloys
scanning electron microscopy (SEM)
  temperature-dependent deformation 276, 278–84, 286–94
  thermomigration 427–34, 436
Scheil solidification 63–4
SCP *see* satellite control processors
self-diffusion
  electromechanical coupling 253, 265
  electromigration 363–4
  microstructure 209, 248
  minor alloying additions 152
  whisker growth 323–4
self-perpetuating coupling events 9
SEM *see* scanning electron microscopy
SGTE pure substance database 101–2
shear loading 448, 453–6
shear strength 171–3
shear-stress–displacement curves 453–5
short circuits 300–301
short-range ordering (SRO) 53
SIF *see* stress intensity factors
silica fillers 186–89
silicon chip technology 429
silver doping 123–4, 126–28, 151
  see also tin–silver alloys; tin–silver–copper alloys
silver–copper alloys 47–48
silver–indium alloys 28
simulated annealing 361
single-crystal tin 251–4, 257–58, 260, 268–70
single-wall carbon nanotubes (SWCNT) 165, 168, 170
sintering processes 164–5
size effect 447, 448–66
SMT *see* surface mount technology
Sn *see* tin
sol-gel methods 163
solder joint responses
  electromigration 5, 7–9
  imposed fields 5
  mechanical integrity 5–6
  polymorphism of tin 8
  synergistic effects 8–9
  thermal migration 5, 8
  thermomechanical fatigue 6–7, 8–9
  whisker growth 7
SOLDERS database 56–68
solid state aging 139–40
solvents 182
Soret effect *see* thermomigration
spalling
  miniaturization 466, 481
  Ni-Sn intermetallics 144–5
spark erosion 163
SPR *see* stencil printing followed by reflow
SRO *see* short-range ordering
steady-state creep 207–209, 212–16, 247, 249
stencil printing followed by reflow (SPR) 471
step soldering 36–7
strain rates 273–5, 277–78, 282–88
stress intensity factors (SIF) 473–4
stress-relaxation tests 251, 254, 260–4, 268–70
stress–strain curves
  electromigration 392–3
  miniaturization 450, 458–9, 476
striation rings 327–8
surface-active materials 166
surface-damage accumulation 289–91
surface finishes 137–8
surface metallization 137–8
surface morphology 255–8
surface mount technology (SMT) 164
surface tension 65–68
surface treatments 317, 333
SWCNT *see* single-wall carbon nanotubes
symmetric IMC layer growth 411
synchrotron radiation X-ray tomography 426
synergistic effects 8–9
syntectic phase reactions 16–17

TC *see* thermal cycling
TEM *see* transmission electron microscopy
temperature to decomposition 188–9

temperature-dependent deformation 273–95
  context 274–5
  crack propagation 278–80, 286–8
  experimental details 275–6
  grain-boundary sliding/decohesion 273, 279–82, 286–7, 289–91, 294–5
  low-temperature microstructural damage 291–5
  mechanical testing 276
  microstructure 274–5, 276, 278–84, 286–94
  residual mechanical properties 286–89
  results and discussion 276–94
  strain rates 273–5, 277–8, 282–8
  surface-damage accumulation 289–91
  test-specimen preparation 275
  thermal cycling 275–6, 289–95
temperature redistribution 390–91
tensile strength
  electromechanical coupling 258–60, 267–8
  electromigration 391–3
  miniaturization 448–9, 451–7, 461–3, 476, 479
ternary phase diagrams 22, 26–7, 29–40, 53–4, 58–62, 85–94
thermal aging 351–58, 365–66
thermal cycling (TC)
  microstructure 201, 203, 236, 246–7
  nanocomposite solder 171–4, 175
  temperature-dependent deformation 275–6, 289–95
  whisker growth 326–8
thermal expansion mismatch 326–7
thermal fatigue resistance 150–51
thermal infrared microscopy 433–4
thermochemical data 94–111
thermodynamic databases 51–68
  conditions of consistency 52–4
  creation 54
  modeling other properties 65–68
  modeling phase diagrams and thermodynamic properties 58–65
  SOLDERS database 56–68
  specialized databases relevant for lead-free solders 54–7
thermoelectric effect 435, 441
thermomechanical analyzers (TMA) 187–88
thermomechanical behavior
  microstructure 233–50
  miniaturization 445–6
  whisker growth 304
thermomechanical cycling (TMC) 199, 200–202
thermomechanical fatigue (TMF) 5, 6–7, 8–9
  microstructure 246–9
  miniaturization 447
  nanocomposite solder 171–4, 175
  temperature-dependent deformation 273–95
thermomigration (TM) 5, 8, 425–42
  composite SnPb solder joints 429–30
  creep 427, 434–5, 439–41
  driving force 435–9
  electromigration 340, 347–51, 385, 394, 427, 429, 437–8, 441
  flip-chip technology 425–42
  in-situ observation 429–30
  intermetallic compounds 432, 435–6, 438
  irreversible processes 438–9
  lead-free solder joints 432–5
  microstructure 436–7
  thermoelectric effect 435, 441
  tin–lead alloys 427–32
  under bump metallization 431, 433, 435, 438
  unpowered composite SnPb solder joints 427–29
  unpowered eutectic SnPb solder joints 431–2
thick-film UBM 383–5
thin-film UBM 382–3
three-dimensional integrated circuits (3DIC) 376
through-Si-via (TSV) technology 376, 395, 402
time to delamination 187–8
tin alloys
  material design 4
  mechanical integrity 6
  polymorphism of tin 8
  whisker growth 7
tin–antimony alloys 26, 32, 54–5
tin–antimony/silver couples 13, 26, 29–32, 36–8
tin–bismuth alloys
  electromechanical coupling 252
  electromigration 342, 404–7
  nanocomposite solder 166, 169, 171, 173, 175
  phase diagrams 25, 34–6, 66–7
  whisker growth 332–3
tin–bismuth/iron couples 13, 34–6
tin–bismuth–zinc alloys 27
tin–cobalt alloys
  electromigration 409–10
  phase diagrams 32–3

tin–cobalt/nickel couples 32–3
tin–copper alloys
  diffusion couples 360–61
  electromigration 343–5, 351–65, 367–8, 375, 381–5, 389, 393–4, 411–13
  material design 4
  microstructure 237–8, 240, 245–9
  miniaturization 461–6
  minor alloying additions 122, 132–4, 137–43, 147–50
  phase diagrams 25, 46, 58–9
  temperature-dependent deformation 273–4, 279–82, 286–7, 289–94
  thermomigration 435–6, 438
  whisker growth 7, 304–7, 309–10, 313–15, 317–18, 325–6, 332
tin–copper–indium alloys 27
tin–copper/nickel couples 38–40
tin–gold alloys 24
tin hillocks *see* hillock growth
tin–indium alloys
  electromigration 407
  miniaturization 468
  phase diagrams 26
tin–lead alloys
  electromechanical coupling 252–3
  electromigration 342–3, 348, 352, 355, 389, 407
  microstructure 234–7, 240–1, 244–9
  miniaturization 446, 448, 474
  phase diagrams 19–21, 28, 57, 60–6
  thermomigration 348, 427–32
  whisker growth 307–8
tin–lead/iron couples 34–6
tin–nickel alloys
  electromigration 346–7, 351–5, 358–63, 367–8, 375, 381–5, 389, 393–4, 411–12
  miniaturization 461–3
  thermomigration 435
  whisker growth 332
tin–silver alloys
  Ag_3Sn plate formation 122, 125, 129–33
  electromigration 343–6, 355, 384–5, 408–9
  interfacial reactions 137
  microstructure 197–231, 237–8, 240, 247–9
  miniaturization 448–9, 464, 477
  minor alloying additions 122, 125, 129–34, 137, 147–50
  phase diagrams 24, 28, 32–3, 66–7
  temperature-dependent deformation 273–95
  thermomigration 433–4, 439
  undercooling 132–4
  whisker growth 332–3
tin–silver–bismuth alloys
  interfacial reactions 137
  minor alloying additions 122, 137
tin–silver–copper (SAC) alloys
  Ag_3Sn plate formation 122, 125, 129–3
  chemical effects on reliability 182, 185
  electromechanical coupling 251–6, 268–70
  electromigration 343–5, 364–5, 392–4, 404, 409–10
  grain-boundary vacancy concentration 268–70
  interfacial reactions 137
  intermetallic compounds 140–1, 143–6
  material design 4
  mechanical properties 149–50
  microstructure 199, 204–13, 218–23, 227, 237–40, 245–6, 248–9
  microstructure modifications 145–9
  miniaturization 448–52, 454–61, 463, 466–75
  minor alloying additions 122, 125, 129–34, 137, 140–41, 143–50, 152–3
  nanocomposite solder 164, 166, 167, 169, 173, 175
  phase diagrams 32, 33–4, 40–1, 58–62
  surface morphology 255–6
  tensile strength 258–60, 268
  thermomechanical fatigue 6–7
  undercooling 132–4
tin whiskers *see* whisker growth
tin–zinc alloys
  electromigration 403–6
  miniaturization 463
  phase diagrams 27
tin–zinc/copper interconnects 252
titanium dioxide nanoparticles 167–8, 170
titanium doping 140, 150–1
TM *see* thermomigration
TMA *see* thermomechanical analyzers
TMC *see* thermomechanical cycling
TMF *see* thermomechanical fatigue
transmission electron microscopy (TEM) 142–3
triaxial tensile stress 458–9, 474
triple points 46–7
TSV *see* through-Si-via

UBM *see* under bump metallization
ultimate tensile strength (UTS) 448–9, 451–7, 461–3, 476

under bump metallization (UBM)
  electromigration 341, 342–50, 354, 358–9, 362–3, 367–8, 375, 377–8, 381–5, 388–9, 393–4, 412
  minor alloying additions 134–8, 149, 151–3
  phase diagrams 14, 32
  thermomigration 431, 433, 435, 438
undercooling
  miniaturization 468
  minor alloying additions 122, 129–30, 132–6, 146
  phase diagrams 32–3
underlayers 317–18, 328, 332
unexpected compound formation 33–4
unexpected growth rates 34–6
unexpected melting of solder 36–8
unified creep model 197–8, 209–19, 227
unpowered composite SnPb solder joints 427–29
unpowered eutectic SnPb solder joints 431–2
uphill diffusion 38–40
UTS *see* ultimate tensile strength

vacancy concentration at grain boundary 264–5, 266–70
vapor arcs 301
vapor–liquid–solid (VLS) mechanism 324–5
vehicles 182
viscosity 167
VLS *see* vapor–liquid–solid
void propagation
  chemical effects on reliability 182–3
  electromigration 342–7, 351, 382–3, 386–91, 404–5
  miniaturization 454, 466–7, 474–5, 478, 480–1
von Mises plasticity 451–4, 457–9

wafer bumping processes 132, 134–5
wafer-level chip-scale package (WL/CSP) joints 469
Waste in Electrical and Electronic Equipment (WEEE) 233
wavelength-dispersive spectroscopy (WDS) 144
WEEE *see* Waste in Electrical and Electronic Equipment
wettability 168
Wheatstone bridges 386
whisker growth 7, 299–21, 323–35
  chemical effects on reliability 184–5
  compressive stress 303–4, 306–16, 325–7, 329, 332
  conformal coatings 316–17
  context 299–302
  electromechanical coupling 265–6
  electromigration whiskers 331–2
  features and causes 303–8
  finite element analysis 310–14
  grain-boundary diffusion 305–6, 310–12, 314–15
  heat treatment 318
  intermetallic compounds 304–15, 317–18, 325–6, 330–2
  kinking 302
  low melting point metals 323–5
  mechanical-compression whiskers 330–1, 333
  mechanisms 308–16, 324–5
  microstructure 312–13, 317, 324, 333
  mitigation strategies 316–18, 332–3
  nonuniformities 316
  nucleation and growth 303–4, 311–12, 314–16
  oxidation/corrosion whiskers 329–30
  plastic deformation 310–12, 314, 316
  room-temperature whiskers 325–6, 332–3
  self-diffusion coefficients 323–4
  short circuits 300–301
  surface treatments 317, 333
  thermal cycling whiskers 326–28
  underlayers 317–18, 328, 332
WL/CSP *see* wafer-level chip-scale package

X-ray diffraction (XRD) 73–4, 76–82, 88, 91–2

Young's modulus
  microstructure 221
  nanocomposite solder 169
yttrium doping 148

Z axis CTE 187
zinc doping
  electromigration 364–5, 368
  minor alloying additions 123–4, 126–8, 135–6, 140–3, 148, 152–4
  see also tin–zinc alloys